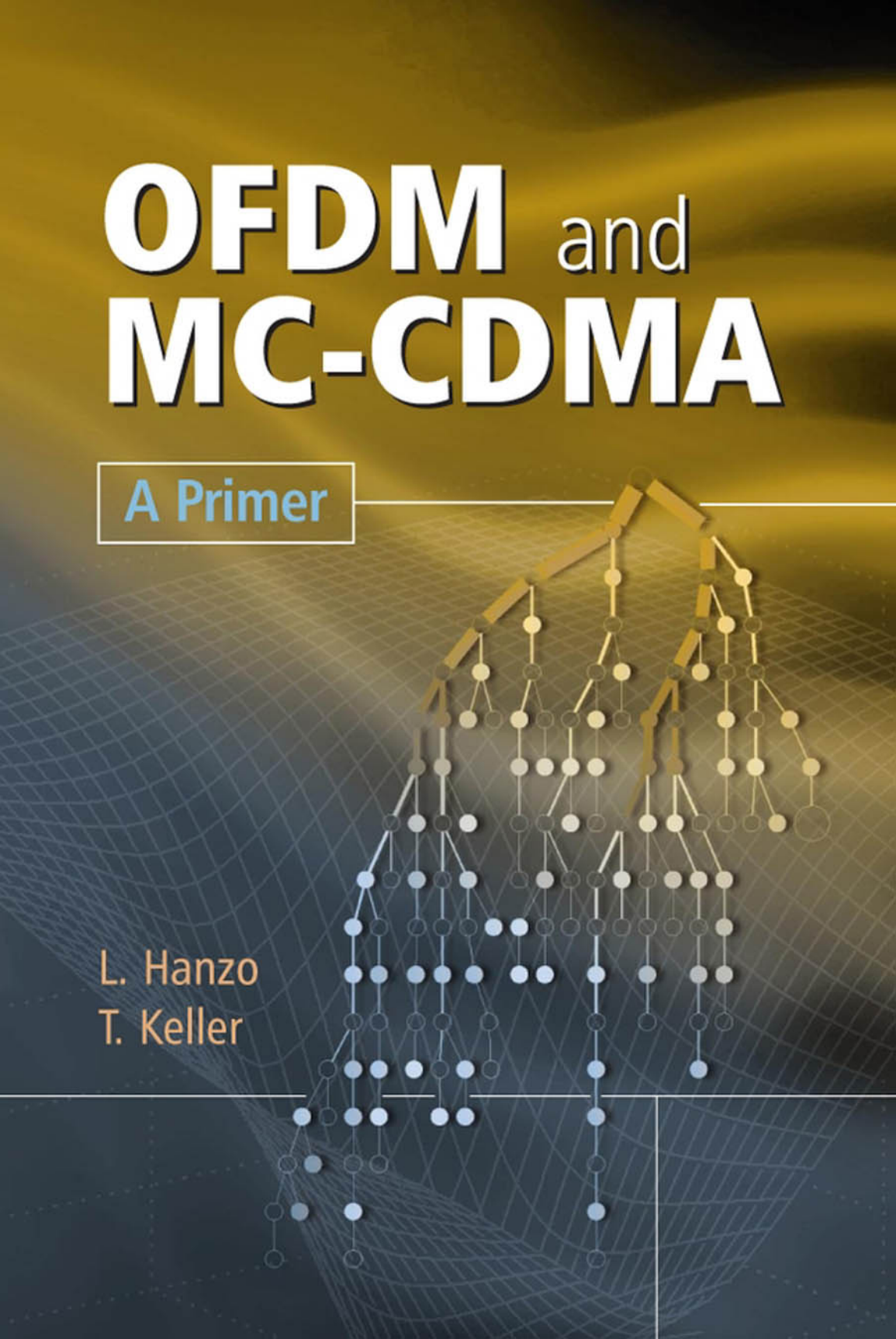
OFDM and MC-CDMA

A Primer



L. Hanzo
T. Keller

OFDM and MC-CDMA
A Primer

L. Hanzo
University of Southampton, UK

T. Keller
Analog Devices Ltd., Cambridge, UK



IEEE PRESS
IEEE Communications Society, Sponsor



John Wiley & Sons, Ltd

OFDM and MC-CDMA

OFDM and MC-CDMA
A Primer

L. Hanzo
University of Southampton, UK

T. Keller
Analog Devices Ltd., Cambridge, UK



IEEE PRESS
IEEE Communications Society, Sponsor



John Wiley & Sons, Ltd

Copyright © 2006 John Wiley & Sons Ltd, The Atrium, Southern Gate, Chichester,
West Sussex PO19 8SQ, England

Telephone (+44) 1243 779777

Email (for orders and customer service enquiries): cs-books@wiley.co.uk
Visit our Home Page on www.wiley.com

All Rights Reserved. No part of this publication may be reproduced, stored in a retrieval system or transmitted in any form or by any means, electronic, mechanical, photocopying, recording, scanning or otherwise, except under the terms of the Copyright, Designs and Patents Act 1988 or under the terms of a licence issued by the Copyright Licensing Agency Ltd, 90 Tottenham Court Road, London W1T 4LP, UK, without the permission in writing of the Publisher. Requests to the Publisher should be addressed to the Permissions Department, John Wiley & Sons Ltd, The Atrium, Southern Gate, Chichester, West Sussex PO19 8SQ, England, or emailed to permreq@wiley.co.uk, or faxed to (+44) 1243 770620.

Designations used by companies to distinguish their products are often claimed as trademarks. All brand names and product names used in this book are trade names, service marks, trademarks or registered trademarks of their respective owners. The Publisher is not associated with any product or vendor mentioned in this book. All trademarks referred to in the text of this publication are the property of their respective owners.

This publication is designed to provide accurate and authoritative information in regard to the subject matter covered. It is sold on the understanding that the Publisher is not engaged in rendering professional services. If professional advice or other expert assistance is required, the services of a competent professional should be sought.

Other Wiley Editorial Offices

John Wiley & Sons Inc., 111 River Street, Hoboken, NJ 07030, USA

Jossey-Bass, 989 Market Street, San Francisco, CA 94103-1741, USA

Wiley-VCH Verlag GmbH, Boschstr. 12, D-69469 Weinheim, Germany

John Wiley & Sons Australia Ltd, 42 McDougall Street, Milton, Queensland 4064, Australia

John Wiley & Sons (Asia) Pte Ltd, 2 Clementi Loop #02-01, Jin Xing Distripark, Singapore 129809

John Wiley & Sons Canada Ltd, 22 Worcester Road, Etobicoke, Ontario, Canada M9W 1L1

Wiley also publishes its books in a variety of electronic formats. Some content that appears in print may not be available in electronic books.

IEEE Communications Society, Sponsor
COMMS-S Liaison to IEEE Press, Mostafa Hashem Sherif

British Library Cataloguing in Publication Data

A catalogue record for this book is available from the British Library

ISBN-13 978-0-470-03007-3 (HB)
ISBN-10 0-470-03007-0 (HB)

Typeset by the authors using LaTeXsoftware.
Printed and bound in Great Britain by Antony Rowe Ltd, Chippenham, England.
This book is printed on acid-free paper responsibly manufactured from sustainable forestry in which at least two trees are planted for each one used for paper production.

We dedicate this monograph to the numerous contributors of this field, many of whom are listed in the Author Index

Contents

About the Authors **xv**

Other Wiley and IEEE Press Books on Related Topics **xvi**

Acknowledgements **xix**

1 Introduction **1**
1.1 Motivation of the Book 1
1.2 Orthogonal Frequency Division Multiplexing History 5
1.2.1 Early Classic Contributions and OFDM Standards 5
1.2.2 Peak-to-Mean Power Ratio 6
1.2.3 Synchronisation 8
1.2.4 OFDM/CDMA 8
1.2.5 Decision-Directed Channel Estimation 8
1.2.6 Uplink Detection Techniques for Multi-User SDMA-OFDM 13
1.2.7 OFDM Applications 16
1.3 Outline of the Book 16
1.4 Chapter Summary and Conclusion 18

I OFDM System Design **19**

2 Introduction to Orthogonal Frequency Division Multiplexing **21**
2.1 Introduction 21
2.2 Principles of QAM-OFDM 23
2.3 Modulation by DFT 25
2.4 Transmission via Bandlimited Channels 29
2.5 Basic OFDM Modem Implementations 32
2.6 Cyclic OFDM Symbol Extension 35
2.7 Decision-Directed Adaptive Channel Equalisation 36
2.8 OFDM Bandwidth Efficiency 38
2.9 Chapter Summary and Conclusion 39

3 OFDM Transmission over Gaussian Channels 41
3.1 Orthogonal Frequency Division Multiplexing 42
3.2 Choice of the OFDM Modulation 42
3.3 OFDM System Performance over AWGN Channels 42
3.4 Clipping Amplification 43
3.4.1 OFDM Signal Amplitude Statistics 43
3.4.2 Clipping Amplifier Simulations 44
3.4.2.1 Introduction to Peak-Power Reduction Techniques 45
3.4.2.2 BER Performance Using Clipping Amplifiers 46
3.4.2.3 Signal Spectrum with Clipping Amplifier 47
3.4.3 Clipping Amplification – Summary 50
3.5 Analogue-to-Digital Conversion 50
3.6 Phase Noise 53
3.6.1 Effects of Phase Noise 53
3.6.2 Phase Noise Simulations 54
3.6.2.1 White Phase Noise Model 54
3.6.2.1.1 Serial Modem 55
3.6.2.1.2 OFDM Modem 55
3.6.2.2 Coloured Phase Noise Model 57
3.6.3 Phase Noise – Summary 60
3.7 Chapter Summary and Conclusion 60

4 OFDM Transmission over Wideband Channels 61
4.1 The Channel Model 61
4.1.1 The Wireless Asynchronous Transfer Mode System 62
4.1.1.1 The WATM Channel 62
4.1.1.2 The Shortened WATM Channel 64
4.1.2 The Wireless Local Area Network 64
4.1.2.1 The WLAN Channel 65
4.1.3 UMTS System 65
4.1.3.1 The UMTS Type Channel 65
4.2 Effects of Time-Dispersive Channels on OFDM 66
4.2.1 Effects of the Stationary Time-Dispersive Channel 67
4.2.2 Non-Stationary Channel 68
4.2.2.1 Summary of Time-Variant Channels 70
4.2.3 Signalling over Time-Dispersive OFDM Channels 70
4.3 Channel Transfer Function Estimation 70
4.3.1 Frequency Domain Channel Transfer Function Estimation 70
4.3.1.1 Pilot Symbol-Assisted Schemes 71
4.3.1.1.1 Linear Interpolation for PSAM 71
4.3.1.1.2 Ideal Lowpass Interpolation for PSAM 73
4.3.1.1.3 Summary 75
4.3.2 Time Domain Channel Estimation 78
4.4 System Performance 78
4.4.1 Static Time-Dispersive Channel 78
4.4.1.1 Perfect Channel Estimation 78

4.4.1.2 Differentially Coded Modulation 81
4.4.1.3 PSAM Aided Channel Transfer Function Estimation 83
4.4.2 Slowly Varying Time-Dispersive Channel 88
4.4.2.1 Perfect Channel Estimation 89
4.4.2.2 Pilot Symbol-Assisted Modulation Summary 90
4.5 Intersubcarrier Interference Cancellation 90
4.5.1 Motivation 90
4.5.2 The Signal Model 94
4.5.3 Channel Estimation 96
4.5.4 Cancellation Schemes 97
4.5.5 ICI Cancellation Performance 99
4.5.6 Conclusions on ICI Cancellation 100
4.6 Chapter Summary and Conclusion 101

5 OFDM Time and Frequency Domain Synchronisation 103
5.1 System Performance with Frequency and Timing Errors 103
5.1.1 Frequency Shift 103
5.1.1.1 The Spectrum of the OFDM Signal 104
5.1.1.2 Effects of Frequency Mismatch on Different Modulation Schemes 108
5.1.1.2.1 Coherent Modulation 108
5.1.1.2.2 Pilot Symbol Assisted Modulation 108
5.1.1.2.3 Differential Modulation 109
5.1.1.2.4 Frequency Error - Summary 109
5.1.2 Time Domain Synchronisation Errors 110
5.1.2.1 Coherent Demodulation 110
5.1.2.2 Pilot Symbol-Assisted Modulation 111
5.1.2.3 Differential Modulation 112
5.1.2.3.1 Time Domain Synchronisation Errors - Summary 114
5.2 Synchronisation Algorithms 114
5.2.1 Coarse Frame and OFDM Symbol Synchronisation Review 115
5.2.2 Fine Symbol Tracking Review 116
5.2.3 Frequency Acquisition Review 116
5.2.4 Frequency Tracking Review 116
5.2.5 Synchronisation based on Auto-Correlation 117
5.2.6 Multiple Access Frame Structure 117
5.2.6.1 The Reference Symbol 117
5.2.6.2 The Correlation Functions 119
5.2.7 Frequency Tracking and OFDM Symbol Synchronisation 120
5.2.7.1 OFDM Symbol Synchronisation 120
5.2.7.2 Frequency Tracking Studies 120
5.2.8 Frequency Acquisition and Frame Synchronisation Studies 122
5.2.8.1 Frame Synchronisation Studies 122
5.2.8.2 Frequency Acquisition Studies 122
5.2.8.3 Block Diagram of the Synchronisation Algorithms 122
5.2.9 Frequency Acquisition Using Pilots 123

5.2.9.1 The Reference Symbol . . . 124
5.2.9.2 Frequency Acquisition . . . 124
5.2.9.3 Performance of the Pilot-Based Frequency Acquisition in AWGN Channels . . . 126
5.2.9.4 Alternative Frequency Error Estimation for Frequency Domain Pilot Tones . . . 131
5.3 Comparison of the Frequency Acquisition Algorithms . . . 133
5.4 BER Performance with Frequency Synchronisation . . . 137
5.5 Chapter Summary and Conclusion . . . 138
5.6 Appendix: OFDM Synchronisation Performance . . . 139
5.6.1 Frequency Synchronisation in an AWGN Channel . . . 139
5.6.1.1 One Phasor in AWGN Environment . . . 139
5.6.1.1.1 Cartesian Coordinates . . . 139
5.6.1.1.2 Polar Coordinates . . . 139
5.6.1.2 Product of Two Noisy Phasors . . . 140
5.6.1.2.1 Joint Probability Density . . . 140
5.6.1.2.2 Phase Distribution . . . 141
5.6.1.2.3 Numerical Integration . . . 141

6 Adaptive Single- and Multi-user OFDM Techniques 145
6.1 Introduction . . . 145
6.1.1 Motivation . . . 145
6.1.2 Adaptive Techniques . . . 146
6.1.2.1 Channel Quality Estimation . . . 147
6.1.2.2 Parameter Adaptation . . . 148
6.1.2.3 Signalling the AOFDM Parameters . . . 148
6.1.3 System Aspects . . . 150
6.2 Adaptive Modulation for OFDM . . . 150
6.2.1 System Model . . . 150
6.2.2 Channel Model . . . 151
6.2.3 Channel Transfer Function Variations . . . 151
6.2.4 Choice of the Modulation Modes . . . 152
6.2.4.1 Fixed Threshold Adaptation Algorithm . . . 152
6.2.4.2 Sub-Band BER Estimator Adaptation Algorithm . . . 155
6.2.5 Constant Throughput Adaptive OFDM . . . 156
6.2.6 AOFDM Mode Signalling and Blind Detection . . . 158
6.2.6.1 Signalling . . . 158
6.2.6.2 Blind Detection by SNR Estimation . . . 159
6.2.6.3 Blind Detection by Multi-Mode Trellis Decoder . . . 161
6.2.7 Sub-Band Adaptive OFDM and Turbo Channel Coding . . . 164
6.2.8 Effects of the Doppler Frequency . . . 164
6.2.9 Channel Transfer Function Estimation . . . 167
6.3 Adaptive OFDM Speech System . . . 168
6.3.1 Introduction . . . 168
6.3.2 System Overview . . . 169
6.3.2.1 System Parameters . . . 169

6.3.3 Constant Throughput Adaptive Modulation . . . 170
6.3.3.1 Constant-Rate BER Performance . . . 171
6.3.4 Multimode Adaptation . . . 173
6.3.4.1 Mode Switching . . . 173
6.3.5 Simulation Results . . . 174
6.3.5.1 Frame Error Results . . . 174
6.3.5.2 Audio Segmental SNR . . . 176
6.4 Pre-equalisation . . . 176
6.4.1 Motivation . . . 176
6.4.2 Pre-equalisation with Sub-Band Blocking . . . 179
6.4.3 Adaptive Modulation with Spectral Predistortion . . . 181
6.5 Comparison of the Adaptive Techniques . . . 184
6.6 Near-Optimum Power- and Bit Allocation in OFDM . . . 186
6.6.1 State of the Art . . . 186
6.6.2 Problem Description . . . 186
6.6.3 Power and Bit Allocation Algorithm . . . 187
6.7 Multi-User AOFDM . . . 191
6.7.1 Introduction . . . 191
6.7.2 Adaptive Transceiver Architecture . . . 192
6.7.2.1 An Overview . . . 192
6.7.2.2 The Signal Model . . . 193
6.7.2.3 The SMI Algorithm . . . 193
6.7.2.4 The Adaptive Bit-Assignment Algorithm . . . 194
6.7.2.5 The Channel Models . . . 194
6.7.3 Simulation Results - Perfect Channel Knowledge . . . 195
6.7.3.1 General Remarks . . . 195
6.7.3.2 Two-Branch Maximum-Ratio Combining . . . 195
6.7.3.3 SMI Co-Channel Interference Suppression . . . 195
6.7.4 Pilot-Based Channel Parameter Estimation . . . 198
6.7.4.1 System Description . . . 198
6.7.4.2 Simulation Results . . . 200
6.8 Chapter Summary and Conclusion . . . 201

II OFDM versus MC-CDMA Systems 203

7 OFDM versus MC-CDMA 205
7.1 Amalgamating DS-CDMA and OFDM . . . 205
7.1.1 The DS-CDMA Component . . . 205
7.1.2 The OFDM Component . . . 208
7.2 Multi-Carrier CDMA . . . 211
7.2.1 MC-CDMA . . . 211
7.2.2 MC-DS-CDMA . . . 214
7.2.3 MT-CDMA . . . 215
7.3 Further Research Topics in MC-CDMA . . . 216
7.4 Chapter Summary and Conclusion . . . 217

8 Basic Spreading Sequences 219
8.1 PN Sequences . . . 219
8.1.1 Maximal Length Sequences . . . 219
8.1.2 Gold Codes . . . 221
8.1.3 Kasami Sequences . . . 222
8.2 Orthogonal Codes . . . 223
8.2.1 Walsh Codes . . . 223
8.2.2 Orthogonal Gold Codes . . . 224
8.2.3 Multi-Rate Orthogonal Gold Codes . . . 226
8.3 Chapter Summary and Conclusion . . . 228

9 MC-CDMA Performance in Synchronous Environments 231
9.1 The Frequency Selective Channel Model . . . 232
9.2 The System Model . . . 233
9.3 Single User Detection . . . 235
9.3.1 Maximal Ratio Combining . . . 236
9.3.2 Equal Gain Combining . . . 239
9.3.3 Orthogonality Restoring Combining . . . 241
9.4 Multi-User Detection . . . 242
9.4.1 Background . . . 242
9.4.2 Maximum Likelihood Detection . . . 243
9.4.3 Concatenated Space-Time Block Coded and Turbo Coded Symbol-by-Symbol Adaptive OFDM and Multi-Carrier CDMA . . . 244
9.5 Chapter Summary and Conclusion . . . 250

III Advanced Topics: Multi-User OFDM Systems 251

10 Maximum-Likelihood Enhanced Sphere Decoding of MIMO-OFDM 253
10.1 Classification of Smart Antennas . . . 253
10.2 Introduction to Space-Time Processing . . . 255
10.3 SDM-OFDM System Model . . . 259
10.3.1 MIMO Channel Model . . . 259
10.3.2 SDM-OFDM Transceiver Structure . . . 260
10.4 Optimised Hierarchy Reduced Search Algorithm-Aided SDM Detection . . . 262
10.4.1 OHRSA-Aided ML SDM Detection . . . 263
10.4.2 Search Strategy . . . 267
10.4.2.1 Generalisation of the OHRSA-ML SDM Detector . . . 269
10.4.3 Bitwise OHRSA ML SDM Detection . . . 272
10.4.3.1 Generalisation of the BW-OHRSA-ML SDM Detector . . . 277
10.4.4 OHRSA-Aided Log-MAP SDM Detection . . . 279
10.4.5 Soft-Output OHRSA-Aided Approximate Log-MAP Detection . . . 290
10.4.5.1 Complexity Analysis. . . . 293
10.4.5.2 Performance Analysis . . . 297
10.5 Chapter Summary and Conclusion . . . 300

11 Genetic Algorithm Aided Joint Channel Estimation and MUD for SDMA OFDM 303
11.1 Introduction . . . 303
11.2 SDMA MIMO Channel Model . . . 305
11.3 System Overview . . . 306
11.4 GA-Aided Iterative Joint Channel Estimation and Multi-User Detection . . . 306
11.4.1 Pilot-Aided Initial Channel Estimation . . . 309
11.4.2 Generating Initial Symbol Estimates . . . 311
11.4.3 GA-Aided Joint FD-CHTF and Data Optimisation Providing Soft Outputs . . . 313
11.4.3.1 Extended GA Individual Structure for MIMO Systems . . . 313
11.4.3.2 Initialisation . . . 314
11.4.3.3 Joint Genetic Optimisation . . . 315
11.4.3.3.1 Cross-Over Operator . . . 315
11.4.3.3.2 Mutation Operator . . . 316
11.4.3.3.3 Comments on the Joint Optimisation Process . . . 317
11.4.3.4 Generating the GA's Soft Outputs . . . 317
11.5 Simulation Results . . . 319
11.5.1 Effects of the Maximum Mutation Step Size . . . 320
11.5.2 Effects of the Doppler Frequency . . . 323
11.5.3 Effects of the Number of GA-JCEMUD Iterations . . . 324
11.5.4 Effects of the Pilot Overhead . . . 325
11.5.5 Joint Optimisation versus Separate Optimisation . . . 325
11.5.6 Comparison of GA-JCEMUDs Having Soft and Hard Outputs . . . 327
11.5.7 MIMO Robustness . . . 327
11.6 Chapter Summary and Conclusion . . . 329

12 Multi-User OFDM Employing Genetic Algorithm Aided Minimum Bit Error Rate Multi-User Detection 331
12.1 Introduction . . . 331
12.1.1 Minimum Bit Error Ratio Detection of OFDM . . . 332
12.2 System Model . . . 332
12.2.1 Space Division Multiple Access . . . 332
12.2.2 Error Probability of a BPSK System . . . 335
12.2.3 Exact MBER Multi-User Detection . . . 336
12.3 Genetic Algorithm . . . 338
12.3.1 Overview of GAs . . . 339
12.3.2 Employing GAs in the MBER MUD Aided SDMA OFDM System . 341
12.4 Simulation Results . . . 342
12.4.1 Performance of a Four-User and Four-Receiver Antenna Scenario . . 342
12.4.2 Performance of the Four-Antenna Scenario versus the Number of Users . . . 343
12.5 Complexity Comparison . . . 346
12.6 Chapter Summary and Conclusion . . . 346

13 Conclusion and Further Research Problems **351**
13.1 Summary and Conclusions of Part I 351
13.1.1 Summary of Part I 351
13.1.2 Conclusions of Part I 352
13.2 Summary and Conclusions of Part II 353
13.2.1 Summary of Part II 353
13.2.2 Conclusions of Part II 353
13.3 Summary and Conclusions of Part III 354
13.3.1 Near-ML Enhanced Sphere Detection of MIMO-OFDM 354
13.3.2 GA-Aided Joint MUD and Channel Estimation 355
13.3.3 GA-Aided MBER MUD 355
13.4 Closing Remarks 356

Glossary **359**

Bibliography **363**

Subject Index **395**

Author Index **401**

About the Authors



Lajos Hanzo, Fellow of the Royal Academy of Engineering, received his first-class degree in electronics in 1976 and his doctorate in 1983. In 2004 he was awarded the Doctor of Sciences (DSc) degree by the University of Southampton, UK. During his career in telecommunications he has held various research and academic posts in Hungary, Germany and the UK. Since 1986 he has been with the Department of Electronics and Computer Science, University of Southampton, UK, where he holds the chair in telecommunications. He has co-authored 12 books, totalling 9000 pages on mobile radio communications, published in excess of 600 research papers, has acted as TPC Chair of numerous major IEE and IEEE conferences, presented various keynote lectures and has been awarded a number of distinctions. Currently he heads an academic research team, working on a range of research projects in the field of wireless multimedia communications sponsored by industry, the Engineering and Physical Sciences Research Council (EPSRC) UK, the European IST Programme and the Mobile Virtual Centre of Excellence (VCE), UK. He is an enthusiastic supporter of industrial and academic liaison and he offers a range of industrial courses. Lajos is also an IEEE Distinguished Lecturer of both the Communications as well as the Vehicular Technology Society, a Fellow of both the IEEE and the IEE. He is an editorial board member of the Proceedings of the IEEE and a Governor of the IEEE VT Society. For further information on research in progress and associated publications, please refer to http://www-mobile.ecs.soton.ac.uk



Thomas Keller studied Electrical Engineering at the University of Karlsruhe, Ecole Superieure d'Ingenieurs en Electronique et Electrotechnique, Paris, and the University of Southampton. He graduated with a Dipl.-Ing. degree in 1995. Between 1995 and 1999 he was with the Wireless Multimedia Communications Group at the University of Southampton, where he completed his PhD in mobile communications. His areas of interest include adaptive OFDM transmission, wideband channel estimation, CDMA and error correction coding. Following the completion of his PhD he joined Ubinetics, Cambridge, UK, where he was involved in the research and development of third-generation wireless systems. Following a reorganization, he was part of a team that was transferred to Analog Devices, Cambridge, UK. Dr. Keller has co-authored three monographs and about 30 various research papers.

Other Wiley and IEEE Press Books on Related Topics[1]

- R. Steele, L. Hanzo (Ed): *Mobile Radio Communications: Second and Third Generation Cellular and WATM Systems*, John Wiley and IEEE Press, 2nd edition, 1999, ISBN 07 273-1406-8, 1064 pages
- L. Hanzo, F.C.A. Somerville, J.P. Woodard: *Voice Compression and Communications: Principles and Applications for Fixed and Wireless Channels*; IEEE Press and John Wiley, 2001, 642 pages
- L. Hanzo, P. Cherriman, J. Streit: *Wireless Video Communications: Second to Third Generation and Beyond*, IEEE Press and John Wiley, 2001, 1093 pages
- L. Hanzo, T.H. Liew, B.L. Yeap: *Turbo Coding, Turbo Equalisation and Space-Time Coding*, John Wiley and IEEE Press, 2002, 751 pages
- J.S. Blogh, L. Hanzo: *Third-Generation Systems and Intelligent Wireless Networking: Smart Antennas and Adaptive Modulation*, John Wiley and IEEE Press, 2002, 408 pages
- L. Hanzo, C.H. Wong, M.S. Yee: *Adaptive Wireless Transceivers: Turbo-Coded, Turbo-Equalised and Space-Time Coded TDMA, CDMA and OFDM Systems*, John Wiley and IEEE Press, 2002, 737 pages
- L. Hanzo, L-L. Yang, E-L. Kuan, K. Yen: *Single- and Multi-Carrier CDMA: Multi-User Detection, Space-Time Spreading, Synchronisation, Networking and Standards*, John Wiley and IEEE Press, June 2003, 1060 pages
- L. Hanzo, M. Münster, T. Keller, B-J. Choi, *OFDM and MC-CDMA for Broadband Multi-User Communications, WLANs and Broadcasting*, John Wiley and IEEE Press, 2003, 978 pages
- L. Hanzo, S-X. Ng, T. Keller and W.T. Webb, *Quadrature Amplitude Modulation: From Basics to Adaptive Trellis-Coded, Turbo-Equalised and Space-Time Coded OFDM, CDMA and MC-CDMA Systems*, John Wiley and IEEE Press, 2004, 1105 pages

[1] For detailed contents and sample chapters please refer to http://www-mobile.ecs.soton.ac.uk

Acknowledgements

We are indebted to our many colleagues who have enhanced our understanding of the subject, in particular to Prof. Emeritus Raymond Steele. These colleagues and valued friends, too numerous to be mentioned, have influenced our views concerning various aspects of wireless multimedia communications. We thank them for the enlightenment gained from our collaborations on various projects, papers and books. We are grateful to Steve Braithwaite, Jan Brecht, Jon Blogh, Marco Breiling, Marco del Buono, Sheng Chen, Peter Cherriman, Stanley Chia, Joseph Cheung, Sheyam Lal Dhomeja, Dirk Didascalou, Lim Dongmin, Stephan Ernst, Peter Fortune, Eddie Green, David Greenwood, Hee Thong How, Ee Lin Kuan, W. H. Lam, C. C. Lee, Xiao Lin, Chee Siong Lee, Tong-Hooi Liew, Vincent Roger-Marchart, Jason Ng, Michael Ng, M. A. Nofal, Jeff Reeve, Redwan Salami, Clare Somerville, Rob Stedman, David Stewart, Jürgen Streit, Jeff Torrance, Spyros Vlahoyiannatos, William Webb, Stephan Weiss, John Williams, Jason Woodard, Choong Hin Wong, Henry Wong, James Wong, Lie-Liang Yang, Bee-Leong Yeap, Mong-Suan Yee, Kai Yen, Andy Yuen, and many others with whom we enjoyed an association.

We also acknowledge our valuable associations with the Virtual Centre of Excellence (VCE) in Mobile Communications, in particular with its chief executive, Dr Walter Tuttlebee, and other leading members of the VCE, namely Dr Keith Baughan, Prof. Hamid Aghvami, Prof. Ed Candy, Prof. John Dunlop, Prof. Barry Evans, Prof. Peter Grant, Prof. Mike Walker, Prof. Joseph McGeehan, Prof. Steve McLaughlin and many other valued colleagues. Our sincere thanks are also due to the EPSRC, UK for supporting our research. We would also like to thank Dr Joao Da Silva, Dr Jorge Pereira, Dr Bartholome Arroyo, Dr Bernard Barani, Dr Demosthenes Ikonomou, Dr Fabrizio Sestini and other valued colleagues from the Commission of the European Communities, Brussels, Belgium.

Without the kind support of Mark Hammond, Sarah Hinton, Jennifer Beal and their colleagues at the Wiley office in Chichester, UK this monograph would never have reached the readers. *Finally, our sincere gratitude is due to the numerous authors listed in the Author Index — as well as to those whose work was not cited owing to space limitations — for their contributions to the state of the art, without whom this book would not have materialised.*

Lajos Hanzo and Thomas Keller
School of Electronics and Computer Science
University of Southampton, UK

Chapter 1

Introduction

1.1 Motivation of the Book

Whilst the concept of Orthogonal Frequency Division Multiplexing (OFDM) has been known since 1966 [1], it only reached sufficient maturity for employment in standard systems during the 1990s. OFDM exhibits numerous advantages over the family of more conventional serial modem schemes [2], although it is only natural that it also imposes a number of disadvantages. The discussion of the associated design tradeoffs of OFDM and Multi-Carrier Code Division Multiple Access (MC-CDMA) systems constitutes the topic of this monograph and in this context our discussions include the following fundamental issues:

1) A particularly attractive feature of OFDM systems is that they are capable of operating without a classic channel equaliser, when communicating over dispersive transmission media, such as wireless channels, while conveniently accommodating the time- and frequency-domain channel quality fluctuations of the wireless channel.

   Explicitly, the channel SNR variation versus both time and frequency of an indoor wireless channel is shown in a three-dimensional form in Figure 1.1 versus both time and frequency, which suggests that OFDM constitutes a convenient framework for accommodating the channel quality fluctuations of the wireless channel, as will be briefly augmented below. This channel transfer function was recorded for the channel impulse response of Figure 1.2, by simply transforming the impulse response to the frequency domain at regular time intervals, while its taps fluctuated according to the Rayleigh distribution.

   These channel quality fluctuations may be readily accommodated with the aid of subband-adaptive modulation as follows. Such an adaptive OFDM (AOFDM) modem is characterised by Figure 1.3, portraying at the top a contour plot of the above-mentioned wireless channel's signal-to-noise ratio (SNR) fluctuation versus both time and frequency for each OFDM subcarrier. We note at this early stage that these channel quality fluctuations may be mitigated with the aid of frequency-domain channel equalisation,

OFDM and MC-CDMA: A Primer L. Hanzo and T. Keller
© 2006 John Wiley & Sons, Ltd

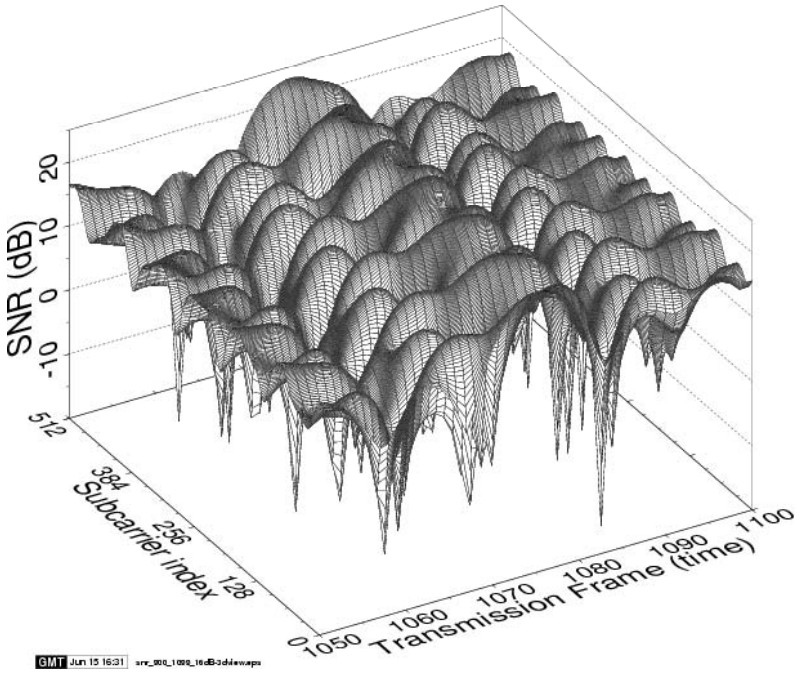


Figure 1.1: Instantaneous channel SNR for all 512 subcarriers versus time, for an average channel SNR of 16 dB over the channel characterised by the channel impulse response (CIR) of Figure 1.2.

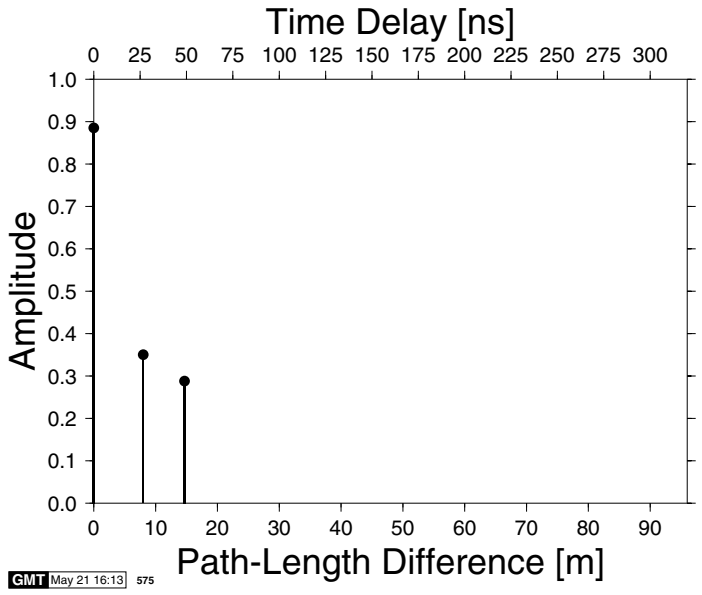


Figure 1.2: Indoor three-path WATM channel impulse response.

as will be detailed throughout the book, but nonetheless, they cannot be entirely eradicated.

More specifically, as can be seen in Figure 1.1, that when the channel is of high quality — as for example in the vicinity of the OFDM symbol index of 1080 — the sub-band-adaptive modem considered here for the sake of illustration has used the same modulation mode, as the identical-throughput conventional fixed-rate OFDM modem in all subcarriers, which was 1 bit per symbol (BPS) in this example, as in conventional Binary Phase Shift Keying (BPSK). By contrast, when the channel is hostile — for example, around frame 1060 — the sub-band-adaptive modem transmitted zero bits per symbol in some sub-bands, corresponding to disabling transmissions in the low-quality sub-bands. In order to compensate for the loss of throughput in this sub-band, a higher-order modulation mode was used in the higher quality sub-bands.

In the centre and bottom subfigures of Figure 1.3 the modulation mode chosen for each 32-subcarrier sub-band is shown versus time for two different high-speed wireless modems communicating at either 3.4 or 7.0 Mbps, respectively, again, corresponding to an average throughput of either 1 or 2 BPS.

However, these adaptive transceiver principles are not limited to OFDM transmissions. In recent years the concept of intelligent multi-mode, multimedia transceivers (IMMT) has emerged in the context of a variety of wireless systems [2–7]. The range of various existing solutions that have found favour in already operational standard systems has been summarised in the excellent overview by Nanda *et al.* [5]. *The aim of these adaptive transceivers is to provide mobile users with the best possible compromise amongst a number of contradicting design factors, such as the power consumption of the hand-held portable station (PS), robustness against transmission errors, spectral efficiency, teletraffic capacity, audio/video quality and so forth [4].*

2) Another design alternative applicable in the context of OFDM systems is that the channel quality fluctuations observed, for example, in Figure 1.1 are averaged out with the aid of frequency-domain spreading codes, which leads to the concept of Multi-Carrier Code Division Multiple Access (MC-CDMA). In this scenario typically only a few chips of the spreading code are obliterated by the frequency-selective fading and hence the chances are that the spreading code and its conveyed data may still be recoverable. The advantage of this approach is that in contrast to AOFDM-based communications, in MC-CDMA no channel quality estimation and signalling are required. Therefore OFDM and MC-CDMA will be comparatively studied in Part II of this monograph. Part III will also consider the employment of Walsh-Hadamard code-based spreading of each subcarrier's signal across the entire OFDM bandwidth, which was found to be an efficient frequency-domain fading counter-measure capable of operating without the employment of adaptive modulation.

3) A further technique capable of mitigating the channel quality fluctuations of wireless channels is constituted by space-time coding, which will also be considered as an attractive anti-fading design option capable of attaining a high diversity gain. Space-time coding employs several transmit and receive antennas for the sake of achieving diversity gain and hence an improved performance.

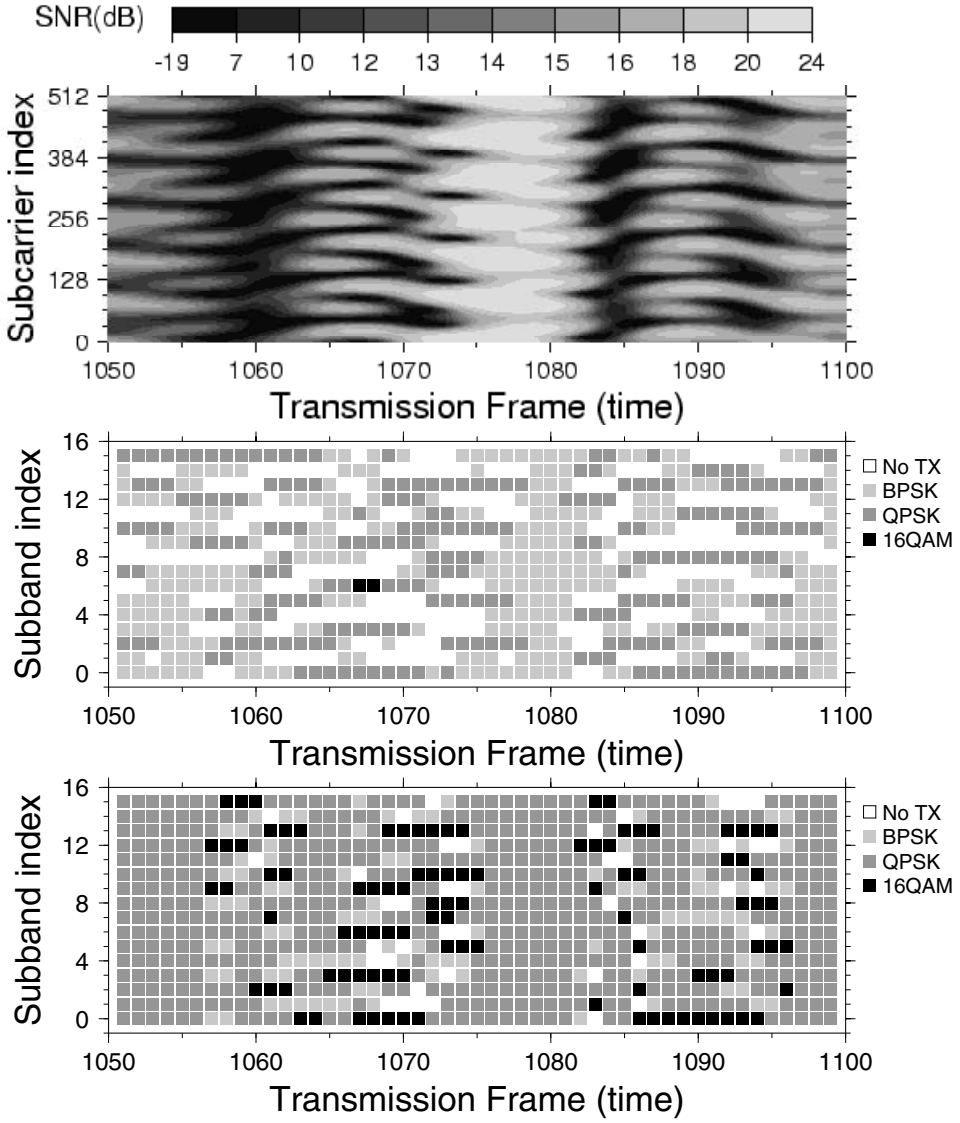


Figure 1.3: The micro-adaptive nature of the sub-band-adaptive OFDM modem. The top graph is a contour plot of the channel SNR for all 512 subcarriers versus time. The bottom two graphs show the modulation modes chosen for all 16 32-subcarrier sub-bands for the same period of time. The middle graph shows the performance of the 3.4 Mbps sub-band-adaptive modem, which operates at the same bit rate as a fixed BPSK modem. The bottom graph represents the 7.0 Mbps sub-band-adaptive modem, which operated at the same bit rate as a fixed QPSK modem. The average channel SNR was 16 dB.

4) By contrast, in Part III of the book we employ multiple antennas at the base-station for a different reason, namely for the sake of supporting multiple users, rather than to achieving transmit diversity gain. This is possible, since the users' channel impulse responses (CIR) or channel transfer functions are accurately estimated and hence these channel transfer functions may be viewed as unique user signature sequences, which allow us to recognise and demultiplex the transmissions of the individual users, in a similar fashion to the unique user-specific spreading codes employed in CDMA systems. We note, however, that this technique is only capable of reliably separating the users communicating within the same bandwidth, if their CIRs are sufficiently different. This assumption is typically valid for the uplink, although it may have a limited validity, when the base station receives from mobile stations in its immediate vicinity. By contrast, different techniques have to be invoked for downlink multi-user transmissions.

Our intention with the book is:

1) First, to pay tribute to all researchers, colleagues and valued friends, who contributed to the field. Hence this book is dedicated to them, since without their quest for better transmission solutions for wireless communications this monograph could not have been conceived. They are too numerous to name here, hence they appear in the author index of the book. Our hope is that the conception of this monograph on the topic will provide an adequate portrayal of the community's research and will further fuel this innovation process.

2) We expect to stimulate further research by exposing open research problems and by collating a range of practical problems and design issues for the practitioners. The coherent further efforts of the wireless research community is expected to lead to the solution of the range of outstanding problems, ultimately providing us with flexible wireless transceivers exhibiting a performance close to information theoretical limits.

1.2 Orthogonal Frequency Division Multiplexing History

1.2.1 Early Classic Contributions and OFDM Standards

The first OFDM scheme was proposed by Chang in 1966 [1] for dispersive fading channels. During the early years of the evolution of OFDM research the contributions due to the efforts of Weinstein, Peled, Ruiz, Hirosaki, Kolb, Cimini, Schüssler, Preuss, Rückriem, Kalet *et al.* [1, 8–20] have to be mentioned. As unquestionable proof of its maturity, OFDM was standardised as the European digital audio broadcast (DAB) as well as digital video broadcast (DVB) scheme. It constituted also a credible proposal for the recent third-generation mobile radio standard competition in Europe. Finally, OFDM was recently selected as the high performance local area network's (HIPERLAN) transmission technique as well as becoming part of the IEEE 802.11 Wireless Local Area Network (WLAN) standard.

The system's operational principle is that the original bandwidth is divided into a high number of narrow sub-bands, in which the mobile channel can be considered non-dispersive. Hence no channel equaliser is required and instead of implementing a bank of sub-channel

modems they can be conveniently implemented with the aid of a single Fast Fourier Transformer (FFT), as it will be outlined in Chapter 2.

These OFDM systems - often also termed frequency division multiplexing (FDM) or multi-tone systems - have been employed in military applications since the 1960s, for example by Bello [21], Zimmermann [8], Powers and Zimmerman [22], Chang and Gibby [23] and others. Saltzberg [24] studied a multi-carrier system employing orthogonal time–staggered quadrature amplitude modulation (O-QAM) of the carriers.

The employment of the discrete Fourier transform (DFT) to replace the banks of sinusoidal generators and the demodulators was suggested by Weinstein and Ebert [9] in 1971, which significantly reduces the implementation complexity of OFDM modems. In 1980, Hirosaki [20] suggested an equalisation algorithm in order to suppress both intersymbol and intersubcarrier interference caused by the channel impulse response or timing and frequency errors. Simplified OFDM modem implementations were studied by Peled [13] in 1980, while Hirosaki [14] introduced the DFT-based implementation of Saltzberg's O-QAM OFDM system. From Erlangen University, Kolb [15], Schüssler [16], Preuss [17] and Rückriem [18] conducted further research into the application of OFDM. Cimini [10] and Kalet [19] published analytical and early seminal experimental results on the performance of OFDM modems in mobile communications channels.

More recent advances in OFDM transmission were presented in the impressive state-of-the-art collection of works edited by Fazel and Fettweis [25], including the research by Fettweis *et al.* at Dresden University, Rohling *et al.* at Braunschweig University, Vandendorp at Loeven University, Huber *et al.* at Erlangen University, Lindner *et al.* at Ulm University, Kammeyer *et al.* at Bremen University and Meyr *et al.* [26, 27] at Aachen University, but the individual contributions are too numerous to mention. Important recent references are the books by van Nee and Prasad [28] as well as by Vandenameele, van der Perre and Engels [29].

As a summary of this section, we outline the milestones and the main contributions found in the OFDM literature in Table 1.1, which culminated in the ratification of numerous OFDM-based standards in recent years.

While OFDM transmission over mobile communications channels can alleviate the problem of multipath propagation, recent research efforts have focused on solving a set of inherent difficulties regarding OFDM, namely the peak-to-mean power ratio, time and frequency synchronisation, and on mitigating the effects of the frequency selective fading channel. These issues are addressed below with reference to the literature, while a more in-depth treatment is given throughout the book.

1.2.2 Peak-to-Mean Power Ratio

It is plausible that the OFDM signal - which is the superposition of a high number of modulated sub-channel signals - may exhibit a high instantaneous signal peak with respect to the average signal level. Furthermore, large signal amplitude swings are encountered, when the time domain signal traverses from a low instantaneous power waveform to a high power waveform, which may results in a high out-of-band (OOB) harmonic distortion power, unless the transmitter's power amplifier exhibits an extremely high linearity across the entire signal level range. This then potentially contaminates the adjacent channels with adjacent channel interference. Practical amplifiers exhibit a finite amplitude range, in which they can be con-

Year	Milestone
1966	First OFDM scheme proposed by Chang [1] for dispersive fading channels.
1967	Saltzberg [24] studied a multi-carrier system employing Orthogonal QAM (O-QAM) of the carriers.
1970	U.S. patent on OFDM issued [30].
1971	Weinstein and Ebert [9] applied DFT to OFDM modems.
1980	Hirosaki designed a subchannel-based equalizer for an orthogonally multiplexed QAM system [20].
	Keasler *et al.* [31] described an OFDM modem for telephone networks.
1985	Cimini [10] investigated the feasibility of OFDM in mobile communications.
1987	Alard and Lasalle [32] employed OFDM for digital broadcasting.
1991	ANSI ADSL standard [33].
1994	ANSI HDSL standard [34].
1995	ETSI DAB standard [35]: the first OFDM-based standard for digital broadcasting systems.
1996	ETSI WLAN standard [36].
1997	ETSI DVB-T standard [37].
1998	ANSI VDSL and ETSI VDSL standards [38, 39].
	ETSI BRAN standard [40].
1999	IEEE 802.11a WLAN standard [41].
2002	IEEE 802.11g WLAN standard [42].
2004	ETSI DVB-H standard [43].
	IEEE 802.16 WMAN standard [44].
	Candidate for IEEE 802.11n standard for next generation WLAN [45].
	Candidate for IEEE 802.15.3a standard for WPAN (using MB-OFDM) [46].
2005	Candidate for 4G standards in China, Japan and South Korea (CJK) [47].

Table 1.1: Milestones in the history of OFDM.

sidered almost linear. In order to prevent severe clipping of the high OFDM signal peaks - which is the main source of OOB emissions - the power amplifier must not be driven to saturation and hence they are typically operated with a certain so-called back-off, creating a certain "head room" for the signal peaks, which reduces the risk of amplifier saturation and OOB emission. Two different families of solutions have been suggested in the literature, in order to mitigate these problems, either reducing the peak-to-mean power ratio, or improving the amplification stage of the transmitter.

More explicitly, Shepherd [48], Jones [49], and Wulich [50] have suggested different coding techniques which aim to minimise the peak power of the OFDM signal by employing different data encoding schemes before modulation, with the philosophy of choosing block codes whose legitimate code words exhibit low so-called crest factors or peak-to-mean power envelope fluctuation. Müller [51], Pauli [52], May [53] and Wulich [54] suggested different algorithms for post-processing the time domain OFDM signal prior to amplification, while Schmidt and Kammeyer [55] employed adaptive subcarrier allocation in order to reduce the crest factor. Dinis and Gusmão [56–58] researched the use of two-branch amplifiers, while the clustered OFDM technique introduced by Daneshrad, Cimini and Carloni [59] operates with a set of parallel partial FFT processors with associated transmitting chains. OFDM systems with increased robustness to non-linear distortion have been proposed by Okada,

Nishijima and Komaki [60] as well as by Dinis and Gusmão [61]. These aspects of OFDM transmissions will be treated in substantial depth in Part II of the book.

1.2.3 Synchronisation

Time and frequency synchronisation between the transmitter and receiver are of crucial importance as regards the performance of an OFDM link [62, 63]. A wide variety of techniques have been proposed for estimating and correcting both timing and carrier frequency offsets at the OFDM receiver. Rough timing and frequency acquisition algorithms relying on known pilot symbols or pilot tones embedded into the OFDM symbols have been suggested by Claßen [26], Warner [64], Sari [65], Moose [66], as well as Brüninghaus and Rohling [67]. Fine frequency and timing tracking algorithms exploiting the OFDM signal's cyclic extension were published by Moose [66], Daffara [68] and Sandell [69]. OFDM synchronisation issues are the topics of Chapter 5.

1.2.4 OFDM/CDMA

Combining multi-carrier OFDM transmissions with code division multiple access (CDMA) allows us to exploit the wideband channel's inherent frequency diversity by spreading each symbol across multiple subcarriers. This technique has been pioneered by Yee, Linnartz and Fettweis [70], by Chouly, Brajal and Jourdan [71], as well as by Fettweis, Bahai and Anvari [72]. Fazel and Papke [73] investigated convolutional coding in conjunction with OFDM/CDMA. Prasad and Hara [74] compared various methods of combining the two techniques, identifying three different structures, namely multi-carrier CDMA (MC-CDMA), multi-carrier direct sequence CDMA (MC-DS-CDMA) and multi-tone CDMA (MT-CDMA). Like non-spread OFDM transmission, OFDM/CDMA methods suffer from high peak-to-mean power ratios, which are dependent on the frequency domain spreading scheme, as investigated by Choi, Kuan and Hanzo [75]. Part II of the book considers the related design trade-offs.

1.2.5 Decision-Directed Channel Estimation

In recent years numerous research contributions have appeared on the topic of channel transfer function estimation techniques designed for employment in single-user, single transmit antenna-assisted OFDM scenarios, since the availability of an accurate channel transfer function estimate is one of the prerequisites for coherent symbol detection with an OFDM receiver. The techniques proposed in the literature can be classified as *pilot-assisted*, *decision-directed* (DD) and *blind* channel estimation (CE) methods, as detailed in the extended version of this monograph [90].

In the context of pilot-assisted channel transfer function estimation a subset of the available subcarriers is dedicated to the transmission of specific pilot symbols known to the receiver, which are used for "sampling" the desired channel transfer function. Based on these samples of the frequency domain transfer function, the well-known process of interpolation is used for generating a transfer function estimate for each subcarrier residing between the pilots. This is achieved at the cost of a reduction in the number of useful subcarriers available for data transmission. The family of *pilot-assisted* channel estimation techniques was

Year	Author	Contribution
'91	Höher [76]	Cascaded 1D-FIR channel transfer factor interpolation was carried out in the frequency- and time-direction for frequency-domain PSAM.
'93	Chow, Cioffi and Bingham [77]	Subcarrier-by-subcarrier-based LMS-related channel transfer factor equalisation techniques were employed.
'94	Wilson, Khayata and Cioffi [78]	Linear channel transfer factor filtering was invoked in the time-direction for DDCE.
'95	van de Beek, Edfors, Sandell, Wilson and Börjesson [79]	DFT-aided CIR-related domain Wiener filter-based noise reduction was advocated for DDCE. The effects of leakage in the context of non-sample-spaced CIRs were analysed.
'96	Edfors, Sandell, van de Beek, Wilson and Börjesson [80]	SVD-aided CIR-related domain Wiener filter-based noise reduction was introduced for DDCE.
	Frenger and Svensson [81]	MMSE-based frequency-domain channel transfer factor prediction was proposed for DDCE.
	Mignone and Morello [82]	FEC was invoked for improving the DDCE's remodulated reference.
'97	Tufvesson and Maseng [83]	An analysis of various pilot patterns employed in frequency-domain PSAM was provided in terms of the system's BER for different Doppler frequencies. Kalman filter-aided channel transfer factor estimation was used.
	Höher, Kaiser and Robertson [84, 85]	Cascaded 1D-FIR Wiener filter channel interpolation was utilised in the context of 2D-pilot pattern-aided PSAM
'98	Li, Cimini and Sollenberger [86]	An SVD-aided CIR-related domain Wiener filter-based noise reduction was achieved by employing CIR-related tap estimation filtering in the time-direction.
	Edfors, Sandell, van de Beek, Wilson and Börjesson [87]	A detailed analysis of SVD-aided CIR-related domain Wiener filter-based noise reduction was provided for DDCE, which expanded the results of [80].
	Tufvesson, Faulkner and Maseng [88]	Wiener filter-aided frequency domain channel transfer factor prediction-assisted pre-equalisation was studied.
	Itami, Kuwabara, Yamashita, Ohta and Itoh [89]	Parametric finite-tap CIR model-based channel estimation was employed for frequency domain PSAM.

Table 1.2: Contributions to channel transfer factor estimation for single-transmit antenna-assisted OFDM [90].

Year	Author	Contribution
'99	Al-Susa and Ormondroyd [91]	DFT-aided Burg algorithm-assisted adaptive CIR-related tap prediction filtering was employed for DDCE.
	Yang, Letaief, Cheng and Cao [92]	Parametric, ESPRIT-assisted channel estimation was employed for frequency domain PSAM.
'00	Li [93]	Robust 2D frequency domain Wiener filtering was suggested for employment in frequency domain PSAM using 2D pilot patterns.
'01	Yang, Letaief, Cheng and Cao [94]	Detailed discussions of parametric, ESPRIT-assisted channel estimation were provided in the context of frequency domain PSAM [92].
	Zhou and Giannakis [95]	Finite alphabet-based channel transfer factor estimation was proposed.
	Wang and Liu [96]	Polynomial frequency domain channel transfer factor interpolation was contrived.
	Yang, Cao and Letaief [97]	DFT-aided CIR-related domain one-tap Wiener filter-based noise reduction was investigated, which is supported by variable frequency domain Hanning windowing.
	Lu and Wang [98]	A Bayesian blind turbo receiver was contrived for coded OFDM systems.
	Li and Sollenberger [99]	Various transforms were suggested for CIR-related tap estimation filtering-assisted DDCE.
	Morelli and Mengali [100]	LS- and MMSE-based channel transfer factor estimators were compared in the context of frequency domain PSAM.
'02	Chang and Su [101]	Parametric quadrature surface-based frequency domain channel transfer factor interpolation was studied for PSAM.
	Necker and Stüber [102]	Totally blind channel transfer factor estimation based on the finite alphabet property of PSK signals was investigated.

Table 1.3: Contributions to channel transfer factor estimation for single-transmit antenna-assisted OFDM [90].

investigated for example by Chang and Su [101], Höher [76, 84, 85], Itami *et al.* [89], Li [93], Tufvesson and Maseng [83], Wang and Liu [96], as well as Yang *et al.* [92, 97, 103].

By contrast, in the context of Decision-Directed Channel Estimation (DDCE) all the sliced and remodulated subcarrier data symbols are considered as pilots. In the absence of symbol errors and also depending on the rate of channel fluctuation, it was found that accurate channel transfer function estimates can be obtained, which often are of better quality, in terms of the channel transfer function estimator's mean-square error (MSE), than the estimates offered by pilot-assisted schemes. This is because the latter arrangements usually invoke relatively sparse pilot patterns.

The family of *decision-directed* channel estimation techniques was investigated for example by van de Beek *et al.* [79], Edfors *et al.* [80, 87], Li *et al.* [86], Li [99], Mignone and Morello [82], Al-Susa and Ormondroyd [91], Frenger and Svensson [81], as well as Wilson *et al.* [78]. Furthermore, the family of *blind* channel estimation techniques was studied by Lu and Wang [98], Necker and Stüber [102], as well as by Zhou and Giannakis [95]. The various contributions have been summarised in Tables 1.2 and 1.3.

In order to render the various DDCE techniques more amenable to use in scenarios associated with a relatively high rate of channel variation expressed in terms of the OFDM symbol normalized Doppler frequency, linear prediction techniques well known from the speech coding literature [104, 105] can be invoked. To elaborate a little further, we will substitute the CIR-related tap estimation filter - which is part of the two-dimensional channel transfer function estimator proposed in [86] - by a CIR-related tap prediction filter. The employment of this CIR-related tap prediction filter enables a more accurate estimation of the channel transfer function encountered during the forthcoming transmission time slot and thus potentially enhances the performance of the channel estimator. We will be following the general concepts described by Duel-Hallen *et al.* [106] and the ideas presented by Frenger and Svensson [81], where frequency domain prediction filter-assisted DDCE was proposed. Furthermore, we should mention the contributions of Tufvesson *et al.* [88, 107], where a prediction filter-assisted frequency domain pre-equalisation scheme was discussed in the context of OFDM. In a further contribution by Al-Susa and Ormondroyd [91], adaptive prediction filter-assisted DDCE designed for OFDM has been proposed upon invoking techniques known from speech coding, such as the Levinson-Durbin algorithm or the Burg algorithm [104, 108, 109] in order to determine the predictor coefficients.

In contrast to the above-mentioned single-user OFDM scenarios, in a multi-user OFDM scenario the signal received by each antenna is constituted by the superposition of the signal contributions associated with the different users or transmit antennas. Note that in terms of the multiple-input multiple-output (MIMO) structure of the channel the multi-user single-transmit antenna scenario is equivalent, for example, to a single-user space-time coded (STC) scenario using multiple transmit antennas. For the latter a Least-Squares (LS) error channel estimator was proposed by Li *et al.* [110], which aims at recovering the different transmit antennas' channel transfer functions on the basis of the output signal of a specific reception antenna element and by also capitalising on the remodulated received symbols associated with the different users. The performance of this estimator was found to be limited in terms of the mean-square estimation error in scenarios, where the product of the number of transmit antennas and the number of CIR taps to be estimated per transmit antenna approaches the total number of subcarriers hosted by an OFDM symbol. As a design alternative, in [111] a DDCE was proposed by Jeon *et al.* for a space-time coded OFDM scenario of two transmit antennas

Year	Author	Contribution
'99	Li, Seshadri and Ariyavisitakul [110]	The LS-assisted DDCE proposed exploits the cross-correlation properties of the transmitted subcarrier symbol sequences.
'00	Jeon, Paik and Cho [111]	Frequency-domain PIC-assisted DDCE is studied, which exploits the channel's slow variation versus time.
	Li [112]	Time-domain PIC-assisted DDCE is investigated as a simplification of the LS-assisted DDCE of [110]. Optimum training sequences are proposed for the LS-assisted DDCE of [110].
'01	Mody and Stüber [113]	Channel transfer factor estimation designed for frequency-domain PSAM based on CIR-related domain filtering is studied.
	Gong and Letaief [114]	MMSE-assisted DDCE is advocated which represents an extension of the LS-assisted DDCE of [114]. The MMSE-assisted DDCE is shown to be practical in the context of transmitting consecutive training blocks. Additionally, a low-rank approximation of the MMSE-assisted DDCE is considered.
	Jeon, Paik and Cho [115]	2D MMSE-based channel estimation is proposed for frequency-domain PSAM.
	Vook and Thomas [116]	2D MMSE based channel estimation is invoked for frequency domain PSAM. A complexity reduction is achieved by CIR-related domain-based processing.
	Xie and Georghiades [117]	Expectation maximization (EM) based channel transfer factor estimation approach for DDCE.
'02	Li [118]	A more detailed discussion on time-domain PIC-assisted DDCE is provided and optimum training sequences are proposed [112].
	Bölcskei, Heath and Paulraj [119]	Blind channel identification and equalisation using second-order cyclostationary statistics as well as antenna precoding were studied.
	Minn, Kim and Bhargava [120]	A reduced complexity version of the LS-assisted DDCE of [110] is introduced, based on exploiting the channel's correlation in the frequency-direction, as opposed to invoking the simplified scheme of [118], which exploits the channel's correlation in the time-direction. A similar approach was suggested by Slimane [121] for the specific case of two transmit antennas.
	Komninakis, Fragouli, Sayed and Wesel [122]	Fading channel tracking and equalisation were proposed for employment in MIMO systems assisted by Kalman estimation and channel prediction.

Table 1.4: Contributions on channel transfer factor estimation for multiple-transmit antenna assisted OFDM [90].

and two receive antennas.

Specifically, the channel transfer function[1] associated with each transmit-receive antenna pair was estimated on the basis of the output signal of the specific receive antenna upon *subtracting* the interfering signal contributions associated with the remaining transmit antennas. These interference contributions were estimated by capitalising on the knowledge of the channel transfer functions of all interfering transmit antennas predicted during the $(n-1)$-th OFDM symbol period for the n-th OFDM symbol, also invoking the corresponding remodulated symbols associated with the n-th OFDM symbol. To elaborate further, the difference between the subtraction-based channel transfer function estimator of [111] and the LS estimator proposed by Li *et al.* in [110] is that in the former the channel transfer functions predicted during the previous, i.e. the $(n-1)$-th OFDM symbol period for the current, i.e. the n-th OFDM symbol are employed for both symbol detection *as well as* for obtaining an updated channel estimate for employment during the $(n+1)$-th OFDM symbol period. In the approach advocated in [111] the subtraction of the different transmit antennas' interfering signals is performed in the frequency domain.

By contrast, in [112] a similar technique was proposed by Li with the aim of simplifying the DDCE approach of [110], which operates in the time domain. A prerequisite for the operation of this parallel interference cancellation (PIC)-assisted DDCE is the availability of a reliable estimate of the various channel transfer functions for the current OFDM symbol, which are employed in the cancellation process in order to obtain updated channel transfer function estimates for the demodulation of the next OFDM symbol. In order to compensate for the channel's variation as a function of the OFDM symbol index, linear prediction techniques can be employed, as it was also proposed for example in [112]. However, due to the estimator's recursive structure, determining the optimum predictor coefficients is not as straightforward as for the transversal FIR filter-assisted predictor as described in Section 15.2.4 of the extended version of this book [90] for single-user DDCE.

A comprehensive overview of further publications on channel transfer factor estimation for OFDM systems supported by multiple transmit antennas is provided in Table 1.4.

1.2.6 Uplink Detection Techniques for Multi-User SDMA-OFDM

Combining adaptive antenna-aided techniques with OFDM transmissions was shown to be advantageous for example in the context of suppressing co-channel interference in cellular communications systems. Amongst others, Li, Cimini and Sollenberger [148–150], Kim, Choi and Cho [151], Lin, Cimini and Chuang [152] as well as Münster *et al.* [153] have investigated algorithms designed for multi-user channel estimation and interference suppression.

The related family of Space-Division-Multiple-Access (SDMA) communication systems has recently drawn wide research interests. In these systems the L different users' transmitted signals are separated at the base-station (BS) with the aid of their unique, user-specific spatial signature, which is constituted by the P-element vector of channel transfer factors between the users' single transmit antenna and the P different receiver antenna elements at the BS, upon assuming flat-fading channel conditions such as those often experienced in the context of each of the OFDM subcarriers.

[1] In the context of the OFDM system the set of K different subcarriers' channel transfer factors is referred to as the channel transfer function, or simply as the channel.

Year	Author	Contribution
'96	Foschini [123]	The concept of the BLAST architecture was introduced.
'98	Vook and Baum [124]	SMI-assisted MMSE combining was invoked on an OFDM subcarrier basis.
	Wang and Poor [125]	Robust sub-space-based weight vector calculation and tracking were employed for co-channel interference suppression, as an improvement of the SMI-algorithm.
	Wong, Cheng, Letaief and Murch [126]	Optimization of an OFDM system was reported in the context of multiple transmit and receive antennas upon invoking the maximum SINR criterion. The computational was reduced by exploiting the channel's correlation in the frequency direction.
	Li and Sollenberger [127]	Tracking of the channel correlation matrix' entries was suggested in the context of SMI-assisted MMSE combining for multiple receiver antenna assisted OFDM, by capitalizing on the principles of [86].
'99	Golden, Foschini, Valenzuela and Wolniansky [128]	The SIC detection-assisted V-BLAST algorithm was introduced.
	Li and Sollenberger [129]	The system introduced in [127] was further detailed.
	Vandenameele, Van der Perre, Engels and de Man [130]	A comparative study of different SDMA detection techniques, namely that of MMSE, SIC and ML detection was provided. Further improvements of SIC detection were suggested by adaptively tracking multiple symbol decisions at each detection node.
	Speth and Senst [131]	Soft-bit generation techniques were proposed for MLSE in the context of a coded SDMA-OFDM system.
'00	Sweatman, Thompson, Mulgrew and Grant [132]	Comparisons of various detection algorithms including LS, MMSE, D-BLAST and V-BLAST (SIC detection) were carried out.
	van Nee, van Zelst and Awater [133–135]	The evaluation of ML detection in the context of a Space-Division Multiplexing (SDM) system was provided, considering various simplified ML detection techniques.
	Vandenameele, Van der Perre, Engels, Gyselinckx and de Man [136]	More detailed discussions were provided on the topics of [130].

Table 1.5: Contributions on multi-user detection techniques designed for multiple transmit antenna assisted OFDM systems [90].

Year	Author	Contribution
'00	Li, Huang, Lozano and Foschini [137]	Reduced complexity ML detection was proposed for multiple transmit antenna systems employing adaptive antenna grouping and multi-step reduced-complexity detection.
'01	Degen, Walke, Lecomte and Rembold [138]	An overview of various adaptive MIMO techniques was provided. Specifically, pre-distortion was employed at the transmitter, as well as LS- or BLAST detection were used at the receiver or balanced equalisation was invoked at both the transmitter and receiver.
	Zhu and Murch [139]	A tight upper bound on the SER performance of ML detection was derived.
	Li, Letaief, Cheng and Cao [140]	Joint adaptive power control and detection were investigated in the context of an OFDM/SDMA system, based on the approach of Farrokhi *et al.* [141].
	van Zelst, van Nee and Awater [142]	Iterative decoding was proposed for the BLAST system following the turbo principle.
	Benjebbour, Murata and Yoshida [143]	The performance of V-BLAST or SIC detection was studied in the context of backward iterative cancellation scheme employed after the conventional forward cancellation stage.
	Sellathurai and Haykin [144]	A simplified D-BLAST was proposed, which used iterative PIC capitalizing on the extrinsic soft-bit information provided by the FEC scheme used.
	Bhargave, Figueiredo and Eltoft [145]	A detection algorithm was suggested, which followed the concepts of V-BLAST or SIC. However, multiple symbols states are tracked from each detection stage, where - in contrast to [136] - an intermediate decision is made at intermediate detection stages.
	Thoen, Deneire, Van der Perre and Engels [146]	A constrained LS detector was proposed for OFDM/SDMA, which was based on exploiting the constant modulus property of PSK signals.
'02	Li and Luo [147]	The block error probability of optimally ordered V-BLAST was studied. Furthermore, the block error probability is also investigated for the case of tracking multiple parallel symbol decisions from the first detection stage, following an approach similar to that of [136].

Table 1.6: Contributions on detection techniques for MIMO systems and for multiple transmit antenna assisted OFDM systems [90].

A whole host of multi-user detection (MUD) techniques known from Code-Division-Multiple-Access (CDMA) communications lend themselves also to an application in the context of SDMA-OFDM on a per-subcarrier basis. Some of these techniques are the Least-Squares (LS) [132, 138, 146, 154], Minimum Mean-Square Error (MMSE) [124–127, 129, 132, 136, 140, 154–156], Successive Interference Cancellation (SIC) [123, 128, 132, 136, 138, 143, 145, 147, 154, 156], Parallel Interference Cancellation (PIC) [144, 154] and Maximum Likelihood (ML) detection [131, 133–137, 139, 142, 154, 156]. A comprehensive overview of recent publications on MUD techniques for MIMO systems is given in Tables 1.5 and 1.6.

1.2.7 OFDM Applications

Due to their implementational complexity, OFDM applications have been scarce until quite recently. Recently, however, OFDM has been adopted as the new European digital audio broadcasting (DAB) standard [11, 12, 157–159] as well as for the terrestrial digital video broadcasting (DVB) system [65, 160].

For fixed-wire applications, OFDM is employed in the asynchronous digital subscriber line (ADSL) and high-bit-rate digital subscriber line (HDSL) systems [161–164] and it has also been suggested for power line communications systems [165, 166] due to its resilience to time dispersive channels and narrow band interferers.

More recently, OFDM applications were studied within the European 4th Framework Advanced Communications Technologies and Services (ACTS) programme [167]. The MEDIAN project investigated a 155 Mbps wireless asynchronous transfer mode (WATM) network [168–171], while the Magic WAND group [172, 173] developed a wireless local area network (LAN). Hallmann and Rohling [174] presented a range of different OFDM systems that were applicable to the European Telecommunications Standardisation Institute's (ETSI) recent personal communications oriented air interface concept [175].

1.3 Outline of the Book

- **Chapter 2**: In this chapter we commence our detailed discourse by demonstrating that OFDM modems can be efficiently implemented by invoking the Fourier transform or the fast Fourier Transform (FFT). A number of basic OFDM design issues are discussed in an accessible style.

- **Chapter 3**: The BER performance of OFDM modems achievable in AWGN channels is studied for a set of different modulation schemes in the subcarriers. The effects of amplitude limiting of the transmitter's output signal, caused by a simple clipping amplifier model, and of finite resolution D/A and A/D conversion on the system performance are investigated. Oscillator phase noise is considered as a source of intersubcarrier interference and its effects on the system performance are demonstrated.

- **Chapter 4**: The effects of time-dispersive frequency-selective Rayleigh fading channels on OFDM transmissions are demonstrated. Channel estimation techniques are presented which support the employment of coherent detection in frequency selective channels. Additionally, differential detection is investigated, and the resultant system performance is compared, when communicating over various channels.

- **Chapter 5**: We focus our attention on the time and frequency synchronisation requirements of OFDM transmissions and the effects of synchronisation errors are demonstrated. Two novel synchronisation algorithms for frame and OFDM symbol synchronisation are suggested and compared. The resulting system performance over fading wideband channels is examined.

- **Chapter 6**: Based on the results of Chapter 4, the employment of adaptive modulation schemes is suggested for duplex point-to-point links over frequency-selective time-varying channels. Different bit allocation schemes are investigated and a simplified sub-band adaptivity OFDM scheme is suggested to alleviate the associated signalling constraints. A range of blind modulation scheme detection algorithms are also investigated and compared. The employment of long-block-length convolutional turbo codes is suggested for improving the system's throughput and the turbo coded adaptive OFDM modem's performance is compared using different sets of parameters. Then the effects of using pre-equalisation at the transmitter are examined, and a set of different pre-equalisation algorithms is introduced. A joint pre-equalisation and adaptive modulation algorithm is proposed and its BER and throughput performance are studied.

- **Chapter 7**: The discussions of **Part II** of the book commence by a rudimentary comparison of OFDM, CDMA and MC-CDMA in Chapter 7.

- **Chapter 8**: Since the properties of spreading sequences are equally important in both multicarrier CDMA and in DS-CDMA, the basic properties of various spreading sequences are reviewed in Chapter 8.

- **Chapter 9**: The basic characterisation of spreading codes provided in Chapter 8 is followed by Chapter 9, analysing the achievable performance of both single- and multi-user detected MC-CDMA. The chapter is concluded by the comparative study of a sophisticated space-time block coded near-instantaneously adaptive OFDM and MC-CDMA system. These conclusions suggest that whilst both near-instantaneously adaptive OFDM and MC-CDMA exhibit a high performance, they require the transmission of channel-quality related side-information, which exhibits a high sensitivity to transmission errors, since in the presence of modem mode signalling errors catastrophic data error propagation may be experienced. A more robust 'all-weather' tool is constituted by space-time coding, which is capable of mitigating the channel-quality fluctuations imposed by co-channel interference and fading, although this is achieved at the cost of a higher complexity owing to the employment of multiple transmitters and receivers.

- **Chapter 10**: Achieving near-ML multi-user MIMO-OFDM performance at a modest complexity is the ambitious aim of this chapter, which proposes an advanced extension of the Complex Sphere Detector (CSD) [176]. The algorithm proposed extends the potential range of applications of the CSD methods, as well as reducing the associated computational complexity, rendering the technique a feasible solution for implementation in practical systems. This technique allows the system to support a higher number of users than the number of antennas.

- **Chapter 11**: This chapter invokes the enhanced CSD of Chapter 10 and combines it with Genetic Algorithms (GA) for the sake of creating a powerful yet modest-complexity joint channel and data estimation scheme. It will be demonstrated that the

proposed GA-aided iterative joint channel estimation and multi-user detection scheme generating soft outputs constitutes an effective solution to the channel estimation problem in multi-user MIMO SDMA-OFDM systems. Furthermore, the GA-JCEMUD is capable of exhibiting a robust performance in the so-called 'over-loaded' scenarios, where the number of users is higher than the number of receiver antenna elements.

Chapter 12: The last in-depth chapter of the book introduces a new design paradigm, which aims for directly minimizing the BER at the output of the SDMA MUD, rather than minimizing the MSE. This results in a potentially complex optimization problem, which may be solved with the aid of GAs applied in the context of an SDMA OFDM system for determining the MBER MUD's array weight vectors. We will demonstrate that the GA-aided system has an edge over the conjugate gradient algorithm-based system, because it does not require an initial SDMA array weight solution. Unlike the family of conventional MUDs, the MBER MUD is capable of supporting more users than the number of receiver antennas.

- **Chapter 13**: In this chapter we offer detailed conclusions and highlight a range of further research problems.

1.4 Chapter Summary and Conclusion

Here we conclude our brief introduction to OFDM and the review of its evolution since its conception by Chang in 1966 [1]. Numerous seminal contributions have been reviewed in chronological order in Tables 1.2–1.6, highlighting the historical development of the subject. These contributions reflect the state of the art at the time of writing in the context of the various OFDM system components, outlining a number of open research topics. Let us now embark on a detailed investigation of the topics introduced in this chapter.

Throughout this monograph we endeavour to highlight the range of contradictory system design trade-offs associated with the conception of OFDM and MC-CDMA systems. We intend to present the material in an unbiased fashion and sufficiently richly illustrated in terms of the associated design trade-offs so that readers will be able to find recipes and examples for solving their own particular wireless communications problems. In this rapidly evolving field it is a challenge to complete a timely, yet self-contained treatise, since new advances are being discovered at an accelerating pace, which should find their way into a timely monograph. Our sincere hope is that you, the readers, will find the book a useful source of information, but above all a catalyst for further research.

Part I

OFDM System Design

Chapter 2

Introduction to Orthogonal Frequency Division Multiplexing

2.1 Introduction

In this introductory chapter we examine orthogonal frequency division multiplexing (OFDM) as a means of counteracting the channel-induced linear distortions encountered when transmitting over a dispersive radio channel. The fundamental principle of orthogonal multiplexing originates from Chang [1], and over the years a number of researchers have investigated this technique [8–10, 13–18, 22–24]. Despite its conceptual elegance, until recently its deployment has been mostly limited to military applications due to implementational difficulties. However, it has recently been adopted as the new European digital audio broadcasting (DAB) standard, and this consumer electronics application underlines its significance as a broadcasting technique [11, 12, 19, 157, 158].

In the OFDM scheme of Figure 2.1 the serial data stream of a traffic channel is passed through a serial-to-parallel convertor which splits the data into a number of parallel channels. The data in each channel is applied to a modulator, such that for N channels there are N modulators whose carrier frequencies are f_0, f_1, ..., f_{N-1}. The difference between adjacent channels is Δf and the overall bandwidth W of the N modulated carriers is $N\Delta f$.

These N modulated carriers are then combined to give an OFDM signal. We may view the serial-to-parallel convertor as applying every Nth symbol to a modulator. This has the effect of interleaving the symbols into each modulator, e.g. symbols S_0, S_N, S_{2N}, ... are applied to the modulator whose carrier frequency is f_1. At the receiver the received OFDM signal is demultiplexed into N frequency bands, and the N modulated signals are demodulated. The baseband signals are then recombined using a parallel-to-serial convertor.

In the more conventional serial transmission approach [177], the traffic data is applied directly to the modulator transmitting at a carrier frequency positioned at the centre of the transmission band $f_0, \ \ldots, \ f_{N-1}$, ie at $(f_{N-1} + f_0)/2$. The modulated signal occupies the

OFDM and MC-CDMA: A Primer L. Hanzo and T. Keller
© 2006 John Wiley & Sons, Ltd

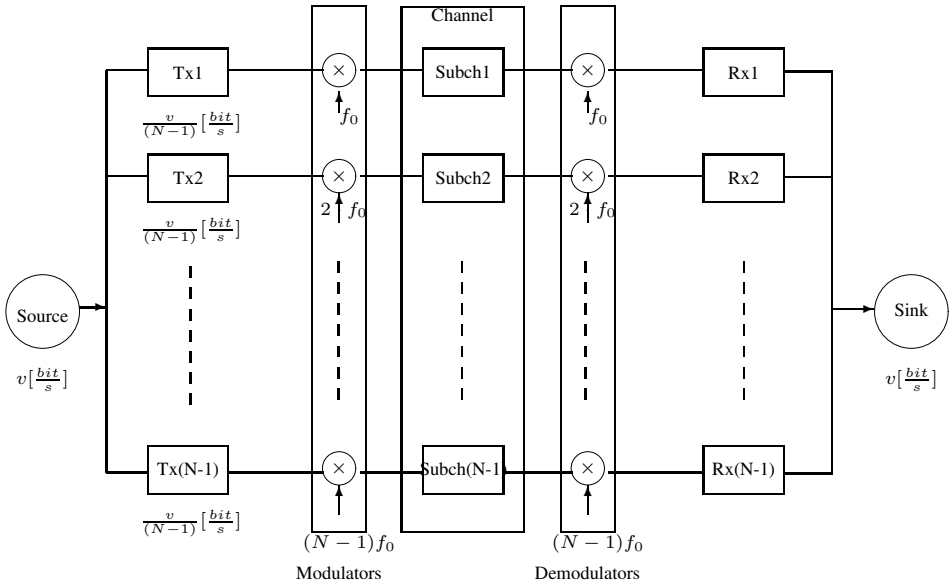


Figure 2.1: Simplified block diagram of the orthogonal parallel modem

entire bandwidth W. When the data is transmitted serially, the effect of a deep fade in a mobile channel is to cause a burst of transmission errors, if the fade extends over the duration of several bits. By contrast, during an N-symbol duration period of the conventional serial system, each of the N number of OFDM subchannel modulators carries only one symbol, each of which has an N times longer duration. Hence an identical-duration channel fade would only affect a fraction of the duration of each of the extended-length subcarrier symbols transmitted in parallel. Therefore the OFDM system may be able to recover all of the partially fading-contaminated N subcarrier symbols. Thus, while the serial system exhibits an error burst, no errors or few errors may occur using the OFDM approach.

A further advantage of OFDM is that because the symbol period has been increased, the channel's delay spread becomes a significantly shorter fraction of a symbol period than in the serial system, potentially rendering the system less sensitive to channel-induced dispersion, than the conventional serial system.

A disadvantage of the OFDM approach portrayed in Figure 2.1 is its increased complexity in comparison to a conventional serial modem, which is a consequence of employing N modulators and transmit filters at the transmitter and N demodulators and receive filters at the receiver. We will demonstrate in Section 2.3 that the associated complexity can be reduced by the employment of the discrete Fourier transform (DFT). When the number of subcarriers is high, the system's complexity may be further reduced by implementing the DFT with the aid of the Fast Fourier transform (FFT), again, as we will demonstrate in Section 2.3. The simple conceptual reason for this is that – as it will be argued in the context of Figure 2.2 in the next section – the OFDM sub-channel modulators use a set of harmonically related sinusoidal and cosinusoidal sub-channel carriers, just like the basis functions of the DFT.

2.2 Principles of QAM-OFDM

The simplest version of the basic OFDM system has N sub-bands, each separated from its neighbour by a sufficiently large guard band in order to prevent interference between signals in adjacent bands. However, the available spectrum can be used much more efficiently if the spectra of the individual sub-bands are allowed to overlap. By using coherent detection and orthogonal sub-band tones, the original data can be correctly recovered.

In the system shown in Figure 2.2, the input serial data stream is rearranged into a sequence $\{d_n\}$ of N QAM symbols at baseband. Each serial QAM symbol is spaced by $\Delta t = 1/f_s$ where f_s is the serial signalling or symbol rate. At the nth symbol instant, the QAM symbol $d(n) = a(n) + jb(n)$ is represented by an in-phase component $a(n)$ and a quadrature component $b(n)$. A block of N QAM symbols is applied to a serial-to-parallel convertor and the resulting in-phase symbols $a(0)$, $a(1)$, ..., $a(N-1)$, and quadrature symbols $b(0)$, $b(1)$, ..., $b(N-1)$ are applied to N pairs of balanced modulators. The quadrature components $a(n)$ and $b(n)$, $n = 0, 1, \ ..., \ N-1$, modulate the quadrature carriers $\cos w_n t$ and $\sin w_n t$, respectively. Notice that the signalling interval of the sub-bands in the parallel system is N times longer than that of the serial system giving $T = N\Delta t$, which corresponds to an N-times lower signalling rate. The sub-band carrier frequencies $w_n = 2\pi n f_0$ are spaced apart by $w_0 = 2\pi/T$.

The modulated carriers $a(n)\cos w_n t$ and $b(n)\sin w_n t$ when added together constitute a QAM signal, and since $n = 0, 1, \ ..., \ N-1$, we have N QAM symbols at RF, where the nth QAM signal is given by:

$$\begin{aligned} X_n(t) &= a(n)\cos w_n t + b(n)\sin w_n t \\ &= \gamma(n)\cos(w_n t + \psi_n) \end{aligned} \tag{2.1}$$

where we have

$$\gamma(n) = \sqrt{a^2(n) + b^2(n)} \tag{2.2}$$

and

$$\psi_n = \tan^{-1}\left(\frac{b(n)}{a(n)}\right) \quad n = 0, 1, \ ..., \ N-1. \tag{2.3}$$

By adding the outputs of each sub-channel signal $X_n(t)$ whose carriers are offset by $\omega_0 = 2\pi/T$ we obtain the FDM/QAM signal in the form of

$$D(t) = \sum_{n=0}^{N-1} X_n(t). \tag{2.4}$$

This set of N FDM/QAM signals is transmitted over the mobile radio channel. At the receiver this OFDM signal is demultiplexed using a bank of N filters to regenerate the N QAM signals. The QAM baseband signals $a(n)$ and $b(n)$ are recovered and turned into serial form $\{d_n\}$. Recovery of the data ensues using the QAM baseband demodulator and differential decoding.

In theory, such a system is capable of achieving the maximum transmission rate of $log_2\, Q\ bits/s/Hz$, where Q is the number of QAM levels. In practice, there is some spectral spillage due to adjacent frequency sub-bands which reduces this efficiency. Spectral spillage

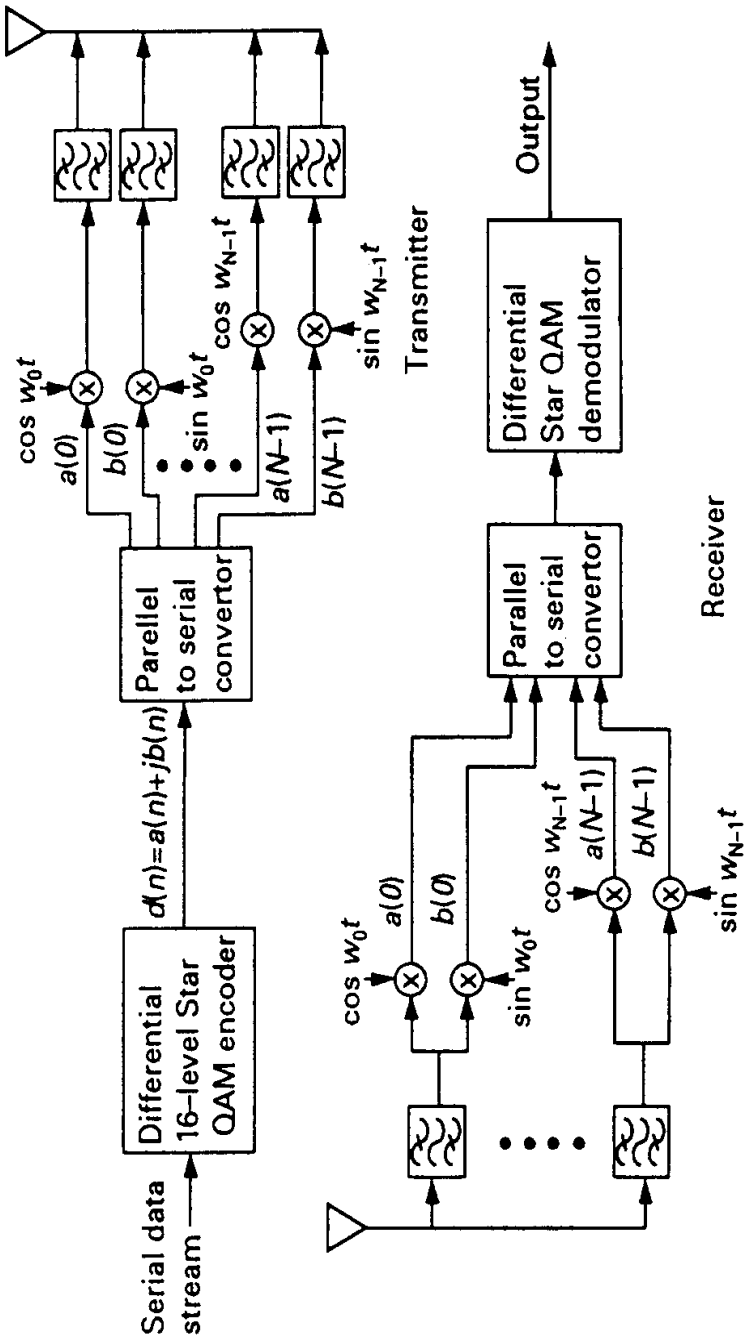


Figure 2.2: Detailed OFDM system schematic ©Hanzo, Webb, Keller, 2000, [177]

due to the sub-bands at the top and bottom of the overall frequency band requires a certain amount of guard space between adjacent users. Furthermore, spectral spillage between OFDM sub-bands due to the imperfections of each of the sub-band filters requires that the sub-bands be spaced further apart than the theoretically required minimum amount, decreasing spectral efficiency. In order to obtain the highest efficiency, the block size should be kept high and the sub-band filters made to meet stringent specifications.

One of the most attractive features of this scheme is that the bandwidth of the sub-channels is very narrow when compared to the communications channel's coherence bandwidth. Therefore, flat-fading narrowband propagation conditions apply. The sub-channel modems can use almost any modulation scheme, and QAM is an attractive choice in some situations.

2.3 Modulation by Discrete Fourier Transform [178, 179]

A fundamental problem associated with the OFDM scheme described is that in order to achieve high resilience against fades in the channels we consider, the block size, N, has to be of the order of 100, requiring a large number of sub-channel modems. Fortunately, it can be shown mathematically that taking the discrete Fourier transform (DFT) of the original block of N QAM symbols and then transmitting the DFT coefficients serially is exactly equivalent to the operations required by the OFDM transmitter of Figure 2.2. Substantial hardware simplifications can be made with OFDM transmissions if the bank of sub-channel modulators/demodulators is implemented using the computationally efficient pair of inverse fast Fourier transform and fast Fourier transform (IFFT/FFT).

The modulated signal $m(t)$ is given by

$$m(t) = \Re\left\{b(t)e^{j2\pi f_0 t}\right\}, \tag{2.5}$$

where $b(t)$ is the equivalent baseband information signal and f_0 is the carrier frequency, as introduced in Equations 2.6, 2.9 and 2.10. Using the rectangular full-response modulation elements $m_T(t-kT) = rect\frac{(t-kT)}{T}$ "weighted" by the complex QAM information symbols $X(k) = I(k) + jQ(k)$ to be transmitted, where $I(k)$ and $Q(k)$ are the quadrature components, the equivalent baseband information signal is given by:

$$b(t) = \sum_{k=-\infty}^{\infty} X(k)m_T(t-kT), \tag{2.6}$$

where k is the signalling interval index and T is its duration. On substituting Equation 2.6 into Equation 2.5 we have:

$$m(t) = \Re\left\{\sum_{k=-\infty}^{\infty} X(k)m_T(t-kT)e^{j2\pi f_0 t}\right\}. \tag{2.7}$$

Without loss of generality let us consider the signalling interval $k = 0$:

$$m_0(t) = m(t)rect\frac{t}{T}, \tag{2.8}$$

where adding the modulated signals of the sub-channel modulators yields

$$m_0(t) = \sum_{n=0}^{N-1} m_{0n}(t). \tag{2.9}$$

Observe that the stream of complex baseband symbols $X(k)$ to be transmitted can be described both in terms of in-phase $I(k)$ and quadrature phase $Q(k)$ components, as well as by magnitude and phase. In the case of a square-shaped QAM constellation [180] $X(k) = I(k)+jQ(k)$ might be a more convenient formalism; for the star QAM constellation introduced in [180], $X(k) = |X(k)|e^{j\Phi(k)}$ appears to be more attractive.

If $X_n = X_{n,k=0}$ is the complex baseband QAM symbol to be transmitted via sub-channel n in signalling interval $k = 0$, then

$$m_0(t) = \begin{cases} \sum_{n=0}^{N-1} \Re\left\{X_{n,0} e^{j2\pi f_{0,n} t}\right\} & \text{for } |t| < \frac{T}{2}, \\ 0 & \text{otherwise.} \end{cases} \tag{2.10}$$

Bearing in mind that $m_0(t)$ is confined to the interval $|t| < \frac{T}{2}$ we drop the sampling interval index $k = 0$ and simplify our formalism to

$$m_0(t) = \sum_{n=0}^{N-1} \Re\left\{X_n e^{j2\pi f_{0n} t}\right\}. \tag{2.11}$$

When computing the $\Re$ part using the complex conjugate we have:

$$\begin{aligned} m_0(t) &= \sum_{n=0}^{N-1} \frac{1}{2}\left\{X_n e^{j2\pi f_{0n} t} + {X_n}^* e^{-j2\pi f_{0n} t}\right\} \\ &= \sum_{n=-(N-1)}^{N-1} \frac{1}{2} X_n e^{j2\pi f_{0n} t}, \end{aligned} \tag{2.12}$$

where for $n = 0, \ldots, N-1$ we have:

$$X_{-n} = {X_n}^*, \quad X_0 = 0, \quad f_{0(-n)} = -f_{0n}, \quad f_{00} = 0.$$

This conjugate complex symmetric sequence is shown in Figure 2.3 in case of the square 16-QAM constellation of [180], where both the I and Q components can assume values of ± 1 and ± 3.

We streamline our formalism in Equation 2.12 by introducing the Fourier coefficients F_n given by

$$F_n = \begin{cases} \frac{1}{2} X_n & if \quad 1 \le n \le N-1 \\ \frac{1}{2} X_n^* & if \quad -(N-1) \le n \le -1 \\ 0 & if \quad n = 0 \end{cases} \tag{2.13}$$

emphasising that the Fourier coefficients of a real signal are conjugate complex symmetric.

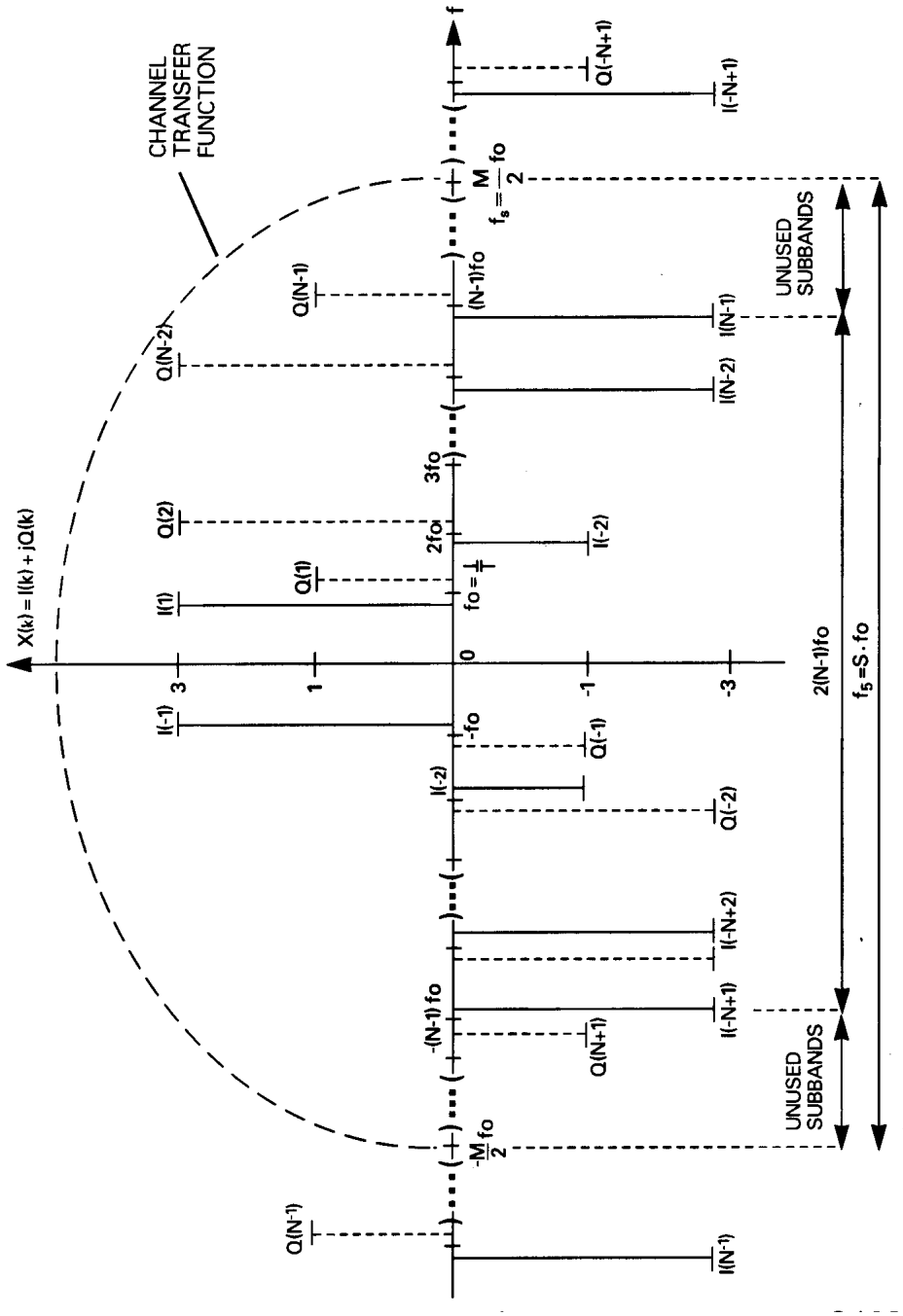


Figure 2.3: Conjugate complex symmetric square 16-QAM transmitted sequence $X(k) = I(k) + jQ(k)$

Then Equation 2.12 can be rewritten as:

$$m_0(t) = \sum_{n=-(N-1)}^{N-1} F_n \cdot e^{j2\pi f_{0n} t}. \tag{2.14}$$

Observe that Equation 2.14 already bears close resemblance to the DFT. Assuming that the sub-channel carriers take values of $f_{0n} = nf_0$, $n = 0, \ldots, N-1$, where again $f_0 = 1/T$ represents the subcarrier spacing chosen to be the reciprocal of the sub-channel signalling interval, then the total one-sided bandwidth is $B = (N-1)f_0$.

So far the sub-channel modulated signals $m_{0n}(t)$ have been assumed to be continuous functions of time within the parallel signalling interval $k = 0$. In order to assist sampled, time-discrete processing by the DFT within the signalling interval $k = 0$ we introduce the discretised time $t = i\Delta t$, where $\Delta t = 1/f_s$ is the reciprocal of the sampling frequency f_s which must be chosen in accordance with Nyquist's sampling theorem to adequately represent $m_0(t)$. Recall furthermore from the previous section that $\Delta t = 1/f_s$ is the original serial QAM symbol spacing and f_s is the serial QAM symbol rate. Then we have:

$$m_0(i\Delta t) = \sum_{n=-(N-1)}^{N-1} F_n e^{j2\pi n f_0 i\Delta t}. \tag{2.15}$$

The Nyquist criterion is met if

$$f_s > 2(N-1)f_0, \tag{2.16}$$

where for practical reasons $f_s = Mf_0$ is assumed, implying that the sampling frequency f_s is an integer multiple of the subcarrier spacing f_0, with $M > 2(N-1)$ being a positive integer, implying also that $f_s = 1/\Delta t = Mf_0$, i.e. $f_0\Delta t = 1/M$. Again, these frequencies are portrayed in Figure 2.3. Bearing in mind that the spectrum of a sampled signal repeats itself at multiples of the sampling frequency f_s with a periodicity of $M = f_s/f_0$ samples, and exploiting the conjugate complex symmetry of the spectrum, for the Fourier coefficients F_n we have:

$$F_n = \begin{cases} F_{n-M} = F^*_{M-n} & if\ (\frac{M}{2}+1) \leq n \leq M-1 \\ 0 & if\ N-1 < n \leq \frac{M}{2}. \end{cases} \tag{2.17}$$

Observe that the frequency region $(N-1)f_0 < f_n \leq \frac{M}{2}f_0$ represents the typical unused transition band of the communications channel, where it exhibits significant amplitude and group delay distortion as suggested by Figure 2.3. However, in the narrow sub-bands the originally wide band frequency selective fading channel can be rendered flat upon using a high number of sub-channels.

The set of QAM symbols can be interpreted as a spectral domain sequence, which due to its conjugate complex symmetry will have a real IDFT pair in the time domain, representing the real modulated signal, which can be written as:

$$m_0(i\Delta t) = \sum_{n=0}^{M-1} F_n e^{j\frac{2\pi}{M}ni},\ i = 0 \ldots M-1. \tag{2.18}$$

This is the standard IDFT that can be computed by the IFFT if the transform length M is an integer power of 2. The rectangular modulation elements $m_T(t) = rect\frac{t}{T}$ introduced in Equation 2.6 have an infinite bandwidth requirement since in effect they rectangularly window the set of orthogonal basis functions constituted by the carriers $rect\frac{t}{T} \cdot \cos w_{0l}t$ and $rect\frac{t}{T} \cdot \sin w_{0l}t$. It is possible to use a time domain raised cosine pulse instead of the $rect\frac{t}{T}$ function [9], but this will impose further slight impairments on the time domain modulated signal which is also exposed to the hostile communications channel.

Observe that the representation of $m_0(t)$ by its $\Delta t = 1/f_s$-spaced samples is only correct if $m_0(t)$ is assumed to be periodic and bandlimited to $2(N-1)f_0$. This is equivalent to saying that $m_0(t)$ can only have a bandlimited frequency domain representation if in the time domain it expands from $-\infty$ to ∞. Due to sampling at a rate of $f_s = 1/\Delta t$ the spectral lobes become periodic at the multiples of f_s, but if the Nyquist sampling theorem is observed, no aliasing occurs. In order to fulfil these requirements, the modulating signal $m_0(t)$ derived by IFFT from the conjugate complex symmetric baseband information signal X_l has to be quasi-periodically extended before transmission via the channel, at least for the duration of the channel's memory. The effects of bandlimited transmission media will be discussed in the following section.

Having provided a justification for employing the FFT for carrying out modulation of all subcarriers in a single step, let us now consider the FFT-based QAM/FDM modem's schematic portrayed in Figure 2.4. The bits provided by the source are serial/parallel converted in order to form the n-level Gray coded symbols, N of which are collected in TX buffer 1, while the contents of TX buffer 2 are being transformed by the IFFT in order to form the time domain modulated signal. The digital-to-analogue (D/A) converted, low-pass filtered modulated signal is then transmitted via the channel and its received samples are collected in RX buffer 1, while the contents of RX buffer 2 are being fast Fourier transformed for deriving the demodulated signal. The twin buffers are alternately filled with data to allow for the finite FFT-based demodulation time. Before the data is Gray decoded and passed to the data sink, it can be decontaminated from the effects of the dispersive channel in the frequency domain, since despite using a high number of subchannels and hence a long subchannel symbol duration, the subchannel symbols may experience some dispersion in case of supporting extremely high transmission rates. In simple terms this operation may be carried out by inserting known pilot symbols into the frequency domain OFDM signal. These pilot subcarriers will allow us to sample and reconstruct the channel's complex frequency domain transfer function. Provided that frequency domain transfer function is sampled at a sufficiently high frequency, which is higher than the channel's Nyquist sampling frequency, we will show in Chapter 3 that the channel's frequency domain transfer function can be reliably recovered at the receiver, despite the contaminating effects of the Additive White Gaussian Noise (AWGN). Naturally, if the vehicular speed is high and hence the channel's Doppler frequency is high, a high "sampling frequency", i.e. high pilot subcarrier density has to be used, which reduces the achievable effective date throughput.

2.4 Transmission via Bandlimited Channels

The DFT/IDFT operations assume that the input signal is periodic in both time and frequency domain with a periodicity of M samples. If the modulated sample sequence of Equation 2.18

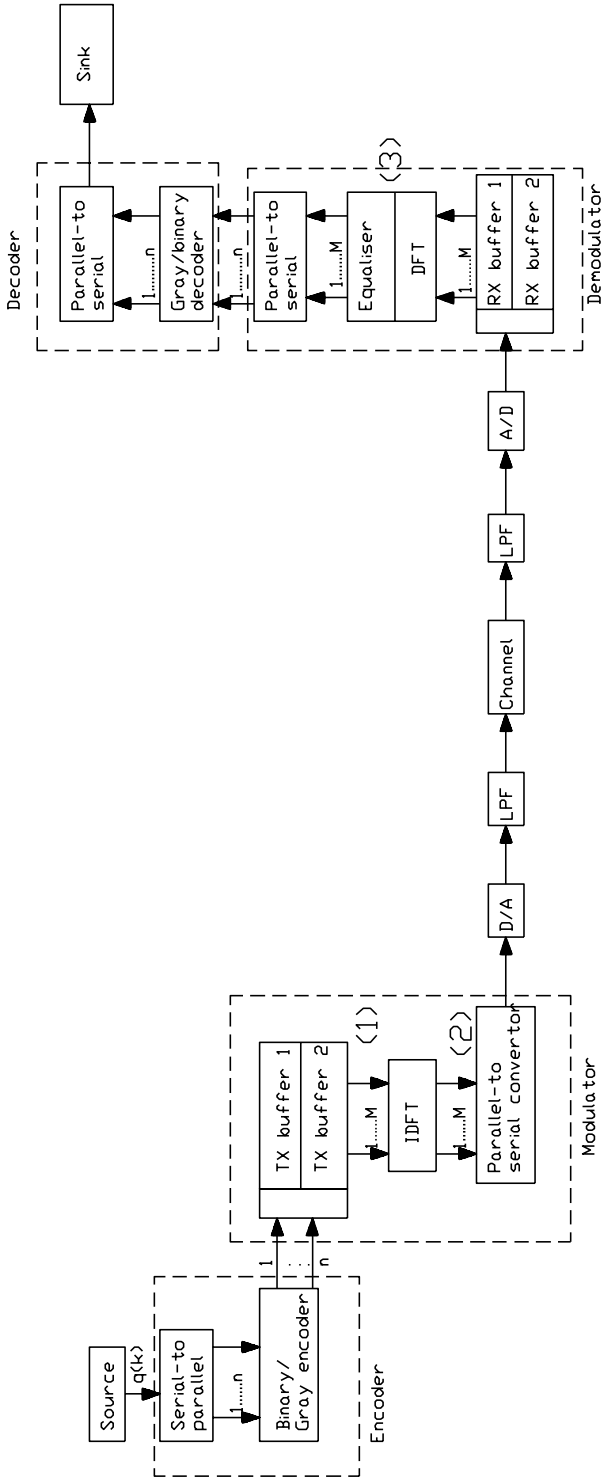


Figure 2.4: FFT-based OFDM modem schematic ©Hanzo, Webb, Keller 2000, [177]

is periodically repeated and transmitted via the lowpass filter (LPF) preceding the channel, the channel is excited with a continuous, periodic signal. However, in order not to waste precious transmission time and hence channel capacity we would like to transmit only one period of $m_0(t)$ constituted by M samples. Assuming a LPF with a cut-off frequency of $f_c = 1/2\Delta t = f_s/2$ and transmitting only one period of $m_0(i\Delta t)$, the channel's input signal becomes:

$$\begin{aligned} m_{0,LPF}(t) &= m_0(i\Delta t) * \frac{1}{\Delta t}\frac{\sin(\pi t/\Delta t)}{\pi t/\Delta t} \\ &= m_0(i\Delta t) * \frac{1}{\Delta t} sinc\frac{\pi t}{\Delta t}, \end{aligned} \tag{2.19}$$

where the LPF's impulse response is given by the *sinc* function and hence $m_{0,LPF}(t)$ has an infinite time domain duration. One period of the periodic modulated signal $m_{0,p}(i\Delta t)$, is given by

$$m_0(i\Delta t) = m_{0,p}(i\Delta t) rect\frac{t}{T}. \tag{2.20}$$

The convolution in Equation 2.19 can be written as:

$$m_{0,LPF}(t) = \sum_{i=0}^{M-1} m_0(i\Delta t)\frac{1}{\Delta t} sinc\frac{\pi(t - i\Delta t)}{\Delta t}. \tag{2.21}$$

In the spectral domain this is equivalent to writing

$$M_{0,LPF}(f) = M_0(f) rect\frac{f}{f_c}, \tag{2.22}$$

where $M_0(f) = FFT\{m_0(i\Delta t)\}$ and $H_{LPF}(f) = rect\frac{f}{f_c}$ is the LPF's frequency domain transfer function. Transforming Equation 2.20 into the frequency domain yields:

$$\begin{aligned} M_0(f) &= FFT\{m_{0,p}(i\Delta t) rect\frac{t}{T}\} \\ &= M_{0,p}(f) * \frac{1}{f_0} sinc\frac{\pi f}{f_0}, \end{aligned} \tag{2.23}$$

where $M_{0,p}(f)$ is the frequency domain representation of $m_{0,p}(i\Delta t)$, which is convolved with the Fourier transform of the $rect\frac{t}{T}$ function. Now $M_0(f)$ of Equation 2.23 is lowpass filtered according to Equation 2.22, giving:

$$\begin{aligned} M_{0,LPF}(f) &= M_0(f) rect\frac{f}{f_c} \\ &= \left[M_{0,p}(f) * \frac{1}{f_0} sinc\frac{\pi f}{f_0}\right] rect\frac{f}{f_c}. \end{aligned} \tag{2.24}$$

So the effect of the time domain truncation of the periodic modulated signal $m_{0,p}(i\Delta t)$ to a single period as in Equation 2.20 manifests itself in the frequency domain as the convolution of Equation 2.23, generating the infinite bandwidth signal $M_0(f)$. When $M_0(f)$ is lowpass

filtered according to Equation 2.24, it becomes bandlimited to f_c, and its Fourier transform pair $m_{0,LPF}(t)$ in Equation 2.19 has an infinite time domain support due to the convolution with $sinc(\pi t/\Delta t)$. This phenomenon results in interference due to time domain overlapping between consecutive transmission blocks, which can be mitigated by quasi-periodically extending $m_0(i\Delta t)$ for the duration of the memory of the channel before transmission. At the receiver only the unimpaired central section is used for signal detection.

In order to portray a practical OFDM scheme and to aid the exposition here and in the previous section, in Figure 2.5 we plotted a few characteristic signals.

Figure 2.5(a) shows the transmitted spectrum using $M = 128$ and rectangular 16-QAM having $I, Q = \pm 1, \pm 3$.

In contrast to Figure 2.3, where the I and Q components were portrayed next to each other in order to emphasise that they belong to the same frequency, here the I and Q components associated with the same frequency are plotted with the same spacing as adjacent sub-bands. In Figure 2.5(a) there are 64 legitimate frequencies between 0 and 4 kHz, corresponding to 128 lines. Observe, however, that for frequencies of 0-300 Hz and 3.4-4.0 kHz we have allocated no QAM symbols. This is because this signal was transmitted after conjugate complex extension and IFFT over the M1020 CCITT telephone channel simulator, which has a high attenuation in these frequency slots. The real modulated signal after IFFT is plotted in Figure 2.5(b), which is constituted by 128 real samples. At the receiver this signal is demodulated by FFT in order to derive the received signal $\tilde{X}(k)$, which is then subjected to hard decision delivering the sequence $\hat{X}(k)$ seen in Figure 2.5(c). Finally, Figure 2.5(d) portrays the error signal $\Delta(k) = X(k) - \tilde{X}(k)$, where large errors can be observed towards the transmission band edges due to the M1020 channel's attenuation. The interpretation of these characteristic signals will be further developed in Section 2.5, as further details of the OFDM system are unravelled.

2.5 Basic OFDM Modem Implementations

A historic OFDM modem implementation was proposed by Hirosaki [14] and is shown in Figure 2.6. This implementation is based on staggered QAM (SQAM) or offset QAM (OQAM), where the quadrature components are delayed by half a signalling interval with respect to each other in order to reduce the signal envelope fluctuation [177]. The system is constituted by M synchronised baseband channels operating with a Baud rate of $f_0 = 1/T$. The baseband modulating signals of sub-channels i and $(i + M/2)$ are amplitude modulated onto the carriers $f_i = [f_0 + (i-1)f_0]$, $i = 1, \ldots, M/2$, with the carrier suppressed. This implies that the sub-channels are spaced according to the Baud rate of $f_0 = 1/T$. Then the sum of the sub-channel signals i and $(i + M/2)$, $i = 1, \ldots, M/2$ form the ith SQAM sub-channel, where the in-phase and quadrature phase modulating signals are shifted by $T/2$ with respect to each other. The transmit and receive filters $G(\omega)$ are identical square-root raised-cosine Nyquist filters and an equaliser implementation is also proposed in [14].

However, Hirosaki's conceptually simple OFDM implementation may become implementationally prohibitive in terms of complexity and cost [14], especially for a high number of sub-channels. Weinstein [9] suggested the digital implementation of OFDM subcarrier modulators/demodulators based on the discrete Fourier transform (DFT).

The DFT and its more efficient implementation, the fast Fourier transform (FFT) are

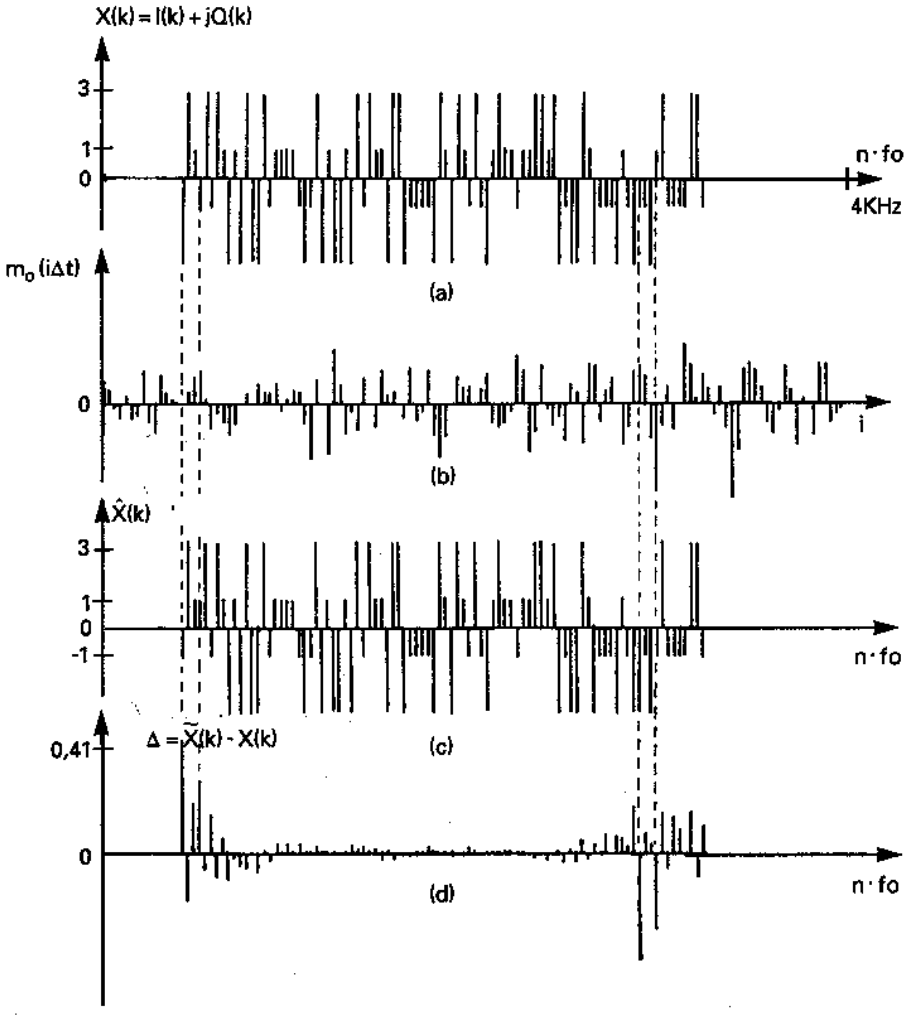


Figure 2.5: Characteristic OFDM signals for $M = 128$ and 16-QAM

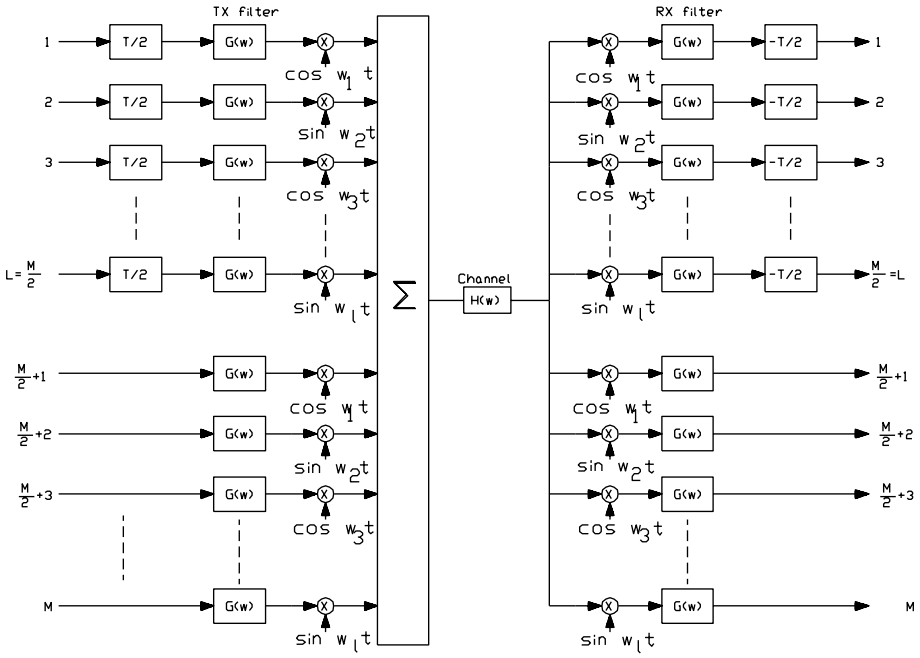


Figure 2.6: Filter-bank implementation of the FDM modem [14] ©IEEE, 1981, Hirosaki

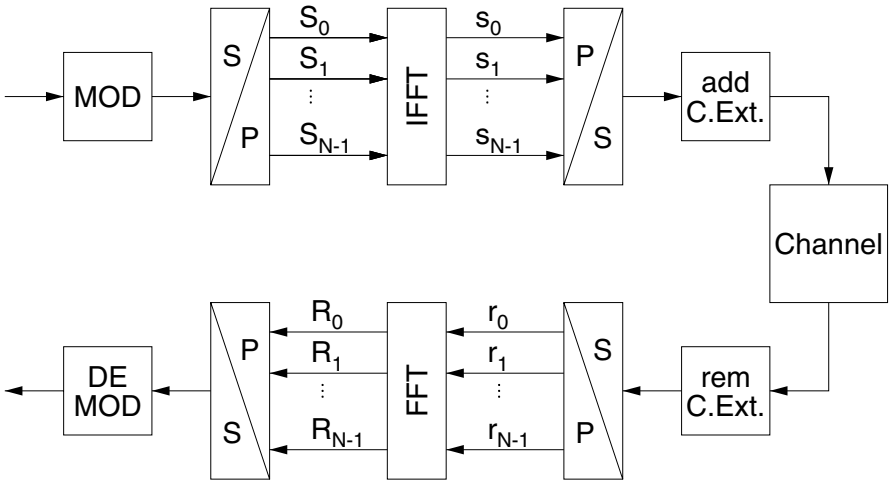


Figure 2.7: Schematic of N-subcarrier OFDM transmission system

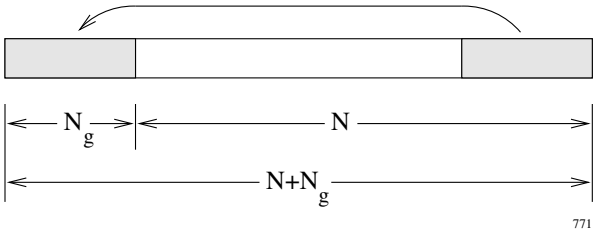


Figure 2.8: Stylised plot of N-subcarrier OFDM time domain signal with a cyclic extension of N_g samples

typically employed in practice in the baseband OFDM modulation/demodulation process, as can be seen in the schematic of Figure 2.7. The serial data stream is mapped to data symbols with a symbol rate of $1/T_s$, employing a general phase and amplitude modulation scheme, and the resulting symbol stream is demultiplexed into a vector of N data symbols S_0 to S_{N-1}. The parallel data symbol rate is $1/N \cdot T_s$, ie. the parallel symbol duration is N times longer than the serial symbol duration T_s. The inverse FFT (IFFT) of the data symbol vector is computed and the coefficients s_0 to s_{N-1} constitute an OFDM symbol. The s_n are the time domain samples of the OFDM symbol and are transmitted sequentially over the channel at a symbol rate of $1/T_s$. At the receiver, a spectral decomposition of the received time domain samples r_n is computed employing an N-tap FFT, and the recovered data symbols R_n are restored in serial order and demultiplexed.

If we assume that the bandwidth of the OFDM spectrum is finite, then simple Fourier theory dictates that the corresponding time domain signal has an infinite duration. The underlying assumption upon invoking the IFFT for modulation is that although N frequency domain samples produce N time domain samples, the time domain signal is assumed to be periodically repeated, theoretically, for an infinite duration. In practice, however, it is sufficient to repeat the time domain signal periodically for the duration of the channel's memory, i.e. for a duration that is comparable to the length of the CIR. Hence, for transmission over time-dispersive channels, each time domain OFDM symbol is extended by the so-called cyclic extension (C. Ext. in Figure 2.7) or a guard interval of N_g samples duration, in order to overcome the inter-OFDM symbol interference due to the channel's memory.

The samples of the cyclic extension are copied from the end of the time domain OFDM symbol, generating the transmitted time domain signal $(s_{N-N_g-1}, \ldots, s_{N-1}, s_0, \ldots, s_{N-1})$ depicted in Figure 2.8. At the receiver, the samples of the cyclic extension are discarded. Clearly, the need for a cyclic extension in time dispersive environments reduces the efficiency of OFDM transmissions by a factor of $N/(N + N_g)$. Since the duration N_g of the necessary cyclic extension depends only on the channel's memory, OFDM transmissions employing a high number of carriers N are desirable for efficient operation. Typically a guard interval length of not more than 10% of the OFDM symbol's duration is employed.

2.6 Cyclic OFDM Symbol Extension

As we have seen in Section 2.4, the response of the low pass filtered OFDM channels to a block of modulated signal is theoretically infinite. A low-complexity technique of pre-

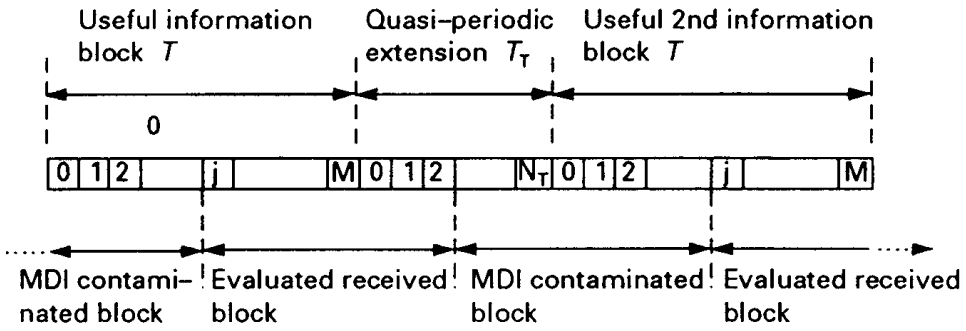


Figure 2.9: Reducing the interference of time-domain OFDM symbols by quasi-periodic block extension

venting the interference of consecutive OFDM symbols is to transmit quasi-periodically extended time domain OFDM symbols, after modulation by IFFT [15]. The required length of the quasi-periodic time-domain OFDM symbol extension depends on the channel's memory, in other words, on the length of the transient response of the channel, when subjected to the quasi-periodic excitation constituted by the time-domain OFDM modulated signal. The method is best explained with reference to Figure 2.9. Every block of length-T modulated signal segment is quasi-periodically extended by a length of T_T transient duration simply repeating N_T samples of the useful information block. Then the total sequence length becomes $(M + N_T)$ samples, corresponding to a duration of $(T + T_T)$. Trailing and leading samples of this extended block are corrupted by the channel's transient response, hence the receiver is instructed to ignore the first j number of samples of the received block and also disregard $(M + N_T - j)$ trailing samples. Only the central M number of samples are demodulated by FFT at the receiver, which are essentially unaffected by the channel's transient response, as seen in Figure 2.9.

The number of quasi-periodic extension samples N_T required depends on the length of the channel's transient response and on the number of modulation levels. If the number of modulation levels is high, the maximum acceptable time-domain OFDM symbol interference imposed by the channel transients must be kept as low as possible in order to maintain sufficient noise margins before the data is corrupted. This then requires a longer quasi-periodic extension, i.e. N_T must be also higher. It must also be appreciated that this interference-contaminated extension actually wastes channel capacity as well as transmitted power. However, if the useful information blocks are long, i.e. $M \geq 128$, the extension length can be kept as low as 10% of the useful information block length.

2.7 Decision-Directed Adaptive Channel Equalisation

In this section it will be assumed that the time-domain inter-OFDM symbol interference was removed by the quasi-periodic block extension. The linear distortions introduced by the unequalised channel transfer function $H(f)$ can be removed by estimating $H(if_0)$ and then dividing the received signal spectrum by $H(if_0)$, before hard decision decoding is performed

using the function $D\{\ \}$.

As mentioned above, $H(if_0)$ can be determined using a preamble having a real-valued "white" spectrum. By setting all real spectral lines to unity and all imaginary lines to zero in the preamble data frame, after modulation by the IFFT the transmitted signal is the Kronecker delta. Therefore the received signal is the channel's impulse response, which after demodulation by FFT gives the channel's frequency domain transfer function $H(if_0)$. The received signal's spectrum after demodulation by FFT becomes:

$$\tilde{X}_i = H(if_0)X_i,\ i = 1, \ldots,\ M, \tag{2.25}$$

where X_i is the ith transmitted spectral line at frequency if_0. After equalisation by dividing the received spectral line $\tilde{X}_i$ with the estimated channel transfer function $H(if_0)$ and taking hard decisions, we obtain the recovered sequence:

$$\hat{X}_i = D\left\{\frac{\tilde{X}_i}{H(if_0)}\right\},\ i = 1, \ldots,\ M. \tag{2.26}$$

If the recovered sequence $\hat{X}_i$ is error-free, it lends itself to the recursive recomputation of the channel's frequency response in order to cope with slowly time-varying transmission media [15]. The updated transfer function is given by:

$$H_a(if_0) = \frac{\tilde{X}_i}{\hat{X}_i} = \frac{\tilde{X}_i}{D\left\{\frac{\tilde{X}_i}{H(if_0)}\right\}},\ i = 1, \ldots,\ M. \tag{2.27}$$

In order to retain robustness for transmissions over channels having high bit error rate a leaky algorithm can be introduced to generate a weighted average of the previous and current transfer function using the leakage factor β in the following fashion:

$$H_{\text{adaptive}}(if_0) = \beta H_a^k(if_0) + (1-\beta)H_a^{k-1}(if_0). \tag{2.28}$$

The leakage factor β is a parameter determined by the prevailing channel bit error rate.

An interesting aspect of our OFDM scheme is that if the channel varies slowly, then using differential coding between corresponding sub-channels of consecutive OFDM transmission frames removes the requirement for a channel equaliser as long as the difference is computed before a hard decision takes place [9]. This is due to the fact that spectral lines of the same sub-channel or same frequency will suffer the same attenuation due to the channel's linear distortion. Hence the effect of channel attenuation and phase shift drops out before hard decision takes place. Similar arguments can be exploited between adjacent lines of the same OFDM transmission frame as well, if the channel's transfer characteristic is sufficiently smooth.

If the frequency domain transfer function $H(if_0)$ is more erratic as a function of frequency or time, a number of known pilot tones can be included in the transmitted spectrum. These pilots facilitate the more accurate estimation and equalisation of the channel transfer function. This technique was proposed by Cimini for wide-band, frequency-selective multipath mobile channels in reference [10] and it will be widely used throughout the forthcoming chapters. In case of narrowband Rayleigh-fading mobile radio channels the fading is "fre-

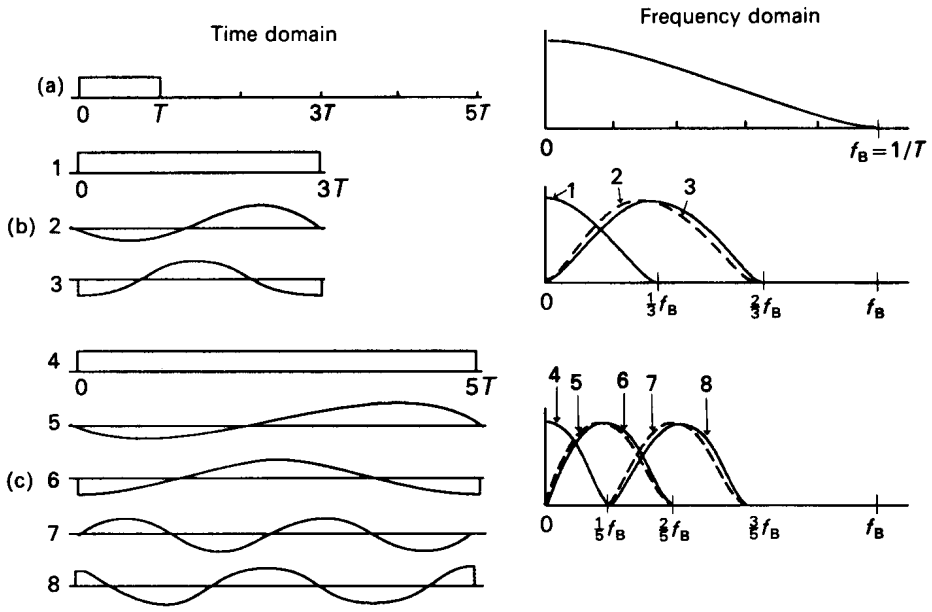


Figure 2.10: OFDM carriers, their stylised spectra and bandwidth requirement: (a) one-carrier system, (b) three-carrier system, (c) five-carrier system [182] ©Springer, 1969, Harmuth

quency flat fading", hence each transmitted frequency component suffers the same attenuation and phase shift. In this case time domain pilot symbols employed as in the Pilot Symbol Assisted Modulation (PSAM) schemes of Chapter 10 in [177] are useful in supporting the tracking of the Rayleigh fading envelope [181]. A detailed discourse on sophisticated two-dimensional pilot symbol-assisted channel estimation techniques is provided in Chapter 14 of the extended version of this book [90].

2.8 OFDM Bandwidth Efficiency

In the OFDM system each symbol to be transmitted modulates an assigned carrier of a set of wide-sense orthogonal basis functions and these modulated sub-channel signals are superimposed for transmission via the communications channel. The received signal can be demodulated for example by the correlation receiver described in the previous section or by FFT.

A set of suitable wide-sense orthogonal basis functions of gradually increasing length T, $3T$ and $5T$, similar to those used in our OFDM schemes, is depicted in Figure 2.10 for a one-carrier, three-carrier and five-carrier system, respectively [182, 183].

Both their time domain waveforms and stylised spectra are shown in Figure 2.10. In a simplistic approach here we assume that the signal spectra can be band limited to the bandwidth of its main spectral lobe, as suggested by the figure.

Using an essentially serial system with one carrier, as seen in Figure 2.10(a), the minimum

bandwidth required is $f_B = 1/T$ and the bandwidth efficiency is $\eta = 1$ Bd/Hz because the spectrum of this pulse is represented by the sinc function whose first zero is at $f_B = 1/T$. The three-carrier system of Figure 2.10(b) expands the length of the basis functions to $3T$, thereby reducing the bandwidth requirement to $B = \frac{2}{3} f_B$, giving $\eta = 1.5$ Bd/Hz. This is because the rectangularly windowed sin and cos spectra are represented by the convolution of a tonal spectral line and a frequency domain sinc function describing the spectrum of the rectangular time domain window. The five-carrier scheme using basis functions of $5T$ length further reduces the bandwidth to $B = \frac{3}{5} f_B$ and increases the spectral efficiency to 1.67 Bd/Hz.

Similarly, the approximate bandwidth of a $(2M + 1)$-carrier system using an impulse as well as M sine and M cosine carriers of length $(2M + 1)T$ becomes

$$B = \frac{M + 1}{2M + 1} \frac{1}{T}, \tag{2.29}$$

yielding a bandwidth efficiency of

$$\eta = \frac{2M + 1}{M + 1} \text{ Bd/Hz}. \tag{2.30}$$

When $M \to \infty$, we have $\lim_{M \to \infty} \eta = 2$ Bd/Hz, which for a typical value of $M = 64$ gives $\eta = 129/65 = 1.98$ Bd/Hz. The interferences caused by the above band limitation are given in closed form in [183] for a variety of carriers, but for the more attractive scenarios using a higher number of carriers it can only be estimated by simulation studies.

2.9 Chapter Summary and Conclusion

In this chapter we have investigated orthogonal multiplexing as an attractive means of transmitting high-rate information over highly dispersive mobile radio channels. The essential premise of orthogonal multiplexing is that of dividing the serial input data stream into a high number of parallel streams and to transmit these low-rate parallel streams simultaneously. This offered two main advantages. First, by increasing the subchannels' symbol duration – owing to the low sub-channel signalling rate – the probability of the subchannel symbols becoming corrupted by dispersion was substantially reduced, thus no channel equaliser was required. The modulation scheme of each of these orthogonal subchannels may be arbitrarily chosen or even adapted on a time-variant basis.

Naturally, OFDM also has a number of disadvantages. One of the most notorious one is that it requires a linear amplification and the corresponding so-called class-A amplifiers exhibit a low power-efficiency. Alternatively, sophisticated peak-to-average power reduction techniques have to be used.

Following this rudimentary introduction to the basic concepts of OFDM, in the forthcoming chapters we will delve into the various design issues of OFDM more deeply, considering a range of associated research and implementational aspects.

Chapter 3

OFDM Transmission over Gaussian Channels

High data rate communications over additive white Gaussian noise (AWGN) channels are limited not only by noise, but especially with increasing symbol rates, often more significantly by the intersymbol interference (ISI) due to the memory of the dispersive wireless communications channel. Explicitly, this channel memory is caused by the dispersive channel impulse response (CIR) due to the different length propagation paths between the transmitting and the receiving antennae. This dispersion effect could theoretically be measured by transmitting an infinitely short impulse and "receiving" the channel impulse response itself. On this basis, several measures of the effective duration of the impulse response can be calculated, one being the delay spread. The multipath propagation of the channel manifests itself by different echoes of possibly different transmitted symbols overlapping at the receiver, which leads to error rate degradation.

This effect occurs not only in wireless communications, but also over all types of electrical and optical waveguides, although for these media the relative time differences are comparatively small, mostly due to multimode transmission or incorrect electrical or optical adaption at interfaces.

In wireless communications systems the duration and the shape of the channel impulse response depend heavily on the propagation environment of the communications system in question. While indoor wireless networks typically exhibit only short relative delays, outdoor networks, like the Global System for Mobile (GSM) [177] can face maximum delays spreads in the order of 15 μs.

As a general rule, the effects of ISI on the transmission error statistics are negligible, as long as the delay spread is significantly shorter than the duration of one transmitted symbol. This implies that the symbol rate of communications systems is practically limited by the channel's memory. For higher symbol rates, there is typically significant deterioration of the system's error rate performance.

If symbol rates exceeding this limit are to be transmitted over the channel, mechanisms

OFDM and MC-CDMA: A Primer L. Hanzo and T. Keller
© 2006 John Wiley & Sons, Ltd

must be implemented in order to combat the effects of ISI. Channel equalisation techniques can be used to suppress the echoes caused by the channel. To perform this operation, the channel impulse response must be estimated. Significant research efforts were invested into the development of such channel equalisers, and most wireless systems in operation use equalisers to combat ISI.

There is, however, an alternative approach towards transmitting data over a multipath channel. Instead of attempting to cancel the effects of the channel's echoes, orthogonal frequency division multiplexing (OFDM) [177] modems employ a set of harmonically related carriers in order to transmit information symbols in parallel over the channel. Since the system's data throughput is the sum of all the parallel channels' throughputs, the data rate per sub-channel is only a fraction of the data rate of a conventional single-carrier system having the same throughput. This allows us to design a system supporting high data rates, while maintaining symbol durations much longer than the channel's memory, thus circumventing the need for channel equalisation.

3.1 Orthogonal Frequency Division Multiplexing

3.2 Choice of the OFDM Modulation

Modulation of the OFDM subcarriers is analogous to the modulation in conventional serial systems. The modulation schemes of the subcarriers are generally quadrature amplitude modulation (QAM) or phase shift keying (PSK) [177] in conjunction with both coherent and non-coherent detection. Differential coded star-QAM (DSQAM) [177] can also be used. If coherently detected modulation schemes are used, then the reference phase of the OFDM symbol must be known, which can be acquired with the aid of pilot tones [181] embedded in the spectrum of the OFDM symbol, as will be discussed in Chapter 4. For differential detection the knowledge of the absolute subcarrier phase is not necessary, and differentially coded signalling can be invoked either between neighbouring subcarriers or between the same subcarriers of consecutive OFDM symbols.

3.3 OFDM System Performance over AWGN Channels

As the additive white Gaussian noise (AWGN) in the time domain channel corresponds to AWGN of the same average power in the frequency domain, an OFDM modem's performance in an AWGN channel is identical to that of a serial modem. Analogously to a serial system, the bit error rate (BER) versus signal-to-noise rate (SNR) characteristics are determined by the frequency domain modulation scheme used. In Figure 3.1 the simulated BER versus SNR curves for binary phase shift keying (BPSK), differential BPSK (DBPSK), quaternary phase shift keying (QPSK), differential QPSK (DQPSK) and coherent 16-quadrature amplitude modulation (16-QAM) are shown, together with the theoretical BER curves of serial modems, as derived in [184]:

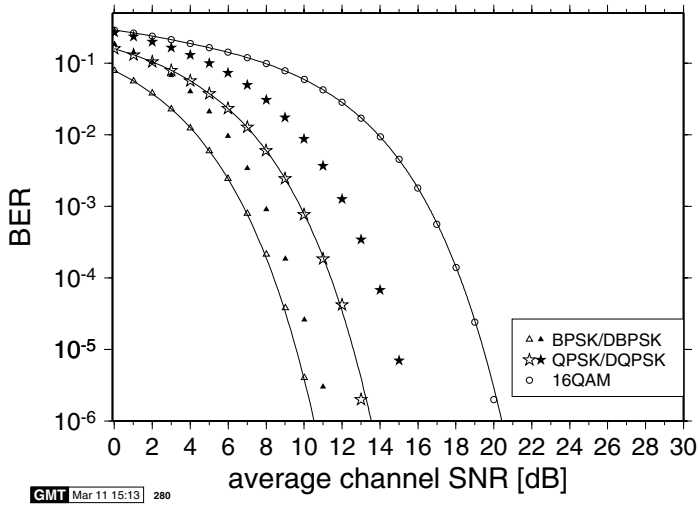


Figure 3.1: BER versus SNR curves for the OFDM modem in AWGN channel using BPSK, DBPSK, QPSK, DQPSK, and 16-QAM. The lines indicate the theoretical performance of the coherently detected modulation schemes in a serial modem over AWGN channels

$$p_{e,BPSK}(\gamma) = Q(\sqrt{2\gamma}), \tag{3.1}$$

$$p_{e,QPSK}(\gamma) = Q(\sqrt{\gamma}), \tag{3.2}$$

$$p_{e,16QAM}(\gamma) = 0.75 \cdot Q\left(\sqrt{\frac{\gamma}{5}}\right) 0.25 \cdot Q\left(\sqrt{\frac{\gamma}{5}}\right), \tag{3.3}$$

where γ is the SNR and the Gaussian $Q()$-function is defined as

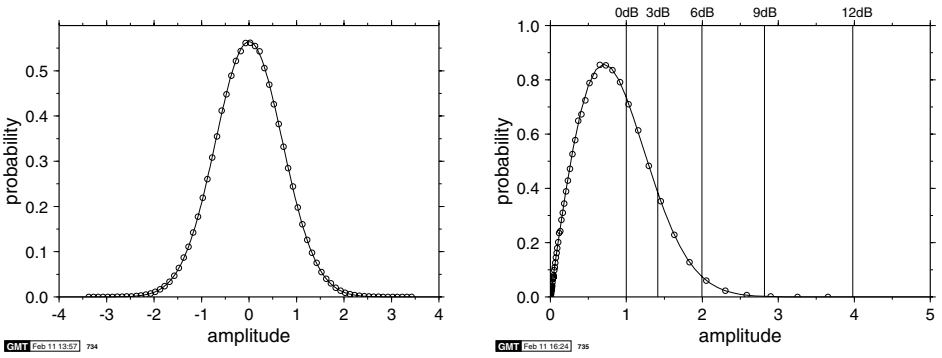
$$Q(y) = \frac{1}{\sqrt{2\pi}} \int_y^\infty e^{-x^2/2} dx = \text{erfc}\left(\frac{y}{\sqrt{2}}\right).$$

It can be seen from Figure 3.1 that the experimental BER performance of the OFDM modem is in very good accordance with the theoretical BER curves of conventional serial modems in AWGN channels.

3.4 Clipping Amplification

3.4.1 OFDM Signal Amplitude Statistics

The time domain OFDM signal is constituted by the sum of complex exponential functions, whose amplitudes and phases are determined by the data symbols transmitted over the different carriers. Assuming random data symbols, the resulting time domain signal exhibits an amplitude probability density function (PDF) approaching the two-dimensional or complex Gaussian distribution for a high number of subcarriers. Figure 3.2(a) explicitly shows that the



(a) I/Q PDF

(b) amplitude PDF

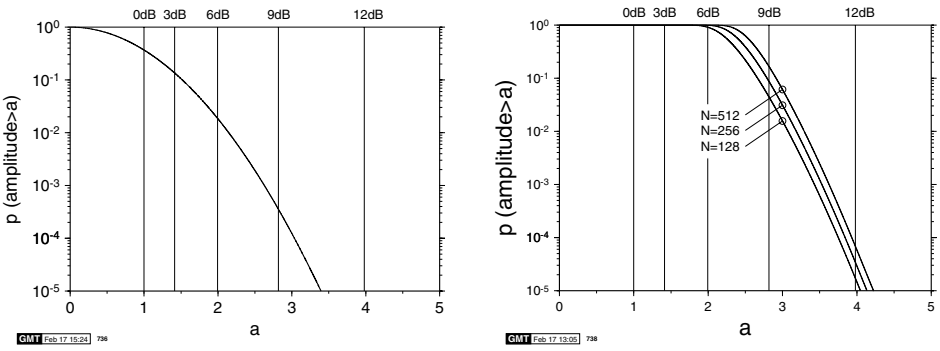
Figure 3.2: Statistics of OFDM time domain signal: (a) amplitude histogram of the I component of a 256-subcarrier OFDM signal (markers) obeying a Gaussian PDF (continuous line) with $\sigma = 1/\sqrt{2}$; (b) two-dimensional amplitude histogram (markers) following a Rayleigh PDF (continuous line) with $\sigma = 1/\sqrt{2}$. The vertical lines in (b) indicate the corresponding powers above mean in decibels

measured amplitude histogram of the in-phase (I) component of a 256-subcarrier OFDM signal obeys a Gaussian distribution with a standard deviation of $\sigma = 1/\sqrt{2}$. The mean power of the signal is $2\sigma^2 = 1$. As the amplitude distribution in both the in-phase and the quadrature phase (Q) component is Gaussian, the two-dimensional amplitude histogram follows a complex Gaussian, or in other words, a Rayleigh distribution [184] with the same standard deviation. The observed amplitude histogram of the 256-subcarrier OFDM signal and the corresponding Rayleigh probability density function are depicted in Figure 3.2(b). The vertical grid lines in the figure indicate the relative amplitude above the mean value in decibels. It can be seen that unlike full response serial modulation schemes – which have a more limited range of possible output amplitudes – the parallel modem's output signal exhibits strong amplitude fluctuations. Note that the standard deviation σ of the probability density functions depicted in Figure 3.2(a) is independent of the number of subcarriers employed, since the mean power of the signal is normalised to 1.

The probability of the instantaneous signal amplitude being above a given threshold, the cumulative density function (CDF), is depicted in Figure 3.3(a). It can be noted that the probability of the signal amplitude exceeding the 6 dB mark is about 1.1%, while the 9dB mark is exceeded with a probability of about $3.5 \cdot 10^{-4}$. The signal amplitude is higher than the average by 10.6 dB with a probability of 10^{-5}.

3.4.2 Clipping Amplifier Simulations

In order to evaluate the effects of a non-linear amplifier on the performance of an OFDM system, simulations have been conducted employing a simple clipping amplifier model. This clipping amplifier limits the amplitude of the transmitted signal to a given level, without perturbing the phase information. This amplitude limitation of the time domain signal affects both the received symbols on all subcarriers in the OFDM symbol, as well as the frequency



(a) signal CDF (b) peak CDF

Figure 3.3: OFDM time domain signal: probability of (a) the instantaneous signal amplitude and (b) the peak amplitude per OFDM symbol being above a given threshold value. The lines indicate the corresponding power levels above the mean. The peak value CDF depends on the number of subcarriers, and curves are shown for 128, 256 and 512 carriers

domain out-of-band emissions, and therefore increases the interference inflicted on adjacent carriers.

In Figure 3.3(a) the probability of the instantaneous signal amplitude exceeding a given level was shown. As amplitude limitation in the time domain affects all the subcarriers in the OFDM symbol, the probability of the time domain peak amplitude per OFDM symbol period being clipped by the amplifier is the probability of at least one of the N time domain samples exceeding a given amplitude limit. This clipping probability for a given maximal amplifier amplitude a is displayed in Figure 3.3(b). It can be observed that the clipping probability per OFDM symbol is dependent on the number of subcarriers employed.

Given the information in Figure 3.3(b), the necessary amplifier back-off for an OFDM transmitter can be determined. If the acceptable clipping probability per OFDM symbol is 10^{-5}, then the necessary amplifier back-off values would be 12.1 dB, 12.3 dB, and 12.5 dB for a 128, 256, and 512 subcarrier OFDM modem, respectively. If a clipping probability of 10^{-4} is acceptable, then these back-off values can be reduced by about 0.6 dB.

3.4.2.1 Introduction to Peak-Power Reduction Techniques

Two main types of peak-to-mean power ratio reduction techniques have been investigated in the literature, which rely on either introducing redundancy in the data stream or on post-processing the time domain OFDM signal before amplification, respectively. In this section we provide a rudimentary introduction to the problem and provide some quantitative results characterising the performance impairments imposed by the peak-to-mean power ratio fluctuations. A significantly more detailed exposure of the associated issues is provided in the detailed version of this monograph [90].

Shepherd [48], Jones [49], and Wulich [50] suggest different coding techniques which aim to ensure that only low peak power OFDM symbols are chosen for transmission, whilst excluding the transmission of the specific combinations of modulating bits that are known to result in the highest peak factors. These schemes can be viewed as simple k out of n block

codes. Depending on the tolerable peak to mean power ratio, the set of acceptable OFDM symbols is computed and the data sequences are mapped onto OFDM symbols from this set only. These techniques reduce the data throughput of the system, but mitigate the severity of clipping amplification.

Müller [51] proposes techniques based on generating a set of OFDM signals by multiplying the modulating data vector in the frequency domain with a set of different phase vectors known to both the transmitter and the receiver, before applying the IDFT. The transmitter will then choose the resulting OFDM symbol exhibiting the lowest peak factor and transmits this together with the chosen phase vector's identification. This technique reduces the average peak factors and requires only a low signalling overhead, but cannot guarantee a given maximum peak factor.

Another group of peak amplitude limiting techniques is based on modifying the time domain signal, where its amplitude exceeds the given peak amplitude limit. Straightforward clipping falls into this category, but induces strong frequency domain out-of-band emissions. In order to avoid the spectral domain spillage of hard clipping, both multiplicative and additive time domain modifications of the OFDM signal have been investigated. Pauli [52] proposes a multiplicative correction of the peak values and their adjacent samples using smooth Gaussian functions for limiting out-of-band emissions. However, multiplying the time domain signal with the time-varying amplitude limiting function introduces intersubcarrier interference.

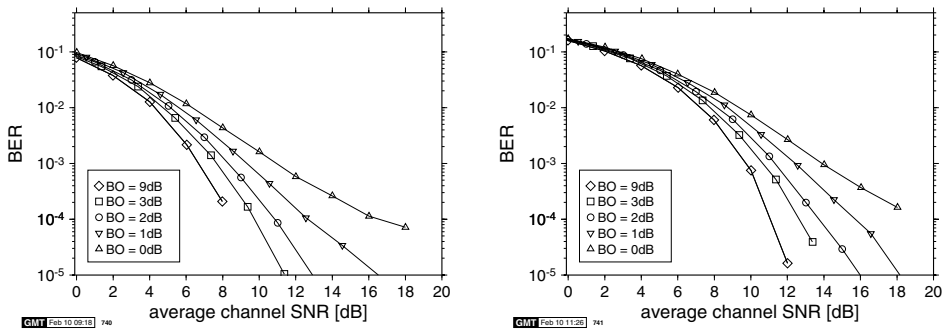
A similar technique, using additive instead of multiplicative amplitude limiting, is described by May [53]. A smoothly varying time domain signal is added to the time domain signal, which has been optimised for low out-of-band emissions. As the DFT is a linear operation, adding a correction signal in the time domain will overlay the frequency domain data symbols with the DFT of the correction signal, introducing additional noise.

As an alternative solution, Wulich [54] suggests measuring the peak amplitude in each OFDM time domain symbol and scaling the amplitude for the whole OFDM symbol, so that the peak value becomes constant from symbol to symbol. At the receiver, an amplitude correction similar to pilot-assisted scaling over fading channels has to be performed. The advantage of this technique is that the system's throughput is not reduced by introducing redundant information, nor is the orthogonality of the subcarriers impaired. As the OFDM symbol energy is fluctuating with the peak power exhibited by the different OFDM symbols, however, the BER performance of the system is impaired.

A further approach to reducing the amplifier linearity requirements, and which relies on the findings of Figure 3.3(b), is to split an OFDM symbol into groups of subcarriers, which are processed by IFFT, amplified and transmitted over separate transmit chains. This system, referred to as clustered OFDM, has been proposed by Daneshrad and Cimini [59], and combines the advantages of reduced peak power in each transmitter chain with additional spatial diversity from the use of multiple transmit antennas, which can be exploited by coding or OFDM-CDMA techniques.

3.4.2.2 BER Performance Using Clipping Amplifiers

If lower back-off values are chosen and no peak power reduction techniques are employed in the OFDM transmission system, then the clipping amplifier will influence both the performance of the OFDM link as well as the out-of-band emissions. The effects of the amplifier



(a) BPSK (b) QPSK

Figure 3.4: Influence of amplitude clipping on BER performance of an OFDM modem

back-off value on the BER performance in an AWGN channel for coherently detected 512-subcarrier BPSK and QPSK OFDM transmission are depicted in Figure 3.4.

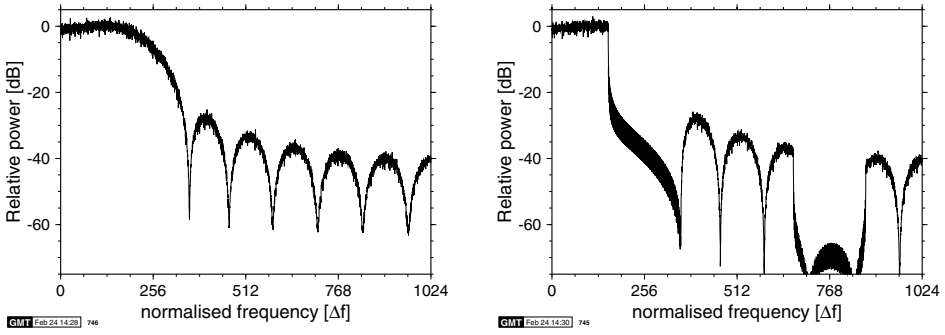
The investigated amplifier back-off values range from 9 dB down to 0 dB. According to Figure 3.3(b), an amplifier back-off of 9 dB results in a clipping probability per OFDM symbol of about 17%, while an amplifier back-off of 0 dB results in nearly certain clipping of every transmitted OFDM symbol.

It can be observed in Figure 3.4 for both BPSK and QPSK that for an amplifier back-off value of 9 dB the BER performance is indistinguishable from the non-limited case, which was portrayed in Figure 3.1. For smaller back-off values, however, the effects of clipping on the BER performance are more severe. A 3 dB amplifier back-off results in a SNR penalty of about 1.3 dB at a BER of 10^{-4}, and a back-off of 0 dB results in more than 8 dB SNR penalty at the same BER.

The BER performance of the OFDM modem can be improved slightly if the receiver's decision boundaries are adjusted according to the amplitude loss in each subcarrier due to the overall signal power loss, which was observed by O'Neill and Lopes [185]. In fading channels this amplitude adjustment would be performed in conjunction with the channel estimation.

3.4.2.3 Signal Spectrum with Clipping Amplifier

The simulated spectrum of a 512-subcarrier OFDM signal is shown in Figure 3.5. Figure 3.5(a) depicts the spectrum of the transmitted signal, when all 512 subcarriers are used for data transmission. A raised cosine Nyquist filter with an excess bandwidth of $\alpha = 0.35$ was used for pulse shaping, resulting in a relatively slow fall-off of the power spectral density outside the FFT bandwidth of $\pm 256\Delta f$. In order to avoid adjacent channel interference due to spectral overlapping, an adjacent carrier must be placed at a frequency distance considerably higher than the data symbol rate. If a tighter spectral packing of adjacent carriers is important, then pulse shaping filters with a steeper frequency transfer function have to be employed, which are more complex to implement. Since in this scenario all the subcarriers are used for data transmission, the time domain samples are uncorrelated and therefore the spectrum in Figure 3.5(a) is equivalent to that of a serial modem transmitting at the same sample rate and



(a) no virtual carriers

(b) 200 virtual carriers

Figure 3.5: Spectrum of a 512-subcarrier OFDM signal using raised-cosine Nyquist pulse shaping filter with an excess bandwidth of $\alpha = 0.35$: (a) no virtual subcarriers, (b) 2×100 subcarriers at the edges of the spectrum. The characteristic sinc-signal shaped curve of this figure is a consequence of rectangular windowing used in the spectral estimation. This effect can be mitigated by smoother windowing.

employing the same pulse shaping filter.

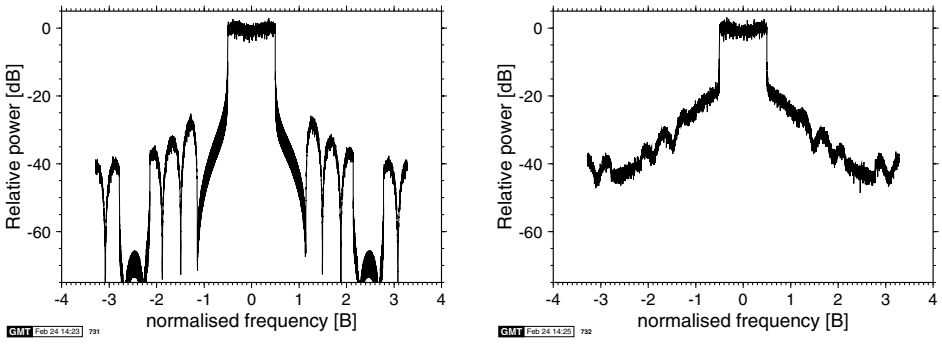
Figure 3.5(b) depicts the signal spectrum of a 512-subcarrier modem employing 200 virtual subcarriers at the edges of the bandwidth, which are effectively disabled and carry no energy. Although the same pulse shaping filter was employed as in Figure 3.5(a), the resulting spectral shape is nearly rectangular, with a drop of approximately 20 dB within one subcarrier distance Δf outside the signal bandwidth. Comparing this spectrum with Figure 3.5(a) it can be observed that the overall shape of the spectrum is determined by the pulse shaping filter, while the employment of disabled virtual subcarriers cuts out parts of the spectrum. It can be seen from the spectrum that by employing virtual subcarriers a very tight power spectrum can be obtained with a simple pulse shaping filter. This rectangular signal spectrum allows tight packing of adjacent carriers, therefore enhancing the spectral efficiency of an OFDM system.

The effects of a clipping amplifier on the OFDM signal spectrum are demonstrated in Figure 3.6. Specifically, Figure 3.6(a) shows the spectrum corresponding to the system employed in the context of Figure 3.5(b), but with the amplifier back-off set to 9 dB. The frequency axis is normalised to the signal bandwidth of $B = 312 \cdot \Delta f$ due to the disabled carriers and the power spectral density is normalised to the average signal power in the signal band. Comparison of Figure 3.6(a) and 3.5(b) shows no discernible change in the spectral domain.

Reducing the amplifier back-off results in increased out-of-band emissions. Figure 3.6(b) shows the averaged power spectral density of the same system with an amplifier back-off of 0 dB. In this case, the spectral spillage is apparent directly outside the signal band.

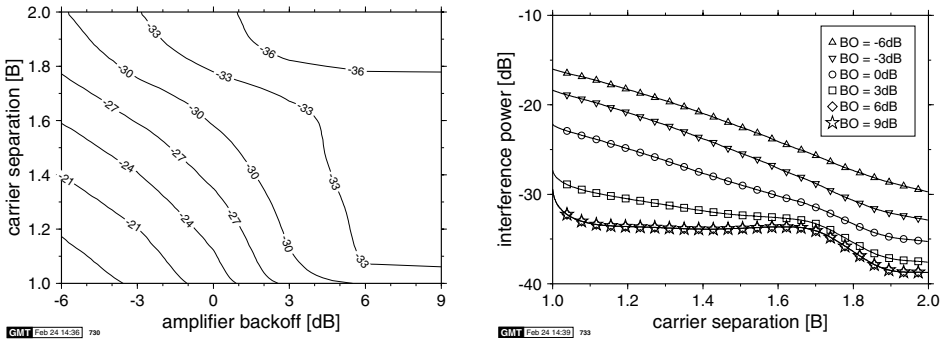
Since the amplitude limiting of the transmitted time domain signal is due to the power amplifier, no bandlimiting filtering is performed after the amplitude distortion. Li and Cimini [186] proposed employing a hard limiter and a lowpass filter before the non-linear amplification stage. In this case, the out-of-band emissions can be reduced, while the BER penalty due to hard limiting the time domain signal still applies.

In order to evaluate the amount of adjacent channel interference caused by non-linear am-



(a) BO = 9dB (b) BO = 0dB

Figure 3.6: Power spectra of a 512-subcarrier OFDM modem employing 200 virtual carriers and Nyquist filtering with an excess bandwidth of 0.35. The frequencies are normalised to the signal bandwidth of $B = 312 \cdot \Delta f$: (a) 9 dB amplifier back-off (BO), (b) 0 dB amplifier back-off



(a) interference power (dB) vs. carrier separation and BO (b) iso-interference plot (dB)

Figure 3.7: Integrated adjacent channel interference power (dB) in a signal bandwidth of B for different values of normalised carrier separation and amplifier back-off

plification of the OFDM signals, the total interference power in a frequency domain window of width B having a variable frequency offset was integrated and normalised by the in-band power for varying values of amplifier back-off. Figure 3.7(b) shows the results of this integration for amplifier back-off values up to 9 dB and adjacent carrier separations from B to $2B$. A carrier separation of B corresponds to directly adjacent signal bands, and such a set-up would approach the maximal possible system throughput of 2 symbols/s/Hz or 2 Baud/Hz.

It can be observed from the figure that the integrated interference levels are indistinguishable for amplifier back-off values of 6 dB and 9 dB. The integrated interference level in this case is below -30 dB with directly adjacent carriers and below -33 dB for all carrier separation values above $1.03B$. The drop in interference for carrier separations above $1.7B$ is due to the frequency domain image of the virtual carriers that can be seen in Figure 3.6(a) at frequencies between $2.2B$ and $3.8B$. For a back-off value of 3 dB the interference is approximately 1 dB worse than for the higher back-off values for carrier separations above $1.5B$, and this difference is up to 5 dB for smaller carrier separations.

For a back-off value of 0 dB, which corresponds to the spectrum shown in Figure 3.6(b), the integrated interference is below -22.5 dB for all carrier separations. The figure also shows two graphs for negative amplifier back-off values for comparison, which exhibit considerably higher interference values. Since negative back-off values imply amplifier clipping below the nominal mean power of the signal, this would not be a likely case at the transmitter's power amplifier.

3.4.3 Clipping Amplification – Summary

We have seen that for OFDM transmission a considerable amplifier back-off is necessary, in order to maintain the BER and spectral characteristics of the ideal OFDM system. This complicates the transmitter design and leads to inefficient power amplifier applications.

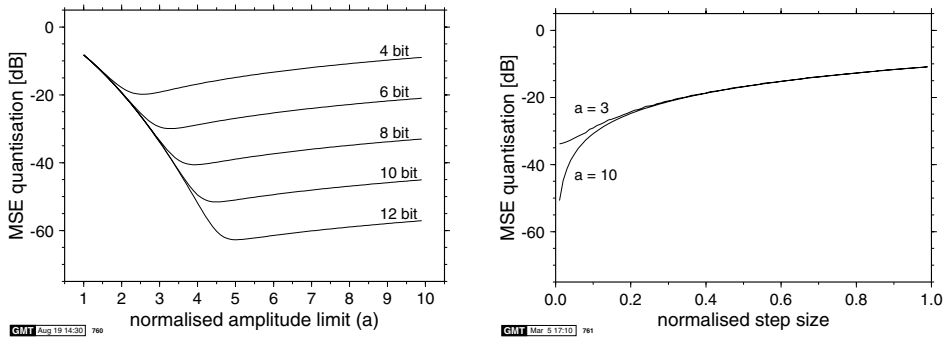
Although a 512-subcarrier OFDM modem is capable of producing a peak-to-average power ratio of up to 27 dB, we have seen that much lower amplifier back-off values result in acceptable system performance. A back-off of 12.5 dB results in only one of 10^5 OFDM symbols suffering clipping at all, and we have seen for a 6 dB back-off that both the BER performance as well as the averaged spectrum are indistinguishable from the ideally amplified scenario.

3.5 Analogue-to-Digital Conversion

We saw in Figure 3.2 that the time domain OFDM signal follows a two-dimensional or complex Gaussian distribution. The distribution of signal amplitudes determines the necessary parameters of the analogue-to-digital convertor (ADC) at the receiver. We have investigated the effects of the receiver input ADC on the BER performance of an OFDM system in an AWGN channel environment.

Since an ADC transforms the continuous analogue input signal to discrete-valued digital information, the original input signal is not preserved perfectly. As the dynamic range of an ADC is limited, there are amplitude clipping effects if the input signal exceeds the ADC's maximal input amplitude.

A linear analogue-to-digital convertor quantises the input signal into a set of n equidistant



(a) (b)

Figure 3.8: Mean square quantisation error for linearly spaced ADC at OFDM receiver: (a) quantisation noise for different amplitude limits normalised to the average input signal amplitude σ versus ADC resolution; (b) quantisation noise for amplitude limits of $a = 3$ and $a = 10$ versus the linear step size

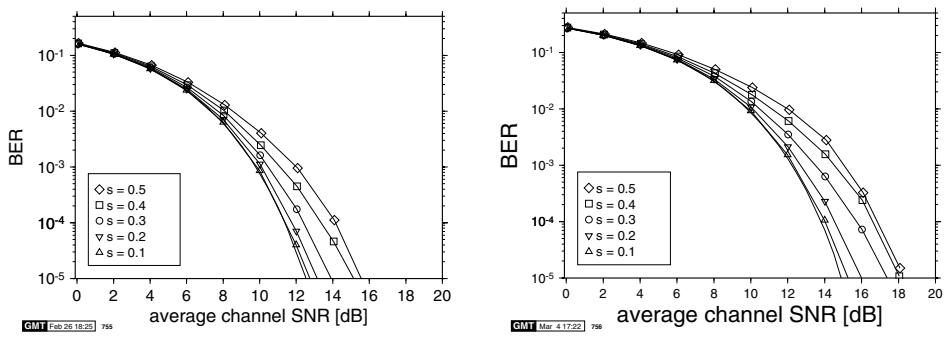
output values, which span an interval with clipping values of $-a$ and a. In this case, the ADC error stems from quantisation error due to the finite step size of $2a/n$ for input values within the dynamic range $[-a, a]$, as well as from amplitude clipping for input values outside this range.

Taking into account the Gaussian nature of the I and Q components of the OFDM signal, the mean square ADC error can be determined for different ADC set-ups. Figure 3.8(a) shows the mean square ADC error normalised to the average input signal power versus clipping amplitude for different quantisation resolution values. For this and the following figures, the input signal is modelled by a white Gaussian noise function with a standard deviation σ. The mean square quantisation error is relative to the mean input power σ^2, and the amplitude limit a is in units of σ.

The mean square ADC error value can be interpreted as the mean power of an additional random noise superimposed on the quantised signal. This ADC noise is not Gaussian, hence estimating the BER performance degradation with the Gaussian noise approximation is inadequate.

It can be seen from the figure that a small dynamic range of $2a$ results in high ADC noise irrespective of the number of ADC bits, which is due to predominant clipping. For $a = 1$, the normalised ADC noise power is about -8 dB, again independently of the resolution of the ADC. For higher values of a, the total ADC noise is dominated by the effects of increasing step size. Depending on the AGC's given resolution, there is an optimal value of a, for which the ADC noise, constituted by clipping and granular noise, is minimal.

In order to separate the effects of the amplitude limitation and the quantisation step size, BER simulations have been conducted with a fixed amplitude limiter and a range of ADC step sizes. The linear ADC step size is given for a range of ADC resolutions b and two amplitude limits a in Table 3.1. The effects of clipping on the OFDM performance have been discussed in the context of non-linear amplification, and Figure 3.4 showed that an amplifier back-off of 9 dB results in no BER performance degradation due to amplifier clipping in an



(a) coherent QPSK (b) differential QPSK

Figure 3.9: BER versus channel SNR for a QPSK modem with coherent and differential detection using different normalised receiver ADC resolution values in an AWGN channel. The maximal normalised amplitude is $a = 3$

AWGN channel for a 512-subcarrier OFDM modem. Setting the amplitude limits of the simulated ADC to $a = 3$ corresponds to a 9.5 dB dynamic range, hence the amplitude clipping contribution to the ADC noise does not significantly impair the modem's BER performance.

$a\backslash b$	4	5	6	7	8	9	10	11	12
3	0.375	0.188	0.094	0.0469	0.0234	0.0117	0.00586	0.00293	0.00146
10	0.625	0.313	0.156	0.0781	0.039	0.0195	0.00977	0.00488	0.00244

Table 3.1: Linear ADC step size for amplitude limits of $a = 3$ and $a = 10$ and ADC resolutions from $b = 4$ bits/sample to $b = 12$ bits/sample

The average ADC noise power for the normalised amplitude limits of $a = 3$ and $a = 10$ is depicted in Figure 3.8(b). The amplitude limit of $a = 3$ results in a residual ADC noise of about -34 dB due to amplitude clipping, while the amplitude clipping noise contribution for a limit of $a = 10$ is below -50 dB. For step sizes above 0.2, which corresponds to ADC resolutions of 5 bits or less, the gap between the two curves is closed, and the noise power is dominated by the quantisation noise.

The BER performance of a 512-subcarrier OFDM modem employing coherently as well as differentially detected QPSK is depicted in Figure 3.9. These experiments have been conducted for a maximal amplitude of $a = 3$ with step sizes from 0.1 to 0.5, which roughly corresponds to ADC resolutions between 6 and 3 bits. In both graphs the curve without markers represents the modem's BER performance in the absence of ADC quantisation and clipping noise.

It can be observed in both figures that the SNR penalty at a BER of 10^{-4} with an ADC step size of 0.1 is 0.15 dB and 0.2 dB for QPSK and DQPSK, respectively. This resolution corresponds to 60 steps in the range from -3 to 3, and therefore would require an ADC of 6-bit resolution. For higher step sizes the SNR penalty is more severe; a step size of 0.5 results in a SNR penalty of about 2.8 dB and 3.2 dB for coherent and differential detection, respectively. Let us now consider the effects of oscillator noise.

3.6 Phase Noise

The presence of phase noise is an important limiting factor for an OFDM system's performance [62, 63, 187], and depends on the quality and the operating conditions of the system's RF hardware. In conventional mobile radio systems around a carrier frequency of 2GHz the phase noise constitutes typically no severe limitation, however, in the 60GHz carrier frequency, 225MHz bandwidth system considered in Section 4.1.1 its effects were less negligible and hence had to be investigated in more depth. Oscillator noise stems from oscillator inaccuracies in both the transmitter and receiver and manifests itself in the baseband as additional phase and amplitude modulation of the received samples [188]. The oscillator noise influence on the signal depends on the noise characteristics of the oscillators in the system and on the signal bandwidth. It is generally split in amplitude noise $A(t)$ and phase noise $\Phi(t)$, and the influence of the amplitude noise $A(t)$ on the data samples is often neglected. The time domain functions $A(t)$ and $\Phi(t)$ have Gaussian histograms, and their time domain correlation are determined by their respective long-term power spectra through the Wiener-Khintchine theorem.

If the amplitude noise is neglected, imperfect oscillators are characterised by the long-term power spectral density (PSD) $N_p(f')$ of the oscillator output signal's phase noise, which is also referred to as the phase noise mask. The variable f' represents the frequency distance from the oscillator's nominal carrier frequency in a bandpass model, or equivalently, the absolute frequency in the baseband. An example of this phase noise mask for a practical oscillator is given in Figure 3.10(a). If the phase noise PSD $N_p(f')$ of a specific oscillator is known, then the variance of the phase error $\Phi(t)$ for noise components in a frequency band $[f_1, f_2]$ is the integral of the phase noise spectral density over this frequency band as in [188]:

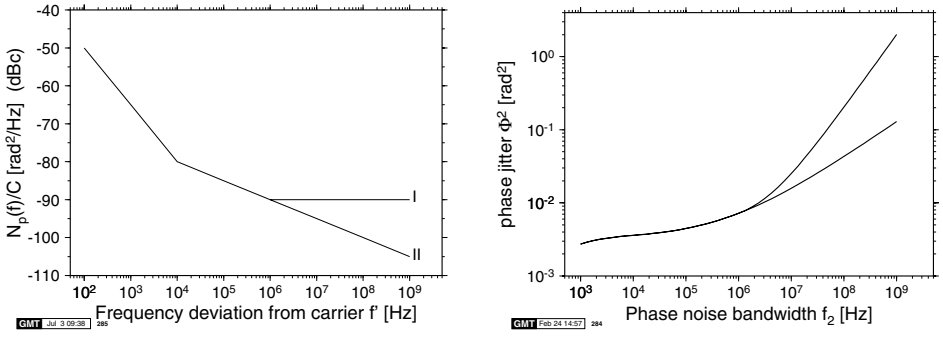
$$\bar{\Phi^2} = \int_{f_1}^{f_2} \left(\frac{2N_p(f')}{C} \right) df', \tag{3.4}$$

where C is the carrier power and the factor 2 represents the double-sided spectrum of the phase noise. The phase noise variance $\bar{\Phi}^2$ is also referred to as the integrated phase jitter, which is depicted in Figure 3.10(b).

3.6.1 Effects of Phase Noise

The phase noise contribution of both the transmitter and receiver can be viewed as an additional multiplicative effect of the radio channel, like fast and slow fading. In serial modulation schemes phase noise manifests itself as random phase errors of the received samples. The effects of this additional random phase component on the received samples depend on the modulation scheme employed, and as expected, they are more pronounced in differential detection schemes than in coherently detected arrangements invoking carrier recovery. The carrier recovery, however, is affected by the phase noise, which in turn degrades the performance of a coherently detected scheme.

For OFDM schemes, multiplication of the received time domain signal with a time-varying channel transfer function is equivalent to convolving the frequency domain spectrum of the OFDM signal with the frequency domain channel transfer function. Since the phase noise spectrum's bandwidth is wider than the subcarrier spacing, this results in energy



(a) $N_p(f')/C$ (b) Φ^2

Figure 3.10: Phase noise characterisation: (a) spectral phase noise density (phase noise mask), (b) integrated phase jitter for two different phase noise masks

spillage into other sub-channels and therefore in intersubcarrier interference, an effect which will be quantified below.

3.6.2 Phase Noise Simulations

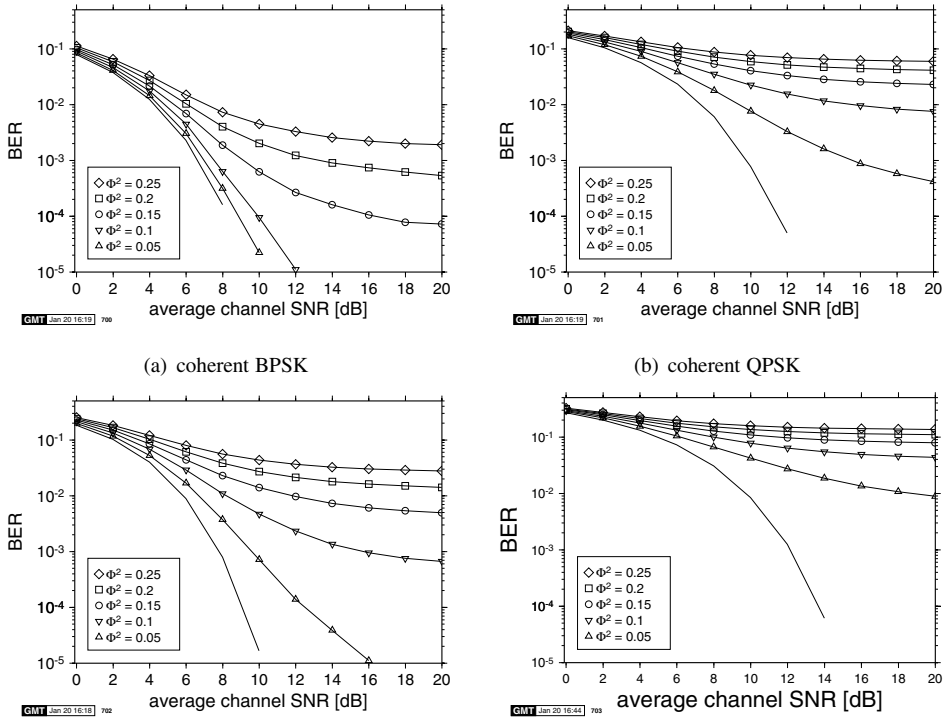
In our studies two different models of the phase noise in an OFDM communications system have been investigated: the simple band-limited white phase noise model, which is solely based on the value of the integrated phase jitter of Equation 3.4, and a coloured phase noise model, which also takes into account the phase noise mask of Figure 3.10(a). Both of these models will be described below.

3.6.2.1 White Phase Noise Model

The simplest way of modelling the effect of phase noise in simulations is to assume uncorrelated Gaussian distributed phase errors with a standard deviation of $\bar{\Phi}$ at the signal sampling instants. This corresponds to the phase noise exhibiting a uniform PSD $N_p(f') = \left(\bar{\Phi}\right)^2 / B$ throughout the signal bandwidth B.

As the phase noise is assumed to be white, the integrated phase jitter, or the variance of the phase noise given in Equation 3.4 constitutes sufficient information for generating the phase error signal $\Phi(t)$. Clearly, since no correlation between the noise samples is assumed, this is the worst-case scenario with the highest possible differences of $\Phi(t)$ between two consecutive samples.

Simulations have been performed for both a 512-subcarrier OFDM modem, as well as for a serial modem for comparison. The serial modem's BER performance curves are depicted in Figure 3.11 for BPSK and QPSK employing both coherent and differential detection, for integrated phase jitter values of $\bar{\Phi}^2 = 0.05\ rad^2$ to $\bar{\Phi}^2 = 0.25\ rad^2$. For coherently detected BPSK, as shown in Figure 3.11(a), white phase noise of $\bar{\Phi}^2 = 0.05\, rad^2$ already causes a measurable SNR penalty of about 0.6 dB at a BER of 10^{-4}, while a phase jitter of $0.1\ rad^2$ results in a SNR penalty of 1.8 dB at this BER. For phase jitter values above $0.1\ rad^2$, residual



(a) coherent BPSK

(b) coherent QPSK

(c) differential BPSK

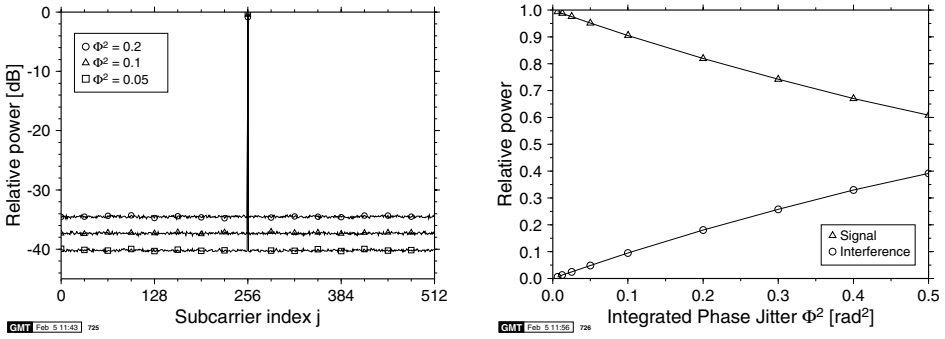
(d) differential QPSK

Figure 3.11: Bit error rate versus channel SNR for a serial modem in an AWGN channel and exposed to white phase noise for integrated phase jitter values of $0.05\ rad^2$ to $0.25\ rad^2$: (a) BPSK, (b) QPSK, (c) DBPSK, (d) DQPSK

bit error rates of $6 \cdot 10^{-5}$, $5 \cdot 10^{-4}$ and $2 \cdot 10^{-3}$ were observed at phase jitters of 0.15, 0.2 and $0.25\ \ rad^2$, respectively.

3.6.2.1.1 Serial Modem The serial QPSK modem's performance is more vulnerable to the effects of phase noise than that of BPSK, as is shown in Figure 3.11(a) and 3.11(b). For all simulated values of $\bar{\Phi}^2$, the bit error rate exceeds 10^{-4}. For a phase jitter of 0.25 rad^2, the observed residual bit error rate is 6%. The curves for differential detection of BPSK and QPSK are shown in Figure 3.11(c) and 3.11(d), respectively. Since for differentially detected PSK schemes both the received modulated symbol as well as the reference phase are corrupted by phase noise, the phase noise effects are severe. The DBPSK modem exhibits residual bit errors of more than 10^{-4} for all simulated phase jitter values above 0.05 rad^2, while the DQPSK modem's BER performance is worse than 0.9% for all simulated values of $\bar{\Phi}^2$.

3.6.2.1.2 OFDM Modem While for serial modems the phase noise results in phase errors of the received samples, the FFT modem's performance is affected by the inter-subcarrier in-



(a) interference from single subcarrier

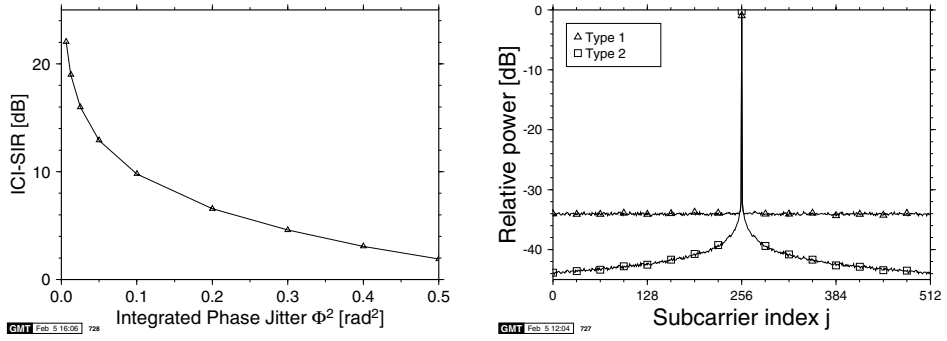
(b) signal and interference level

Figure 3.12: The effect of white phase noise on OFDM: (a) power spillage due to white phase noise, (b) average signal and interference levels for one subcarrier

terference caused by the convolution of the phase noise spectrum with the OFDM spectrum. The average amount of power spillage from one subcarrier into the rest of the OFDM spectrum observed for different values of integrated phase jitter is depicted in Figure 3.12(a). It can be seen that the white phase noise results in uniform spreading of inter-subcarrier interference over all subcarriers, and a loss of signal power in the desired subcarrier number 256. It can be noted that doubling the variance of the phase noise results approximately in doubling the interference power in the other subcarriers, as demonstrated by the 3 dB differences seen in Figure 3.12(a). The received signal power in the central subcarrier drops accordingly.

The total interference power received in each subcarrier is the sum of all active subcarriers' contributions, which is shown in Figure 3.12(b) for a 512-subcarrier OFDM modem. It can be seen that the signal energy drops while the interference energy rises for rising values of the integrated phase jitter, with the signal-to-interference ratio (SIR) dropping to about 1.5, which corresponds to 2 dB for $\bar{\Phi}^2 = 0.5$. For small values of phase jitter up to approximately 0.1, the interference power rises linearly with the phase jitter, and more slowly for higher values of phase jitter. The interchannel-interference (ICI) experienced in each subcarrier for the white phase noise channel depending on the phase jitter is shown in Figure 3.13(a). The SIR is above 10 dB for phase jitter values below approximately 0.1, and 20 dB for values phase jitter values of 0.01. This is in accordance to the linear relationship of interference power and phase jitter for small values observed above.

Figure 3.14 shows the BER performance results observed for a 512-subcarrier OFDM modem in the white phase noise channels. For coherently detected OFDM BPSK the BER performance is generally worse than for the serial modem, characterised in Figure 3.11(a). For differential detection, however, the OFDM modem's BER performance is better than the serial modem's depicted in Figure 3.11(c). This different behaviour can be explained by the different effects of the phase noise on the different systems. It has been observed in Figure 3.12(b) that for the investigated values of the integrated phase jitter the mean interference power in each subcarrier of an OFDM modem increases approximately linearly with the mean square of the phase error in the serial modem. For the same values of noise variance, coherent serial BPSK is more robust to the phase errors in the received serial symbols than



(a) ICI-SIR for OFDM modem in white phase noise

(b) interference from single subcarrier, coloured phase noise

Figure 3.13: OFDM in phase noise channel: (a) ICI-SIR for OFDM modem in white phase noise channel; (b) average signal and interference levels for one subcarrier in the coloured phase noise channels corresponding to the phase noise masks shown in Figure 3.10(a)

f'[Hz]	100	1k	10k	100k	1M
N_p/C[dB]	-50	-65	-80	-85	-90

Table 3.2: Two-sided phase noise mask used for simulations. f' = frequency distance from carrier, N_p/C = normalised phase noise density

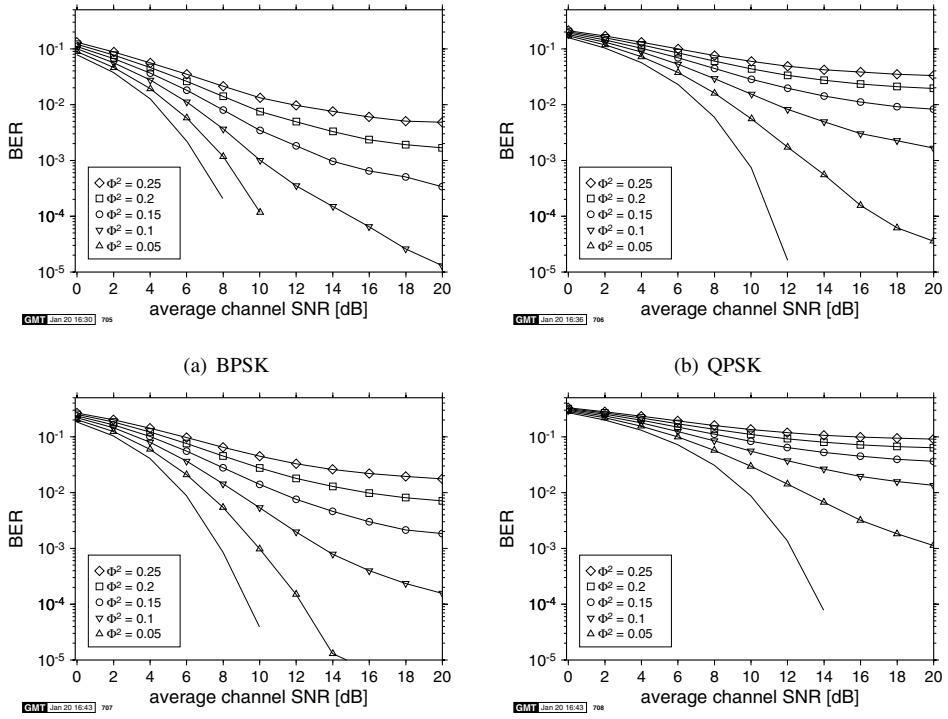
DBPSK, while the noise-like interference observed in the OFDM system is less detrimental to the differentially detected BPSK than to coherent BPSK.

For both differential and coherent QPSK the OFDM modem performs better than the serial modem, as can be seen comparing Figure 3.14(b) with 3.11(b) and 3.14(d) with 3.11(d). There is, however, considerable degradation of the BER performance in both cases. Having considered the worst-case scenario of uncorrelated white phase noise, let us now focus our attention on the more practical case of coloured phase noise sources.

3.6.2.2 Coloured Phase Noise Model

The integral $\bar{\Phi^2}$ of Equation 3.4 characterises the long-term statistical properties of the oscillator's phase and frequency errors due to phase noise. In order to create a time domain function satisfying the standard deviation $\bar{\Phi}^2$, a white Gaussian noise spectrum was filtered with the phase noise mask $N_p(f')$ depicted in Figure 3.10(a), which was transformed into the time domain. A frequency resolution of about 50 Hz was assumed in order to model the shape of the phase noise mask at low frequencies, which led to a FFT transform length of $2^{22} = 4194304$ samples for the frequency range of Figure 3.10(a).

The resulting time domain phase noise channel data is a stream of phase error samples, which were used to distort the incoming signal at the receiver. The double-sided phase noise mask used for the simulations is given in Table 3.2. Between the points given in Table 3.2, a log-linear interpolation is assumed, as shown in Figure 3.10(a). As the commercial oscil-



(a) BPSK

(b) QPSK

(c) differential BPSK

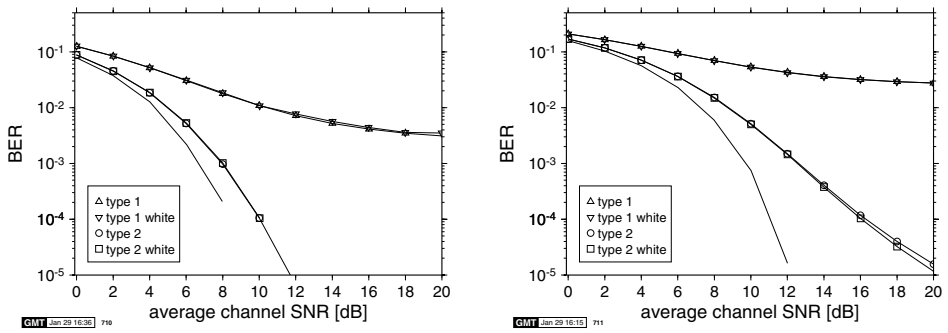
(d) differential QPSK

Figure 3.14: Bit error rate versus channel SNR for a 512 subcarrier OFDM modem in an AWGN channel and white phase noise for different values of integrated phase jitter of $0.05\ rad^2$ to $0.25\ rad^2$: (a) BPSK, (b) QPSK, (c) DBPSK, (d) DQPSK (compared with Figure 3.11)

lator's phase noise mask used in our investigations was not specified for frequencies beyond 1 MHz, two different cases were considered for frequencies beyond 1 MHz: (I) a phase noise floor at -90 dB, and (II) an $f^{-1/2}$ law. Both of these extended phase noise masks are shown in Figure 3.10(a). The integrated phase jitter has been calculated using Equation 3.4 for both scenarios, and the value of the integral for different noise bandwidths is depicted in Figure 3.10(b).

For the investigated 155 Mbits/s wireless ATM (WATM) system's [168–171] double-sided bandwidth of 225 MHz, the integration of the phase noise masks results in phase jitter values of $\bar{\Phi}^2 = 0.2303\, rad^2$ and $\bar{\Phi}^2 = 0.04533\, rad^2$ for the phase noise mask with and without noise floor, respectively.

The simulated BER performance of a 512-subcarrier OFDM system with a subcarrier distance $\Delta f = 440\ kHz$ over the two different phase noise channels is depicted in Figure 3.15 for coherently detected BPSK and QPSK. In addition to the BER graphs corresponding to the coloured phase noise channels described above, graphs of the modems' BER performance over white phase noise channels with the equivalent integrated phase jitter values were also plotted in the figures. It can be observed that the BER performance for both modulation



(a) BPSK (b) QPSK

Figure 3.15: Bit error rate versus channel SNR for a 512-subcarrier OFDM modem in the presence of phase noise. Type 1 represents the coloured phase noise channel with the phase noise mask depicted in Figure 3.10(a) assuming a noise floor of $90\ rad^2/\text{Hz}$, while Type 2 is the channel without phase noise floor. The curves designated "white" are the corresponding white phase noise results. The lines without markers give the corresponding results in the absence of phase noise

schemes and for both phase noise masks is very similar for the coloured and the white phase noise models.

The interference caused by one OFDM subcarrier in the two coloured phase noise channels is depicted in Figure 3.13(b). It can be seen that the Type 1 channel exhibits a virtually white interference spectrum, very similar to the white phase noise channels depicted in Figure 3.12(a). Only the subcarriers directly adjacent to the signal bearer show higher interference influence than in the white phase noise channel. This is due to the Type 1 phase noise density given in the phase noise mask; it is non-flat only for frequencies below 1 MHz, which corresponds to approximately 2.3 subcarrier distances at a separation of 440 kHz. It can be observed in Figure 3.13(b) that higher interference was measured in the two subcarriers adjacent to the signal carrier. If the interference caused by all subcarriers is combined, then all but the very closest subcarriers have equal contributions to the interference signal, resulting in interference like Gaussian noise.

The Type 2 channel, which exhibits no noise floor in the phase noise mask, results in interference that is dependent on the distance from the interfering subcarrier. The summation of the interference is dominated by the interference contribution of the carriers in close vicinity, hence the resulting interference is less Gaussian than for the Type 1 channel.

The simulated BER results shown in Figure 3.15 show virtually indistinguishable performance for the modems in both the coloured and the white phase noise channels. Only a slight difference can be observed for QPSK between the Type 1 and Type 2 phase noise masks, where the corresponding white phase noise results in a better performance than the coloured noise. This difference can be explained with the interference being caused by fewer interferers compared to the white phase noise scenario, resulting in a non-Gaussian error histogram.

3.6.3 Phase Noise – Summary

Phase noise, like all time-varying channel conditions experienced by the time domain signal, results in intersubcarrier interference in OFDM transmissions. If the bandwidth of the phase noise is high compared to the OFDM subcarrier spacing, then this interference is caused by a high number of contributions from different subcarriers, resulting in a Gaussian noise interference. Besides this noise inflicted upon the received symbols, the signal level in the subcarriers drops by the amount of energy spread over the adjacent subcarriers.

The integral over the phase noise mask, termed phase jitter, is a measure of the signal-to-interference ratio that can be expected in the received subcarriers, if the phase noise has a wide bandwidth and is predominantly white. The relationship between the phase jitter and the SIR is shown in Figure 3.13(a). For narrowband phase noise this estimation is pessimistic.

3.7 Chapter Summary and Conclusion

In this chapter we discussed some of basic components of OFDM modems as well as a number of design factors, which influence the achievable performance. Specifically, in Section 3.3 we characterised the OFDM modem's performance, when communicating over conventional wireline type AWGN channels using various modulation schemes. We have shown in Section 3.4 that a particular characteristic of the OFDM signal is that owing to the presence of a high number of randomly modulated subcarrier signals the power of the composite modulated signal of an OFDM symbol may exhibit a high fluctuation. The corresponding signal PDFs were portrayed in Subsection 3.4.1. In order to avoid the spillage of out-of-band non-linear distortion products into the adjacent transmission bands, high-linearity power amplifiers are required for the transmission of OFDM signals. Furthermore, for the sake of reducing the chances that the highest signal peaks are clipped by the power amplifier, the input signal level is typically reduced by a certain amount by invoking a technique, which is often referred to as amplifier back-off, as was discussed in Section 3.4.2. The related issues of peak factor reduction techniques is covered in significantly more detail the full-length version of this monograph [90].

The effects of the ADC conversion accuracy on the achievable BER were quantified in Section 3.5. The chapter was concluded in Section 3.6 by considering the effects of phase noise on the OFDM system's BER. We are now ready to discuss the performance of OFDM modems communicating over dispersive fading channels, which constitutes the topic of the next chapter.

Chapter 4

OFDM Transmission over Wideband Channels

Orthogonal frequency division multiplexing modems were originally conceived in order to transmit data reliably in time-dispersive or frequency selective channels without the need for a complex time domain channel equaliser. In this chapter, the techniques employed for the transmission of quadrature amplitude modulated (QAM) OFDM signals over a time-dispersive channel are discussed and channel estimation methods are investigated.

4.1 The Channel Model

The channel model assumed in this chapter is that of a finite impulse response (FIR) filter with time-varying tap values. Every propagation path i is characterised by a fixed delay τ_i and a time-varying amplitude $A_i(t) = a_i \cdot g_i(t)$, which is the product of a complex amplitude a_i and a Rayleigh fading process $g_i(t)$. The Rayleigh processes g_i are independent from each other, but they all exhibit the same normalised Doppler frequency f'_d, depending on the parameters of the simulated channel.

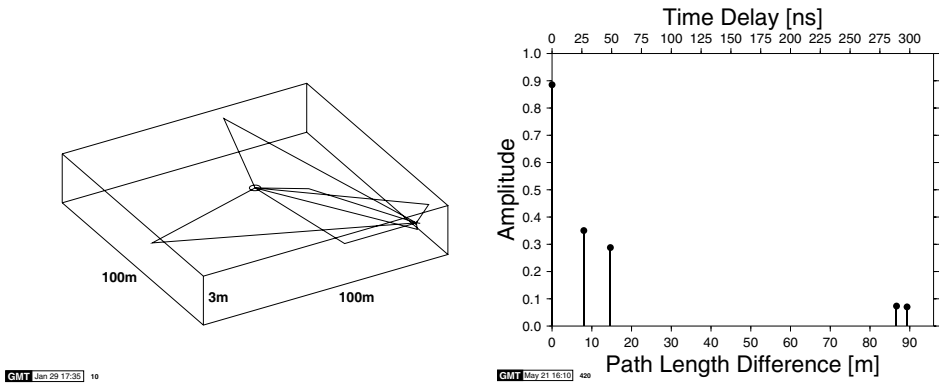
The ensemble of the p propagation paths constitutes the impulse response

$$h(t,\tau) = \sum_{i=1}^{p} A_i(t) \cdot \delta(\tau - \tau_i) = \sum_{i=1}^{p} a_i \cdot g_i(t) \cdot \delta(\tau - \tau_i), \tag{4.1}$$

which is convolved with the transmitted signal.

All the investigations carried out in this chapter were based on one of the system and channel models characterised below. Each of the models represents a framework for a class of similar systems, grouped into three categories: wireless asynchronous transfer mode (WATM), wireless local area networks (WLAN) and a time division multiple access (TDMA) OFDM form of a personal communications type scheme, in a similar framework to the universal

© 2006 John Wiley & Sons, Ltd



(a) paths (b) impulse response

Figure 4.1: The 60GHz, 225MHz bandwidth WATM channel: five-path model and resulting impulse response

mobile telecommunication system (UMTS).

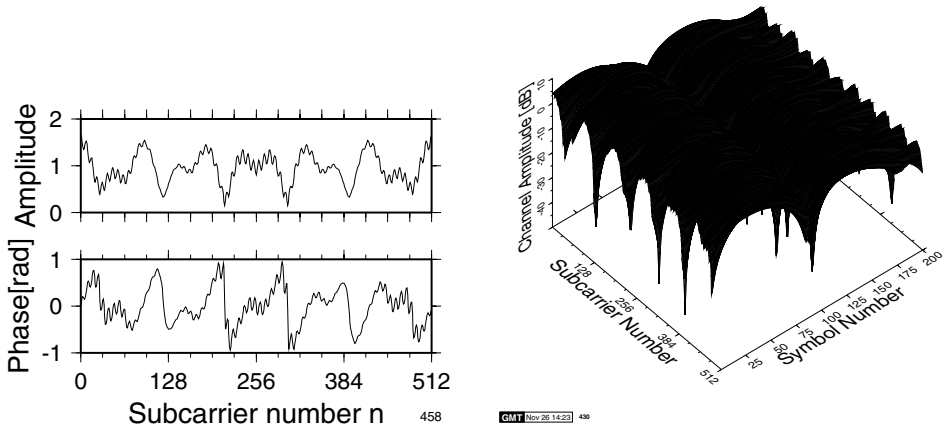
4.1.1 The Wireless Asynchronous Transfer Mode System

The wireless asynchronous transfer mode (WATM) system parameters used for our investigations follow closely the specifications of the Advanced Communications Technologies and Services (ACTS) Median system, which is a proposed wireless extension to fixed-wire ATM-type networks. In the Median system, the OFDM FFT length is 512, and each symbol is padded with a cyclic prefix of length 64. The sampling rate of the Median system is 225 Msamples/s, and the carrier frequency is 60 GHz. The uncoded target data rate of the Median system is 155 MBps.

4.1.1.1 The WATM Channel

The WATM channel employed here is a pessimistic model of the operating environment of an indoor wireless ATM network similar to that of the ACTS Median system. For our simulations, we assumed a vehicular velocity of about 50 km/h or 13.9 m/s, resulting in a normalised Doppler frequency of $f'_d = 1.235 \cdot 10^{-5}$. The impulse response was determined by simple ray tracing in a warehouse-type environment of 100 m $\times$ 100 m $\times$ 3 m, which is shown schematically in Figure 4.1(a). The resultant impulse response, which is shown in Figure 4.1(b), exhibits a maximum path delay of 300 ns, which corresponds to 67 sampling intervals. The five taps of the impulse response were derived assuming free space propagation, using the inverse second power law.

The Fourier transform of this impulse response leads to the static frequency domain channel transfer function depicted in Figure 4.2(a). Note that the central frequency of the bandwidth is in FFT bin 0, hence the spectrum appears wrapped around in this graph. Throughout this work the subcarrier index 0 contains the central frequency, with the subcarriers 1 to $N/2$ spanning the positive relative frequencies, and the subcarriers $N/2 - 1$ to $N - 1$ contain-



(a) channel frequency response

(b) time-variant amplitude

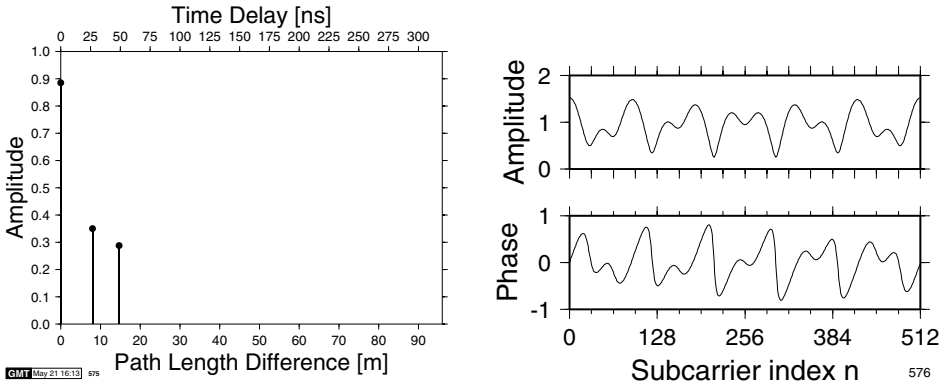
Figure 4.2: WATM channel: (a) unfaded frequency domain channel transfer function $H(n)$; (b) time-variant channel amplitude for 200 consecutive OFDM symbols

ing the negative relative frequency range. Since the impulse response is assumed to be real, the resultant channel transfer function is conjugate complex symmetric around the central frequency bin.

If each of the impulses in Figure 4.1(b) is faded according to a Rayleigh fading process with the normalised Doppler frequency f'_d, then the resulting time-varying impulse response will lead to a time-varying frequency domain channel transfer function, which is depicted in Figure 4.2(b). In this figure, the amplitude of the channel transfer function has been plotted over the bandwidth of the OFDM system for 200 consecutive OFDM symbol time slots.

Figure 4.2(b) reveals a relatively high correlation of the channel transfer function amplitude both along the time and the frequency axes. The correlation in the frequency domain is dependent on the impulse response; the longer the tap delays, the lower the correlation in the transfer function. The similarity of the channel transfer functions along the time axis stems from the slowly changing nature, i.e. the low normalised Doppler frequency, of the assumed narrowband channels. The impulse response changes only little between consecutive OFDM symbol intervals; the correlation between neighbouring channel transfer functions is therefore affected by the Doppler frequency of the constituting narrowband fading channels relative to the duration of one OFDM symbol. For this graph, the impulse response was kept constant for the duration of each OFDM symbol. We will show in Section 4.2.2 that the notion of defining a frequency domain channel transfer function is problematic in environments exhibiting rapid changes of the impulse response.

As the channel impulse response (CIR) depicted in Figure 4.1(b) is of the line-of-sight (LOS) type with one dominant path, fading of this LOS path results in an amplitude variation across the whole signal bandwidth. This is seen in Figure 4.2(b) at around symbol number 100, where a substantial amplitude fade across all subcarriers occurs.



(a) channel impulse response

(b) channel frequency response

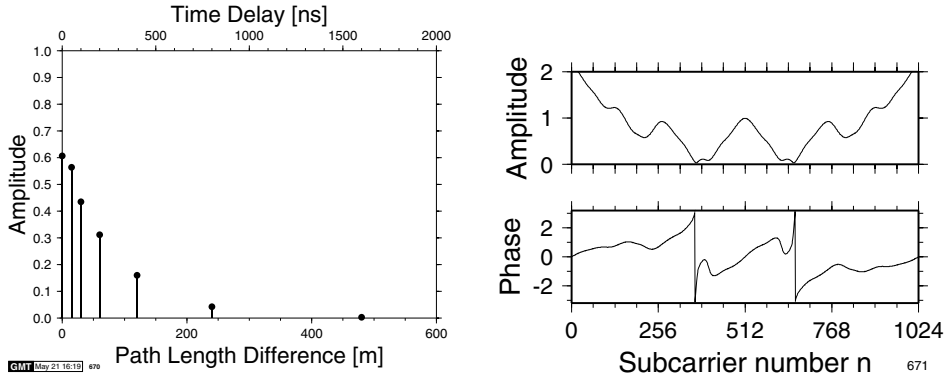
Figure 4.3: Short WATM channel: (a) impulse response, (b) unfaded frequency domain channel transfer function $H(n)$

4.1.1.2 The Shortened WATM Channel

Since the WATM channel discussed above is the worst-case scenario for an indoor wireless high data rate network, we have introduced a truncated version of the original WATM channel impulse response depicted in Figure 4.1(b), by only retaining the first three impulses. This reduces the total length of the impulse response, with the last path arriving at a delay of 48.9 ns due to the reflection with an excess path length of about 15 m with respect to the line-of-sight path, which corresponds to 11 sample periods. Omitting the two long delay pulses in the impulse response does not affect the total impulse response energy significantly, lowering the power by only 0.045 dB, hence no renormalisation of the impulse response was necessary. The resulting impulse response exhibits a root mean squared (RMS) delay spread of $1.5276 \cdot 10^{-8}$s, and it is shown in Figure 4.3(a). The resulting frequency domain transfer function for the unfaded short WATM impulse response is given in Figure 4.3(b), and comparison with Figure 4.2(a) reveals a close correspondence with the original WATM channel transfer function. As the first three low delay paths are the same for both channel models, the general shape of the channel transfer function is very similar; the last two paths in the WATM impulse response result in fast ripple on top of the dominant lower frequency components of the channel transfer function of Figure 4.2(a), which is absent in the shortened channel of Figure 4.3(b).

4.1.2 The Wireless Local Area Network

The main wireless local area network (WLAN) system parameters we opted for were loosely based on the high performance local area network (HIPERLAN) system [189], leading to a sampling rate of 20 MHz and a carrier frequency of 17 GHz. The assumed data symbols utilise a 1024-point FFT and a cyclic extension of 168 samples.



(a) modified HIPERLAN CM1 150

(b) channel frequency response

Figure 4.4: WLAN channel: (a) modified HIPERLAN CM1 150 ns impulse response, (b) unfaded frequency domain channel transfer function $H(n)$

4.1.2.1 The WLAN Channel

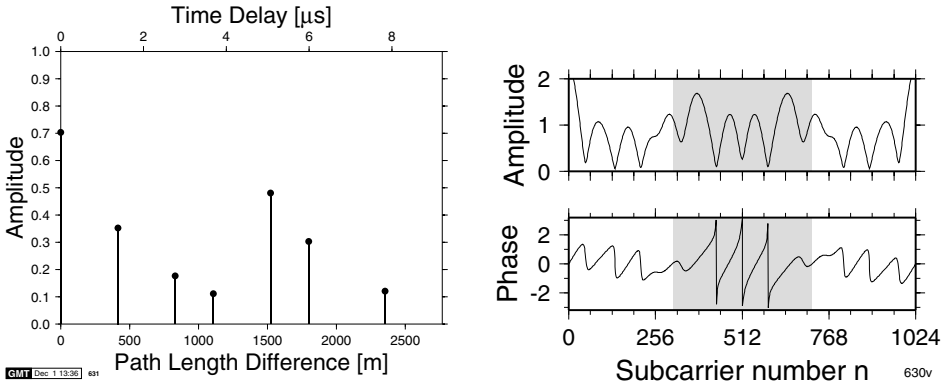
The WLAN channel's impulse response is based on the HIPERLAN CM1 impulse response with a RMS delay spread of 150 ns, as described by Tellambura *et al.* [189]. The second and third path of the original impulse response were combined to achieve a symbol-spaced impulse response pattern. The resulting impulse response is shown in Figure 4.4(a). The corresponding frequency domain channel transfer function is displayed in Figure 4.4(b). Assuming a worst-case vehicular velocity of 50km/h, fading channel simulations were conducted employing Rayleigh fading narrowband channels with a normalised Doppler frequency of $f'_d = 3.94 \cdot 10^{-5}$.

4.1.3 UMTS System

The set of parameters used, for the UMTS-type investigations was based on a version of the ACTS FRAMES Mode 1 proposal [190], resulting in a sampling rate of 2.17 MHz, a carrier frequency of 2 GHz, and a bandwidth of 1.6 MHz. A 1024-point FFT OFDM symbol with 410 virtual subcarriers is employed, in order to comply with the spectral constraints. The data segment of the OFDM symbol is padded with a 168-sample cyclic extension.

4.1.3.1 The UMTS Type Channel

A discretised COST 207 bad urban (BU) impulse response, as described in the COST 207 final report [191], was chosen for the UMTS-type channel. The symbol-spaced discretised impulse response employed for our investigations is depicted in Figure 4.5(a). This impulse response results in a strongly frequency selective channel, as shown in Figure 4.5(b). The area shaded in grey shows the location of the virtual subcarriers in the OFDM spectrum. Since no signal is transmitted in this range of frequencies, the channel transfer function for the virtual subcarriers does not affect the modem's performance. For simulations under Rayleigh fading conditions, a carrier frequency of 1.9 GHz and a vehicular velocity of 50 km/h were assumed,



(a) COST 207 BU

(b) channel frequency response

Figure 4.5: UMTS channel: (a) COST 207 BU impulse response, (b) unfaded frequency domain channel transfer function $H(n)$

	f_c	$1/T_s$	$f_{d,max}$	$f'_{d,max}$	τ_{max}	RMS(τ)
UMTS	2 GHz	2.17 MHz	87.9 Hz	$4.05 \cdot 10^{-5}$	7.83 μs	3.28 μs
WLAN	17 GHz	20 MHz	787 Hz	$3.94 \cdot 10^{-5}$	1.6 μs	0.109 μs
WATM	60 GHz	225 MHz	2278 Hz	$2.345 \cdot 10^{-5}$	300 ns	34.3 ns
WATM - short	-"-	-"-	-"-	-"-	48.9 ns	16.9 ns

Table 4.1: Carrier frequency f_c, sample rate $1/T_s$, maximal Doppler frequency $f_{d,max}$, normalised maximal Doppler frequency $f'_{d,max}$, maximal path delay τ_{max}, and channel RMS delay spread RMS(τ) of the various system frameworks

leading to a normalised Doppler frequency of $f'_d = 4.0534 \cdot 10^{-5}$.

4.2 Effects of Time-Dispersive Channels on OFDM

The effects of the time-variant and time-dispersive channels on the data symbols transmitted in an OFDM symbol's subcarriers are diverse. First, if the impulse response of the channel is longer than the duration of the OFDM guard interval, then energy will spill over between consecutive OFDM symbols, leading to inter-OFDM symbol interference. We will not investigate this effect here, as the length of the guard interval is generally chosen to be longer than the longest anticipated channel impulse response.

If - as a consequence of a low Doppler frequency - the Rayleigh-fading CIR taps fluctuate only slowly compared to the duration of an OFDM symbol, then an essentially time-invariant CIR response can be associated with each transmitted OFDM symbol. Naturally, all of the Rayleigh-fading CIR tap values change gradually over the duration of a number of consecutive OFDM symbols. Viewing this phenomenon in the frequency domain, the channel transfer function of a specific OFDM symbols can be considered time-invariant for the duration of one OFDM symbol, while in a number of consecutive OFDM symbol durations it changes grad-

ually. In this case, the frequency domain effects of the channel result in a time-invariant, but frequency-dependent multiplicative linear distortion of the frequency domain received symbols. This phenomenon is analogous to the effects of a multiplicative, non-dispersive time domain Rayleigh-fading channel envelope in the context of a serial modem, which does not result in inter-symbol interference. A low-Doppler scenario associated with slowly fluctuating Rayleigh-faded CIR taps will be investigated in Section 4.2.1.

By contrast, when the Rayleigh-fading CIR taps fluctuate rapidly owing to a high vehicular speed and hence impose CIR tap fluctuations associated with a high Doppler frequency, the system experiences Inter-subcarrier Interference (ICI). In simple tangible terms this CIR-tap fluctuation may be interpreted in the frequency domain as a frequency domain channel transfer function change during the reception of the OFDM symbol. When communicating over a channel exhibiting no linear distortions, the individual subchannels have a sinc-function shaped frequency response. All of the sinc-shaped subchannel spectra exhibit zero-crossings at the other subcarrier frequencies and the individual subchannel spectra are orthogonal to each other. This ensures that the subcarrier signals do not interfere with each other, when communicating over perfectly distortionless channels, as a consequence of their orthogonality. However, the orthogonality of the sinc-shaped subchannel spectra may be destroyed by the channel, when the Rayleigh-fading CIR taps change substantially during the transmission of an OFDM symbol and hence the corresponding frequency domain channel transfer function changes during this time interval. The quantitative effects of the ICI will be studied in Section 4.2.2.

4.2.1 Effects of the Stationary Time-Dispersive Channel

Here a channel is referred to as stationary, if the Rayleigh-fading CIR taps do not fluctuate significantly over the duration of an OFDM symbol, but do change over longer periods of time. In this case, the time domain convolution of the transmitted time domain signal with the channel impulse response corresponds simply to the multiplication of the spectrum of the signal with the channel frequency transfer function $H(f)$:

$$s(t) * h(t) \longleftrightarrow S(f) \cdot H(f), \tag{4.2}$$

where the channel's frequency domain transfer function $H(f)$ is the Fourier transform of the impulse response $h(t)$:

$$h(t) \longleftrightarrow H(f). \tag{4.3}$$

Since the information symbols $S(n)$ are encoded into the amplitude of the transmitted spectrum at the subcarrier frequencies f_n, the received symbols $r(n)$ are the product of the transmitted symbol and the channel's frequency domain transfer function $H(n)$ plus the additive complex Gaussian noise samples $n(n)$:

$$r(n) = S(n) \cdot H(n) + n(n). \tag{4.4}$$

4.2.2 Non-Stationary Channel

A channel is classified here as non-stationary, if the Rayleigh-fading CIR taps change significantly over the duration of an OFDM symbol, as a consequence of experiencing a high Doppler frequency. In this case, the frequency domain transfer function is time-variant during the transmission of an OFDM symbol and this time-variant frequency domain transfer function leads to the loss of orthogonality between the OFDM symbol's sinc-shaped subcarrier spectra. The amount of intersubcarrier interference imposed by this phenomenon depends on the rate of change, i.e. the Doppler frequency governing the fluctuation speed of the Rayleigh-fading CIR taps.

The simplest environment that may be considered for studying the effects of non-stationary channels is the narrowband channel, whose impulse response consists of a single Rayleigh-fading path. If the amplitude of this path changes as a function of time owing to fading, then the received OFDM symbol's spectrum will be the original OFDM spectrum convolved with the time-variant channel transfer function experienced during the transmission of the OFDM symbol. As this short-term channel transfer function changes between the consecutive transmission bursts, we will investigate the effects of the time-variant narrowband channel averaged over a high number of transmission bursts.

Since the ICI is caused by the variation of the channel impulse response during the transmission of each OFDM symbol, we introduce the "OFDM symbol normalised" Doppler frequency F_d:

$$F_d = f_d \cdot NT_s = f'_d \cdot N, \tag{4.5}$$

where N is the FFT length, $1/T_s$ is the sampling rate, f_d is the Doppler frequency characterising the fading channel and $f'_d = f_d \cdot T_s$ is the conventional normalised Doppler frequency.

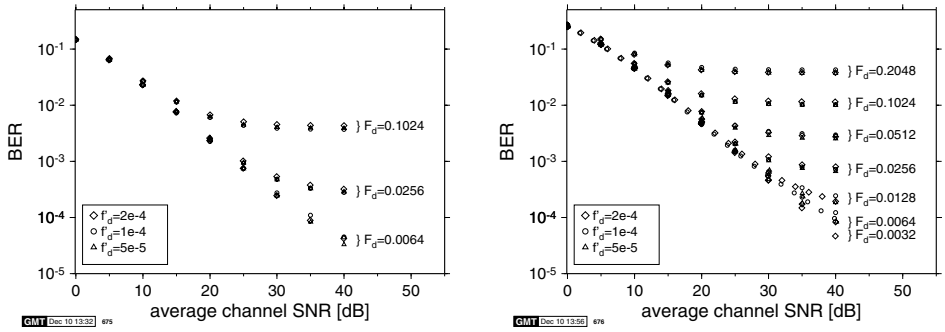
f'_d / N	16	32	64	128	256	512	1024	2048	4096
5×10^{-5}	-	-	0.0032	0.0064	0.0128	0.0256	0.0512	0.1024	0.2048
1×10^{-4}	-	0.0032	0.0064	0.0128	0.0256	0.0512	0.1024	0.2048	-
2×10^{-4}	0.0032	0.0064	0.0128	0.0256	0.0512	0.1024	0.2048	-	-

Table 4.2: OFDM symbol normalised Doppler frequency of $F_d = f_d NT_s = f'_d N$ as a function of the FFT length between 16 and 4096, when using the set of system parameters employed in the experiments characterising the non-stationary transmission scenario

The BER performance for the OFDM modem configurations shown in Table 4.2 was determined by simulation and the simulation results for BPSK are given in Figure 4.6. Figure 4.6(a) depicts the BER performance of an OFDM modem employing BPSK with perfect narrowband fading channel estimation, where it can be observed that for any given value of F_d the different FFT lengths and channels behave similarly. For an F_d value of 0.0256, a residual bit error rate of about $2.8 \cdot 10^{-4}$ is observed, while for $F_d = 0.1024$ the residual BER is about 0.37%.

Figure 4.6(b) shows the performance of an OFDM system without the assumption of perfect phase recovery. Instead, differential detection is employed at the receiver, and, as in Figure 4.6(a), there is good correspondence between the BER curves for the same value of F_d. It can be seen that for F_d values from 0.0128 on, there is already a visible performance penalty at a SNR value of 40 dB. The highest observed residual BER is 4.2% for $f_d = 0.2048$.

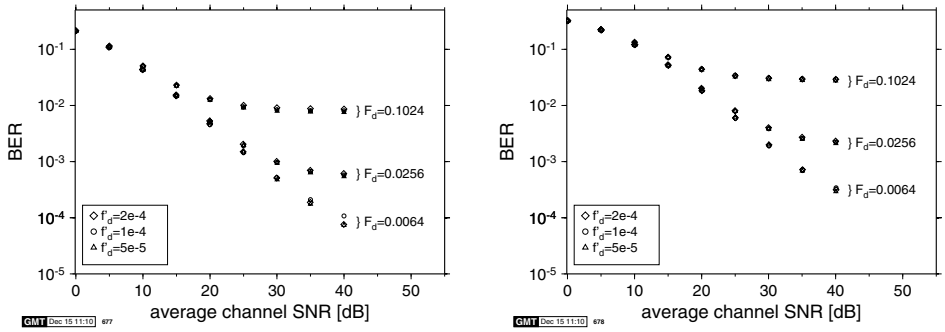
Higher-order modulation schemes, such as QPSK and 16-QAM, are more affected by the



(a) perfect phase recovery BPSK

(b) differential BPSK

Figure 4.6: BPSK OFDM modem performance in a fading narrowband channel for normalised Doppler frequencies of $f'_d = 5 \cdot 10^{-5}$, $1 \cdot 10^{-4}$ and $2 \cdot 10^{-4}$ and FFT lengths between 16 and 4096. The FFT length for a given normalised Doppler frequency f'_d and an OFDM symbol normalised Doppler frequency F_d can be obtained from Table 4.2.



(a) QPSK

(b) 16QAM

Figure 4.7: OFDM modem performance assuming perfect phase recovery in a fading narrowband channel with normalised Doppler frequencies of $f'_d = 5 \cdot 10^{-5}$, $1 \cdot 10^{-4}$ and $2 \cdot 10^{-4}$ and FFT lengths between 16 and 2048 symbols. The FFT length for a given normalised Doppler frequency f'_d and an OFDM symbol normalised Doppler frequency F_d can be obtained from Table 4.2.

intersubcarrier interference caused by the time-varying narrowband fading channel characteristics, as shown in Figure 4.7. Again, the correspondence between different set-ups resulting in the same value of F_d is very good. Since the BER performance is limited by the intersubcarrier interference instead of noise, the BER curves of Figures 4.6(a), 4.7(a) and 4.7(b) do not exhibit the expected fixed SNR shift of 3 dB between BPSK and QPSK and 9.5 dB between BPSK and 16-QAM, as experienced for noise-only limited systems. From the BER curves and residual BER values of Figures 4.6 and 4.7, it can be deduced that the effects of the intersubcarrier interference for $F_d = 0.1024$ and $F_d = 0.0256$ are equivalent to the effects of noise at SNR values of $\gamma = 17$ dB and $\gamma = 28$ dB, respectively. These values are

long-term averages and appear to be valid for all the modulation schemes used.

4.2.2.1 Summary of Time-Variant Channels

Time-variant channels impose a major influence on the BER performance of OFDM systems. The intersubcarrier interference caused by the time-varying nature of the transmission channel limits the attainable bit error rates for the UMTS and the WLAN scenarios, where normalised Doppler frequencies of around $4 \cdot 10^{-5}$ and FFT lengths of 1024 are assumed, leading to $F_d \approx 0.04$. Therefore, an error floor of about 10^{-3} has to be faced by these systems, even if perfect channel estimation is assumed.

4.2.3 Signalling over Time-Dispersive OFDM Channels

Analogously to the case of serial modems in narrowband fading channels, the amplitude and phase variations inflicted by the channel's frequency domain transfer function $H(n)$ upon the received symbols will severely affect the bit error probabilities, where different modulation schemes suffer to different extents from the effects of the channel transfer function. Coherent modulation schemes rely on the knowledge of the symbols' reference phase, which will be distorted by the phase of $H(n)$. If such a modulation scheme is to be employed, then this phase distortion has to be estimated and corrected. For multilevel modulation schemes, where also the magnitude of the received symbol bears information, the magnitude of $H(n)$ will affect the demodulation. Clearly, the performance of such a system depends on the quality of the channel estimation.

A simpler approach to signalling over fading channels is to employ differential modulation, where the information is encoded in the difference between consecutive symbols. Differential phase shift keying (DPSK) employs the phase of the previously received symbol as phase reference, encoding information in the phase difference between symbols. DPSK is thus only affected by the differential channel phase distortion between two consecutive symbols, rather than by the channel phase distortion's absolute value.

4.3 Channel Transfer Function Estimation

Frequency domain channel estimation algorithms generate the channel transfer function estimates $\hat{H}(n)$ for subsequent correction of the received symbols prior to demodulation. The accuracy of the algorithm influences the total system performance to a great extent, especially for systems employing multilevel modulation and coherent detection. We have investigated several different wideband channel estimation techniques, which can be split into two groups: those operating on the spectrum of the received OFDM symbol and those employing time domain correlation algorithms.

4.3.1 Frequency Domain Channel Transfer Function Estimation

Frequency domain channel estimation algorithms exploit the knowledge of the pilot subcarrier positions in the frequency domain representation of the OFDM symbols, that is after the receiver's FFT-based demodulation stage. At this stage, the frequency domain channel transfer function $H(n)$ can be estimated by using known frequency domain pilot subcarriers

embedded in the OFDM symbol's spectrum. These pilot subcarriers facilitate the sampling of the frequency domain channel transfer function $H(n)$, provided that the corresponding sampling frequency is higher than the Nyquist frequency required for the aliasing-free representation of the channel's transfer function at the Doppler frequency encountered. Our treatment of channel transfer function estimation is conceptual in this chapter. A significantly deeper discussion on channel transfer function estimation using both pilot-based as well as decision directed principles in single- as well as multi-user contexts is provided in Chapters 14-16 of the extended version of this monograph [90].

4.3.1.1 Pilot Symbol-Assisted Schemes

Pilot symbol-assisted modulation (PSAM) schemes obtain a channel transfer function estimate on the basis of known frequency domain pilot symbols that are interspersed with the transmitted data symbols [181]. Conventionally, PSAM schemes have been utilised in narrowband fading environments for sampling the time domain fading envelope of the channel in the context of conventional serial modems. For each received pilot subcarrier the corresponding channel transfer function value is estimated as the quotient of the received and the expected subcarrier value. The channel transfer function estimate for the information-bearing subcarrier positions of the OFDM symbol is derived from these pilot-based channel transfer function estimates by means of interpolation between them. A range of different interpolation techniques were comparatively studied by Torrance *et al.* [192] in the context of serial modems communicating over Rayleigh fading narrowband channels, ultimately favouring linear interpolation as a consequence of its low complexity and good performance. We will address the issues of choosing an interpolation scheme in the context of OFDM transmissions over fading wideband channels below.

In parallel modems, PSAM can be utilised for estimating the frequency domain channel transfer function $H(n)$ in a time dispersive environment, if no inter-subcarrier interference is present. Accordingly, n_p pilot symbols P_i are transmitted in the subcarriers with indices $p_i, i = 1, \ldots, n_p$ within the total OFDM symbol bandwidth of N subcarriers. At the receiver, the channel transfer function $\hat{H}(p_i)$ at the pilot subcarriers is estimated from the received samples $r(p_i)$:

$$\hat{H}(p_i) = r(p_i)/P_i. \tag{4.6}$$

In a second step, the values of the channel transfer function are estimated for the unknown data symbols by interpolation using the $\hat{H}(p_i)$ values of Equation 4.6. Clearly, the placement of the pilots and the interpolation technique will influence the quality of the channel estimation. In this chapter we will investigate two different interpolation techniques, linear and lowpass interpolation, both with a varying number of pilot subcarriers.

4.3.1.1.1 Linear Interpolation for PSAM The simplest interpolation technique that can be used to estimate the channel transfer function for the subcarriers between two neighbouring channel estimation samples $\hat{H}(p_i)$ and $\hat{H}(p_{i+1})$ is a linear function:

$$\hat{H}(n) = \hat{H}(p_i) + \frac{\hat{H}(p_{i+1}) - \hat{H}(p_i)}{p_{i+1} - p(i)} \cdot (n - p_i) \quad \text{for} \quad p_i \leq n \leq p_{i+1}. \tag{4.7}$$

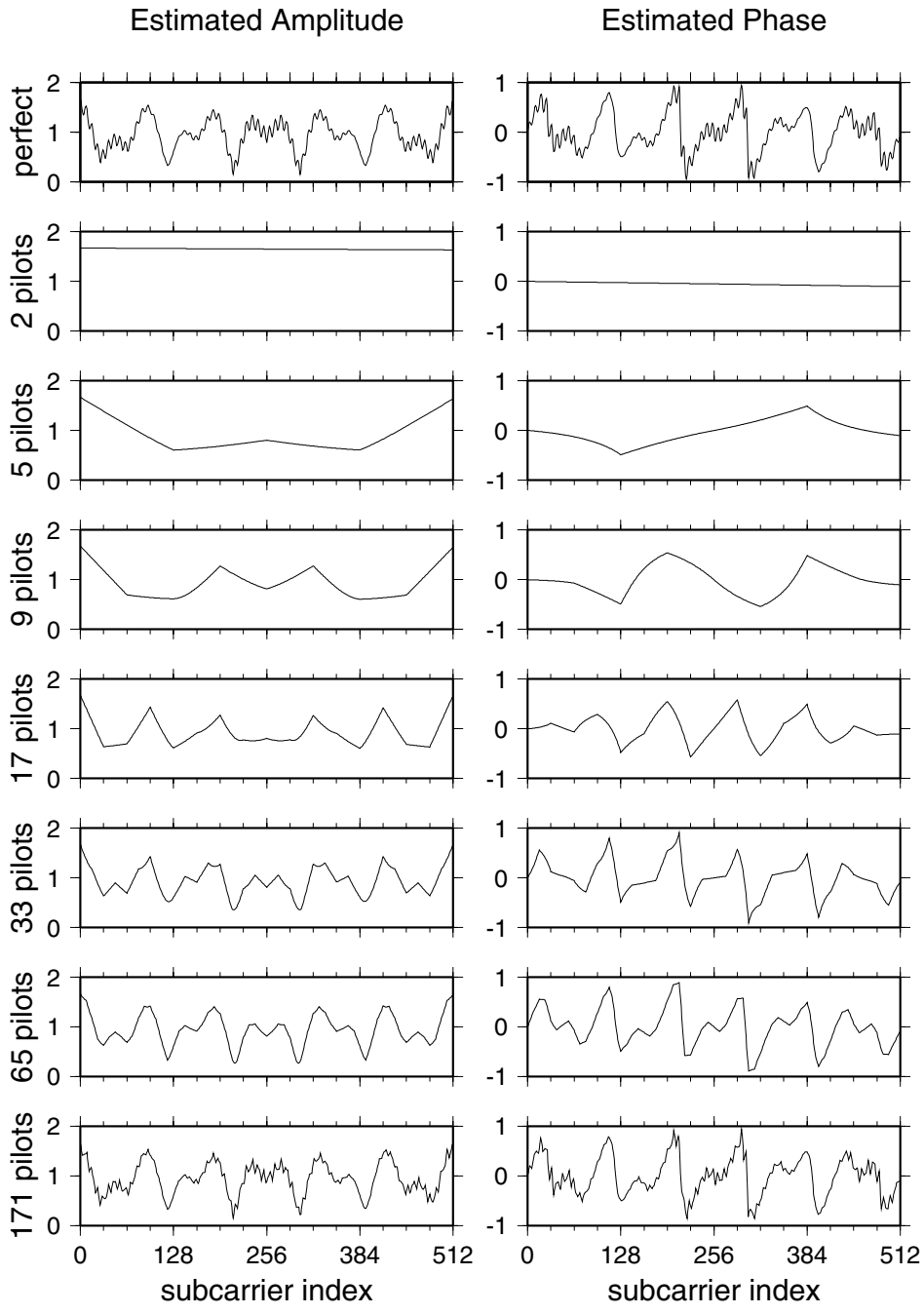


Figure 4.8: Estimation of the stationary WATM channel of Figure 4.2, a noiseless environment using linear interpolation between pilots employing $2 \ldots 171$ pilots per 512-subcarrier OFDM symbol

Figure 4.8 shows the amplitude and the phase of the stationary WATM channel's frequency domain transfer function $H(n)$ for different numbers of equidistant pilot symbols in the frequency domain in an ideal noiseless environment. It can be seen that the channel estimation accuracy improves with increasing number of pilot tones in the spectrum. The number of pilot tones in the OFDM spectrum necessary to sample the channel transfer function can be determined on the basis of the sampling theorem as follows.

The frequency domain channel's transfer function $H(f)$ is the Fourier transform of the channel impulse response $h(t)$. Each of the impulses in the impulse response will result in a complex exponential function $e^{-(j2\pi\tau/T_s)f}$ in the frequency domain, depending on its time delay τ. In order to sample this contribution to $H(f)$ according to the sampling theorem, the maximum pilot spacing Δp in the OFDM symbol is:

$$\Delta p \leq \frac{N}{2\tau/T_s}\Delta f. \tag{4.8}$$

In the case of the WATM channel impulse response with a maximum delay of $\tau/T_s = 67$, the resulting pilot spacing in the OFDM symbol is three subcarriers, requiring 171 pilot carriers per 512-subcarrier OFDM symbol. If the channel estimation is to resolve only the effects of the first three dominant paths with a maximum delay of $\tau/T_s = 11$ in Figure 4.1(b), then the minimal pilot spacing can be increased from 3 to 23 subcarriers.

Inspection of Figure 4.8 underlines these points: in order to resolve the full detail of the original transfer function, as depicted at the top of the figure, 171 pilots must be used. Furthermore, even using 171 pilots in the OFDM symbol, the estimated curve is not a very close match of the original. This is due to the linear interpolation algorithm used.

Nonetheless, the estimations performed with 33 and 65 pilots, respectively, show very similar levels of detail. Both schemes can appropriately sample the effects of the first three paths, but they are undersampled for capturing information concerning the two long-delay paths. If the pilot spacing is higher than the calculated number of 23, then the accuracy of the estimation declines further.

The shortened WATM channel, as characterised in Figure 4.3(a), can be sampled adequately utilising any pilot spacing of less than 23 subcarriers, which for our 512-subcarrier system corresponds to a minimum number of 23 pilots per OFDM symbol. Figure 4.9 shows the linearly interpolated channel estimation values for PSAM channel estimation using $2, \ldots, 171$ pilots in the 512-subcarrier OFDM symbol for the noiseless shortened WATM channel. Again, it can be seen that the accuracy of the channel transfer function estimation improves with the number of pilots, but that a total of 171 pilots is necessary to yield a channel estimation that is indistinguishable from the perfect channel estimation curve in this scale. As 33 and 65 pilot subcarriers already exceed the 23 pilots required to sample the frequency domain channel transfer function according to the Nyquist sampling theorem, it becomes clear that the estimation errors are due to the linear interpolation algorithm and that – for optimal channel estimation accuracy – substantial oversampling of the channel has to be employed, thus deteriorating the system's bandwidth efficiency.

4.3.1.1.2 Ideal Lowpass Interpolation for PSAM The perfect interpolator for the measured channel transfer function samples $\hat{H}(p_i)$ is the ideal lowpass filter with a cut-off frequency of $1/\Delta p$, where Δp is the spectral distance between consecutive pilot subcarriers.

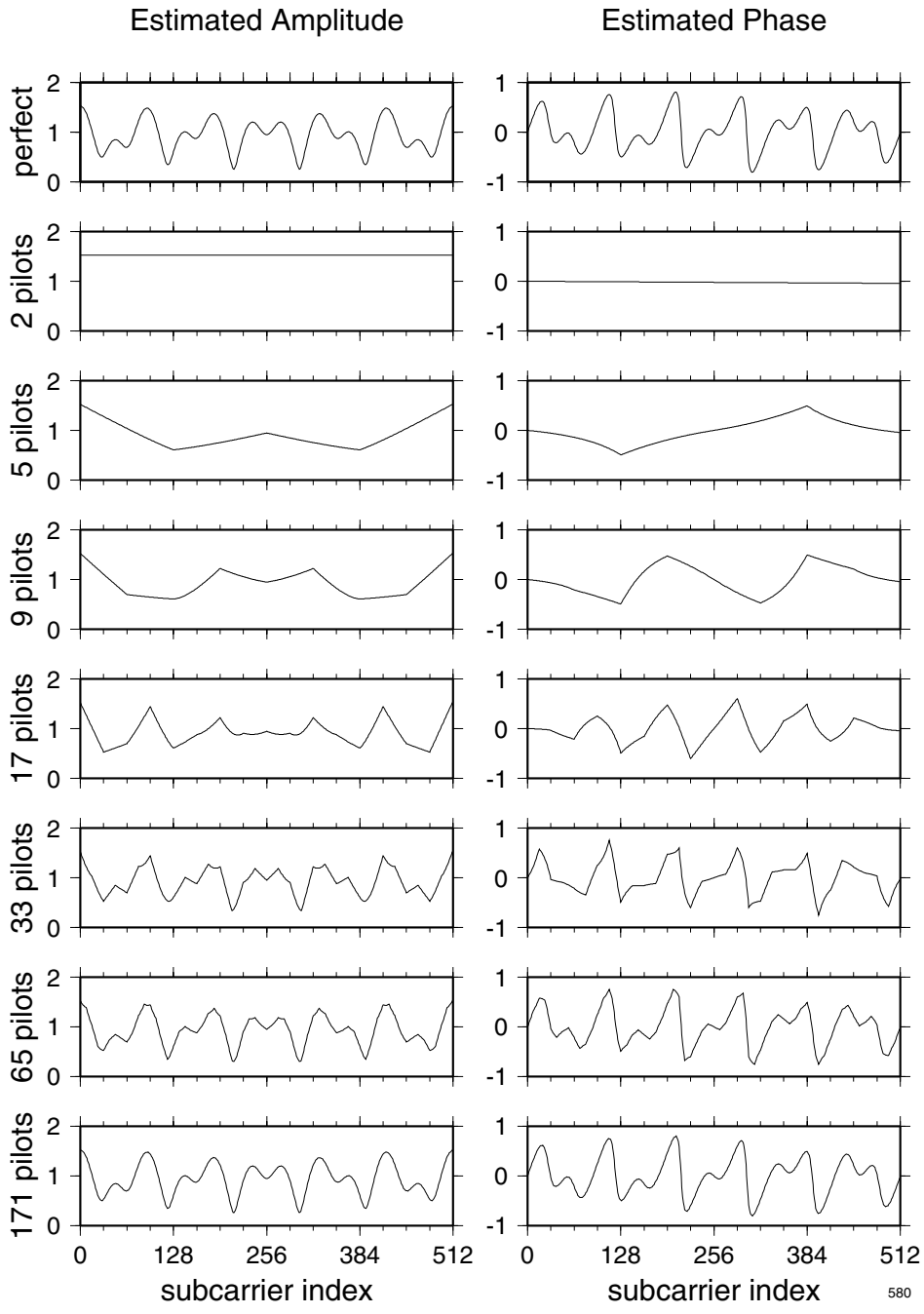


Figure 4.9: Estimation of the stationary shortened WATM channel of Figure 4.3, a noiseless environment using linear interpolation between pilots employing 2 ..., 171 pilots per 512-subcarrier OFDM symbol

Unlike the linear interpolation, this requires equidistant pilot placement in the OFDM symbol.

While an ideal rectangular filter transfer function is impossible to implement perfectly in the time domain due to its infinitely long impulse response, we employed an ideal rectangular frequency domain filter based on a FFT/IFFT operation. A perfect FFT-based lowpass filter can be implemented if its bandwidth coincides with a FFT bin of the chosen Fourier transform, which limits the set of possible pilot numbers. In our case, a 512-point FFT/IFFT operation was employed, therefore allowing for sets of 2^n with $1 \leq n \leq 9$ pilots.

For comparison with the linear interpolation, the same set of pilot distances Δp has been employed for the experiments. Since the lowpass interpolator does not require a pilot in the last subcarrier, the corresponding number of pilots is reduced by one for the lowpass interpolator, when compared to the linear interpolator.

Figure 4.10 gives an overview of the estimation accuracy of the PSAM scheme with ideal lowpass interpolation in a noiseless environment. Again, the resolution of the estimation depends on the number of pilots per OFDM symbol. The estimated transfer functions for 32 and for 64 pilots are identical and exactly correspond to the effect of the first three impulses in $h(t)$. In order to resolve $H(f)$ more finely, at least 170 pilot subcarriers must be employed. Closer inspection of the estimated $\hat{H}(n)$ for 170 pilots reveals relatively high errors in the estimation. This is due to non-optimal lowpass filtering; the optimum bandwidth of the lowpass filter corresponding to $\Delta p = 3\Delta f$ does not line up with the filter's FFT bins, hence the passband is too wide. This leads to considerable estimation errors, especially at the highest subcarrier indices, since there is no pilot symbol at the last subcarrier. If a perfect lowpass interpolation scheme was to be used over the WATM channel, then a pilot distance of $\Delta p = 2\Delta f$ would have to be used, resulting in 256 pilot subcarriers per 512-subcarrier OFDM symbol.

The equivalent estimated channel transfer functions for the case of the shortened WATM channel are depicted in Figure 4.11. It can be seen from the figure that the channel estimation is indistinguishable from the perfect case for the 32-pilot scenario and the 64-pilot scenario. Since the number of pilots necessary for the perfect sampling of this channel is 23, which corresponds to a pilot spacing of 23, the channel estimation utilising less than 23 pilots yields inaccurate results. If 170 pilot subcarriers are employed in each OFDM symbol, then the same effect as observed for the full-length WATM channel applies; because the frequency resolution of the FFT employed for the lowpass filter implementation is insufficient, the filter passband does not correspond exactly to the pilot frequency.

4.3.1.1.3 Summary The Nyquist sampling theorem applies to the channel estimation in the frequency domain utilising pilot subcarriers in the OFDM symbol, but delivers only a lower bound for the number of pilots necessary, which is valid for perfect lowpass interpolation. If linear interpolation is employed, then oversampling beyond the Nyquist rate is necessary, in order to achieve high estimation accuracy. The number of pilot subcarriers that has to be used is dependent on the modulation scheme employed for signalling over the subcarriers.

The ideal lowpass interpolator yields better estimation accuracy than the linear interpolator for a given number of pilots, but the choice of pilot sets is limited by the implementation of the lowpass filter. If a FFT/IFFT based filter implementation is chosen, then only a limited set of possible pilot distances is available. This, in the WATM channel, leads to the need for

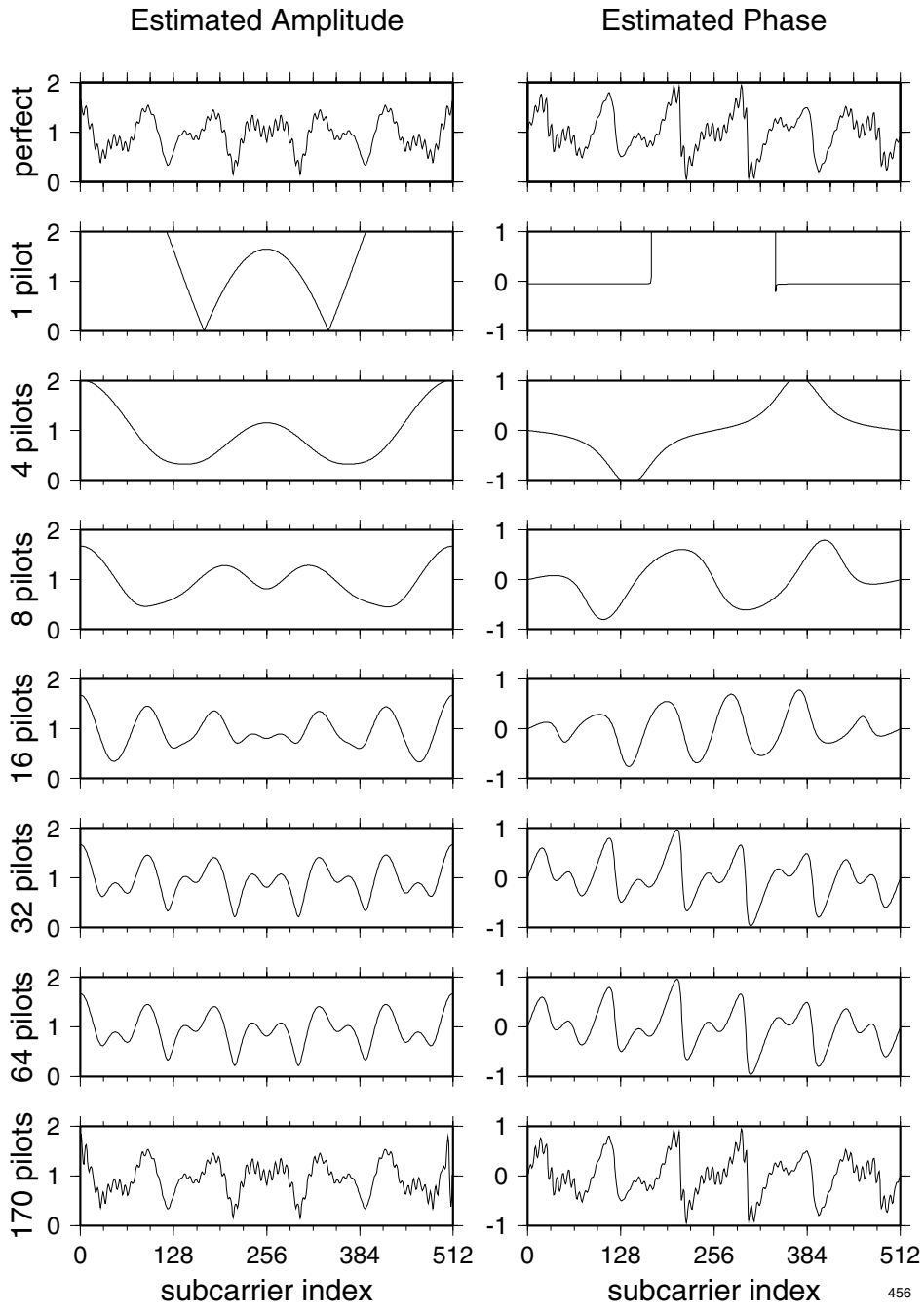


Figure 4.10: Estimation of the stationary WATM channel of Figure 4.2, a noiseless environment using ideal lowpass interpolation between pilots employing 2, ..., 171 pilots per 512-subcarrier OFDM symbol

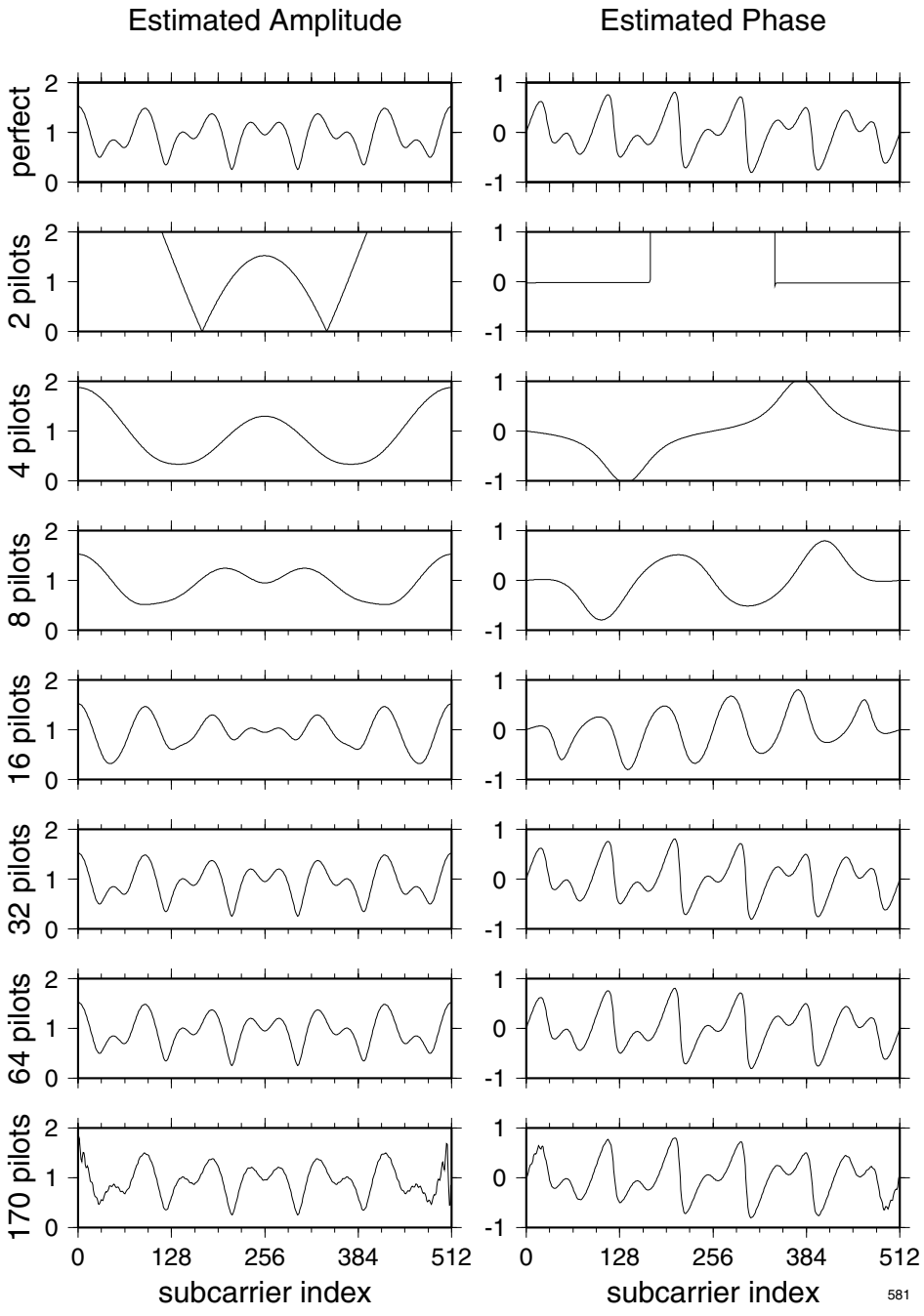


Figure 4.11: Estimation of the stationary shortened WATM channel of Figure 4.3, a noiseless environment using ideal lowpass interpolation between pilots employing $2, \ldots, 171$ pilots per 512-subcarrier OFDM symbol

a substantially higher number of pilots than would be necessary for the more flexible linear interpolator.

4.3.2 Time Domain Channel Estimation

An alternative approach to channel estimation in OFDM transmission systems is to estimate the channel directly from the time domain received signal. Analogous to wideband estimation in serial modems, a training sequence in the transmitted data stream can be employed in order to perform a correlation-based impulse response estimation. The corresponding frequency domain channel transfer function can be computed by FFT from this impulse response.

Again, our treatment of channel transfer function estimation was conceptual in this chapter. A significantly deeper discussion on channel transfer function estimation using both pilot-based as well as decision directed principles in single- as well as multi-user contexts is provided in Chapters 14-16 of the extended version of this monograph [90].

4.4 System Performance

The various channel estimation techniques discussed above have been studied in a perfectly noiseless environment and without considering the effects of the channel estimation upon the system's bit error rate performance. In this section, we will consider the attainable performance of data transmission systems over the time-dispersive channel, for both non-fading and stationary channels.

4.4.1 Static Time-Dispersive Channel

The static time-dispersive channel exhibits a time-invariant channel impulse response, which inflicts no intersubcarrier interference as described in Section 4.2.2. Therefore, the OFDM subcarriers are independent and each subcarrier n corresponds to an AWGN channel with a signal-to-noise ratio of γ_n. If the average channel SNR is γ, then the sub-channel SNR values γ_n depend on the magnitude of the frequency domain channel transfer function $H(n)$:

$$\gamma_n = \gamma \cdot |H(n)|^2 . \tag{4.9}$$

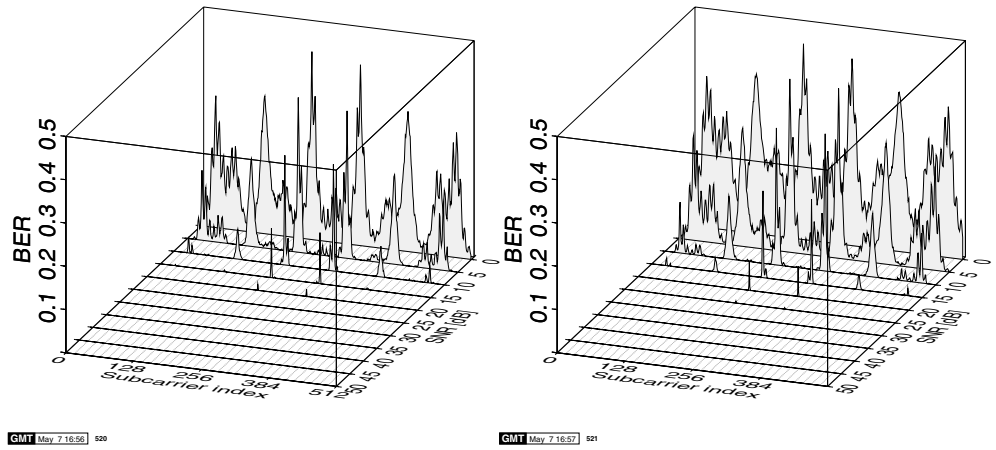
If we assume perfect channel estimation, corresponding to $\hat{H}(n) = H(n)$, then the bit error rate $p_{e,n}$ for each subcarrier n depends exclusively on the sub-channel SNR γ_n, which allows the calculation of the overall system bit error rate p_e by simply averaging over the sub-channel SNR values:

$$p_e = \frac{1}{N_u} \sum_n p_{e,n} = \frac{1}{N_u} \sum_n p_e(\gamma_n), \tag{4.10}$$

where N_u is the number of subcarriers used for data signalling and the use of the same modulation scheme for all subcarriers is assumed.

4.4.1.1 Perfect Channel Estimation

Perfect channel estimation is the best-case scenario for OFDM transmission over time-dispersive channels, as the performance is only limited by the SNR of the subcarriers, not by



(a) BPSK (b) QPSK

Figure 4.12: Simulated BER per subcarrier over the static WATM channel of Figure 4.1(b) with perfect channel estimation for (a) coherent BPSK transmission and (b) coherent QPSK transmission. The symmetry of the BER curves indicates that the unfaded CIR was real.

the reference phase and amplitude estimation errors in the receiver. Simulations have been performed for both coherent and non-coherent modulation schemes, where the frequency domain channel transfer function $H(n)$ was calculated at the receiver by applying the Fourier transform to the perfectly known noiseless impulse response of the channel, as depicted in Figure 4.1(b). The resulting channel transfer function is shown in Figure 4.2(a).

Figure 4.12(a) shows the measured BER per subcarrier for different levels of average OFDM SNR for the simulated 512-subcarrier modem over the WATM channel employing coherent binary phase shift keying (BPSK) in the subcarriers. It is apparent that the bit error probability varies significantly between different subcarriers, from about 2% in good sub-channel conditions, up to 40% in the deep fades of the channel transfer function $H(f)$ at an average OFDM SNR of 0 dB. At an average SNR of 5 dB, groups of virtually error-free subcarriers can be observed, interspersed with bundles of carriers exhibiting high bit error probabilities. At 15 dB, only a very small number of carriers experience measurable transmission error rates at all.

The recorded bit error rates in the simulation correspond very closely to the theoretical results obtained by calculating the sub-channel SNR γ_n for each subcarrier index n following Equation 4.9 and evaluating the appropriate bit error probability function for the chosen modulation scheme. Specifically, the BER over the AWGN channel was calculated employing Equations 3.1 to 3.3 For coherent modulation, the bit error probabilities $p_e(\gamma)$ for BPSK, QPSK and 16-QAM are depicted in Figure 3.1, and Figure 4.13 shows good correspondence between the obtained theoretical bit error rates and the simulation results.

The corresponding graph for QPSK, as shown in Figure 4.12(b), is similar to the BPSK case, only exhibiting higher bit error probabilities. Again, the bit error rate per subcarrier varies strongly with the channel transfer function, which is due to the variation in sub-channel SNR.

The OFDM bit error probability averaged over all subcarriers versus the channel SNR

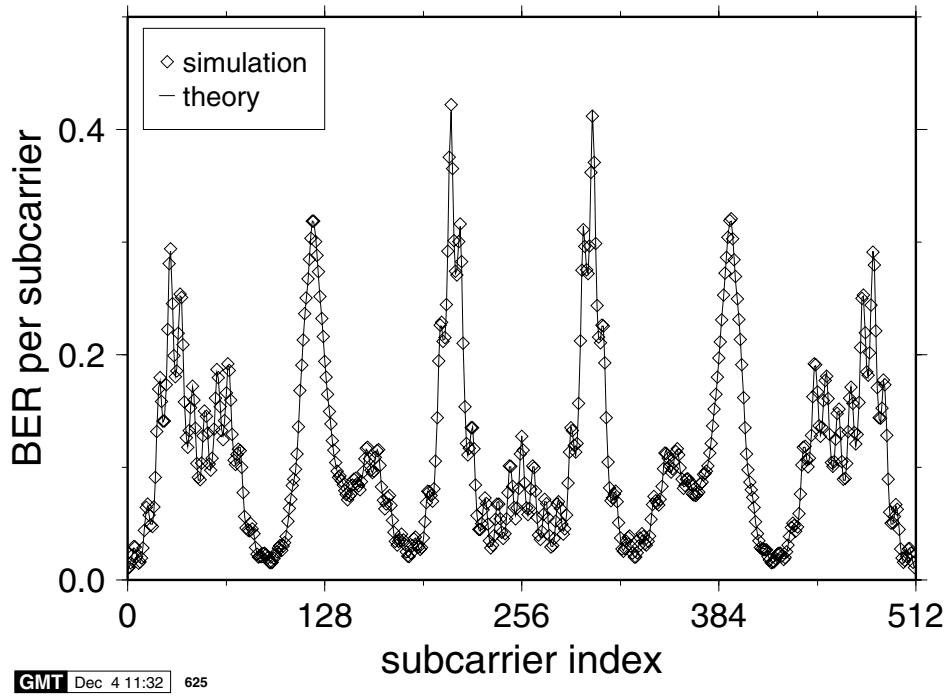
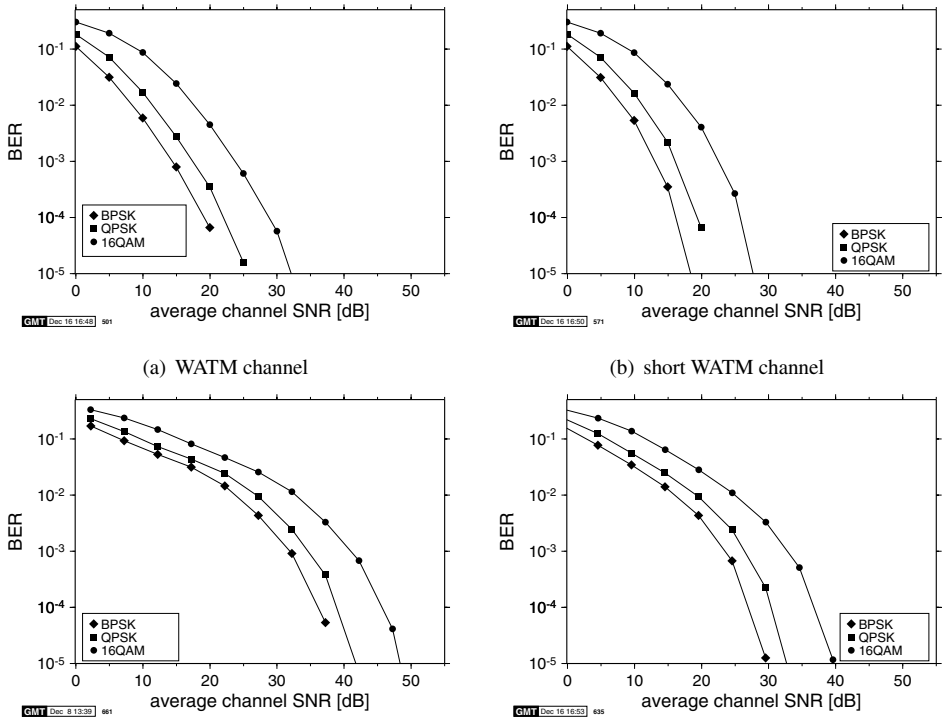


Figure 4.13: Simulated and theoretical BER per subcarrier for coherently detected BPSK transmission with perfect channel estimation over the static WATM channel of Figure 4.1(b) at an average OFDM SNR of 0 dB

for BPSK, QPSK and 16-QAM transmission over the non-fading WATM channel is shown in Figure 4.14(a). The QPSK curve is shifted to the right by 3 dB compared to the BPSK performance curve, which is in accordance with the performance in a narrowband channel, as demonstrated in Section 3.3. The same observation can be made for the performance difference between 16-QAM and the other signalling schemes.

Although the relative BER performance relationship between the different modulation schemes corresponds to the BER results found in the narrowband AWGN channel, the absolute bit error rate values depend on the channel transfer function. Figure 4.14(b) depicts the corresponding BER versus channel SNR graph for the shortened WATM channel of Figure 4.3. The relative BER performance relationship between the different modulation schemes is the same as over the other channels, but the shape of the BER curve is different from that of the WATM channel. Comparing the frequency domain channel transfer function of the shortened WATM channel of Figure 4.3(b) and that of the original WATM channel of Figure 4.2(a) it can be seen that the fading is less severe in the shortened WATM channel, leading to better BER performance at high SNR values.

The UMTS channel characterised in Figure 4.5(b) exhibits even stronger fading in the frequency domain than the two WATM channels, and consequently the BER performance is worse than that of both the WATM systems. At a BER of 10^{-3} the required SNR for the corresponding modulation schemes is about 9 dB higher for the UMTS system than for the



(a) WATM channel

(b) short WATM channel

(c) WLAN channel

(d) UMTS channel

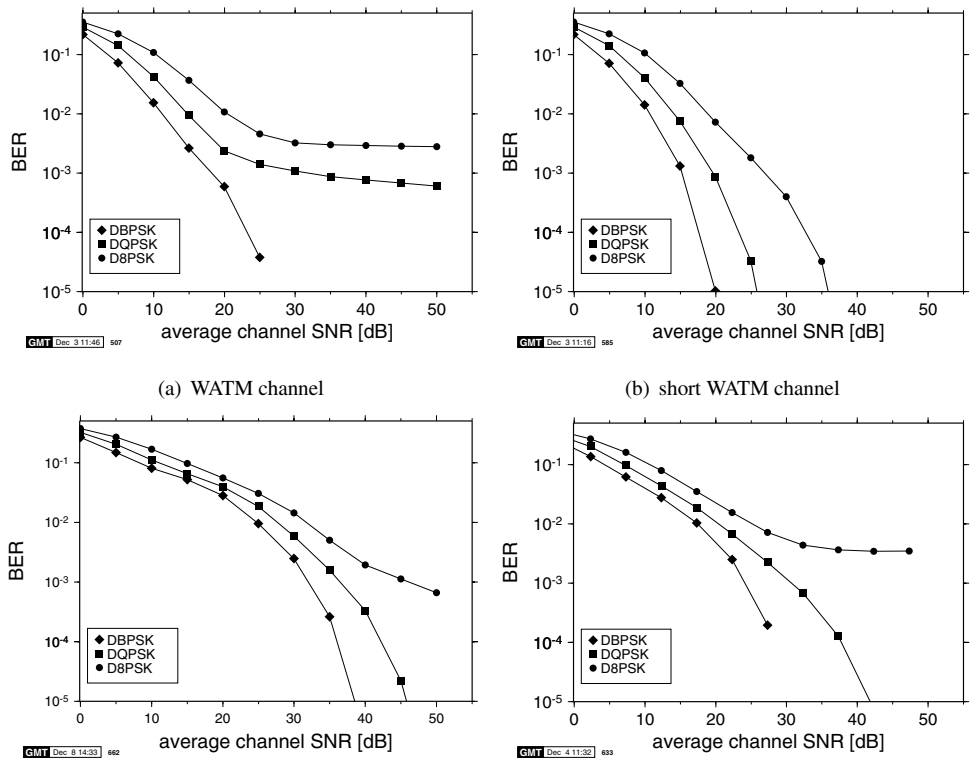
Figure 4.14: Bit error rate versus channel SNR for static (a) WATM channel (Figure 4.1(b)), (b) shortened WATM channel (Figure 4.3), (c) WLAN channel (Figure 4.4), (d) UMTS channel (Figure 4.5(a)); perfect channel estimation and coherent detection

WATM system.

4.4.1.2 Differentially Coded Modulation

Differentially coded modulation enables the receiver to detect the data symbols without knowledge of the reference phase, therefore no channel estimation is required, if differential phase shift keying (DPSK) is used for modulating the subcarriers. Since the transmitted information is encoded in the phase difference between two consecutive subcarriers, there needs to be one phase reference subcarrier per OFDM symbol, typically in the first subcarrier.

While the absolute phase of the frequency domain channel transfer function $H(n)$ at subcarrier n does not affect the reception, the phase change of $H(n)$ between two consecutive subcarriers does influence the reception of the symbols. Note that the BER performance of both the WATM system in Figure 4.15(a) as well as that of the UMTS system in Figure 4.15(d) exhibit a residual bit error rate for high SNR levels for certain modulation schemes. These noise-independent errors are caused by channel effects and are investigated for the UMTS system below.



(a) WATM channel

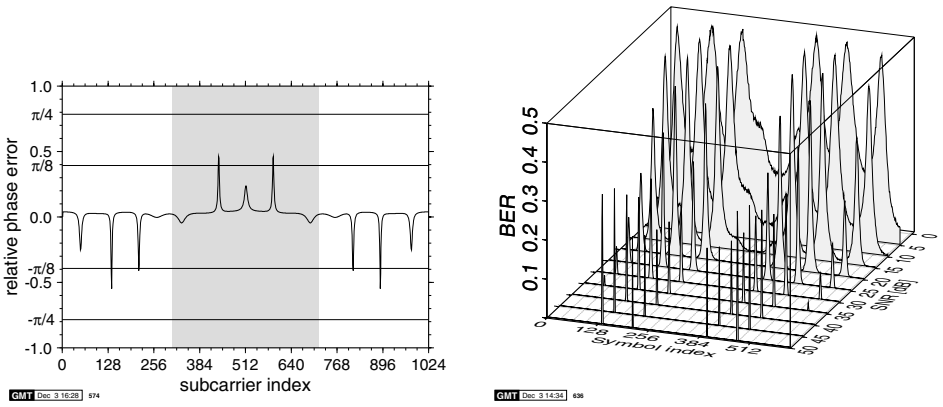
(b) short WATM channel

(c) WLAN channel

(d) UMTS channel

Figure 4.15: Bit error rate versus channel SNR for static (a) WATM channel (Figure 4.1(b)), (b) shortened WATM channel (Figure 4.3), (c) WLAN channel (Figure 4.4), (d) UMTS channel (Figure 4.5(a)), using differential detection

In differential phase shift keying, the information to be transmitted is mapped to the phase difference between two consecutively received symbols. As all the symbols transmitted over the wideband OFDM channel suffer different phase rotations from the channel's frequency domain transfer function $H(n)$, the channel phase rotation difference $(\measuredangle H(n) - \measuredangle H(n-1))$ between subcarrier $(n-1)$ and subcarrier n offsets the receiver's decision boundaries for detected signals. Figure 4.16(a) shows the phase difference $(\measuredangle H(n) - \measuredangle H(n-1))$ between adjacent subcarriers for the UMTS channel of Figure 4.5. The grey area in the graph marks the positions of the virtual subcarriers, which are not used for transmission, and therefore do not have an impact on the system's performance. The horizontal lines at $\pm\pi/8$ and $\pm\pi/4$ mark the receiver's decision boundaries for DQPSK and D8PSK, respectively. If the channel transfer function's differential phase shift crosses the appropriate decision boundary for a given subcarrier index, then the data symbol transmitted over this subcarrier suffers from residual bit errors. In our example of Figure 4.16(a), there are four visible peaks comprising actually 6 out of 612 data-bearing subcarriers crossing the $\pi/8$ decision boundary for D8PSK. As the data is grey mapped on the PSK symbols, exactly one residual bit error will occur on



(a) differential phase error

(b) BER per subcarrier

Figure 4.16: Differential modulation over the static UMTS channel of Figure 4.5. (a) Phase difference between consecutive frequency domain samples of the frequency domain channel transfer function $H(n)$; the grey area designates the virtual subcarriers, which are not used for data transmission. (b) Simulated BER per subcarrier in static UMTS channel for D8PSK without channel estimation

each of the six subcarriers, resulting in a residual bit error rate of $6/1836 = 3.268 \cdot 10^{-3}$. Figure 4.16(b) gives an overview of the resulting BER per subcarrier for the data-bearing subcarriers for SNR values from 0 dB up to 50 dB. It can be seen that the residual bit errors are concentrated in four bursts, comprising the six symbols with subcarrier indices 136, 137, 312, 401, 477, and 478. At 50 dB SNR the symbols in the outer two bursts have a bit error rate of $1/3$, corresponding to one bit error per D8PSK symbol. The bit error rate of the inner two error bursts is lower, at about 23%, but is rising with higher SNR values to $1/3$. This rising BER with higher SNR values for the two inner error bursts is explained by the channel transfer function shown in Figure 4.16(a). The channel induces exactly one bit error for the symbols in each of the corresponding subcarriers in the absence of noise. Since the phase error due to the channel's phase rotation is very close to the decision 8-DPSK boundary, the presence of noise can influence the reception towards the correct decision, therefore reducing the long-term bit error rate.

In addition to residual bit errors, the decision boundary offset caused by the differential phase shift of the channel transfer function as depicted in Figure 4.16(a) will also compromise the noise sensitivity of the subcarriers that are not directly affected by residual errors.

4.4.1.3 Pilot Symbol-Assisted Modulation Aided Channel Transfer Function Estimation

As discussed in Section 4.3.1.1, pilot symbol-assisted modulation (PSAM) schemes acquire a channel transfer function estimate $\hat{H}(n)$ by sampling $H(n)$ with the aid of known pilot symbols embedded in the transmission burst and interpolating between the received pilots. We have seen that the minimal number of pilots needed to sample the channel transfer function follows the sampling theorem and that the maximal pilot distance in the OFDM symbol

System	FFT length	Max. delay $[T_s]$	max. Δp $[\Delta f]$	min. N_p
WATM	512	67	3	171
short WATM	512	11	23	22
WLAN	1024	32	16	64
UMTS	1024	17	30	34

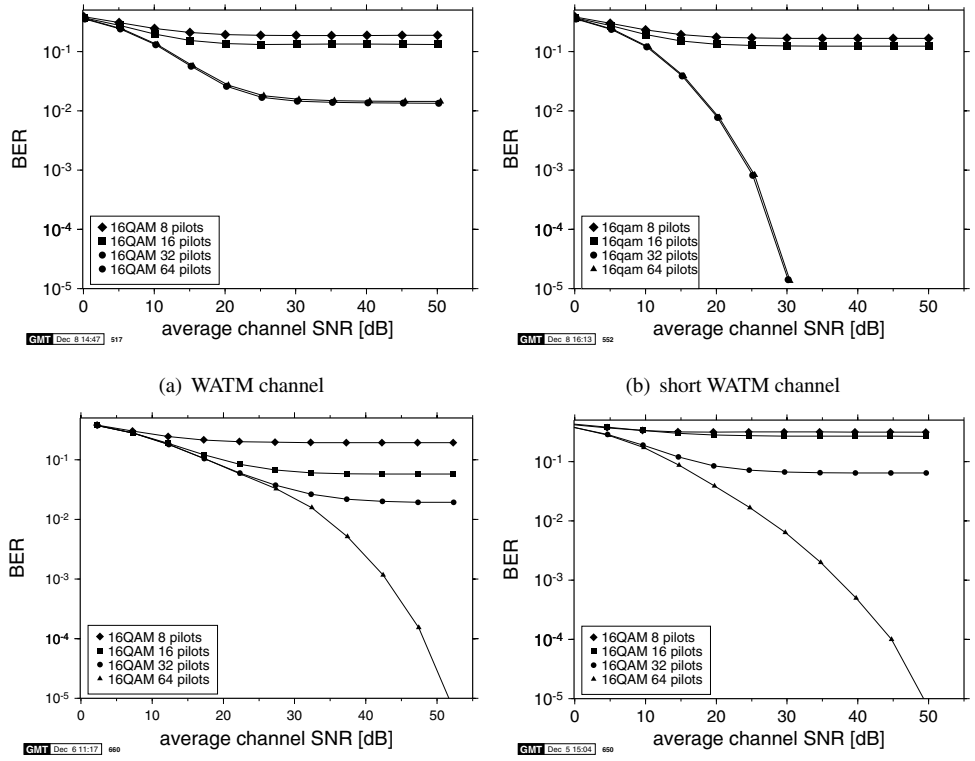
Table 4.3: Theoretical maximum pilot distance and minimal number of pilots for the WATM, short WATM, WLAN and UMTS systems

is given by Equation 4.8. Furthermore, we have seen that this minimal number of pilots only applies to the ideal lowpass filter interpolation algorithm, and more pilot symbols have to be employed, if linear rather than lowpass interpolation is to be used, therefore trading receiver complexity for transmission overhead.

Here we will characterise the performance of the four different OFDM systems in their respective non-fading channel environments. A more detailed discourse on channel transfer function estimation using both pilot-based as well as decision directed principles in single- as well as multi-user contexts is provided in Chapters 14-16 of the extended version of this monograph [90]. Each system was investigated using a range of pilot numbers. Using Equation 4.8, we can predict the number of pilot symbols necessary for each scenario, if ideal interpolation is assumed, and these numbers are given in Table 4.3. The performance evaluation for all these scenarios was carried out for 8, 16, 32 and 64 pilots with ideal lowpass interpolation and with the equivalent 9, 17, 33 and 65 pilot sets for linear interpolation. We will concentrate on our most robust and least robust modulation schemes, namely BPSK and 16-QAM.

Figure 4.17 shows the BER performance for all the discussed systems in their respective non-fading channels employing PSAM-16-QAM with ideal lowpass interpolation as modulation scheme. It can be seen in Figure 4.17(a) that the WATM system faces high residual bit error rates for all sets of pilot symbols investigated. This is expected, because the number of pilot subcarriers employed in these simulations was lower than the minimum number of 171 stated in Table 4.3. Therefore, the channel transfer function is not adequately sampled in the frequency domain and the resulting channel estimation is of insufficient accuracy for coherently detecting 16-QAM. Note that the residual bit error rate drops with increasing number of pilots employed for the channel estimation, but that the curves for 32-pilot and 64-pilot PSAM exhibit virtually equal performance. Figure 4.17(a) reveals that the estimated channel transfer function for these two cases is the same, owing to the twin-burst structure of the WATM impulse response of Figure 4.1(b). Therefore, increasing the number of pilots from 32 to 64 will not increase the system's performance, since this does not allow the modem to resolve the channel effects due to the two paths around 90 m.

According to Table 4.3, the short WATM channel can be adequately sampled with 22 pilot symbols equidistantly interspersed with the data symbols. This is in accordance with the system's performance curves in Figure 4.17(b). The BER curves for 32 and 64 subcarriers exhibit essentially identical performance, while for 8 and 16 pilot symbols the residual bit error rate is above 10%. For the WLAN channel, at least 64 pilots have to be employed in order to sample all the frequency components of $H(f)$. We can see in Figure 4.17(c) that all but the 60 pilot symbol systems exhibit residual bit error rates and that the BER performance



(a) WATM channel

(b) short WATM channel

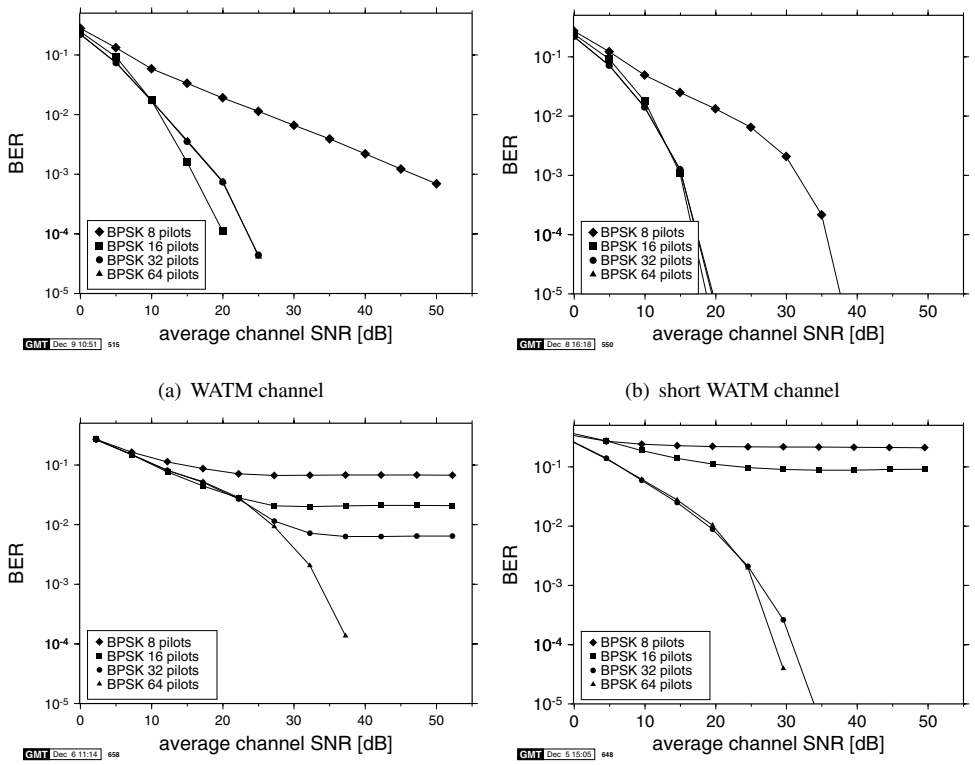
(c) WLAN channel

(d) UMTS channel

Figure 4.17: Bit error rate versus channel SNR for static (a) WATM channel (Figure 4.1(b)), (b) shortened WATM channel (Figure 4.3), (c) WLAN channel (Figure 4.4), (d) UMTS channel (Figure 4.5(a)), PSAM-16QAM with ideal lowpass interpolation

increases with an increased number of pilots.

If the more robust BPSK modulation scheme is used in the subcarriers, then the effects of inaccurate channel estimation are less pronounced. Figure 4.18 gives an overview of the BER performance for BPSK modems in the four operational environments, employing a perfect lowpass filter interpolator. The BER performance curves for the WATM system, shown in Figure 4.18(a), exhibit no residual errors. Like the 16-QAM curves, the performance is identical, irrespective of whether 32 or 64 pilot symbols are employed. Unlike in the 16-QAM case, however, the performance is best for 16-pilot subcarriers employed in the OFDM symbol. This oddity can be explained comparing the channel phase estimation errors for 16 and for 32 subcarriers, which are depicted in Figure 4.19. The phase estimation error for the WATM channel transfer function estimated with 16 pilot symbols is shown in Figure 4.19(a), which exhibits high fluctuations of the phase error of up to 0.7 radians. The phase estimation error for 32 pilot symbols, as shown in Figure 4.19(b), while substantially smaller on average, exhibits a peak error value of about 1.0 rad, which is closer to the BPSK decision boundary of $\pm\pi/2$ than the maximum error of the 16-pilot estimation. For higher SNR values the overall



(a) WATM channel

(b) short WATM channel

(c) WLAN channel

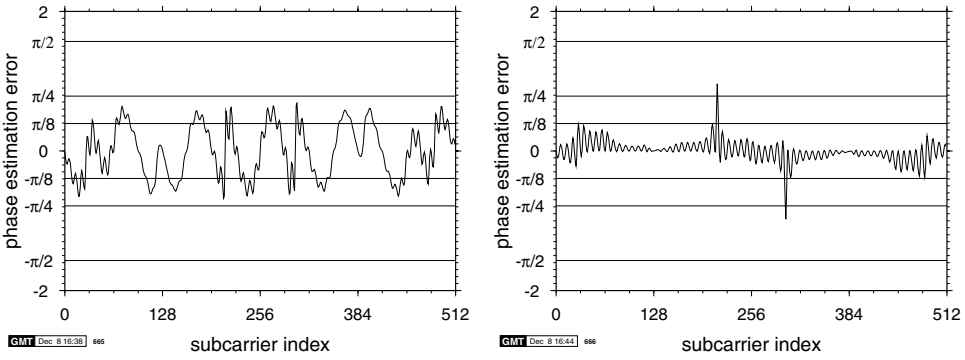
(d) UMTS channel

Figure 4.18: Bit error rate versus channel SNR for static (a) WATM channel (Figure 4.1(b)), (b) shortened WATM channel (Figure 4.3), (c) WLAN channel (Figure 4.4), (d) UMTS channel (Figure 4.5(a)), PSAM-BPSK with ideal lowpass interpolation

BER will be dominated by the bit errors occurring in the subcarriers with the highest phase estimation errors, therefore leading to the 16-pilot system performing better than the overall more accurate 32 and 64 pilot symbol estimation systems.

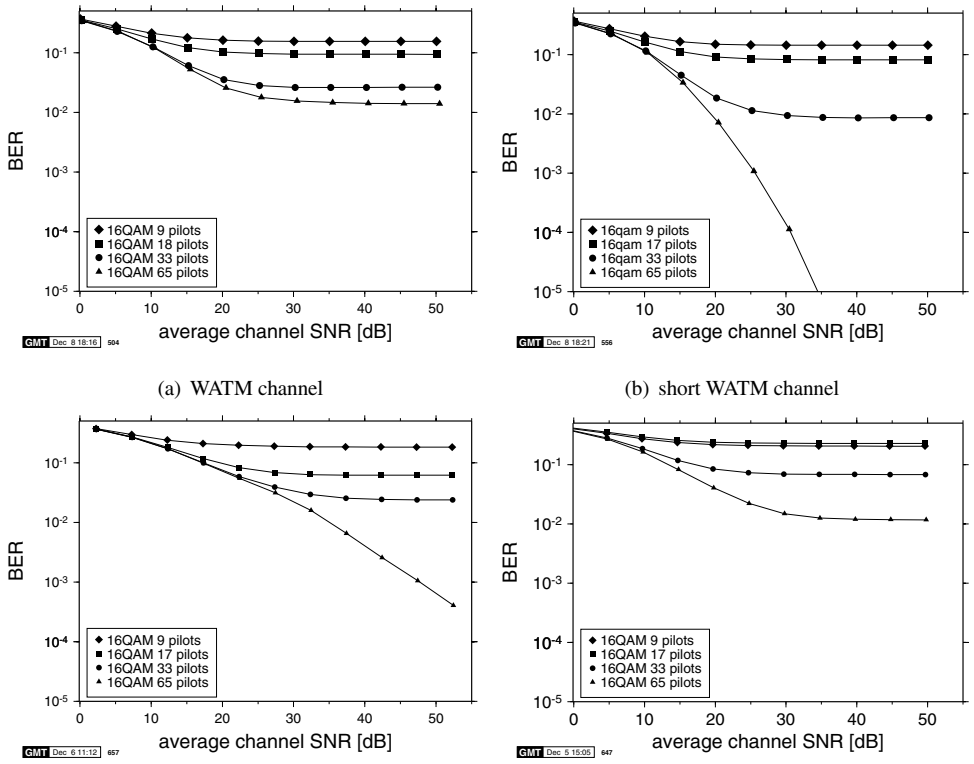
The WATM system's performance over the short WATM channel of Figure 4.3 is depicted in Figure 4.18(b). No residual bit error rates are observed and the BER performance with 32 and 64 pilots is identical. The 16-pilot BER curve is close to the 32- and 64-pilot results, and the modem performs about 18 dB worse with 8 pilot symbols. Both the WLAN as well as the UMTS channels exhibit residual bit errors for 8 and 16 pilot symbols and show an improving BER performance with increasing numbers of pilots. The WLAN system, whose performance is shown in Figure 4.18(c), performs without residual errors only when using 64 pilot symbols. For the UMTS channel, however, 32-pilot channel estimation results in a BER performance comparable to that of the 64-pilot estimation.

If the linear interpolation algorithm is employed instead of the ideal lowpass filter, then the BER performance of all the systems investigated is degraded. This is in accordance with the channel estimation experiments, as evidenced for example by the WATM channel estima-



(a) 16 pilots (b) 32 pilots

Figure 4.19: Channel transfer function phase estimation error for the WATM channel of Figure 4.1(b) employing ideal lowpass filter interpolator: (a) 16 pilot symbols, (b) 32 pilot symbols



(a) WATM channel (b) short WATM channel

(c) WLAN channel (d) UMTS channel

Figure 4.20: Bit error rate versus channel SNR for static (a) WATM channel (Figure 4.1(b)), (b) shortened WATM channel (Figure 4.3), (c) WLAN channel (Figure 4.4), (d) UMTS channel (Figure 4.5(a)), using PSAM 16-QAM with linear interpolation

tion plots in Figures 4.8 and 4.10. The BER performance curves for 16-QAM transmission employing linearly interpolated PSAM are given in Figure 4.20, and it can be seen that for all modems, the performance is worse than that associated with the lowpass interpolation curves shown in Figure 4.17. The least differences between the two interpolation algorithms are visible for the WATM modem. In both cases, 64-pilot symbols are insufficient for combating residual bit errors and the residual bit error rates for both schemes are similar. In the short UMTS channel, the differences are more obvious. While the performance of the 32- and 64-pilot estimation systems was the same for lowpass interpolation, the linear interpolation algorithm shows residual errors for 32 pilot symbols. Compared to the lowpass interpolation, the BER results for the linear interpolator using 64 pilots are about 3 dB worse.

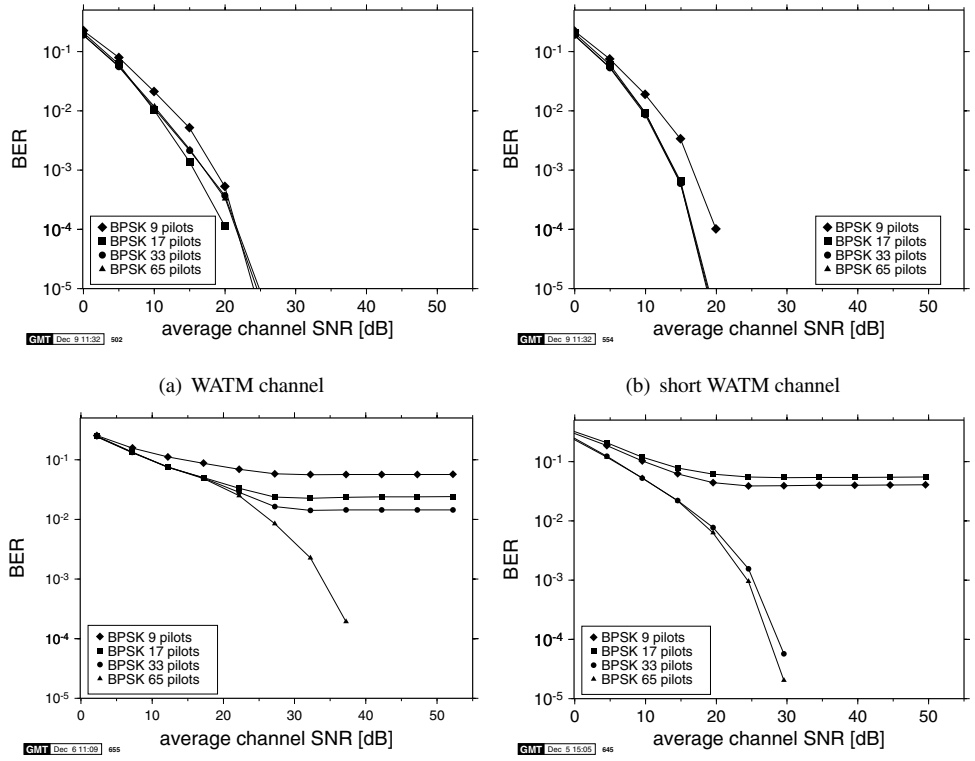
The BER performance for the WLAN system, as depicted in Figures 4.20(c) and 4.17(c), shows relatively minor differences between lowpass and linear interpolation. The residual bit error rates for 8, 16 and 32 pilots are similar, while for 64 pilots there is a SNR loss of about 5 dB for the linearly interpolated system at a BER of 10^{-3}. The UMTS, whose performance curves are plotted in Figure 4.20(d), exhibits a residual BER of about 1% for 64 pilots.

For BPSK-PSAM transmission over the OFDM systems, the difference in performance between lowpass and linear interpolation algorithms are much less apparent than for 16-QAM. Figure 4.21 gives an overview of the BER performance of the simulated systems in their respective environments using BPSK with linear interpolation-based channel estimation. The BER performance of the WATM system, as depicted in Figure 4.21(a), does not vary significantly with the number of pilots employed. This differs from the curves observed for the lowpass interpolator in Figure 4.18(a), where much higher bit error rates were observed, if only 8 pilots were employed for the channel estimation. Both the linear as well as the lowpass interpolator results show best performance for 17 and 16 pilot symbols, respectively. Over the short WATM channel, systems employing either interpolator exhibit an essentially identical performance for all but 8 and 9 pilots, respectively. In the latter case, there is a performance difference of 13-dB SNR for a BER of 10^{-3} in favour of the linear interpolation. For the WLAN and the UMTS, the BER performance with lowpass and linear interpolation is fairly similar, the difference being slightly lower residual bit error rates for the linearly interpolated channel estimation.

4.4.2 Slowly Varying Time-Dispersive Channel

The slowly varying time-dispersive channel is characterised by an impulse response that is time-varying, but which is assumed constant for the duration of one OFDM symbol. Hence we also refer to this channel model as an OFDM symbol time-invariant channel. This stationary property prevents intersubcarrier interference and renders the wideband channel estimation possible. In this case, the channel can be viewed as a succession of static impulse responses generated upon fading the constituting paths. The rate of change for each of the paths' fading is described by the Doppler frequency of the fading channel.

As we saw in Section 4.2.2, the time-varying nature of the channel transfer function will introduce intersubcarrier interference depending on the symbol normalised Doppler frequency $F_d = f_d \cdot T_s \cdot N$. Performance degradations can be observed even for small values of f_d. We will investigate the validity of the assumption of the stationary channel for our four scenarios in the case of perfect channel estimation.



(a) WATM channel

(b) short WATM channel

(c) WLAN channel

(d) UMTS channel

Figure 4.21: Bit error rate versus channel SNR for static (a) WATM channel (Figure 4.1(b)), (b) shortened WATM channel (Figure 4.3), (c) WLAN channel (Figure 4.4), (d) UMTS channel (Figure 4.5(a)), using PSAM-BPSK with linear interpolation

4.4.2.1 Perfect Channel Estimation

Perfect channel estimation is the best-case scenario for transmission over wideband channels and the system performance in these circumstances constitutes an upper bound to the achievable performance with realistic channel estimation algorithms. As the results for perfect channel estimation are not influenced by sub-optimal channel estimation, the effects of the time-varying channel on the transmitted data symbols can be studied and the validity of the static channel assumption for the four operating frameworks, namely WATM, short WATM, WLAN and UMTS, can be verified.

Perfect channel estimation of the time-varying wideband channel was achieved by taking a snapshot of the channel impulse response in the centre of the OFDM symbol and calculating the corresponding frequency domain channel transfer function from this impulse response by the help of the FFT. This transfer function does not fully characterise the channel, unlike in the static channel case, since it does not give any information concerning the intersubcarrier interference and only takes into account the time-varying nature of the impulse response. Nonetheless, the achieved channel estimation constitutes a best-case benchmark for realistic

channel estimation algorithms.

In order to isolate the influence of the time domain variations of the channel during the transmission of an OFDM symbol, experiments have been conducted for all four operating frameworks of Table 4.1 with two different models of the fading channel. First, the channel impulse response was updated after every transmitted sample, resulting in a realistic model for a time-varying wideband channel. The second set of experiments employed a stationary channel model, where the impulse response was kept constant for the duration of each transmitted OFDM symbol. The resulting BER results from these experiments are shown in Figure 4.22. A BER performance degradation due to the time-varying channel can be observed for all the systems. The BER degradation is low for the WATM system over both the WATM and the shortened WATM channel with $F_d = 0.0063$, exhibiting a residual BER of under $2 \cdot 10^{-4}$ for 16-QAM. For the WLAN system and the UMTS, whose F_d values are about 0.04, the BER degradation is much more evident. In both cases, the residual BER for 16-QAM transmission is about $6 \cdot 10^{-3}$ and for BPSK the BER residual is $7.4 \cdot 10^{-4}$. Clearly, for the UMTS and WLAN at the given vehicular speed, the channel cannot be assumed to be stationary.

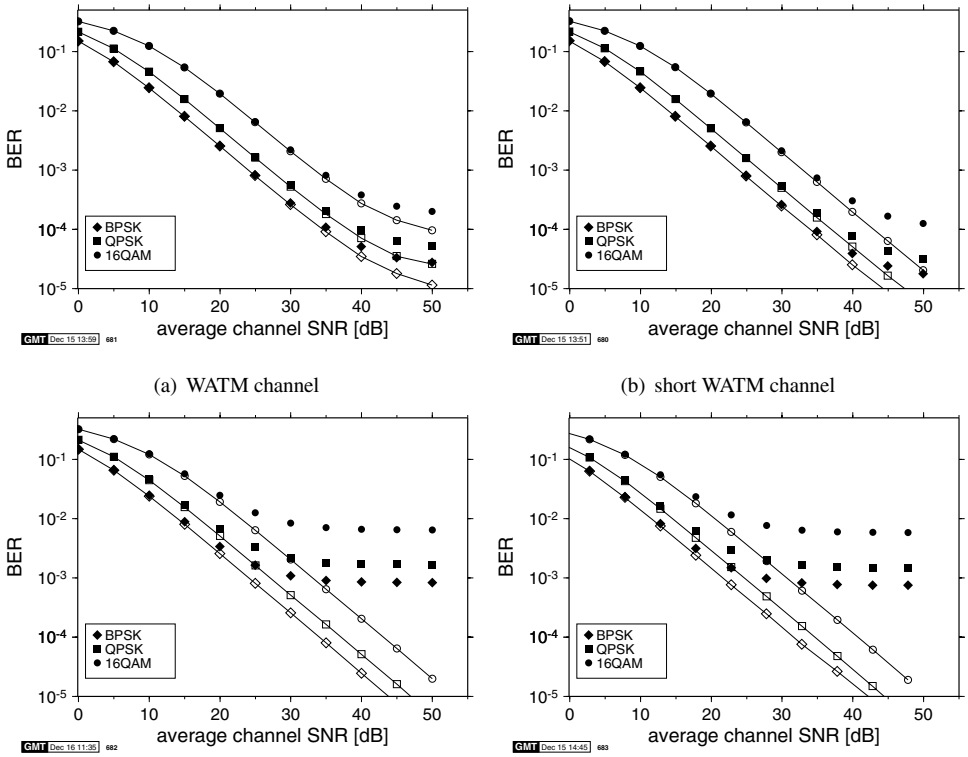
4.4.2.2 Pilot Symbol-Assisted Modulation Summary

In order to investigate the effects of imperfect channel estimation on the system's BER performance in wideband fading channels separately from the effects of time domain variations of the impulse response, the PSAM experiments have been conducted in the stationary channel. Therefore, the observed performance degradation compared to the perfect channel estimation results depicted in Figure 4.22 are caused by incorrect amplitude and phase estimations. The experimental results for 16-QAM transmission employing PSAM in conjunction with ideal lowpass and linear interpolation techniques are given in Figures 4.23 and 4.24, respectively. The estimation accuracy of the PSAM interpolation algorithms depends on each faded impulse response actually encountered by the modem, with some impulse amplitude combinations resulting in very poor estimation quality for the linear interpolation algorithm.

4.5 Intersubcarrier Interference Cancellation

4.5.1 Motivation

In the previous subsection it was argued that OFDM transmission is sensitive against the fading-induced CIR-tap variations incurred during an OFDM symbol period. This phenomenon leads to ICI and hence in this subsection we consider various techniques that may be invoked for mitigating the effects of ICI. ICI can be considered as an additional noise contribution, which linearly depends on the signal power and thus it potentially limits the achievable BER at relatively high SNRs. Here we propose a time domain CIR tap variation estimator, which relies on both the received signal as well as on tentative symbol decisions. Our simulation results obtained in the context of a system employing decision-directed channel-prediction demonstrate that with the aid of the proposed algorithm, ICI cancellation can be performed even in transmission scenarios associated with high Doppler frequencies. We will demonstrate that this may be achieved without inserting additional time domain pilot symbols.



(a) WATM channel

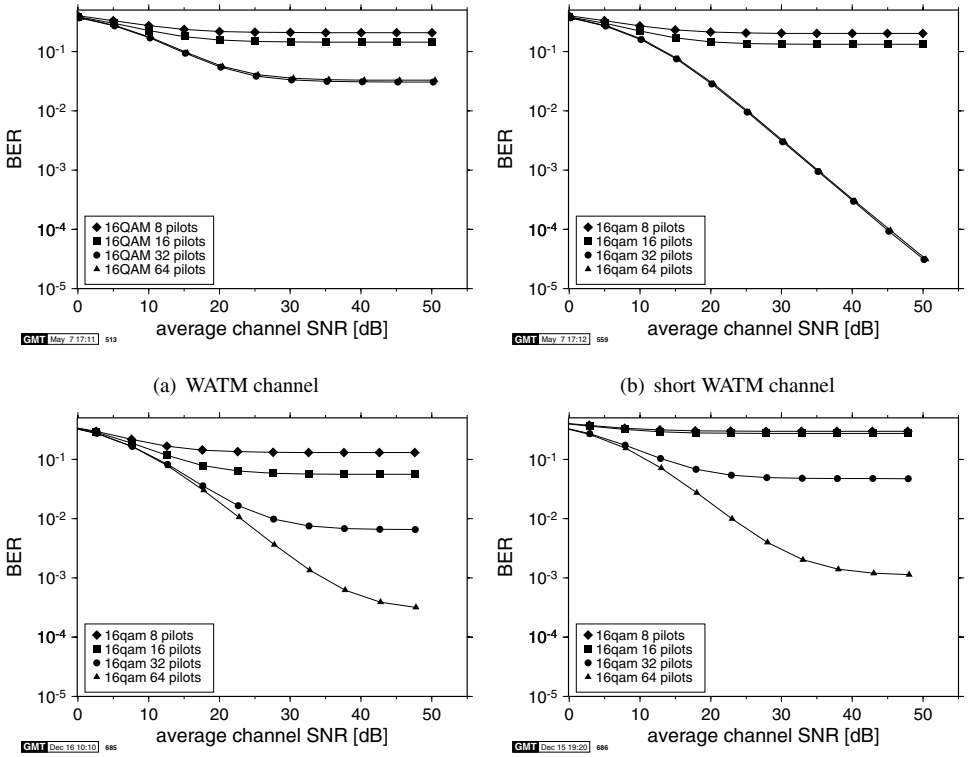
(b) short WATM channel

(c) WLAN channel

(d) UMTS channel

Figure 4.22: Bit error rate versus channel SNR for fading (a) WATM channel (Figure 4.1(b)), (b) shortened WATM channel (Figure 4.3), (c) WLAN channel (Figure 4.4), (d) UMTS channel (Figure 4.5(a)), using coherent detection and perfect channel estimation. The open symbols correspond to the stationary channel model and the filled symbols correspond to the continuously fading channel model

To elaborate a little further, the ICI contribution imposed on each subcarrier can be viewed as additional noise, which becomes - assuming a sufficiently high number of subcarriers - near-Gaussian distributed as a consequence of the central limit theorem. However, in contrast to the effects of AWGN, the ICI imposed on the different subcarriers is correlated. Since the ICI power is a linear function of the signal power, the AWGN power may be exceeded by the ICI power, when the transmitted signal power is high. Several schemes have been proposed in the literature for reducing the ICI noise power [193–195]. For example, Hasholzner *et al.* [193] propose to model the ICI generation by means of a Multiple-Input Multiple-Output (MIMO) system. Equalised and potentially less ICI contaminated subcarrier signals are obtained by a weighted superposition of the signal received in each subcarrier with the contributions from its neighbours. Adaptation of the frequency domain MIMO equaliser weights is achieved by means of the Recursive Least Squares (RLS) algorithm upon invoking the difference between the complex signals at the symbol detector output and at the equaliser output.



(a) WATM channel

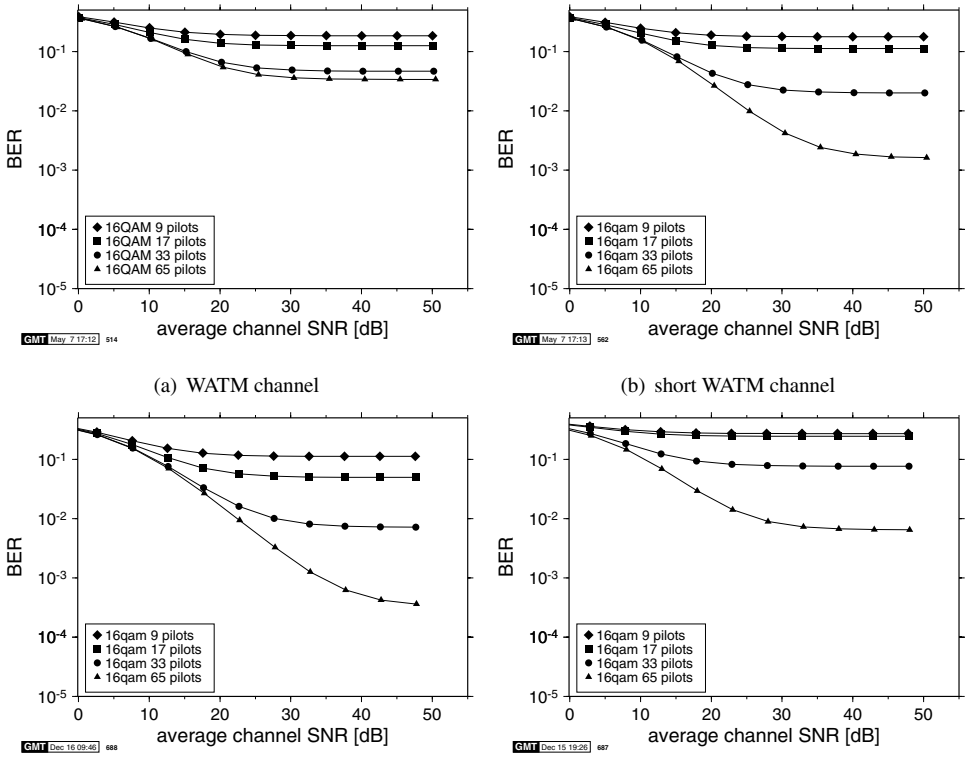
(b) short WATM channel

(c) WLAN channel

(d) UMTS channel

Figure 4.23: Bit error rate versus channel SNR for fading (a) WATM channel (Figure 4.1(b)), (b) shortened WATM channel (Figure 4.3), (c) WLAN channel (Figure 4.4), (d) UMTS channel (Figure 4.5(a)), using coherent detection and pilot symbol assisted channel estimation with ideal lowpass filter interpolation for 16-QAM

A drawback of this approach is the RLS algorithm's limited CIR tracking capability under rapid fading channel conditions. An algorithm which follows a similar strategy was proposed in [194]. Here the equaliser weights are obtained by directly inverting the channel matrix describing the MIMO system inflicting the ICI. This approach is equivalent to de-coupling the subcarriers. However, the dimension of the channel matrix is in most cases excessive for direct inversion. Hence, the inversion of multiple lower-dimensional sub-matrices hosting only a limited subset of complex ICI transfer factors between the subcarrier to be decontaminated and its nearest neighbours was proposed in both [193] and [194]. Since the rate of change of the CIR tap values is limited by the channel's Doppler frequency, the ICI is predominantly restricted to neighbouring subcarriers. The estimation of the channel matrix was achieved in [194] upon regularly inserting time domain pilot symbols into the OFDM symbol stream. More specifically, the channel sounding symbol was a Dirac-impulse like time domain pilot tone surrounded by zero-samples, where the length of each zero-segment was identical to that of the OFDM symbol's cyclic prefix. For the simulations presented



(a) WATM channel

(b) short WATM channel

(c) WLAN channel

(d) UMTS channel

Figure 4.24: Bit error rate versus channel SNR for fading (a) WATM channel (Figure 4.1(b)), (b) shortened WATM channel (Figure 4.3), (c) WLAN channel (Figure 4.4), (d) UMTS channel (Figure 4.5(a)), using coherent detection and pilot symbol-assisted channel estimation with linear interpolation for 16-QAM

in [194], a propagation scenario having a relatively small delay spread was assumed, since otherwise the additional channel-sounding overhead would have been prohibitive. In the context of the Wireless Asynchronous Transfer Mode (WATM) system model, 512 subcarriers and a 64-sample guard interval were assumed [2]. Using the channel sounding symbols proposed in [194], this would impose a pilot overhead of 25%, which is excessive. A potential solution requiring no additional pilot information for estimating the CIR tap's variation will be detailed in Sections 4.5.3 of our contribution. Another approach which we would like to mention is that of Hutter *et al.* [195], where a reduction of the ICI was achieved upon exploiting the correlation between the ICI contributions imposed on adjacent subcarriers. In contrast to the algorithms outlined in [193, 194], in [195] no explicit knowledge concerning the frequency domain MIMO channel transfer factors between the different subcarriers was invoked. An estimate of the short-term channel correlation matrix was obtained by evaluating the vector of error signals between the sliced and remodulated symbol and the received symbol for each subcarrier, followed by multiplication with its Hermitean transpose.

A refinement was achieved through averaging with the corresponding tentative estimate associated with the previous OFDM symbol period. The rest of this section is organized as follows. In Section 4.5.2 the ICI generation procedure will be highlighted, followed by the evaluation of the potentially achievable ICI reduction. The philosophy of an attractive CIR tap variation estimator will be detailed in Section 4.5.3, while the ICI canceller is described in Section 4.5.4. The system's BER performance is characterised in Section 4.5.5 and we will draw our conclusions in Section 4.6.

4.5.2 The Signal Model

It has been demonstrated for example in [194] that the signal $x[n,k]$ received in the k-th subcarrier of the n-th OFDM symbol is a weighted superposition of the complex symbol $s[n,k]$ assigned to this subcarrier at the transmitter, with the contributions $s[n,\acute{k}]$ from all other subcarriers $\acute{k} \neq k$:

$$\begin{aligned} x[n,k] &= \sum_{\acute{k}=0}^{N-1} \left(\sum_{m=0}^{M-1} H_m[n,k-\acute{k}] e^{-j\frac{2\pi}{N}m\acute{k}} \right) s[n,\acute{k}] + \\ &\quad + n[n,k], \end{aligned} \tag{4.11}$$

where:

$$H_m[n,k-\acute{k}] = \frac{1}{N} \sum_{t=0}^{N-1} h_m[n,t] e^{-j\frac{2\pi}{N}t(k-\acute{k})}, \tag{4.12}$$

$$n[n,k] = \sum_{t=0}^{N-1} \acute{n}[n,t] e^{-j\frac{2\pi}{N}tk}. \tag{4.13}$$

Specifically, $H_m[n,k-\acute{k}]$ defined in Equation 4.12 denotes the $(k-\acute{k})$-th frequency bin of the DFT associated with the complex time domain fading signal $h_m[n,t]$ of the m-th CIR tap during the n-th OFDM symbol period - normalised to the number of subcarriers N. Furthermore, $n[n,k]$ is the k-th DFT bin of the complex time domain AWGN noise process $\acute{n}[n,t]$, again for the n-th OFDM symbol period. The term $M-1$ represents the maximum multipath-delay imposed by the channel, given as an integer multiple of the sampling interval duration T_s. It should be noted that in Equation 4.11 the contributions for $k \neq \acute{k}$ constitute the ICI inflicted by the neighbouring subcarriers upon the k-th subcarrier. In [195, 196] the variance of the ICI has been evaluated, employing the standard definition $\sigma^2_{ICI} = E\{x[n,k]x^*[n,k]|_{k\neq\acute{k}}\}$ with the aid of Equation 4.11, where $E\{\}$ denotes the expectation. Similarly, we can evaluate the variance of the residual ICI, $\sigma^2_{ICI,resid}$ at the output of an ideal ICI cancellation scheme which is capable of suppressing the undesired ICI contri-

$matrix_size$	1	3	5
$\sigma^2_{ICI,cancel}/\sigma^2_s\|_{lin}$	0.012896	0.005008	0.003063
$reduction\|_{dB}$		-4.108	-2.135

Table 4.4: *Residual* ICI variance normalised to the signal variance for an OFDM symbol normalised Doppler frequency of $f_dT_f = 0.1$ in the context of the indoor WATM channel environment using $N = 512$ and $N_g = 64$.

butions in the range of $\{k - sym, \ldots, k + sym\}\backslash\{k\}$ around the subcarrier k, as follows:

$$\frac{\sigma^2_{ICI,resid}}{\sigma^2_s} = 1 - \frac{1}{N^2}\Bigg[(1 + 2 \cdot sym)N + \\ + 2\sum_{\Delta n=1}^{N-1}(N - \Delta n)\frac{sin\left((sym + \frac{1}{2})\frac{2\pi}{N}\Delta n\right)}{sin\left(\frac{\pi}{N}\Delta n\right)} \cdot J_0\left(2\pi T_s f_D \Delta n\right)\Bigg], \tag{4.14}$$

where a normalization to the signal variance σ^2_s has been performed. In Equation 4.14, $J_0()$ denotes the zero-order Bessel function of the first kind, assuming Jakes fading [150], T_s is the sampling interval duration and f_D is the maximum Doppler frequency of the channel. It should be noted that by setting the one-sided ICI cancellation range sym equal to zero, Equation 4.14 degenerates into the corresponding expression for the ICI noise variance given in [195, 196]. We have evaluated Equation 4.14 for channel sub-matrix sizes of 1, 2 and 4, where the sub-matrix size is related to the one-sided ICI cancellation range according to $matrix_size = 1 + 2 \cdot sym$. Hence, a sub-matrix size of 1 corresponds to the case of no ICI cancellation. Here we employed the parameters of the indoor WATM system model [2]. Specifically $N = 512$ and $f_dT_f = 0.1$ was assumed as a worst-case scenario, where T_f denotes the frame duration, which is related to the sampling interval duration T_s by $T_f = (N + N_g)T_s$, with N_g as the number of guard samples. The results are listed in Table 4.4, where we have also calculated the differential ICI variance reduction in terms of dB, achieved by increasing the ICI cancellation range. In accordance with [194] the highest improvement is achieved by employing ICI cancellation with a one-sided range of 1 instead of no cancellation. Specifically this results in an ICI reduction of about $4.1dB$. A prerequisite for attaining this performance is the availability of perfect channel- and error-free symbol knowledge, so that the ICI contributions can be perfectly reconstructed and subtracted from the received signal. Upon invoking Equation 4.14 and by considering the first two elements of the Taylor approximation of $J_0(x)$, which is $\tilde{J}_0(x) = 1 - \frac{1}{4}x^2 \; \forall \; x \ll 1$ [108], we also confirm that in the range of f_DT_f of interest, the ICI variance is proportional to the square of the Doppler frequency f_D: $\sigma^2_{ICI,red} = c \cdot f^2_D\sigma^2_s$, where c is the proportionality constant inherent in Equation 4.14. We conclude furthermore that the maximum achievable ICI reduction is independent of the Doppler frequency f_D. In the next section we will embark on a description of the system model.

4.5.3 Channel Estimation

In Section 4.5.1 we outlined that a prerequisite for the cancellation of CIR variation induced ICI considered here is the availability of an estimate of the variation of each CIR tap during a specific OFDM symbol period. In contrast to [194], our aim is to avoid using dedicated time domain pilot symbols while also circumventing the employment of an iterative MIMO equaliser weight update strategy. **Explicitly, our strategy is to obtain tentative symbol decisions without using ICI cancellation in a first iteration, followed by an estimation of the CIR tap variations on the basis of these tentative symbol decisions and by also capitalising on the knowledge of the received time domain signal. This is followed by frequency domain ICI cancellation and a final iteration to obtain symbol decisions on the basis of a potentially less ICI-contaminated signal.** Hence, our aim in this section is to develop the CIR tap variation estimator. The received time domain signal $r[n,t]$, $t \in \{0,\ldots,N-1\}$ within the FFT window of the n-th OFDM symbol period is given by the convolution of the time-variant CIR tap values $h_m[n,t]$, where $m \in \{0,\ldots,M-1\}$ denotes the tap index, with the output $t[n,t]$ of the OFDM modulator, yielding:

$$r[n,t] = \sum_{m=0}^{M-1} h_m[n,t]t[n,t-m] + \acute{n}[n,t]. \tag{4.15}$$

Here we follow the philosophy that the evolution of each CIR tap value during the FFT window of an OFDM symbol period can be linearly approximated, which was also advocated in [194], resulting in:

$$\tilde{h}_m[n,t] = \tilde{c}_m[n] \cdot t + \tilde{b}_m[n], \tag{4.16}$$

where $\tilde{c}_m[n]$ and $\tilde{b}_m[n]$, $m \in \{0,\ldots,M-1\}$ are the CIR tap variation estimator coefficients to be determined. Hence, a cost-function given by the aggregate mean-square error between the received time domain signal and the appropriately synthesized signal can be defined as follows:

$$C[n] = \sum_{t=0}^{N-1} \left| r[n,t] - \sum_{m=0}^{M-1} (\tilde{c}_m[n]t + \tilde{b}_m[n])t[n,t-m] \right|^2. \tag{4.17}$$

In order to determine the estimator coefficients $\tilde{c}_m[n]$ and $\tilde{b}_m[n]$ for all $m \in \{0,\ldots,M-1\}$, a suitable approach is to minimise Equation 4.17 using standard optimisation techniques, namely by evaluating the partial derivatives with respect to the desired variables:

$$\begin{aligned} \frac{\partial C[n]}{\partial \tilde{b}_m[n]} &= \sum_{t=0}^{N-1} \Bigg\{ - r^*[n,t]t[n,t-m] + \\ &\quad + \sum_{\acute{m}=0}^{M-1} (\tilde{c}^*_{\acute{m}}t + \tilde{b}^*_{\acute{m}}) \cdot t[n,t-m]t^*[n,t-\acute{m}] \Bigg\}, \end{aligned} \tag{4.18}$$

$$\frac{\partial C[n]}{\partial \tilde{c}_m[n]} = \sum_{t=0}^{N-1} \Bigg\{ - r^*[n,t] \cdot t \cdot t[n,t-m] + \\ + \sum_{\acute{m}=0}^{M-1} (\tilde{c}^*_{\acute{m}} t + \tilde{b}^*_{\acute{m}}) \cdot t \cdot t[n,t-m] t^*[n,t-\acute{m}] \Bigg\}. \tag{4.19}$$

At the optimum point the partial derivatives $\partial C[n]/\partial \tilde{b}_m$ and $\partial C[n]/\partial \tilde{c}_m$ are zero for all $m \in \{0, \ldots, M-1\}$. Hence, a system of equations can be established assuming knowledge of the received signal $r[n,t]$ and that of the transmitted signal $t[n,t]$, yielding estimates for the desired estimator coefficients upon inverting a matrix of dimensions $2M \times 2M$. In [110] it was proposed - assuming a similar estimation problem - to identify the path delays exhibiting the highest signal power and hence only to incorporate these so-called significant taps in the estimation process. This could be achieved with the aid of dedicated OFDM training symbols employed in the context of decision-directed channel estimation [150, 197]. The advantage would potentially be a significant size reduction of the matrix to be inverted. In the next section we will outline a range of different ICI cancellation schemes applicable to our system.

4.5.4 Cancellation Schemes

We commence with a brief review of the most prominent ICI-cancellation schemes employed. Let us recall Equation 4.11, which established a relationship between the symbols $s[n,\acute{k}]$ transmitted in different subcarriers $\acute{k}$ and the complex symbol $x[n,k]$ received on the k-th subcarrier, as a function of the subcarrier coupling factors and that of the channel noise. This relation could also be expressed in matrix form, potentially leading to an $N \times N$ frequency domain MIMO channel matrix, where N denotes the number of subcarriers. Fully compensating for the effects of ICI would require as alluded to in Section 4.5.2 the inversion of the channel matrix, which is impractical in terms of computational complexity. Hence, a more practical solution is to exploit the band structure of the channel matrix, which is a direct consequence of the sharply decaying ICI influence as a function of the frequency domain separation of subcarriers. This is a ramification of the relatively low Doppler frequency in comparison to the OFDM symbol's bandwidth. Therefore we perform ICI cancellation only for a limited subset of the subcarriers, namely within a range of sym around the subcarrier considered [193, 194]. Hence, for the k-th subcarrier a simplified relation between the transmitted symbol $s[n,k]$ and the received symbol $x[n,k]$ - assuming a cancellation range of $sym = 1$ is given by [194]:

$$\mathbf{x}[k] = \mathbf{H}[k]\mathbf{s}[k] + \mathbf{n}_r[k], \tag{4.20}$$

where

$$\mathbf{x}[k] = (x[k-1], x[k], x[k+1])^T \tag{4.21}$$

$$\mathbf{s}[k] = (s[k-1], s[k], s[k+1])^T \tag{4.22}$$

$$\mathbf{n}_r[k] = (n^k_r[k-1], n^k_r[k], n^k_r[k+1])^T, \tag{4.23}$$

and

$$\mathbf{H}[k] = \begin{pmatrix} H[k-1,k-1] & H[k-1,k] & 0 \\ H[k,k-1] & H[k,k] & H[k,k+1] \\ 0 & H[k+1,k] & H[k+1,k+1] \end{pmatrix}. \quad (4.24)$$

For notational convenience we have omitted the OFDM symbol index n. The vector $\mathbf{n}_r[k]$ of residual noise contributions requires further explanation. Each of its elements $n_r^k[x]$ is constituted by the sum of the AWGN in the x-th subcarrier and the residual ICI taking into account the partial ICI cancellation. For example, following from the structure of the matrix $\mathbf{H}[k]$ defined in Equation 4.24, the residual ICI contribution in the $(k-1)$-th subcarrier is identical to the original contribution minus the contribution from the k-th subcarrier. By contrast, the residual ICI in the k-th subcarrier is constituted by the difference between the original contribution in this subcarrier minus the interference due to the $(k-1)$-th and the $(k+1)$-th subcarrier. The elements of the matrix $\mathbf{H}[k]$ can be directly inferred from Equation 4.11, specifically from the term in round brackets. Equation 4.20 suggests several approaches for recovering the symbol transmitted on the k-th subcarrier. The authors of [194] proposed the direct inversion of the partial channel matrix $\mathbf{H}[k]$, which will be referred to during our comparative study as the **zero-forcing (ZF)** solution. Hence, the signal at the output of the combiner is given by:

$$\tilde{\mathbf{s}}_{ZF}[k] = \mathbf{H}^{-1}[k]\mathbf{x}[k], \quad (4.25)$$

where finally only the desired element in the center of the vector $\tilde{\mathbf{s}}_{ZF}[k]$ is retained. An exception is given by the first and the last vector of recovered symbols, where the first $sym+1$ elements and the last $sym+1$ elements are retained [194], respectively. A well-known disadvantage of the ZF solution is the associated potential noise amplification. A more attractive, but also more complex approach is the minimum mean-square error (MMSE) solution, which was also advocated in [195]:

$$\tilde{\mathbf{s}}_{MMSE}[k] = \left(\mathbf{H}^H[k]\mathbf{H}[k] + \left(\frac{\sigma_{n,\sum}^2}{\sigma_s^2} + dl \right) \mathbf{I} \right)^{-1} \mathbf{H}^H[k]\mathbf{x}[k]. \quad (4.26)$$

It should be noted that in contrast to [195] we have not taken into account the correlation between the residual ICI associated with the subcarriers encompassed by the partial MIMO channel matrix $H[k]$, since the merit of doing so appears to be relatively limited. The residual noise variance $\sigma_{n,\sum}^2$ in Equation 4.26 is given by the sum of the AWGN noise variance σ_n^2 and the residual ICI variance $\sigma_{ICI,cancel}^2$, where in the context of our simulations we have employed the estimated noise variance given in the second column of Table 4.4. Furthermore, in Equation 4.26, dl denotes a diagonal loading constant, which is often employed in the literature [195] for facilitating the inversion of ill-conditioned matrices. In the context of our simulations in Section 4.5.5 we experimentally found a value of $dl = 0.055$ to operate best for BPSK and $dl = 0$ for QPSK. A third approach to ICI cancellation, which - in contrast to the previously mentioned ZF- and MMSE solutions - requires the knowledge of the transmitted symbols, is that of subtractive cancellation, which is defined here simply by the subtraction

of the reconstructed signal from the received signal. This can be expressed as:

$$\tilde{\mathbf{s}}_{MMSE}[k] = r[k] - \sum_{\substack{\acute{k}=k-sym \\ \acute{k}\neq k}}^{k+sym} H[k,\acute{k}]\hat{s}[\acute{k}], \tag{4.27}$$

where $\hat{s}[\acute{k}]$ denotes the tentative symbol decision of the $\acute{k}$-th subcarrier symbol obtained during the first iteration. In next section the above ICI cancellation schemes will be characterised in conjunction with the CIR tap variation estimator introduced in Section 4.5.3.

4.5.5 ICI Cancellation Performance

In this section we will assess the performance of the proposed system using a decision-directed channel estimator similar to that proposed in [150] for obtaining initial symbol decisions. In [150] Wiener filtering of the CIR taps in the time domain is employed for obtaining a potentially less noise-contaminated estimate of the channel transfer function for the current timeslot, which is then employed as an initial channel estimate during the next timeslot. This implies assuming the invariance of the channel transfer function between two consecutive OFDM symbols. By contrast, we employ a Wiener prediction filter in order to compensate for the CIR tap variations actually incurred in the high-Doppler propagation scenarios considered here. As outlined in [197], the conceptual difference between the interpolation and the prediction filter resides in the structure of the co-variance vector, which is part of the Wiener equation. In our simulations we employed a decision-directed channel estimator capitalising on an 8-tap CIR predictor, a training period of 32 OFDM symbols and a training block length of two OFDM symbols. It should be noted that the training period or equivalently the time domain distance between two training blocks is a crucial parameter, especially at low SNRs, where error propagation is known to deteriorate the decision-directed channel estimator's performance. The training block length has two implications. Firstly, at low SNRs error propagation extending over the training period is experienced as the result of using past CIR estimates in the process of CIR tap prediction. Secondly, the CIR tap predictor is required to deliver sufficiently accurate channel estimates already during the reception of the first information-bearing OFDM symbol. It should be noted that the proposed CIR tap variation estimator could also be employed in a system, which invokes for example frequency domain pilot symbols for obtaining a tentative CIR estimate, in order to assist in the tentative initial demodulation required. Our simulations have been conducted in the context of the 512-subcarrier indoor WATM channel [2] employing a worst-case Doppler scenario of $f_D T_f = 0.1$. Our BER results for BPSK modulation are portrayed in Figure 4.25, while those for QPSK modulation are depicted in Figure 4.26. In both figures we have also plotted the system's performance without ICI cancellation. We considered both, a "frame-invariant" fading scenario, where the fading envelope was kept constant during an OFDM symbol period in order to avoid the generation of ICI, and a "frame-variant" fading scenario. We observe that even in the context of "frame-invariant" fading, where no ICI was generated, the BER performance is limited at high SNRs, which is attributed to the imperfections of the CIR predictor. Amongst the different ICI cancellation schemes the MMSE canceller exhibits the best performance. Specifically, in the context of BPSK the BER is reduced by a factor of 5, while in conjunction with QPSK a reduction by a factor of 3 is observed. The BER dif-

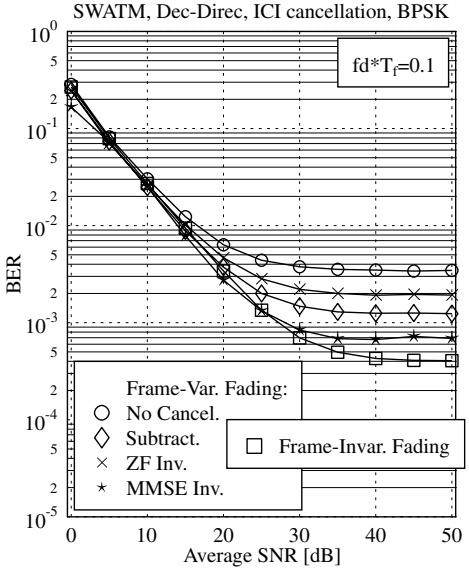


Figure 4.25: BER performance of a system employing 8-tap Wiener filter prediction assisted decisions-directed channel estimation and two-stage ICI cancellation according to Sections 4.5.3 and 4.5.4 by using **BPSK modulation**.

ference between these schemes can be explained by pointing out that the minimum distance between signal points hosted by a QPSK constellation are located closer to each other than in the BPSK constellation and hence a higher vulnerability against channel estimation errors and channel noise can be observed. Another phenomenon, which requires further explanation is that for BPSK the ZF-inversion performs worse, than subtraction based cancellation. By contrast, for QPSK the situation was reversed. An explanation is that in the case of BPSK, when relatively reliable first-iteration symbol decisions are available, the subtractive combiner does not encounter the problem of noise amplification, which was associated with the ZF-inversion based solution. Again, by contrast, for QPSK more erroneous symbol decisions are employed in the subtractive cancellation process and hence the ZF-inversion, which does not capitalise directly on tentative symbol decisions is advantageous.

4.5.6 Conclusions on ICI Cancellation

In this section we have demonstrated the feasibility of CIR tap variation-induced ICI cancellation without requiring additional time domain pilot symbols as in [194] or without necessitating iterative weight update techniques as in [193]. We employed a two-stage detection technique, where during the first iteration tentative symbol decisions are provided on the basis of the initially ICI-contaminated received signal. These initial estimates are then employed to estimate the CIR tap variations incurred during the current OFDM symbol period. Following the process of ICI cancellation, the potentially less ICI-impaired received signal is employed in a second demodulation iteration to provide symbol decisions. As a result, the BER was reduced by a factor of five in the context of BPSK and a factor of three in the context of

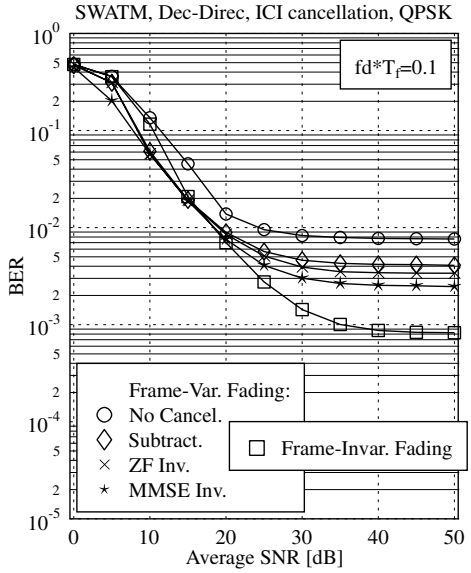


Figure 4.26: BER performance of a system employing 8-tap Wiener filter prediction assisted decisions-directed channel estimation and two-stage ICI cancellation according to Sections 4.5.3 and 4.5.4 by using **QPSK modulation**.

QPSK, when using decision-directed channel estimation as a basis for first-stage detection.

4.6 Chapter Summary and Conclusion

The performance of OFDM transmission over time-varying and time-dispersive channels is mainly limited by two factors, namely the long-term shape and the rate of time-variability of the channel's impulse response. The maximum impulse response dispersion determines the rate of frequency domain fluctuation of the channel transfer function, which manifests itself as frequency domain fading across the bandwidth of the OFDM symbol. The effects of this frequency domain channel transfer function fading can be combated with the aid of similar PSAM methods employed in the frequency domain as known from the time domain fading envelope estimation technique employed in conventional narrowband serial modems. Similarly to conventional serial time domain transmission schemes, frequency domain PSAM requires the transmission of known pilot symbols and hence increases the system's overhead.

As an alternative solution, differential detection of the received data symbols may be invoked, where we exploit that the adjacent subcarriers of an OFDM typically experience similar frequency domain attenuations and phase rotations. Similar statements may be made also for the subcarriers at the same frequency of consecutive OFDM symbols. Hence the effects of channel transfer function fluctuations may be eliminated, when the adjacent subcarriers are used as the reference required for differential detection. We have to note, however, that differential detection typically shows a 3 dB SNR performance loss compared to coherently detected schemes. For both differential detection and PSAM the channel's impulse response

determines the achievable performance. High-dispersion channels result in rapid fading in the frequency domain, either requiring more pilots per OFDM symbol for PSAM or degrading the achievable BER performance of differential detection.

Variations of the channel's impulse response, caused by fast fading of the constituting paths, result in interference between the OFDM symbol's subcarriers. This intersubcarrier interference is low, if the channel varies only insignificantly during an OFDM symbol, but causes severe performance degradation, if the rate of the channel variation is not much slower than the OFDM symbol rate. The effect of intersubcarrier interference therefore limits the maximum number of subcarriers employed in an OFDM system, depending on the channel's Doppler frequency and the robustness of the modulation scheme employed. Finally, the chapter was closed by proposing an ICI cancellation technique, which was capable of substantially improving the achievable system performance.

In the next chapter we will study a range of time and frequency synchronisation issues encountered in the context of OFDM transmission schemes.

Chapter 5

OFDM Time and Frequency Domain Synchronisation

In this chapter we will investigate the effects of time and frequency domain synchronisation errors on the performance of an OFDM system, and two different synchronisation algorithms will be presented for time domain burst-based OFDM communications systems.

5.1 System Performance with Frequency and Timing Errors

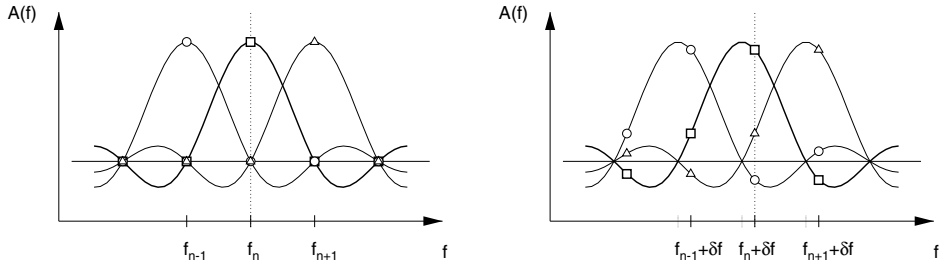
The performance of the synchronisation subsystem, in particular the accuracy of the frequency and timing error estimations, is of major influence on the overall OFDM system performance. In order to investigate the effects of carrier frequency and time domain FFT window alignment errors, a series of investigations has been performed over different channels.

5.1.1 Frequency Shift

Carrier frequency errors result in a shift of the received signal's spectrum in the frequency domain. If the frequency error is an integer multiple n of the subcarrier spacing Δf, then the received frequency domain subcarriers are shifted by $n \cdot \Delta f$. The subcarriers are still mutually orthogonal, but the received data symbols, which were mapped to the OFDM spectrum, are in the wrong position in the demodulated spectrum, resulting in a bit error rate of 0.5.

If the carrier frequency error is not an integer multiple of the subcarrier spacing, then energy is spilling over between the subcarriers, resulting in loss of their mutual orthogonality. In other words, interference is observed between the subcarriers, which deteriorates the bit error rate of the system. The amount of this intersubcarrier interference can be evaluated by investigating the spectrum of the OFDM symbol.

OFDM and MC-CDMA: A Primer L. Hanzo and T. Keller
© 2006 John Wiley & Sons, Ltd



(a) perfect sampling (b) frequency error

Figure 5.1: Stylised plot of OFDM symbol spectrum with sampling points for three subcarriers. The symbols on the curves signify the contributions of the three subcarriers to the sum at the sampling point: (a) no frequency offset between transmitter and receiver, (b) frequency error δf present

5.1.1.1 The Spectrum of the OFDM Signal

The spectrum of the OFDM signal is derived from its time domain representation transmitted over the channel. A single OFDM symbol in the time domain can be described as:

$$u(t) = \left[\sum_{n=0}^{N-1} a_n e^{j\omega_n \cdot t}\right] \times \text{rect}\left(\frac{t}{N \cdot T_s}\right), \tag{5.1}$$

which is the sum of N subcarriers $e^{\omega_n \cdot t}$, each modulated by a QAM symbol a_n and windowed by a rectangular window of the OFDM symbol duration T_s. The Fourier transform of this rectangular window is a frequency domain sinc function, which is convolved with the Dirac delta subcarriers, determining the spectrum of each of the windowed complex exponential functions, leading to the spectrum of the nth single subcarrier in the form of

$$A_n(\omega) = \frac{\sin(N \cdot T_s \cdot \omega/2)}{N \cdot T_s \cdot \omega/2} * \delta(\omega - \omega_n).$$

Replacing the angular velocities ω by frequencies and using the relationship $N \cdot T_s = 1/\Delta f$, the spectrum of a subcarrier can be expressed as:

$$A_n(f) = \frac{\sin(\pi \frac{f-f_n}{\Delta f})}{\pi \frac{f-f_n}{\Delta f}} = \text{sinc}\left(\frac{f - f_n}{\Delta f}\right).$$

The OFDM receiver samples the received time domain signal, demodulates it by invoking the FFT and in the case of a carrier frequency shift, it generates the sub-channel signals in the frequency domain at the sampling points $f_n + \delta f$, which are spaced from each other by the subcarrier spacing Δf and misaligned by the frequency error δf. This scenario is shown in Figure 5.1. Figure 5.1(a) shows the sampling of the subcarrier at frequency f_n at the optimum frequency raster, resulting in a maximum signal amplitude and no intersubcarrier interference. If the frequency reference of the receiver is offset with respect to that of the

transmitter by a frequency error of δf, then the received symbols suffer from intersubcarrier interference, as depicted in Figure 5.1(b).

The total amount of intersubcarrier interference experienced by subcarrier n is the sum of the interference amplitude contributions of all the other subcarriers in the OFDM symbol:

$$I_n = \sum_{j,j\neq n} a_j \cdot A_j(f_n + \delta f).$$

Since the QAM symbols a_j are random variables, the interference amplitude in subcarrier n, I_n, is also a random variable, which cannot be calculated directly. If the number of interferers is high, however, then the power spectral density of I_n can be approximated with that of a Gaussian process, according to the central limit theorem. Therefore, the effects of the intersubcarrier interference can be modelled by additional white Gaussian noise superimposed on the frequency domain data symbols.

The variance of this Gaussian process σ_{ISI_n} is the sum of the variances of the interference contributions,

$$\sigma^2_{ISI_n} = \sum_{j,j\neq n} \sigma^2_{a_j} \cdot \left|A_j(f_n + \delta f)\right|^2.$$

The quantities $\sigma^2_{a_j}$ are the variances of the data symbols, which are the same for all j in a system that is not varying the average symbol power across different subcarriers. Additionally, because of the constant subcarrier spacing of Δf, the interference amplitude contributions can be expressed more conveniently as:

$$A_j(f_n + \delta f) = A_j n(\delta f) = sinc((n-j) + \frac{\delta f}{\Delta f}).$$

The sum of the interferer powers leads to the intersubcarrier interference variance expression:

$$\sigma^2_{ISI} = \sigma^2_a \cdot \sum_{i=-N/2-1}^{N/2} \left|sinc(i + \frac{\delta f}{\Delta f})\right|. \tag{5.2}$$

The value of the intersubcarrier interference (ISI) variance for FFT lengths of $N = 64$, 512 and 4096 and for a range of frequency errors δf is shown in Figure 5.2. It can be seen that the number of subcarriers does not influence the ISI noise variance for OFDM symbol lengths of more than 64 subcarriers. This is due to the rapid decrease of the interference amplitude with increasing frequency separation, so that only the interference from close subcarriers contributes significantly to the interference load on the subcarriers.

In order to investigate the accuracy of the Gaussian approximation, simulations were conducted and histograms of the measured interference amplitude were produced for QPSK and 16-QAM modulation of the subcarriers. The triangles in Figure 5.3 depict the histograms of ISI noise magnitudes recorded for a 512-subcarrier OFDM modem employing QPSK and 16-QAM in a system having a frequency error of $\delta f = 0.3\Delta f$. The continuous line drawn in the same graph is the corresponding approximation of the histogram by a Gaussian probability density function (PDF) of the variance calculated using Equation 5.2. It can be observed that the Gaussian curve is a reasonable approximation for both histograms in the central region, but that for the tails of the distributions the Gaussian function exhibits high relative errors.

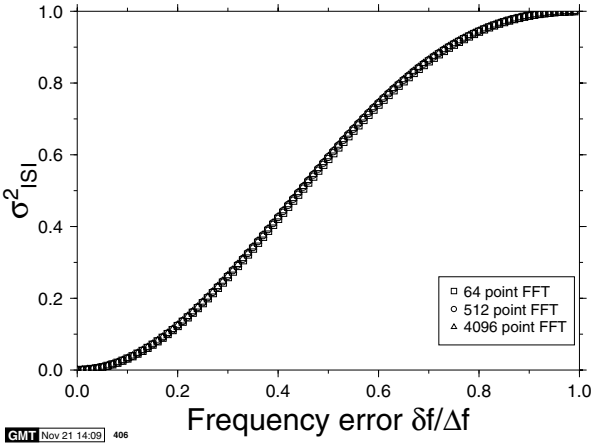
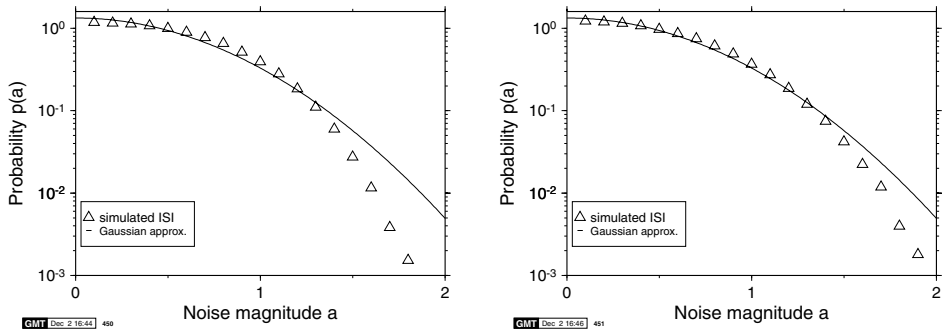


Figure 5.2: Intersubcarrier interference variance due to a frequency shift δf FFT lengths of $N = 64$, 512 and 4096 for normalised frequency errors $\delta f/\Delta f$ between 0 and 1



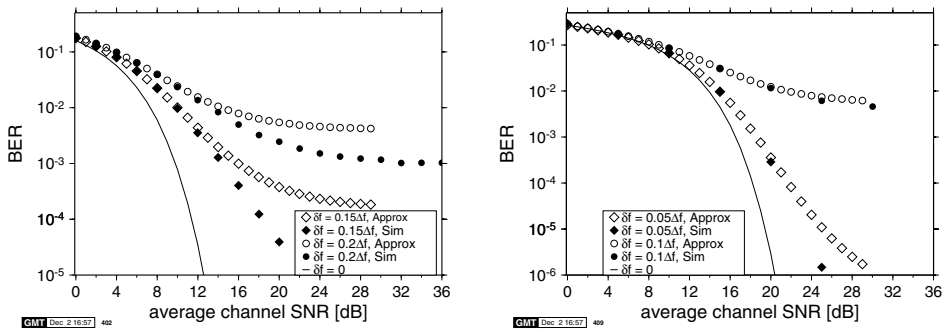
(a) QPSK (b) 16QAM

Figure 5.3: Histogram of the ISI magnitude for a simulated 512-subcarrier OFDM modem using QPSK or 16-QAM for $\delta f = 0.3\Delta f$; the line represents the Gaussian approximation having the same variance

The histogram of the interference caused by the 16-QAM signal is, however, closer to the Gaussian curve than the QPSK interference histogram.

However, the frequency mismatch between the transmitter and receiver of an OFDM system not only results in intersubcarrier interference, but it also reduces the useful signal amplitude at the frequency domain sampling point by a factor of $f(\delta f) = \text{sinc}(\delta f/\Delta f)$. Using this and σ^2_{ISI}, the theoretical influence of the inter-subcarrier interference, approximated by a Gaussian process, can be calculated for a given modulation scheme in an AWGN channel. In the case of coherently detected QPSK, the closed-form expression for the BER $P_e(\gamma)$ at a channel SNR γ is given [184] by:

$$P_e(\gamma) = Q(\sqrt{\gamma}),$$



(a) QPSK (b) 16QAM

Figure 5.4: The effect of intersubcarrier interference due to frequency synchronisation error on the BER over AWGN channels: (a) bit error probability versus channel SNR for frequency errors of $0.15\Delta f$ and $0.2\Delta f$ for a QPSK modem. (b) BER versus channel SNR for frequency errors of $0.05\Delta f$ and $0.1\Delta f$ for a 16-QAM modem. In both graphs, the filled symbols are simulated BER results, while the open symbols are the predicted BER curves using the Gaussian intersubcarrier interference model

where the Gaussian $Q()$-function is defined as

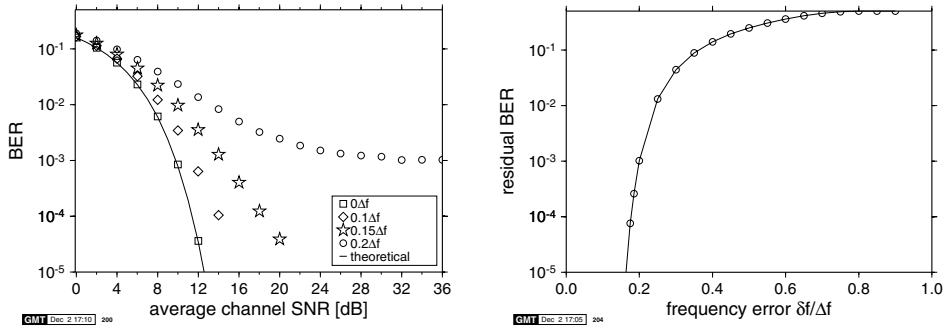
$$Q(y) = \frac{1}{\sqrt{2\pi}} \int_y^\infty e^{-x^2/2} dx = \text{erfc}\left(\frac{y}{\sqrt{2}}\right).$$

Assuming that the effects of the frequency error can be approximated by white Gaussian noise of variance σ_{ISI}^2 and taking into account the attenuated signal magnitude $f(\delta f) = sinc(\delta f/\Delta f)$, we can adjust the equivalent SNR to:

$$\gamma' = \frac{f(\delta f) \cdot \sigma_a^2}{\sigma_{ISI}^2 + \sigma_a^2/\gamma},$$

where σ_a^2 is the average symbol power and γ is the real channel SNR. Comparison between the theoretical BER calculated using γ' and simulation results for different frequency errors δf are shown in Figure 5.4(a). While for both frequency errors the theoretical BER using the Gaussian approximation fits the simulation results well for channel SNR values of up to 12 dB, the predictions and the simulation results diverge for higher values of SNR. The pessimistic BER prediction is due to the pronounced discrepancy between the histogram and the Gaussian curve in Figure 5.3 at the tail ends of the amplitude histograms, since for high noise amplitudes the Gaussian model is a poor approximation for the intersubcarrier interference.

The equivalent experiment, conducted for coherently detected 16-QAM, results in the simulated and predicted bit error rates depicted in Figure 5.4(b). For 16-QAM transmission, the noise resilience is much lower than for QPSK, hence for our experiments smaller values of δf have been chosen. It can be observed that the Gaussian noise approximation is a much better fit for the simulated BER in a 16-QAM system than for a 4-QAM modem. This is



(a) BER versus SNR

(b) Residual BER

Figure 5.5: Bit error rate versus channel SNR performance for a non-pilot-assisted QPSK OFDM modem in an AWGN channel: (a) bit error rate versus signal-to-noise ratio plot for different constant frequency errors, (b) plot of residual bit error rate versus the frequency error

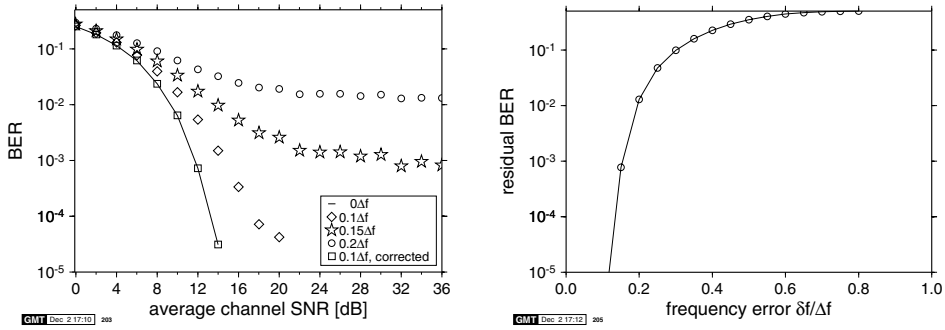
in accordance with Figure 5.3, where the histograms of the interference magnitudes were depicted.

5.1.1.2 Effects of Frequency Mismatch on Different Modulation Schemes

In order to investigate the effects of frequency mismatch on different modulation schemes, a series of simulations was conducted employing both coherently and differentially detected, as well as pilot symbol assisted QPSK systems. Figures 5.5(a), 5.6(a) and 5.7(a) show the performance of the QPSK, pilot symbol-assisted QPSK (PSA-QPSK) and differential QPSK (DQPSK) OFDM schemes, respectively. As a benchmark, the BER performance of the equivalent serial modulation scheme is plotted [184] as a line on all the graphs, which also represents the performance that is achieved by the parallel modem, when $\delta f = 0$.

5.1.1.2.1 Coherent Modulation Figure 5.5(a) reveals the BER performance degradation due to increasing the carrier frequency offset δf. The adjacent sub-channel interference effects are considerable, even for small frequency errors. It is clear that for a carrier frequency offset of $\delta f = 0.2 \cdot \Delta f$, the BER reaches a residual value of about 10^{-3} at approximately 26 dB of SNR. The minimal possible BER for different values of carrier frequency mismatch are plotted in Figure 5.5(b). For relative frequency errors above $0.18 \cdot \Delta f$, the attainable bit error rate is worse than 10^{-4}.

5.1.1.2.2 Pilot Symbol Assisted Modulation Figure 5.6(a) shows the bit error rate performance of the pilot-assisted QPSK system over an AWGN channel, which is consistently worse than that of an equivalent coherently demodulated system without pilot assistance. This is in accordance with the performance of PSAM schemes over AWGN channels, where PSAM systems are generally handicapped by errors in the channel estimation, which is unnecessary for non-fading channels. Since the frequency error mismatch results in additional noise in the received frequency domain pilots, the quality of the channel estimation dete-



(a) BER versus SNR

(b) Residual BER

Figure 5.6: Bit error rate versus channel SNR performance for a 3-pilot-assisted QPSK OFDM modem in an AWGN channel: (a) bit error rate versus signal-to-noise ratio plot for different fixed frequency errors, (b) plot of residual bit error rate versus the frequency error

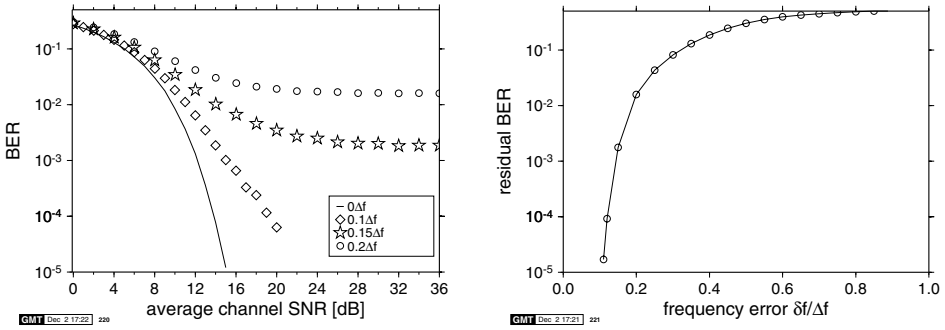
riorates. This reduces the BER performance of a PSAM system compared to a coherently demodulated system refraining from using pilots.

The bit error rate curves given in the figure were computed for three pilot subcarriers per 512-subcarrier OFDM symbol, which were invoked to mitigate the effects of the channel's fading envelope in a time or frequency fading environment. The corresponding relationship between the residual bit error rate and the frequency error is given in Figure 5.6(b). In the simulations presented here linear interpolation was employed between the pilots. Clearly, the BER performance of the system depends on the number of pilots employed as well as on the interpolation method, and these effects are discussed in Section 4.3.1.1 in more depth.

5.1.1.2.3 Differential Modulation The corresponding simulation results for differentially encoded QPSK are shown in Figure 5.7. Again, the impact of the intersubcarrier interference is severe even for small relative frequency errors. Figure 5.7(b) shows that a frequency error of only $0.12\Delta f$ results in a BER residual of 10^{-4}.

5.1.1.2.4 Frequency Error - Summary A frequency error in an OFDM system results in a shift of the received frequency domain symbols relative to the receiver's raster. This leads to intersubcarrier interference, whose nature is noise-like, owing to the great number of contributing interfering subcarriers. Because of the frequency domain aliasing, the variance of this interference is constant for all subcarriers in the OFDM symbol, if all subcarriers carry the same average power. The variance of the interference can be computed and used to model the interference effects by additional white noise superimposed on the data symbols. Depending on the modulation scheme employed, this model typically yields a good estimation of the actual BER.

Different modulation schemes are affected differently by the presence of frequency errors in the system, analogously to their performance in purely AWGN environments. Coherent detection suffers the least penalty, followed by differential detection and PSAM schemes. Let us now consider the effects of time domain synchronisation errors.



(a) BER versus SNR

(b) Residual BER

Figure 5.7: Bit error rate versus channel SNR performance for differential QPSK modulation scheme in AWGN channel. The OFDM FFT length is 512. (a) Bit error rate versus signal-to-noise ratio plot for different fixed frequency errors, (b) plot of residual bit error rate versus the frequency error

5.1.2 Time Domain Synchronisation Errors

Unlike frequency mismatch, as discussed above, time synchronisation errors do not result in intersubcarrier interference. Instead, if the receiver's FFT window spans samples from two consecutive OFDM symbols, inter-OFDM symbol interference occurs.

Additionally, even small misalignments of the FFT window result in an evolving phase shift in the frequency domain symbols, leading to BER degradation. Initially, we will concentrate on these phase errors.

If the receiver's FFT window is shifted with respect to that of the transmitter, then the time shift property of the Fourier transform, formulated as:

$$\begin{aligned} f(t) &\longleftrightarrow F(\omega) \\ f(t-\tau) &\longleftrightarrow e^{-j\omega\tau}F(\omega) \end{aligned}$$

describes its effects on the received symbols. Any misalignment τ of the receiver's FFT window will introduce a phase error of $2\pi\Delta f\tau/T_s$ between two adjacent subcarriers. If the time shift is an integer multiple m of the sampling time T_s, then the phase shift introduced between two consecutive subcarriers is $\delta\phi = 2\pi m/N$, where N is the FFT length employed. This evolving phase error has a considerable influence on the BER performance of the OFDM system, clearly depending on the modulation scheme used.

5.1.2.1 Coherent Demodulation

Coherent modulation schemes suffer the most from FFT window misalignments, since the reference phase evolves by 2π throughout the frequency range for every sampling time misalignment. Clearly, this results in a total loss of the reference phase, and hence coherent modulation cannot be employed without phase correction mechanisms, if realistic imperfect time synchronisation has to be expected.

5.1.2.2 Pilot Symbol-Assisted Modulation

Pilot symbol assisted modulation (PSAM) schemes can be employed in order to mitigate the effects of spectral attenuation and the phase rotation throughout the FFT bandwidth. Pilots are interspersed with the data symbols in the frequency domain and the receiver can estimate the evolving phase error from the received pilots' phases.

This operation is performed with the aid of the wideband channel estimation discussed in Section 4.3.1.1, and the number of pilot subcarriers necessary for correctly estimating the channel transfer function depends on the maximum anticipated time shift τ. Following the notion of the frequency domain channel transfer function $H(n)$ introduced in Chapter 4, the effects of phase errors can be written as:

$$H(f) = e^{-j2\pi f\tau}. \tag{5.3}$$

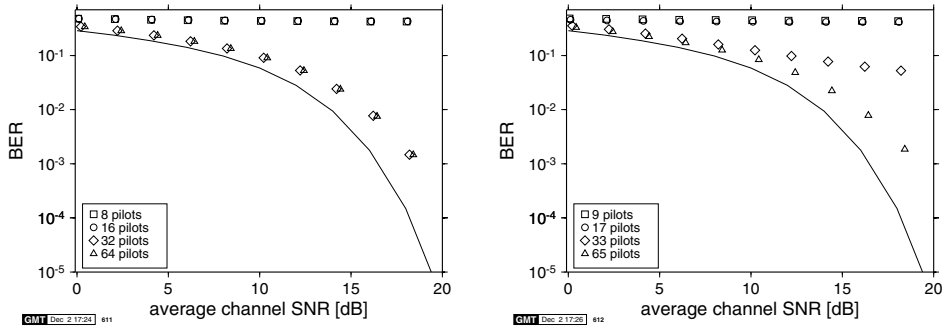
Replacing the frequency variable f by the subcarrier index n, where $f = n\Delta f = n/(NT_s)$ and normalising the time misalignment τ to the sampling time T_s, so that $\tau = m \cdot T_s$, the frequency domain channel transfer function can be expressed as:

$$H(n) = e^{-j2\pi\frac{nm}{N}}. \tag{5.4}$$

The number of pilots necessary for correctly estimating this frequency domain channel transfer function $H(n)$ is dependent on the normalised time delay m. Following the Nyquist sampling theorem, the distance Δp between two pilot tones in the OFDM spectrum must be less than or equal to half the period of $H(n)$, so that

$$\Delta p \leq \frac{N}{2m}. \tag{5.5}$$

The simulated performance of a 512-subcarrier 16-QAM PSAM modem in the presence of a constant timing error of $\tau = 10T_s$ in an AWGN channel is depicted in Figure 5.8 for both of the PSAM interpolation algorithms investigated in Section 4.3.1.1. Following Equation 5.5, the maximum acceptable pilot subcarrier distance required for resolving a normalised FFT window misalignment of $m = \tau/T_s = 10$ is $\Delta p = N/20 = 512/20 = 25.6$, requiring at least 20 pilot subcarriers equidistantly spaced in the OFDM symbol. We can see in both graphs of Figure 5.8 that the bit error rate is 0.5 for both schemes if less than 20 pilot subcarriers are employed in the OFDM symbol. For pilot numbers above the required minimum of 20, however, the performance of the ideal lowpass interpolated PSAM scheme does not vary with the number of pilots employed, while the linearly interpolated PSAM scheme needs higher numbers of pilot subcarriers for achieving a similar performance to the lowpass interpolator scheme. The continuous lines in the graphs show the BER curve for a coherently detected 16-QAM OFDM modem in the absence of timing errors, while utilising no PSAM. The BER penalty of PSAM in a narrowband AWGN channel as well as the performance differences between the two PSAM schemes are in accordance with the results found in Section 4.3.1.1.



(a) perfect lowpass interpolation

(b) linear interpolation

Figure 5.8: Bit error rate versus channel SNR performance for 16-level PSA-QAM in an AWGN channel for different pilot subcarrier spacings in the presence of a fixed FFT window misalignment of $\tau = 10T_s$. The OFDM FFT length is 512. (a) PSAM interpolation using ideal lowpass interpolator, (b) PSAM using linear interpolator. In both graphs, the line marks the coherently detected 16-QAM performance in the absence of both FFT window misalignment and PSAM

5.1.2.3 Differential Modulation

Differential encoding of OFDM symbols can be implemented both between corresponding subcarriers of consecutive OFDM symbols or between adjacent subcarriers of the same OFDM symbol. We found the latter more advantageous in TDMA environments and hence this principle is employed here. The BER performance of differentially encoded modulation schemes is affected by the phase shift $\delta\phi$ between adjacent subcarriers introduced by timing errors and this influence can be evaluated for example for DPSK systems, as will be shown below.

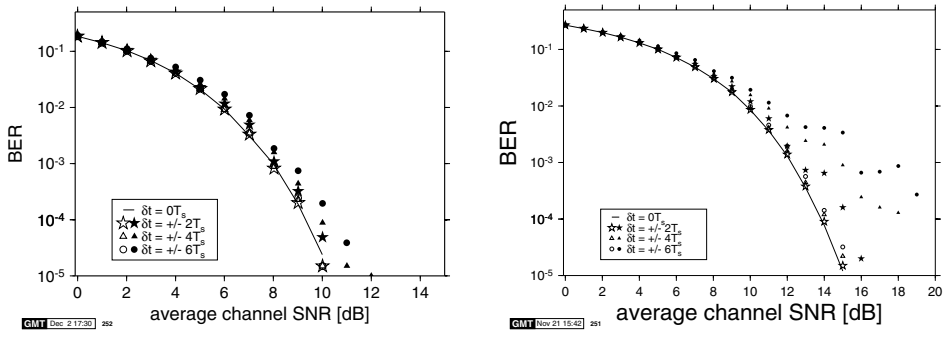
The two-dimensional probability density function of a noisy phasor in polar coordinates is calculated in Appendix 5.6 and is given by Equation 5.49, if we assume the transmitted phase to be zero. Integration of this function over the magnitude r gives the phase probability function $p_\phi(\phi)$:

$$p_\phi(\phi) = \int_0^\infty \frac{r}{2\pi\sigma^2} \cdot e^{-(r^2+\mathcal{A}^2-2r\mathcal{A}\cos\phi)/2\sigma^2} dr, \tag{5.6}$$

where $\mathcal{A}$ is the amplitude of the noiseless phasor. For differential phase modulation, the error of the difference between the phases of two consecutive symbols, $\Phi = \phi_k - \phi_{k-1}$, determines the symbol error rate (SER). The PDF $p_\Phi(\Phi)$ of this difference can be expressed by a variable transform, which results in the following integral:

$$p_\Phi(\Phi) = \int_{-\pi}^{\pi} p_\phi(\psi - \Phi) \cdot p_\phi(\psi) d\psi, \tag{5.7}$$

where ψ is an auxiliary variable. The received symbol will be demodulated correctly, if the difference error $\Delta\phi$ is within the decision boundaries of the PSK constellation. For M-DPSK,



(a) DBPSK (b) DQPSK

Figure 5.9: Bit error rate versus SNR over AWGN channels for a 512-subcarrier OFDM modem employing DBPSK and DQPSK, respectively. Positive time shifts imply time-advanced FFT window or delayed received data

the symbol error rate (SER) is given by:

$$SER = 1 - \int_{-\pi/M}^{\pi/M} p_{\Phi}(\Phi) d\Phi. \tag{5.8}$$

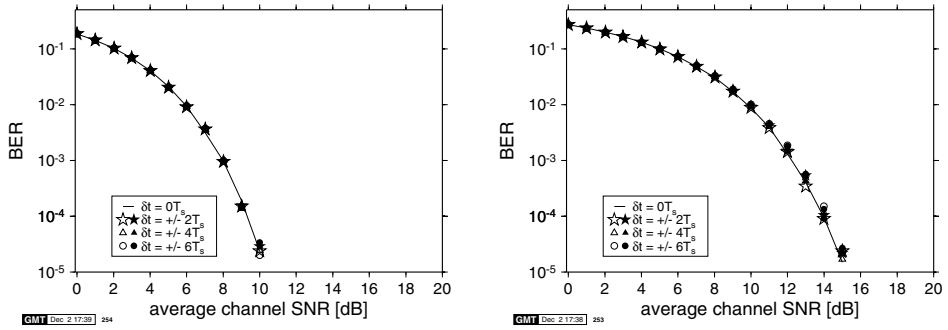
If there is an FFT window misalignment induced phase shift $\delta\phi$ between consecutive symbols, then the integration limits in Equation 5.8 are biased by this shift:

$$SER = 1 - \int_{-\pi/M+\delta\phi}^{\pi/M+\delta\phi} p_{\Phi}(\Phi) d\Phi. \tag{5.9}$$

Simulations have been performed for a 512-subcarrier OFDM system, employing DBPSK and DQPSK for different FFT window misalignment values. The BER performance curves for timing errors up to six sampling intervals are displayed in Figure 5.9. Note that one sample interval misalignment represents a phase error of $2\pi/512$ between two consecutive samples, which explains why the BER effects of the simulated positive timing misalignments marked by the hollow symbols are negligible for DBPSK. Specifically, a maximum SNR degradation of 0.5 dB was observed for DQPSK.

Positive FFT window time shifts correspond to a delayed received data stream and hence all samples in the receiver's FFT window belong to the same quasi-periodically extended OFDM symbol. In the case of negative time shifts, however, the effects on the bit error rate are much more severe due to inter OFDM-symbol interference. Since the data is received prematurely, the receiver's FFT window contains samples of the forthcoming OFDM symbol, not from the cyclic extension of the wanted symbol.

This non-symmetrical behaviour of the OFDM receiver with respect to positive and negative relative timing errors can be mitigated by adding a short postamble, consisting of copies of the OFDM symbol's first samples. Figure 5.10 shows the BER versus SNR curves for the same offsets, while using a 10-sample postamble. Now, the behaviour for positive and negative timing errors becomes symmetrical. Clearly, the required length of this postamble



(a) DBPSK (b) DQPSK

Figure 5.10: Bit error rate versus SNR over AWGN channels for a 512-subcarrier OFDM modem employing a postamble of 10 symbols for DBPSK and DQPSK, respectively. Positive time shifts correspond to time-advanced FFT window or delayed received data

depends on the largest anticipated timing error, which adds further redundancy to the system. This postamble can be usefully employed, however, to make an OFDM system more robust to time misalignments and thus to simplify the task of the time domain FFT window synchronisation system.

5.1.2.3.1 Time Domain Synchronisation Errors - Summary Misalignment of the receiver's FFT window relative to the received sample stream leads to possible inter-OFDM symbol interference as well as to an evolving shift of the reference phase throughout the received frequency domain OFDM symbol. While the effects of inter-OFDM symbol interference can be mitigated for moderate misalignments by appending a cyclic postamble to the OFDM symbol, the phase errors in the frequency domain make it impossible to use coherently detected modulation schemes without phase recovery methods. Instead, differentially detected schemes can be employed, which nonetheless suffer from performance degradation due to the phase errors. Alternatively, pilot symbol-assisted channel estimation schemes can be employed in conjunction with coherent detection.

5.2 Synchronisation Algorithms

The results of Section 5.1 indicate that the accuracy of a modem's time and frequency domain synchronisation system dramatically influences the overall BER performance. We have seen that carrier frequency differences between the transmitter and the receiver of an OFDM system will introduce additional impairments in the frequency domain caused by intersubcarrier interference, while FFT window misalignments in the time domain will lead to phase errors between the subcarriers. Both of these effects will degrade the system's performance and have to be kept to a minimum by the synchronisation system.

In a TDMA-based OFDM system, the frame synchronisation between a master station – in cellular systems generally the base station – and the portable stations has also to be maintained. For these systems, a reference symbol marking the beginning of a new time frame is

commonly used. This added redundancy can be exploited for both frequency synchronisation and FFT window alignment, if the reference symbol is correctly chosen.

In order to achieve synchronisation with a minimal amount of computational effort at the receiver, while also minimising the amount of redundant information added to the data signal, the synchronisation process is normally split into an acquisition phase and a tracking phase, if the characteristics of the random frequency and timing errors are known. In the acquisition phase, an initial estimate of the errors is acquired, using more complex algorithms and possibly a higher amount of synchronisation information in the data signal, whereas later the tracking algorithms only have to correct for small short-term deviations.

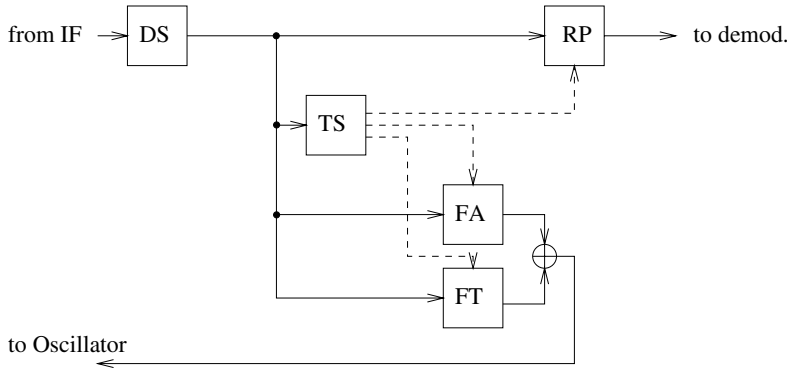


Figure 5.11: Block diagram of the synchronisation system: **DS**-downsampling and clock recovery, **TS**-time synchronisation, **FA**-frequency acquisition, **FT**-frequency tracking, **RP**-remove cyclic extension prefix

The block diagram of a possible synchronisation system is shown in Figure 5.11. The down sampling and clock recovery module DS has to determine the optimum sampling instant. The time synchronisation TS controls the frequency acquisition FA, the frequency tracking FT as well as the time domain alignment of the FFT window, which is carried out by the "remove prefix" or RP block. These operations will be detailed during our further discourse.

At the beginning of the synchronisation process neither the frequency error nor the timing misalignment are known, hence synchronisation algorithms must be found that are sufficiently robust to initial timing and frequency errors.

5.2.1 Coarse Frame and OFDM Symbol Synchronisation Review

Coarse frame and symbol synchronisation algorithms presented in the literature all rely on additional redundancy inserted in the transmitted data stream. The pan-European digital video broadcasting (DVB) system uses a so-called null symbol as the first OFDM symbol in the time frame. No energy is transmitted [198], during the null symbol and it is detected by monitoring the received baseband power in the time domain, without invoking FFT processing. Claßen [26] proposed an OFDM synchronisation burst of at least three OFDM symbols per time frame. Two of the OFDM symbols in the burst would contain synchronisation subcarriers bearing known symbols along with normal data transmission carriers, but one of the

OFDM symbols would be the exact copy of one of the other two, thus resulting in more than one OFDM symbol synchronisation overhead per synchronisation burst. For the ALOHA environment, Warner [64] proposed the employment of a power detector and subsequent correlation-based detection of a set of received synchronisation subcarriers embedded in the data symbols. The received synchronisation tones are extracted from the received time domain signal using an iterative algorithm for updating the synchronisation tone values once per sampling interval. For a more detailed discussion on these techniques the interested reader is referred to the literature [26, 64], while for a variety of further treatises to the contributions by Mammela and his team [199–201].

5.2.2 Fine Symbol Tracking Review

Fine symbol tracking algorithms are generally based on correlation operations either in the time or in the frequency domain. Warner [64] and Bingham [202] employed frequency domain correlation of the received synchronisation pilot tones with known synchronisation sequences, while de Couasnon [203] utilised the redundancy of the cyclic prefix by integrating over the magnitude of the difference between the data and the cyclic extension samples. Sandell [69] proposed exploiting the auto-correlation properties of the received time domain samples imposed by the cyclic extension for fine time domain tracking.

5.2.3 Frequency Acquisition Review

The frequency acquisition algorithm has to provide an initial frequency error estimate, which is sufficiently accurate for the subsequent frequency tracking algorithm to operate reliably. Generally the initial estimate must be accurate to half a subcarrier spacing. Sari [65] proposed the use of a pilot tone embedded into the data symbol, surrounded by zero-valued virtual subcarriers, so that the frequency-shifted pilot can be located easily by the receiver. Moose [66] suggested a shortened repeated OFDM symbol pair, analogous to his frequency tracking algorithm to be highlighted in the next section. By using a shorter DFT for this reference symbol pair, the subcarrier distance is increased and thus the frequency error estimation range is extended. Claßen [26, 27] proposed using binary pseudo-noise (PN) or so-called CAZAC training sequences carried by synchronisation subcarriers, which are also employed for the frequency tracking. The frequency acquisition, however, is performed by a search for the training sequence in the frequency domain. This is achieved by means of frequency domain correlation of the received symbol with the training sequence.

5.2.4 Frequency Tracking Review

Frequency tracking generally relies on an already established coarse frequency estimation having a frequency error of less than half a subcarrier spacing. Moose [66] suggested the use of the phase difference between subcarriers of repeated OFDM symbols in order to estimate frequency deviations of up to one-half of the subcarrier spacing, while Claßen [26] employed frequency domain synchronisation subcarriers embedded into the data symbols, for which the phase shift between consecutive OFDM symbols can be measured. Daffara [68] and Sandell [69] used the phase of the received signal's auto-correlation function, which represents a

phase shift between the received data samples and their repeated copies in the cyclic extension of the OFDM symbols.

Following the above brief literature survey, we will investigate two different synchronisation algorithms, both making use of a reference symbol marking the beginning of a new time frame. This limits the use of both algorithms to systems whose channel access scheme is based on time division multiple access (TDMA) frames.

5.2.5 Time and Frequency Domain Synchronisation Based on Auto-Correlation

Both the frequency and the time domain synchronisation control signals can be derived from the received signal samples' cyclic nature upon exploiting the OFDM symbols' cyclic time domain extension by means of correlation techniques. A range of symbol timing and fine frequency tracking algorithms were proposed by Mandarini and Falaschi [204]. Originally, Moose [66] proposed a synchronisation algorithm using repeated data symbols, and methods for the frequency error estimation using the cyclic extension of OFDM symbols were presented by Daffara *et al.* [68] and Sandell *et al.* [69]. The frequency acquisition and TDMA frame synchronisation proposed here are based on similar principles, employing a dedicated reference symbol exploited in the time domain [205].

No added redundancy in the data symbols and no *a priori* knowledge of the synchronisation sequences constituting the reference symbol are required, since only the repetitive properties of the OFDM symbols and those of the reference symbol (REF) in the proposed time division duplex (TDD) frame structure seen in Figure 5.13 are exploited. All the processing is carried out in the time domain, hence no FFT-based demodulation of the reference symbol is necessary.

5.2.6 Multiple Access Frame Structure

The proposed 64-slot TDMA/TDD frame structure is depicted at the top of Figure 5.12, which is constituted by a null symbol, a reference symbol and 62 data symbols. Let us initially consider the role of the reference symbol.

5.2.6.1 The Reference Symbol

The reference symbol shown in Figure 5.13 was designed to assist in the operation of the synchronisation scheme and consists of repetitive copies of a synchronisation pattern SP of N_s pseudorandom complex samples. The synchronisation algorithm at the receiver needs no knowledge of the employed synchronisation pattern, hence this sequence could be used for channel-sounding training sequences or for base station identification signals. Note therefore that there are three hierarchical periodic time domain structures in the proposed framing scheme: the short-term intrinsic periodicity in the reference symbol of Figure 5.13, the medium-term periodicity associated with the quasi-periodic extension of the OFDM symbols and the long-term periodicity of the OFDM TDMA/TDD frame structure, repeating the reference symbol every 64 OFDM symbols, as portrayed in Figure 5.12. The long-term reference symbol periodicity is exploited in order to maintain OFDM frame synchronisation, while the medium-term synchronism of the cyclic extension assists in the process of OFDM sym-

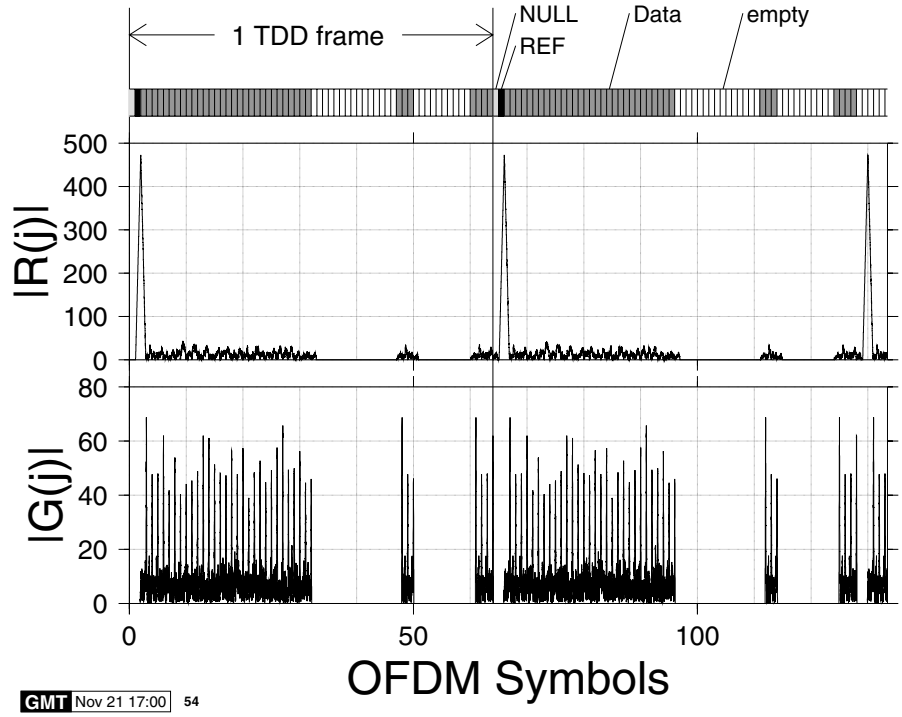


Figure 5.12: Time synchronisation: plots of the correlation terms $R(j)$ and $G(j)$ from Equation 5.10 and 5.11 for two consecutive 64-slot TDD frames under perfect channel conditions. The peaks indicate the correct TDD frame and OFDM symbol synchronisation instants, respectively

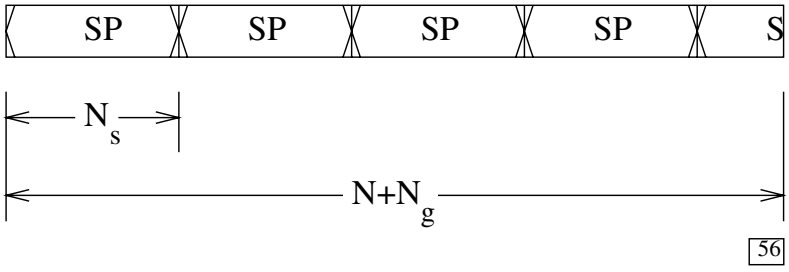
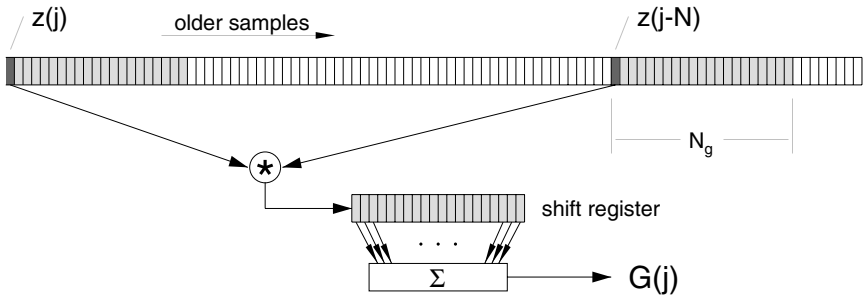


Figure 5.13: Reference symbol consisting of consecutive copies of a synchronisation pattern (SP) in the time domain

bol synchronisation. A detailed discussion of this figure will be provided during our further discourse. Let us begin with the macroscopic structure.



GMT Jul 24 17:07 67

Figure 5.14: Schematic plot of the computation of the correlation function $G(j)$. The grey area represents the memory of the shift register

5.2.6.2 The Correlation Functions

The synchronisation algorithms rely on the evaluation of the following correlation functions $G(j)$ and $R(j)$, where j is the index of the most recent input sample:

$$G(j) = \sum_{m=0}^{N_g-1} z(j-m) \cdot z(j-m-N)^* \tag{5.10}$$

$$R(j) = \sum_{m=0}^{N+N_g-N_s-1} z(j-m) \cdot z(j-m-N_s)^*, \tag{5.11}$$

where $z(j)$ are the received complex signal samples, N is the number of subcarriers per OFDM symbol, N_g is the length of the cyclic extension and N_s is the periodicity within the reference symbol, as seen in Figure 5.13. The asterisk * denotes the conjugate of a complex value.

$G(j)$ is used for both frequency tracking and OFDM symbol synchronisation, expressing the correlation between two sequences of N_g samples length spaced by N in the received sample stream, as shown in Figure 5.14. The second function, $R(j)$, is the corresponding expression for the reference symbol, where the period of the repetitive synchronisation pattern is N_s, as seen in Equation 5.11 and Figure 5.13. In this case, (N_g+N-N_s) samples are taken into account for the correlation computation, and they are spaced by a distance of N_s samples. Having defined the necessary correlation functions for quantifying the time and frequency synchronisation error, let us now concentrate on how the synchronisation algorithms rely on their evaluation.

5.2.7 Frequency Tracking and OFDM Symbol Synchronisation

In this section we consider details of the frequency tracking and OFDM symbol synchronisation algorithms, which make use of $G(j)$, as defined by Equation 5.10.

5.2.7.1 OFDM Symbol Synchronisation

The magnitude of $G(j_{max})$ is maximum, if $z(j_{max})$ is the last sample of the current OFDM symbol, since then the guard samples constituting the cyclic extension and their copies in the current OFDM symbol are perfectly aligned in the summation windows. Figure 5.12 shows the simulated magnitude plots of $G(j)$ and $R(j)$ for two consecutive WATM frames, with $N = 512$ and $N_g = N_s = 50$, under perfect channel conditions. The observed correlation peaks of $|G(j)|$ can be easily identified at the last sample of an OFDM symbol. The amplitudes of the correlation peaks fluctuate, since the transmitted OFDM data symbols differ. The correlation peak magnitude is equal to the energy contained in the N_g samples of the cyclic extension and averages 50 for our system with $N_g = 50$ and an average sample power of unity.

The simulated accuracy of the OFDM symbol synchronisation in an AWGN channel is characterised in Figure 5.15. Observe in the figure that for SNRs in excess of about 7 dB the histogram is tightly concentrated around the perfect estimate, typically resulting in OFDM symbol timing estimation errors below $\pm 20T_s$. However, as even slightly misaligned time domain FFT windows cause phase errors in the frequency domain, this estimation accuracy is insufficient. In order to improve the OFDM symbol timing synchronisation, the estimates must be lowpass filtered. Let us now concentrate on the issues of fine frequency tracking.

5.2.7.2 Frequency Tracking Studies

A carrier frequency error of δf results in an evolving phase error $\Psi(j)$ of the received samples $z(j)$:

$$\Psi(\delta f, j) = 2\pi \delta f \cdot j \cdot T_s \tag{5.12}$$

$$= 2\pi \frac{j\delta f}{N\Delta f}. \tag{5.13}$$

Clearly, the phase error difference between two received time domain samples $z(j_1)$ and $z(j_2)$ is a function of the frequency error and their time delay, and is given by $\Psi(\delta f, j_2) - \Psi(\delta f, j_1) = \Psi(\delta f, |j_2 - j_1|)$. If the original phase difference between the two received symbols $z(j_1)$ and $z(j_2)$ is known, and all other phase distortion is absent, then the phase difference error can be used to determine the frequency error δf.

Since the time domain samples of the cyclic extension or the guard interval are known to be a copy of the last N_g data samples of the OFDM symbol, the frequency error can be estimated using each of these N_g pairs of identical samples. In order to improve the estimation accuracy when exposed to noise and other channel impairments, averaging can be carried out over the N_g estimates.

The phase of $G(j)$ at $j = j_{max}$ equals the averaged phase shift between the guard time samples and the corresponding data samples of the current OFDM symbol. Since the corresponding sample pairs are spaced by N samples, rearranging Equation 5.13 leads to the fine

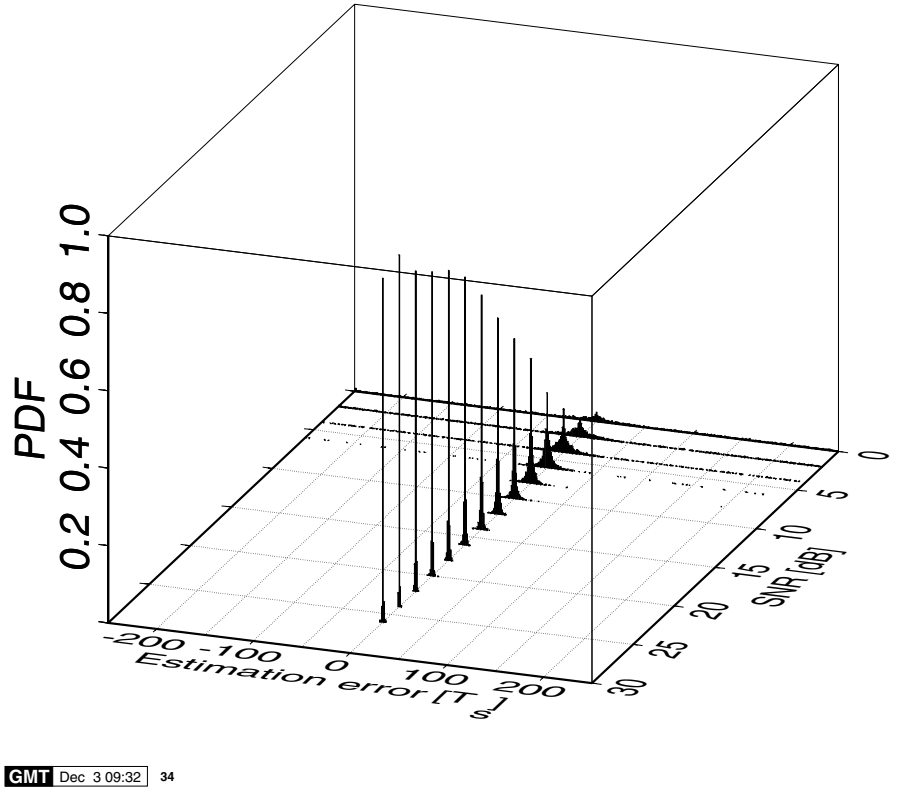


Figure 5.15: Histogram of the symbol timing estimation errors normalised to the sample interval T_s in an AWGN channel for $N = 512$ and $N_g = 50$ with no lowpass filtering of the estimates

frequency error estimation δf_t given by:

$$\delta f_t = \frac{\Delta f}{2\pi} \cdot \measuredangle G(j_{max}). \tag{5.14}$$

Because of the 2π ambiguity of the phase, the frequency error must be smaller than $\Delta f/2$. Therefore, the initial frequency acquisition must ensure a rough frequency error estimate with an accuracy of better than $\Delta f/2$, if the proposed fine frequency tracking is used.

Assuming perfect estimation of the position j_{max} of the correlation peak $G(j_{max})$, as we have seen in Figure 5.12, the performance of the fine frequency error estimation in an AWGN environment is shown in Figure 5.16(a). Observe that for AWGN SNR values above 10 dB, the estimation error histogram is concentrated on errors below about $0.02\Delta f$, where Δf is the subcarrier spacing.

Having resolved the issues of OFDM symbol synchronisation and fine frequency tracking, let us now focus our attention on the aspects of frequency acquisition and frame synchronisation.

5.2.8 Frequency Acquisition and Frame Synchronisation Studies

Our proposed frequency acquisition and frame synchronisation techniques are based on the same algorithms as the fine frequency and OFDM symbol synchronisation. However, instead of using the medium-term periodicity of the cyclic extension of the OFDM data symbols, the dedicated reference symbol with shorter cyclic period $N_s < N$ is exploited in order to improve the frequency capture range, as will be highlighted below.

5.2.8.1 Frame Synchronisation Studies

Similarly to the OFDM symbol synchronisation, the magnitude of $R(j)$ in Equation 5.11 and Figure 5.12 is maximum when the periodic synchronisation segments SP of length N_s of the reference symbol shown in Figure 5.13 perfectly overlap. Again, the magnitude of $R(j)$ for two simulated TDD frames is shown at the top of Figure 5.12. The OFDM frame timing is synchronised with the peak of $R(j)$, which can additionally be taken into account for the OFDM symbol synchronisation. The peak height is constant under perfect channel conditions, owing to the fixed reference symbol.

5.2.8.2 Frequency Acquisition Studies

The frequency acquisition algorithm uses the same principle as the frequency tracking scheme of Section 5.2.7.2. Specifically, the phase of $R(j)$ at the last sample of the reference symbol j_{max} contains information on the frequency error:

$$\measuredangle R(j_{max}) = 2\pi \cdot \delta f_a \cdot N_s \cdot T_s = 2\pi \cdot \delta f_a \cdot \frac{N_s}{N \cdot \Delta f} \tag{5.15}$$

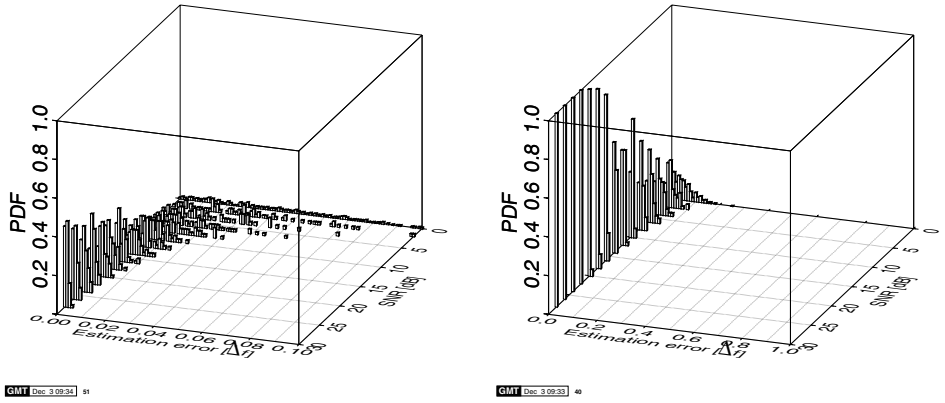
leading to

$$\delta f_a = \frac{N}{N_s} \frac{\Delta f}{2\pi} \cdot \measuredangle R(j_{max}). \tag{5.16}$$

Since the spacing between the sample pairs used in the computation of $R(j)$ is smaller than in the case of $G(j)$, which was used for the frequency tracking ($N_s < N$), the maximum detectable frequency error is now increased from $\Delta f/2$ to $N/N_s \cdot \Delta f/2$, where Δf is the subcarrier spacing of the OFDM symbols. The simulated performance of the frequency acquisition algorithm for $N = 512$, $N_s = 50$ and perfect time synchronisation is shown in Figure 5.16(b) for transmissions over an AWGN channel. As seen in the figure, the scheme maintains an acquisition error below $\Delta f/2$ even for SNR values down to 0 dB, which exceeds the system's operational specifications.

5.2.8.3 Block Diagram of the Synchronisation Algorithms

To summarise our previous elaborations, Figure 5.17 shows the detailed block diagram of the synchronisation algorithms. The received samples are multiplied with the complex conjugate of the delayed input sequences and summed up over $(N + N_g - N_s)$ and N_g samples, respectively. The magnitude maxima of the two sequences $G(j)$ and $R(j)$ are detected and they trigger the sampling of the phase estimates $\measuredangle G$ and $\measuredangle R$ in order to derive the two frequency error estimates δf_a and δf_t. Let us now describe an alternative frequency synchronisation



(a) frequency tracking (b) frequency acquisition

Figure 5.16: Histogram of the simulated frequency estimation error for the frequency acquisition and frequency tracking algorithms using $N = 512$ and $N_s = N_g = 50$ over AWGN channels

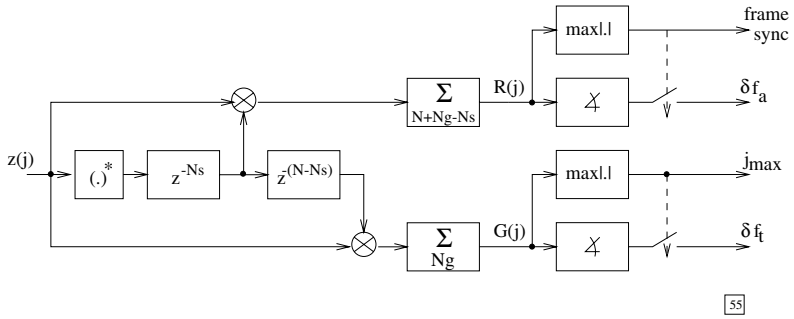


Figure 5.17: Block diagram of the synchronisation algorithms

technique, which can be used as a benchmark in order to assess the potential of our previously described technique.

5.2.9 Frequency Acquisition Using Frequency Domain Pilots

The algorithm described in this section has been proposed by Mandarini and Falaschi [204]. In contrast to the reference symbol of Figure 5.13, the technique advocated by Mandarini and Falaschi relies on the reference symbol shown in Figure 5.18 containing a set of pilot tones, which is transmitted once per TDD frame. The reference symbol is processed in the frequency domain, after demodulation by FFT.

The idea of the pilot tone algorithm is that a frequency mismatch between the transmitter and the receiver will result in a shift of the pilot tones in the received spectrum. This shift is measured at the receiver by searching for the FFT frequency bin with the maximum amplitude, resulting in an estimation accuracy of half a subcarrier spacing. This estimation is

improved further in a second stage by considering the relative amplitudes of the adjacent FFT bins.

5.2.9.1 The Reference Symbol

The reference symbol is transmitted once at the beginning of every TDD frame, as depicted in Figure 5.12. This reference symbol consists of a set of M pilot tones spanning the OFDM signal's bandwidth, spaced from each other by ΔN subcarriers or by a frequency gap of $\Delta F = \Delta N \cdot \Delta f$. Accordingly, the maximum detectable frequency error is $\Delta F/2 = \Delta N/2 \cdot \Delta f$ and hence the higher the number of pilots, the lower the frequency capture range. A stylised plot of the reference symbol in the frequency domain is shown in Figure 5.18.

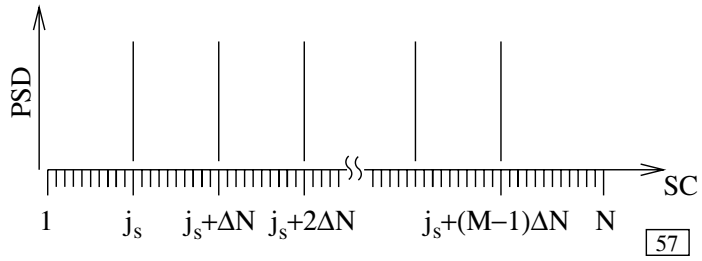


Figure 5.18: Stylised plot of the power spectral density (PSD) of the pilot-tone-based reference symbol using M pilot tones in the N subcarrier (SC) spectrum, spaced by $(\Delta N - 1)$ blank subcarriers

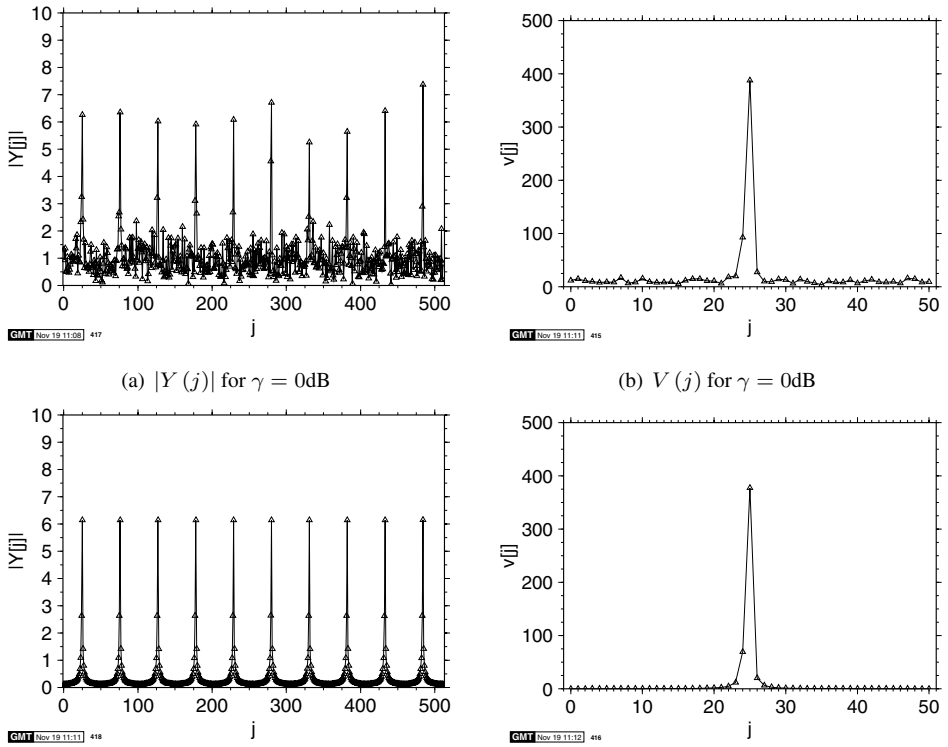
In order to keep the overall OFDM symbol energy constant, the total energy of the reference symbol is set equal to the average OFDM symbol energy and split equally between the M pilot tones.

5.2.9.2 Frequency Acquisition

The frequency acquisition algorithm estimates the frequency error by searching for the position of the pilot tones in the spectrum of the received reference symbol. In order to accomplish this, the received time domain signal of the reference symbol is demodulated by FFT. In order to minimise the influence of noise, the sum of the received power spectral amplitudes over all the M frequency ranges depicted in Figure 5.18 is then calculated as follows:

$$V(j) = \sum_{m=0}^{M-1} |Y(j + j_s + m\Delta N)|^2 \quad \text{for} \quad -\frac{\Delta N - 1}{2} \leq j \leq \frac{\Delta N - 1}{2}, \tag{5.17}$$

where $Y(j)$ represents the frequency domain samples of the received demodulated reference symbol. Observe that for the sample position identified by j $V(j)$ corresponds to the superposition of the powers of the ΔN-spaced $Y(j)$ samples, one from each of the M frequency ranges. In Figure 5.19 simulated values for both $|Y(j)|$ and $V(j)$ are given for SNR values of 0 dB and 50 dB, respectively, for a 10-pilot reference symbol in a 512-subcarrier OFDM system with $\delta f = 0.3\Delta f$ frequency error. It can be seen that the positions of the pilot tones in the received spectrum are easily determined even for SNR values of 0 dB, thanks to the



(a) $|Y(j)|$ for $\gamma = 0$dB

(b) $V(j)$ for $\gamma = 0$dB

(c) $|Y(j)|$ for $\gamma = 50$dB

(d) $V(j)$ for $\gamma = 50$dB

Figure 5.19: Magnitude of the received frequency domain samples $|Y(j)|$ and averaged samples $V(j)$ for SNR values of $\gamma = 0$ dB and $\gamma = 50$ dB for a 512-subcarrier OFDM modem employing 10 pilot tone subcarriers in the reference symbol. The simulated frequency mismatch between the transmitter and the receiver was $\delta f = 0.3\Delta f$

high power of the pilot tones relative to the average data symbol power. The total energy of the reference is 512, leading to a pilot tone amplitude of $\sqrt{512/10} = 7.15$. Because of the subcarrier energy spillover caused by the frequency error, the amplitude of the peaks of $Y(j)$ in the figure is lowered to about 6.2. Accordingly, the peak value of $V(j)$ is about 390 instead of 512, with the rest of the received energy located in the adjacent FFT bins.

The frequency error is determined by estimating the position of the highest peak in $V(j)$ over the range of j given in Equation 5.17. First, the index j_{max} of the maximum value of $V(j)$ is found. This gives a rough estimate of the frequency error with a frequency resolution of the subcarrier spacing Δf. As can be observed in Figure 5.19, this rough frequency error estimation is very noise resilient, resulting in a reliable detection of the frequency error. The accuracy of this estimation, however, is insufficient for low BER modem operation. If a subsequent frequency error tracking algorithm like the proposed time domain correlation-based approach is employed in the system, then the $0.5\Delta f$ estimation accuracy can be an adequate starting point for the tracking algorithm. If a better estimate is needed, however, then the amplitudes in the neighbouring bins around the peak value in $V(j)$ can be exploited

to refine the first estimate, as follows.

Since the frequency error is not generally an integer multiple of the resolution Δf of the FFT, a better frequency error estimate can be derived by determining the position of the peak value of $V(j)$ around j_{max}. The proposed algorithm exploits the amplitude of $V(j)$ at $j = j_{max}$ and the two adjacent values $V(j_{max} \pm 1)$ in order to derive the following quantities:

$$\rho_1 = \frac{\sqrt{V(j_{max}+1)}}{\sqrt{V(j_{max})}} \tag{5.18}$$

$$\rho_{-1} = \frac{\sqrt{V(j_{max}-1)}}{\sqrt{V(j_{max})}}, \tag{5.19}$$

which represent the normalised frequency domain pilot values at the positions adjacent to the $V(j)$ peak at $j = j_{max}$. Their difference $(\rho_1 - \rho_{-1})$ is computed and the rough frequency error estimate of $j_{max} \cdot \Delta f$ is corrected by the help of the estimated deviation d as follows:

$$d = \frac{\rho_1 - \rho_{-1}}{2} \tag{5.20}$$

$$\delta f = \Delta f \cdot (j_{max} + \text{sgn}\{d\} \cdot \sqrt{|d|}), \tag{5.21}$$

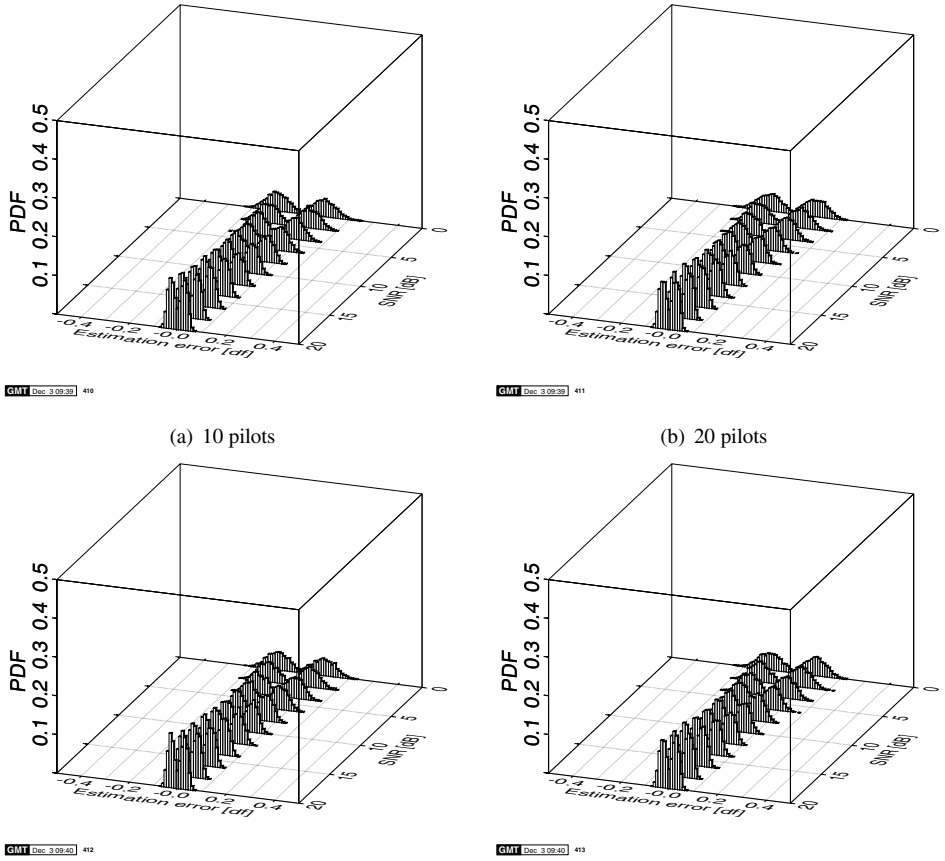
where the value of $\sqrt{|d|}$ is the estimation of the true peak position between the peak $V(j_{max})$ and the higher of the two adjacent values of $V(j_{max} \pm 1)$.

Clearly, the number of pilot tones included in the reference symbol, M, determines the maximal frequency deviation that can be detected using this algorithm, which is given by $\delta f_{max} = \Delta f \cdot \lfloor N/2M \rfloor$, where $\lfloor x \rfloor$ means the highest integer number smaller or equal to x. Not only the frequency capture range, but also the peak-to-average power ratio or crest factor (CF) of the reference symbol in the time domain depends on the number of pilot tones used. If the phase of all the M pilot tones is equal, then the upper bound for the resulting crest factor equals M, which would be the result of all M sinusoids adding constructively to a peak value. Experimental results in Figure 5.21(b) show that the actually measured CF for pilot symbols with a varying number of pilot tones is very close to the stated upper bound. For comparison, the histogram of the simulated CF values for pseudorandom OFDM data symbols is shown in Figure 5.21(b). This PDF shows that the average CF value for a 512-subcarrier 4-QAM OFDM system is about 8.5 dB, although peak values up to 12 dB have been occasionally observed. For small numbers of pilot tones, the crest factor of the reference symbol is therefore not worse than that of the average data symbols.

5.2.9.3 Performance of the Pilot-Based Frequency Acquisition in AWGN Channels

A series of simulations was performed in order to characterise the performance of the pilot tone-based frequency acquisition algorithm in an AWGN environment. For different fixed frequency errors and noise levels, the frequency error estimation was invoked and the difference between the estimated and the actual error was recorded. Figure 5.20 shows the histograms of the frequency mismatch estimation errors for 10, 20, 30 and 40 pilots and for a range of SNR values in the case of an actual frequency error of $\delta f = 0.0$.

Inspection of the figure reveals that the estimation accuracy is not sensitive to the number of pilot tones used in the reference symbol; in fact, the differences in the simulated histograms



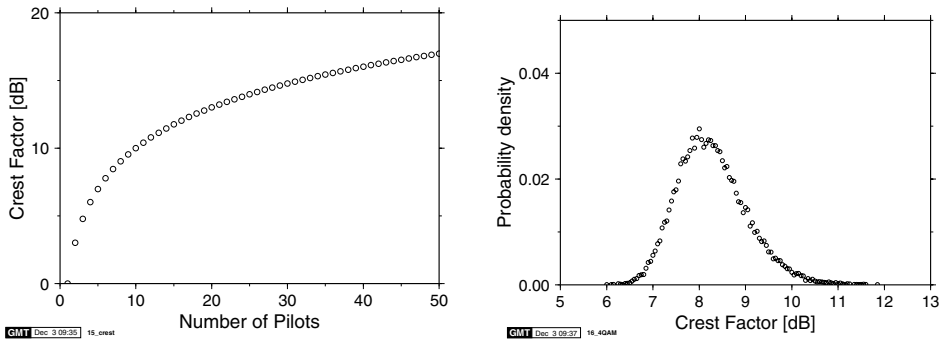
(a) 10 pilots

(b) 20 pilots

(c) 30 pilots

(d) 40 pilots

Figure 5.20: Histograms of simulated frequency mismatch estimation error for a 512-subcarrier OFDM modem in a narrowband AWGN channel for 10, 20, 30 and 40 pilot tones. The simulated frequency error was $\delta f = 0.0$



(a) reference symbol (b) data symbols

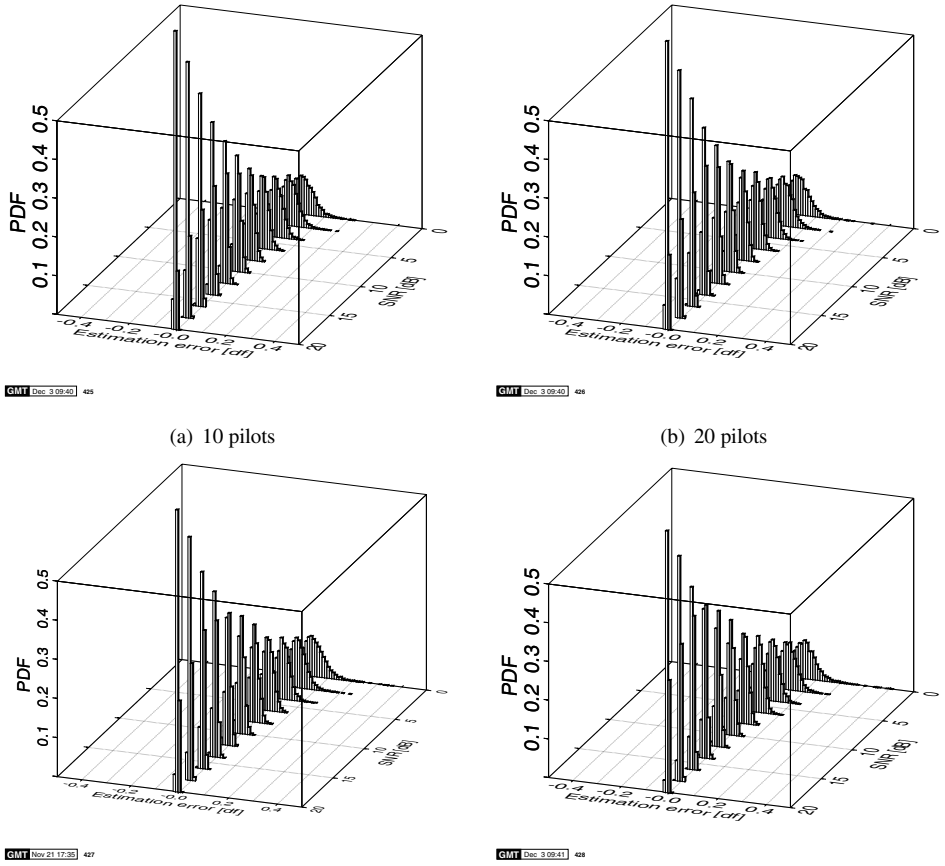
Figure 5.21: Characterisation of the coarse frequency synchronisation using the reference symbol of Figure 5.18: (a) crest factor versus number of pilot tones for non-optimised reference symbols, (b) histogram of simulated data symbol crest factors for a 512-subcarrier, 4-QAM OFDM system

are hardly visible. The estimation accuracy is significantly better than $0.5\Delta f$ throughout the simulated SNR range and hence meets the requirements of the subsequent fine frequency synchronisation for all simulated signal-to-noise ratios. It can be observed, however, that there is a bifurcation of the estimation error histogram which leads to two distinct probability maxima on both sides of the true value, with a low probability for a perfect estimation. This behaviour can be explained by the fine peak location estimation, which exhibits a high noise sensitivity for low δf values and hence small differences in the noise samples on either side of the correlation peak lead to considerable estimation errors.

The gap between the maxima closes with increasing SNR, but even at 20 dB there are frequency estimation errors of up to 8% of the subcarrier spacing, which underlines the need for subsequent fine frequency synchronisation. Alternatively, averaging the estimated frequency errors for several estimations would improve the estimation accuracy, but it would slow down the system's response time to frequency deviations. The histogram is symmetric around the perfect estimation value, hence a longer-term averaging would yield the correct frequency error estimate.

The estimation accuracy of the pilot tone frequency acquisition algorithm depends on the actual frequency error. In order to illustrate this, frequency estimation error histograms for a given frequency mismatch of $\delta f = 0.3\Delta f$ are shown in Figure 5.22, and they exhibit rather different characteristics from the previous case with $\delta f = 0$. The histograms are offset with respect to the perfect estimation value, hence averaging over multiple estimations will result in a residual estimation error. Subsequent fine frequency sychronisation is therefore necessary for low SNR values . For low noise levels, however, the estimation accuracy is greatly improved with respect to the earlier case. For SNRs in excess of 10 dB, the estimation errors do not exceed 5% of the subcarrier spacing, and will therefore not affect the system performance to a great extent. It can be observed that the asymmetry of the estimation errors is dependent on the number of pilots employed.

The frequency deviation estimation error histogram for $\delta f = 0.5\Delta f$ is shown in Figure 5.23, where it can be observed that in this case the histogram is split into two distinct parts,



(a) 10 pilots

(b) 20 pilots

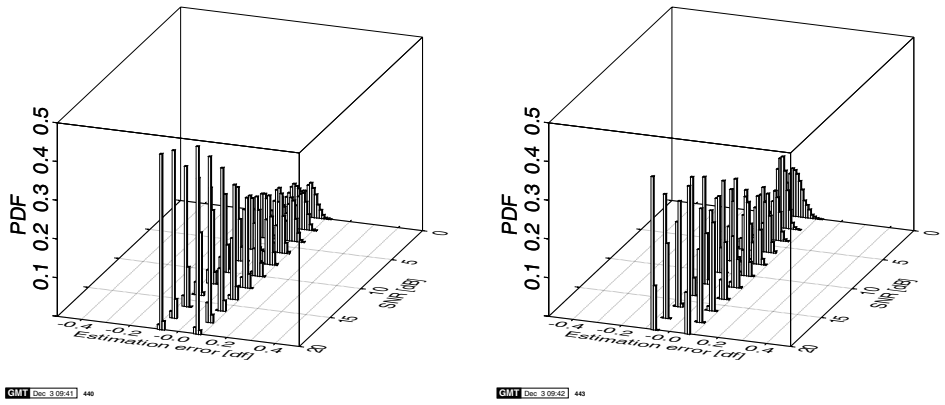
(c) 30 pilots

(d) 40 pilots

Figure 5.22: Histograms of simulated frequency mismatch estimation error for a 512-subcarrier OFDM modem in a narrowband AWGN channel for 10, 20, 30 and 40 pilot tones. The simulated frequency error was $\delta f = 0.3$

and that each of the groups is centred at 8% of the subcarrier distance above and below the correct value. Again, fine frequency synchronisation would be necessary to ensure optimal system performance.

In order to evaluate the residual estimation errors, Figure 5.24 depicts the estimated versus the actual frequency error for a perfect, noiseless channel. For frequency errors close to an integer multiple of Δf the estimation accuracy is very good, but values close to $(n + 1/2)\Delta f$ are estimated with errors of up to 8% of the subcarrier spacing. This observation is in accordance with the results of the above experiments, which showed a residual estimation error of about 1% of the carrier separation at $\delta f = 0.3\Delta f$ and of $\pm 8\%$ at $\delta f = 0.5\Delta f$.



(a) $\delta f = 0.5\Delta f$, 10 pilots

(b) $\delta f = 0.5\Delta f$, 40 pilots

Figure 5.23: Histograms of simulated frequency mismatch estimation error for a 512-subcarrier OFDM modem in a narrowband AWGN channel for 10 and 40 pilot tones. The simulated frequency error was $\delta f = 0.5\Delta f$

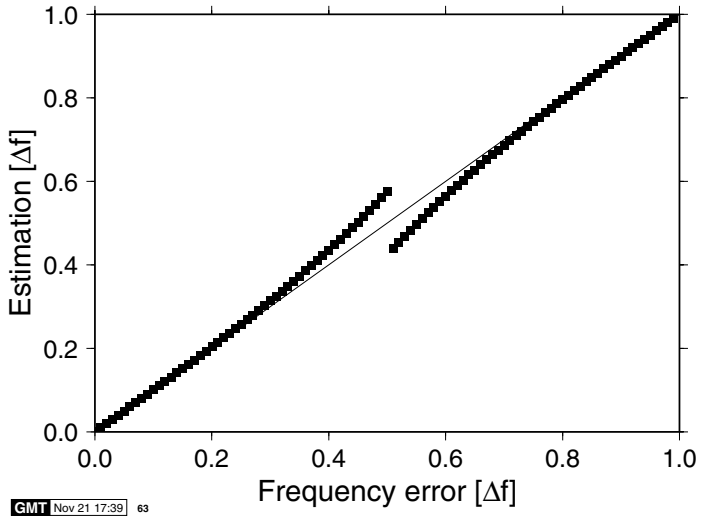


Figure 5.24: Estimated versus actual frequency error for the pilot tone-based coarse frequency synchronisation algorithm in a perfect noiseless channel

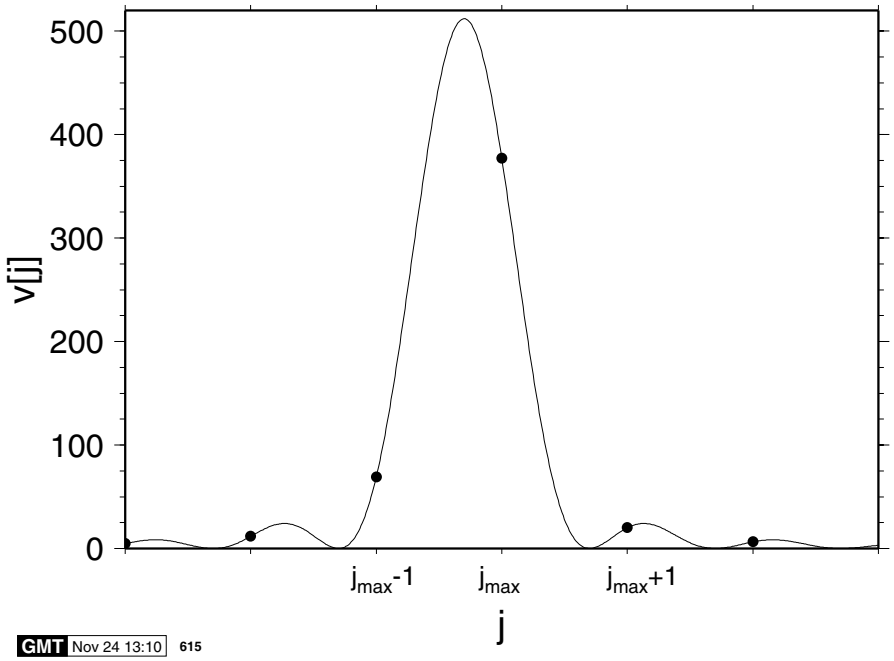


Figure 5.25: Detail from Figure 5.19(d): $V(j)$ for an SNR value of $\gamma = 50$ dB for a 512-subcarrier OFDM modem employing 10 pilot tones in the reference symbol. The simulated frequency mismatch is $0.3\Delta f$. The symbols represent the simulated $V(j)$ values, while the continuous line corresponds to the sinc^2 approximation of Equation 5.23

5.2.9.4 Alternative Frequency Error Estimation for Frequency Domain Pilot Tones

In order to improve the frequency error dependent performance of the frequency domain pilot-based frequency synchronisation algorithm outlined above, an alternative peak position estimation has been investigated in order to enhance the algorithm based on Equation 5.21. As we saw earlier, the continuous spectrum of each OFDM subcarrier follows a sinc function centred around the subcarrier frequency. In the presence of a frequency error between the transmitter and receiver, the receiver's sampling raster in the frequency domain is not aligned with the received spectrum's maximum and nulls, but shifted by the frequency error δf.

The spectrum of the received reference symbol – which contains M pilot tones at the frequencies $(j_s + m\Delta N) \cdot \Delta f$ with $0 \leq m \leq (M-1)$ – in the presence of a frequency error δf in a noiseless environment can be expressed as:

$$Y(j) = \sqrt{\frac{N}{M}} \cdot \sum_{m=0}^{M-1} \text{sinc}\left(j - j_s - m\Delta N + \frac{\delta f}{\Delta f}\right). \tag{5.22}$$

The factor $\sqrt{N/M}$ is the amplitude of each pilot tone, ensuring that the overall energy of the reference symbol is equal to the average OFDM symbol energy. If the frequency distance ΔN between two consecutive pilot tones is sufficiently large so that the received spectra

of the different pilot tones do not significantly overlap, then the vector $V(j)$, as defined by Equation 5.17, can be approximated as:

$$V(j) = \sum_{m-0}^{M-1} |Y(j + j_s + m\Delta N)|^2 \tag{5.23}$$

$$\approx N \cdot \text{sinc}^2\left(j + \frac{\delta f}{\Delta f}\right). \tag{5.24}$$

Figure 5.25 shows the simulated values of $V(j)$ from Figure 5.19(d) in greater detail around the peak, along with the continuous line corresponding to the sinc approximation of Equation 5.23. It can be seen that there is a very good correspondence between the simulated and the approximated values for the pilot spacing of $M = 50$ employed in this case.

Using the sinc^2 approximation of Equation 5.23, the values for $V(j_{max})$, $V(j_{max} + 1)$ and $V(j_{max} - 1)$ can be expressed in terms of the normalised fine frequency error estimation $\nu = \delta f/\Delta f - j_{max}$ as follows:

$$V(j_{max}) \approx N\text{sinc}^2(\nu), \tag{5.25}$$

$$V(j_{max} + 1) \approx N\text{sinc}^2(1 + \nu), \quad \text{and} \tag{5.26}$$

$$V(j_{max} - 1) \approx N\text{sinc}^2(-1 + \nu). \tag{5.27}$$

Then the following normalised terms can be defined:

$$\rho_1 = \frac{\sqrt{V(j_{max} + 1)}}{\sqrt{V(j_{max})}} \tag{5.28}$$

$$\approx \frac{\sqrt{N}\,|\sin(\pi(1 + \nu))|}{|\pi(1 + \nu)|} \cdot \frac{|\pi\nu|}{\sqrt{N}\,|\sin(\pi\nu)|} \tag{5.29}$$

$$= \frac{|\nu|}{|1 + \nu|} \quad \text{and} \tag{5.30}$$

$$\rho_{-1} = \frac{\sqrt{V(j_{max} - 1)}}{\sqrt{V(j_{max})}} \tag{5.31}$$

$$\approx \frac{\sqrt{N}\,|\sin(\pi(-1 + \nu))|}{|\pi(-1 + \nu)|} \cdot \frac{|\pi\nu|}{\sqrt{N}\,|\sin(\pi\nu)|} \tag{5.32}$$

$$= \frac{|\nu|}{|-1 + \nu|}. \tag{5.33}$$

The value d, defined as half the difference between ρ_1 and ρ_{-1} in Equation 5.20, can therefore be approximated as:

$$d = \frac{\rho_1 - \rho{-}1}{2} \approx \frac{1}{2}\left(\frac{|\nu|}{|1 + \nu|} - \frac{|\nu|}{|-1 + \nu|}\right). \tag{5.34}$$

Solving Equation 5.34 for ν values smaller than one subcarrier distance yields:

$$\nu = \begin{cases} -\sqrt{\frac{d}{d+1}} & \text{for} \quad -1 < \nu < 0 \quad (\text{or} \quad (d > 0) \\ \sqrt{\frac{d}{d-1}} & \text{for} \quad 0 \leq \nu < 1 \quad (\text{or} \quad d \leq 0) \end{cases} . \tag{5.35}$$

An alternative pilot-based frequency synchronisation algorithm can therefore be contrived by calculating the peak position estimate ν from d, as defined in Equation 5.20, using Equation 5.35 and replacing the δf estimate in Equation 5.21 by:

$$\delta f = \Delta f \cdot (j_{max} + \nu). \tag{5.36}$$

A series of simulations were conducted in order to investigate the performance of this modified peak position estimation algorithm in noisy conditions. All the investigations have been performed for a 512-subcarrier system employing a 10-pilot reference symbol in a narrowband Gaussian white noise channel.

Histograms of the estimation errors for fixed frequency errors of $\delta f = 0$, $\delta f = 0.3\Delta f$ as well as for $\delta f = 0.5\Delta f$ are given in Figure 5.26. In all cases, the estimation accuracy was better than $0.5\Delta f$, therefore allowing the subsequent use of the OFDM data symbol-based tracking algorithm of Section 5.2.7. Comparison of Figure 5.26(a) with the corresponding results for the original peak position estimation algorithm in Figure 5.20(a) reveals a similar performance for both algorithms. This was expected, since the modified estimation terms $\sqrt{d/(d-1)}$ and $-\sqrt{d/(d+1)}$ are close to the term $\sqrt{d}$ in Equation 5.21 of the original algorithm for small values of d.

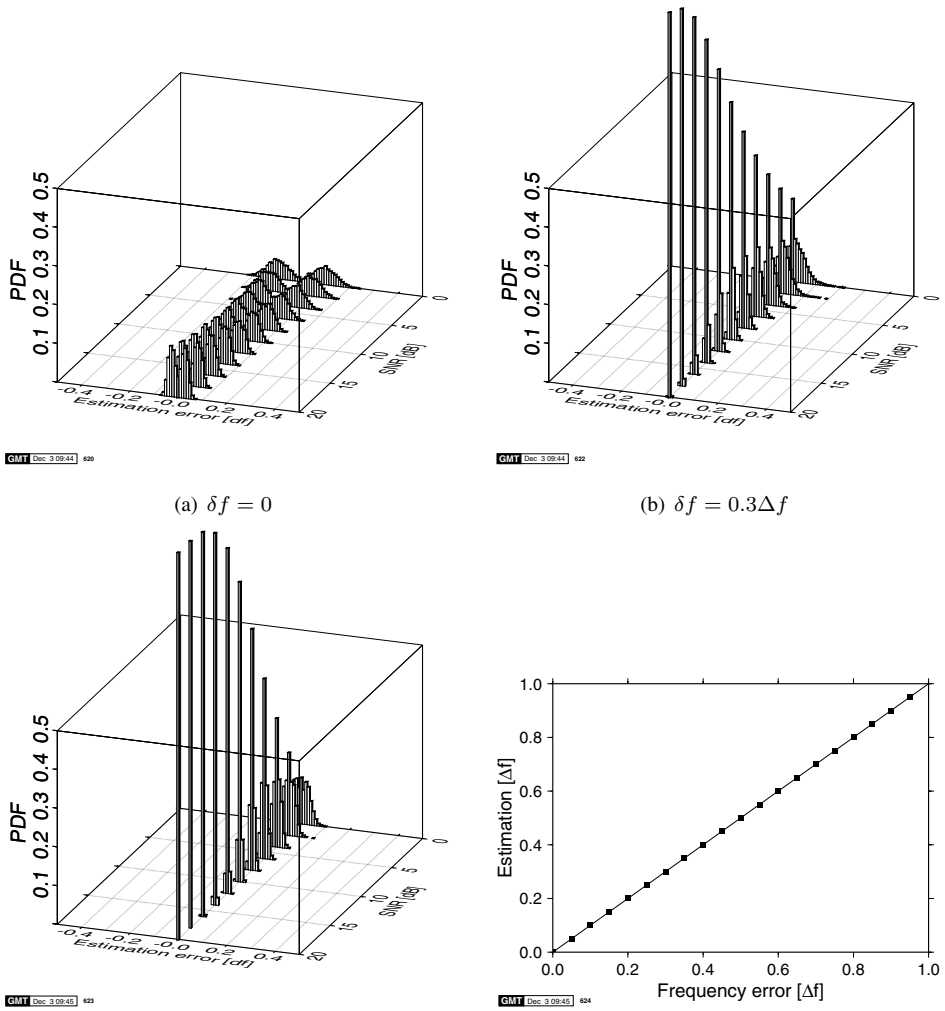
For a frequency error of $\delta f = 0.3\Delta f$, as depicted in Figure 5.26(b), the estimation accuracy was dramatically improved, when compared to the case of $\delta f = 0$. This was in accordance with the results achieved using the original peak position estimation, as shown in Figure 5.22(a). Although both schemes achieved accurate estimation results, the modified algorithm of Equation 5.36 exhibited a lower estimation bias and it was slightly more accurate than the original algorithm of Equation 5.21.

Imposing the third simulated frequency error of $\delta f = 0.5\Delta f$ revealed the different behaviour of the two investigated algorithms. While the original version of the algorithm exhibited a split histogram with systematic estimation errors of about 8% of the subcarrier distance, as can be seen in Figure 5.23(a), the modified algorithm delivered a significantly more accurate frequency error estimate. The estimation accuracy of the modified algorithm in a noiseless environment is demonstrated in Figure 5.26(d). There are no systematic estimation errors for the whole frequency error range that the peak position estimation is expected to handle.

5.3 Comparison of the Frequency Acquisition Algorithms

Both the frequency acquisition algorithms examined achieve the minimum requirements of an estimation accuracy better than half a subcarrier spacing for AWGN channel SNR levels down to 0 dB and hence ensure reliable operation of the subsequent fine frequency synchronisation algorithm.

There is, however, a difference in their absolute accuracy. While the pilot tone algorithm



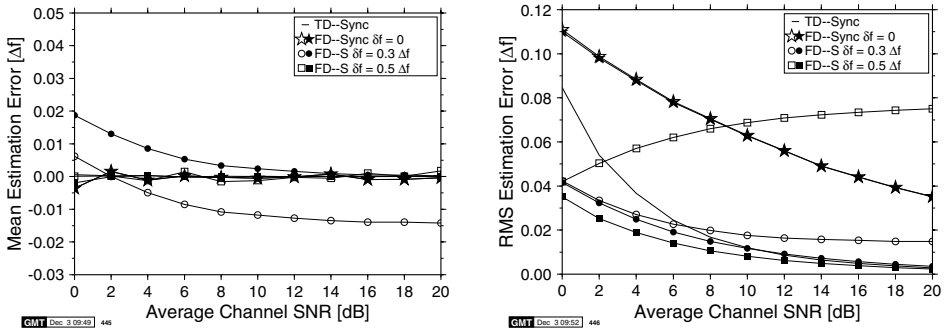
(a) $\delta f = 0$

(b) $\delta f = 0.3\Delta f$

(c) $\delta f = 0.5\Delta f$

(d) residual accuracy

Figure 5.26: (a, b, c): Histograms of the simulated frequency mismatch estimation error for a 512-subcarrier OFDM modem in a narrowband AWGN channel for 10 pilot tones employing the alternative peak position estimation algorithm. The simulated frequency error was $\delta f = 0.3$. (d) Estimated versus actual frequency error for pilot tone-based frequency synchronisation employing the alternative peak position estimation algorithm



(a) mean error (b) RMS

Figure 5.27: Comparison of the frequency acquisition algorithms over AWGN channels: (a) mean estimation error, (b) RMS estimation error. TD = time domain estimation algorithm, FD = frequency domain estimation algorithm employing a 10-pilot reference symbol. The open symbols show the performance associated with the original peak position estimation of Equation 5.21, while the closed symbols signify the alternative peak position estimation algorithm of Equation 5.36 for given frequency errors δf of 0, 0.3 and 0.5 times the subcarrier distance Δf

of Section 5.2.9 suffers from residual estimation errors for certain ranges of frequency errors, the correlation-based algorithm of Section 5.2.5 delivers the same estimation accuracy throughout its frequency capture range. Values for the long-term mean and RMS estimation error are shown in Figure 5.27. The solid lines without markers in the two graphs are the mean and RMS error curves for the time domain correlation algorithm, which are valid for all frequency errors within the frequency capture range of the algorithm ($\pm 5.12\Delta f$ for $N = 512$ and $N_s = 50$). The curves with markers correspond to the pilot tone synchronisation system employing a 10-pilot reference symbol, for frequency errors of 0, 0.3, and 0.5 times the subcarrier distance Δf. For these frequency error values, curves are drawn for the original as well as for the modified peak position estimation algorithm. The performance of both the pilot tone algorithms is clearly dependent on the frequency error, both in terms of the mean as well as the RMS errors.

The mean estimation error curves in Figure 5.27(b) show the long-term averaged estimation errors for the different schemes. While none of the algorithms exhibits mean errors above 0.5% of the subcarrier distance for frequency deviations of 0 or 0.5% Δf over the SNR range investigated, frequency errors of $0.3\Delta f$ cause both the pilot tone estimation algorithms to deliver biased estimates. The amount of this mean estimation error depends on the SNR, and the noise level dependency of the estimation is the same for both the original as well as for the alternative peak search algorithm. The residual estimation error in the absence of noise is different for the two peak position estimators, however. While the alternative estimation algorithm delivers a non-biased estimation for high SNR values, the original algorithm exhibits an estimation error of about 1.5% of the subcarrier distance. This is in accordance with Figure 5.24, which shows the residual estimation errors for the original peak position estimation. It is interesting to note that the original peak search algorithm does not result in a biased non-zero mean error estimate for frequency errors of $\delta f = 0.5\Delta f$, although the

instantaneous estimation errors at this point are at a maximum, as can be seen from Figures 5.24 and 5.23(a). This is because of the symmetry of the histogram, which will result in a non-biased mean estimation value. For all other frequency errors between 0 and $0.5\Delta f$, however, the histogram of estimation errors will be asymmetrical and the estimation will therefore be biased, as seen for example in Figure 5.22.

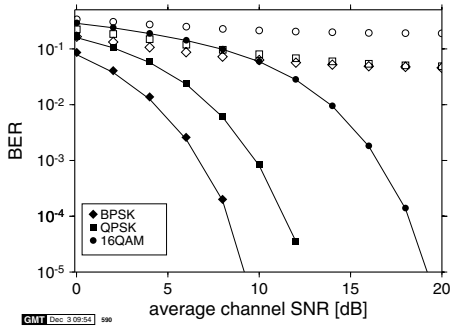
The modified peak search algorithm of Section 5.2.9.4, too, delivers biased estimations for frequency errors between 0 and $0.5\Delta f$, as seen in Figure 5.27. Since these are due to the noise affecting the estimation, there is no residual estimation error in noiseless environments. For SNR values in excess of 8 dB, the mean estimation error is smaller than 0.5% of the subcarrier distance for $\delta f = 0.3\Delta f$. The time domain frequency synchronisation algorithm of Section 5.2.5 does not exhibit any significant bias in the estimation error for the range of SNR values investigated. Therefore, long-term averaging of the time domain algorithm's estimates will result in correct frequency error estimation at the cost of reduced agility.

Figure 5.27(b) depicts the RMS estimation error curves for the investigated synchronisation algorithms for the same set of frequency errors. It can be seen that for both frequency domain pilot-based error estimation algorithms the estimation quality varies greatly with the frequency error to be estimated. The original peak position estimation algorithm exhibits residual RMS values of $0.015\Delta f$ and about $0.8\Delta f$ for frequency errors δf of $0.3\Delta f$ and $0.5\Delta f$, respectively. For $\delta f = 0.3\Delta f$ this corresponds to the bias of 1.5% of the subcarrier distance, which has been observed in Figure 5.27(a). For $\delta f = 0.5\Delta f$, this residual estimation error can be observed in the histogram, as shown in Figure 5.23(a). Although the long-term mean of the estimation is the correct value, each single estimation exhibits an error of about 8% of the subcarrier distance. This value corresponds to the residual level of RMS estimation error for $\delta f = 0.5\Delta f$ in Figure 5.27(b).

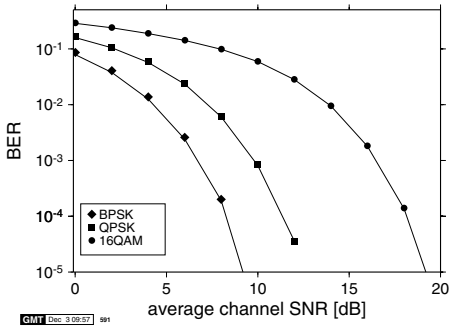
The frequency domain pilot-based algorithm employing the alternative peak position estimation of Section 5.2.9.4 does not exhibit residual RMS estimation errors. The estimation accuracy does, however, vary with the frequency error to be estimated. For $\delta f = 0$, its performance is virtually the same as that of the original peak position estimation algorithm, with high estimation errors for the whole AWGN SNR range. At $\delta f = 0.3\Delta f$ and $0.5\Delta f$, the estimation accuracy is much better, at RMS estimation errors of around 1% of the subcarrier distance for SNR values in excess of 12 dB and 10 dB, respectively.

The time domain correlation-based algorithm's accuracy does not depend on the frequency error to be estimated. Its performance is comparable to that of the frequency domain algorithm employing the alternative peak search algorithm of Section 5.2.9.4 for frequency errors δf of $0.3\Delta f$ or $0.5\Delta f$ for SNR values above 10 dB, but it performs significantly better at $\delta f = 0$.

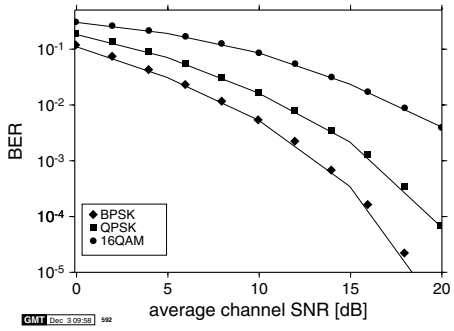
Comparing frequency error with the estimation accuracy of the different algorithms it becomes clear that all the algorithms would satisfy the estimation accuracy of $0.5\Delta f$, necessary if subsequent fine frequency tracking mechanisms are used data symbol by data symbol. If no fine frequency tracking is to be employed, however, then the constraints on the estimation accuracy are significantly tighter. We saw in Section 5.1.1.2 that, depending on the modulation scheme used, frequency errors of 5–10% of the subcarrier spacing lead to degradation of the system's SNR performance. In this case – and if no lowpass filtering of the estimated value is to be employed – the time domain correlation-based synchronisation algorithm of Section 5.2.5 would be the only applicable algorithm, since its accuracy is consistently high and its estimation is unbiased throughout the frequency error range.



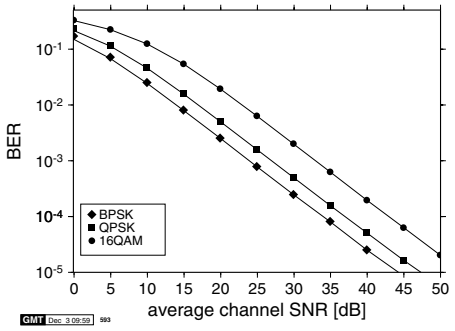
(a) $\delta f = 0.3\Delta f$, AWGN channel



(b) $\delta f = 7.5\Delta f$, AWGN channel



(c) $\delta f = 0.3\Delta f$, short WATM channel, non fading



(d) $\delta f = 0.3\Delta f$, short WATM channel, fading

Figure 5.28: BER versus channel SNR performance curves for the 512-subcarrier OFDM system in the presence of fixed frequency errors. The lines indicate the performance for perfectly corrected frequency error, and the hollow symbols show the performance for uncorrected frequency errors. The filled symbols indicate simulations with our proposed frequency error estimation using the time domain correlation technique. The short WATM channel impulse response is shown in Figure 4.3(a).

If the pilot tone reference symbol-based frequency synchronisation algorithms are to be employed without subsequent frequency tracking, then the estimation accuracy has to be improved using lowpass filtering techniques of the estimates. Let us now consider the system's BER performance when subjected to frequency synchronisation errors.

5.4 BER Performance with Frequency Synchronisation

In order to investigate the effects of the proposed frequency synchronisation algorithm on an OFDM modem, a series of experiments was conducted. The synchronisation algorithm chosen was the time domain correlation algorithm of Section 5.2.5, because of its frequency error independent estimation accuracy. We modelled a system employing one reference symbol and one data symbol per 64-slot TDMA frame. The frequency error estimates were not lowpass filtered, instead every estimate was used directly to correct the frequency error of the

subsequent data symbol. Coherently detected BPSK, QPSK and 16-QAM were employed as modulation schemes in the subcarriers and the BER performance of the modem was investigated in both narrowband AWGN as well as in fading and non-fading wideband channels. In all the simulations, a 512-subcarrier OFDM scheme employing no virtual carriers and perfect wideband channel estimation was used.

The BER performance of the simulated modems in all the channels is given in Figure 5.28. Figure 5.28(a) depicts the BER versus channel SNR for BPSK, QPSK and 16-QAM in an AWGN channel with a frequency error of $\delta f = 0.3\Delta f$. The white symbols in the graph portray the BER performance of an OFDM modem employing no frequency synchronisation. It can be seen that the frequency error results in heavy intersubcarrier interference, which manifests itself by a high residual bit error rate of about 5% for BPSK and QPSK and about 20% for 16-QAM. The lines in the graph characterise the performance of the modem in the absence of frequency errors. The black markers correspond to the BER recorded with the frequency synchronisation algorithm in operation. It can be seen that the performance of the modem employing the proposed frequency synchronisation algorithm of Section 5.2.5 is nearly indistinguishable from the perfectly synchronised case. In Figure 5.28(b), the modem's BER curves for an AWGN channel at a frequency error of $7.5\Delta f$ are depicted. Since the synchronisation algorithm's accuracy does not vary with varying frequency errors, the modem's BER performance employing the proposed synchronisation algorithm at $\delta f = 7.5\Delta f$ is the same as at $\delta f = 0.3\Delta f$. The BER for the non-synchronised modem is, however, 50% and the corresponding markers are off the graph.

The synchronised modem's BER performance in wideband channels is given in Figure 5.28(c) and 5.28(d). The impulse response used in these investigations was the short WATM impulse response, which is depicted in Figure 4.3(a). Perfect knowledge of the channel impulse response was assumed for perfect phase and amplitude correction of the data symbols with coherent detection. Again, the BER curves for both the non-fading and the fading channels show a remarkable correspondence between the ideal performance lines and the performance of the synchronised modems. In all the investigated environments, the modem's performance was unaffected by the estimation accuracy of the time domain reference symbol synchronisation algorithm.

5.5 Chapter Summary and Conclusion

In this chapter, the effects of frequency and timing errors in OFDM transmissions have been characterised. While frequency errors result in frequency domain inter-subcarrier interference, timing errors lead to time domain inter-OFDM symbol interference and to frequency domain phase rotations.

In order to overcome the effects of moderate timing errors, a cyclic postamble and the use of pilot symbol-assisted modulation or differential detection was proposed. Different frequency and timing error estimation algorithms were portrayed, and their performance was investigated. A new combined frequency and timing synchronisation algorithm based on a dedicated reference symbol exploited in the time domain was proposed and the system's performance employing this algorithm was investigated in AWGN and fading channels. The solution of Section 5.2.5 was finally advocated for implementation in a 34Mbit/s real-time demonstration testbed.

5.6 Appendix: Theoretical Performance of OFDM Synchronisation Algorithms

5.6.1 Frequency Synchronisation in an AWGN Channel

The correlation operation used in the frequency synchronisation algorithm is based on the conjugate complex multiplication of the noisy input sample with its noisy and phase-shifted copy. To derive the theoretical performance of this algorithm, the influence of the noise on the phase of this product must be known. Throughout the calculations, we will assume no frequency and time invariant phase errors, in order to simplify the notation.

5.6.1.1 One Phasor in AWGN Environment

5.6.1.1.1 Cartesian Coordinates Every received sample is a superposition of the transmitted phasor and two statistically independent quadrature noise samples; if the received phasor is real and of magnitude $\mathcal{A}$, the noisy signal is described by the complex stochastic variable Z:

$$\begin{aligned} Z &= \mathcal{A} + N && (5.37)\\ &= X + jY && (5.38) \end{aligned}$$

As the two quadrature noise processes are statistically independent, the joint probability density function (PDF) of the two quadrature components x and y is given by the product of two one-dimensional Gaussian PDFs:

$$\begin{aligned} p_{x,y}(x,y) &= p(x) \cdot p(y) && (5.39)\\ &= \left(\frac{1}{\sqrt{2\pi}\sigma}\right)^2 \cdot e^{-(x-\mathcal{A})^2/2\sigma^2} \cdot e^{-y^2/2\sigma^2} && (5.40)\\ &= \frac{1}{2\pi\sigma^2} \cdot e^{-((x-\mathcal{A})^2+y^2)/2\sigma^2} && (5.41) \end{aligned}$$

5.6.1.1.2 Polar Coordinates The stochastic variable Z can be expressed in polar coordinates:

$$\begin{aligned} Z &= R \cdot e^{j\Phi} && (5.42)\\ with R &= \sqrt{X^2+Y^2} && (5.43)\\ \Phi &= \tan^{-1}\tfrac{Y}{X} && (5.44) \end{aligned}$$

To derive the PDF in polar coordinates $p_{r,\phi}(r,\phi)$ from the expression in Cartesian coordinates $p_{x,y}(x,y)$, given in Equation 5.41, the variable transform $(x,y) \Rightarrow (r,\phi)$ is performed:

$$\begin{aligned} x(r,\phi) &= r \cdot \cos\phi && (5.45)\\ y(r,\phi) &= r \cdot \sin\phi && (5.46) \end{aligned}$$

The determinant J of the corresponding Jacobean matrix is:

$$J = \begin{vmatrix} \frac{\partial x(r,\phi)}{\partial r} & \frac{\partial y(r,\phi)}{\partial r} \\ \frac{\partial x(r,\phi)}{\partial \phi} & \frac{\partial y(r,\phi)}{\partial \phi} \end{vmatrix} = \begin{vmatrix} \cos\phi & \sin\phi \\ -r \cdot \sin\phi & r \cdot \cos\phi \end{vmatrix} = r \tag{5.47}$$

This leads to the probability density function of one noisy phasor in polar coordinates:

$$p_{r,\phi}(r,\phi) = |J| \cdot p_{x,y}(x(r,\phi), y(r,\phi)) \tag{5.48}$$

$$= \frac{r}{2\pi\sigma^2} \cdot e^{-(r^2+\mathcal{A}^2-2r\mathcal{A}\cos\phi)/2\sigma^2} \tag{5.49}$$

5.6.1.2 Product of Two Noisy Phasors

5.6.1.2.1 Joint Probability Density To derive the probability density function of the product of two noisy phasors, we will assume that both of the phasors are stochastic variables with a PDF given in Equation 5.49, with the same signal amplitude $\mathcal{A}$ and zero signal phase. The new stochastic variable Π represents the product of the two noisy phasors Z_1 and Z_2:

$$\Pi = \Xi * e^{j\Psi} = Z_1 \cdot Z_2 \tag{5.50}$$

The joint probability density function $p_\Pi(\Xi = \xi, \Psi = \psi)$ is derived from Equation 5.49 using complex multiplication:

$$\Xi = R_1 \cdot R_2 \tag{5.51}$$

$$\Psi = \Phi_1 + \Phi_2 \tag{5.52}$$

Two auxiliary variables must be introduced in order to solve the system. We choose $\Lambda = R_2$ and $\Omega = \Phi_2$. The resulting transformation functions and their inverse functions are:

$$\left.\begin{array}{rcl} \xi &=& r_1 \cdot r_2 \\ \psi &=& \phi_1 + \phi_2 \\ \lambda &=& r_2 \\ \omega &=& \phi_2 \end{array}\right\} \Leftrightarrow \left\{\begin{array}{rcl} r_1 &=& \xi/\lambda \\ \phi_1 &=& \psi - \omega \\ r_2 &=& \lambda \\ \phi_2 &=& \omega \end{array}\right. \tag{5.53}$$

The determinant J of the corresponding Jacobean matrix is:

$$J = \begin{vmatrix} \frac{\partial r_1}{\partial \xi} & \frac{\partial r_2}{\partial \xi} & \frac{\partial \phi_1}{\partial \xi} & \frac{\partial \phi_2}{\partial \xi} \\ \frac{\partial r_1}{\partial \psi} & \frac{\partial r_2}{\partial \psi} & \frac{\partial \phi_1}{\partial \psi} & \frac{\partial \phi_2}{\partial \psi} \\ \frac{\partial r_1}{\partial \lambda} & \frac{\partial r_2}{\partial \lambda} & \frac{\partial \phi_1}{\partial \lambda} & \frac{\partial \phi_2}{\partial \lambda} \\ \frac{\partial r_1}{\partial \omega} & \frac{\partial r_2}{\partial \omega} & \frac{\partial \phi_1}{\partial \omega} & \frac{\partial \phi_2}{\partial \omega} \end{vmatrix} = \begin{vmatrix} 1/\lambda & 0 & 0 & 0 \\ 0 & 1 & 0 & 0 \\ \xi \ln\lambda & 0 & 1 & 0 \\ 0 & 0 & 0 & 1 \end{vmatrix} = 1/\lambda \tag{5.54}$$

The resulting probability density function depending on the four new variables is:

$$p_\Pi(\xi,\psi,\lambda,\omega) = |J| \cdot p_Z(r_1 = \xi/\lambda, \phi_1 = \psi - \omega, r_2 = \lambda, \phi_2 = \omega) \tag{5.55}$$

The two probability density functions $p_Z(r1, \phi_1)$ and $p_Z(r2, \phi_2)$ are statistically independent, therefore

$$p_Z(r_1, \phi_1, r_2, \phi_2) = p_Z(r1, \phi_1) \cdot p_Z(r2, \phi_2) \tag{5.56}$$

Using the Equations 5.49 and 5.56 in 5.55, we find the expression for the PDF of the product of two noisy phasors as a function of the four transformed variables ξ, ψ, λ and ω:

$$p_\Pi(\xi, \psi, \lambda, \omega) = \frac{\xi}{\psi} \cdot \frac{1}{4\pi^2\sigma^4} \cdot e^{-\frac{\xi^2/\lambda^2+\lambda^2+2\mathcal{A}^2-2\mathcal{A}(\lambda\cos\omega+\xi/\lambda\cos(\psi-\omega)))}{2\sigma^2}} \tag{5.57}$$

Eliminating the auxiliary variables λ and ω by integrating Equation 5.57 yields:

$$p_\Pi(\Xi = \xi, \Psi = \psi) = \int_0^\infty \int_{-\pi}^{\pi} p_\Pi(\xi, \psi, \lambda, \omega) d\omega d\lambda \tag{5.58}$$

5.6.1.2.2 Phase Distribution The distribution of the phase of Π is obtained by integrating Equation 5.58 over the amplitude ξ:

$$p_\Pi(\Psi = \psi) = \int_0^\infty p_\Pi(\xi, \psi) d\xi \tag{5.59}$$

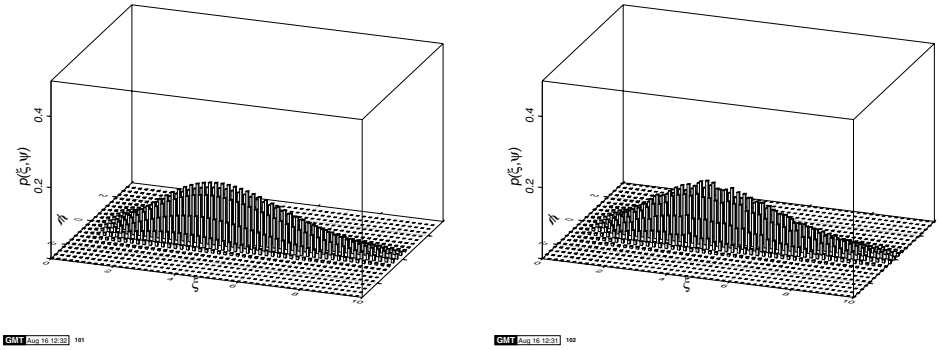
5.6.1.2.3 Numerical Integration The integrals in Equations 5.58 and 5.59 cannot be solved analytically, therefore numerical integration has to be employed to determine the probability density functions $p_\Pi(\xi, \psi)$ and $p_\Pi(\psi)$. This numerical integral has been evaluated for a range of different signal-to-noise (SNR) values γ:

$$\gamma = \frac{\mathcal{A}}{2\sigma^2} \tag{5.60}$$

Simulations have been performed for the same SNR values to verify the expressions 5.58 and 5.59. The simulated histograms have been employed to perform a χ^2–test with the numerical results. The χ^2 value gives a distance measure between an expected probability distribution and a N-binned set of experimental data:

$$\chi^2 = \sum_{i=0}^{N-1} \frac{(p(i) - h(i))^2}{p(i)} \tag{5.61}$$

where $h(i)$ is the value of the ith data bin, and $p(i)$ its expected value. As an example, Figure 5.6.1.2.3 illustrates both the numerical evaluation of Equation 5.58 and the histogram of the simulation for a SNR value of 6dB and a phasor amplitude of $\mathcal{A} = 2$. The figures reflect a high degree of correspondence between the numerical and the simulation results. This is confirmed by a quantitative measure, the χ^2 test, which yields a confidence-level in excess of 99% when testing the hypothesis that the simulated results are of the same distribution as given in Equation 5.58. Table 5.1 displays the values of χ^2 and the resulting confidence level $\Gamma(2100, \chi^2)$ for SNR values between 0 and 10dB. The numerically integrated phase probability density function Equation 5.59 and the histogram of the simulated values are



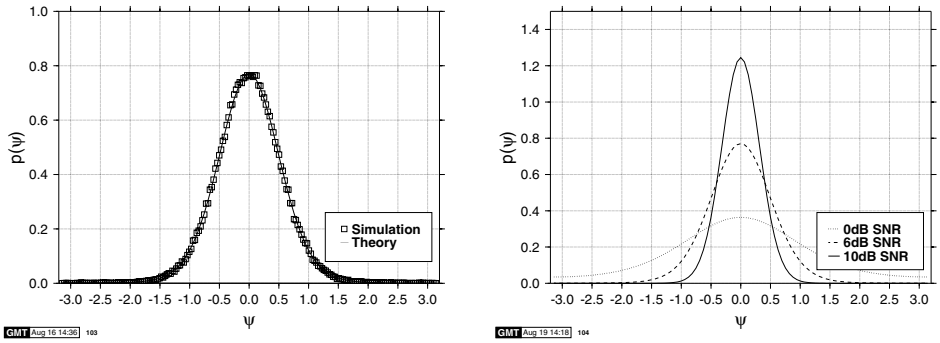
(a) $p_{\Pi}(\xi, \chi)$ (b) simulated histogram

Figure 5.29: Product of two noisy phasors with $\mathcal{A} = 2$ and $\gamma = 6$dB: (a): numerical solution of Equation 5.58, (b): histogram of 100000 simulated products

SNR	χ^2	Confidence level
0	3.959337e-1	$> 99\%$
2	3.344832e-1	–”–
4	3.012187e-1	–”–
6	2.110520e-1	–”–
8	1.835500e-1	–”–
10	1.718824e-1	–”–

Table 5.1: χ^2 values and confidence levels for $p_{\Pi}(\xi, \psi)$ for different SNR values

shown in Figure 5.30(a). Figure 5.30(b) depicts the phase PDF for different SNR values.



(a) phase PDF, theory and simulation

(b) phase PDFs for different SNR values

Figure 5.30: Product of two noisy phasors: phase probability density functions. (a): theoretical PDF and simulated histogram of the phase distribution for SNR = 6dB (b): theoretical PDFs for different SNR values

Chapter 6

Adaptive Single- and Multi-user OFDM Techniques

6.1 Introduction

Steele and Webb [206] proposed adaptive modulation for exploiting the time-variant Shannonian channel capacity of fading narrowband channels, and further research was conducted at Osaka University by Sampei *et al.* [207], at the University of Stanford by Goldsmith and Chua [208], by Pearce, Burr and Tozer at the University of York [209], Lau and McLeod at the University of Cambridge [210], and at Southampton University [211,212]. The associated principles can also be invoked in the context of parallel modems, as it has been demonstrated by Kalet [19], Czylwik [213] as well as by Chow, Cioffi and Bingham [214]. Our treatment of adaptive modulation is conceptual in this chapter. For a more detailed treatise on adaptive modulation please refer to [7, 90, 215–217].

6.1.1 Motivation

We saw in Figure 4.12 that the bit error probability of different OFDM subcarriers transmitted in time-dispersive channels depends on the frequency domain channel transfer function. The occurrence of bit errors is normally concentrated in a set of severely faded subcarriers, while in the rest of the OFDM spectrum often no bit errors are observed. If the subcarriers that will exhibit high bit error probabilities in the OFDM symbol to be transmitted can be identified and excluded from data transmission, the overall BER can be improved in exchange for a slight loss of system throughput. As the frequency domain fading deteriorates the SNR of certain subcarriers, but improves that of others above the average SNR value, the potential loss of throughput due to the exclusion of faded subcarriers can be mitigated by employing higher-order modulation modes on the subcarriers exhibiting high SNR values.

In addition to excluding sets of faded subcarriers and varying the modulation modes employed, other parameters such as the coding rate of error correction coding schemes can

OFDM and MC-CDMA: A Primer L. Hanzo and T. Keller
© 2006 John Wiley & Sons, Ltd

be adapted at the transmitter according to the perceived channel transfer function. This issue is addressed in substantial detail in the full-length version of this monograph [90] and in [215, 216].

Adaptation of the transmission parameters is based on the transmitter's perception of the channel conditions in the forthcoming time slot. Clearly, this estimation of future channel parameters can only be obtained by extrapolation of previous channel estimations, which are acquired upon detecting each received OFDM symbol. The channel characteristics therefore have to vary sufficiently slowly compared to the estimation interval.

Adapting the transmission technique to the channel conditions on a time slot by time slot basis for serial modems in narrowband fading channels has been shown to considerably improve the BER performance [218] for time division duplex (TDD) systems assuming duplex reciprocal channels. However, the Doppler fading rate of the narrowband channel has a strong effect on the achievable system performance: if the fading is rapid, then the prediction of the channel conditions for the next transmit time slot is inaccurate, and therefore the wrong set of transmission parameters may be chosen. If, however, the channel varies slowly, then the data throughput of the system is varies dramatically over time, and large data buffers are required at the transmitters in order to smoothen the bit rate fluctuation. For time critical applications, such as interactive speech transmission, the potential delays can become problematic. A given single-carrier adaptive system in narrowband channels will therefore operate efficiently only in a limited range of channel conditions.

Adaptive OFDM modem channels can ease the problem of slowly time-varying channels, since the variation of the signal quality can be exploited in the time domain and the frequency domain. The channel conditions still have to be monitored based on the received OFDM symbols, and relatively slowly varying channels have to be assumed, since we saw in Section 4.2.2 that OFDM transmissions are not well suited to rapidly varying channel conditions.

6.1.2 Adaptive Techniques

Adaptive modulation is only suitable for duplex communication between two stations, since the transmission parameters have to be adapted using some form of two-way transmission in order to allow channel measurements and signalling to take place.

Transmission parameter adaptation is a response of the transmitter to time-varying channel conditions. In order to efficiently react to the changes in channel quality, the following steps have to be taken:

(1) *Channel quality estimation:* In order to appropriately select the transmission parameters to be employed for the next transmission, a reliable estimation of the channel transfer function during the next active transmit time slot is necessary.

(2) *Choice of the appropriate parameters for the next transmission:* Based on the prediction of the channel conditions for the next time slot, the transmitter has to select the appropriate modulation modes for the subcarriers.

(3) *Signalling or blind detection of the employed parameters:* The receiver has to be informed, which demodulator parameters to employ for the received packet. This information can either be conveyed within the OFDM symbol itself, with the loss of effective data throughput, or the receiver can attempt to estimate the parameters employed by the remote transmitter by means of blind detection mechanisms.

6.1.2.1 Channel Quality Estimation

The transmitter requires an estimate of the expected channel conditions for the time when the next OFDM symbol is to be transmitted. Since this knowledge can only be gained by prediction from past channel quality estimations, the adaptive system can only operate efficiently in an environment exhibiting relatively slowly varying channel conditions.

The channel quality estimation can be acquired from a range of different sources. If the communication between the two stations is bidirectional and the channel can be considered reciprocal, then each station can estimate the channel quality on the basis of the received OFDM symbols, and adapt the parameters of the local transmitter to this estimation. We will refer to such a regime as *open-loop adaptation*, since there is no feedback between the receiver of a given OFDM symbol and the choice of the modulation parameters. A time division duplex (TDD) system in absence of interference is an example of such a system, and hence a TDD regime is assumed to generate the performance results below. Channel reciprocity issues were addressed for example in [219, 220].

If the channel is not reciprocal, as in a frequency division duplex (FDD) system, then the stations cannot determine the parameters for the next OFDM symbol's transmission from the received symbols. In this case, the receiver has to estimate the channel quality and explicitly signal this perceived channel quality information to the transmitter in the reverse link. Since in this case the receiver explicitly instructs the remote transmitter as to which modem modes to invoke, this regime is referred to as *closed-loop adaptation*. With the aid of this technique the adaptation algorithms can take into account effects such as interference as well as non-reciprocal channels. If the communication between the stations is essentially unidirectional, then a low-rate signalling channel must be implemented from the receiver to the transmitter. If such a channel exists, then the same technique as for non-reciprocal channels can be employed.

Different techniques can be employed to estimate the channel quality. For OFDM modems, the bit error probability in each subcarrier is determined by the fluctuations of the channel's instantaneous frequency domain channel transfer function H_n, if no interference is present. The estimate of the channel transfer function $\hat{H}_n$ can be acquired by means of pilot tone based channel estimation, as demonstrated in Section 4.3.1.1. More accurate measures of the channel transfer function can be gained by means of decision directed or time domain training sequence based techniques. The estimate of the channel transfer function $\hat{H}_n$ does not take into account effects, such as co-channel or intersubcarrier interference. Alternative channel quality measures that include interference effects can be devised on the basis of the error correction decoder's soft output information or by means of decision feedback local SNR estimations.

The delay between the channel quality estimate and the actual transmission of the OFDM symbol in relation to the maximal Doppler frequency of the channel is crucial to the adaptive system's performance. If the channel estimate is obsolete at the time of transmission, then poor system performance will result. For a closed-loop adaptive system the delays between channel estimation and transmission of the packet are generally longer than for an open-loop adaptive system, and therefore the Doppler frequency of the channel is a more critical parameter for the system's performance than in the context of open-loop adaptive systems.

6.1.2.2 Parameter Adaptation

Different transmission parameters can be adapted to the anticipated channel conditions, such as the modulation and coding modes. Adapting the number of modulation levels in response to the anticipated local SNR encountered in each subcarrier can be employed, in order to achieve a wide range of different trade-offs between the received data integrity and throughput. Corrupted subcarriers can be excluded from data transmission and left blank or perhaps used for crest factor reduction.

The adaptive channel coding parameters entail code rate, adaptive interleaving and puncturing for convolutional and turbo codes, or varying block lengths for block codes [177]. These techniques can be combined with adaptive modulation mode selection, as detailed in the full-length version of this monograph [90] and in [215, 216].

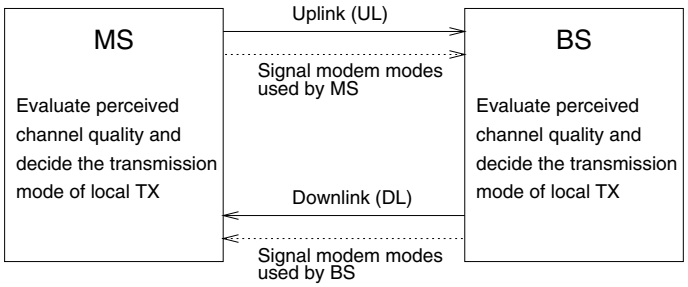
Based on the estimated frequency domain channel transfer function, spectral predistortion at the transmitter of one or both communicating stations can be invoked, in order to partially or fully counteract the frequency selective fading of the time-dispersive channel. Unlike frequency domain equalisation at the receiver – which corrects for the amplitude and phase errors inflicted upon the subcarriers by the channel but cannot improve the signal-to-noise ratio in poor quality channels – spectral predistortion at the OFDM transmitter can deliver near-constant signal-to-noise levels for all subcarriers and can be thought of as power control on a subcarrier-by-subcarrier basis.

In addition to improving the system's BER performance in time dispersive channels, spectral predistortion can be employed in order to perform all channel estimation and equalisation functions at only one of the two communicating duplex stations. Low cost, low power consumption mobile stations can communicate with a base station that performs the channel estimation and frequency domain equalisation of the uplink, and uses the estimated channel transfer function for predistorting the down-link OFDM symbol. This set-up would lead to different overall channel quality on the uplink and the downlink, and the superior downlink channel quality could be exploited by using a computationally less complex channel decoder having weaker error correction capabilities in the mobile station than in the base station.

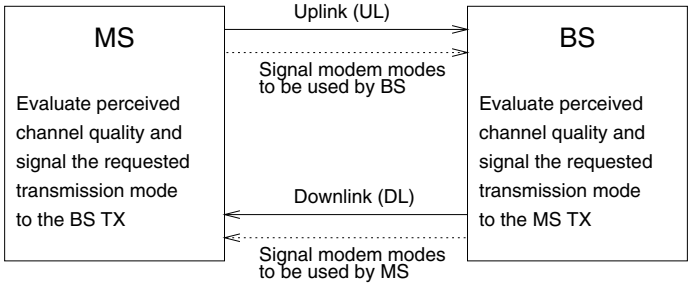
If the channel's frequency domain transfer function is to be fully counteracted by the spectral predistortion upon adapting the subcarrier power to the inverse of the channel transfer function, then the output power of the transmitter can become excessive, if heavily faded subcarriers are present in the system's frequency range. In order to limit the transmitter's maximal output power, hybrid channel predistortion and adaptive modulation schemes can be devised, which would deactivate transmission in deeply faded sub-channels, while retaining the benefits of predistortion in the remaining subcarriers.

6.1.2.3 Signalling the AOFDM Parameters

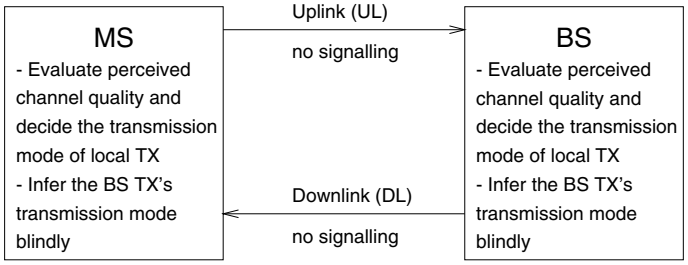
Signalling plays an important role in adaptive systems and the range of signalling options is summarised in Figure 6.1 for both open-loop and closed-loop signalling, as well as for blind detection. If the channel quality estimation and parameter adaptation have been performed at the transmitter of a particular link, based on open-loop adaptation, then the resulting set of parameters has to be communicated to the receiver in order to successfully demodulate and decode the OFDM symbol. If the receiver itself determines the requested parameter set to be used by the remote transmitter, the closed-loop scenario, then the same amount of information has to be transported to the remote transmitter in the reverse link. If this



(a) Reciprocal channel, open-loop control



(b) Non-reciprocal channel, closed-loop signalling



(c) Reciprocal channel, blind modem-mode detection

Figure 6.1: Signalling scenarios in adaptive modems

signalling information is corrupted, then the receiver is generally unable to correctly decode the OFDM symbol corresponding to the incorrect signalling information.

Unlike adaptive serial systems, which employ the same set of parameters for all data symbols in a transmission packet [211, 212], adaptive OFDM systems have to react to the frequency selective nature of the channel, by adapting the modem parameters across the subcarriers. The resulting signalling overhead may become significantly higher than that for serial modems, and can be prohibitive for subcarrier-by-subcarrier modulation mode adaptation. In order to overcome these limitations, efficient and reliable signalling techniques have to be employed for practical implementation of adaptive OFDM modems.

If some flexibility in choosing the transmission parameters is sacrificed in an adaptation

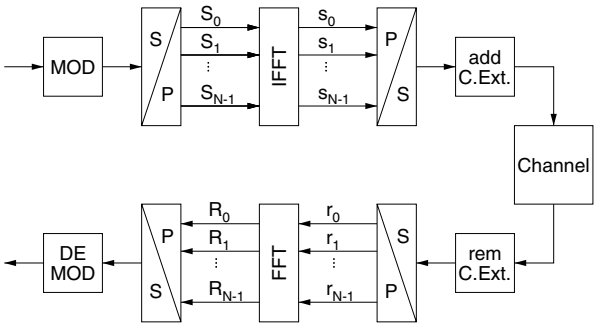


Figure 6.2: Schematic model of the OFDM system

scheme, as in the sub-band adaptive OFDM schemes described below, then the amount of signalling can be reduced. Alternatively, blind parameter detection schemes can be devised, which require little or no signalling information, respectively. Two simple blind modulation scheme detection algorithms are investigated in Section 6.2.6.2 [221].

6.1.3 System Aspects

The effects of transmission parameter adaptation for OFDM systems on the overall communication system have to be investigated in at least the following areas: data buffering and latency due to varying data throughput, the effects of co-channel interference and bandwidth efficiency.

6.2 Adaptive Modulation for OFDM

6.2.1 System Model

The system model of the N-subcarrier orthogonal frequency division multiplexing (OFDM) modem is shown in Figure 6.2 [1]. At the transmitter, the modulator generates N data symbols S_n, $0 \leq n \leq N-1$, which are multiplexed to the N subcarriers. The time domain samples s_n transmitted during one OFDM symbol are generated by the inverse fast Fourier transform (IFFT) and transmitted over the channel after the cyclic extension (C. Ext.) has been inserted. The channel is modelled by its time-variant impulse response $h(\tau, t)$ and AWGN. At the receiver, the cyclic extension is removed from the received time domain samples, and the data samples r_n are fast Fourier transformed, in order to yield the received frequency domain data symbols R_n.

The channel's impulse response is assumed to be time invariant for the duration of one OFDM symbol, therefore it can be characterised for each OFDM symbol period by the N-point Fourier transform of the impulse response, which is referred to as the frequency domain channel transfer function H_n. The received data symbols R_n can be expressed as:

$$R_n = S_n \cdot H_n + n_n,$$

where n_n is an AWGN sample. Coherent detection is assumed for the system, therefore the received data symbols R_n have to be defaded in the frequency domain with the aid of an estimate of the channel transfer function H_n. This estimate $\hat{H}_n$ can be obtained by the use of pilot subcarriers in the OFDM symbol, or by employing time domain channel sounding training sequences embedded in the transmitted signal. Since the noise energy in each subcarrier is independent of the channel's frequency domain transfer function H_n, the "local" signal-to-noise ratio SNR in subcarrier n can be expressed as

$$\gamma_n = |H_n|^2 \cdot \gamma,$$

where γ is the overall SNR. If no signal degradation due to intersubcarrier interference (ISI) or interference from other sources appears, then the value of γ_n determines the bit error probability for the transmission of data symbols over the subcarrier n.

The goal of adaptive modulation is to choose the appropriate modulation mode for transmission in each subcarrier, given the local SNR γ_n, in order to achieve a good trade-off between throughput and overall BER. The acceptable overall BER varies depending on other systems parameters, such as the correction capability of the error correction coding and the nature of the service supported by this particular link.

The adaptive system has to fulfil these requirements:

(1) Channel quality estimation,

(2) Choice of the appropriate modulation modes.

(3) Signalling or blind detection of the modulation modes.

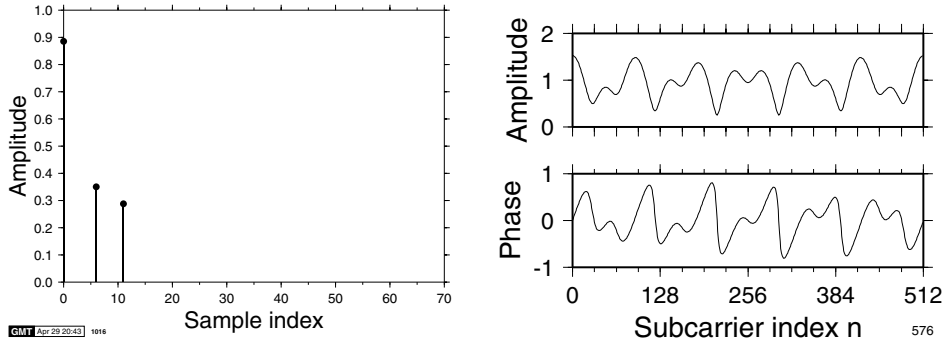
We will examine these three points with reference to Figure 6.1 in the following sections for the example of a 512-subcarrier OFDM modem in the shortened WATM channel of Section 4.1.1.2.

6.2.2 Channel Model

The impulse response $h(\tau, t)$ used in our experiments was generated on the basis of the symbol-spaced impulse response shown in Figure 6.3(a) by fading each of the impulses obeying a Rayleigh distribution of a normalised maximal Doppler frequency of $f'_d = 1.235 \cdot 10^{-5}$, which corresponds to the WLAN channel experienced by a modem transmitting at a carrier frequency of 60 GHz with a sample rate of 225 MHz and a vehicular velocity of 50 km/h. The complex frequency domain channel transfer function H_n corresponding to the unfaded impulse response is shown in Figure 6.3(b).

6.2.3 Channel Transfer Function Variations

The most convenient setting for an adaptive OFDM (AOFDM) system is a time division duplex (TDD) system in a slowly varying reciprocal channel, allowing open-loop adaptation. Both stations transmit an OFDM symbol in turn, and at each station the most recent received symbol is used for the channel estimation employed for the modulation mode adaptation for the next transmitted OFDM symbol. The channel estimation on the basis of the received



(a) $h(n)$ (b) H_n

Figure 6.3: WATM wideband channel: (a) unfaded symbol spaced impulse response, (b) the corresponding frequency domain channel transfer function

symbol can be performed by PSAM (see Section 4.3.1.1), or upon invoking more sophisticated methods, such as decision-directed channel estimation. Initially, we will assume perfect knowledge of the channel transfer function during the received time slot.

6.2.4 Choice of the Modulation Modes

The two communicating stations use the open-loop predicted channel transfer function acquired from the most recent received OFDM symbol, in order to allocate the appropriate modulation modes to the subcarriers. The modulation modes were chosen from the set of binary phase shift keying (BPSK), quadrature phase shift keying (QPSK), 16-quadrature amplitude modulation (16-QAM), as well as "no transmission", for which no signal was transmitted. These modulation modes are denoted by M_m, where $m \in (0, 1, 2, 4)$ is the number of data bits associated with one data symbol of each mode.

In order to keep the system complexity low, the modulation mode is not varied on a subcarrier-by-subcarrier basis, but instead the total OFDM bandwidth of 512 subcarriers is split into blocks of adjacent subcarriers, referred to as sub-bands, and the same modulation scheme is employed for all subcarriers of the same sub-band. This substantially simplifies the task of signalling the modem mode and renders the employment of alternative blind detection mechanisms feasible, which will be discussed in Section 6.2.6.

Three modulation mode allocation algorithms were investigated in the sub-bands: a fixed threshold controlled algorithm, an upper bound BER estimator and a fixed throughput adaptation algorithm.

6.2.4.1 Fixed Threshold Adaptation Algorithm

The fixed threshold algorithm was derived from the adaptation algorithm proposed by Torrance for serial modems [218]. In the case of a serial modem, the channel quality is assumed to be constant for all symbols in the time slot, and hence the channel has to be slowly varying in order to allow accurate channel quality prediction. Under these circumstances, all data symbols in the transmit time slot employ the same modulation mode, chosen according to

	l_0	l_1	l_2	l_4
speech system	$-\infty$	3.31	6.48	11.61
data system	$-\infty$	7.98	10.42	16.76

Table 6.1: Optimised switching levels for adaptive modulation over Rayleigh fading channels for the "speech" and "data" systems, shown in instantaneous channel SNR [dB] (from [222])

the predicted SNR. The SNR thresholds for a given long-term target BER were determined by Powell optimisation [222]. Torrance assumed two uncoded target bit error rates: 1% for a high data rate "speech" system, and 10^{-4} for a higher integrity, lower data rate "data" system. The resulting SNR thresholds l_n for activating a given modulation mode M_n in a slowly Rayleigh fading narrowband channel for both systems are given in Table 6.1. Specifically, the modulation mode M_n is selected if the instantaneous channel SNR exceeds the switching level l_n.

As noted before, a more detailed analytically motivated discussion on the optimisation of the modem mode switching thresholds can be found in [90]. More specifically, it is shown in [90] that the multi-dimensional Powell optimisation technique may be replaced by a single-dimensional Lagrangian optimisation procedure, which is capable of further improving the achievable system throughput. More explicitly, the optimisation may be rendered one-dimensional, since the switching thresholds of the high-throughput modem modes are actually at a constant distance from the activation threshold of the lowest-throughput BPSK mode.

This adaptation algorithm originally assumed a constant instantaneous SNR over all of the block's symbols, but in the case of an OFDM system in a frequency selective channel the channel quality varies across the different subcarriers. For sub-band adaptive OFDM transmission, this implies that if the sub-band width is wider than the channel's coherence bandwidth [177], then the original switching algorithm cannot be employed. For our investigations, we have therefore employed the lowest quality subcarrier in the sub-band for the adaptation algorithm based on the thresholds given in Table 6.1. The performance of the 16 sub-band adaptive system over the shortened WATM Rayleigh fading channel of Figure 4.3 is shown in Figure 6.4.

Adjacent or consecutive time slots have been used for the uplink and downlink slots in these simulations, so that the delay between channel estimation and transmission was rendered as short as possible. Figure 6.4 shows the long-term average BER and throughput of the studied modem for the "speech" and "data" switching levels of Table 6.1 as well as for a subcarrier-by-subcarrier adaptive modem employing the "data" switching levels. The results show the typical behaviour of a variable throughput AOFDM system, which constitutes a trade-off between the best BER and best throughput performance. For low SNR values, the system achieves a low BER by transmitting very few bits and only when the channel conditions allow. With increasing long-term SNR, the throughput increases without significant change in the BER. For high SNR values the BER drops as the throughput approaches its maximum of 4 bits per symbol, since the highest-order constellation was 16-QAM.

It can be seen from the figure that the adaptive system performs better than its target bit error rates of 10^{-2} and 10^{-4} for the "speech" and "data" systems, respectively, resulting in measured bit error rates lower than the targets. This can be explained by the adaptation

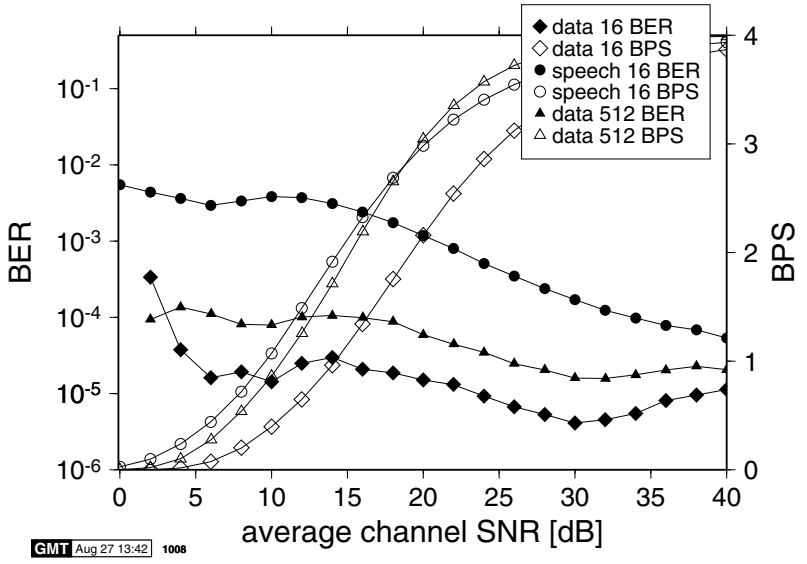


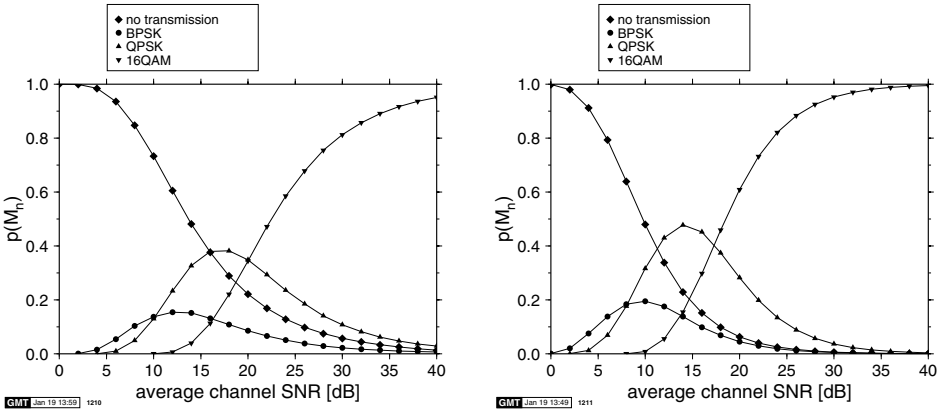
Figure 6.4: BER and BPS throughput performance of the 16 sub-band, 512 subcarrier switching level adaptive OFDM modem employing BPSK, QPSK, 16-QAM and "no transmission" over the Rayleigh fading time-dispersive channel of Figure 4.3 using the switching thresholds of Table 6.1

regime, which was based on the conservative principle of using the lowest quality subcarrier in each sub-band for channel quality estimation, leading to a pessimistic channel quality estimate for the entire sub-band. For low values of SNR, the throughput in bits per data symbol is low and exceeds the fixed BPSK throughput of 1 bit/symbol only for SNR values in excess of 9.5 dB and 14 dB for the "speech" and "data" systems, respectively.

The upper bound performance of the system with subcarrier-by-subcarrier adaptation is also portrayed in the figure, shown as 512 independent sub-bands, for the "data" optimised set of threshold values. It can be seen that in this case the target BER of 10^{-4} is closely met over a wide range of SNR values from about 2 dB to 20 dB, and that the throughput is considerably higher than in the case of the 16 sub-band modem. This is the result of more accurate subcarrier-by-subcarrier channel quality estimation and fine-grained adaptation, leading to better exploitation of the available channel capacity.

Figure 6.5 shows the long-term modulation mode histograms for a range of channel SNR values for the "data" switching levels in both the 16 sub-band and the subcarrier-by-subcarrier adaptive modems using the switching thresholds of Table 6.1. Comparison of the graphs shows that higher-order modulation modes are used more frequently by the subcarrier-by-subcarrier adaptation algorithm, which is in accordance with the overall throughput performance of the two modems in Figure 6.4.

The throughput penalty of employing sub-band adaptation depends on the frequency domain variation of the channel transfer function. If the sub-band bandwidth is lower than the channel's coherence bandwidth, then the assumption of constant channel quality per sub-band is closely met, and the system performance is equivalent to that of a subcarrier-by-subcarrier



(a) 16 sub-bands

(b) subcarrier-by-subcarrier

Figure 6.5: Histograms of modulation modes versus channel SNR for the "data" switching level adaptive 512 subcarrier, 16 sub-band OFDM modem over the Rayleigh fading time-dispersive channel of Figure 4.3 using the switching thresholds of Table 6.1

adaptive scheme.

6.2.4.2 Sub-Band BER Estimator Adaptation Algorithm

We saw above that the fixed switching level based algorithm leads to a throughput performance penalty, if used in a sub-band adaptive OFDM modem, when the channel quality is not constant throughout each sub-band. This is due to the conservative adaptation based on the subcarrier experiencing the most hostile channel in each sub-band.

An alternative scheme taking into account the non-constant SNR values γ_j across the N_s subcarriers in the jth sub-band can be devised by calculating the expected overall bit error probability for all available modulation modes M_n in each sub-band, which is denoted by $\bar{p}_e(n) = 1/N_s \sum_j p_e(\gamma_j, M_n)$. For each sub-band, the mode having the highest throughput, whose estimated BER is lower than a given threshold, is then chosen. While the adaptation granularity is still limited to the sub-band width, the channel quality estimation does not include only the lowest quality subcarrier, which leads to an improved throughput.

Figure 6.6 shows the BER and throughput performance for the 16 sub-band adaptive OFDM modem employing the BER estimator adaptation algorithm in the Rayleigh fading time-dispersive channel of Figure 4.3. The two sets of curves in the figure correspond to target bit error rates of 10^{-2} and 10^{-1}, respectively. Comparing the modem's performance for a target BER of 10^{-2} with that of the "speech" modem in Figure 6.4, it can be seen that the BER estimator algorithm results in significantly higher throughput while meeting the BER requirements. The BER estimator algorithm is readily adjustable to different target bit error rates, which is demonstrated in the figure for a target BER of 10^{-1}. Such adjustability is beneficial when combining adaptive modulation with channel coding, as will be discussed in Section 6.2.7.

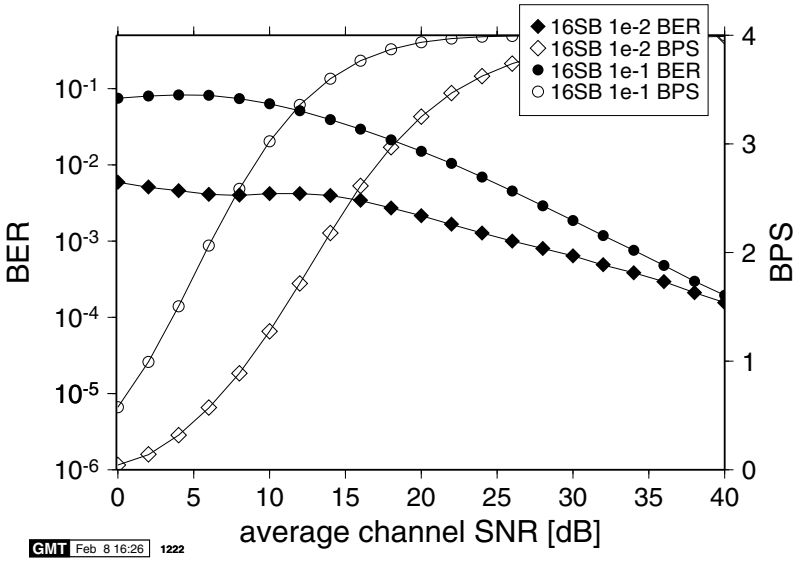


Figure 6.6: BER and BPS throughput performance of the 16 sub-band, 512 subcarrier BER estimator adaptive OFDM modem employing BPSK, QPSK, 16-QAM and "no transmission" over the Rayleigh fading time-dispersive channel of Figure 4.3

6.2.5 Constant Throughput Adaptive OFDM

The time-varying data throughput of an adaptive OFDM modem operating with either of the two adaptation algorithms discussed above makes it difficult to employ such a scheme in a variety of constant rate applications. Torrance [218] studied the system implications of variable-throughput adaptive modems in the context of narrowband channels, stressing the importance of data buffering at the transmitter, in order to accommodate the variable data rate. The required length of the buffer is related to the Doppler frequency of the channel, and a slowly varying channel – as required for adaptive modulation – results in slowly varying data throughput and therefore the need for a high buffer capacity. Real-time interactive audio or video transmission is sensitive to delays, and therefore different modem mode adaptation algorithms are needed for such applications.

The constant throughput AOFDM scheme proposed here exploits the frequency selectivity of the channel, while offering a constant bit rate. Again, sub-band adaptivity is assumed, in order to simplify the signalling or the associated blind detection of the modem schemes.

The modulation mode allocation of the sub-bands is performed on the basis of a cost function to be introduced below, based on the expected number of bit errors in each sub-band. The expected number of bit errors $e_{n,s}$, for each sub-band n and for each possible modulation mode index s, is calculated on the basis of the estimated channel transfer function $\hat{H}$, taking into account the number of bits transmitted per sub-band and per modulation mode, $b_{n,s}$.

Each sub-band is assigned a state variable s_n holding the index of a modulation mode. Each state variable is initialised to the lowest-order modulation mode, which in our case is 0

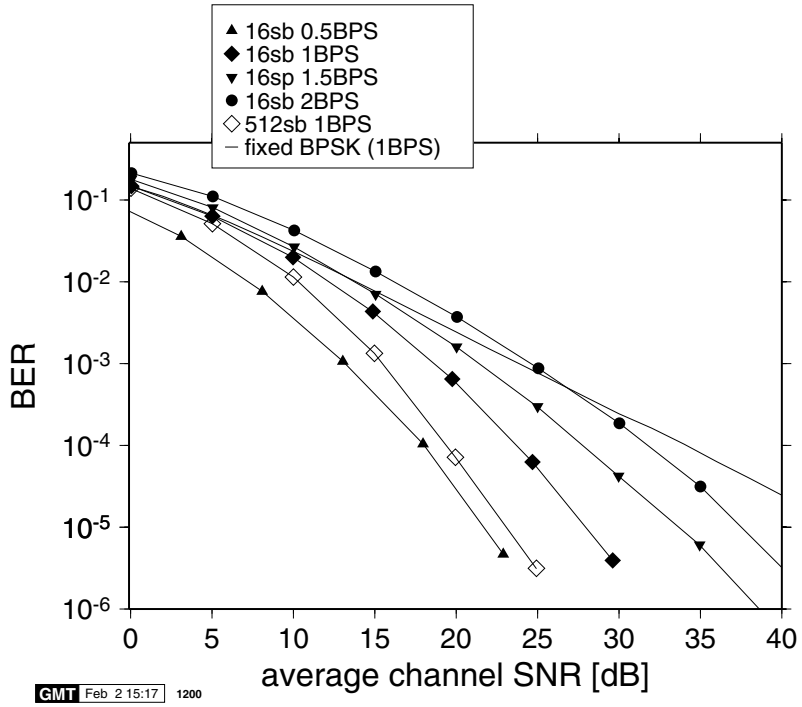


Figure 6.7: BER performance versus SNR for the 512 subcarrier, 16 sub-band constant throughput adaptive OFDM modem employing BPSK, QPSK, 16-QAM and "no transmission" in the Rayleigh fading time-dispersive channel of Figure 4.3 for 0.5, 1, 1.5 and 2 bits per symbol (BPS) target throughput

for "no transmission". A set of cost values $c_{n,s}$ is calculated for each sub-band n and state s:

$$c_{n,s} = \frac{e_{n,s+1} - e_{n,s}}{b_{n,s+1} - b_{n,s}} \tag{6.1}$$

for all but the highest modulation mode index s. This cost value is related to the expected increase in the number of bit errors, divided by the increase of throughput, if the modulation mode having the next higher index is used instead of index s in sub-band n. In other words, Equation 6.1 quantifies the expected incremental bit error rate of the state transition $s \rightarrow s+1$ in sub-band n.

The modulation mode adaptation is performed by repeatedly searching for the block n having the lowest value of c_{n,s_n}, and incrementing its state variable s_n. This is repeated until the total number of bits in the OFDM symbol reaches the target number of bits. Because of the granularity in bit numbers introduced by the sub-bands, the total number of bits may exceed the target. In this case, the data is padded with dummy bits for transmission.

Figure 6.7 gives an overview of the BER performance of the fixed throughput 512-subcarrier OFDM modem over the time dispersive channel of Figure 4.3 for a range of target bit numbers. In Figure 6.7 the curve without symbols represents the performance of a fixed

BPSK OFDM modem over the same channel and where the modem transmits, i.e. 1 bit over each data subcarrier per OFDM symbol. The diamond shapes give the performance of the equivalent throughput adaptive scheme for the 16 sub-band arrangement filled shapes and for the subcarrier-by-subcarrier adaptive scheme open shapes. It can be seen that the 16 sub-band adaptive scheme yields a significant improvement in BER terms for SNR values above 10 dB. The SNR gain for a bit error rate of 10^{-4} is 8 dB compared to the non-adaptive case. Subcarrier-by-subcarrier adaptivity increases this gain by a further 4 dB. The modem can readily be adapted to the system requirements by adjusting the target bit rate, as shown in Figure 6.7. Halving the throughput to 0.5 BPS, the required SNR is reduced by 6 dB for a BER of 10^{-4}, while increasing the throughput to 2 BPS deteriorates the noise resilience by 8 dB at the same BER.

6.2.6 AOFDM Mode Signalling and Blind Detection

The adaptive OFDM receiver has to be informed of the modulation modes used for the different sub-bands. This information can either be conveyed using signalling subcarriers in the OFDM symbol itself, or the receiver can employ blind detection techniques in order to estimate the transmitted symbols' modulation modes, as seen in Figure 6.1.

6.2.6.1 Signalling

The simplest way of signalling the modulation mode employed in a sub-band is to replace one data symbol by an M-PSK symbol, where M is the number of possible modulation modes. In this case, reception of each of the constellation points directly signals a particular modulation mode in the current sub-band. In our case, for four modulation modes and assuming perfect phase recovery, the probability of a signalling error $p_s(\gamma)$, when employing one signalling symbol, is the symbol error probability of QPSK. Then the correct sub-band mode signalling probability is:

$$(1 - p_s(\gamma)) = (1 - p_{b,QPSK}(\gamma))^2,$$

where $p_{b,QPSK}$ is the bit error probability for QPSK:

$$p_{b,QPSK}(\gamma) = Q(\sqrt{\gamma}) = \frac{1}{2} \cdot \text{erfc}\left(\sqrt{\frac{\gamma}{2}}\right),$$

which leads to the expression for the modulation mode signalling error probability of

$$p_s(\gamma) = 1 - \left(1 - \frac{1}{2} \cdot \text{erfc}\left(\sqrt{\frac{\gamma}{2}}\right)\right)^2.$$

The modem mode signalling error probability can be reduced by employing multiple signalling symbols and maximum ratio combining of the received signalling symbols $R_{s,n}$, in order to generate the decision variable R'_s prior to decision:

$$R'_s = \sum_{n=1}^{N_s} R_{s,n} \cdot \hat{H}^*_{s,n},$$

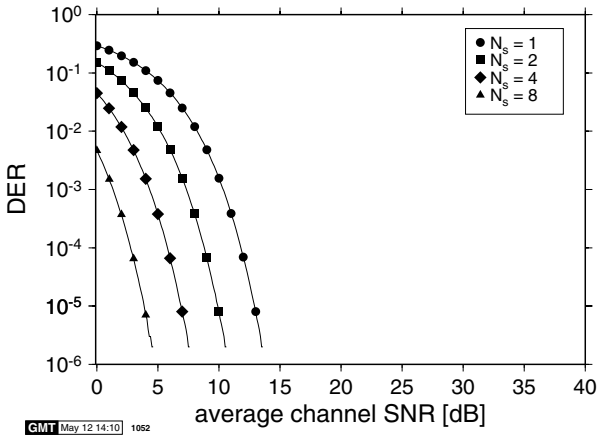


Figure 6.8: Modulation mode detection error ratio (DER) if signalling with maximum ratio combining is employed for QPSK symbols in an AWGN channel for 1, 2, 4 and 8 signalling symbols per sub-band, evaluated from Equation 6.2

where N_s is the number of signalling symbols per sub-band, the quantities $R_{s,n}$ are the received symbols in the signalling subcarriers, and $\hat{H}_{s,n}$ represents the estimated values of the frequency domain channel transfer function at the signalling subcarriers. Assuming perfect channel estimation and constant values of the channel transfer function across the group of signalling subcarriers, the signalling error probability for N_s signalling symbols can be expressed as:

$$p'_s(\gamma, N_s) = 1 - \left(1 - \frac{1}{2} \cdot \text{erfc}\left(\sqrt{\frac{N_s\gamma}{2}}\right)\right)^2 . \tag{6.2}$$

Figure 6.8 shows the signalling error rate in an AWGN channel for 1, 2, 4 and 8 signalling symbols per sub-band, respectively. It can be seen that doubling the number of signalling subcarriers improves the performance by 3 dB. Modem mode detection error ratios (DER) below 10^{-5} can be achieved at 10 dB SNR over AWGN channels if two signalling symbols are used. The signalling symbols for a given sub-band can be interleaved across the entire OFDM symbol bandwidth, in order to benefit from frequency diversity in fading wideband channels.

As seen in Figure 6.1, blind detection algorithms aim to estimate the employed modulation mode directly from the received data symbols, therefore avoiding the loss of data capacity due to signalling subcarriers. Two algorithms have been investigated, one based on geometrical SNR estimation and another incorporating error correction coding.

6.2.6.2 Blind Detection by SNR Estimation

The receiver has no *a priori* knowledge of the modulation mode employed in a particular received sub-band and estimates this parameter by quantising the defaded received data symbols $R_n/\hat{H}_n$ in the sub-band to the closest symbol $\hat{R}_{n,m}$ for all possible modulation modes M_m for each subcarrier index n in the current sub-band. The decision-directed error energy

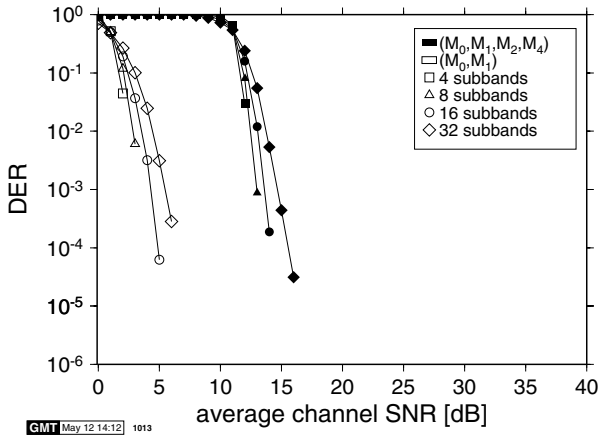


Figure 6.9: Blind modulation mode detection error ratio (DER) for 512-subcarrier OFDM systems employing (M_0, M_1) as well as for (M_0, M_1, M_2, M_4) for different numbers of sub-bands in an AWGN channel

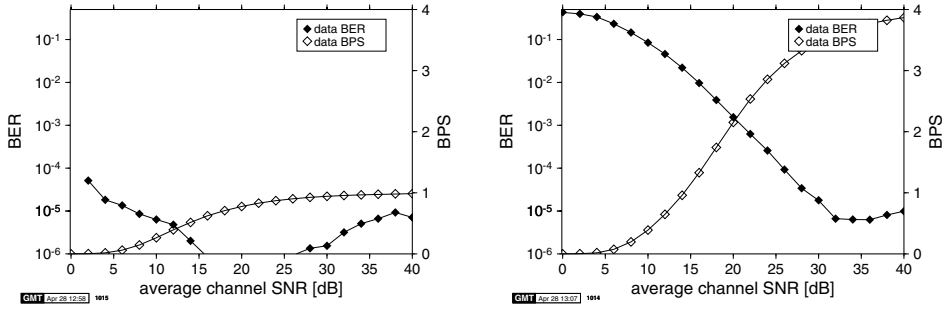
e_m for each modulation mode is calculated:

$$e_m = \sum_n \left(R_n / \hat{H}_n - \hat{R}_{n,m} \right)^2$$

and the modulation mode M_m which minimises e_m is chosen for the demodulation of the sub-band.

The DER of the blind modulation mode detection algorithm described in this section for a 512-subcarrier OFDM modem in an AWGN channel is depicted in Figure 6.9. It can be seen that the detection performance depends on the number of symbols per sub-band, with fewer sub-bands and therefore longer symbol sequences per sub-band leading to a better detection performance. It is apparent, however, that the number of available modulation modes has a more significant effect on the detection reliability than the block length. If all four legitimate modem modes are employed, then reliable detection of the modulation mode is only guaranteed for AWGN SNR values of more than 15-18 dB, depending on the number of sub-bands per OFDM symbol. If only M_0 and M_1 are employed, however, the estimation accuracy is dramatically improved. In this case, AWGN SNR values above 5-7 dB are sufficient to ensure reliable detection. The estimation accuracy could be improved by using the estimate of the channel quality, in order to predict the modulation mode, which is likely to have been employed at the transmitter. For example, at an estimated channel SNR of 5 dB it is unlikely that 16-QAM was employed as the modem mode and hence this *a priori* knowledge can be exploited, in order increase our confidence in the corresponding decision.

Figure 6.10 shows the BER performance of the fixed threshold "data" 16 sub-band adaptive system in the fading wideband channel of Figure 4.3 for both sets of modulation modes, namely for (M_0, M_1) and (M_0, M_1, M_2, M_4) with blind modulation mode detection. Erroneous modulation mode decisions were assumed to yield a BER of 50% in the received block. This is optimistic, since in a realistic scenario the receiver would have no knowl-



(a) (M_0, M_1) (b) (M_0, M_1, M_2, M_4)

Figure 6.10: BER and BPS throughput performance of a 16 sub-band, 512 subcarrier adaptive OFDM modem employing (a) no transmission (M_0) and BPSK (M_1), or (b) (M_0, M_1, M_2, M_4), both using the data-type switching levels of Table 6.1 and the SNR-based blind modulation mode detection of Section 6.2.6.2 over the Rayleigh fading time-dispersive channel of Figure 4.3

edge of the number of bits actually transmitted, leading to loss of synchronisation in the data stream. This problem is faced by all systems having a variable throughput and not employing an ideal reliable signalling channel. This problem must be mitigated by data synchronisation measures.

It can be seen from Figure 6.10 that while blind modulation mode detection yields poor performance for the quadruple-mode adaptive scheme, the twin-mode scheme exhibits BER results consistently better than 10^{-4}.

6.2.6.3 Blind Detection by Multi-Mode Trellis Decoder

If error correction coding is invoked in the system, then the channel decoder can be employed to estimate the most likely modulation mode per sub-band. Since the number of bits per OFDM symbol is varied in this adaptive scheme, and the channel encoder's block length is therefore not constant, for the sake of implementational convenience we have chosen a convolutional encoder at the transmitter. Once the modulation modes to be used are decided upon at the transmitter, the convolutional encoder is employed to generate a zero-terminated code word having the length of the OFDM symbol's capacity. This code word is modulated on the subcarriers according to the different modulation modes for the different sub-bands, and the OFDM symbol is transmitted over the channel.

At the receiver, each received data subcarrier is demodulated by all possible demodulators, and the resulting hard decision bits are fed into parallel trellises for Viterbi decoding. Figure 6.11 shows a schematic sketch of the resulting parallel trellis if 16-QAM (M_4), QPSK (M_2), BPSK (M_1), and "no transmission" (M_0) are employed, for a convolutional code having four states. Each sub-band in the adaptive scheme corresponds to a set of four parallel trellises, whose inputs are generated independently by the four demodulators of the legitimate modulation modes. The number of transitions in each of the trellises depends on the number of output bits received from the different demodulators, so that the 16-QAM (M_4)

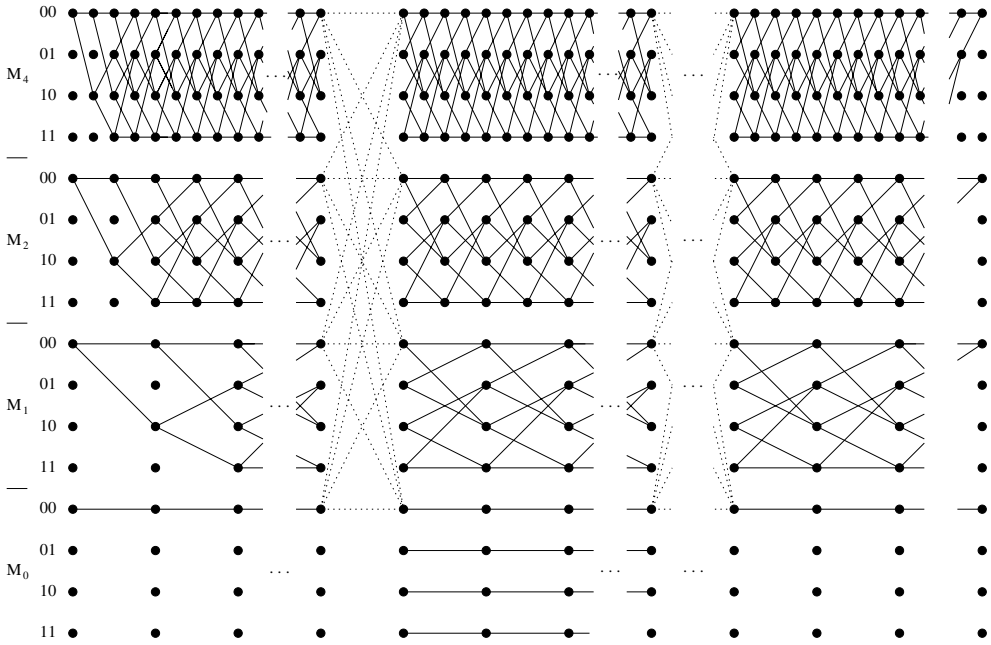


Figure 6.11: Schematic plot of the parallel trellises for blind modulation mode detection employing convolutional coding. In this example, a four-state 00-terminated convolutional encoder was assumed. The dotted lines indicate the intersub-band transitions for the 00 state, and are omitted for the other three states

trellis contains four times as many transitions as the BPSK and "no transmission" trellises. Since in the case of "no transmission" no coded bits are transmitted, the state of the encoder does not change. Therefore, legitimate transitions for this case are only horizontal ones.

At sub-band boundaries, transitions are allowed between the same state of all the parallel trellises associated with the different modulation modes. This is not a transition due to a received bit, and therefore preserves the metric of the originating state. Note that in the figure only the possible allowed transitions for the state 00 are drawn; all other states originate the equivalent set of transitions. The initial state of the first sub-band is 00 for all modulation modes, and since the code is terminated in 00, the last sub-band's final states are 00.

The receiver's Viterbi decoder calculates the metrics for the transitions in the parallel trellises, and once all the data symbols have been processed, it traces back through the parallel trellis on the surviving path. This backtracing commences at the most likely 00 state at the end of the last sub-band. If no termination was used at the decoder, then the backtracing would start at the most likely of all the final states of the last block.

Figure 6.12 shows the modulation mode detection error ratio (DER) for the parallel trellis decoder in an AWGN channel for 16 and 8 sub-bands, if a convolutional code of constraint length 7 is used. Comparison with Figure 6.9 shows considerable improvements relative to the BER estimation-based blind detection scheme of Section 6.2.6.2, both for 16 and 8 sub-bands. Higher sub-band lengths improve the estimation accuracy by a greater degree than

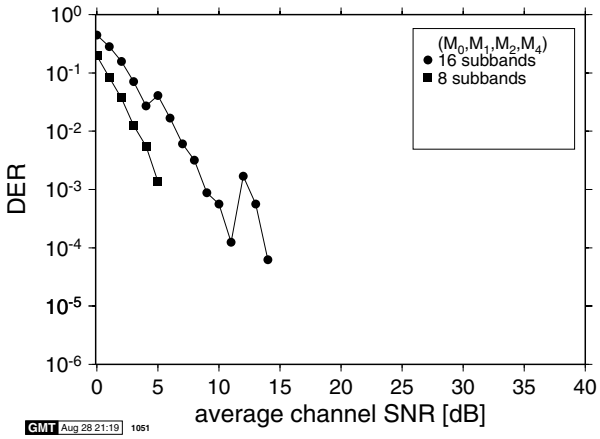


Figure 6.12: Blind modulation mode detection error ratio (DER) using the parallel trellis algorithm of Section 6.2.6.3 with a $K = 7$ convolutional code in an AWGN channel for a 512-subcarrier OFDM modem

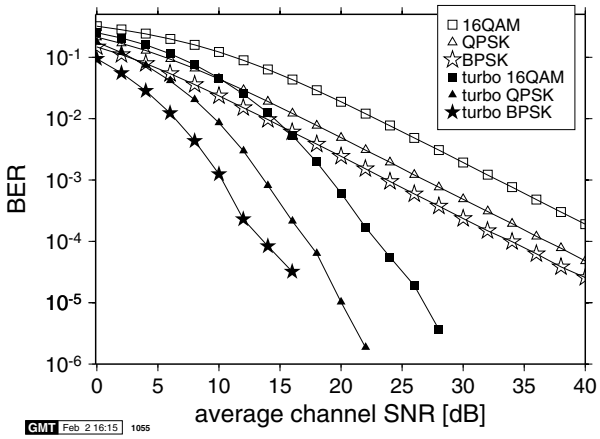


Figure 6.13: BER performance of the 512-subcarrier OFDM modem in the fading time-dispersive channel of Figure 4.3 for both uncoded and half-rate turbo-coded transmission, using 8-iteration log-MAP turbo decoding, 1000-bit random interleaver, and a constraint length of 3

has been observed for the BER estimation algorithm of Figure 6.9. A DER of less than 10^{-5} was observed for AWGN SNR values of 6 dB and 15 dB in the 8 and 16 sub-band scenarios, respectively. The use of stronger codes could further improve the estimation accuracy, at the cost of higher complexity.

6.2.7 Sub-Band Adaptive OFDM and Turbo Channel Coding

Adaptive modulation can reduce the BER to a level where channel decoders can perform well. Figure 6.13 shows both the uncoded and coded BER performance of a 512-subcarrier OFDM modem in the fading wideband channel of Figure 4.3, assuming perfect channel estimation. The channel coding employed in this set of experiments was a turbo coder [223] with a data block length of 1000 bits, employing a random interleaver and 8 decoder iterations. The log-MAP decoding algorithm was used [224]. The constituent half-rate convolutional encoders were of constraint length 3, with octally represented generator polynomials of $(7, 5)$ [177]. It can be seen that the turbo decoder provides a considerable coding gain for the different fixed modulation schemes, with a BER of 10^{-4} for SNR values of 13.8 dB, 17.3 dB and 23.2 dB for BPSK, QPSK and 16-QAM transmission, respectively.

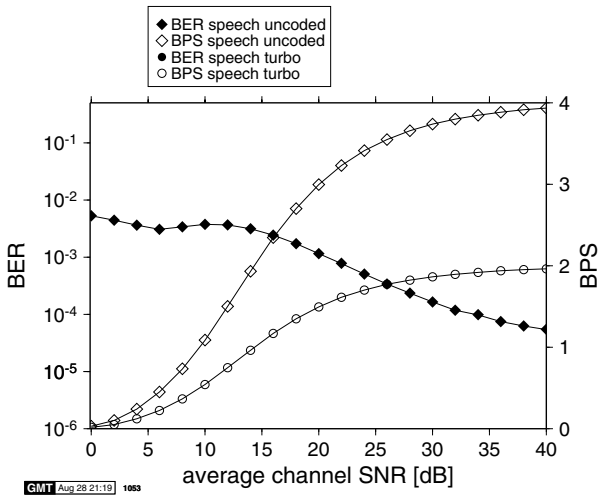
Figure 6.14 depicts the BER and throughput performance of the same decoder employed in conjunction with the adaptive OFDM modem for different adaptation algorithms. Figure 6.14(a) shows the performance for the "speech" system employing the switching levels listed in Table 6.1. As expected, the half-rate channel coding results in a halved throughput compared to the uncoded case, but offers low BER transmission over the channel of Figure 4.3 for SNR values of down to 0 dB, maintaining a BER below 10^{-6}.

Further tuning of the adaptation parameters can ensure a better average throughput, while retaining error-free data transmission. The switching level-based adaptation algorithm of Table 6.1 is difficult to control for arbitrary bit error rates, since the set of switching levels was determined by an optimisation process for uncoded transmission. Since the turbo codec has a non-linear BER versus SNR characteristic, direct switching level optimisation is an arduous task. The sub-band BER predictor of Section 6.2.4.2 is easier to adapt to a channel codec, and Figure 6.14(b) shows the performance for the same decoder, with the adaptation algorithm employing the BER prediction method having an upper BER bound of 1%. It can be seen that the less stringent uncoded BER constraints when compared to Figure 6.14(a) lead to a significantly higher throughput for low SNR values. The turbo-decoded data bits are error-free, hence a further increase in throughput is possible while maintaining a high degree of coded data integrity.

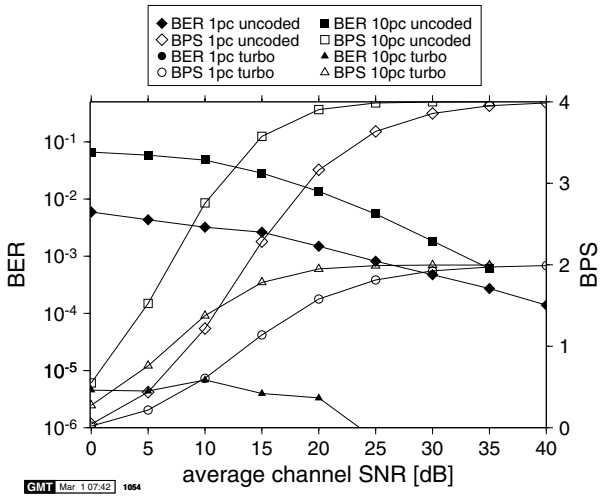
The second set of curves in Figure 6.14(b) show the system's performance, if an uncoded target BER of 10% is assumed. In this case, the turbo decoder's output BER is below 10^{-5} for all the SNR values plotted, and shows a slow decrease for increasing values of SNR. The throughput of the system, however, exceeds 0.5 data bits per symbol for SNR values of more than 2 dB.

6.2.8 Effects of the Doppler Frequency

Since the adaptive OFDM modem employs the most recently received OFDM symbol in order to predict the frequency domain transfer function of the reverse channel for the next transmission, the quality of this prediction suffers from the time variance of the channel transfer function between the uplink and downlink time slots. We assume that the time delay between the uplink and downlink slots is the same as the delay between the downlink and uplink slots, and we refer to this time as the frame duration T_f. We normalise the maximal Doppler frequency f_d of the channel to the frame duration T_f, and define the frame normalised Doppler frequency F'_d as $F'_d = f_d \cdot T_f$. Figure 6.15 depicts the fixed switching level (see Table 6.1)

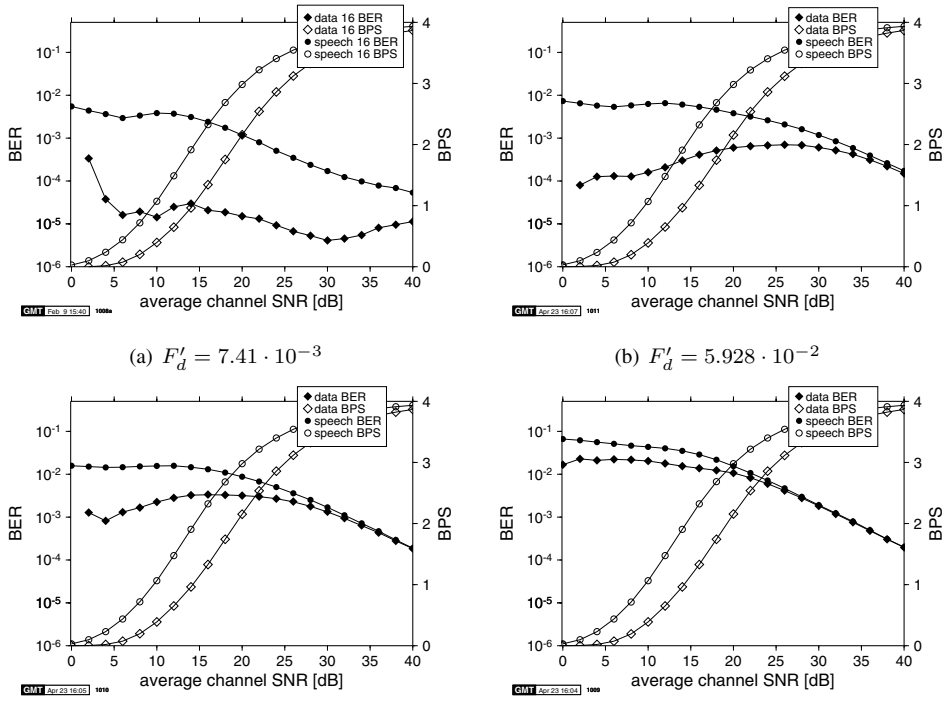


(a) speech system



(b) maximal BER 1% and 10%

Figure 6.14: BER and BPS throughput performance of 16 sub-band, 512 subcarrier adaptive turbo coded and uncoded OFDM modem employing (M_0, M_1, M_2, M_4) for (a) speech-type switching levels of Table 6.1 and (b) a maximal estimated sub-band BER of 1% and 10% over the channel of Figure 4.3. The turbo-coded transmission over the speech system and the 1% maximal BER system are error-free for all examined SNR values and therefore the corresponding BER curves are omitted from the graphs, hence the lack of black circles on (a) and (b)



(a) $F'_d = 7.41 \cdot 10^{-3}$

(b) $F'_d = 5.928 \cdot 10^{-2}$

(c) $F'_d = 1.1856 \cdot 10^{-1}$

(d) $F'_d = 2.3712 \cdot 10^{-1}$

Figure 6.15: BER and BPS throughput performance of 16 sub-band, 512 subcarrier adaptive OFDM modem employing (M_0, M_1, M_2, M_4) for both data-type and speech-type switching levels with perfect modulation mode detection and different frame normalised Doppler frequencies F'_d over the channel of Figure 4.3. The triangular markers in (a) show the performance of a subcarrier-by-subcarrier adaptive modem using the data-type switching levels of Table 6.1 for comparison

modem's BER and throughput performance in bits per symbol (BPS) for values of F'_d between $7.41 \cdot 10^{-3}$ and $2.3712 \cdot 10^{-1}$. These values stem from the studied WATM system with a time slot duration of 2.67 μs and up/downlink delays of 1, 8, 16 and 32 time slots at a channel Doppler frequency of 2.78 kHz. As mentioned in Section 4.1.1.1, this corresponds to a system employing a carrier frequency of 60 GHz, a sampling rate of 225 Msamples/s and a vehicular velocity of 50 km/h or $13.\overline{8}$ m/s.

Figure 6.15(a) shows the BER and BPS throughput of the studied modems in a framework with consecutive uplink and downlink time slots. This corresponds to $F'_d = 7.41 \cdot 10^{-3}$, while the target bit error rates for the speech and data system are met for all SNR values above 4 dB, and the BER performance is generally better than the target error rates. This was explained above with the conservative choice of modulation modes based on the most corrupted subcarrier in each sub-band, resulting in lower throughput and lower bit error rates for the switching level based sub-band adaptive modem.

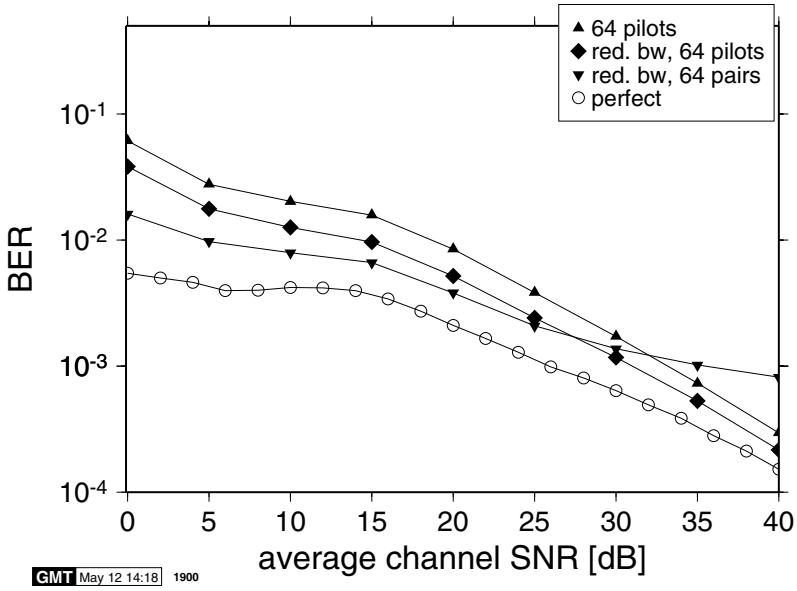


Figure 6.16: BER versus channel SNR performance for the 1% target BER adaptive 16 sub-band, 512 subcarrier OFDM modem employing pilot symbol assisted channel transfer function estimation over the channel of Figure 4.3

Comparing Figure 6.15(a) with the other performance curves, it can be seen that the bit error rate performance for both the speech and the data system suffer from increasing decorrelation of the predicted and actual channel transfer function for increasing values of F'_d. In Figure 6.15(b) an 8 time slot delay was assumed between uplink and downlink time slots, which corresponds to $F'_d = 5.928 \cdot 10^{-2}$, and therefore the BER performance of the modem was significantly deteriorated. The "speech" system still maintains its target BER, but the "data" system delivers a BER of up to 10^{-3} for SNR values between 25 and 30 dB. It is interesting to observe that the delayed channel prediction mainly affects the higher-order modulation modes, which are employed more frequently at high SNR values. This explains the shape of the BER curve for the "data" system, which is rising from below 10^{-4} at 2 dB SNR up to 10^{-3} at 26 dB SNR. The average throughput of the modem is mainly determined by the statistics of the estimated channel transfer function at the receiver, and this is therefore not affected by the delay between the channel estimation and the packet transmission.

6.2.9 Channel Transfer Function Estimation

All the adaptive modems above rely on the estimate of the frequency domain channel transfer function, both for equalisation of the received symbols at the receiver, as well as for the modem mode adaptation of the next transmitted OFDM symbol. Figure 6.16 shows the BER versus SNR curves for the 1% target BER modem, as presented above, if pilot symbol-assisted channel estimation [181] is employed instead of the previously used delayed, but otherwise perfect, channel estimation.

Comparing the curves for perfect channel estimation and for the 64-pilot lowpass interpolation algorithm, it can be seen that the modem falls short of the target bit error rate of 1% for channel SNR values of up to 20 dB. More noise resilient channel estimation algorithms can improve the modem's performance. If the passband width of the interpolation lowpass filter (see Section 4.3.1.1) is halved, which is indicated in Figure 6.16 as the reduced bandwidth (red. bw.) scenario, then the BER gap between the perfect and the pilot symbol assisted channel estimation narrows, and a BER of 1% is achieved at a SNR of 15 dB. Additionally, employing pairs of pilots with the above bandwidth-limited interpolation scheme further improves the modem's performance, which results in BER values below 1% for SNR values above 5 dB. The averaging of the pilot pairs improves the noise resilience of the channel estimation, but introduces estimation errors for high SNR values. This can be observed in the residual BER in the figure.

Having studied a range of different AOFDM modems, let us now embark on a system design study in the context of an adaptive interactive speech system.

6.3 Adaptive OFDM Speech System[1]

6.3.1 Introduction

In this section we introduce a bidirectional high-quality audio communications system, which will be used to highlight the systems aspects of adaptive OFDM transmissions over time-dispersive channels. Specifically, the channel-coded adaptive transmission characteristics and a potential application for joint adaptation of modulation, channel coding and source coding are studied.

The basic principle of adaptive modulation is to react to the anticipated channel capacity for the next OFDM symbol transmission burst, by employing modulation modes of different robustness to channel impairments and of different data throughput. The trade-off between data throughput and integrity can be adapted to different system environments. For data transmission systems, which are not dependent on a fixed data rate and do not require low transmission delays, variable-throughput adaptive schemes can be devised that operate efficiently with powerful error correction coders, such as long block length turbo codes [226]. Real-time audio or video communications employing source codecs, which allow variable bit rates, can also be used in conjunction with variable-rate adaptive schemes, but in this case block-based error correction coders cannot be readily employed.

Fixed-rate adaptive OFDM systems, which sacrifice a guaranteed BER performance for the sake of a fixed data throughput, are more readily integrated into interactive communications systems, and can coexist with long block-based channel coders in real-time applications.

For these investigations, we propose a hybrid adaptive OFDM scheme, based on a multi-mode constant throughput algorithm, consisting of two adaptation loops: an inner constant throughput algorithm, having a bit rate consistent with the source and channel coders, and an outer mode switching control loop, which selects the target bit rate of the whole system from a set of distinct operating modes. These issues will become more explicit during our further discourse.

[1] T. Keller, M. Münster, L. Hanzo: "A Turbo-coded Burst-by-burst Adaptive Wideband Speech Transceiver", ©IEEE JSAC, 2000, November 2000, Vol. 18, No. 11, pp. 2363-2372 [225]. Details concerning the source codec and its performance are discussed in the above publication and in [6].

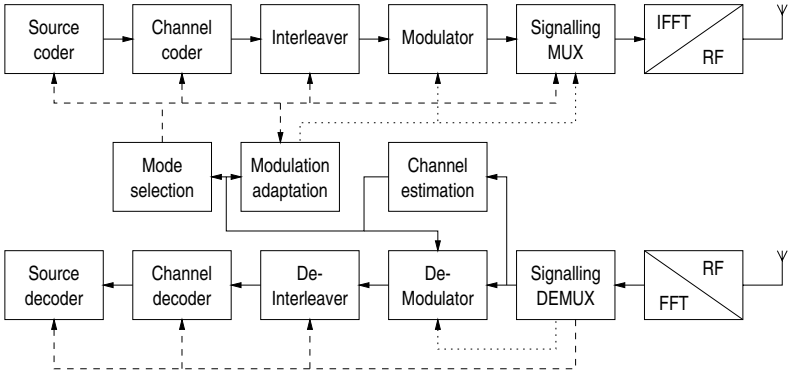


Figure 6.17: Schematic model of the multimode adaptive OFDM system

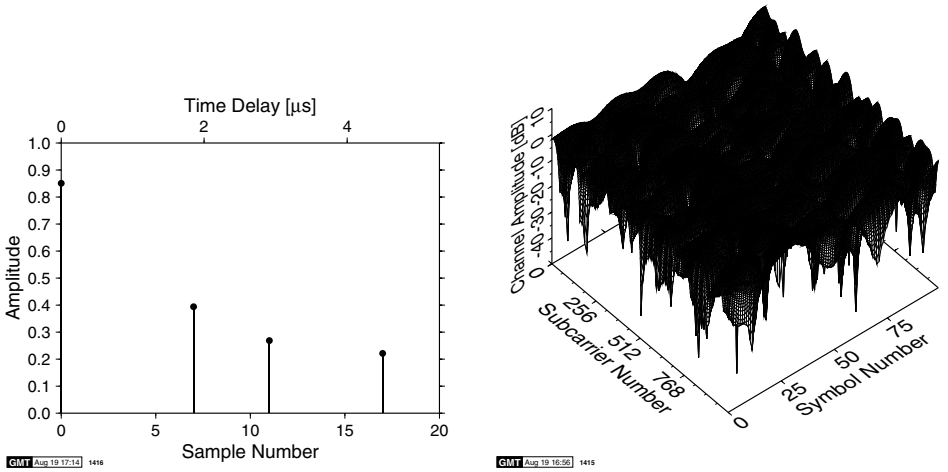
6.3.2 System Overview

The structure of the studied adaptive OFDM modem is depicted schematically in Figure 6.17. The top half of the diagram is the transmitter chain, which consists of the source and channel coders, a channel interleaver decorrelating the channel's frequency domain fading, an adaptive OFDM modulator, a multiplexer adding signalling information to the transmit data, and an IFFT/RF OFDM block. The receiver seen at the bottom of the figure consists of a RF/FFT OFDM receiver, a demultiplexer extracting the signalling information, an adaptive demodulator, a de-interleaver/channel decoder and the source decoder. The parameter adaptation linking the receiver and transmitter chain consists of a channel estimator, and the throughput mode selection as well as the modulation adaptation blocks.

The open-loop control structure of the adaptation algorithms can be seen in the figure: the receiver's operation is controlled by the signalling information that is contained in the received OFDM symbol, while the channel quality information generated by the receiver is employed to determine the remote transmitter's matching parameter set by the modulation adaptation algorithms. The two distinct adaptation loops distinguished by the dotted and dashed lines are the inner and outer adaptation loops, respectively. The outer adaptation loop controls the overall throughput of the system, which is chosen from a finite set of predefined modes, so that a fixed delay decoding of the received OFDM data packets becomes possible. This outer loop controls the block length of the channel encoder and interleaver, and the target throughput of the inner adaptation loop. The operation of the adaptive modulator, controlled by the inner loop, is transparent to the rest of the system. The operation of the adaptation loops is described in more detail below.

6.3.2.1 System Parameters

The transmission parameters have been adopted from the TDD mode of the UMTS system of Section 4.1.3, with a carrier frequency of 1.9 GHz, a time frame and time slot duration of 4.615 ms and 122 μs, respectively. The sampling rate is assumed to be 3.78 MHz, leading to a 1024-subcarrier OFDM symbol with a cyclic extension of 64 samples in each time slot.



(a) unfaded impulse response

(b) time varying amplitude

Figure 6.18: Channel for PictureTel experiments: (a) unfaded channel impulse response (b) time-varying channel amplitude for 100 OFDM symbols

For spectral shaping of the OFDM signal, there are a total of 206 virtual subcarriers at the bandwidth boundaries.

The 7 kHz bandwidth PictureTel audio codec [6][2] has been chosen for this system because of its good audio quality, robustness to packet dropping and adjustable bit rate. The channel encoder/interleaver combination is constituted by a convolutional turbo codec [223] employing block turbo interleavers in conjunction with a subsequent pseudorandom channel interleaver. The constituent half-rate recursive systematic convolutional (RSC) encoders are of constraint length 3, with octal generator polynomials of $(7, 5)$ [177]. At the decoder, 8 iterations are performed, utilising the so-called maximum *a posteriori* (MAP) [224] algorithm and log-likelihood ratio soft inputs from the demodulator.

The channel model consists of a four-path COST 207 typical urban impulse response [191], where each impulse is subjected to independent Rayleigh fading with a normalised Doppler frequency of $2.25 \cdot 10^{-6}$, corresponding to a pedestrian scenario with a walking speed of 3 mph.

The unfaded impulse response and the time- and frequency-varying amplitude of the channel transfer function are depicted in Figure 6.18.

6.3.3 Constant Throughput Adaptive Modulation

The constant throughput adaptive algorithm attempts to allocate a given number of bits for transmission in subcarriers exhibiting a low BER, while the use of high BER subcarriers is minimised. We employ the open-loop adaptive regime of Figure 6.1, basing the decision concerning the next transmitted OFDM symbol's modulation scheme allocation on the channel estimation gained at the reception of the most recently received OFDM symbol by the local

[2] See http://www.picturetel.com

station. Sub-band adaptive modulation [227] – where the modulation scheme is adapted not on a subcarrier-by-subcarrier basis, but for sub-bands of adjacent subcarriers – is employed in order to simplify the signalling requirements. The adaptation algorithm was highlighted in Section 6.2.5. For these investigations we employed 32 sub-bands of 32 subcarriers in each OFDM symbol. Perfect channel estimation and signalling were used.

6.3.3.1 Constant-Rate BER Performance

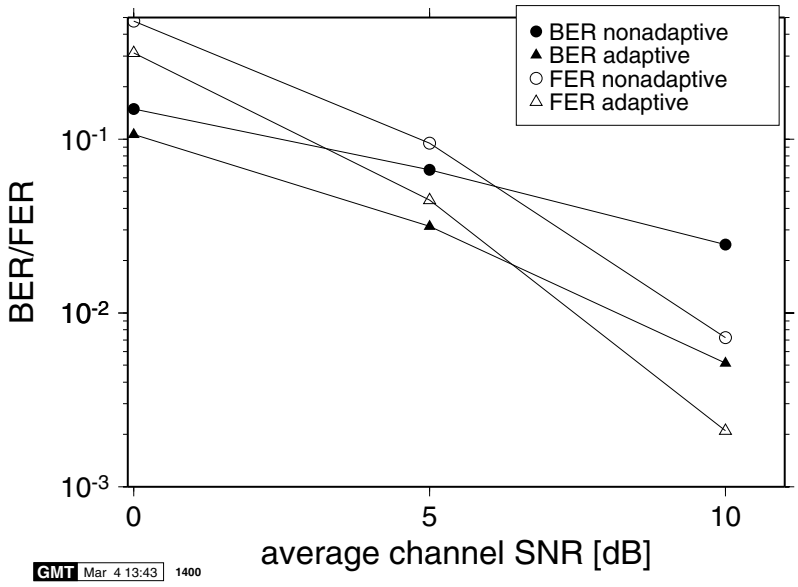
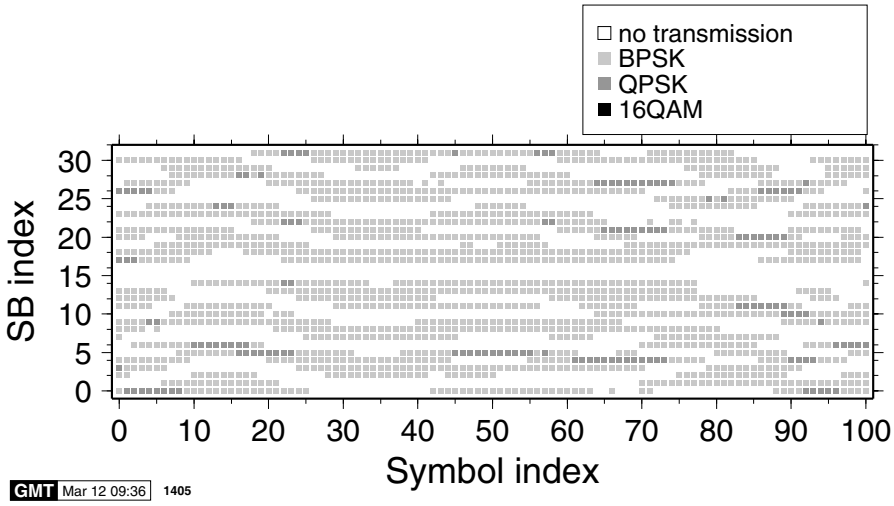


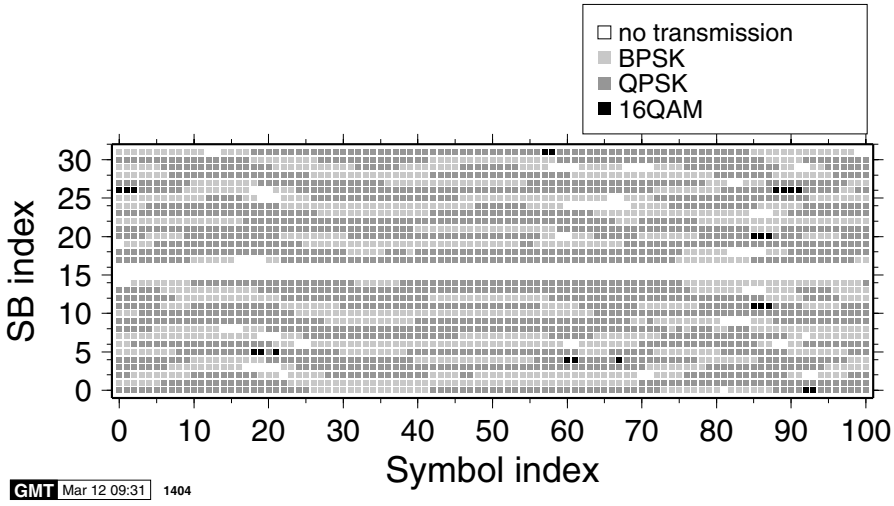
Figure 6.19: BER and FER performance for the fixed-throughput adaptive and non-adaptive OFDM modems in the fading time-dispersive channel of Section 4.1.3 for a block length of 578 coded bits

Figure 6.19 characterises the fixed-throughput adaptive modulation scheme's performance under the channel conditions characterised above, for a block length of 578 coded bits. As a comparison, the BER curve of a fixed BPSK modem transmitting the same number of bits in the same channel, employing 578 out of 1024 subcarriers, is also depicted. The number of useful audio bits per OFDM symbol was based on a 200-bit target data throughput, which corresponds to a 10 kbps data rate, padded with 89 bits, which can contain a checksum for error detection and high-level signalling information. Furthermore, half-rate channel coding was used.

The BER plotted in the figure is the hard decision-based bit error rate at the receiver before channel decoding. It can be seen that the adaptive modulation scheme yields a significantly improved performance, which is also reflected in the frame error rate (FER). This FER approximates the probability of a decoded block containing errors, in which case it is unusable for the audio source decoder and hence it is dropped. This error event can be detected by using the checksum in the OFDM data symbol.



(a) 578 data bits per OFDM symbol



(b) 1458 data bits per OFDM symbol

Figure 6.20: Overview of modulation mode allocation for fixed-throughput adaptive modems over the fading time-dispersive channel of Figure 6.18(b) at 5 dB average channel SNR

As an example, the modulation mode allocation for the 578 data bit adaptive modem at an average channel SNR of 5 dB is given in Figure 6.20(a) for 100 consecutive OFDM symbols. The unused sub-bands with indexes 15 and 16 contain the virtual carriers, and therefore do not transmit any data. It can be seen that the constant throughput adaptation algorithm of Section 6.2.5 allocates data to the higher quality subcarriers on a symbol-by-symbol basis, while keeping the total number of bits per OFDM symbol constant. As a comparison, Figure 6.20(b) shows the equivalent overview of the modulation modes employed for a fixed bit rate of 1458 bits per OFDM symbol. It can be seen that in order to meet this increased throughput target, hardly any sub-bands are in "no transmission" mode, and overall higher-order modulation schemes have to be employed.

6.3.4 Multimode Adaptation

While the fixed-throughput adaptive algorithm described above copes with the frequency domain fading of the channel, there is a medium-term variation of the overall channel capacity due to time domain channel quality fluctuations as indicated in Figure 6.18(b). While it is not straightforward to employ powerful block-based channel coding schemes, such as turbo coding, in variable-throughput adaptive OFDM schemes for real-time applications like voice or video telephony, a multimode adaptive system can be designed that allows us to switch between a set of different source and channel codecs as well as transmission parameters, depending on the overall channel quality. We have investigated the use of the estimated overall BER at the output of the receiver, which is the sum of all the $e(j, s_j)$ quantities of Equation 6.1 after adaptation. On the basis of this expected bit error rate at the input of the channel decoder, the probability of a frame error (FER) must be estimated and compared with the estimated FER of the other modem modes. Then the mode having the highest throughput exhibiting an estimated FER of less than 10^{-6} – or alternatively the mode exhibiting the lowest FER – is selected and the source encoder, the channel encoder and the adaptive modem are set up accordingly.

We have defined four different operating modes, which correspond to unprotected audio data rates of 10, 16, 24, and 32 kbps at the source codec's interface. With half-rate channel coding and allowing for checksum and signalling overhead, the number of transmitted coded bits per OFDM symbol was 578, 722, 1058 and 1458 for the four modes, respectively.

6.3.4.1 Mode Switching

Figure 6.21 shows the *observed* FER for all four modes versus the unprotected BER that was *predicted* at the transmitter. The predicted unprotected BER was discretised into intervals of 1%, and the channel-coded FER was evaluated over these BER intervals. It can be seen from the figure that for estimated protected BER values below 5% no frame errors were observed for any of the modes. For higher estimated unprotected BER values, the higher throughput modes exhibited a lower FER than the lower throughput modes, which was consistent with the turbo coder's performance increase for longer block lengths. A FER of 1% was observed for a 7% predicted unprotected error rate for the 10 kbps mode, and BER values of 8% to 9% were allowed for the longer blocks, while maintaining a FER of less than 1%

For this experiment, we assumed the best-case scenario of using the actual measured FER statistics of Figure 6.21 for the mode switching algorithm rather than estimating the FER on

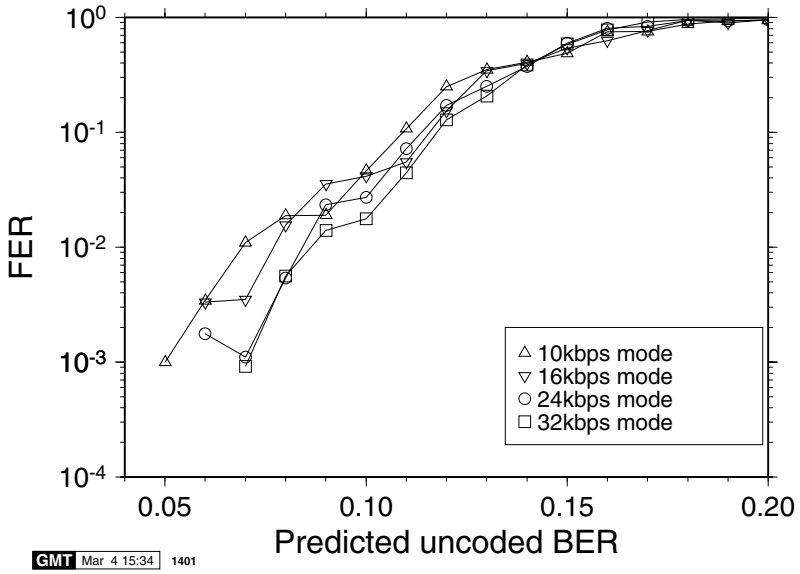


Figure 6.21: Frame error rate versus the predicted unprotected BER for 10 kbps, 16 kbps, 24 kbps and 32 kbps modes

the basis of the estimated uncoded BER. In this case, the previously observed FER corresponding to the predicted overall BER values for the different modes were compared, and the mode having the lowest FER was chosen for transmission. The mode switching sequence for the first 500 OFDM symbols at 5 dB channel SNR over the channel of Figure 6.18(b) is depicted in Figure 6.22. It can be seen that in this segment of the sequence 32 kbps transmission is the most frequently employed mode, followed by the 10 kbps mode. The intermediate modes are mostly transitory, as the improving or deteriorating channel conditions make it necessary to switch between the 10 kbps and 32 kbps modes. This behaviour is consistent with Table 6.2, for the Switch-I scheme.

6.3.5 Simulation Results

The comparison between the different adaptive schemes will be based on a channel SNR of 5 dB over the channel of Figure 6.18(b), since the audio codec's performance is unacceptable for SNR values around 0 dB, and as the adaptive modulation is most effective for channel SNR values below 10 dB.

6.3.5.1 Frame Error Results

The audio experiments [225] have shown that the audio quality is acceptable for frame dropping rates of about 5%, and that the perceived audio quality increases with increasing throughput. Table 6.2 gives an overview of the frame error rates and mode switching statistics of the system for a channel SNR of 5 dB over the channel of Figure 6.18(b). It can be seen that for the fixed modes the FER increases with the throughput, from 4.45% in the 10 kbps mode

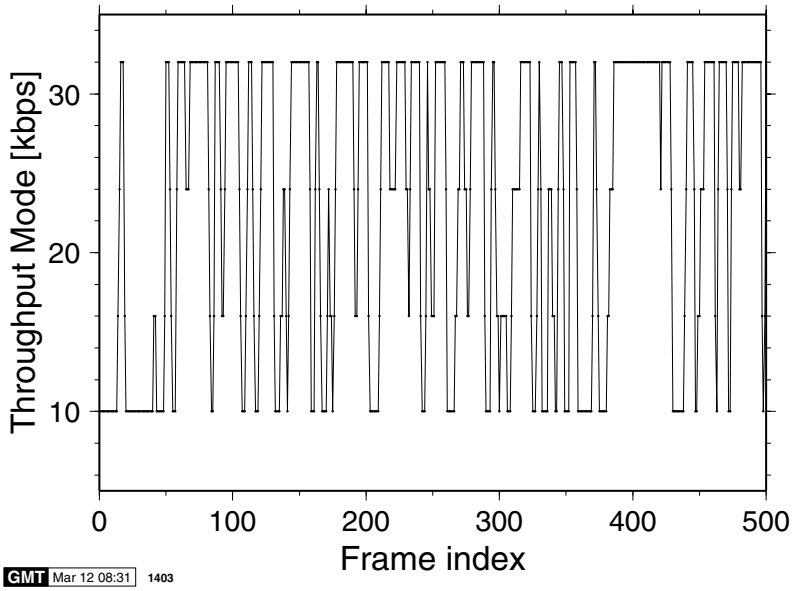


Figure 6.22: Mode switching pattern at 5 dB channel SNR over the channel of Figure 6.18(b)

Scheme	FER [%]	Rate-10kbps [%]	Rate-16kbps [%]	Rate-24kbps [%]	Rate-32kbps [%]
Fixed-10kbps	4.45	95.55	0.0	0.0	0.0
Fixed-16kbps	5.58	0.0	94.42	0.0	0.0
Fixed-24kbps	10.28	0.0	0.0	89.72	0.0
Fixed-32kbps	18.65	0.0	0.0	0.0	81.35
Switch-I	4.44	21.87	13.90	11.59	48.20
Switch-II	5.58	0.0	34.63	11.59	48.20

Table 6.2: FER and relative usage of different bit rates in the fixed bit rate schemes and the variable schemes Switch-I and Switch-II (successfully transmitted frames) for a channel SNR of 5 dB over the channel of Figure 6.18(b)

up to 18.65% for the 32 kbps mode. This is because the turbo codec performance improves for longer interleavers, the OFDM symbol had to be loaded with more bits, hence there was a higher unprotected BER. The time-variant bit rate mode-switching schemes, referred to as Switch-I and Switch-II for the four- and three-mode switching regimes used, deliver frame dropping rates of 4.44% and 5.58%, respectively. Both these FER values are acceptable for the audio transmission. It can be seen that upon incorporating the 10 kbps mode in the switching regime Switch-I of Table 6.2, the overall FER is lowered only by an insignificant amount, while the associated average throughput is reduced considerably.

6.3.5.2 Audio Segmental SNR

Figure 6.23 displays the cumulative density function (CDF) of the segmental SNR (SEGSNR) [177] obtained from the reconstructed signal of an audio test sound for all the modes of Table 6.2 discussed above at a channel SNR of 5 dB over the channel of Figure 6.18(b).

Focusing our attention on the figure, we can draw a whole range of interesting conclusions. As expected, for any given SEGSNR it is desirable to maintain as low a proportion as possible of the audio frames' SEGSNRs below a given abscissa value. Hence we conclude that the best SEGSNR CDF was attributable to the Switch-II scheme, while the worst performance was observed for the fixed 10 kbps scheme. Above a SEGSNR of 15 dB the CDFs of the fixed 16, 24 and 32 kbps modes follow our expectations. Viewing matters from a different perspective, the Switch-II scheme exhibits a SEGSNR of less than 20 dB with a probability of 0.8, compared to 0.95 for the fixed 10 kbps scheme.

Before concluding we also note that the CDFs do not have a smoothly tapered tail, since for the erroneous audio frames a SEGSNR of 0 dB was registered. This results in the step-function-like behaviour associated with the discontinuities corresponding to the FER values in the FER column of Table 6.2.

6.4 Pre-equalisation

We have seen above how the receiver's estimate of the channel transfer function can be used by the transmitter in order to dramatically improve the performance of an OFDM system by adapting the subcarrier modulation modes to the channel conditions. For sub-channels exhibiting a low signal-to-noise ratio, robust modulation modes were used, while for subcarriers having a high SNR, high throughput multi-level modulation modes can be used. An alternative approach to combating the frequency selective channel behaviour is to apply pre-equalisation to the OFDM symbol prior to transmission on the basis of the anticipated channel transfer function. The optimum scheme for the power allocation to the subcarriers is Shannon's water-pouring solution [228]. We will investigate a range of related topics in this section.

6.4.1 Motivation

As discussed above, the received data symbol R_n of subcarrier n over a stationary time-dispersive channel can be characterised by:

$$R_n = S_n \cdot H_n + n_n,$$

where S_n is the transmitted data symbol, H_n is the channel transfer function of subcarrier n, and n_n is a noise sample.

The frequency domain equalisation at the receiver, which is necessary for non-differential detection of the data symbols, corrects the phase and amplitude of the received data symbols using the estimate of the channel transfer function $\hat{H}_n$ as follows:

$$R'_n = R_n/\hat{H}_n = S_n \cdot H_n/\hat{H}_n + n_n/\hat{H}_n.$$

If the estimate $\hat{H}_n$ is accurate, this operation defades the constellation points before decision.

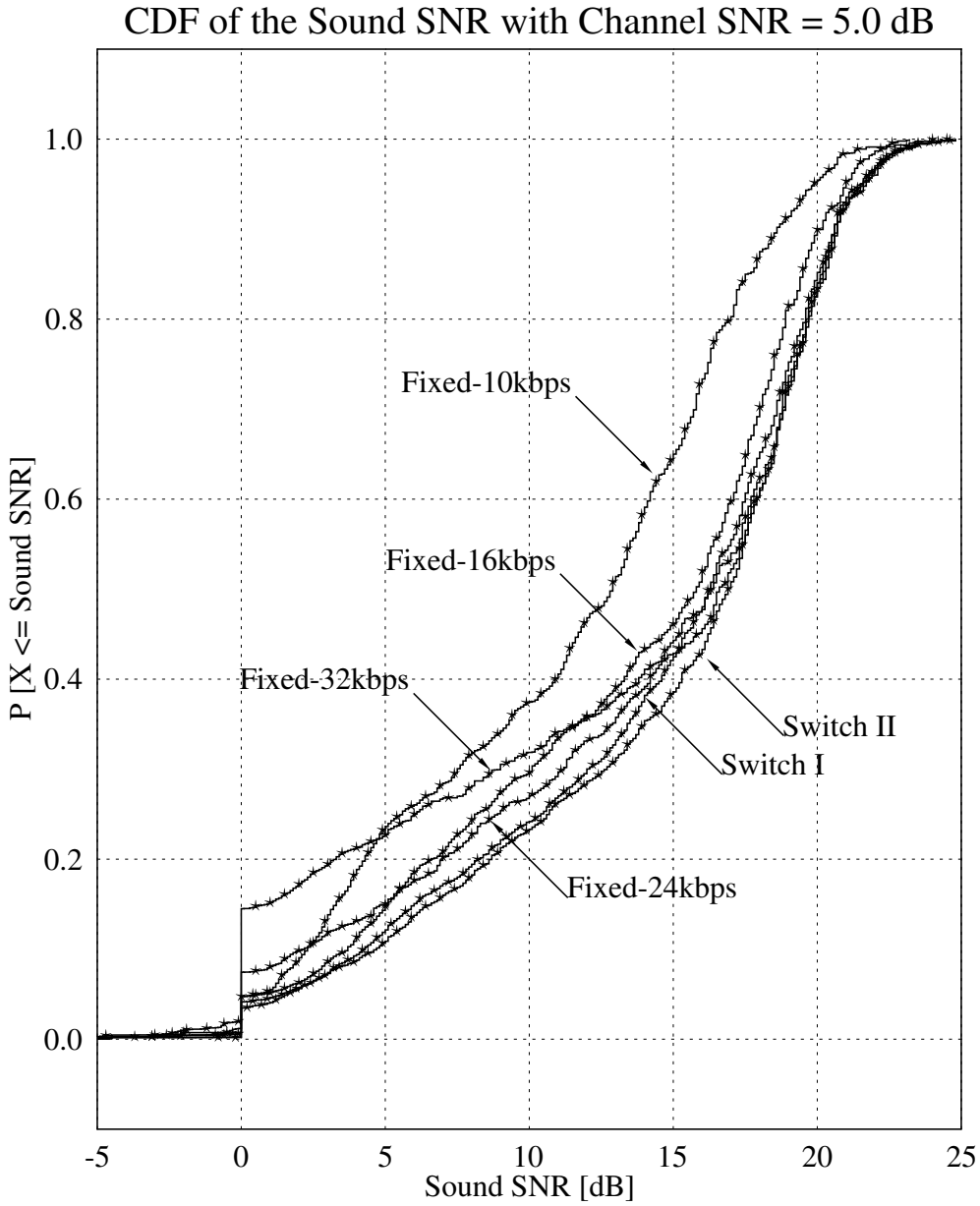


Figure 6.23: Typical CDF of the segmental SNR of a reconstructed audio signal transmitted over the fading time-dispersive channel of Section 4.1.3 at a channel SNR of 5 dB (from [225])

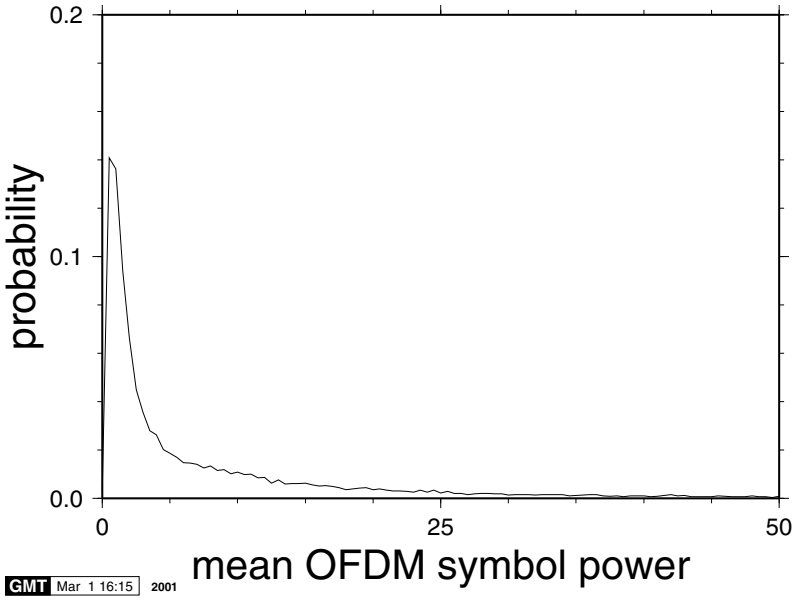


Figure 6.24: OFDM symbol energy histogram for 512-subcarrier 16-QAM with full channel inversion over the short WATM channel of Figure 4.3

However, upon defading, the noise sample n_n is amplified by the same amount as the signal, therefore preserving the SNR of the received sample.

Pre-equalisation for the OFDM modem operates by scaling the data symbol of subcarrier n, S_n, by a predistortion function E_n, computed from the inverse of the anticipated channel transfer function, prior to transmission. At the receiver, no equalisation is performed, hence the received symbols can be expressed as:

$$R_n = S_n \cdot E_n \cdot H_n + n_n.$$

Since no equalisation is performed, there is no noise amplification at the receiver. Similarly to the adaptive modulation techniques illustrated above, pre-equalisation is only applicable to a duplex link, since the transmitted signal is adapted to the specific channel conditions perceived by the receiver. As in other adaptive schemes, the transmitter needs an estimate of the current frequency domain channel transfer function, which can be obtained from the received signal in the reverse link, as seen in Figure 6.1.

The simplest choice of the pre-equalisation transfer function E_n is the inverse of the estimated frequency domain channel transfer function, $E_n = 1/\hat{H}_n$. If the estimation of the channel transfer function is accurate, then perfect channel inversion would result in an AWGN-like channel perceived at the receiver, since the anticipated time- and frequency-dependent behaviour of the channel is precompensated at the transmitter. The BER performance of such a system, accordingly, is identical to that of the equivalent modem in an AWGN channel with respect to the received signal power.

Since the pre-equalisation algorithm amplifies the power in each subcarrier by the corres-

ponding estimate of the channel transfer function, the transmitter's output power fluctuates in an inverse fashion with respect to time variant channel. The fades in the frequency domain channel transfer function can be deep, hence the transmit power in the corresponding subcarriers may be high. Figure 6.24 shows the histogram of the total OFDM symbol energy at the transmitter's output for the short WLAN channel of Figure 4.3 in conjunction with "full channel inversion", normalised to the fixed average output energy. It can be seen that the OFDM symbol energy fluctuates widely, with observed peak values in excess of 55. The long-term mean symbol energy was measured to be 22.9, which corresponds to an average output power increase of 13.6 dB. This naturally would impose unacceptable constraints on the required perfectly linear dynamic range of the power amplifier. Hence in practice only limited dynamic scenarios can be considered.

Explicitly, in order to limit the associated transmit power fluctuations, the dynamic range of the pre-equalisation algorithm can be limited to a value l, so that the following relations apply:

$$E_n = a_n \cdot e^{-j\phi_n}, \text{with} \tag{6.3}$$

$$\phi_n = \angle \hat{H}_n \quad \text{and} \tag{6.4}$$

$$a_n = \begin{cases} \left|\hat{H}_n\right| & \text{for} \left|\hat{H}_n\right| \leq l \\ l & \text{otherwise.} \end{cases} \tag{6.5}$$

Limiting the values of E_n to the value of l does not affect the phase of the channel pre-equalisation. Depending on the modulation mode employed for transmission, reception of the symbols affected by the amplitude limitation is still possible, perhaps for phase shift keying. Multilevel modulation modes exploiting the received symbol's amplitude will be affected by the imperfect pre-equalisation. The associated mean OFDM symbol power histogram is shown in Figure 6.25. Given, for example, a maximum allowed amplification factor of 6 and 12 dB, the normalised transmitted OFDM symbol power in the figure should be limited to 4 and 16, respectively. However, in practice even higher values may be observed, which is due to the OFDM symbol's energy fluctuation as a function of the specific data sequence, if multilevel modulation modes are used. In order to circumvent the above peak-to-mean envelope fluctuation problems, it is in practical terms more attractive to combine pre-equalisation with sub-band blocking, which is the topic of the next section.

6.4.2 Pre-equalisation with Sub-Band Blocking

Limiting the maximal amplification of the subcarriers leads to a reduced BER performance compared to the full channel inversion, but the system performance can be improved by identifying the subcarriers that cannot be fully pre-equalised and by disabling subsequent transmission in these subcarriers. This "blocking" of the transmission in certain subcarriers can be seen as adaptive modulation with two modulation modes, which introduces the problem of modulation mode signalling. As was discussed in the context of Figure 6.1 for the adaptive modulation modems above, this signalling task can be solved in different ways, namely by blind detection of blocked subcarriers, or by transmitting explicit signalling information contained in the data block. We have seen above that employing sub-band adaptivity – rather than subcarrier-by-subcarrier adaptivity – simplifies both the modem mode detection as well

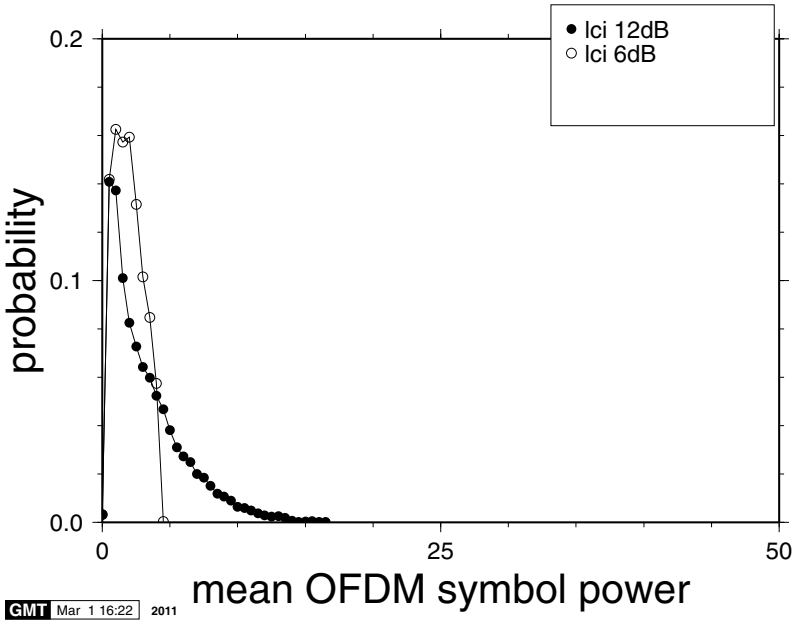


Figure 6.25: OFDM symbol energy histogram for 512-subcarrier 16-QAM transmission with limited dynamic range channel inversion (lci) over the WATM channel of Figure 4.3.

as the mode signalling, at the expense of a lower system throughput. In order to keep the system's complexity low and to allow for simple modem mode signalling or blind detection, we will assume a 16 sub-band adaptive scheme here.

Analogously to the adaptive modulation schemes above, the transmitter decides for all subcarriers in each sub-band, whether to transmit data or not. If pre-equalisation is possible under the power constraints, then the subcarriers are modulated with the pre-equalised data symbols. The information on whether or not a sub-band is used for transmission, and this is signalled to the receiver.

Since no attempt is made to transmit in the sub-bands that cannot be power-efficiently pre-equalised, the power conserved in the blank subcarriers can be used to "boost" the data-bearing sub-bands. This scheme allows for a more flexible pre-equalisation algorithm than the fixed threshold method described above; here is a summary:

(1) Calculate the necessary transmit power p_n for each sub-band n, assuming perfect pre-equalisation.

(2) Sort sub-bands according to their required transmit power p_n.

(3) Select sub-band n with the lowest power p_n, and add p_n to the total transmit power. Repeat this procedure with the next lowest power, until no further sub-bands can be added without the total power $\sum p_j$ exceeding power limit l.

Figure 6.26 depicts the 16-QAM BER performance over the short WATM channel of Figure 4.3. The BER floor stems from the channel's time-variant nature, since there is a delay be-

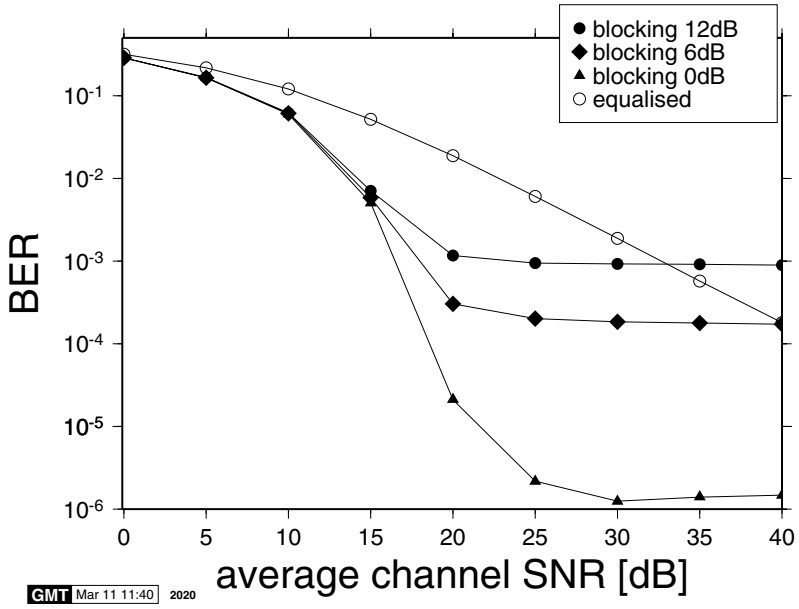


Figure 6.26: BER performance of the 512-subcarrier 16-QAM OFDM modem over the fading short WATM channel of Figure 4.3 employing 16 sub-band pre-equalisation with blocking and a delay of 1 time slot between the instants of perfect channel estimation and reception. Note that the transmit power is not shown in this figure

tween the channel estimation instant and the instant of transmission. The average throughput figures for the 6 dB and 12 dB symbol energy limits are 3.54 and 3.92 bits per data symbol, respectively. It can be noted that the BER floor is lower for $l = 6$ dB than for $l = 12$ dB. This is because the effects of the channel variation due to the delay between the instants of channel estimation and reception in the faded subcarriers on the equalisation function are more dramatic than in the higher quality subcarriers. The lower the total symbol energy limit l, the smaller the number of low quality subcarriers used for transmission. If the symbol energy is limited to 0 dB, then the BER floor drops to $1.5 \cdot 10^{-6}$ at the expense of the throughput, which attains 2.5 BPS. Figure 6.27 depicts the mean OFDM symbol energy histogram for this scenario. It can be seen that, compared with the limited channel inversion scheme of Figure 6.25, the allowable symbol energy is more efficiently allocated, with a higher probability of high energy OFDM symbols. This is the result of the flexible reallocation of energy from blocked sub-bands, instead of limiting the output power on a subcarrier-by-subcarrier basis.

6.4.3 Adaptive Modulation with Spectral Predistortion

The pre-equalisation algorithms discussed above invert the channel's anticipated transfer function, in order to transform the resulting channel into a Gaussian-like non-fading channel, whose SNR is dependent only on the path loss. Sub-band blocking has been introduced above, in order to limit the transmitter's output power, while maintaining the near-constant

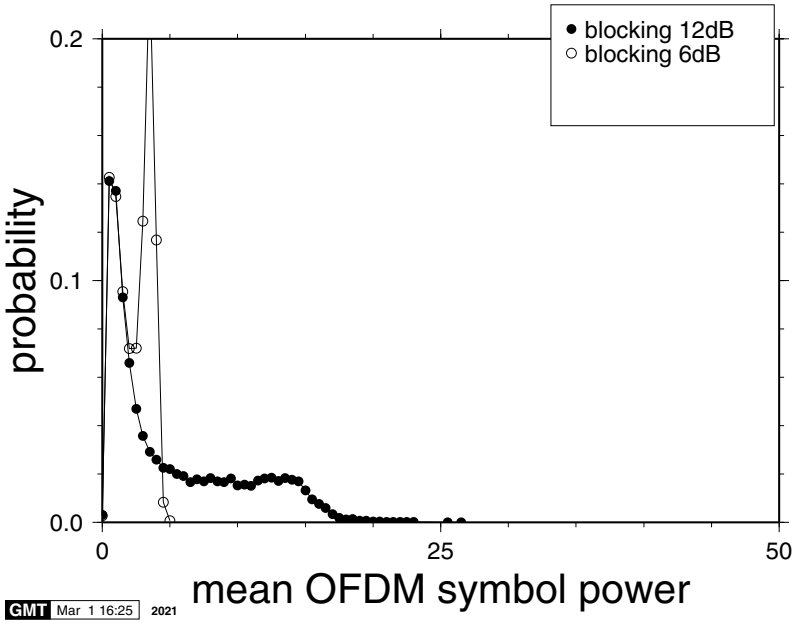


Figure 6.27: OFDM symbol energy histogram for 512 subcarrier, 16 sub-band pre-equalisation with blocking over the short WATM channel of Figure 4.3 using 16-QAM. The corresponding BER curves are given in Figure 6.26

SNR across the used subcarriers. The pre-equalisation algorithms discussed above do not cancel out the channel's path loss, but rely on the receiver's gain control algorithm to automatically account for the channel's average path loss.

We have already shown that maintaining Gaussian channel characteristics is not the most efficient way of exploiting the channel's time variant capacity. If maintaining a constant data throughput is not required by the rest of the communications system, then a fixed BER scheme in conjunction with error correction coding can assist in maximising the system's throughput. The results presented for the target BER adaptive modulation scheme in Figure 6.14(b) showed that, for the particular turbo coding scheme used, an uncoded BER of 1% resulted in error-free channel coded data transmission, and that for an uncoded target BER of 10% the turbo decoded data BER was below 10^{-5}. We have seen that it is impossible to exactly reach the anticipated uncoded target BER with the adaptive modulation algorithm, since the adaptation algorithm operates in discrete steps between modulation modes.

Combining the target BER adaptive modulation scheme and spectral pre-distortion allows the transmitter to react to the channel's time and frequency variant nature, in order to fine-tune the behaviour of the adaptive modem in fading channels. It also allows the transmitter to invest the energy that is not used in "no transmission" sub-bands into the other sub-bands without affecting the equalisation at the receiver.

The combined algorithm for adaptive modulation with spectral predistortion described here does not intend to invert the channel's transfer function across the OFDM symbol's range of subcarriers, it is therefore not a pure pre-equalisation algorithm. Instead, the aim is

Target BER	10^{-4}	1%	10%
SNR(BPSK)[dB]	8.4	4.33	−0.85
SNR(QPSK)[dB]	11.42	7.34	2.16
SNR(16QAM)[dB]	18.23	13.91	7.91

Table 6.3: Required target SNR levels for 1% and 10% target BER for the different modulation schemes over an AWGN channel

to transmit a sub-band's data symbols at a power level which ensures a given target SNR at the receiver, that is constant for all subcarriers in the sub-band, which in turn results in the required BER. Clearly, the receiver has to anticipate the different relative power levels for the different modulation modes, so that error-free demodulation of the multilevel modulation modes employed can be ensured.

The joint adaptation algorithm requires the estimates of the noise floor level at the receiver as well as the channel transfer function, which includes the path loss. On the basis of these values, the necessary amplitude of E_n required to transmit a data symbol over the subcarrier n for a given received SNR of γ_n can be calculated as follows:

$$|E_n| = \frac{\sqrt{N_0 \cdot \gamma_n}}{\left|\hat{H}_n\right|},$$

where N_0 is the noise floor at the receiver. The phase of E_n is used for the pre-equalisation, and hence:

$$\angle E_n = -\angle \hat{H}_n.$$

The target SNR, of subcarrier n, γ_n, is dependent on the modulation mode that is signalled over the subcarrier, and determines the system's target BER. We have identified three sets of target SNR values for the modulation modes, with uncoded target BER values of 1% and 10% for use in conjunction with channel coders, as well as 10^{-4} for transmission without channel coding. Table 6.3 gives an overview of these levels, which have been read from the BER performance curves of the different modulation modes in a Gaussian channel.

Figure 6.28 shows the performance of the joint predistortion and adaptive modulation algorithm over the fading time-dispersive short WATM channel of Figure 4.3 for the set of different target BER values of Table 6.3, as well as the comparison curves of the perfectly equalised 16-QAM modem under the same channel conditions. It can be seen that the BER achieved by the system is close to the BER targets. Specifically, for a target BER of 10%, no perceptible deviation from the target has been recorded, while for the lower BER targets the deviations increase for higher channel SNRs. For a target BER of 1%, the highest measured deviation is at the SNR of 40 dB, where the recorded BER is 1.36%. For the target BER of 10^{-4}, the BER deviation is small at 0 dB SNR, but at an SNR of 40 dB the experimental BER is $2.2 \cdot 10^{-3}$. This increase of the BER with increasing SNR is due to the rapid channel variations in the deeply faded subcarriers, which are increasingly used at higher SNR values. The light grey curve in the figure denotes the system's performance if no delay is present between the channel estimation and the transmission. In this case, the simulated BER shows only very little deviation from the target BER value. This is consistent with the behaviour of

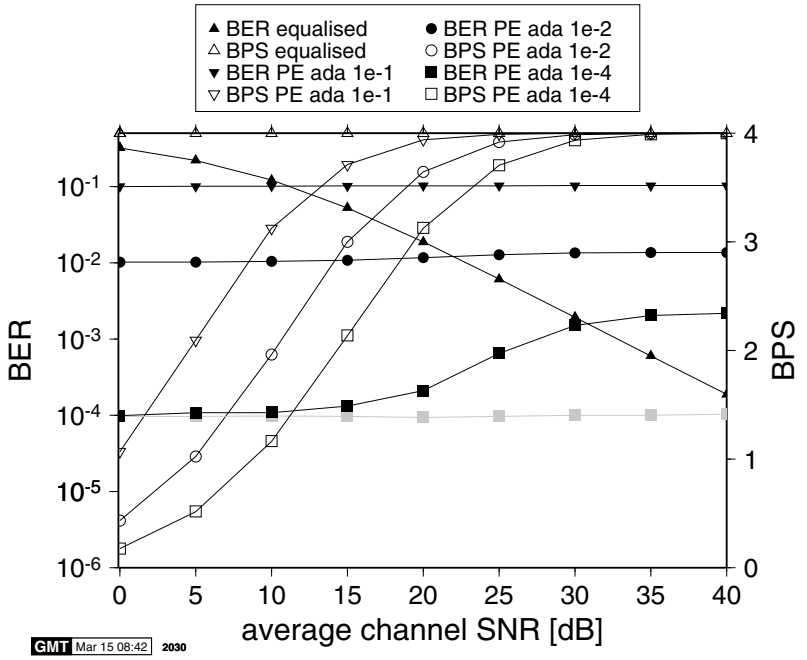


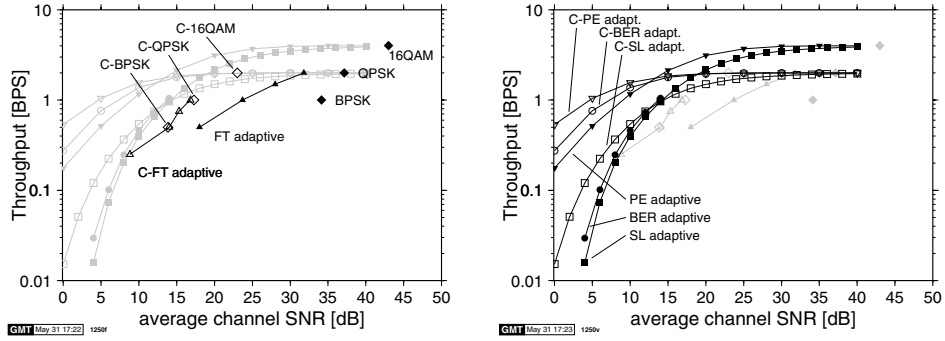
Figure 6.28: BER performance and BPS throughput of the 512 subcarrier, 16 sub-band adaptive OFDM modem with spectral predistortion over the Rayleigh fading time dispersive short WATM channel of Figure 4.3, and that of the perfectly equalised 16-QAM modem. The light grey BER curve gives the performance of the adaptive modem for a target BER of 10^{-4} with no delay between channel estimation and transmission, while the other results assume 1 time slot delay between uplink and downlink.

the full channel inversion pre-equalising modem.

6.5 Comparison of the Adaptive Techniques

Figure 6.29 compares the different adaptive modulation schemes discussed in this chapter. The comparison graph is split into two sets of curves, depicting the achievable data throughput for a data BER of 10^{-4} highlighted for the fixed throughput systems in Figure 6.29(a), and for the time-variant throughput systems in Figure 6.29(b).

The fixed throughput systems, highlighted in black in Figure 6.29(a), comprise the non-adaptive BPSK, QPSK and 16-QAM modems, as well as the fixed-throughput adaptive scheme, both for coded and uncoded applications. The non-adaptive modems' performance is marked on the graph as diamonds, and it can be seen that the uncoded fixed schemes require the highest channel SNR of all examined transmission methods to achieve a data BER of 10^{-4}. Channel coding employing the advocated turbo coding schemes dramatically improves the SNR requirements, at the expense of half the data throughput. The uncoded fixed-throughput (FT) adaptive scheme, marked by filled triangles, yields consistently worse data



(a) fixed throughput schemes

(b) variable throughput schemes

Figure 6.29: BPS throughput versus average channel SNR for non-adaptive and adaptive modulation as well as for pre-equalised adaptive techniques, for a data bit error rate of 10^{-4}. Note that for the coded schemes the achieved BER values are lower than 10^{-4}. (a) Fixed-throughput systems: coded (C-) and uncoded BPSK, QPSK, 16-QAM, and fixed-throughput (FT) adaptive modulation. (b) Variable-throughput systems: coded (C-) and uncoded switching level adaptive (SL), target BER adaptive (BER) and pre-equalised adaptive (PE) systems. Note that the separately plotted variable-throughput graph also shows the light grey benchmark curves of the complementary fixed-rate schemes and vice versa

throughput than the coded (C-) fixed modulation schemes C-BPSK, C-QPSK and C-16QAM, with its throughput being about half the coded fixed scheme's at the same SNR values. The coded FT (C-FT) adaptive system, however, delivers very similar throughput to the C-BPSK and C-QPSK transmission, and can deliver a BER of 10^{-4} for SNR values down to about 9 dB.

The variable throughput schemes, highlighted in Figure 6.29(b), outperform the comparable fixed throughput algorithms. For high SNR values, all uncoded schemes' performance curves converge to a throughput of 4 bits/symbol, which is equivalent to 16-QAM transmission. The coded schemes reach a maximal throughput of 2 bits/symbol. Of the uncoded schemes, the "data" switching level (SL) and target BER adaptive modems deliver a very similar BPS performance, with the target-BER scheme exhibiting slightly better throughput than the SL adaptive modem. The adaptive modem employing pre-equalisation (PE) significantly outperforms the other uncoded adaptive schemes and offers a throughput of 0.18 BPS at an SNR of 0 dB.

The coded transmission schemes suffer from limited throughput at high SNR values, since the half-rate channel coding limits the data throughput to 2 BPS. For low SNR values, however, the coded schemes offer better performance than the uncoded schemes, with the exception of the "speech" SL adaptive coded scheme, which is outperformed by the uncoded PE adaptive modem. The poor performance of the coded SL scheme can be explained by the lower uncoded target BER of the "speech" scenario, which was 1%, in contrast to the 10% uncoded target BER for the coded BER and PE adaptive schemes. The coded PE adaptive modem outperforms the target-BER adaptive scheme, thanks to its more accurate control of the uncoded BER, leading to a higher throughput for low SNR values.

It is interesting to observe that for the given set of four modulation modes, the uncoded

PE adaptive scheme is close in performance to the coded adaptive schemes, and that for SNR values of more than 14 dB, it outperforms all other studied schemes. It is clear, however, that the coded schemes would benefit from higher-order modulation modes, which would allow these modems to increase the data throughput further when the channel conditions allow. Before concluding this chapter, in the next section let us consider the generic problem of optimum power and bit allocation in the context of uncoded OFDM systems.

6.6 A Fast Algorithm for Near-Optimum Power and Bit Allocation in OFDM Systems [229]

6.6.1 State of the Art

In this section the problem of efficient OFDM symbol-by-symbol based power and bit allocation is analysed in the context of highly dispersive time-variant channels. A range of solutions published in the literature is reviewed briefly and Piazzo's [229] computationally efficient algorithm is discussed in somewhat more detail.

When OFDM is invoked over highly frequency selective channels, each subcarrier can be allocated a different transmit power and a different modulation mode. This OFDM symbol-by-symbol based "resource" allocation can be optimised with the aid of an algorithm which, if the channel is time variant, has to be repeated on an OFDM symbol-by-symbol basis. Some of the existing algorithms [19, 230] are mainly of theoretical interest due to their high complexity. Amongst the practical algorithms [213, 214, 229, 231, 232] the Hughes-Hartog algorithm (HHA) [232–234] is perhaps best known, but its complexity is somewhat high, especially for real-time OFDM symbol-by-symbol based applications at high bit rates. Hence the HHA has stimulated extensive research for computationally more efficient algorithms [213, 214, 229, 231, 232]. The most efficient appears to be that of Lai *et al.* [232], which is a fast version of the HHA and that of Piazzo [229].

6.6.2 Problem Description

Piazzo [229] considered an OFDM system using N subcarriers, each employing a potentially different modulation mode and transmit power. Below we follow the notation and approach proposed by Piazzo [229]. The different modes use different modem constellations and thus carry a different number of bits per subcarrier, ranging from 1 to I bits per subcarrier, corresponding to BPSK and 2^I-ary QAM. We denote the transmit power and the number of bits allocated to subcarrier k ($k = 0, \ldots, N-1$) by p_k and b_k, respectively. If $b_k = 0$, subcarrier k is allocated no power and no bits, hence it is disabled. The total transmit power is $P = \frac{1}{N}\sum_{k=0}^{N-1} p_k$ and the number of transmitted bits per OFDM symbol is $B = \sum_{k=0}^{N-1} b_k$. The i-bit modulation mode is characterised by the function $R_i(S)$, denoting the SNR required at the input of the detector, in order to achieve a target bit error rate (BER) equal to S. Finally, we denote the channel's power attenuation at subcarrier k by a_k, and the power of the Gaussian noise by P_N, so that the SNR of subcarrier k is $r_k = p_k/(a_k \cdot P_N)$.

We consider the problem of minimising the transmit power for a fixed target BER of S and for a fixed number of transmitted bits B per OFDM symbol. We impose an additional constraint, namely that the BER of every carrier has to be equal to S. This constraint

simplifies the problem, while producing a system close to the unconstrained optimum system [214, 232, 234], while [230] considers an unconstrained system. Furthermore, from an important practical point of view, it produces a near-constant BER at the input of the channel decoder, if FEC is used, which maximises the achievable coding gain, since the channel does not become overwhelmed by the plethora of transmission errors, which would be the case for a more bursty error statistics without this constraint. In order to satisfy this constraint, the power transmitted on subcarrier k has to be $p_k = P_N a_k R_{b_k}(S)$, and the total power to be minimised is given by the sum of the N subcarriers' powers across the OFDM symbol:

$$P = \frac{P_N}{N} \sum_{k=0}^{k=N-1} a_k \cdot R_{b_k}(S). \tag{6.6}$$

We now state a property of the optimum system. Namely, in the optimum system if a subcarrier has a lower attenuation than another one – i.e. it exhibits a higher frequency domain transfer function value and hence experiences a higher received SNR – then it must carry at least as many bits as the lower SNR subcarrier. More explicitly:

$$a_k < a_h \;\Rightarrow\; b_k \geq b_h. \tag{6.7}$$

The above property in Equation 6.7 can be readily proven. Let us briefly consider a system, which does not satisfy Equation 6.7, where for subcarriers k and h the above condition is violated and hence we have $a_k < a_h$ and $b_k = i_1 < b_h = i_2$. In other words, although the attenuation a_k is lower than a_h, $i_1 < i_2$. Consider now a second system, where the lower attenuation subcarrier was assigned the higher number of bits, i.e. $b_k = i_2$ and $b_h = i_1$. Since the required SNR for maintaining the target BER of S is lower for a lower number of bits, i.e. we have $R_{i_1}(S) < R_{i_2}(S)$, upon substituting these SNR values in Equation 6.6 we can infer that the second system requires a lower total power P per OFDM symbol for maintaining the target BER S. Thus the first system is not optimum in this sense.

Equation 6.7 states a necessary condition of optimality, which was also exploited by Lai *et al.* in [232], but it can be exploited further, as we will demonstrate below. From now on, we consider the channel's transfer function or attenuation vector sorted in the order of $a_0 \leq a_1 \leq a_2 \ldots$, which simplifies our forthcoming discussions.

6.6.3 Power and Bit Allocation Algorithm

Piazzo's algorithm [229] solves the above resource allocation problem for the general system by repeatedly solving the problem for a simpler system. Explicitly, the simpler system employs only two modulation modes, those carrying J and $J-1$ bits. This system can be termed the twin-mode system (TMS). On the basis of Equation 6.7 and since the channel's frequency domain attenuation vector was sorted in the order of $a_0 \leq a_1 \leq a_2 \ldots$, for the optimum TMS (OTMS) the OFDM subcarriers will be divided in three groups:

(1) Group J comprises the first or lowest attenuation OFDM subcarriers using a J-bit modulation mode.

(2) Group 0 is constituted by the last or highest attenuation OFDM subcarriers transmitting zero bits.

(3) Group $(J-1)$ hosts the remaining OFDM subcarriers using a $(J-1)$-bit modem mode.

In order to find the OTMS – minimising the required transmit power of the OFDM symbol for a fixed target BER of S and for a fixed number of transmitted bits B per OFDM symbol – we initially assign all the B bits of the OFDM symbol to the highest quality, i.e. lowest attenuation, group J. This of course would be a sub-optimum scheme, leaving the medium quality subcarriers of group $J-1$ unused, since even the highest quality subcarriers would require an excessive SNR, i.e. transmit power, for maintaining the target BER, when transmitting B bits per OFDM symbol. We note furthermore that the above bit allocation may require padding of the OFDM symbol with dummy bits if J is not an integer divisor of B.

Following the above initial bit allocation, Piazzo suggested performing a series of *bit reallocations, reducing the transmit power upon each reallocation*. Specifically, in each power and bit reallocation step we move the $J \cdot (J-1)$ bits allocated to the last, i.e. highest attenuation or lowest quality, $(J-1)$ OFDM subcarriers of group J to group $(J-1)$. For example, if 1 bit/symbol BPSK and 2 bit/symbol 4-QAM are used, then we move $2 \cdot 1 = 2$ bits, which were allocated to the highest attenuation 4-QAM subcarrier to two BPSK modulated subcarriers. The associated trade-off is that while previously the lowest quality subcarrier of class J had to carry 2 bits, it will now be conveying only 1 bit and additionally the highest quality and previously unused subcarrier has to be assigned 1 bit. This reallocation was motivated by the fact that before reallocation the lowest quality subcarrier of class J would have required a higher power for meeting the target BER requirement of S upon carrying 2 bits, than the regime generated by the reallocation step.

In general, for the sake of performing this power-reducing bit reallocation we have to add J subcarriers to group $(J-1)$. Hence we assign the last, i.e. lowest quality, $(J-1)$ OFDM subcarriers of group J and the first, i.e. highest quality, unused subcarrier to group $(J-1)$. Based on Equation 6.6 and upon denoting the index of the last, i.e. lowest quality, subcarrier of group J before reallocation by M_J and the index of the first, i.e. highest quality, unused subcarrier before reallocation by M_0, the condition of successful power reduction after the tentative bit reallocation can be formulated. Specifically, the bit reallocation results in a system using less power, if the sum of the subcarriers' attenuations carrying J bits weighted by their SNR $R_J(S)$ required for the J-bit modem mode for maintaining the target BER of S is higher than that of the corresponding constellation after the above bit reallocation process, when an extra previously unused subcarrier was invoked for transmission. This can be expressed in a more compact form as:

$$R_J(S) \sum_{k=0}^{J-2} a_{M_J-k} > R_{J-1}(S)(a_{M_0} + \sum_{k=0}^{J-2} a_{M_J-k}). \tag{6.8}$$

If Equation 6.8 is satisfied, the reallocation is performed and another tentative reallocation step is attempted. Otherwise the process is terminated, since the optimum twin-mode power and bit allocation scheme has been found.

According to Piazzo's proposition [229] the above procedure can be further accelerated. Since the attenuation vector was sorted, we have $a_{M_J-k} \approx a_{M_J}$ in Equation 6.8. Upon replacing a_{M_J-k} by a_{M_J}, after some manipulations we can reformulate Equation 6.8, i.e. the condition for the modem mode allocation after the bit reallocation to become more efficient

as:

$$K_J(S)a_{M_J} - a_{M_0} > 0, \tag{6.9}$$

where $K_J(S) = (J-1)(\frac{R_J(S)}{R_{J-1}(S)} - 1)$ and $K_J(S) > 0$ holds, since $R_J(S) > R_{J-1}(S)$. Piazzo denoted the values of M_J and M_0 after m reallocation steps by $M_J(m)$ and $M_0(m)$. Since initially all the bits were allocated to group J, we have for the index of the last subcarrier of group J at the commencement of the bit reallocation steps $M_J(0) = \lfloor B/J \rfloor - 1$, while for the index of the first unused subcarrier is $M_0(0) = \lfloor B/J \rfloor$, where $\lfloor x \rfloor$ is the smallest integer greater than or equal to x. Furthermore, since in each bit reallocation step the last $(J-1)$ OFDM subcarriers of group J and the first subcarrier of group 0 are moved to group $(J-1)$, after m reallocations we have $M_J(m) = \lfloor B/J \rfloor - 1 - (J-1)m$ and $M_0(m) = \lfloor B/J \rfloor + m$. Upon substituting these values in Equation 6.9 the left-hand side becomes a function of m, namely $f(m) = K_J(S)a_{M_J(m)} - a_{M_0(m)}$. Because the frequency domain channel transfer function's attenuation vector was ordered and since $K_J(S) > 0$, hence it is readily seen that $f(m)$ is a monotonically decreasing function of the reallocation index m. Therefore the method presented above essentially attempts to find the specific value of the reallocation index m, for which we have $f(m) > 0$ and $f(m+1) < 0$. In other words, when we have $f(m+1) < 0$, the last reallocation step resulted in a power increase, not a decrease, hence the reallocation procedure is completed.

The search commences from $m = 0$ and increases m by one at each bit reallocation step. In order to accelerate the search procedure, Piazzo replaced the linearly incremented search by a logarithmic search. This is possible, since the $f(m)$ function is monotonically decreasing upon increasing the reallocation index m. Piazzo [229] stipulated the search range by commencing from the minimum value of the reallocation index m, namely from $m_0 = 0$.

The maximum value, denoted by m_1, is determined by the number of OFDM subcarriers N or by the number of bits B to be transmitted per OFDM symbol, as will be argued below. There are two limitations, which determine the maximum possible number of reallocation steps. Namely, the reallocation steps have to be curtailed when there are no more bits left in the group of subcarriers associated with the J-bit modem mode group or when there are no more unused carriers left after iteratively invoking the best unused carrier from the group of disabled carriers. These limiting factors, which determine the maximum possible number of bit reallocation steps, are discussed further below.

Recall that at the commencement of the algorithm all the bits were assigned to the subcarrier group associated with the J-bit modem mode and hence there were $\lceil B/J \rceil$ subcarriers in group J. Upon reallocating the $J \cdot (J-1)$ bits allocated to the last, i.e. highest attenuation or lowest quality, $(J-1)$ OFDM subcarriers of group J to group $(J-1)$ until no more bits were left in the subcarrier group associated with the J-bit modem mode naturally constitutes an upper limit for the maximum number of reallocation steps m_1, which is given by $\lceil B/J \rceil/(J-1)$. Again, the other limiting factor of the maximum number of bit reallocation steps is the number of originally unused carriers, which was $N - \lceil B/J \rceil$). Hence the maximum possible number of reallocations is given by $m_1 = min(\lfloor \lfloor B/J \rfloor/(J-1) \rfloor; N - \lfloor B/J \rfloor)$, where $\lceil x \rceil$ is the highest integer smaller than or equal to x.

The accelerated logarithmic search proposed by Piazzo [229] halves the maximum possible range at each bit reallocation step, by testing the value of $f(m)$ at the centre of the range and by updating the range accordingly. Piazzo's proposed algorithm can be summarised in a

compact form as follows [229]:

Algorithm 1 $OTMS(B, S, J, N, a_k)$
(1) Initialise $m_0 = 0$, $m_1 = min(\lfloor \lfloor B/J \rfloor / (J-1) \rfloor, N - \lfloor B/J \rfloor)$.
(2) Compute $m_x = m_0 + \lfloor m_1 - m_0 \rfloor / 2$.
(3) If $f(m_x) \geq 0$ *let* $m_0 = m_x + 1$*; else let* $m_1 = m_x$.
(4) If $m_1 = m_0 + 1$ *goto step 5); else goto step 2).*
(5) Stop. The number of carriers in group J *is* $N_J = \lfloor B/J \rfloor - m_0 \cdot (J-1)$.

When the algorithm is completed, the value N_J becomes known and this specifies the number of OFDM subcarriers in the group J associated with the J-bit modem mode.

Having generated the optimum twin-mode system, Piazzo also considered the problem of finding the optimum general system (OGS) employing OFDM subcarrier modulation modes carrying $1, ..., I$ bits. The procedure proposed initially invoked Algorithm 1 in order to find the optimum twin-mode system carrying a total of B bits per OFDM symbol using the I-bit and the $(I-1)$-bit per subcarrier modulation modes. At the completion of Algorithm 1 we know N_I, the number of OFDM subcarriers carrying I bits. These subcarriers are now confirmed. These OFDM subcarriers as well as the associated $I \cdot N_I$ bits can now be eliminated from the resource allocation problem, and the optimum system transmitting the remaining $B - I \cdot N_I$ bits of the remaining $(N - N_I)$ subcarriers can be sought, using subcarrier modulation modes transmitting $(I-1), (I-2), ...$ bits.

Again, Algorithm 1 can be applied to this new system, now using the modulation modes with $(I-1)$ and $(I-2)$ bits per subcarrier and repeating the procedure. After each application of Algorithm 1 a new group of subcarrier is confirmed. Piazzo's general algorithm can be summarised in a compact form as follows [229]:

Algorithm 2 $OGS(B, S, I, N, a_k)$
(1) Initialise $\hat{B} = B$, $\hat{N} = N$, $\hat{a}_k = a_k$, $J = I$.
(2) Perform $OTMS(\hat{B}, S, J, \hat{N}, \hat{a}_k)$ *to compute* N_J.
(3) If $J = 2$*, let* $N_1 = \hat{B} - 2 \cdot N_2$ *and stop.*
(4) Remove the first N_J *carriers from* $\hat{a}_k$*, let* $\hat{B} = \hat{B} - J \cdot N_J$, $\hat{N} = \hat{N} - N_J$, $J = J - 1$ *and goto step 2).*

When the algorithm is completed, the values N_i specifying the number of OFDM subcarriers conveying i bits, become known for all the legitimate modes carrying $i = I, (I-1), ..., 1$ bits per subcarrier. Hence we know the number of bits allocated to subcarrier k ($k = 0, \ldots, N-1$) expressed in terms of the b_k values as well as the associated minimum power requirements. Hence the system is specified in terms of $p_k = P_N a_k R_{b_k}(S)$. In closing it is worthwhile noting that the algorithm can be readily modified to handle the case where the two modes of the twin-mode system carry J and $K < J - 1$ bits.

Having considered the above near-optimum power- and bit allocation algorithm, in the next section we will consider a variety of OFDM systems supporting multiple users and invoking adaptive beam-steering.

6.7 Multi-User AOFDM[3]

6.7.1 Introduction

Signal fading as well as co-channel interference are known to have a severe impact on the system performance in multi-cellular mobile environments. Adaptive modulation as a method of matching the system to fading induced variations of the channel quality was originally proposed for single carrier transmission, but its potential was also soon discovered in the context of multicarrier transmissions, with the aim of concentrating the throughput on subcarriers least affected by frequency selective fading [227]. On the other hand, adaptive antenna array techniques have been shown to be effective in reducing co-channel interference at the receiver side [155, 235], when supporting multiple users.

This particular application of smart antennas is often referred to as **Space Division Multiple Access** (SDMA), which exploits the unique, user-specific "spatial signature" of the individual users for differentiating amongst them. In simple conceptual terms one could argue that both a conventional CDMA spreading code and the Channel Impulse Response (CIR) affect the transmitted signal similarly - they are namely convolved with it. Hence, provided that the CIR is accurately estimated, it becomes known and certainly unique, although - as opposed to orthogonal Walsh-Hadamad spreading codes, for example - not orthogonal to the other users' CIRs. Nonetheless, an accurately estimated CIR may be used for uniquely identifying users after channel estimation and hence for supporting several users within the same bandwidth. Provided that a powerful multi-user detector is available, one can support even more users than the number of antennas. Hence this method enhances the achievable spectral efficiency directly. These techniques are discussed in great detail in Chapters 10 - 12, hence in this introductory part of the book only a rudimentary exposé of the basic concepts is offered.

It is worth noting that the family of Multiple Input Multiple Output (MIMO) systems [123] is also closely related to the SDMA arrangements discussed here, since they also employ multiple antennas. However, in contrast to the SDMA arrangements, MIMOs are typically invoked not for the sake of supporting multiple users, but for increasing the throughput of a wireless system in terms of the number of bits per symbol that can be transmitted by a single user in a given bandwidth at a given integrity.

One of the most prominent schemes that may be used for detecting multiple users with the aid of SDMA is the so-called Sample Matrix Inversion (SMI) technique, which has recently drawn wide interest [124, 149, 150]. We commence our discussions in the next section with a brief description of a system amalgamating adaptive modulation and co-channel interference suppression. Initial performance results will be presented in Subsection 6.7.3 assuming perfect knowledge of all channel parameters, while in Subsection 6.7.4 the problem of channel parameter estimation will be addressed by means of orthogonal pilot sequences, leading to our conclusions.

[3]This section is based on M. Münster, T. Keller and L. Hanzo, "Co-Channel Interference Suppression Assisted Adaptive OFDM in Interference Limited Environments", ©IEEE, VTC'99, Amsterdam, NL, 17-19 Sept. 1999.

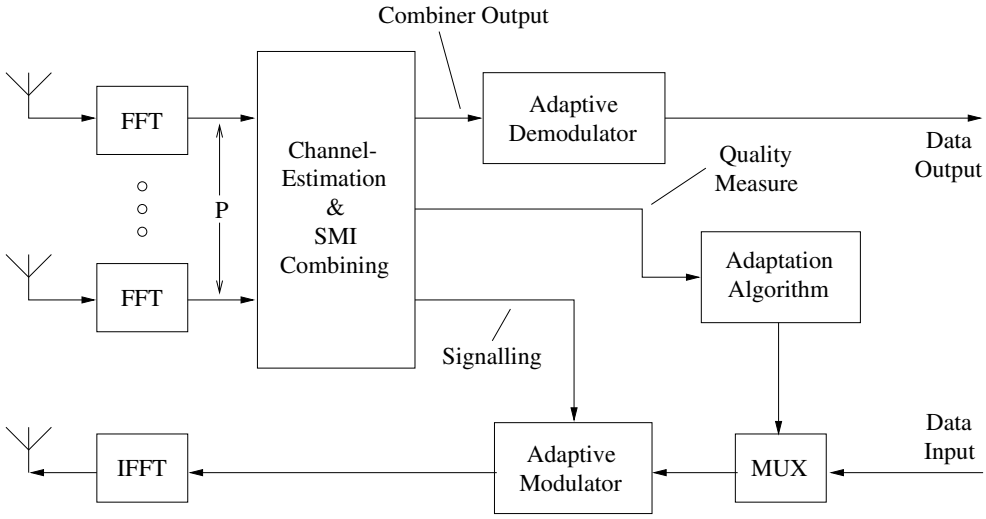


Figure 6.30: Schematic structure of the adaptive transceiver with interference suppression at the receiver

6.7.2 Adaptive Transceiver Architecture

6.7.2.1 An Overview

The transceiver schematic is shown in Figure 6.30, where the receiver employs a multiple-antenna assisted front end. The signal received by each individual antenna element is fed to an FFT block, and the resulting parallel received OFDM symbols are combined on a subcarrier-by-subcarrier basis. The combining is accomplished on the basis of the weight vector, which has been obtained by solving the Wiener equation, constituting the core of the sample matrix inversion algorithm [155, 235]. After combining, the signal is fed into the adaptive demodulator of Figure 6.30, which delivers the output bits in the form of soft-decision information to an optional channel decoder. The demodulator operates in one of a set of four modes, namely "no transmission", BPSK, QPSK and 16-QAM. Since an interfered channel cannot be considered to constitute a reciprocal system, the modem mode adaptation operates in a closed-loop fashion, where each of the receivers instructs the remote transmitter as to the required set of modulation modes for the next AOFDM symbol, which is necessary for maintaining a given target Bits per Symbol (BPS) performance. On reception of a packet, the adaptation algorithm computes the set of modulation modes to be employed by the remote transmitter for the next transmitted AOFDM symbol on the basis of a channel quality measure, namely the subcarrier SNR, which can be estimated by the interference suppression algorithm. The set of requested modulation modes is signalled to the remote receiver along with the next transmitted AOFDM symbol, which is then used by the remote transmitter in its next transmission.

6.7.2.2 The Signal Model

The $P \times 1$ vector of complex signals, $\mathbf{x}[n,k]$, received by the antenna array in the k-th subcarrier of the n-th OFDM symbol is constituted by a superposition of the independently faded signals associated with the desired user and the L undesired users plus the Gaussian noise at the array elements:

$$\begin{aligned} \mathbf{x}[n,k] &= \mathbf{d}[n,k] + \mathbf{u}[n,k] + \mathbf{n}[n,k], \quad \text{with} \\ \mathbf{d}[n,k] &= \mathbf{H}^{(0)}[n,k]s_0[k] \\ \mathbf{u}[n,k] &= \sum_{l=1}^{L} \mathbf{H}^{(l)}[n,k]s_l[k], \end{aligned} \tag{6.10}$$

where $\mathbf{H}^{(l)}[n,k]$ for $l = 0,\ldots,L$ denotes the $P \times 1$ vector of complex channel coefficients between the l-th user and the P antenna array elements. We assume that the vector components $H_m^{(l)}[n,k]$ for different array elements m or users l are independent, stationary, complex Gaussian distributed processes with zero-mean and different variance σ_l^2, $l = 0,\ldots,L$. The variable $s_l[n,k]$ – which is assumed to have zero-mean and unit variance – represents the complex data of the l-th user and $\mathbf{n}[n,k]$ denotes the aforementioned $P \times 1$ vector of additive white Gaussian noise contributions with zero mean and variance σ^2 [149].

6.7.2.3 The SMI Algorithm

The idea behind minimum mean-square error (MMSE) beamforming [155] is to adjust the antenna weights, such that the power of the differential signal between the combiner output and a reference signal – which is characteristic of the desired user – is minimised. The solution to this problem is given by the well-known Wiener equation, which can be directly solved by means of the SMI algorithm in order to yield the optimum weight vector $\mathbf{w}[n,k]$ of dimension $P \times 1$. Once the instantaneous correlation between the received signals, which is represented by the $P \times P$ matrix $\mathbf{R}[n,k]$, and the channel vector $\mathbf{H}^{(0)}[n,k]$ of the desired user are known, the weights are given by [124, 149, 155]:

$$\mathbf{w}[n,k] = (\mathbf{R}[n,k] + \gamma\mathbf{I})^{-1}\mathbf{H}^{(0)}[n,k], \tag{6.11}$$

where γ represents the so-called diagonal augmentation factor [149]. Assuming knowledge of all channel parameters and the noise variance σ^2, the correlation matrix can be determined by:

$$\begin{aligned} \mathbf{R}[n,k] &\triangleq E_c\{\mathbf{x}[n,k]\mathbf{x}^H[n,k]\} \\ &= \mathbf{R}_d[n,k] + \mathbf{R}_u[n,k] + \mathbf{R}_n[n,k], \quad \text{with} \\ \mathbf{R}_d[n,k] &= \mathbf{H}^{(0)}[n,k]{\mathbf{H}^{(0)}}^H[n,k] \\ \mathbf{R}_u[n,k] &= \sum_{l=1}^{L} \mathbf{H}^{(l)}[n,k]{\mathbf{H}^{(l)}}^H[n,k] \\ \mathbf{R}_n[n,k] &= \sigma^2\mathbf{I}, \end{aligned} \tag{6.12}$$

which is a superposition of the correlation matrices $\mathbf{R}_d[n,k]$, $\mathbf{R}_u[n,k]$ and $\mathbf{R}_n[n,k]$ of the desired and undesired users as well as of the array element noise, respectively. The combiner output can now be inferred from the array output vector $\mathbf{x}[n,k]$ by means of:

$$y[n,k] = \mathbf{w}^H[n,k]\mathbf{x}[n,k]. \tag{6.13}$$

The Signal-to-Noise Ratio (SNR) at the combiner output – which is of vital importance for the modulation mode adaptation – is given by [155]:

$$\begin{aligned} SNR &= \frac{E\{|\mathbf{w}^H[n,k]\mathbf{d}[n,k]|^2\}}{E\{|\mathbf{w}^H[n,k]\mathbf{n}[n,k]|^2\}} \\ &= \frac{\mathbf{w}^H[n,k]\mathbf{R}_d[n,k]\mathbf{w}[n,k]}{\mathbf{w}^H[n,k]\mathbf{R}_n[n,k]\mathbf{w}[n,k]} \end{aligned} \tag{6.14}$$

and correspondingly the Signal-to-Interference+Noise Ratio (SINR) is given by [155]:

$$SINR = \frac{\mathbf{w}^H[n,k]\mathbf{R}_d[n,k]\mathbf{w}[n,k]}{\mathbf{w}^H[n,k](\mathbf{R}_u[n,k]+\mathbf{R}_n)\mathbf{w}[n,k]}. \tag{6.15}$$

Equation 6.12 is the basis for our initial simulations, where perfect channel knowledge has been assumed. Since in a real environment the receiver does not have perfect knowledge of the channel, its parameters have to be estimated, a problem which we will address in Section 6.7.4 on an OFDM symbol-by-symbol basis by means of orthogonal pilot sequences.

6.7.2.4 The Adaptive Bit-Assignment Algorithm

The adaptation performed by the modem is based on the choice between a set of four modulation modes, namely 4, 2, 1 and 0 bit/subcarrier, where the latter corresponds to "no transmission". The modulation mode could be assigned on a subcarrier-by-subcarrier basis, but the signalling overhead of such a system would be prohibitive. Hence, we have grouped adjacent subcarriers into "sub-bands" and assign the same modulation mode to all subcarriers in a sub-band. Note that the frequency domain channel transfer function is typically not constant across the subcarriers of a sub-band, hence the modem mode adaptation will be suboptimal for some of the subcarriers. The Signal-to-Noise Ratio (SNR) of the subcarriers will be shown to be in most cases an effective measure for controlling the modulation assignment. The modem mode adaptation is hence achieved by calculating in the first step for each sub-band and for all four modulation modes the expected overall sub-band bit error rate (BER) by means of averaging the estimated individual subcarrier BERs. Throughout the second step of the algorithm – commencing with the lowest modulation mode in all sub-bands – in each iteration the number of bits/subcarrier of that sub-band is increased, which provides the best compromise in terms of increasing the number of expected bit errors compared to the number of additional data bits accommodated, until the target number of bits is reached.

6.7.2.5 The Channel Models

Simulations have been conducted for the indoor Wireless Asynchronous Transfer Mode (WATM) channel impulse response (CIR) of Section 4.1 [227]. This three-path impulse re-

sponse exhibits a maximal dispersion of 11 time domain OFDM samples, with each path faded according to a Rayleigh distribution of a normalised maximal Doppler frequency of $f'_d = 1.235 \cdot 10^{-5}$, where the normalisation interval was the OFDM symbol duration. This model corresponds to the channel experienced by a mobile transmitting at a carrier frequency of 60 GHz with a sampling rate of 225 MHz and travelling at a vehicular velocity of 50 km/h. An alternative channel model, which we considered in our simulations is a Wireless Local Area Network (WLAN) model associated with a seven-path impulse response having a maximal dispersion of 32 samples. However, for this more dispersive and higher Doppler frequency channel adaptive modulation has turned out to be less effective due to its significantly increased normalised Doppler frequency of $f'_d = 3.935 \cdot 10^{-5}$ corresponding to a carrier frequency of 17 GHz, sampling rate of 20 MHz and vehicular velocity of 50 km/h.

6.7.3 Simulation Results - Perfect Channel Knowledge

6.7.3.1 General Remarks

In our initial simulations we assumed that the receiver had perfect knowledge of all channel parameters, which enabled the estimation of the correlation matrix required by the SMI algorithm upon using Equation 6.12. Furthermore, we initially assumed that the receiver was capable of signalling the modulation modes to the transmitter without any additional delay. Throughout our discussions we will gradually remove the above idealistic assumptions. In all simulations we assumed a partitioning of the 512-subcarrier OFDM symbol's total bandwidth into 16 equal-sized 32-subcarrier sub-bands. This has been shown to provide a reasonable compromise between signalling overhead and performance degradation compared to a subcarrier-by-subcarrier based modulation mode assignment.

6.7.3.2 Two-Branch Maximum-Ratio Combining

Initial simulations were conducted in the absence of co-channel interference. In this scenario the SMI equations take the form of the MMSE maximum-ratio combiner, resulting in a high diversity gain even with the minimal configuration of only two reception elements. Adaptive modulation was performed on the basis of the estimated SNR of each subcarrier, which is given by Equation 6.14. Since due to diversity reception the dramatic fades of the channel frequency response have been mitigated, the performance advantage of adaptive modulation is more modest, as illustrated by Figure 6.31 for the "transmission frame-invariant" WATM channel, for which the fading profile is kept constant for the OFDM symbol duration, in order to avoid inter-subcarrier interference. For the equivalent simulations in the "transmission frame-invariant" WLAN channel environment we observed a more distinct performance gain due to adaptive modulation, which is justified by the higher degree of frequency selectivity introduced by the WLAN channel's seven-path impulse response.

6.7.3.3 SMI Co-Channel Interference Suppression

In these simulations we considered first of all the case of a single dominant co-channel interferer of the same signal strength as the desired user. It is well known that if the total number of users – whose signals arrive at the antenna array – is less or equal to the number of array elements, the unwanted users are suppressed quite effectively. Hence, for our

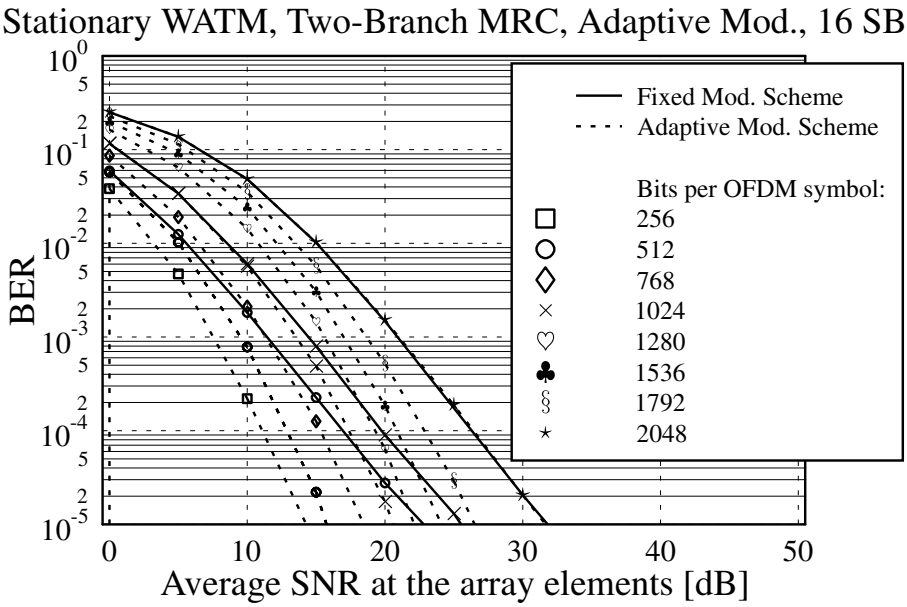


Figure 6.31: BER of 16-sub-band AOFDM modem with two-branch maximum-ratio combining in a "frame-invariant" indoor WATM environment, assuming perfect channel knowledge and zero-delay signalling of the modulation modes

modulation adaptation requirements we can assume that $SNR \approx SINR$, which enables us to use the algorithm described in Section 6.7.2, on the basis of the SNR estimated with the aid of Equation 6.14. Figure 6.32 illustrates the impact of adaptive modulation in the WATM channel environment under the outlined conditions. At a given SNR the performance gain due to adaptive modulation decreases with an increasing bitrate, since the higher bitrate imposes a more stringent constraint on the modulation mode assignment, invoking a higher number of low-SNR subcarriers. Upon comparing Figure 6.32 and 6.33 we observe that AOFDM attains a significantly higher SNR gain in the presence of co-channel interference, than without interference. As alluded to in the previous section this is because under co-channel interference the SMI scheme exploits most of its diversity information extracted from the antenna array for suppressing the unwanted signal components, rather than mitigating the frequency domain channel fades experienced by the wanted user. For decreasing values of the Interference-to-Noise Ratio (INR) at the antenna array output, the system performance will gradually approach the performance observed for the MRC system. In order to render our investigations more realistic in our next experiment we allow a continuous, i.e. "frame-variant" fading across the OFDM symbol duration. The system performance corresponding to this scenario is illustrated in Figure 6.33. At low SNRs the observed performance is identical to that recorded in Figure 6.32 for the "frame-invariant" channel model, whereas at high SNRs we experience a residual BER due to inter-subcarrier interference. Again, for a

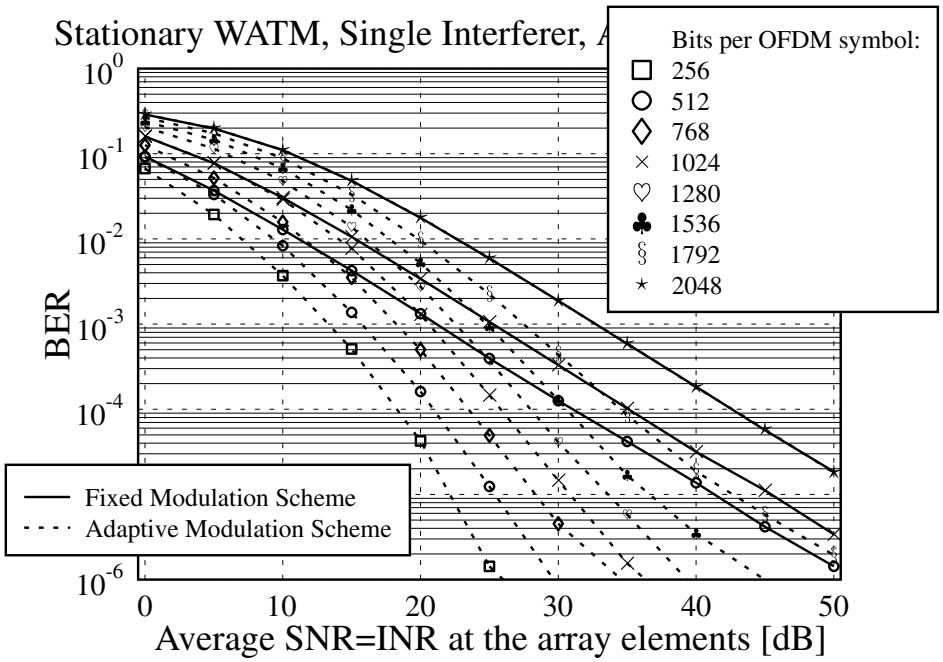


Figure 6.32: BER of 16-sub-band AOFDM modem with two-branch SMI and 2 users in a "frame-invariant" indoor WATM environment, assuming perfect channel knowledge and zero-delay signalling of the modulation modes

low number of bits per OFDM symbol the adaptive scheme is capable of reducing the "loading" of subcarriers with low SNR values, which are particularly impaired by inter-subcarrier interference. Hence AOFDM exhibits a BER improvement in excess of an order of magnitude. So far we have assumed that the receiver is capable of instantaneously signalling the required modulation modes for the next OFDM symbol to the transmitter. This assumption cannot be maintained in practice. Here we assume a time division duplexing (TDD) system with identical transceivers at both ends of the link, which communicate with each other using adjacent uplink and downlink slots. Hence we have to account for this by incorporating an additional delay of at least one OFDM symbol, while neglecting the finite signal processing delay. Simulation results for this scenario are depicted in Figure 6.34. We observe that the performance gain attained by adaptive modulation is reduced compared to that associated with the zero-delay assumption in Figure 6.33. This could partly be compensated for by channel prediction. When employing a higher number of array elements, the performance gain achievable by adaptive modulation will mainly depend on the number of users and their signal strength. If the number of users is lower than the number of array elements, or if the interferers are predominantly weak, the remaining degrees of freedom for influencing the array response are dedicated by the SMI scheme to providing diversity for the reception

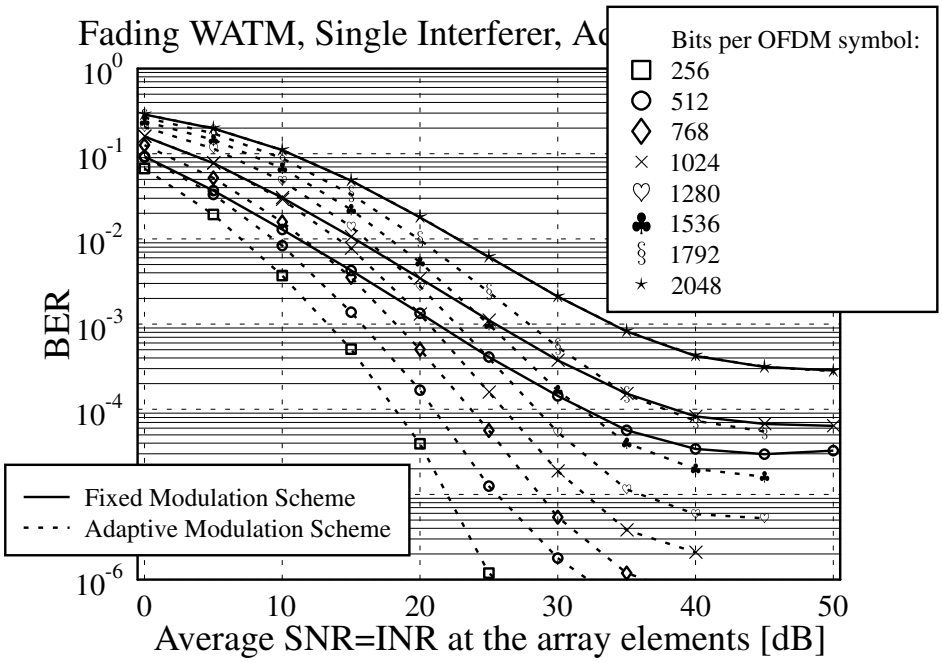


Figure 6.33: Performance results of Figure 6.32 repeated for a fading indoor WATM environment

of the wanted user and hence adaptive modulation proves less effective. If the number of users exceeds the number of array elements, the system becomes incapable of suppressing the undesired users effectively, resulting in a residual BER at high SNRs due to the residual co-channel interference. Since for a relatively high number of users the residual interference exhibits Gaussian-noise like characteristics, the SINR given by Equation 6.15 could be a suitable measure for performing the modulation mode assignment. By contrast, for a low number of interferers it is difficult to predict the impact on the system performance analytically. A possible approach would be to use the instantaneous number of errors in each sub-band (e.g. at the output of a turbo decoder) as a basis for the modulation assignment, which constitutes our future work. Let us now consider the issues of channel parameter estimation.

6.7.4 Pilot-Based Channel Parameter Estimation

6.7.4.1 System Description

Vook and Baum [124] have proposed SMI parameter estimation for OFDM by means of orthogonal reference sequences carrying pilot slots, which are transmitted over several OFDM symbol durations. This principle can also be applied on an OFDM symbol-by-symbol basis, as required for adaptive modulation. Upon invoking the idea of pilot-based channel esti-

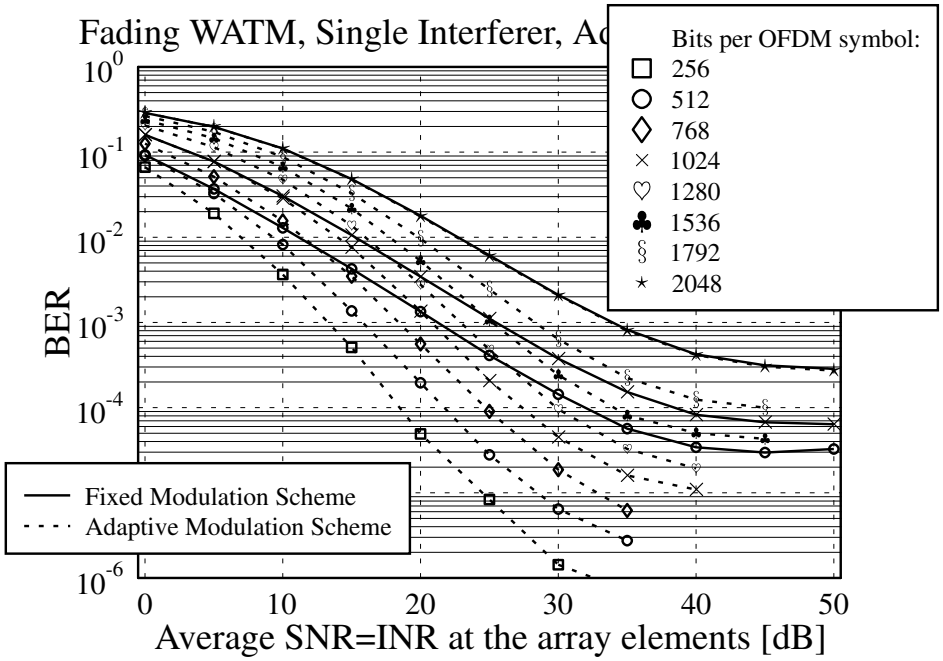


Figure 6.34: Performance results of Figure 6.33 repeated for one OFDM symbol delayed signalling

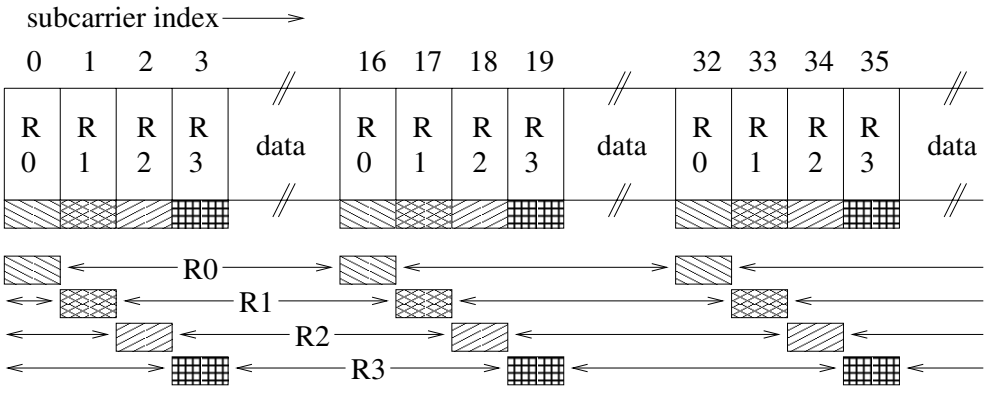


Figure 6.35: Pilot arrangement in each OFDM symbol for a reference length of 4 bit and a group distance of 16 subcarriers; interpolation is performed between pilots associated with the same bit position within the reference sequence

code/bit	0	1	2	3
0	1	1	1	1
1	1	1	-1	-1
2	1	-1	-1	1
3	1	-1	1	-1

Table 6.4: Orthogonal Walsh codes with a length of 4 bit

mation by means of sampling and low-pass interpolating the channel transfer function, we replace each single pilot subcarrier by a group of pilots, which carries a replica of the user's unique reference sequence. This is illustrated in Figure 6.35 for a reference sequence having a length of 4 bit, and for a pilot group distance of 16 subcarriers, which corresponds to the frequency required for sampling the WATM channel's transfer function. The corresponding 4-bit orthogonal Walsh code-based reference sequences are listed in Table 6.4. Each of these 4 bits is assigned using BPSK to one of the 4 pilots in a pilot-group. The complex signal received by the m-th antenna in a pilot subcarrier at absolute index k and local index i within the reference sequence is constituted by a contribution of all users, each of which consists of the product of the Walsh code value associated with the user at bit position i of the reference sequence of Table 6.4 and the complex channel coefficient between the transmitter and the m-th antenna. MMSE lowpass interpolation is performed between all pilot symbols of the same relative index i within the k-spaced pilot blocks – as seen in Figure 6.35 – in order to generate an interpolated estimate of the reference for each subcarrier. An estimate of the channel vector $\hat{\mathbf{H}}^{(0)}[n,k]$ and the correlation matrix $\hat{\mathbf{R}}[n,k]$ for the k-th subcarrier of the n-th OFDM symbol is then given by [124, 155, 235]:

$$\hat{\mathbf{H}}^{(0)}[n,k] = \frac{1}{N}\sum_{i=0}^{N-1} r^{(0)^*}(i)\mathbf{x}_{LP}[n,k](i) \tag{6.16}$$

$$\hat{\mathbf{R}}[n,k] = \frac{1}{N}\sum_{i=0}^{N-1} \mathbf{x}_{LP}[n,k](i)\mathbf{x}_{LP}^{H}[n,k](i), \tag{6.17}$$

where $r^{(0)}(i)$ denotes the i-th value of the reference sequence associated with the desired user, $\mathbf{x}_{LP}[n,k](i)$ represents the low-pass interpolated received signal at sequence position i and N denotes the total reference length.

6.7.4.2 Simulation Results

The performance of this scheme is characterised by the simulation results presented in Figure 6.36. Compared to the results presented in Figure 6.34 for "perfect channel knowledge", in Figure 6.36 we observe that besides the reduced range of supported bitrates there is an additional performance degradation, which is closely related to the choice of the reference length. Specifically, there is a reduction in the number of useful data subcarriers due to the pilot overhead, which reduces the "adaptively" exploitable diversity potential. Second, a relatively short reference sequence results in a limited accuracy of the estimated channel

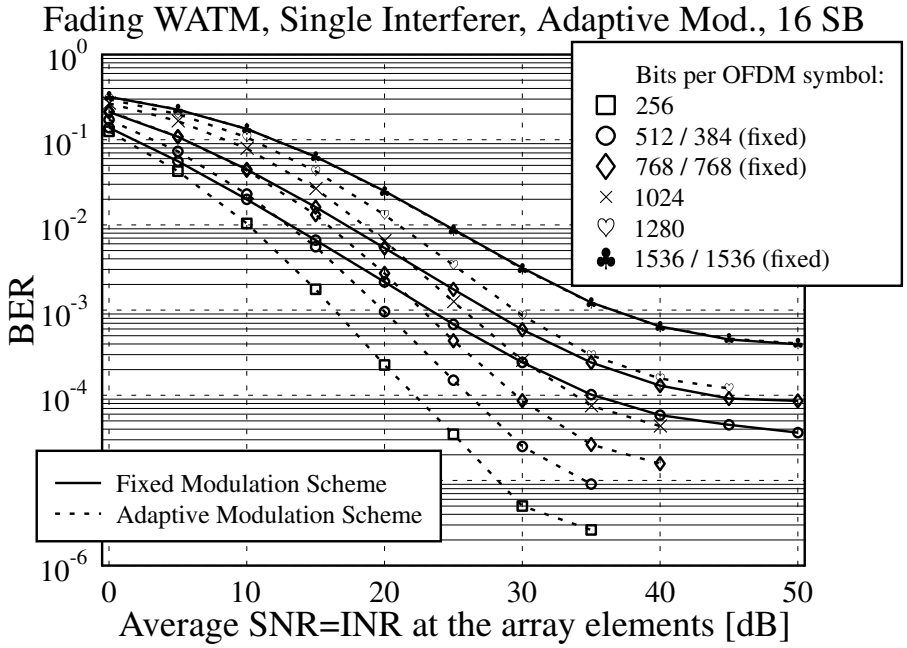


Figure 6.36: BER of 16-sub-band adaptive OFDM modem with two-branch SMI and 2 users in a fading indoor WATM environment, with pilot -based channel parameter estimation and one OFDM symbol delayed signalling of the modulation assignment using a diagonal loading of $\gamma = 1.0$

parameters – an effect which can be partly compensated for by a technique referred to as diagonal loading [149]. However, the effect of short reference sequences becomes obvious for a higher number of antenna elements, since more signal samples are required, in order to yield a reliable estimate of the correlation matrix. Hence our scheme proposed here is attractive for a scenario having 2–3 reception elements, where the interference is due to 1–2 dominant interferers and an additional Gaussian noise-like contribution of background interferers, which renders the SINR of Equation 6.15 to be an effective measure of channel quality. In conclusion, the proposed adaptive array-assisted AOFDM scheme resulted typically in an order of magnitude BER reduction due to employing adaptive modulation.

6.8 Chapter Summary and Conclusion

A range of adaptive modulation and spectral predistortion techniques have been presented in this chapter, all of which aim to react to the time and frequency dependent channel transfer function experienced by OFDM modems in fading time-dispersive channels. It has been

demonstrated that by exploiting the knowledge of the channel transfer function at the transmitter, the overall system performance can be increased substantially over the non-adaptive case. It has been pointed out that the prediction of the channel transfer function for the next transmission time slot and the signalling of the parameters are the main practical problems in the context of employing adaptive techniques in duplex communications.

The channel prediction accuracy is dependent on the quality of the channel estimation at the receiver, as well as on the temporal correlation of the channel transfer function between the uplink and downlink time slots. Two-dimensional channel estimation techniques [150, 236] can be invoked in order to improve the channel prediction at the receivers.

It has been demonstrated that sub-band adaptivity instead of subcarrier-by-subcarrier adaptivity can significantly decrease the necessary signalling overhead, with a loss of system performance that is dependent on the channel's coherence bandwidth. We have seen that sub-band adaptivity allows the employment of blind detection techniques in order to minimise the signalling overhead. Further work on blind detection algorithms as well as new signalling techniques is needed to improve the overall bandwidth efficiency of adaptive OFDM systems.

Pre-equalisation or spectral predistortion techniques have been demonstrated to significantly improve an OFDM system's performance in time-dispersive channels, while not increasing the system's output power. It has been shown that spectral predistortion can integrate well with adaptive modulation techniques, improving the system's performance significantly. We saw in Figure 6.1 that a data throughput of 0.5 bits/symbol has been achieved at 0 dB average channel SNR with a BER of below 10^{-4}.

An adaptive power and bit allocation algorithm was also highlighted and the performance of AOFDM in a beam-forming assisted multi-user scenario was characterised. Our treatment of adaptive modulation was conceptual in this chapter. By contrast, numerous analytical expressions were derived for characterising the achievable BER performance as well as for determining the modem mode switching thresholds in [90]. For more detailed aspects of adaptive modulation, please refer to [7, 215–217].

Part II

OFDM versus MC-CDMA Systems

Chapter 7

OFDM versus MC-CDMA

In 1993, a number of hybrid transmission techniques employing an amalgam of Code Division Multiple Access (CDMA) and Orthogonal Frequency Division Multiplexing (OFDM) were proposed [70, 73], which are expected to combine the benefits of pure CDMA and OFDM techniques. The aim of Chapters 7–9 is to examine various aspects of these techniques.

Since multi-carrier CDMA techniques rely on the combination of CDMA and OFDM, the two conventional techniques will be reviewed briefly. The concept of multi-carrier CDMA will be presented next.

7.1 Amalgamating DS-CDMA and OFDM

7.1.1 The DS-CDMA Component

Direct-Sequence (DS) CDMA is a spread-spectrum communication technique. DS-CDMA systems [237, 238] are capable of supporting a multiplicity of users within the same bandwidth by assigning different – typically unique user-specific – codes to different users for their communications, in order to be able to distinguish their signals from each other at the receiver. Spread-spectrum techniques were developed originally for military guidance and communications systems [239]. During the Second World War, radar engineers used spread-spectrum techniques to mitigate intentional jamming and to achieve high resolution ranging. During the late 1970s, the employment of spread-spectrum techniques was proposed for efficient cellular communication [240]. It is interesting to note that [240] addressed most essential issues involved in DS-CDMA cellular communications at such an early stage, although the proposed scheme was based on frequency hopping spread-spectrum communication. For a detailed historical review of spread-spectrum based communications, the reader is referred to the overview papers by Scholtz [239], by Yue [241] or to Chapter 2 of [242] by Simon, Omura, Scholtz and Levitt.

In CDMA systems, users share the same broad bandwidth all the time, using different

© 2006 John Wiley & Sons, Ltd

spreading codes. This unique feature of CDMA results in a soft capacity limit [240], while conventional Frequency Division Multiple Access (FDMA) and Time Division Multiple Access (TDMA) have hard capacity limits, since they use a finite number of orthogonal resources. The limiting factor of the capacity of CDMA systems is self-interference and Multi-User Interferences (MUI). The effects of these interference sources depend on the channel's characteristics and on the properties of the spreading codes used. Since any method, which reduces the interference is capable of increasing the overall user capacity in CDMA, significant research efforts have been invested in reducing the interference [243]. Several simple techniques, such as spatial isolation of users by cell sectorisation and discontinuous transmission relying on a voice activity detection or on the burstiness of the information source were shown to increase the user capacity [244]. Other sophisticated techniques employing interference cancellation [245], joint detection [246, 247] and adaptive antenna arrays [248] are realistic at the time of writing and offer further capacity gains.

One of the important merits of CDMA in cellular environments is its near-unity frequency reuse factor [244]. In TDMA and FDMA systems, the same frequency could be reused in different cells only beyond a sufficiently hight reuse distance, where the effects of interference between users of the same channel became negligible [2, 249, 250]. By contrast, in CDMA systems, the adjacent cells can use the same frequency in conjunction with unique cell-specific spreading sequences assigned for each cell site. Frequency planning is not required any more, while cell planning still remains an important issue, for example, for reasons of transmit power reduction [251]. An obvious advantage of the universal frequency reuse is the substantial potential increase in user capacity per unit bandwidth in comparison to 7-cell clusters. Another important advantage is the ability to use soft hand-off [244]. When a mobile roams across a cell boundary, its communication channel has to be handed over to a more suitable base station [2, 249]. In conventional multiple access systems often this means an abrupt RF channel change. Hence the communication link typically experiences a short discontinuity, while this RF channel change takes place. This is referred to as hard hand-off or hard hand-over [249]. In CDMA systems all base stations may use the same frequency. So-called Rake receivers [252, 253] are used in the mobile stations for combining the signals from the two base stations involved in the hand-over [251]. This soft hand-off makes seamless communications possible [254]. The soft hand-off also mitigates the multi-path fading effects during the hand-over period with the aid of cell site diversity [251].

In mobile communication the transmitted signal passes through multiple paths generally exhibiting different path lengths. The arrival time of the signals at a receiver spans from several tens of ns to several tens of μs, depending on the environments. The channel impulse characterises the scattering of the transmitted energy in the time domain. The associated time domain description results in Inter-Symbol Interference (ISI), where each impulse response component is exposed to fast Rayleigh fading. In conventional FDMA and TDMA systems complex channel equalisers are required for combating dispersion. As the transmission rate is increased, the number of ISI-contaminated adjacent symbols is proportionately increased [2]. Ironically, CDMA communication systems intentionally use significantly higher transmission rates, or chip rates, in order to take advantage of these scattered multi-path signals. Rake receivers [252,253] are capable of resolving each delayed signal component with an accuracy of a chip period. Each demodulated component is combined by the Rake receivers in order to make effective use of the channel-induced multi-path diversity. A system having a shorter chip period or wider bandwidth is capable of resolving lower delay differences and hence may

benefit from higher-order diversity. This characteristic together with the demands of higher data transfer rates render wide-band CDMA (W-CDMA) more attractive than the existing Pan-American narrow-band CDMA system known as IS-95 [255].

DS-CDMA systems typically suffer from the so-called near/far problem [256, 257]. This problem is more acute in the up-link due to its asynchronous nature, than in the synchronous down-link [251]. The base station's receiver will experience excessive multi-user interferences resulting from the undesirable non-zero asynchronous cross-correlation between the spreading sequences. This is so, even when the asynchronous cross-correlations of the sequences employed are low, due to the effects of the multi-path channel. Thus, a mobile station near the base station should reduce its transmit power so that all the reverse link signals at the base station's receiver can have an equal power, independent of their geographical locations. In open-loop power control schemes [257] a mobile station measures the power of the signal received from the base station for determining its required transmit power, assuming that the transmit path and the receiving path have approximately equal attenuations. Sometimes this is not the case, especially in frequency division duplex (FDD) CDMA systems. Thus closed-loop power control is required. In closed-loop power control schemes [258, 259] the base station sends power adjustment commands to each mobile station based on several measures, such as the received signal strength, the ratio of signal energy per bit to noise density (E_b/N_o) and the Bit Error Ratio (BER). Stability problems may arise in closed-loop power control and hence the global stability of the system has to be ensured [258]. Control latency and power adjustment levels are two key parameters in designing a closed-loop power control system [257].

Although power control is typically capable of tracking the power variation due to slow fading, it is almost impossible to compensate for the effects of fast Rayleigh fading, simply because the actual power variation speed exceeds the power control speed. In this case, interleaving combined with channel coding can support the operation of the power control in attaining the target performance. It is desirable to design the interleaver such that the originally consecutive symbols become separated in time by more than the channel's coherence time at the output of interleaver [257]. This implies that a higher interleaver depth is desirable for mobile stations travelling at lower speed, for example. However, a higher interleaver depth implies a longer processing delay, which is undesirable, for example, in interactive voice communications.

CDMA systems use a significantly higher bandwidth than the modulating signal's bandwidth by spreading the original signal with the aid of high rate spreading sequences. The noise-like spreading sequences play an important role in characterising a CDMA communication system. In frequency selective multi-path fading environments ensuring low off-peak, auto-correlation of the spreading sequences is necessary to reduce the Inter-Symbol Interference (ISI) and to combine the energy scattered in the time domain using Rake receivers. In multi-user environments additionally a low cross-correlation of the different user's sequences is required to distinguish the desired users' signals. The family of various spreading sequences will be reviewed in Chapter 8, while a range of related classic CDMA design aspects are treated in the excellent monographs by Viterbi and Lee [237, 238].

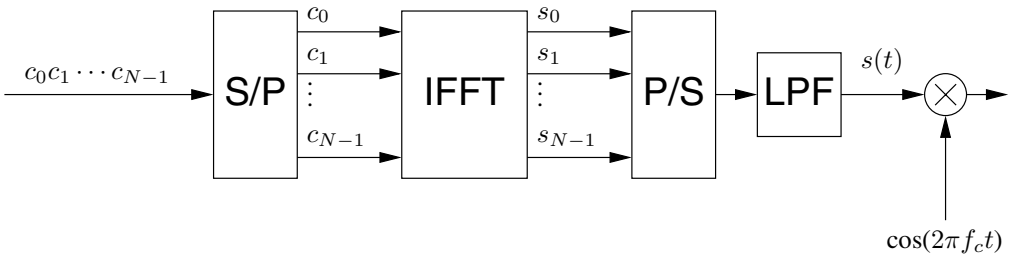


Figure 7.1: OFDM transmitter schematic

7.1.2 The OFDM Component

Orthogonal Frequency Division Multiplexing (OFDM) constitutes a specific form of multi-carrier modulation technique [260]. The basic approach of OFDM [1, 24, 261] is to group serial message symbols and transmit each message symbol on different frequency domain carriers at a reduced signalling rate. The conventional Frequency Division Multiplexing (FDM) technique requires guard bands between adjacent channels, since the receivers make use of band-pass filters to isolate each channel's signal. However, OFDM exploits the orthogonality of the subcarrier signals, although the actual frequency spectra of the different subchannels partially overlap with each other. The receiver in OFDM systems makes use of the orthogonality between the subcarriers to recover the symbols mapped on to a given subcarrier.

The complex baseband equivalent of the OFDM signal $s(t)$ in a symbol duration can be represented as [10]:

$$s(t) = \sum_{k=0}^{N-1} c_k \, e^{j2\pi \frac{k}{T} t} \, , \tag{7.1}$$

where N is the number of carriers and T is the subchannel signalling interval, while c_k is the symbol modulating the subcarrier k. In the next signalling interval a new set of symbols c_k is transmitted. At the receiver, the received signal is multiplied by $e^{-j2\pi \frac{n}{T} t}$ and integrated over a symbol duration in order to recover c_n. The resultant signal becomes, assuming perfect carrier frequency and symbol time recovery over an ideal channel:

$$\frac{1}{T} \int_0^T s(t) e^{-j2\pi \frac{n}{T} t} dt \quad = \quad \frac{1}{T} \sum_{k=0}^{N-1} c_k \int_0^T e^{j2\pi \frac{k}{T} t} e^{-j2\pi \frac{n}{T} t} dt = c_n \, . \tag{7.2}$$

In order to implement directly the transmitter and the receiver of an OFDM system, N oscillators are required.

Weinstein and Ebert [9] presented a method involving the Discrete Fourier Transform (DFT) to perform baseband modulation and demodulation, which spurred the development of OFDM systems with the advent of efficient real-time Digital Signal Processing (DSP) technology. By sampling the modulated signal N times during an OFDM symbol at instants of $t = \frac{m}{N}T$, Equation 7.1 becomes:

$$s(\frac{m}{N}T) = \sum_{k=0}^{N-1} c_k e^{j2\pi \frac{km}{N}} \ , \ (\text{for } m \ = \ 0, \ 1, \ \cdots \ , \ N-1) \ . \tag{7.3}$$

Since $s(\frac{m}{N}T)$ depends only on m, it can be represented as s_m in discrete form, and Equation 7.3 can also be written as:

$$s_m = N \cdot \text{IDFT}(\{c_k\}) \ , \ (\text{for } m \ = \ 0, \ 1, \ \cdots \ , \ N-1), \tag{7.4}$$

where IDFT represents the Inverse Discrete Fourier Transform operator. The efficient implementation of the IDFT is the Inverse Fast Fourier Transform (IFFT). The overall structure of the OFDM transmitter is shown in Figure 7.1.

The N message sequences, $c_0, \ c_1, \ \cdots \ , \ c_{N-1}$, form a frame, which is converted into a parallel form, where c_k is modulating the kth carrier. The IFFT module takes the parallel data and calculates N sampled time domain signals, $s_0, \ s_1, \ \cdots \ , \ s_{N-1}$, which are low-pass filtered to generate the continuous time domain signal. This baseband time domain signal modulates a single carrier frequency and transmitted. The IFFT eliminates the use of N oscillators and renders the OFDM transmitter implementationally attractive [10].

At the OFDM receiver, the reverse action takes place. The down-converted received signal is sampled at a rate of N/T and converted into a parallel stream of N values. Then, the FFT is applied in order to recover the desired frequency components, i.e. the information symbols, c_k.

In mobile channel environments the transmitted signals experience reflection and refraction [2]. This results in different path delays ranging from several ns to tens of μs, depending on the environments encountered. The receiver has to have a channel equaliser in order to cope with the time-dispersion of the received signals. OFDM reduces this requirement by increasing the signalling interval duration. However, it needs a guard time between the OFDM signaling intervals in order to reduce the ISI. Instead of a passive guard space, inserting a quasi-periodically repeated cyclic prefix is used to remove inter-symbol interference [260]. Let us assume that the channel impulse response, $h(t)$, spans $(\nu + 1)\frac{T}{N}$, where $\nu \ll N$ and the corresponding discrete channel impulse response, $h_n, \ 0 \ \leq \ n \ \leq \ \nu$, is $h(\frac{n}{N}T)$. Let $s_{i,n}$ be the nth transmitted symbol in the ith frame as defined in Equation 7.4. The cyclic prefix consists of $s_{i,N-\nu}, \ s_{i,N-\nu+1}, \ \cdots \ , \ s_{i,N-1}$, which is inserted before $s_{i,0}, \ s_{i,1}, \ \cdots \ , \ s_{i,N-1}$. Then, the sampled baseband received signal, $r_{i,n}$, for

$n = -\nu,\ -\nu+1,\ \cdots,\ -1,\ 0,\ 1,\ 2,\ \cdots,\ N-1$, becomes

$$\begin{aligned}
r_{i,-\nu} &= h_0 s_{i,N-\nu} + h_1 s_{i-1,N-1} + h_2 s_{i-1,N-2} + \cdots + h_\nu s_{i-1,N-\nu} \\
r_{i,-\nu+1} &= h_0 s_{i,N-\nu+1} + h_1 s_{i,N-\nu} + h_2 s_{i-1,N-1} + \cdots + h_\nu s_{i-1,N-\nu+1} \\
&\vdots \quad\quad \vdots \\
r_{i,-1} &= h_0 s_{i,N-1} + h_1 s_{i,N-2} + h_2 s_{i,N-1} + \cdots + h_\nu s_{i-1,N-1} \\
r_{i,0} &= h_0 s_{i,0} + h_1 s_{i,N-1} + h_2 s_{i,N-2} + \cdots + h_\nu s_{i,N-\nu} \\
r_{i,1} &= h_0 s_{i,1} + h_1 s_{i,0} + h_2 s_{i,N-1} + \cdots + h_\nu s_{i,N-\nu+1} \\
&\vdots \quad\quad \vdots \\
r_{i,\nu} &= h_0 s_{i,\nu} + h_1 s_{i,\nu-1} + h_2 s_{i,\nu-2} + \cdots + h_\nu s_{i,0} \\
&\vdots \quad\quad \vdots \\
r_{i,N-1} &= h_0 s_{i,N-1} + h_1 s_{i,N-2} + h_2 s_{i,N-3} + \cdots + h_\nu s_{i,N-\nu+1}\ .
\end{aligned}$$

The first ν samples are discarded and the remaining N samples are processed by FFT in the receiver. The remaining N samples can be represented in a more compact form:

$$r_{i,n} = \sum_{j=0}^{\nu} h_j s_{i,(n-j \bmod N)} \text{ for } n = 0,\ \cdots, N-1\ . \tag{7.5}$$

The recovered data symbol, $\hat{c}_{i,k}$, becomes

$$\begin{aligned}
\hat{c}_{i,k} &= \sum_{n=0}^{N-1} r_{i,n} e^{-j2\pi \frac{n}{N} k} &(7.6)\\
&= c_{i,k} \sum_{n=0}^{\nu} h_n e^{-j2\pi \frac{n}{N} k} &(7.7)\\
&= c_{i,k} H_k\ , &(7.8)
\end{aligned}$$

where H_k is the frequency domain channel transfer function and $c_{i,k} = \sum_{n=0}^{N-1} s_{i,n} e^{-j2\pi \frac{n}{N} k}$ was used to arrive at Equation 7.7. Equation 7.8 states that the original symbol, $c_{i,k}$, can be recovered without inter-frame interference or inter-subcarrier interference given the knowledge of $\{H_k\}$, which can be estimated.

The frequency spectrum of an OFDM signal using no pulse shaping is presented in Figure 7.2. The required bandwidth is approximately $N \times \frac{1}{T}$, which is the minimum bandwidth imposed by Nyquist's sampling theorem. Since the first spectral sidelobes are only about -17.3dB below the passband level, various pulse shaping and wavelet based transform methods were proposed to suppress the sidelobes [260] which result in adjacent channel interference.

One of the main drawbacks of the above OFDM system is the "peaky" time domain signal, which requires amplifiers having a high dynamic range [49, 262]. This issue is discussed in

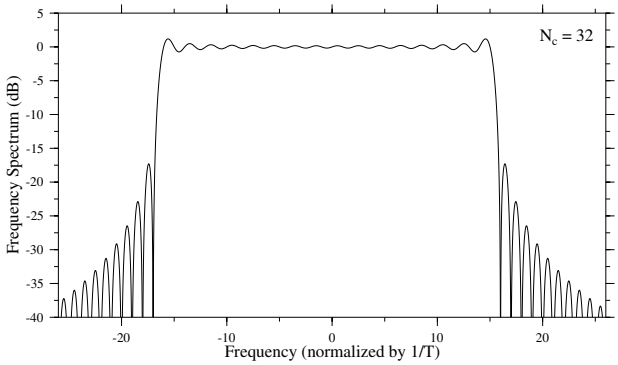


Figure 7.2: Power spectrum of OFDM signal using 32 carriers, without any pulse shaping

more depth in Chapter 11 of the extended version of this book [90]. Another impediment is that OFDM systems are more sensitive to carrier frequency drift, than single carrier [62, 65] systems.

7.2 Multi-Carrier CDMA

A range of novel techniques combining DS-CDMA and OFDM have been presented in the literature [70, 71, 73, 263, 264].

A DS-CDMA system applies spreading sequences in the time domain and uses Rake receivers to optimally combine the time-dispersed energy in order to combat the effects of multi-path fading. However, in indoor wireless environments the time-dispersion is low, on the order of nano seconds, and hence a high chip rate, of the order of tens of MHz, is required for resolving the multi-path components. This implies a high clock-rate, high power consumption as well as implementation difficulties. In order to overcome these difficulties, several techniques have been proposed, which combine DS-CDMA and multi-carrier modulation, such as MC-CDMA [70, 71, 73], MC-DS-CDMA [263] and Multi-Tone CDMA (MT-CDMA) [264]. This overview is mainly based on references [74, 265] by Prasad and Hara, [266] by Scott *et al.*

7.2.1 MC-CDMA

In MC-CDMA, instead of applying spreading sequences in the time domain, we can apply them in the frequency domain, mapping a different chip of a spreading sequence to an individual OFDM subcarrier. Hence each OFDM subcarrier has a data rate identical to the original input data rate and the multicarrier system "absorbs" the increased rate due to spreading in a wider frequency band. The transmitted signal of the ith data symbol of the jth user $s_i^j(t)$ is

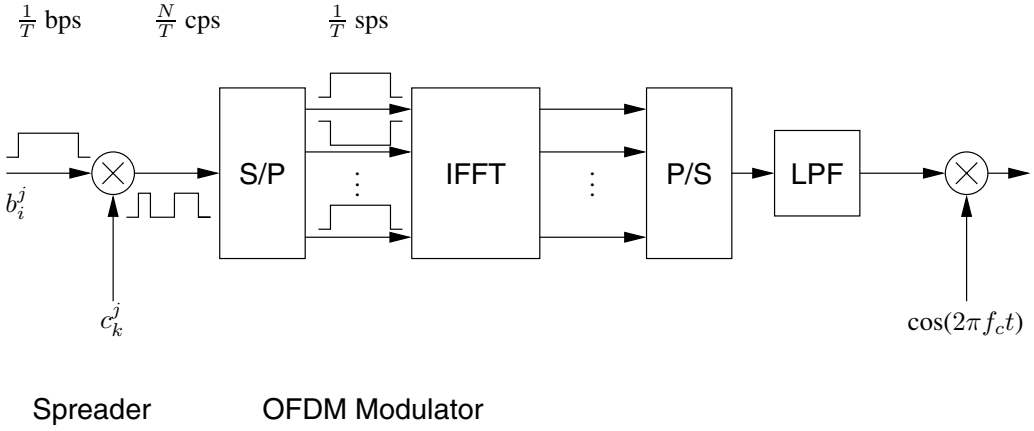


Figure 7.3: Transmitter schematic of MC-CDMA

written as [70, 267]:

$$s_i^j(t) = \sum_{k=0}^{N-1} b_i^j \, c_k^j \, e^{2\pi(f_0 + k f_d)t} \, p(t - iT) \, , \tag{7.9}$$

where

- N is the number of subcarriers
- b_i^j is the ith message symbol of the jth user
- c_k^j represents the kth chip, $k = 0, \cdots, N-1$, of the spreading sequence of the jth user
- f_0 is the lowest subcarrier frequency
- f_d is the subcarrier separation
- $p(t)$ is a rectangular signalling pulse shifted in time given by:

$$p(t) \triangleq \begin{cases} 1 & \text{for } 0 \leq t \leq T \\ 0 & \text{otherwise .} \end{cases} \tag{7.10}$$

If $1/T$ is used for f_d, the transmitted signal can be generated using the IFFT, as in the case of an OFDM system. The overall transmitter structure can be implemented by concatenating a DS-CDMA spreader and an OFDM transmitter, as shown in Figure 7.3. At the spreader, the information bit, b_i^j, is spread in the time domain by the jth user's spreading sequence, c_k^j, $k = 0, \cdots, N-1$. In this implementation, high speed operations are required at the output of the spreader in order to carry out the chip-related operations. The spread chips are fed into the serial-to-parallel (S/P) block and IFFT is applied to these N parallel chips. The output values of the IFFT in Figure 7.3 are time domain samples in parallel form. After being

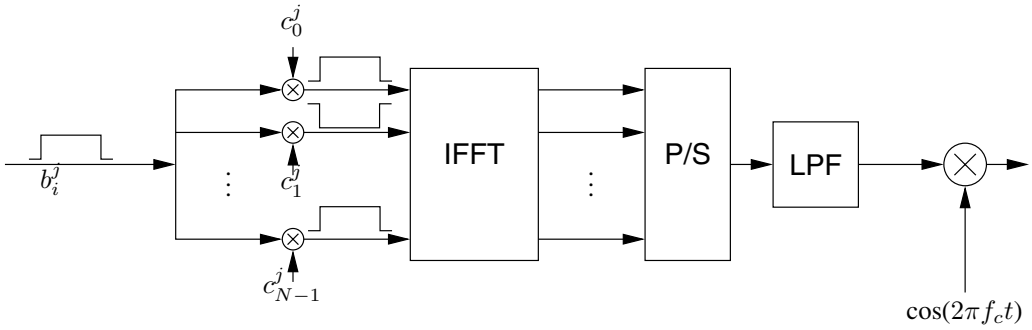


Figure 7.4: Alternative transmitter schematic of MC-CDMA

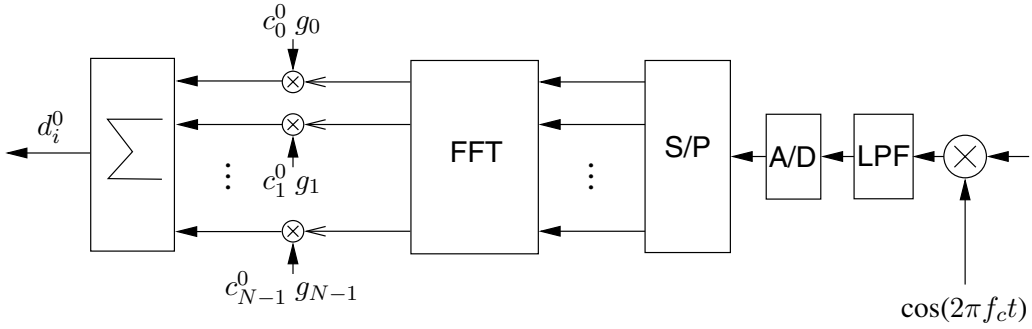


Figure 7.5: Receiver schematic of MC-CDMA

parallel to serial (P/S) conversion these time domain samples are low-pass-filtered, in order to obtain the continuous time domain signal. The signal modulates the carrier and is transmitted to the receiver.

Figure 7.4 shows another implementation, which removes the time domain spreader. In this implementation, the spreading sequence is applied directly to the identical parallel input bits. Hence, the high speed spreading operation is not required.

The spreading sequences in MC-CDMA separate other users' signal from the desired signal, provided that their spreading sequences are orthogonal to each other. Orthogonal codes have zero cross-correlation and hence they are particularly suitable for MC-CDMA. Walsh codes and orthogonal Gold codes are two well known such codes, which will be examined in Chapter 8.

At the MC-CDMA receiver shown in Figure 7.5 each carrier's symbol, i.e. the corresponding chip c_k^j of user j, is recovered using FFT after sampling at a rate of N/T samples/sec and the recovered chip sequence is correlated with the desired user's spreading code in order to recover the original information, b_i^j. Let us define the ith received symbol at the kth carrier

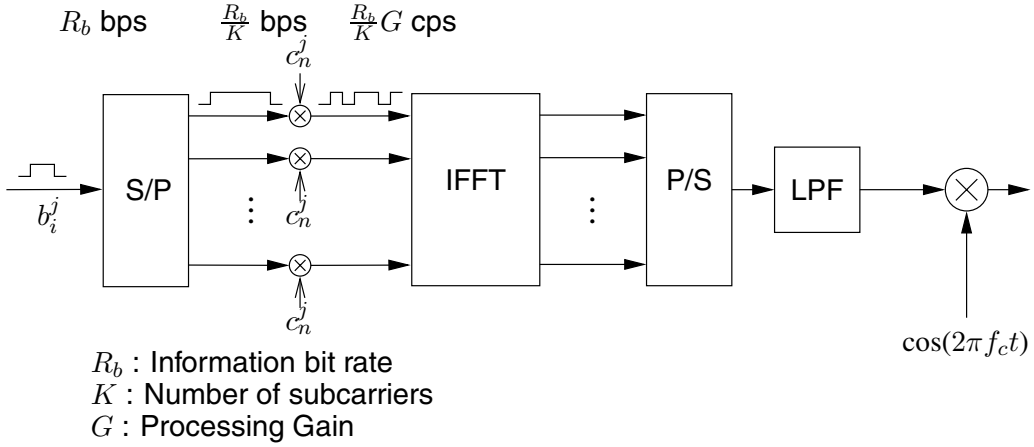


Figure 7.6: Transmitter schematic of MC-DS-CDMA

in the downlink as:

$$r_{k,i} = \sum_{j=0}^{J-1} H_k \, b_i^j \, c_k^j + n_{k,i} \; , \tag{7.11}$$

where J is the number of users, H_k is the frequency response of the kth subcarrier and $n_{k,i}$ is the corresponding noise sample. The MC-CDMA receiver of the 0-th user multiplies $r_{k,i}$ of Equation 7.11 by its spreading sequence chip, c_k^0, as well as by the gain, g_k, which is given by the reciprocal of the estimated channel transfer factor of subcarrier k, for each received subcarrier symbol for $k = 0, \cdots, N-1$, and sums all these products, in order to arrive at the decision variable, d_i^0, which is given by:

$$d_i^0 = \sum_{k=0}^{N-1} c_k^0 \, g_k \, r_{k,i} \; . \tag{7.12}$$

Without the frequency domain equalisation of the received subcarrier symbols, the orthogonality between the different users cannot be maintained. Several methods have been proposed for choosing g_k [70, 74, 267]. The associated BER analysis was performed using various equalisation methods over both the Rayleigh channels and Rician channels by Yee and Linnartz [70]. The comparative summary of numerical results for various equalisation strategies was given, for example, by Prasad and Hara [74, 265].

7.2.2 MC-DS-CDMA

In order to transmit high-rate data with sufficient processing gain, the chip rate of the DS-CDMA system should be significantly higher than the practical limit imposed mainly by the processing speed and power consumption of state-of-the-art electronics. In this case, parallel transmissions of DS-CDMA signals using the OFDM structure [74, 263] can be a solution.

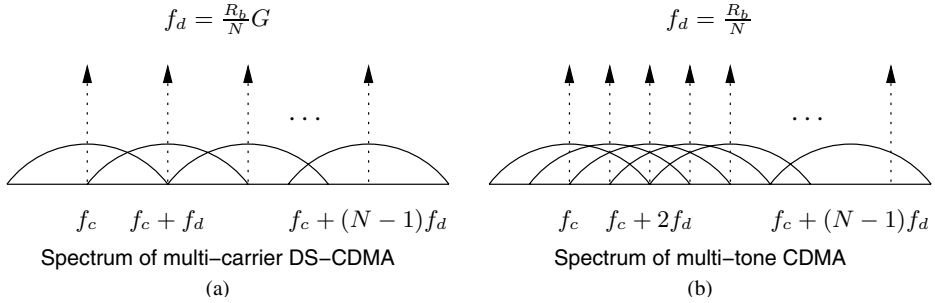


Figure 7.7: Typical power spectra of MC-DS-CDMA and MT-CDMA

Figure 7.6 shows the transmitter structure of a MC-DS-CDMA system.The N consecutive input bits of the jth user, $b_i^j,\ i = 0 \cdots N-1$, are serial-to-parallel converted first. Then, each bit b_i^j is spread by the jth user's spreading sequence in the time domain. The other operations are identical to those of MC-CDMA. In other words, in the MC-CDMA scheme of Figure 7.3 the data bits arriving at a rate of $1/T$ are first spread and hence have a rate of N/T, before reducing the rate again to $1/T$. By contrast, in the MC-DS-CDMA scheme of Figure 7.6 the bit rate of R_b is first reduced to R_b/N and then we produce the rate R_bG/N using spreading.

Figure 7.7(a) shows the typical spectrum of the MC-DS-CDMA signal operated using the schematic of Figure 7.6. The subcarrier separation, f_d, meets the orthogonality condition [74] of:

$$f_d = \frac{R_b}{N}G\ , \tag{7.13}$$

where R_b is the source bit rate, N is the number of subcarriers and G is the processing gain. When N is equal to G, the MC-DS-CDMA spectrum [263] has the same shape, as that of an MC-CDMA system [70]. While the spectra of MC-CDMA signals [70] and MC-DS-CDMA signals [263] exhibit orthogonality between the subcarriers, that of the MT-CDMA scheme of Figure 7.7(b) does not maintain orthogonality between the subcarriers.

The transmitted signal $s_i^j(t)$ of the jth user during the ith signalling interval is written as:

$$s_i^j(t) = \sum_{k=0}^{N-1}\sum_{g=0}^{G-1} b_{k,i}^j c_g^j\ p(t - iT_s - gT_c)\cdot e^{2\pi(f_0+kf_d)t}\ , \tag{7.14}$$

where $b_{k,i}^j$ is the ith bit of the jth user modulating the kth subcarrier after serial-to-parallel conversion, $c_g^j,\ g = 0 \cdots G-1$ represents the jth user's spreading sequence, $T_s = \frac{N}{R_b}$ is the signalling interval, $T_c = \frac{T_s}{G}$ is the chip duration and $p(t)$ is defined in Equation 7.10.

7.2.3 MT-CDMA

MT-CDMA is a combined technique employing time domain spreading and a similar multi-carrier transmission scheme to that of the MC-DS-CDMA scheme of Figure 7.6. However,

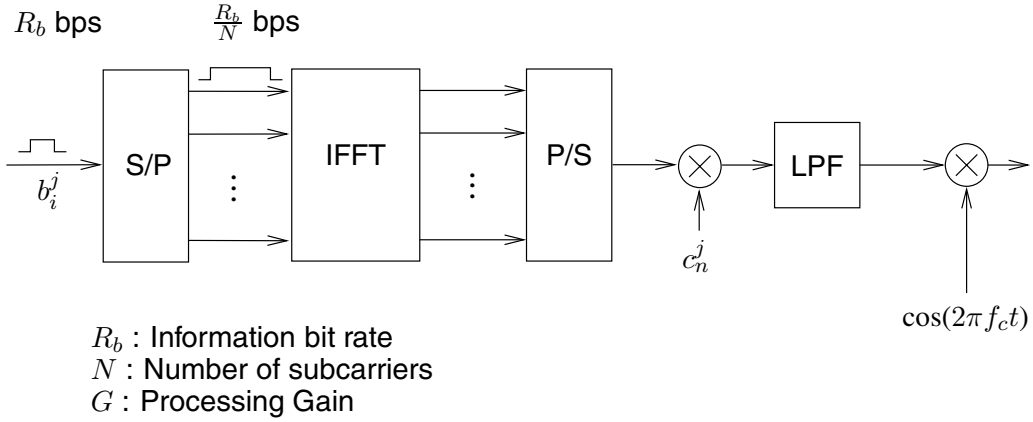


Figure 7.8: Transmitter schematic of MT-CDMA

the time domain spreading is applied after the IFFT stage. Figure 7.8 represents a simple block diagram of the transmitter structure. The required operations are the same as in OFDM, but spreading takes place after the IFFT stage. In this way, the system has a multiple access capability. The corresponding power spectrum is shown in Figure 7.7(b). Each subcarrier's spectrum overlaps with other subcarriers' spectra. The subcarrier frequency spacing is given by [74]:

$$f_d = \frac{R_b}{N}\,, \tag{7.15}$$

which does not retain the subcarriers' orthogonality. The main intention of this operation is to increase the processing gain within a given bandwidth.

7.3 Further Research Topics in MC-CDMA

The seminal contributions of [70, 71, 73, 263, 264] have motivated intensive further research in the field of wireless communications [70, 71, 74, 268–311].

The fundamental aim of MC-CDMA research has been the support of high data rate services in hostile wireless environments. As noted before, the main benefit of combining OFDM with DS-spreading is that it is possible to prevent the obliteration of certain subcarriers by deep frequency domain fades. This is achieved by spreading each subcarrier's signal with the aid of a spreading code and thereby increasing the achievable error-resilience, since in case of corrupting a few chips of a spreading code the chances are that the subcarrier signal still may be recovered.

The performance of both OFDM and MC-CDMA can be improved also by frequency hopping, when a fraction of the subcarriers is activated, concentrating for example on activating the high-quality subcarriers. The frequency domain repetition of the same information symbols may also be invoked, where the same symbols are mapped to several sub-

carriers, although this inevitably results in the reduction of the system's effective throughput [70, 71, 296, 305]. Multicarrier DS-CDMA using adaptive frequency-hopping has been studied in [311], while adaptive subchannel allocation based multicarrier DS-CDMA was the subject of [288]. Yang *et al.* studied constant-weight code aided multicarrier DS-CDMA in conjunction with slow frequency-hopping [271, 272, 300].

7.4 Chapter Summary and Conclusion

In this chapter we commenced by a rudimentary discourse on combining DS-CDMA and OFDM. We have briefly reviewed three types of multi-carrier spread-spectrum schemes combining DS-CDMA and OFDM techniques, namely MC-CDMA [70, 71, 73], MC-DS-CDMA [263] and MT-CDMA [264]. While MC-CDMA employs frequency domain spreading, the other two schemes, i.e. the MC-DS-CDMA and MT-CDMA schemes, employ time domain spreading. Hence, MC-CDMA is capable of exploiting frequency diversity in an explicit manner, since the energy of a symbol is spread over several subcarriers. On the other hand, since all the energy of a symbol is confined to one subcarrier in the MC-DS-CDMA and MT-CDMA schemes, the potential frequency diversity provided by the independently fading different subcarriers cannot be exploited, unless a channel coding scheme is employed in conjunction with cross-subcarrier interleaving [74].

Compared to a MC-DS-CDMA scheme requiring the same frequency band, MT-CDMA is capable of providing a significantly higher spreading factor than that of MC-DS-CDMA, resulting in lower self-interference and in a better suppression of the Multiple Access Interference (MAI) [264]. However, MT-CDMA suffers from inter-subcarrier interference due to the fact that the subcarriers are not orthogonal to each other. Since MC-DS-CDMA is capable of providing backward compatibility with the existing IS-95 DS-CDMA system, a specific form of MC-DS-CDMA has been chosen as one of the Third Generation (3G) mobile communication standards [312].

Prasad and Hara reported that MC-CDMA employing Minimum Mean Square Error Combining (MMSEC) shows the lowest BER among the three above-mentioned multi-carrier spread-spectrum schemes in a downlink scenario [265]. Hence, the performance of MC-CDMA in a downlink scenario will be investigated in more depth in Chapter 9.

The further outline and the rationale of Part II of the book, which entails Chapters 8–9 is highlighted below. Since the properties of spreading sequences are equally important in multicarrier CDMA as in DS-CDMA, the properties of various spreading sequences are reviewed in Chapter 8. One of the main problems associated with the implementation of multi-carrier communication systems is their high Peak-to-Mean Envelope-Power Ratio (PMEPR), requiring highly linear power amplifiers. The envelope power of the MC-CDMA signal is analysed in intricate detail in Chapter 11 of the extended version of this book [90]. Several orthogonal spreading sequences are examined, in order to assess their ability to maintain low PMEPR of the transmitted signal. The effects of reduced PMEPR are investigated in terms of the BER performance and the out-of-band frequency spectrum.

Chapter 8

Basic Spreading Sequences

A spread spectrum communication system spreads the original information signal using user-specific signature sequences. The receiver then correlates the synchronised replica of the signature sequences with the received signal, in order to recover the original information. Due to the noise-like properties of the spreading sequences, "eavesdropping" is not straightforward. DS-CDMA exploits the code's autocorrelation properties in order to optimally combine the multipath signals of a particular user. By contrast, the different users' codes exhibit a low cross-correlation, which can be exploited for separating each user's signal. MC-CDMA also relies on this cross-correlation property in supporting multi-user communications. The characteristics of the spreading sequences play an important role in terms of the achievable system performance and hence the properties of several sequences will be examined in this chapter.

8.1 PN Sequences

Pseudo-Noise (PN) sequences are binary sequences, which exhibit noise-like properties. Maximal length sequences (m-sequences), Gold sequences and Kasami sequences are well-known PN sequences. Other important PN sequences are considered in [242].

8.1.1 Maximal Length Sequences

Various pseudo-random codes can be generated using Linear Feedback Shift Registers (LFSR). The so-called generator polynomial or LFSR connection polynomial governs all the characteristics of the generator. For a given generator polynomial, there are two ways of implementing LFSRs [242, 313]. The sequence generator shown in Figure 8.1 uses only the LFSR's output bits for feeding information back into several intermediate stages of the shift register, which is attractive for high speed hardware as well as software implementations. The other implementation known as the Fibonacci feedback generator [313], which is shown in Figure 8.2, is capable of generating several delayed versions of the same sequence at the output of each shift register without any additional logic. Note that the connection position is

OFDM and MC-CDMA: A Primer L. Hanzo and T. Keller
© 2006 John Wiley & Sons, Ltd

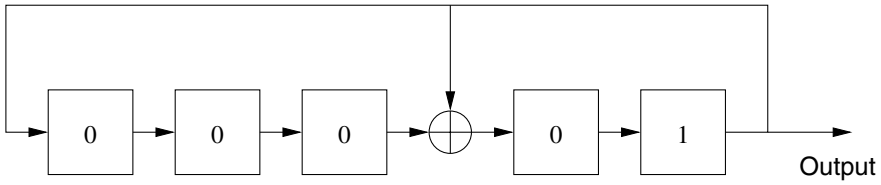


Figure 8.1: Galois Field based feedback implementation of the m-sequence generator. The generator polynomial of $g(x) = 1 + x^2 + x^5$ determines the positions of the non-zero feedback taps. Note that Galois Field 2 additions and subtractions are equivalent.

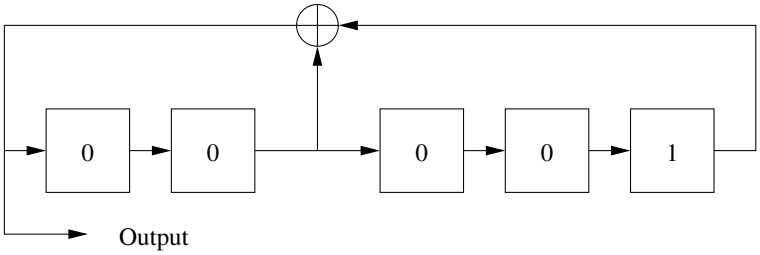


Figure 8.2: Fibonacci feedback implementation of the m-sequence generator. The same generator polynomial was employed as in Figure 8.1.

reversed in Figure 8.2, in order to generate the same sequences as the Galois implementation of [313] as shown in Figure 8.1. Shift-register sequences having the maximum possible repetition period of $2^r - 1$ for an *r*-stage shift register are referred to as maximal-length sequences or *m*-sequences. A so-called primitive generator polynomial [313] always yields an *m*-sequence. The *m*-sequences have three important properties, namely the so-called balance property, the run-length property as well as the shift-and-add property [314]. The periodic autocorrelation function $R_a(k)$ of the sequence $\{a_n\}$ is defined as:

$$R_a(k) \triangleq \frac{1}{N} \sum_{n=0}^{N-1} a_n a_{n+k} \ , \tag{8.1}$$

where N is the period of the sequence. The periodic autocorrelation function of an m-sequence is given by:

$$R_a(k) = \begin{cases} 1.0 & k = lN \\ -\frac{1}{N} & k \neq lN \ , \end{cases} \tag{8.2}$$

where l is an integer and N is the period of the *m*-sequence. The excellent auto-correlation property manifested by the high ratio of these two $R_a(k)$ values is a consequence of the above-mentioned first and third properties, as justified in references [242, 313, 314]. The above-mentioned good autocorrelation features justify the employment of m-sequences for example in the Pan-American IS-95 standard CDMA system [255]. Moreover, as the cross-correlation property of these sequences is relatively poor compared to that of the family of

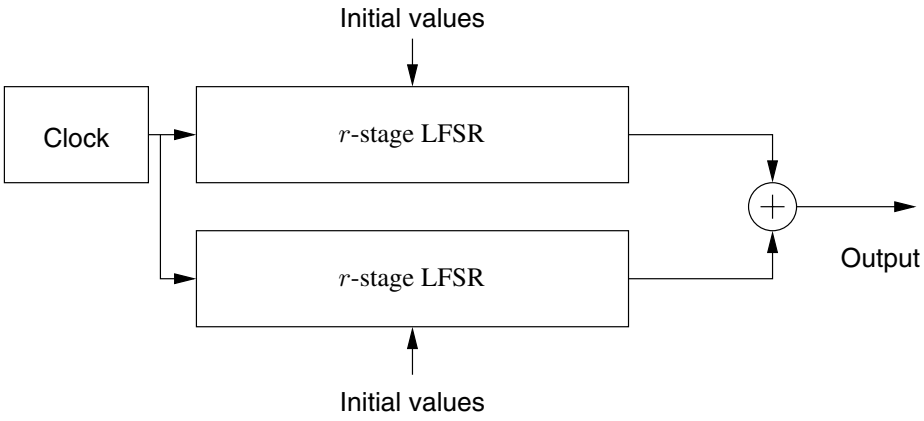


Figure 8.3: Schematic of a Gold code generator

Gold codes, usually the same sequences with different offsets are employed for different users or for different base stations in IS-95 based networks.

8.1.2 Gold Codes

Certain pairs of m-sequences having the same degree can be used for generating the so-called Gold codes by linearly combining two *m*-sequences associated with different offsets, where the operations are defined over the so-called finite Galois field [242, 313]. Not all pairs of *m*-sequences yield Gold codes and those which do are referred to as *preferred pairs*. The autocorrelations and cross-correlations of Gold codes may exhibit the legitimate values of $\{-1, -t(m), t(m) - 2\}$, where

$$t(m) = \begin{cases} 2^{(m+1)/2} + 1 & \text{for odd } m \\ 2^{(m+2)/2} + 1 & \text{for even } m \ . \end{cases} \tag{8.3}$$

Gold codes exhibit lower peak cross-correlations, than m-sequences, as shown in Table 13-2-1 of [260] and hence they differentiate among different users more confidently or distinctively. Furthermore, the cross-correlation function of Gold codes exhibits numerous "-1" values, which is the lowest value among the three possible cross-correlation values. By contrast, Kasami sequences exhibit a lower proportion of "-1"s in their cross-correlation functions, while exhibiting a peak cross-correlation, which is half of that of the Gold codes.

The generation of Gold codes is straightforward. The simple block diagram of a Gold code generator is shown in Figure 8.3. Using two preferred *m*-sequence generators of degree *r*, in conjunction with a set of r initial values in the upper LFSR where at least one value is non-zero, 2^r number of different Gold codes can be obtained by changing the set of r initial values of the bottom LFSR according to the range of 0 to $2^r - 1$. Additional Gold sequences can be obtained by setting the contents of the upper LFSR to all zeros, which results in a Gold sequence that is identical to the second *m*-sequence itself, which is generated from the bottom LFSR of Figure 8.3. Hence in total, $2^r + 1$ Gold codes can be obtained from a Gold

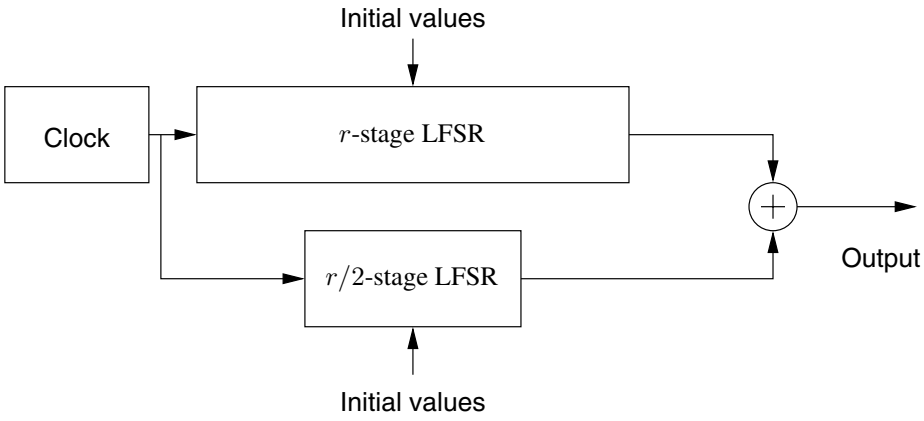


Figure 8.4: Schematic of a Kasami sequence generator

code generator, which is characterised by a pair of preferred m-sequences.

8.1.3 Kasami Sequences

Kasami sequences have optimal cross-correlation values, reaching the so-called Welch lower bound [242, 260]. The lower bound on the cross-correlation between any pair of binary sequences of period *n* in a set of *m*-sequences is [260]:

$$\phi_{max} \geq n\sqrt{\frac{M-1}{Mn-1}}\,. \tag{8.4}$$

Kasami sequences can be generated by the following procedure [242]. For the *m*-sequence $\mathbf{a}$, the so-called decimated sequence of $\mathbf{a}$ is obtained by taking every qth bit of $\mathbf{a}$, which is denoted by $\mathbf{a}[\mathbf{q}]$. By choosing $q = 2^{r/2} + 1$, where r is the degree of sequence $\mathbf{a}$, having retained every qth bit of $\mathbf{a}$, $\mathbf{a}[\mathbf{q}]$ is periodic with the period of $2^{r/2} - 1$. By repeating $\mathbf{a}[\mathbf{q}]$ q times, a new sequence $\mathbf{b}$ of length $2^r - 1$ is obtained. With the aid of $\mathbf{a}$ and $\mathbf{b}$, we form a new set of sequences by module-two adding $\mathbf{a}$ and the $2^{r/2} - 2$ number of cyclically shifted versions of the sequence $\mathbf{b}$. Including $\mathbf{a}$ and $\mathbf{b}$, we get a total of $2^{r/2}$ number of sequences. These sequences are the so-called Kasami sequences [242]. The hardware implementation of Kasami sequences is daunting, because the decimation process requires a high clock frequency. Fortunately, the decimated sequence itself is an *m*-sequence [242] of order $r/2$ and this fact can be exploited for implementing Kasami sequence generators, as shown in Figure 8.4. The *m*-sequence generated by the r-stage LFSR and the other *m*-sequence output by the $r/2$-stage LFSR are added in the binary Galois field in order to form a Kasami sequence.

8.2 Orthogonal Codes

Orthogonal codes have zero cross-correlation. They may appear attractive in terms of replacing PN codes, which have non-zero cross-correlations. However, the cross-correlation value is zero only, when there is no offset between the codes. In fact, they exhibit higher cross-correlations at non-zero offsets, than PN codes. Their autocorrelation properties are usually not attractive either. Nonetheless, orthogonal codes have found application, for example, in perfectly synchronised environments, such as in the down-link of mobile communications.

There are several so-called code expansion techniques that can be used in order to generate orthogonal codes. Probably the Hadamard transform [313] is the best-known technique. A modified Hadamard transform also appeared in the literature [315], which is essentially constituted by the Hadamard transform using a different transform coefficient indexing. Orthogonal Gold codes show reasonable cross-correlation and off-peak autocorrelation values, while providing perfect orthogonality in the zero-offset case. Finally, the multi-rate orthogonal codes of Section 8.2.3 are attractive, since they can provide variable spreading factors depending on the information rate to be supported.

8.2.1 Walsh Codes

Walsh codes are generated by applying the Hadamard transform [313] to a one by one dimensional zero matrix repeatedly. The Hadamard transform is defined as [313]:

$$\begin{aligned} \mathbf{H}_1 &= [0] \\ \mathbf{H}_{2n} &= \begin{bmatrix} \mathbf{H}_n & \mathbf{H}_n \\ \mathbf{H}_n & \overline{\mathbf{H}}_\mathbf{n} \end{bmatrix}. \end{aligned} \tag{8.5}$$

This transform gives us a Hadamard matrix, $\mathbf{H}_n$, only for $n = 2^i$, where i is an integer. The Hadamard matrix is a symmetric square-shaped matrix. Each column or row corresponds to a Walsh code of length n. Every row of $\mathbf{H}_n$ is orthogonal to all other rows.

As an example, let us consider the case of n = 8. We can generate 8-bit Walsh codes, $\mathbf{H}_8$, applying the transform continuously from $\mathbf{H}_1$ three times repeatedly. The resultant matrix is as follows:

$$\mathbf{H}_8 = \begin{bmatrix} 0 & 0 & 0 & 0 & 0 & 0 & 0 & 0 \\ 0 & 1 & 0 & 1 & 0 & 1 & 0 & 1 \\ 0 & 0 & 1 & 1 & 0 & 0 & 1 & 1 \\ 0 & 1 & 1 & 0 & 0 & 1 & 1 & 0 \\ 0 & 0 & 0 & 0 & 1 & 1 & 1 & 1 \\ 0 & 1 & 0 & 1 & 1 & 0 & 1 & 0 \\ 0 & 0 & 1 & 1 & 1 & 1 & 0 & 0 \\ 0 & 1 & 1 & 0 & 1 & 0 & 0 & 1 \end{bmatrix} \tag{8.6}$$

The first column is the all-zero sequence and the second one is an alternating sequence of "0" and "1". This is true for all Hadamard matrices. Let $\mathbf{H}_8[i]$ and $\mathbf{H}_8[j]$, $i,\ j\ =\ 0 \cdots 7$, be two sequences formed from the ith and the jth rows of $\mathbf{H}_8$. Then, we can verify that $\mathbf{H}_8[i]$ and $\mathbf{H}_8[j]$ are orthogonal to each other. Let us refer to i and j as the indices of $\mathbf{H}_8$.

A possible hardware implementation of the $\mathbf{H}_8$ Walsh code is shown in Figure 8.5. It comprises two T-flipflops, a clock generator, three AND gates denoted as $\otimes$ and one XOR

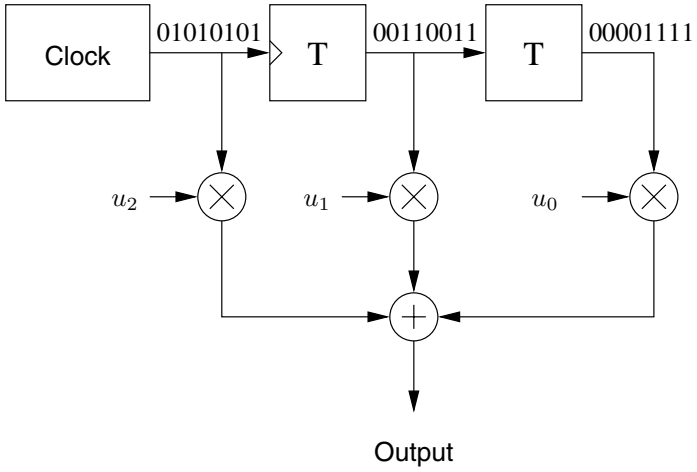


Figure 8.5: Implementation of a Walsh code generator of length=2^3. (© 1995 Prentice-Hall. Inc. [Figure 9-8, page 542] [313])

gate denoted as $\oplus$. The clock source generates the $010101\cdots$ sequence, which corresponds to $\mathbf{H}_8[1]$. After the first T-flipflop, the sequence becomes $00110011\cdots$, which is $\mathbf{H}_8[2]$, since the T-flipflop simply halves the clock rate. The output sequence of the second T-flipflop becomes $00001111\cdots$, which represents $\mathbf{H}_8[4]$. In fact, these three sequences, namely $\mathbf{H}_8[1]$, $\mathbf{H}_8[2]$ and $\mathbf{H}_8[4]$, form bases so that the remaining rows of $\mathbf{H}_8$ can be generated by the linear combination of these three sequences. The desired Walsh code index is described by $u_2,\ u_1,\ u_0$, which is a binary bit-based representation of the index. For example, we can set $u_2 = 0,\ u_1 = 1,\ u_0 = 1$, in order to obtain the $\mathbf{H}_8[3]$ sequence. This can be verified by showing that $\mathbf{H}_8[1] \oplus \mathbf{H}_8[2]$ actually yields $\mathbf{H}_8[3]$. A specific disadvantage of this implementation, however, is that the total delay of generating a specific code is not fixed, it is proportional to the length of the Walsh code to be generated.

8.2.2 Orthogonal Gold Codes

Experiments show that the cross-correlation values of the Gold codes of Section 8.1.2 are "-1" for many code offsets. This suggests that it may be possible to render the cross-correlation values associated with these offsets "0" by attaching an additional "0" to the original Gold codes. In fact, 2^r orthogonal codes can be obtained by this simple zero-padding from a preferred pair of two r-stage LFSR. These codes are referred to as orthogonal Gold codes.

As an example, let us consider a Gold code characterised by a preferred pair of m-sequences, which are denoted by $g_0(x) = 1 + x + x^3$ and $g_1(x) = 1 + x^2 + x^3$ of order three. We can obtain eight Gold codes of length 7 with the aid of the schematic of Figure 8.3 by changing the initial values of the upper LFSR from "000" to "111", while maintaining the bottom LFSR's initial values as "001". We arrive at eight orthogonal Gold codes by attaching

a "0" at the tails, which are given below:

$$\mathbf{G}_8 = \begin{bmatrix} 1 & 0 & 1 & 1 & 1 & 0 & 0 & 0 \\ 0 & 1 & 0 & 1 & 0 & 0 & 0 & 0 \\ 1 & 1 & 0 & 0 & 1 & 1 & 0 & 0 \\ 0 & 0 & 1 & 0 & 0 & 1 & 0 & 0 \\ 1 & 0 & 0 & 0 & 0 & 0 & 1 & 0 \\ 0 & 1 & 1 & 0 & 1 & 0 & 1 & 0 \\ 1 & 1 & 1 & 1 & 0 & 1 & 1 & 0 \\ 0 & 0 & 0 & 1 & 1 & 1 & 1 & 0 \end{bmatrix} \tag{8.7}$$

The ith row of $\mathbf{G}_8$, namely $\mathbf{G}_8[i]$, is the ith orthogonal Gold code of length 8. Let us define an n by n dimensional *cross-correlation matrix* $\mathbf{C}(\mathbf{G})$ of an n by n dimensional code matrix $\mathbf{G}$, where each row is a code of length n, defined as $\mathbf{G}\mathbf{G}^T$, and the operations take place after replacing "0" and "1" with "1" and "-1", respectively. Then, the element in the ith row of the jth column, namely $\mathbf{C}_{ij}$, is the cross-correlation between the two codes, $\mathbf{G}[i]$ and $\mathbf{G}[j]$. Let us also define an n by n dimensional *auto-correlation matrix* $\mathbf{A}(\mathbf{G})$, which comprises $\mathbf{A}_{ij}$, the element in the ith row of the jth column, defined as the auto-correlation value of $\mathbf{G}[i]$ with offset j. Now we get the cross-correlation matrices of $\mathbf{H}_8$ in Equation 8.6 and $\mathbf{G}_8$ in Equation 8.7 as:

$$\mathbf{C}(\mathbf{H}_8) = 8\,\mathbf{I}_8 \tag{8.8}$$

$$\mathbf{C}(\mathbf{G}_8) = 8\,\mathbf{I}_8\,, \tag{8.9}$$

where $\mathbf{I}_8$ is the 8 by 8 dimensional identity matrix. Equations 8.8 and 8.9 show that there is no difference between the Walsh codes and the orthogonal Gold codes in terms of their cross-correlations. However, their auto-correlation properties are different. The auto-correlation matrix of the Walsh codes of length 8 is shown below:

$$\mathbf{A}(\mathbf{H}_8) = \begin{bmatrix} 8 & 8 & 8 & 8 & 8 & 8 & 8 & 8 \\ 8 & -8 & 8 & -8 & 8 & -8 & 8 & -8 \\ 8 & 0 & -8 & 0 & 8 & 0 & -8 & 0 \\ 8 & 0 & -8 & 0 & 8 & 0 & -8 & 0 \\ 8 & 4 & 0 & -4 & -8 & -4 & 0 & 4 \\ 8 & -4 & 0 & 4 & -8 & 4 & 0 & -4 \\ 8 & 4 & 0 & -4 & -8 & -4 & 0 & 4 \\ 8 & -4 & 0 & 4 & -8 & 4 & 0 & -4 \end{bmatrix}. \tag{8.10}$$

Let us compare (Equation 8.10 with the auto-correlation matrix of the orthogonal Gold codes

of length 8 formulated as:

$$\mathbf{A}(\mathbf{G}_8) = \begin{bmatrix} 8 & 0 & 0 & -4 & 0 & -4 & 0 & 0 \\ 8 & 0 & 4 & 0 & 0 & 0 & 4 & 0 \\ 8 & 0 & -8 & 0 & 8 & 0 & -8 & 0 \\ 8 & 0 & 0 & 4 & 0 & 4 & 0 & 0 \\ 8 & 0 & 4 & 0 & 0 & 0 & 4 & 0 \\ 8 & -4 & 0 & 0 & 0 & 0 & 0 & -4 \\ 8 & 0 & 0 & 4 & 0 & 4 & 0 & 0 \\ 8 & 4 & 0 & -4 & -8 & -4 & 0 & 4 \end{bmatrix} . \tag{8.11}$$

Observe in Equation 8.11 that $\mathbf{A}(\mathbf{H}_8)$ has 24 number of "± 8"s and 16 number of "0"s at the various offsets, while $\mathbf{A}(\mathbf{G}_8)$ has 4 number of "± 8"s and 36 number of "0"s. Both have sixteen "± 4"s. Hence, the orthogonal Gold codes exhibit better characteristics than the Walsh codes in terms of their auto-correlations. We can conclude that orthogonal Gold codes are desirable in some applications, where the codes' auto-correlations have to be low, which is desirable, in order to be able to avoid falsely registering the main peak of the autocorrelation function.

8.2.3 Multi-Rate Orthogonal Gold Codes

State-of-the-art wireless communication systems are expected to support multi-rate transmissions. CDMA systems can use multi-rate orthogonal codes for supporting this feature. Despite the terminology "multi-rate", typically a constant physical chip rate is maintained during variable bit rate transmissions and it is the number of chips per information bit, i.e. the spreading factor, which is varied, as it will be described during our further discourse. Generating multi-rate orthogonal codes is fairly straightforward. Commencing from any orthogonal code set, multi-rate codes can be obtained by applying one of the orthogonal transformation techniques described in [313]. Using the Walsh code generator of Figure 8.5 and the orthogonal Gold code generator of Section 8.2.2, one can readily implement multi-rate orthogonal code generators, as shown in Figure 8.6. The clock rate of the Walsh code generator is R_c/L, where R_c is the chip rate and L is the length of the orthogonal Gold code. In other words, the Walsh code generator is clocked once per orthogonal Gold code word. The maximum Walsh code length, n, is given by:

$$n = \frac{SF_{max}}{L} , \tag{8.12}$$

where SF_{max} is the maximum spreading factor and the orthogonal Gold code generator is clocked at the chip-rate of R_c, where SF_{max} is given by $SF_{max} = R_c/R_b$, and R_b is the lowest transmission symbol rate of the multi-rate system. The Walsh code index, $(u_{n-1}, \cdots u_1, u_0)_2$, has to be assigned carefully, in order to preserve the orthogonality between the spread multi-rate data symbols [316]. For the lowest-rate bit stream any free Walsh code index can be assigned from the range of 0 to $n-1$. However, for a $2^k \cdot R_b$-rate data stream, a total of 2^i free Walsh code indices has to be assigned corresponding to the codes $\{W_j\}$, $j = u + \frac{n}{2^i}v$, where u is selected from the set of $\{0, \cdots, \frac{n}{2^i} - 1\}$ and v from the set of $0, \cdots, 2^i - 1$. From the above set of indices only the first assigned index associated with $v = 0$ should be actually used.

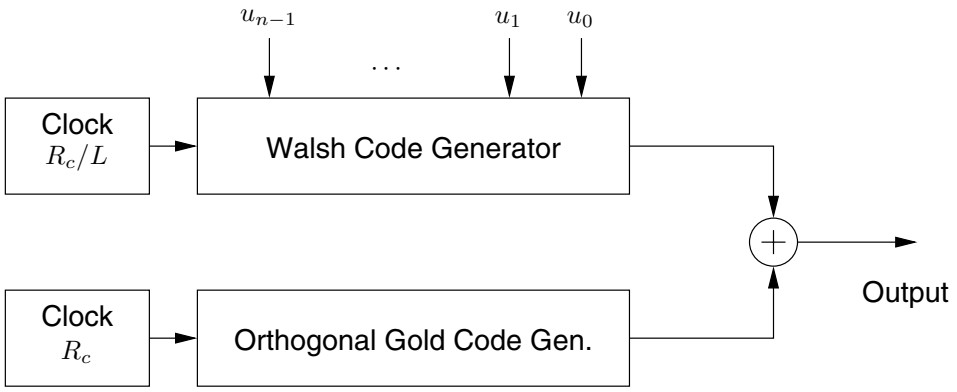


Figure 8.6: A multi-rate orthogonal Gold code generator. L is the length of the orthogonal Gold code, R_c is the chip rate and n is the length of Walsh code.

In order to augment the concept of index assignment, let us now consider a simple example. Let us assume that we have to design a multi-rate CDMA system, which supports two rates, namely 8 kbps and 16 kbps, and that the chip rate, R_c, is 256 kcps. The maximum spreading factor is given by:

$$SF_{max} = R_c/R_b = 256\,kcps/8\,kbps = 32\,, \tag{8.13}$$

where we used $R_b = 8$kbps as the lowest transmission symbol rate. Let us select $L = 8$, so that we can use $\mathbf{G}_8$ of Equation 8.7. According to Equation 8.12, the maximum Walsh code length n, is $SF_{max}/L = 32/8 = 4$. Thus, we use the 4 by 4 dimensional matrix $\mathbf{H}_4$, given as:

$$\mathbf{H}_4 = \begin{bmatrix} 0 & 0 & 0 & 0 \\ 0 & 1 & 0 & 1 \\ 0 & 0 & 1 & 1 \\ 0 & 1 & 1 & 0 \end{bmatrix}\,, \tag{8.14}$$

according to the schematic of Figure 8.6 for expanding $\mathbf{G}_8$, in order to generate the multi-rate orthogonal Gold code of dimension 32, $\mathbf{M}_{32}$, by using $\mathbf{G}_8$ of Equation 8.7 in its original form in those positions of $\mathbf{H}_4$ in Equation 8.14, where there is a "0" and its complementary form in the positions, where there is "1", yielding:

$$\mathbf{M_{32}} = \begin{bmatrix} \mathbf{G}_8 & \mathbf{G}_8 & \mathbf{G}_8 & \mathbf{G}_8 \\ \mathbf{G}_8 & \overline{\mathbf{G}_8} & \mathbf{G}_8 & \overline{\mathbf{G}_8} \\ \mathbf{G}_8 & \mathbf{G}_8 & \overline{\mathbf{G}_8} & \overline{\mathbf{G}_8} \\ \mathbf{G}_8 & \overline{\mathbf{G}_8} & \overline{\mathbf{G}_8} & \mathbf{G}_8 \end{bmatrix}\,. \tag{8.15}$$

Let us now consider the properties of $\mathbf{M}_{32}$. Each row of $\mathbf{M}_{32}$ is orthogonal to other rows. The codes $\mathbf{M}_{32}[0],\ \mathbf{M}_{32}[8],\ \mathbf{M}_{32}[16]$ and $\mathbf{M}_{32}[24]$ are expanded from $\mathbf{G}_8[0]$. In general, $\mathbf{M}_{32}[i],\ \mathbf{M}_{32}[8+i],\ \mathbf{M}_{32}[16+i]$ and $\mathbf{M}_{32}[24+i]$, where i spans the range of $0,\ \cdots,\ 7$, are generated from $\mathbf{G}_8[i]$ and hence they are not orthogonal, when they are used for multi-

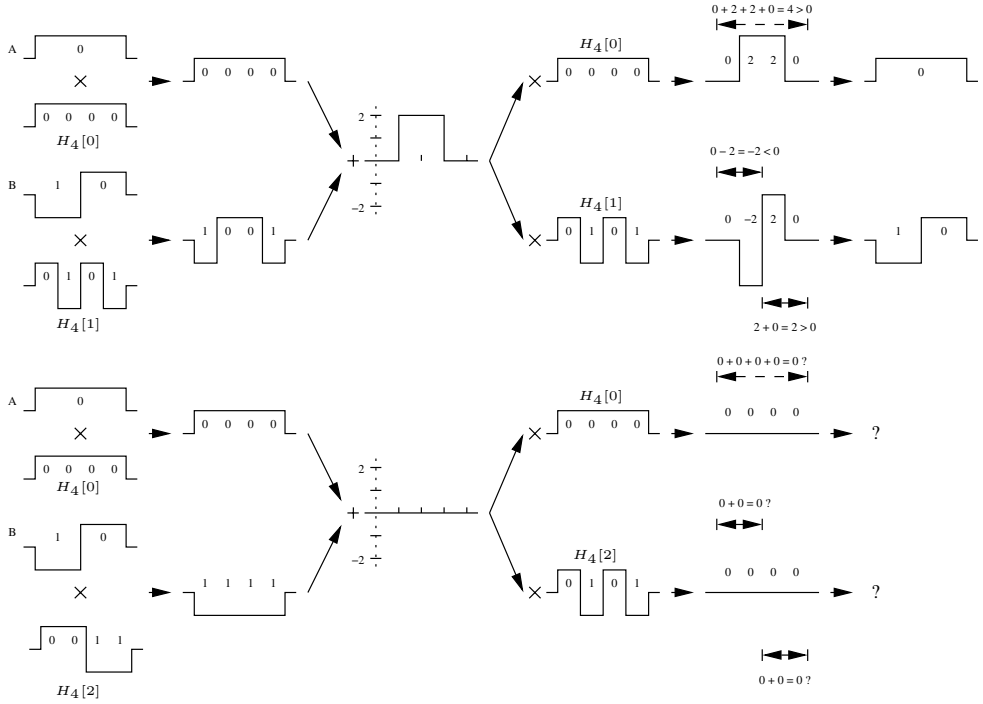


Figure 8.7: A conceptual diagram for multi-rate spreading: "A" transmits at half the rate of the transmission rate of "B". "A;' uses $\mathbf{H}_4[0]$ and "B" $\mathbf{H}_4[1]$ in the upper graph, which results in perfect information recovery at the receiver. In the lower graph, "B" uses $\mathbf{H}_4[2]$, which breaks the orthogonality and makes information recovery impossible.

rate spreading. This lack of orthogonality is a consequence of the fact that when supporting a high transmission rate, while fixing the chip-rate, the number of chips per data bit has to be reduced. For example, when doubling the bit-rate, the number of chips per bit is halved, which inevitably halves the number of orthogonal sequences available. Hence a double bit-rate user has to be assigned two orthogonal codes, which otherwise could be assigned to two basic-rate users. Figure 8.7 shows this concept more explicitly. Since $\mathbf{H}_4[0]$ and $\mathbf{H}_4[2]$ are not orthogonal in a multi-rate environment, the receiver may not be able to recover the original symbols from the received signal, as shown in the graph at the bottom of Figure 8.7. In order to prevent this, two free Walsh codes have to be assigned to user "B", transmitting at twice the transmission rate of user "A" although effectively only one of these codes is transmitted. More explicitly, this potential non-orthogonality problem only arises in conjunction with the codes, which have the same generating orthogonal Gold code.

8.3 Chapter Summary and Conclusion

This chapter examined the correlation properties of a set of PN sequences, specifically those of the m-sequences, Gold codes and Kasami codes, as well as the correlation properties of

a set of orthogonal sequences, namely those of Walsh codes, orthogonal Gold codes and multi-rate orthogonal Gold codes. The schematic diagram of each sequence generator was presented in Figure 8.1 through Figure 8.6. Based on these schematics, a sequence generator library[1] was constructed for employment in our numerical and simulation studies.

It was observed in Section 8.2.2 that orthogonal Gold codes result in lower autocorrelation values, than those of the Walsh codes studied in Section 8.2.1. The effects of the different autocorrelation values of the spreading sequences on the envelope power of the corresponding MC-CDMA signal employing those sequences was examined in detail in Chapter 11 of the extended version of this monograph [90].

Specifically, when studying the structure of multi-rate orthogonal Gold codes in Section 8.2.3, we observed that for supporting 2^k times higher bit-rate users than the basic transmission rate we have to assign 2^k number of code indices, even though only one is actually used, in order to preserve the code's orthogonality with respect to the lower bit-rate user's spread signal.

[1] http://www-mobile.ecs.soton.ac.uk/bjc97r/pnseq/index.html

Chapter 9

MC-CDMA Performance in Synchronous Environments

In wireless environments the transmitted signals may travel through different propagation paths having different lengths and hence these multi-paths components arrive at the receiver with different delays. This time-dispersive nature of the channel causes Inter-Symbol Interference (ISI) and frequency selective fading [249]. The *RMS delay spread* or multi-path spread, τ_{rms}, of the channel determines the amount of ISI inflicted and the gravity of the channel-induced linear distortions. The reciprocal of the delay spread, namely $1/\tau_{rms} = (\Delta f)_c$, is referred to here as the *coherence bandwidth* of the channel [2]. If the total signal bandwidth is wider than $(\Delta f)_c$, the signal experiences *frequency selective* fading [260]. Typically, this is the case, when high rate data is transmitted in a wide signal bandwidth.

In highly frequency selective channels the ISI becomes a major problem in serial modems and hence usually complex channel equalisers are required. In OFDM systems the ISI becomes negligible, as long as a sufficiently high number of guard symbols is introduced [234]. However, due to the frequency selective nature of the channel, each subcarrier has a different bit error ratio (BER). In order to combat this phenomenon several techniques have been used in OFDM, such as error correcting codings in conjunction with frequency domain interleaving [65] and frequency domain adaptive loading [234].

Another traditional method of combating the effect of fading is to involve diversity techniques [260]. The main benefit of MC-CDMA in comparison to other OFDM-based multiple access methods [317] is the inherent provision of frequency diversity. By contrast, a disadvantage of MC-CDMA is the Multi-User Interference (MUI) encountered. These key factors predetermine the performance of MC-CDMA.

When the MC-CDMA signal experiences severe channel fades, the receiver is likely to make a wrong decision concerning the bit carried by the signal. Diversity techniques arrange for generating several replicas of the signal arriving at the receiver over independent fading paths. From the family of various diversity techniques, frequency diversity, time diversity and

© 2006 John Wiley & Sons, Ltd

antenna diversity are most widely used [260]. Although both MC-CDMA and DS-CDMA use frequency diversity, their receiver structures differ in many aspects. DS-CDMA systems use so-called Rake receivers [252] and the number of fingers in the Rake receiver determines the number of diversity paths exploited. In most cases, the number of fingers in DS-CDMA Rake receivers is limited due to their affordable complexity and size. MC-CDMA systems, on the other hand, use a simpler approach, since they transmit the same information on several subcarriers in order to achieve diversity. The number of subcarriers transmitting the same information determines the order of diversity. Thus, in general, it is easier to achieve a higher-order diversity in MC-CDMA, than in DS-CDMA [318].

However, the maximum achievable order of frequency diversity, L, in a specific channel is approximately given by [260, 319]

$$L \approx \frac{W}{(\Delta f)_c} , \tag{9.1}$$

where W is the total bandwidth of the channel and $(\Delta f)_c$ is its coherence bandwidth. Hence, spreading a symbol over more than this number of subcarriers is expected to have no more benefits in terms of diversity gain. Instead, as the number of users increases, the MUI will increase significantly, thus, reducing the overall performance of the MC-CDMA system.

In this chapter, the performance of the various diversity techniques and the multi-user interference reduction techniques applicable to MC-CDMA are investigated over a frequency selective indoor fading channel, assuming that all users' signals are synchronous, which is typically the case in the downlink.

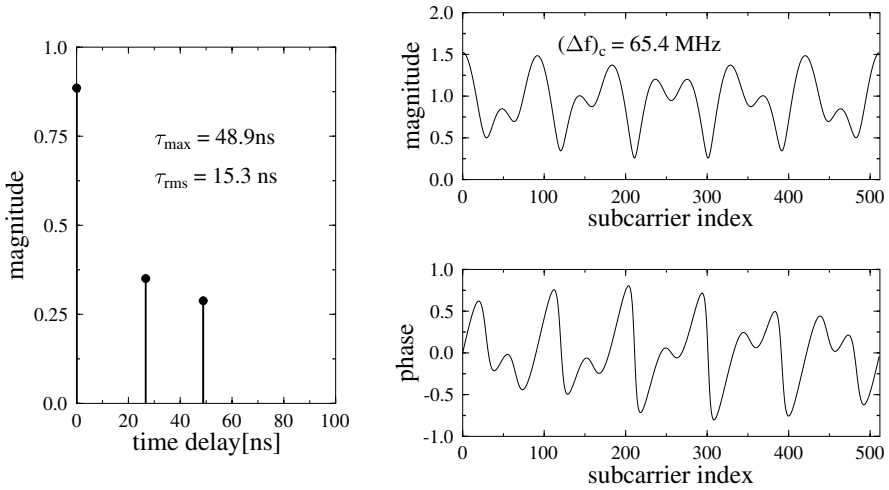
9.1 The Frequency Selective Channel Model

A narrow-band fading channel can be modelled as a Rayleigh process associated with a specific Doppler spectrum [2]. This channel model is based on the worst case scenario, assuming that no line-of-sight path is available between the transmitter and the receiver. On the other hand, a wideband fading channel can be modelled as a sum of several differently delayed, independent Rayleigh fading processes. The corresponding channel impulse response is described as

$$h(t, \tau) = \sum_{p=1}^{P} a_p \cdot R_p(t) \cdot \delta(\tau - \tau_p) , \tag{9.2}$$

where a_p is the normalised amplitude such that $\sum_{p=1}^{P} a_p^2 = 1.0$, $R_p(t)$ is the Rayleigh fading process with $E[R_p^2] = 1.0$ and τ_p is the delay of the p-th path. For the computer simulation purposes, τ_p is given in units of the sampling interval duration.

An indoor channel model is considered for investigating the performance of MC-CDMA in synchronous environments. It is a shortened Wireless Asynchronous Transfer Mode (W-ATM) channel model used for example in [2]. The impulse response and frequency domain response of the channel are shown in Figure 9.1. The impulse response was derived by simple ray-tracing in a warehouse-type room of $100 \times 100 \times 3\text{m}^3$ [2] . The main system parameters and channel parameters of the system investigated are summarised in Table 9.1.



(a) impulse response

(b) frequency response

Figure 9.1: The shortened W-ATM channel model, where τ_{max} is the longest delay, τ_{rms} is the RMS delay spread and $(\Delta f)_c$ is the coherence bandwidth of the channel

parameters	Shortened W-ATM
Carrier frequency, f_c	60 GHz
Sampling rate, $1/T_s$	225 MHz
BPSK data rate, R_b	155 Mbps
Max. speed of mobile, v_{max}	50 Km/h
Max. Doppler frequency, $f_{d,max}$	2277.8 Hz
Normalised Doppler freq., $f_{n,max}$	$1.23 \cdot 10^{-5}$
Max. delay, τ_{max}	11 samples
RMS delay spread, τ_{rms}	15.3 ns
Coherence bandwidth, $(\Delta f)_c$	65.4 MHz
No. of subcarriers, N	512
No. of guard symbols, N_g	64

Table 9.1: Main system parameters of the considered W-ATM system and the channel parameters

9.2 The System Model

The MC-CDMA system considered here employs N subcarriers and each user transmits M bits during a signalling interval, leading to the spreading factor or, synonymously, to the processing gain, G, of N/M [74, 319]. Figure 9.2 shows the transmitter structure of the system model. The data stream of user u is converted into M parallel streams and each stream is spread with the aid of orthogonal spreading sequences of Section 8.2, which maps the same

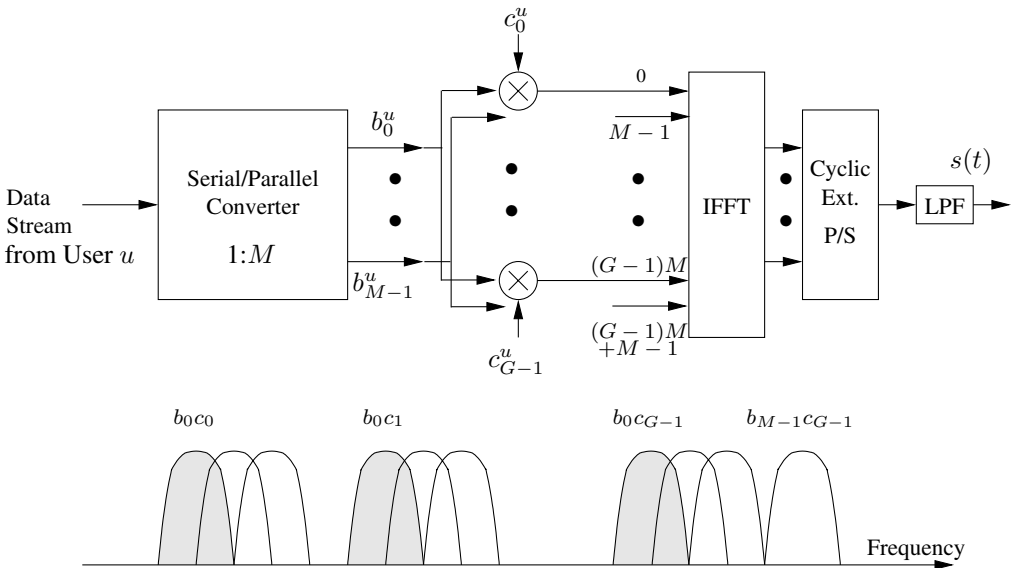


Figure 9.2: MC-CDMA transmitter model and its spectrum for a single user

bit to G number of subcarriers. The subcarrier spacing between the subcarriers conveying the same bit is set to M, in order to minimise the correlation of the fading of these subcarriers. For simplicity, only a single user is depicted in the figure, but a number of users up to G can be incorporated. The uth user's spreading sequence, $c_g^u,\ g\ =\ 0,\ 1,\ \cdots\ , G-1$, is orthogonal to other users' spreading sequences. The Walsh codes and the orthogonal Gold codes described in Section 8.2 can be used as the spreading sequences. In this model, each user transmits its data at the rate of M/T bps, where T is the frame duration. If the transmission rate can be lowered, the maximum number of users, U, can be increased such that the data streams generated by the M users replace the $1 : M$ serial-to-parallel converter in Figure 9.2 [319]. In this case, the total number of users supported can reach the total number of subcarriers, yielding $U = N$. Bearing this in mind, in our discourse, only the configuration shown in Figure 9.2 will be considered.

The complex baseband representation of the transmitted signal, $s(t)$, in a certain signalling interval can be written as:

$$s(t) = \sum_{u=0}^{U-1} \sum_{m=0}^{M-1} \sum_{g=0}^{G-1} \sqrt{E_c}\, b_m^u\, c_g^u\, e^{j2\pi \frac{1}{T}(gM+m)t}\ , \tag{9.3}$$

where

U is the number of users, which has a maximum of G
M is the number of bits transmitted per user
G is the spreading factor or the processing gain given as N/M, where N is the

number of subcarriers
E_c is the energy per subcarrier, or chip, and $E_c = E_b/N$, where E_b is the energy per bit before spreading
T is the signalling interval, during which M number of bits per user are transmitted and $1/T$ is equal to the spacing between adjacent subcarriers
$b_m^u \in \{\pm 1\}$ is the mth bit of user u
$c_g^u \in \{\pm 1\}$ is the gth chip of the uth user's spreading sequence.

9.3 Single User Detection

At the receiver the mth bit of user u is detected independently from the m'th bits, where $m' \neq m$, for all users. Furthermore, assume that there is no inter-subcarrier interference. Thus, without loss of generality, the subscript m can be omitted and the G subcarriers conveying the same bit can be considered for the detection of a bit. In view of Equation 7.8, the demodulated received symbol r_g of the gth subcarrier can be expressed as:

$$r_g = \sum_{u=0}^{U-1} \sqrt{E_c}\, b^u\, c_g^u\, H_g + n_g\,, \tag{9.4}$$

where H_g is the $(gM+m)$th subcarrier's frequency domain channel transfer factor, and n_g is a discrete AWGN process having zero mean and a one-sided power spectral density of N_o. The decision variable of the u'th user's bit, $d^{u'}$, is given for a single user detector as:

$$d^{u'} = \sum_{g=0}^{G-1} q_g\, c_g^{u'}\, r_g\,, \tag{9.5}$$

where q_g is a frequency domain equalisation gain factor, which is dependent upon the diversity combining scheme employed. The decision variable $d^{u'}$ can be expanded with the aid of Equations 9.4 and 9.5 as:

$$\begin{aligned} d^{u'} &= \sum_{g=0}^{G-1} q_g\, c_g^{u'} \left(\sum_{u=0}^{U-1} \sqrt{E_c}\, b^u\, c_g^u\, H_g + n_g \right) \\ &= \sqrt{E_c}\, b^{u'} \sum_{g=0}^{G-1} H_g\, q_g + \sqrt{E_c} \sum_{u=0, u\neq u'}^{U-1} b^u \sum_{g=0}^{G-1} c_g^u\, c_g^{u'}\, H_g\, q_g + \sum_{g=0}^{G-1} c_g^{u'}\, n_g\, q_g \\ &= \alpha + \zeta + \eta\,, \end{aligned} \tag{9.6}$$

where α is the desired signal component given by

$$\alpha = \sqrt{E_c} b^{u'} \sum_{g=0}^{G-1} H_g q_g\,, \tag{9.7}$$

ζ is the MUI given by

$$\zeta \;=\; \sqrt{E_c} \sum_{u=0, u\neq u'}^{U-1} b^u \sum_{g=0}^{G-1} c_g^u c_g^{u'} H_g q_g \;, \tag{9.8}$$

and η is the noise component given by

$$\eta \;=\; \sum_{g=0}^{G-1} c_g^{u'} n_g q_g \;. \tag{9.9}$$

These three signal components predetermine the performance of the single user detector considered.

9.3.1 Maximal Ratio Combining

In Maximal Ratio Combining (MRC) [70, 260] a stronger signal is assigned a higher weight by the diversity combiners, than a weaker signal, since its contribution is more "reliable". The corresponding equalisation gain, q_g, introduced in Equation 9.5 is given as:

$$q_g \;=\; H_g^* \;. \tag{9.10}$$

This equalisation gain attempts to de-attenuate and de-rotate the fading-induced attenuation and phase rotation. The corresponding user's received signal component, α, is given by:

$$\alpha \;=\; \sqrt{E_c}\, b^{u'} \sum_{g=0}^{G-1} |H_g|^2. \tag{9.11}$$

On the other hand, the MUI associated with MRC is given by:

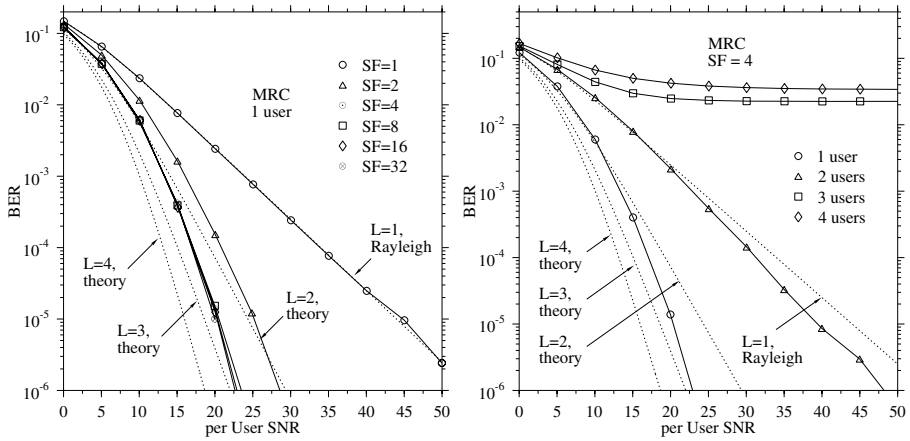
$$\zeta \;=\; \sqrt{E_c} \sum_{u=0, u\neq u'}^{U-1} b^u \sum_{g=0}^{G-1} c_g^u \, c_g^{u'} \, |H_g|^2 \;. \tag{9.12}$$

Finally, the noise term, η, of Equation 9.9 can be calculated as:

$$\eta \;=\; \sum_{g=0}^{G-1} c_g^{u'} \; n_g \; H_g^* \;. \tag{9.13}$$

The effect of MRC is equivalent to that of matched filtering, where the filtering is matched to the channel's transfer function. Matched filtering constitutes the optimal receiver, which maximises the SNR at the output of the decision device [260]. The single user performance of MRC has been widely studied for transmission over a Rayleigh fading channel having L-independent propagation paths and the achievable bit error rate, P_e, is given by [260]:

$$P_e = \left[\frac{1}{2}(1-\mu)\right]^L \sum_{k=0}^{L-1} \binom{L-1+k}{k} \left[\frac{1}{2}(1+\mu)\right]^k \;, \tag{9.14}$$



(a) single user

(b) multiple users for SF=4

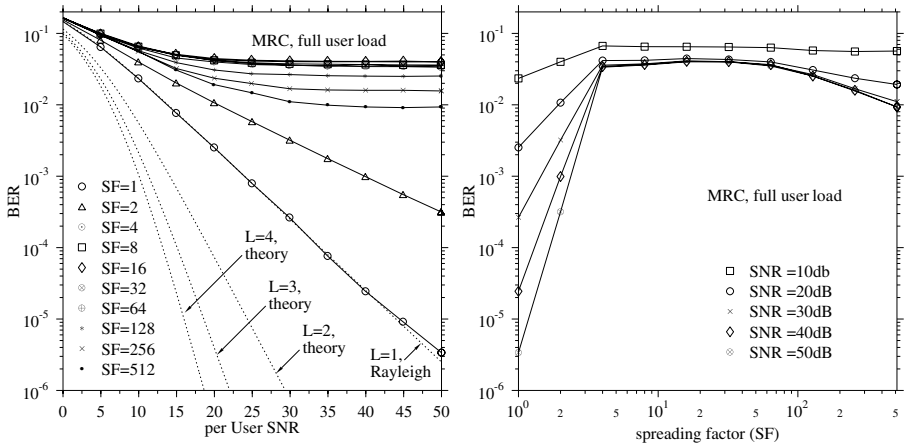
Figure 9.3: BER of synchronous MC-CDMA for the downlink in conjunction with MRC for transmission over W-ATM channel. The theoretical curves were evaluated from Equation 9.14.

where μ is defined as

$$\mu \triangleq \sqrt{\frac{\overline{\gamma}_b}{L + \overline{\gamma}_b}}\,, \tag{9.15}$$

and $\overline{\gamma}_b$ is the average energy per bit, $\overline{E}_b$, divided by the noise power spectral density, N_o. The associated BER curves for $L = 1, \cdots, 4$ are shown in Figure 9.3. More specifically, the simulation results for a single-user scenario are shown in Figure 9.3(a). The available diversity order, L, is given in Equation 9.1. For the shortened W-ATM channel, we have $225MHz/65.4MHz = 3.44$. Hence, a system having a spreading factor of 4 is expected to reach the diversity-assisted performance enhancement limit. When a spreading factor of 1 is employed corresponding to no spreading, the BER performance of MC-CDMA was identical to the BER of single carrier scheme operating over a Rayleigh fading channel. As the spreading factor was increased, the BER performance was improved. However, as can be seen in Figure 9.3(a), the systems having a Spreading Factor (SF) in excess of 4 did not improve the achievable bit error rate. As the SNR increased, the simulation-based BER approached the theoretical BER associated with $L = 3$ which was evaluated from Equation 9.14 under the assumption of independent fadings over L paths. The discrepancy between the simulation-based and theoretical results was due to the correlated fading over G number of subcarriers.

It is interesting to observe the effects of the number of users on the bit error rate, when MRC is used. Figure 9.3(b) shows our simulation results for the spreading factor of four. As the number of users was increased, the bit error rate increased significantly due to the increased amount of MUI. We can view the frequency domain spreading as a form of repetition coding. Thus, the two-user scenario employing SF = 4 in MC-CDMA corresponds to a half rate encoder, since 2 information bits are transmitted using a total of 4 symbols. If we compare the BER curves of this two-user system with that of the single-user scenario in MC-CDMA in conjunction with SF=2, where the code rate can also be regarded as $1/2$, we



(a) BER vs SNR

(b) BER vs spreading factor (SF)

Figure 9.4: BER of the synchronous MC-CDMA downlink using MRC for full user load over the W-ATM channel described in Figure 9.1, where SF is the spreading factor and L represents the diversity order

can conclude that the latter scheme performs significantly better. However, in general, more complex channel coding techniques will perform better than this simple repetition code [260].

In so-called fully loaded conditions when the number of users is equal to the SF, the multi-user interference as opposed to the noise component dominates the system's performance, which becomes poor. The corresponding simulation results are given in Figure 9.4. The BER performance of fully loaded MC-CDMA is worse, than that of OFDM, which corresponds to having SF = 1. In Figure 9.4(b) it can be observed that the BER increased to a certain limit and then decreased across the SNR range spanning from 20dB to 50dB, as the spreading factor was increased. In order to investigate this phenomenon, we have to consider the statistical properties of α and ζ given in Equations 9.11 and 9.12, respectively.

As the total power conveyed by the Channel's Impulse Response (CIR) is normalised such that we have $E\{\sum_{n=0}^{N-1}|h_n|^2\} = 1.0$, the frequency domain channel response satisfies $E\{\sum_{n=0}^{N-1}|H_n|^2\} = N$ according to the discrete form of Parseval's theorem [320], where E denotes the expected value. Hence we can assume that $E\left[\sum_{g=0}^{G-1}|H_g|^2\right]$ becomes G. Thus, the average signal power, $E\left[\alpha^2\right]$ becomes

$$\begin{aligned} E\left[\alpha^2\right] &= E_c \cdot G^2 \\ &= E_b \cdot G\,, \end{aligned}$$

where E_b is the signal energy per bit during the bit interval. If we assume that the absolute value of the subcarrier channel transfer factor H_g obeys an independent identically distributed (iid) Rayleigh process with $E\left[|H_g|^2\right] = 2\sigma^2 = 1$ and $c_g^u c_g^{u'}$ has an equal probability of $+1$ or -1, then Equation 9.12 can be regarded as a zero mean Gaussian process, provided

that U and G are sufficiently high. The variance, $E\left[\zeta^2\right]$ becomes:

$$\begin{aligned} E\left[\zeta^2\right] &= E_c\,(U-1)\,G\,\left(E\left[|H_g|^4\right] - E\left[|H_g|^2\right]^2\right) \\ &= E_c\,(U-1)\,G \\ &= E_b\,(U-1)\,, \end{aligned}$$

where $E\left[|H_g|^4\right] = 8\sigma^4 = 2$ is used. In high SNR scenarios supporting a full user load of $U = G$, the bit error probability, P_e, can be approximated as

$$\begin{aligned} P_e &\simeq \frac{1}{2}\text{erfc}\left(\sqrt{\frac{E\left[\alpha^2\right]}{E\left[\zeta^2\right]}}\right) \\ &= \frac{1}{2}\text{erfc}\left(\sqrt{\frac{E_b\,\cdot\,G}{E_b(U-1)}}\right) \\ &\simeq \frac{1}{2}\text{erfc}(1) \\ &= 0.08\,. \end{aligned}$$

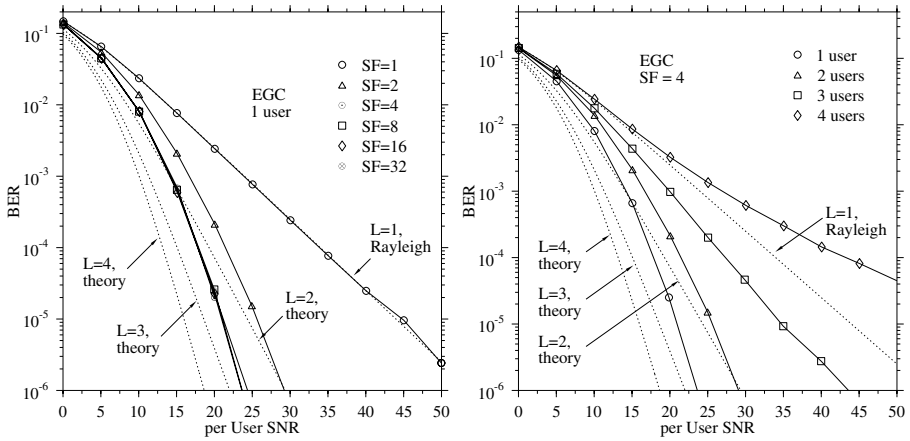
This approximate analysis is supported by Figure 9.4. Specifically, at high SNRs the bit error ratio was constant, namely approximately 0.08 for the spreading factors of 8 to 64. Figure 9.4(b) is a plot of the BER versus the spreading factor. As the spreading factor was increased beyond 64, the associated bit error ratios were reduced. This can be interpreted as follows. The MUI defined in Equation 9.12 is reduced, when the channel transfer factors $\{H_g\}$ are correlated, which is the case for high SFs, when the subcarriers conveying the same bit are close to each other.

In conclusion, we observed that the channel exhibits a limited amount of diversity and the MUI plays a major role in terms of determining the BER, when MRC is used as the diversity combining method.

9.3.2 Equal Gain Combining

Although the spreading codes are orthogonal, due to the differently delayed multi-path components received, their orthogonality is destroyed. The MRC scheme, which is characterised by the equalisation gain given by Equation 9.10, optimally combines these multi-path components in an effort to maximise the SNR, but at the same time it may further impair the orthogonality of the codes. In order to avoid this problem, Equal Gain Combining (EGC) attempts to correct the channel-induced phase rotations [249], leaving the faded magnitudes uncorrected [70]. In this case, the equalisation gain, q_g, is given by:

$$q_g = \frac{H_g^*}{|H_g|}\,. \tag{9.16}$$



(a) single user

(b) multiple users for SF=4

Figure 9.5: BER performance of the synchronous MC-CDMA downlink using EGC over W-ATM channel, where SF is the spreading factor and L is the diversity order

The corresponding three signal components defined in Equations 9.7 to 9.9 are given as:

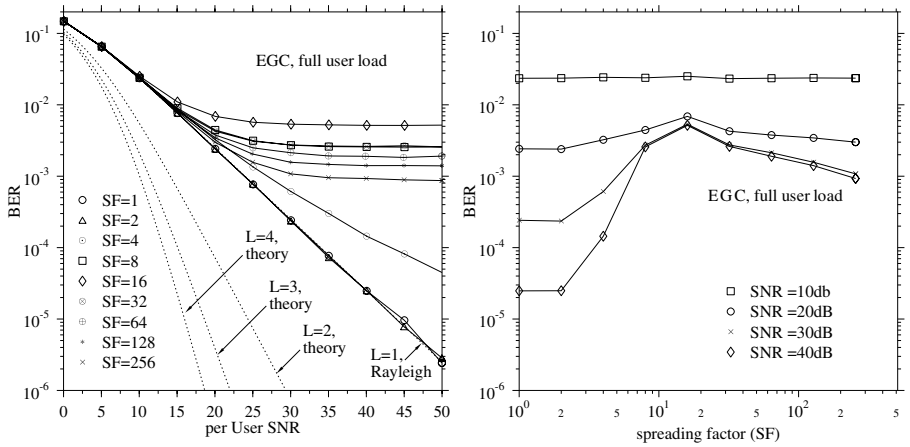
$$\alpha = \sqrt{E_c}\, b^{u'} \sum_{g=0}^{G-1} |H_g| \tag{9.17}$$

$$\zeta = \sqrt{E_c} \sum_{u=0, u\neq u'}^{U-1} b^{u} \sum_{g=0}^{G-1} c_g^{u} c_g^{u'} |H_g| \tag{9.18}$$

$$\eta = \sum_{g=0}^{G-1} c_g^{u'} n_g \frac{H_g^*}{|H_g|} \,. \tag{9.19}$$

Our simulation results are shown in Figure 9.5. In the single user case shown in Figure 9.5(a), the BER curves approached the theoretical ones, but overall EGC performed slightly worse than MRC. No further improvement was observed for the systems having a SF higher than four, as in the case of MRC. When the number of users was increased for the system employing SF = 4, the performance was degraded but remained better, than that of MRC. This results corroborates the BER comparison reported in [70].

When all users are transmitting, the multi-user interference increases significantly, eroding the benefits of the frequency diversity and the performance becomes worse than that of OFDM, corresponding to SF = 1. The corresponding simulation results are given in Figure 9.6. As in the case of MRC, the bit error ratio curve converged to a BER floor, when the SNR was high. The BER floor was dependent on the spreading factor. The worst BER floor was observed for SF = 16. As the spreading factor increases beyond SF = 16, the BER floor is reduced. This can be interpreted using the similar arguments to those in Section 9.3.1.



(a) BER vs SNR

(b) BER vs spreading factor (SF)

Figure 9.6: BER performance of the synchronous MC-CDMA downlink using EGC for a full user load, where SF is the spreading factor and L is the diversity order

9.3.3 Orthogonality Restoring Combining

As argued before, frequency selective fading destroys the orthogonality of the different users' spreading codes. The drawback of the MRC and the EGC scheme is that they inflict MUI due to the above mentioned lack of orthogonality, which is not desirable. If we cancel the effect of the channel transfer function by estimating it and reversing its effects, the orthogonality of the different users can be maintained. This is the aim of Orthogonality Restoring Combining (ORC) or Zero Forcing (ZF) equalisation, which uses the equalisation gain, q_g, given by:

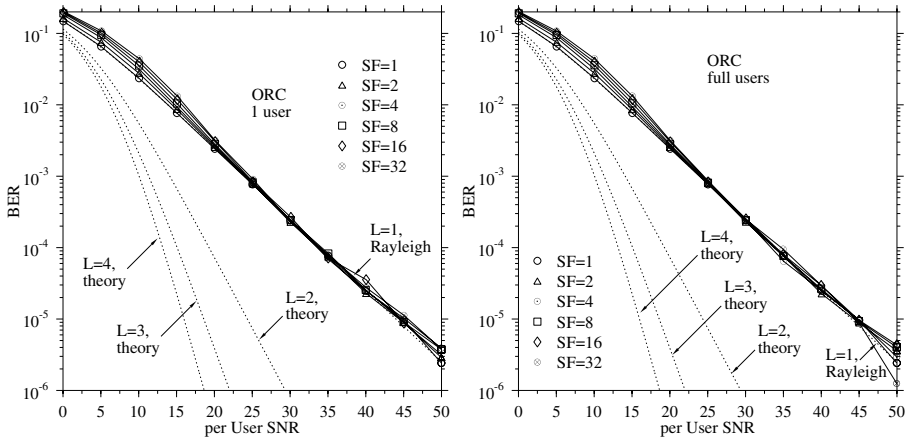
$$q_g \;=\; \frac{H_g^*}{|H_g|^2}. \tag{9.20}$$

We have only two components in the decision variable of Equation 9.6 as $\zeta = 0$, which are given by:

$$\alpha \;=\; \sqrt{E_c}\, G\, b^{u'} = \sqrt{E_b G}\, b^{u'} \tag{9.21}$$

$$\eta \;=\; \sum_{g=0}^{G-1} c_g^{u'}\, n_g\, \frac{H_g^*}{|H_g|^2}\,. \tag{9.22}$$

Figure 9.7 shows our simulation results for the various spreading factors, when ORC is applied in our MC-CDMA scheme. The MC-CDMA system using various spreading factors, i.e. different-order diversity schemes, performed worse than the single-user OFDM scheme associated with SF = 1, when the average per user SNR, $\overline{\gamma}_b$, was less than 25dB. In fact, as the spreading factor was increased, the performance degraded, since the ORC scheme using perfect channel estimation had already removed the frequency selectivity of the channel transfer function, leaving no room for improvement with the aid of frequency domain diversity. The



(a) single user (b) full users

Figure 9.7: BER of the synchronous MC-CDMA downlink using ORC for a single user over the W-ATM channel

source of performance degradation in comparison to OFDM was the noise enhancement, particularly at lower SNR values. More specifically, when the fading was severe for a specific subcarrier, the value of n_g/H_g became high, inevitably amplifying both the signal and the noise. As the spreading factor increased, it became more likely that $\{H_g\}$ encountered deep frequency domain fades, leading to an excessive noise enhancement. This effect is less significant at high SNRs. In order to combat to the noise enhancement problem, the technique of Controlled Equalisation (CE) was proposed by Yee and Linnartz [267], which uses a subset of subcarriers for the ORC scheme, associated with the channel transfer factors that are above a certain threshold.

No noticeable differences were observed between the bit error ratios for the various number of users, as shown in Figure 9.7(b). This result is consistent with the fact that no MUI exists, when ORC is employed.

9.4 Multi-User Detection

9.4.1 Background

The detection methods of Section 9.3 exploited single user information only, thus the performance was interference limited except in the case of ORC. Moreover, when using all the available information at the receiver, such as the spreading codes of all users and their CIRs, the performance can be improved with the aid of Multi-User Detection (MUD).

In the third-generation W-CDMA system referred to as IMT2000 [217] a range of powerful optional performance enhancement techniques have been proposed, which are expected to be used only in mature implementations. For example, powerful but complex Multi-user Detectors (MUDs) [321–323] can be used at the base station to achieve a near-single-user performance in the uplink, while supporting a multiplicity of users. The fundamental approach

of MUDs, which are also often referred to as multi-user equalisers, accrues from recognising the fact that the nature of the interference is similar, regardless whether its source is dispersive multipath propagation or multi-user interference. In other words, the effects of imposing interference on the received signal by a K-path dispersive channel or by a K-user system are similar. Hence MUDs offer the benefit of jointly counteracting both MUI and multipath interference.

MUDs [321, 322] may be categorised in a number of ways, such as linear versus non-linear, adaptive versus non-adaptive algorithms or burst transmission versus continuous transmission regimes. Excellent summaries of some of these sub-optimum detectors can be found in the monographs by Verdu [321], Prasad [324], Glisic and Vucetic [325] or in the tutorial reviews by Woodward and Vucetic [326], Moshavi [327] as well as Duel-Hallen, Holtzman and Zvonar [328], just to mention a few. Other MAI-mitigating techniques include the employment of interference rejection techniques, which typically impose a lower implementation complexity than MUDs [329].

Adaptive antenna arrays (AAAs) [217] are also capable of mitigating the level of MAI at the receiver by forming a beam in the direction of the wanted user and a null towards the interfering users. It is worth noting, however, that since the angle of arrival of the multipath components becomes more limited owing to the focused beam of the AAAs, which limits the number of received rays and hence the achievable diversity gain. Therefore often alternative fading counter-measures, such as the employment of adaptive modulation [90, 215] become necessary, further advocating the techniques reviewed in Chapter 6. Research efforts invested in the area of AAAs area include, amongst others, the investigations carried out by Thompson, Grant and Mulgrew [248, 330]; Naguib and Paulraj [331]; Godara [332]; as well as Kohno, Imai, Hatori and Pasupathy [333]. However, the area of adaptive antenna arrays is beyond the scope of this monograph and the reader is referred to the references cited for further discussions. The Maximum Likelihood Detector (MLD) is investigated in the rest this section as an example. For an in-depth study of MUDs the interested reader is referred to [321–323].

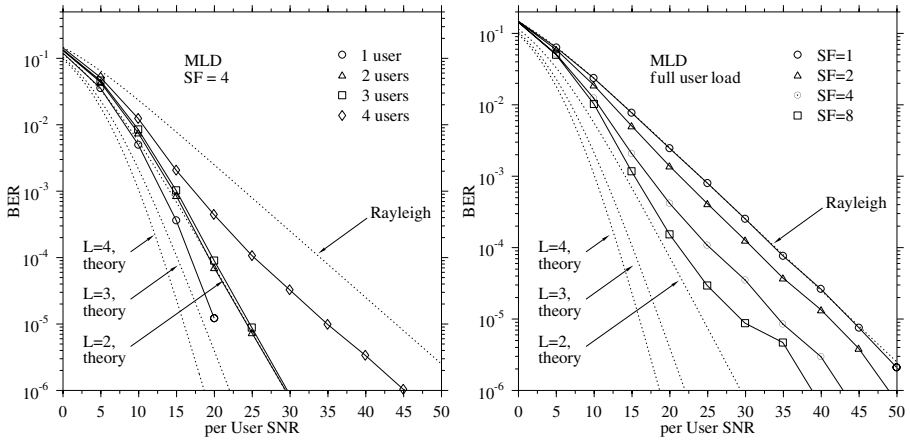
9.4.2 Maximum Likelihood Detection

In this scheme the receiver constructs all possible combinations of the transmitted signals of all users and applies their estimated channel transfer functions in order to generate the expected received signals [319]. Explicitly, the receiver chooses the legitimate transmitted signal, which has the smallest Euclidean distance from the received signal.

Let $\mathbf{C}$ be a $G \times U$-dimensional matrix containing the uth user's spreading code in column u, where $u = 1, 2, \cdots, U$, and $\mathbf{b}$ be a column vector, $(b^0\ b^1\ \cdots\ b^{U-1})^T$ comprised of possible source bits combination. If we define the channel's transfer factor matrix, $\mathbf{H}$, as a $G \times G$-dimensional diagonal matrix having H_g at $\mathbf{H_{gg}}$, then the expected received column vector $\hat{\mathbf{r}}$ is given by $\hat{\mathbf{r}} = \mathbf{HCb}$. The Euclidean distance, d, between the actually received signal vector $\mathbf{r}$ containing $r_g,\ g = 1, 2, \cdots, G$ of Equation 9.4, and the received vector candidate $\hat{\mathbf{r}}$, is given by:

$$d = || \mathbf{r} - \hat{\mathbf{r}} ||^{\mathbf{2}} . \tag{9.23}$$

Our simulation results characterising this MUD are given in Figure 9.8. As can be seen from Figure 9.8(a), the BER curve approached the theoretical BER curve of the single-user scenario for $L = 3$. As the number of users increased, the performance degraded, but nonetheless remained better than the OFDM BER associated with SF = 1. The effect of MUI



(a) SF=4, users=1,2,3 and 4

(b) full user load

Figure 9.8: BER of MC-CDMA downlink with MLD

was considerably reduced compared to the MRC and EGC assisted scenario. Figure 9.8(b) shows the simulation results for the "fully loaded" MC-CDMA system using the MLD. Even in this condition, the BER was lower than that of OFDM. This implies that MC-CDMA systems employing the MLD are superior to the conventional OFDM scheme in terms of their bit error ratio, while providing the same spectral efficiency. In Section 9.3.1 we observed that spreading a bit to more subcarriers than the available diversity order of the channel does not improve the performance of single user detection schemes. However, Figure 9.8(b) suggests that in a multi-user scenario spreading the same bit to more subcarriers than the available diversity order of the channel can improve the bit error ratio due to both the reduced MUI and the better exploitation of the available diversity.

9.4.3 Concatenated Space-Time Block Coded and Turbo Coded Symbol-by-Symbol Adaptive OFDM and Multi-Carrier CDMA[1]

In the previous sections we studied the performance of uncoded adaptive schemes. Since a Forward Error Correction (FEC) code reduces the SNR required for achieving a given target BER at the expense of a reduced BPS throughput, it is interesting to investigate the performance of adaptive schemes employing FEC techniques. A variety of FEC techniques have been used in the context of adaptive modulation schemes. In their pioneering work on adaptive modulation, Webb and Steele [335] used a set of binary BCH codes. Vucetic [336] employed various punctured convolutional codes in response to the time-variant channel status. On the other hand, various Trellis Coded Modulation (TCM) [337, 338] schemes were used in the context of adaptive modulation by Alamouti and Kallel [339], Goldsmith and Chua [340], as well as Hole, Holm and Øien [341]. Keller, Liew and Hanzo studied the performance of Redundant Residue Number System (RRNS) codes in the context of adaptive

[1]This section is based on collaborative research with T.H. Liew [334].

multi-carrier modulation [342, 343]. Various turbo coded adaptive modulation schemes have been investigated also by Liew, Wong, Yee and Hanzo [344–346]. With the advent of space-time (ST) coding techniques [347–349], various concatenated coding schemes combining ST coding and FEC coding can be applied in adaptive modulation schemes. In this section, we investigate the performance of various concatenated space-time block-coded and turbo-coded adaptive OFDM and MC-CDMA schemes.

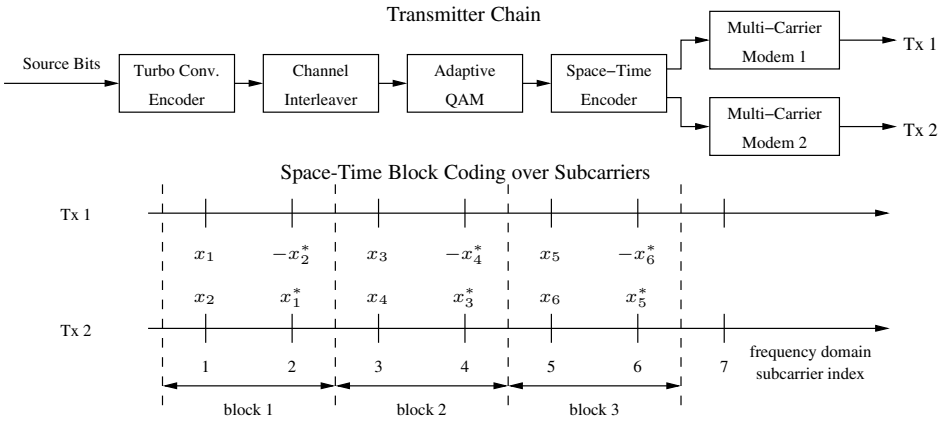
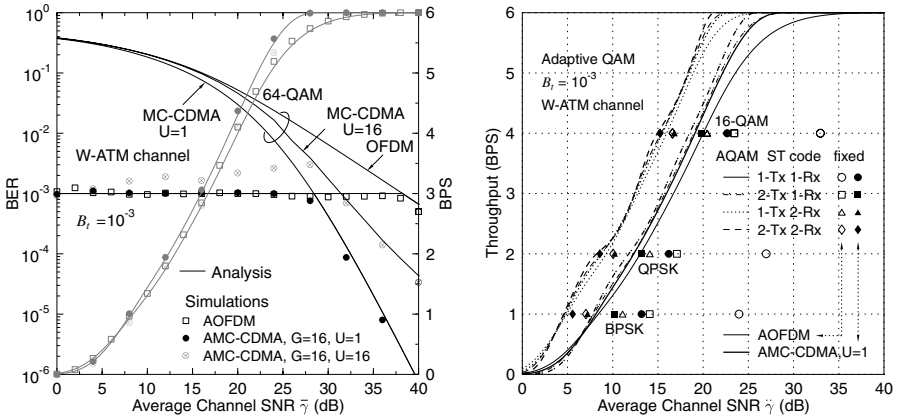


Figure 9.9: Transmitter structure and space-time block encoding scheme

Figure 9.9 portrays the stylised transmitter structure of our system. The source bits are channel coded by a half-rate turbo convolutional encoder [350] using a constraint length of $K = 3$ as well as a random block interleaver having a memory of $L = 3072$ bits. Then, the AQAM block selects a modulation mode from the set of no transmission, BPSK, QPSK, 16-QAM and 64-QAM depending on the instantaneous channel quality perceived by the receiver, according to the SNR-dependent optimum switching levels derived in Chapter 12 of [90]. It is assumed that the perfectly estimated channel quality experienced by receiver A is fed back to transmitter B superimposed on the next burst transmitted to receiver B. The modulation mode switching levels of our AQAM scheme determine the average BER as well as the average throughput.

The modulated symbol is now space-time encoded. As seen at the bottom of Figure 9.9, Alamouti's space-time block code [348] is applied across the frequency domain. A pair of the adjacent sub-carriers belonging to the same space-time encoding block is assumed to have the same channel quality. We employed a Wireless Asynchronous Transfer Mode (W-ATM) channel model [page 474] of [2] transmitting at a carrier frequency of 60GHz, at a sampling rate of 225MHz and employing 512 sub-carriers. Specifically, we used a three-path fading channel model, where the average SNR of each path is given by $\bar{\gamma}_1 = 0.79192\bar{\gamma}$, $\bar{\gamma}_2 = 0.12424\bar{\gamma}$ and $\bar{\gamma}_3 = 0.08384\bar{\gamma}$. The Multi-path Intensity Profile (MIP) of the W-ATM channel is illustrated in Figure 4.3. Each channel associated with a different antenna is assumed to exhibit independent fading.

The simulation results related to our uncoded adaptive modems are presented in Figure 9.10. Since we employed the optimum switching levels derived in Chapter 12 of [90], both our adaptive OFDM (AOFDM) and the adaptive single-user MC-CDMA (AMC-



(a) BER and Throughput, No ST coding

(b) Throughput with ST coding

Figure 9.10: Performance of uncoded five-mode AOFDM and AMC-CDMA. The target BER is $B_t = 10^{-3}$ when transmitting over the W-ATM channel [page 474] of [2]. (a) The constant average BER is maintained for AOFDM and single user AMC-CDMA, while "full-user" AMC-CDMA exhibits a slightly higher average BER due to the residual MUI. (b) The SNR gain of the adaptive modems decreases, as ST coding increases the diversity order. The BPS curves appear in pairs, corresponding to AOFDM and AMC-CDMA – indicated by the thin and thick lines, respectively – for each of the four different ST code configurations. The markers represent the SNRs required by the fixed-mode OFDM and MC-CDMA schemes for maintaining the target BER of 10^{-3} in conjunction with the four ST-coded schemes considered.

CDMA) modems maintain the constant target BER of 10^{-3} up to the "avalanche" SNR value, and then follow the BER curve of the 64-QAM mode. However, "full-user" AMC-CDMA, which is defined as an AMC-CDMA system supporting $U = 16$ users with the aid of a spreading factor of $G = 16$ and employing the MMSE-BDFE Joint Detection (JD) receiver [247], exhibits a slightly higher average BER, than the target of $B_t = 10^{-3}$ due to the residual Multi-User Interference (MUI) of the imperfect joint detector. Since in Chapter 12 of [90] we derived the optimum switching levels based on a single-user system, the levels are no longer optimum, when residual MUI is present. The average throughputs of the various schemes expressed in terms of BPS steadily increase and at high SNRs reach the throughput of 64-QAM, namely 6 BPS. The throughput degradation of "full-user" MC-CDMA imposed by the imperfect JD was within a fraction of a dB. Observe in Figure 9.10(a) that the analytical and simulation results are in good agreement, which we denoted by the lines and distinct symbols, respectively.

The effects of ST coding on the average BPS throughput are displayed in Figure 9.10(b). Specifically, the thick lines represent the average BPS throughput of our AMC-CDMA scheme, while the thin lines represent those of our AOFDM modem. The four pairs of hollow and filled markers associated with the four different ST-coded AOFDM and AMC-CDMA scenarios considered represent the BPS throughput versus SNR values associated with fixed-mode OFDM and fixed-mode MMSE-BDFE JD assisted MC-CDMA schemes.

Specifically, observe for each of the 1, 2 and 4 BPS fixed-mode schemes that the right-most markers, namely the circles, correspond to the 1-Tx / 1-Rx scenario, the squares to the 2-Tx / 1-Rx scheme, the triangles to the 1-Tx / 2-Rx arrangement and the diamonds to the 2-Tx / 2-Rx scenarios. First of all, we can observe that the BPS throughput curves of OFDM and single-user MC-CDMA are close to each other, namely within 1 dB for most of the SNR range. This is surprising, considering that the fixed-mode MMSE-BDFE JD assisted MC-CDMA scheme was reported to exhibit around 10dB SNR gain at a BER of 10^{-3} and 30dB gain at a BER of 10^{-6} over OFDM [75]. This is confirmed in Figure 9.10(b) by observing that the SNR difference between the $\circ$ and $\bullet$ markers is around 10dB, regardless of whether the 4, 2 or 1 BPS scenario is concerned.

Let us now compare the SNR gains of the adaptive modems over the fixed modems. The SNR difference between the BPS curve of AOFDM and the fixed-mode OFDM represented by the symbol $\circ$ at the same throughput is around 15dB. The corresponding SNR difference between the adaptive and fixed-mode 4, 2 or 1 BPS MC-CDMA modem is around 5dB. More explicitly, since in the context of the W-ATM channel model [page 474] of [2] fixed-mode MC-CDMA appears to exhibit a 10dB SNR gain over fixed-mode OFDM, the additional 5dB SNR gain of AMC-CDMA over its fixed-mode counterpart results in a total SNR gain of 15dB over fixed-mode OFDM. Hence ultimately the performance of AOFDM and AMC-CDMA becomes similar.

Let us now examine the effect of ST block coding. The SNR gain of the fixed-mode schemes due to the introduction of a 2-Tx / 1-Rx ST block code is represented as the SNR difference between the two right-most markers, namely circles and squares. These gains are nearly 10dB for fixed-mode OFDM, while they are only 3dB for fixed-mode MC-CDMA modems. However, the corresponding gains are less than 1dB for both adaptive modems, namely for AOFDM and AMC-CDMA. Since the transmitter power is halved due to using two Tx antennas in the ST codec, a 3dB channel SNR penalty was already applied to the curves in Figure 9.10(b). The introduction of a second receive antenna instead of a second transmit antenna eliminates this 3dB penalty, which results in a better performance for the 1-Tx/2-Rx scheme than for the 2-Tx/1-Rx arrangement. Finally, the 2-Tx / 2-Rx system gives around 3-4dB SNR gain in the context of fixed-mode OFDM and a 2-3dB SNR gain for fixed-mode MC-CDMA, in both cases over the 1-Tx / 2-Rx system. By contrast, the SNR gain of the 2-Tx / 2-Rx scheme over the 1-Tx / 2-Rx based adaptive modems was, again, less than 1dB in Figure 9.10(b). More importantly, for the 2-Tx / 2-Rx scenario, the advantage of employing adaptive modulation erodes, since the fixed-mode MC-CDMA modem performs as well as the AMC-CDMA modem in this scenario. Moreover, the fixed-mode MC-CDMA modem still outperforms the fixed-mode OFDM modem by about 2dB. We conclude that since the diversity-order increases with the introduction of ST block codes, the channel quality variation becomes sufficiently small for the performance advantage of adaptive modems to erode. This is achieved at the price of a higher complexity due to employing two transmitters and two receivers in the ST coded system.

When channel coding is employed in the fixed-mode multi-carrier systems, it is expected that OFDM will benefit more substantially from the frequency domain diversity than MC-CDMA, which benefited more than OFDM without channel coding. The simulation results depicted in Figure 9.11 show that the various turbo-coded fixed-mode MC-CDMA systems consistently outperform OFDM. However, the SNR differences between the turbo-coded BER curves of OFDM and MC-CDMA are reduced considerably.

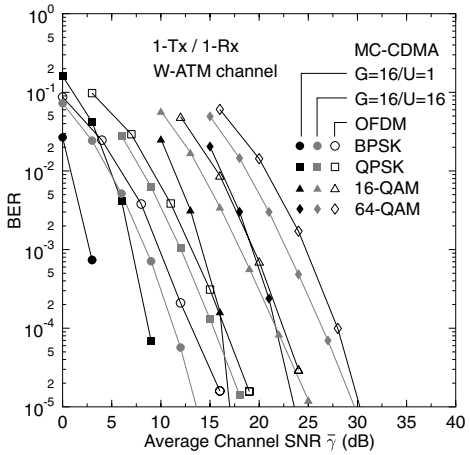
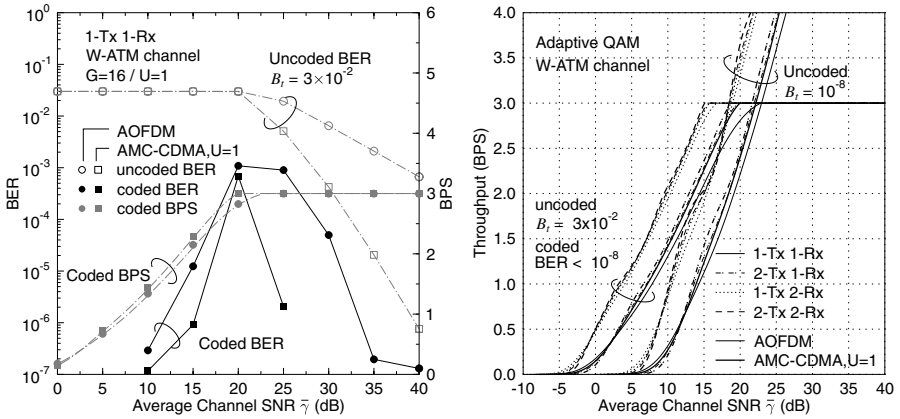


Figure 9.11: Performance of turbo convolutional coded fixed-mode OFDM and MC-CDMA for transmission over the W-ATM channel of [page 474] of [2], indicating that JD MC-CDMA still outperforms OFDM. However, the SNR gain of JD MC-CDMA over OFDM is reduced to 1-2dB at a BER of 10^{-4}.

The performance of the concatenated ST block coded and turbo convolutional coded adaptive modems is depicted in Figure 9.12. We applied the optimum set of switching levels designed in Chapter 12 of [90] for achieving an uncoded BER of 3×10^{-2}. This uncoded target BER was stipulated after observing that it is reduced by half-rate, $K = 3$ turbo convolutional coding to a BER below 10^{-7}, when transmitting over AWGN channels. However, our simulation results yielded zero bit errors, when transmitting 10^9 bits, except for some SNRs, when employing only a single antenna.

Figure 9.12(a) shows the BER of our turbo coded adaptive modems, when a single antenna is used. We observe in the figure that the BER reaches its highest value around the "avalanche" SNR point, where the adaptive modulation scheme consistently activates 64-QAM. The system is most vulnerable around this point. In order to interpret this phenomenon, let us briefly consider the associated interleaving aspects. For practical reasons we have used a fixed interleaver length of $L = 3072$ bits. When the instantaneous channel quality was high, the $L = 3072$ bits were spanning a shorter time-duration during their passage over the fading channel, since the effective BPS throughput was high. Hence the channel errors appeared more bursty, than in the lower-throughput AQAM modes, which conveyed the $L = 3072$ bits over a longer time duration, hence dispersing the error bursts over a longer duration of time. The uniform dispersion of erroneous bits versus time enhances the error correction power of the turbo code. On the other hand, in the SNR region beyond the "avalanche" SNR point seen in Figure 9.12(a) the system exhibited a lower uncoded BER, reducing the coded BER even further. This observation suggests that further research ought to determine the set of switching thresholds directly for a coded adaptive system, rather than by simply estimating the uncoded BER, which is expected to result in near-error-free transmission.

We can also observe that the turbo coded BER of AOFDM is higher than that of AMC-CDMA in the SNR rage of 10-20dB, even though the uncoded BER is the same. This appears to be the effect of the limited exploitation of frequency domain diversity of coded OFDM,



(a) BER (b) Throughput

Figure 9.12: Performance of the concatenated ST block coded and turbo convolutional coded adaptive OFDM and MC-CDMA systems over the W-ATM channel of [page 474] of [2]. The uncoded target BER is 3×10^{-2}. The coded BER was less than 10^{-8} for most of the SNR range, resulting in virtually error-free transmissions. (a) The coded BER becomes higher near the "avalanche" SNR point, when a single antenna was used. (b) The coded adaptive modems have SNR gains up to 7dB compared to their uncoded counterparts achieving a comparable average BER.

compared to MC-CDMA, which leads to a more bursty uncoded error distribution, hence degrading the turbo coded performance. The fact that ST block coding aided multiple antenna systems show virtually error-free performance corroborates our argument.

Figure 9.12(b) compares the throughputs of the coded adaptive modems and the uncoded adaptive modems exhibiting a comparable average BER. The SNR gains due to channel coding were in the range of 0dB to 8dB, depending on the SNR region and on the scenarios employed. Each bundle of throughput curves corresponds to the scenarios of 1-Tx/1-Rx OFDM, 1-Tx/1-Rx MC-CDMA, 2-Tx/1-Rx OFDM, 2-Tx/1-Rx MC-CDMA, 1-Tx/2-Rx OFDM, 1-Tx/2-Rx MC-CDMA, 2-Tx/2-Rx OFDM and 2-Tx/2-Rx MC-CDMA starting from the far right curve, when viewed for throughput values higher than 0.5 BPS. The SNR difference between the throughput curves of the ST and turbo coded AOFDM and those of the corresponding AMC-CDMA schemes was reduced compared to the uncoded performance curves of Figure 9.10(b). The SNR gain owing to ST block coding assisted transmit diversity in the context of AOFDM and AMC-CDMA was within 1dB due to the halved transmitter power. Therefore, again, ST block coding appears to be less effective in conjunction with adaptive modems.

In conclusion, the performance of ST block coded constant-power adaptive multi-carrier modems employing optimum SNR-dependent modem mode switching levels was investigated in this section. The adaptive modems maintained the constant target BER stipulated, whilst maximising the average throughput. As expected, it was found that ST block coding reduces the relative performance advantage of adaptive modulation, since it increases the diversity order and eventually reduces the channel quality variations. When turbo convolutional

coding was concatenated to the ST block codes, near-error-free transmission was achieved at the expense of halving the average throughput. Compared to the uncoded system, the turbo coded system was capable of achieving a higher throughput in the low SNR region at the cost of higher complexity. The study of the relationship between the uncoded BER and the corresponding coded BER showed that adaptive modems obtain higher coding gains, than that of fixed modems. This was due to the fact that the adaptive modem avoids burst errors even in deep channel fades by reducing the number of bits per modulated symbol eventually to zero.

9.5 Chapter Summary and Conclusion

The BER performance of synchronous MC-CDMA operating in the downlink was investigated in Section 9.3 using simulation based studies. In Section 9.3 we employed single-user detectors, namely MRC, EGC and ORC, while in Section 9.4 an MLD multi-user detector operating over the W-ATM channel was used. It was observed in Section 9.3.1 that while MRC is the optimum detector in a single-user scenario, its BER performance was the worst among the three single-user detector investigated in a fully loaded scenario. Neither the EGC nor the ORC-assisted MC-CDMA performed better than OFDM in a fully loaded scenario. However, in the same scenario the MLD multi-user detector-assisted MC-CDMA scheme of Section 9.4.2 exhibited SNR gains of 5dB, 10dB and 15dB for SF = 2, 4 and 8, respectively, in comparison to OFDM, when viewed at the BER of 10^{-6}. We can conclude that the employment of multi-user detectors is essential for MC-CDMA in order to successfully support a multiplicity of simultaneous users.

Concatenated space-time block coded and turbo convolutional-coded adaptive multi-carrier systems were investigated in Section 9.4.3. The coded schemes reduced the required average SNR by about 6-7 dB at a throughput of 1 BPS achieving near error-free transmission. It was also observed in Section 9.4.3 that increasing the number of transmit antennas in adaptive schemes was not very effective, achieving less than 1dB SNR gain owing to the fact that the transmit power per antenna had to be reduced in order to maintain the same constant total transmit power for the sake of a fair comparison.

Part III

Advanced Topics: Multi-User OFDM Systems

Chapter 10

Maximum-Likelihood Enhanced Sphere Decoding of MIMO-OFDM[1]

J. Akhtman and L. Hanzo

10.1 Classification of Smart Antennas

In recent years various smart antenna designs have emerged, which have found application in diverse scenarios, as seen in Table 10.1. The main objective of employing smart antennas is that of combating the effects of multipath fading on the desired signal and suppressing interfering signals, thereby increasing both the performance and capacity of wireless systems [351]. Specifically, in smart antenna-assisted systems, multiple antennas may be invoked at the transmitter and/or the receiver, where the antennas may be arranged for achieving spatial diversity, directional beamforming or for attaining both diversity and beamforming. In smart antenna systems the achievable performance improvements are usually a function of the antenna spacing and that of the algorithms invoked for processing the signals received by the antenna elements.

In beamforming arrangements [217] typically $\lambda/2$-spaced antenna elements are used for the sake of creating a spatially selective transmitter/receiver beam. Smart antennas using beamforming have been widely employed for mitigating the effects of various interfering signals and for providing beamforming gain. Furthermore, the beamforming arrangement is capable of suppressing co-channel interference, which allows the system to support multiple

[1] Acknowledgements: The work reported in this paper has formed part of the Wireless Enabling Techniques work area of the Core 3 Research Programme of the Virtual Centre of Excellence in Mobile and Personal Communications, Mobile VCE, www.mobilevce.com, whose funding support, including that of EPSRC, is gratefully acknowledged. Fully detailed technical reports on this research are available to Industrial Members of Mobile VCE.

© 2006 John Wiley & Sons, Ltd

Beamforming [217]	Typically $\lambda/2$-spaced antenna elements are used for the sake of creating a spatially selective transmitter/receiver beam. Smart antennas using beamforming have been employed for mitigating the effects of co-channel interfering signals and for providing beamforming gain.
Spatial Diversity [216] and Space-Time Spreading	In contrast to the $\lambda/2$-spaced phased array elements, in spatial diversity schemes, such as space-time block or trellis codes [216] the multiple antennas are positioned as far apart as possible, so that the transmitted signals of the different antennas experience independent fading, resulting in the maximum achievable diversity gain.
Space Division Multiple Access	SDMA exploits the unique, user-specific "spatial signature" of the individual users for differentiating amongst them. This allows the system to support multiple users within the same frequency band and/or time slot.
Multiple Input Multiple Output Systems [123]	MIMO systems also employ multiple antennas, but in contrast to SDMA arrangements, not for the sake of supporting multiple users. Instead, they aim for increasing the throughput of a wireless system in terms of the number of bits per symbol that can be transmitted by a given user in a given bandwidth at a given integrity.

Table 10.1: Applications of multiple antennas in wireless communications

users within the same bandwidth and/or same time-slot by separating them spatially. This spatial separation however becomes only feasible, if the corresponding users are separable in terms of the angle of arrival of their beams. These beamforming schemes, which employ appropriately phased antenna array elements that are spaced at distances of $\lambda/2$ typically result in an improved SINR distribution and enhanced network capacity [217].

In contrast to the $\lambda/2$-spaced phased array elements, *in spatial diversity schemes*, such as space-time coding aided transmit diversity arrangements [216], the multiple antennas are positioned as far apart as possible. A typical antenna element spacing of 10λ [351] may be used, so that the transmitted signals of the different antennas experience independent fading, when they reach the receiver. This is because the maximum diversity gain can be achieved, when the received signal replicas experience independent fading. Although spatial diversity can be achieved by employing multiple antennas at either the base station, mobile station, or both, it is more cost-effective and practical to employ multiple transmit antennas at the base station. A system having multiple receiver antennas has the potential of achieving receiver diversity, while that employing multiple transmit antennas exhibits transmit diversity. Recently, the family of transmit diversity schemes based on space-time coding, either space-time block codes or space-time trellis codes, has received wide attention and has been invoked in the 3rd-generation systems [217,352]. The aim of using spatial diversity is to provide both transmit as well as receive diversity and hence enhance the system's integrity/robustness. This typically results in a better physical-layer performance and hence a better network-layer per-

formance, hence space-time codes indirectly increase not only the transmission integrity, but also the achievable spectral efficiency.

A third application of smart antennas is often referred to as *Space Division Multiple Access* (SDMA), which exploits the unique, user-specific "spatial signature" of the individual users for differentiating amongst them. In simple conceptual terms one could argue that both a conventional CDMA spreading code and the Channel Impulse Response (CIR) affect the transmitted signal similarly - they are namely convolved with it. Hence, provided that the CIR is accurately estimated, it becomes known and is certainly unique, although - as opposed to orthogonal Walsh-Hadamad spreading codes, for example - not orthogonal to the other CIRs. Nonetheless, it may be used for uniquely identifying users after channel estimation and hence for supporting several users within the same bandwidth. Provided that a powerful multi-user detector is available, one can support even more users than the number of antennas. Hence this method enhances the achievable spectral efficiency directly.

Finally, Multiple Input Multiple Output (MIMO) systems [123, 353–356] also employ multiple antennas, but in contrast to SDMA arrangements, not for the sake of supporting multiple users. Instead, they aim for increasing the throughput of a wireless system in terms of the number of bits per symbol that can be transmitted by a single user in a given bandwidth at a given integrity.

10.2 Introduction to Space-Time Processing

The ever-increasing demand for both high data-rates, as well as for improved transmission integrity requires efficient utilisation of the limited system resources, while supporting a high grade of mobility in diverse propagation environments. Consequently, the employment of an appropriate modulation format, as well as efficient exploitation of the available bandwidth constitute crucial factors in achieving high performance.

The Orthogonal Frequency Division Multiplexing (OFDM) modulation scheme employed in conjunction with a Multiple-Input Multiple-Output (MIMO) architecture [90], where multiple antennas are employed at both the transmitter and the receiver of the communication system, constitutes an attractive solution in terms of satisfying these requirements. Firstly, the OFDM modulation technique is capable of coping with the highly frequency-selective, time-variant channel characteristics associated with mobile wireless communication channels, while possessing a high grade of structural flexibility for exploiting the beneficial properties of MIMO architectures.

It is highly beneficial that OFDM and MIMOs may be conveniently combined, since the information-theoretical analysis predicts [357] that substantial capacity gains are achievable in communication systems employing MIMO architectures. Specifically, if the fading processes corresponding to different transmit-receive antenna pairs may be assumed to be independently Rayleigh distributed,[2] the attainable capacity has been shown to increase linearly with the smaller of the numbers of the transmit and receive antennas [357]. Additionally, the employment of MIMO architectures allows the efficient exploitation of the spatial diversity available in wireless MIMO environments, thus improving the system's BER, as well as further increasing the system's capacity, as a benefit of the reduced channel quality fluctuations.

[2]This assumption is typically regarded as valid, if the appropriate antenna spacing is larger than $\lambda/2$, where λ is the corresponding wavelength.

The family of space-time signal processing methods, which allow the efficient implementation of communication systems employing MIMO architectures, are commonly referred to as smart antennas. In recent years, the concept of smart antennas has attracted intense research interest in both the academic and the industrial communities. As a result, a multiplicity of smart antenna-related methods has been proposed. These include methods implemented at the transmitter, the receiver or both.

The classification of smart-antenna aided wireless transmission techniques was already briefly addressed in the context of Table 10.1. A slightly more detailed classification is illustrated in Figure 10.1. It should be noted, however, that the classification presented here is somewhat informal and its sole purpose is to appropriately position the content of this chapter in the context of the extensive material available on the subject.

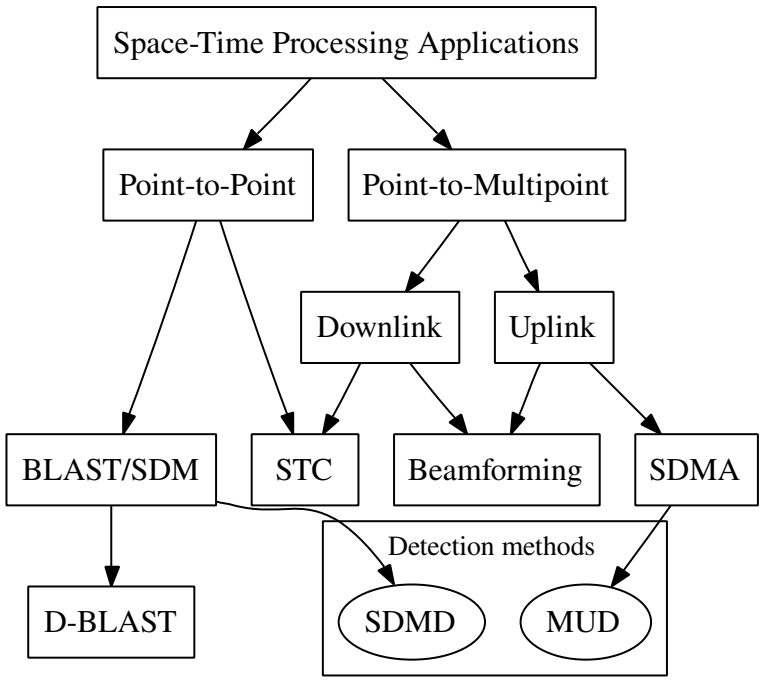


Figure 10.1: Classification of space-time processing techniques

Two distinctive system scenarios employing smart antennas can be identified. The first is the point-to-point SDM-type scenario, where two peer terminals each employing multiple antennas, communicate with each other over a MIMO channel and the multiple antennas are primarily used for achieving a multiplexing gain, i.e. a higher throughput [123]. The second scenario corresponds to the point-to-multipoint configuration, where a single base-station, employing multiple antennas communicates simultaneously using a single carrier frequency with multiple user terminals, each employing one or several antennas.

The various point-to-multipoint smart antenna applications can be further subdivided into

uplink- and downlink-related applications. The uplink-related methods constitute a set of techniques, which can be employed in the base station in order to detect the signals simultaneously transmitted by multiple user terminals. More specifically, provided that the Channel Impulse Response (CIR) of all users is accurately estimated, it may be used as their unique, user-specific spatial signature for differentiating them, despite communicating within the same frequency band [90]. Hence, the corresponding space-time signal processing problem is commonly referred to as Multi-User Detection (MUD) [90], while the multi-antenna multi-user systems employing uplink space-time MUD are commonly referred to as Space Division Multiple Access (SDMA) systems [90]. In contrast to the SDM-type systems designed for achieving the highest possible multiplexing gain, the design objective of the SDMA techniques is the maximisation of the number of users supported. By contrast, the class of beamformers [217] creates angularly selective beams for both the uplink and downlink in the direction of the desired user, while forming nulls towards the interfering users. Finally, the family of Space-Time Codes (STC) [216] was optimised for achieving the highest possible transmit diversity gain, rather than for attaining the highest possible spatial multiplexing gain in the context of a single user or for increasing the number of users supported. At the time of writing new research is aiming for increasing both the attainable diversity and multiplexing gain with the aid of eigen-value decomposition [358].

On the other hand, the host of downlink-related smart antenna applications comprises techniques which can be employed in both the base station terminal and/or each of the user terminals in order to efficiently resolve the high-datarate signal concurrently communicated from multiple antennas of the base station terminal. The downlink smart antenna implementations, which rely on transmitter-end space-time processing only are usually jointly referred to as beamforming [217]. Other downlink methods, which involve space-time processing at both the transmitter and the receiver ends are largely associated with Space-Time Codes (STC) [216].

As stated above, two benefits of employing smart antennas are the system's improved integrity, as well as the increased aggregate throughput. Hence an adequate performance criterion of the particular smart antenna implementation is a combination of the system's attainable aggregate data-throughput, as well as the corresponding data integrity, which can be quantified in terms of the average BER. Consequently, in the context of point-to-multipoint-related smart antenna applications, the achievable capacity associated with the particular space-time processing method considered may be assessed as a product of the simultaneously supported number of individual users and the attainable data-rate associated with each supported user. The measure of data-integrity may be the average BER of all the users supported. Thus, the typical objective of the multi-user-related smart antenna implementations, such as that of an SDMA scheme is that of increasing the number of the simultaneously supported users, while sustaining the highest possible integrity of all the data communicated.

For the sake of distinction, in this work we employ the alternative terminology of Space Division Multiplexing (SDM) in order to refer to a generic MIMO architecture. The corresponding detection methods are referred to as SDM Detection (SDMD) techniques, as opposed to the MUD techniques employed in the context of SDMA systems [90]. Naturally, however, the SDMD and MUD schemes share the same signal detection methods, regardless of whether the signal has arrived from multiple antennas of the same or different users. The classification of the most popular SDMD/MUD schemes is depicted in Figure 10.2. The methods considered include the linear LS and MMSE techniques, as well as non-linear tech-

niques, such as Maximum Likelihood (ML), Successive Interference Cancellation (SIC), Genetic Algorithm-aided MMSE (GA-MMSE) [359, 360] as well as the novel OHRSA methods proposed in this chapter.

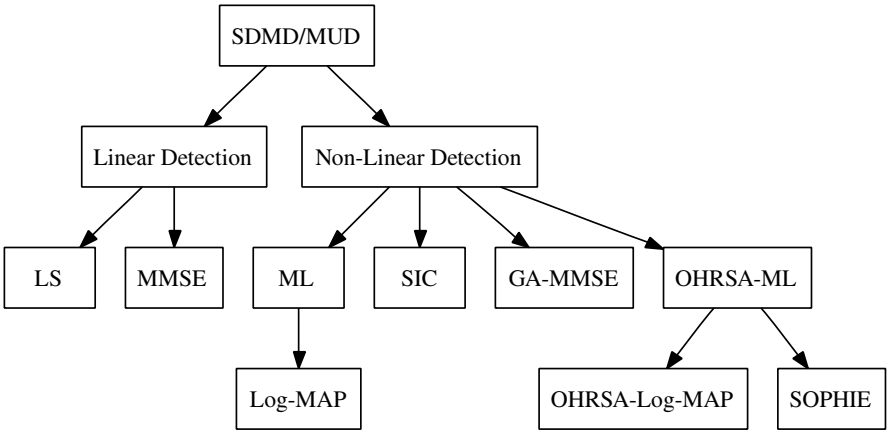


Figure 10.2: SDM detection methods classification.

The rest of this chapter is structured as follows. Both the MIMO channel model considered as well as the SDM-OFDM system model are described in Section 10.3. The OHRSA-aided SDM detection methods considered are outlined in Section 10.4. Specifically, in Section 10.4.1 we derive the OHRSA-aided ML SDM detector, which benefits from the optimal performance of the ML detector briefly introduced in Chapter 9, while exhibiting a relatively low computational complexity, which is only slightly higher than that required by the low-complexity MMSE detector of Chapter 12 in [90]. To elaborate a little further, in Section 10.4.3 we will derive a bit-wise OHRSA-aided ML SDM detector, which allows us to apply the OHRSA method of Section 10.4 in high-throughput systems, which employ multi-level modulation schemes, such as M-ary QAM [90].

In Section 10.4.4 our discourse evolves further by deducing the OHRSA-aided Log-MAP SDM detector, which allows an efficient evaluation of the soft-bit information and therefore results in highly efficient turbo decoding. Unfortunately however, in comparison to the OHRSA-aided ML SDM detector of Section 10.4.3 the OHRSA-aided Log-MAP SDM detector of Section 10.4.4 exhibits a substantially higher complexity. Consequently, in Section 10.4.5 we derive an approximate Log-MAP method, which we refer to as Soft-output OPtimised HIErarchy (SOPHIE) SDM detector. The SOPHIE SDM detector combines the advantages of both the OHRSA-aided ML and the OHRSA-aided Log-MAP SDM detectors of Sections 10.4.3 and 10.4.4, respectively. Specifically, it exhibits a similar performance to that of the optimal Log-MAP detector, while imposing a modest complexity, which is only slightly higher than that required by the low-complexity MMSE SDM detector [90]. The computational complexity as well as the achievable performance of the SOPHIE SDM detector of Section 10.4.5 are analysed and quantified in Sections 10.4.5.1 and 10.4.5.2, respectively. Finally, our conclusions are summarised in Section 10.5.

10.3 SDM-OFDM System Model

10.3.1 MIMO Channel Model

We consider a MIMO wireless communication system employing m_{t} transmit and n_{r} receive antennas, hence, the corresponding MIMO wireless communication channel is constituted by $(n_{\mathrm{r}} \times m_{\mathrm{t}})$ propagation links, as illustrated in Figure 10.3. Furthermore, each of the corresponding $(n_{\mathrm{r}} \times m_{\mathrm{t}})$ Single Input Single Output (SISO) propagation links comprises a multiplicity of statistically independent components, termed as paths. Thus, each of these SISO propagation links can be characterised as a multipath SISO channel discussed in detail in [90]. Similarly to the SISO case, the multi-carrier structure of our SDM-OFDM transceiver allows us to characterise the broadband frequency-selective channel considered as an OFDM subcarrier-related vector of flat-fading Channel Transfer Function (CTF) coefficients. However, as opposed to the SISO case, for each OFDM symbol n and subcarrier k the MIMO channel is characterised by a $(n_{\mathrm{r}} \times m_{\mathrm{t}})$-dimensional matrix $\mathbf{H}[n,k]$ of the CTF coefficients associated with the different propagation links, such that the element $H_{ij}[n,k]$ of the CTF matrix $\mathbf{H}[n,k]$ corresponds to the propagation link connecting the jth transmit and ith receive antennas.

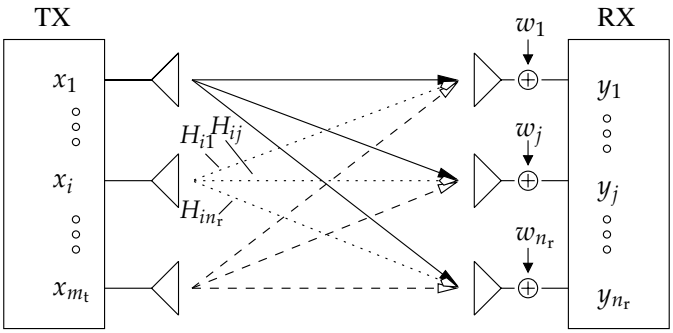


Figure 10.3: Illustration of a MIMO channel constituted by m_{t} transmit and n_{r} receive antennas. The corresponding MIMO channel is characterized by the $(n_{\mathrm{r}} \times m_{\mathrm{t}})$-dimensional matrix $\mathbf{H}$ of CTF coefficients.

Furthermore, the correlation properties of the MIMO-OFDM channel can readily be derived as a generalisation of the SISO-OFDM channel scenario discussed in detail in [90]. As was shown in [361], the cross-correlation function $r_H[m,l]$, which characterises both the time- and frequency-domain correlation properties of the discrete CTF coefficients $H_{ij}[n,k]$ associated with the particular (i,j)th propagation link of the MIMO channel, as well as with the different OFDM symbol and subcarrier indices n and k can be described as

$$\begin{aligned} r_{H;ij}[m,l] &= \mathtt{E}\left\{H_{ij}^{*}[n+m,k+l], H_{ij}[n,k]\right\} \\ &= \sigma_H^2 r_t[m] r_f[l], \end{aligned} \tag{10.1}$$

where $r_t[m]$ is the time-domain correlation function, which may be characterised by a time-

domain correlation model proposed by Jakes in [362], where we have

$$r_t[m] \triangleq r_J[m] = J_0(nw_d), \tag{10.2}$$

and $J_0(x)$ is a zero-order Bessel function of the first kind, while $w_d = 2\pi T f_D$ is the normalised Doppler frequency. On the other hand, the frequency-domain correlation function $r_f[l]$ can be expressed as [93]

$$r_f[l] = |C(l\Delta f)|^2 \sum_{i=1}^{L} \frac{\sigma_i^2}{\sigma_H^2} e^{-\jmath 2\pi l \Delta f \tau_i}, \tag{10.3}$$

where $C(f)$ is the frequency response of the pulse-shaping filter employed by the particular system, σ_i^2 and $\tau_i,\ i = 1, \cdots, L$ are the average power and the corresponding delay of the L-tap Power Delay Profile (PDP) encountered, while σ_H^2 is the average power per MIMO channel link, such that we have $\sigma_H^2 = \sum_{i=1}^{L} \sigma_i^2$.

In this chapter we assume the different MIMO channel links to be mutually uncorrelated. This common assumption is usually valid, if the spacing between the adjacent antenna elements exceeds $\lambda/2$, where λ is the wavelength corresponding to the RF signal employed. Thus, the overall cross-correlation function can be described as

$$\begin{aligned} r_{H;ij}[m,l] &= \mathtt{E}\left\{H_{i'j'}^*[n+m, k+l], H_{ij}[n,k]\right\} \\ &= \sigma_H^2 r_t[m] r_f[l] \delta[i-i'] \delta[j-j'], \end{aligned} \tag{10.4}$$

where $\delta[i]$ is the discrete Kronecker Delta function.

10.3.2 SDM-OFDM Transceiver Structure

The schematic of a typical SDM-OFDM system's physical layer is depicted in Figure 10.4.

The transmitter of the SDM-OFDM system considered is typically constituted by the Encoder and Modulator seen in Figure 10.4, generating a set of m_{t} complex-valued base-band time-domain signals [90]. The modulated base-band signals are then processed in parallel. Specifically, they are oversampled and shaped using a Nyquist filter, such as, for example, a root-raised-cosine filter. The resultant oversampled signals are then converted into an analog pass-band signal using a bank of D/A converters and upconverted to the Radio Frequency (RF) band. At the receiver side of the SDM-OFDM transceiver the inverse process takes place, where the set of received RF signals associated with the n_{r} receive antenna elements are amplified by the RF amplifier and down-converted to an intermediate frequency pass-band. The resultant pass-band signals are then sampled by a bank of A/D converters, down-converted to the base-band, filtered by a matched Nyquist filter and finally decimated, in order to produce a set of discrete complex-valued base-band signals. The resultant set of discrete signals is processed by the corresponding Demodulator and Decoder module seen in Figure 10.4, where the transmitted information-carrying symbols are detected.

In this chapter we consider the link between the output of the SDM-OFDM Modulator and the input of the corresponding SDM-OFDM Demodulator of Figure 10.4 as an effective base-band MIMO channel. The proof of feasibility for this assumption is beyond the scope this chapter, however it can be found for example in [249,363]. The structure of the resultant base-

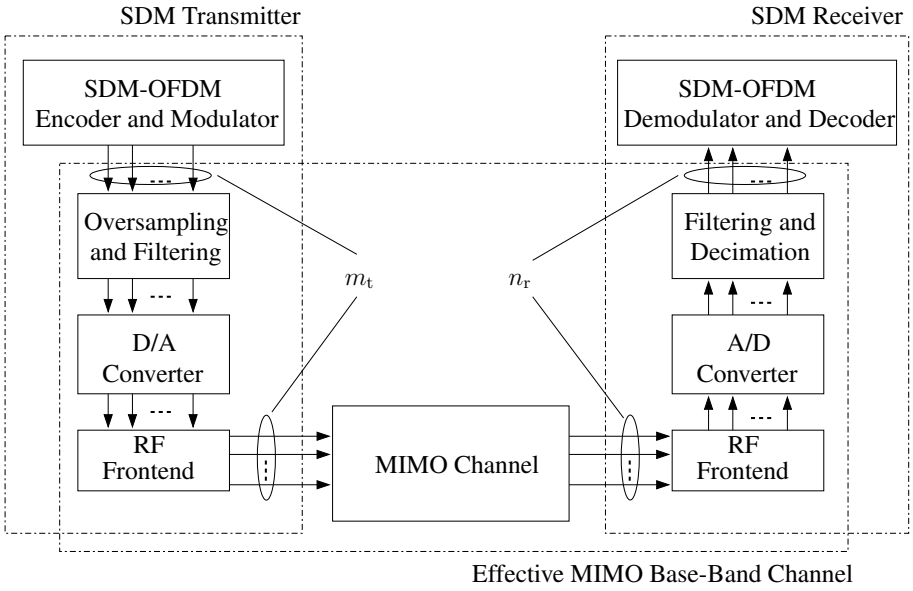


Figure 10.4: Schematic of a typical SDM-OFDM system's physical layer.

band SDM-OFDM system is depicted in Figure 10.5, where the bold grey arrows illustrate subcarrier-related signals represented by the vectors $\mathbf{x}_i$ and $\mathbf{y}_i$, while the black thin arrows accommodate scalar time-domain signals.

The discrete frequency-domain model of the SDM-OFDM system, illustrated in Figure 10.5, may be characterised as a generalisation of the SISO case described in [90]. Namely, we have

$$y_i[n,k] = \sum_{j=1}^{m_t} H_{ij}[n,k]x_j[n,k] + w_i[n,k], \tag{10.5}$$

where $n = 0, 1, \cdots$ and $k = 0, \ldots, K-1$ are the OFDM symbol and subcarrier indices, respectively, while $y_i[n,k], x_j[n,k]$ and $w_i[n,k]$ denote the symbol received at the ith receive antenna, the symbol transmitted from the jth transmit antenna and the Gaussian noise sample encountered at the ith receive antenna, respectively. Furthermore, $H_{ij}[n,k]$ represents the complex-valued CTF coefficient associated with the propagation link connecting the jth transmit and ith receive antennas at the kth OFDM subcarrier and time instance n. Note that in the case of an M-QAM modulated OFDM system, $x_j[n,k]$ corresponds to the M-QAM symbol accommodated by the kth subcarrier of the nth OFDM symbol transmitted from the jth transmit antenna element.

The SDM-OFDM system model described by Equation (10.5) can be interpreted as the per OFDM-subcarrier vector expression of

$$\mathbf{y}[n,k] = \mathbf{H}[n,k]\mathbf{x}[n,k] + \mathbf{w}[n,k], \tag{10.6}$$

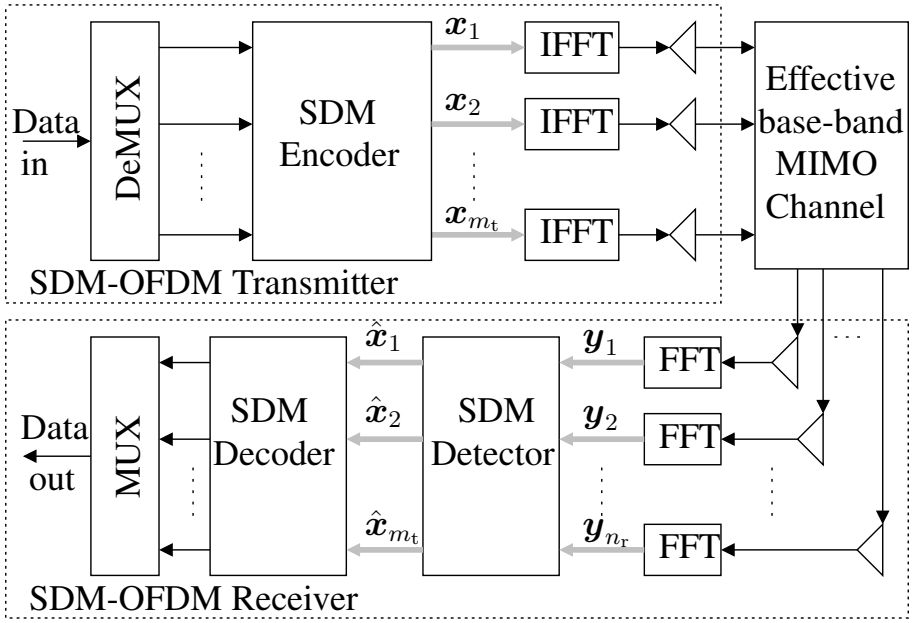


Figure 10.5: Schematic of a generic SDM-OFDM BLAST-type transceiver.

where we introduce the space-division-related vectors $\mathbf{y}[n,k]$, $\mathbf{x}[n,k]$ and $\mathbf{w}[n,k]$, as well as a space-division-related $(n_\mathrm{r} \times m_\mathrm{t})$-dimensional matrix of CTF coefficients $\mathbf{H}[n,k]$. Note that similarly to the SISO case, the multi-carrier structure of the SDM-OFDM transceiver allows us to represent the broadband frequency-selective MIMO channel as a subcarrier-related vector of flat-fading MIMO-CTF matrices $\mathbf{H}[n,k]$.

10.4 Optimised Hierarchy Reduced Search Algorithm-Aided SDM Detection

As it was pointed out in [90] , the "brute-force" ML detection method does not provide a feasible solution to the generic SDM detection problem as a result of its excessive computational complexity. Nevertheless, since typical wireless communication systems operate at moderate-to-high SNRs, Reduced Search Algorithms (RSA) may be employed, which are capable of obtaining the ML solution at a complexity which is considerably lower than that imposed by the ML detector of [90] . The most powerful of the RSA methods found in the literature is constituted by the Sphere Decoder (SD) [364]. The SD was first proposed for employment in the context of space-time processing in [365], where it is used for computing the ML estimates of the modulated symbols transmitted simultaneously from multiple transmit antennas. The complex-valued version of the sphere decoder was proposed by Hochwald and Brink in [176]. The subject was further investigated by Damen *et al.* in [366]. Subsequently, an improved version of the Complex Sphere Decoder (CSD) was advocated by Pham *et al.*

in [367].

Furthermore, CSD-aided detection was considered by Tellambura *et al.* in a joint channel estimation and data detection scheme considered in [368], while a revised version of the CSD method, namely the so-called Multistage Sphere Decoding (MSD) was introduced in [369]. The generalized version of the Sphere Decoder, which is suitable for employment in rank-deficient MIMO systems was introduced by Damen *et al.* in [370] and further refined by Cui and Tellambura in [371].

In this section we would like to introduce a novel Optimised Hierarchy (OH) RSA-aided SDM detection method, which may be regarded as an advanced extension of the CSD method portrayed in [367]. The algorithm proposed extends the potential range of applications of the CSD methods of [176] and [367], as well as reduces the associated computational complexity, rendering the algorithm attractive for employment in practical systems.

The method proposed, which we refer to as the Soft-output OPtimised HIErarchy (SOPHIE) algorithm exhibits the following attractive properties:

1) The method can be used in the so-called over-loaded scenario, where the number of transmit antenna elements exceeds that of the receive antenna elements. A particularly interesting potential application is found in a Multiple Input Single Output scenario, where the system employs multiple transmit antennas and a single receive antenna. Moreover, the associated computational complexity is only moderately increased even in heavily over-loaded scenarios and it is almost independent of the number of receive antennas.

2) As opposed to the conventional CSD schemes, the calculation of the sphere radius is not required and therefore the method proposed is robust to the particular choice of the initial parameters both in terms of the achievable performance and the associated computational complexity.

3) The method proposed allows a selected subset of the transmitted information-carrying symbols to be detected, while the interference imposed by the undetected signals is suppressed.

4) The overall computational complexity required is only slightly higher than that imposed by the linear MMSE multi-user detector designed for detecting a similar number of users.

5) Finally, the associated computational complexity is fairly independent of the channel conditions quantified in terms of the Signal-to-Noise Ratio encountered.

10.4.1 Optimised Hierarchy Reduced Search Algorithm-aided ML SDM Detection

We commence our discourse by deriving an OHRSA-aided ML SDM detection method for a constant-envelope modulation scheme, such as M-PSK, where the transmitted symbols s satisfy the condition of $|s|^2 = 1,\ \forall s \in \mathcal{M}$, and $\mathcal{M}$ denotes the set of M complex-valued constellation points. In the next section, we will then demonstrate that the method derived is equally applicable to arbitrary signal constellations, particularly for high-throughput multi-level modulation schemes, such as M-QAM.

Let us recall that our channel model described in detail in Section 10.3 is given by

$$\mathbf{y} = \mathbf{H}\mathbf{s} + \mathbf{w}, \tag{10.7}$$

where we omit the OFDM subcarrier and symbol indices k and n, respectively. As outlined in [90] , the ML SDM detector provides an m_{t}-antenna-based estimated signal vector candidate $\hat{\mathbf{s}}$, which maximises the objective function defined as the conditional *a posteriori* probability function $\mathtt{P}\left\{\check{\mathbf{s}}|\mathbf{y}, \mathbf{H}\right\}$ over the set $\mathcal{M}^{m_{\mathrm{t}}}$ of legitimate solutions. More explicitly, we have

$$\hat{\mathbf{s}} = \arg \max_{\check{\mathbf{s}} \in \mathcal{M}^{m_{\mathrm{t}}}} \mathtt{P}\left\{\check{\mathbf{s}}|\mathbf{y}, \mathbf{H}\right\}, \tag{10.8}$$

where $\mathcal{M}^{m_{\mathrm{t}}}$ is the set of *all possible* m_{t}-dimensional candidate symbol vectors of the m_{t}-antenna-based transmitted signal vector $\mathbf{s}$. More specifically, we have

$$\mathcal{M}^{m_{\mathrm{t}}} = \left\{\check{\mathbf{s}} = (\check{s}_1, \cdots, \check{s}_{m_{\mathrm{t}}})^{\mathtt{T}};\ \check{s}_i \in \mathcal{M}\right\}. \tag{10.9}$$

Furthermore, it was shown in [90] that we have

$$\mathtt{P}\left\{\check{\mathbf{s}}|\mathbf{y}, \mathbf{H}\right\} = A \exp\left[-\frac{1}{\sigma_w^2}\|\mathbf{y} - \mathbf{H}\check{\mathbf{s}}\|^2\right], \tag{10.10}$$

where A is a constant, which is independent of any of the values $\{\check{s}_i\}_{i=1,\cdots,m_{\mathrm{t}}}$. Thus, it may be shown [90] that the probability maximisation problem of Equation (10.8) is equivalent to the corresponding Euclidean distance minimisation problem. Specifically, we have

$$\hat{\mathbf{s}} = \arg \min_{\check{\mathbf{s}} \in \mathcal{M}^{m_{\mathrm{t}}}} \|\mathbf{y} - \mathbf{H}\check{\mathbf{s}}\|^2, \tag{10.11}$$

where the probability-based objective function of Equation (10.8) is substituted by the objective function determined by the Euclidean distance between the received signal vector $\mathbf{y}$ and the corresponding product of the channel matrix $\mathbf{H}$ with the *a priori* candidate of the transmitted signal vector $\check{\mathbf{s}} \in \mathcal{M}^{m_{\mathrm{t}}}$.

Consequently, our detection method relies on the observation, which may be summarised in the following lemma.

Lemma 1 *The ML solution of Equation* (10.8) *of a noisy linear problem described by Equation* (10.7) *is given by*

$$\hat{\mathbf{s}} = \arg \min_{\check{\mathbf{s}} \in \mathcal{M}^{m_{\mathrm{t}}}} \left\{\|\mathbf{U}(\check{\mathbf{s}} - \hat{\mathbf{x}})\|^2\right\}, \tag{10.12}$$

where $\mathbf{U}$ *is an upper-triangular matrix having positive real-valued elements on the main diagonal and satisfying*

$$\mathbf{U}^{\mathtt{H}}\mathbf{U} = (\mathbf{H}^{\mathtt{H}}\mathbf{H} + \sigma_w^2\mathbf{I}), \tag{10.13}$$

while

$$\hat{\mathbf{x}} = (\mathbf{H}^{\mathtt{H}}\mathbf{H} + \sigma_w^2\mathbf{I})^{-1}\mathbf{H}^{\mathtt{H}}\mathbf{y} \tag{10.14}$$

is the unconstrained MMSE estimate of the transmitted signal vector $\mathbf{s}$*, which was derived in [90] .*

Note 1: Observe that Lemma 1 imposes no constraints on the dimensions, or rank of the matrix $\mathbf{H}$ of the linear system described by Equation (10.7). This property is particularly important, since it enables us to apply our proposed detection technique to the scenario of *over-loaded* systems, where the number of transmit antenna elements exceeds that of the receive antenna elements.

Note 2: As substantiated by Equation (10.11), it is sufficient to prove that the following minimisation problems are equivalent

$$\hat{\mathbf{s}} = \arg \min_{\check{\mathbf{s}} \in \mathcal{M}^{m_t}} \|\mathbf{y} - \mathbf{H}\check{\mathbf{s}}\|^2 \tag{10.15}$$

$$\Leftrightarrow \quad \hat{\mathbf{s}} = \arg \min_{\check{\mathbf{s}} \in \mathcal{M}^{m_t}} \|\mathbf{U}(\check{\mathbf{s}} - \hat{\mathbf{x}})\|^2. \tag{10.16}$$

Proof of Lemma 1: It is evident that in contrast to the matrix $\mathbf{H}^H\mathbf{H}$, the matrix $(\mathbf{H}^H\mathbf{H} + \sigma_w^2\mathbf{I})$ of Equation (10.12) is always Hermitian and positively definite, regardless of the rank of the channel matrix $\mathbf{H}$ associated with the particular MIMO channel realisation encountered. Consequently, it may be represented as the product of an upper-triangular matrix $\mathbf{U}$ and its Hermitian adjoint matrix $\mathbf{U}^H$ using for example the Cholesky factorisation method [372].

Let $\mathbf{U}$ be the matrix generated by the Cholesky decomposition of the Hermitian positive definite matrix $(\mathbf{H}^H\mathbf{H} + \sigma_w^2\mathbf{I})$ of Equation (10.13). More specifically, we have

$$\mathbf{U}^H\mathbf{U} = (\mathbf{H}^H\mathbf{H} + \sigma_w^2\mathbf{I}), \tag{10.17}$$

where $\mathbf{U}$ is an upper-triangular matrix having positive real-valued elements on its main diagonal.

Upon expanding the objective function of Equation (10.12) and subsequently invoking Equation (10.13) we obtain

$$\begin{aligned} J(\check{\mathbf{s}}) &= \|\mathbf{U}(\check{\mathbf{s}} - \hat{\mathbf{x}})\|^2 \\ &= (\check{\mathbf{s}} - \hat{\mathbf{x}})^H\mathbf{U}^H\mathbf{U}(\check{\mathbf{s}} - \hat{\mathbf{x}}) \\ &= (\check{\mathbf{s}} - \hat{\mathbf{x}})^H(\mathbf{H}^H\mathbf{H} + \sigma_w^2\mathbf{I})(\check{\mathbf{s}} - \hat{\mathbf{x}}) \\ &= \check{\mathbf{s}}^H(\mathbf{H}^H\mathbf{H} + \sigma_w^2\mathbf{I})\check{\mathbf{s}} - \hat{\mathbf{x}}^H(\mathbf{H}^H\mathbf{H} + \sigma_w^2\mathbf{I})\check{\mathbf{s}} \\ &\quad - \check{\mathbf{s}}^H(\mathbf{H}^H\mathbf{H} + \sigma_w^2\mathbf{I})\hat{\mathbf{x}} + \hat{\mathbf{x}}^H(\mathbf{H}^H\mathbf{H} + \sigma_w^2\mathbf{I})\hat{\mathbf{x}}. \end{aligned} \tag{10.18}$$

Furthermore, substituting Equation (10.14) into (10.18) yields

$$\begin{aligned} J(\check{\mathbf{s}}) &= \check{\mathbf{s}}^H\mathbf{H}^H\mathbf{H}\check{\mathbf{s}} - \mathbf{y}^H\mathbf{H}\check{\mathbf{s}} - \check{\mathbf{s}}^H\mathbf{H}^H\mathbf{y} \\ &\quad + \sigma_w^2\check{\mathbf{s}}^H\check{\mathbf{s}} + \mathbf{y}^H\mathbf{H}(\mathbf{H}^H\mathbf{H} + \sigma_w^2\mathbf{I})^{-1}\mathbf{H}^H\mathbf{y} \\ &= \|\mathbf{y} - \mathbf{H}\check{\mathbf{s}}\|^2 + \underbrace{\sigma_w^2\check{\mathbf{s}}^H\check{\mathbf{s}} + \mathbf{y}^H(\mathbf{H}(\mathbf{H}^H\mathbf{H} + \sigma_w^2\mathbf{I})^{-1}\mathbf{H}^H - \mathbf{I})\mathbf{y}}_{\psi}. \end{aligned} \tag{10.19}$$

Observe that in the case of a system employing a constant-envelope modulation scheme, such as M-PSK, where we have $\check{\mathbf{s}}^{\mathrm{H}}\check{\mathbf{s}} = 1$, ψ constitutes a real-valued scalar and its value does not depend on the argument $\check{\mathbf{s}}$ of the minimisation problem formulated in Equation (10.12). Consequently, the minimisation of the objective function $J(sv\check{e}cs)$ of Equation (10.19) can be reduced to the minimisation of the term $\|\mathbf{y} - \mathbf{Hx})\|^2$, which renders it equivalent to the minimisation problem of Equation (10.15). This completes the proof.

Using Lemma 1, in particular the fact that the matrix $\mathbf{U}$ is an upper-triangular matrix, the objective function $J(\check{\mathbf{s}})$ of Equation (10.19) may be reformulated as follows

$$\begin{aligned} J(\check{\mathbf{s}}) &= \|\mathbf{U}(\check{\mathbf{s}} - \hat{\mathbf{x}})\|^2 \\ &= (\check{\mathbf{s}} - \hat{\mathbf{x}})^{\mathrm{H}}\mathbf{U}^{\mathrm{H}}\mathbf{U}(\check{\mathbf{s}} - \hat{\mathbf{x}}) \\ &= \sum_{i=1}^{m_{\mathrm{t}}} \Big| \sum_{j=i}^{m_{\mathrm{t}}} u_{ij}(\check{s}_j - \hat{x}_j) \Big|^2 = \sum_{i=1}^{m_{\mathrm{t}}} \phi_i(\check{\mathbf{s}}_i), \end{aligned} \tag{10.20}$$

where $J(\check{\mathbf{s}})$ and $\phi_i(\check{\mathbf{s}}_i)$ are positive real-valued cost and sub-cost functions, respectively. Elaborating a little further we have

$$\begin{aligned} \phi_i(\check{\mathbf{s}}_i) &= \Big| \sum_{j=i}^{m_{\mathrm{t}}} u_{ij}(\check{s}_j - \hat{x}_j) \Big|^2 \\ &= \Big| u_{ii}(\check{s}_i - \hat{x}_i) + \underbrace{\sum_{j=i+1}^{m_{\mathrm{t}}} u_{ij}(\check{s}_j - \hat{x}_j)}_{a_i} \Big|^2. \end{aligned} \tag{10.21}$$

Note that the term a_i is a complex-valued scalar, which is independent of the specific symbol value $\check{s}_i$ of the ith element of the *a priori* candidate signal vector $\check{\mathbf{s}}$.

Furthermore, let $J_i(\check{\mathbf{s}}_i)$ be a Cumulative Sub-Cost (CSC) function recursively defined as

$$J_{m_{\mathrm{t}}}(\check{s}_{m_{\mathrm{t}}}) = \phi_{m_{\mathrm{t}}}(\check{s}_{m_{\mathrm{t}}}) = |u_{m_{\mathrm{t}}m_{\mathrm{t}}}(\check{s}_{m_{\mathrm{t}}} - \hat{x}_{m_{\mathrm{t}}})|^2 \tag{10.22a}$$

$$J_i(\check{\mathbf{s}}_i) = J_{i+1}(\check{\mathbf{s}}_{i+1}) + \phi_i(\check{\mathbf{s}}_i), \quad i = 1, \cdots, m_{\mathrm{t}}\text{–}1, \tag{10.22b}$$

where we define the candidate subvector as $\check{\mathbf{s}}_i = [\check{s}_i, \cdots, \check{s}_{m_{\mathrm{t}}}]$. Clearly, $J_i(\check{\mathbf{s}}_i)$ exhibits the following properties

$$J(\check{\mathbf{s}}) = J_1(\check{\mathbf{s}}_1) > J_2(\check{\mathbf{s}}_2) > \cdots > J_{m_{\mathrm{t}}}(\check{s}_{m_{\mathrm{t}}}) > 0 \tag{10.23a}$$

$$J_i(\check{\mathbf{s}}_i) = J_i(\{\check{s}_j\},\ j = i, \cdots, m_{\mathrm{t}}) \tag{10.23b}$$

for all possible realisations of $\hat{\mathbf{x}} \in \mathbb{C}^{m_{\mathrm{t}}}$ and $\check{\mathbf{s}} \in \mathcal{M}^{m_{\mathrm{t}}}$, where the space $\mathbb{C}^{m_{\mathrm{t}}}$ contains all possible unconstrained MMSE estimates $\hat{\mathbf{x}}$ of the transmitted signal vector $\mathbf{s}$.

Equations (10.23a) and (10.23b) enable us to employ a highly efficient reduced search algorithm, which decreases the number of objective function evaluations of the minimisation problem outlined in Equation (10.12) to a small fraction of the set $\mathcal{M}^{m_{\mathrm{t}}}$. This reduced-complexity search algorithm is outlined in the next section.

10.4.2 Search Strategy

Example 1 (OHRSA-ML 3x3 BPSK)

Consider a BPSK system having $n_{\mathrm{r}} = m_{\mathrm{t}} = 3$ transmit and receive antennas, which is described by Equation (10.7). The transmitted signal $\mathbf{s}$, the received signal $\mathbf{y}$ as well as the channel matrix $\mathbf{H}$ of Equation (10.7) are exemplified by the following values

$$\mathbf{s} = \begin{bmatrix} 1 \\ -1 \\ 1 \end{bmatrix}, \quad \mathbf{y} = \begin{bmatrix} 0.2 \\ 0.8 \\ -1.2 \end{bmatrix}, \quad \mathbf{H} = \begin{bmatrix} 0.5 & 0.4 & -0.2 \\ 0.4 & -0.3 & 0.2 \\ 0.9 & 1.8 & -0.1 \end{bmatrix}. \tag{10.24}$$

Our task is to obtain the ML estimate of the transmitted signal vector $\mathbf{s}$. Firstly, we evaluate the triangular matrix $\mathbf{U}$ of Equation (10.13) as well as the unconstrained MMSE estimate $\hat{\mathbf{x}}$ of Equation (10.14). The resultant quantities are given by

$$\mathbf{U} = \begin{bmatrix} 1.15 & 1.48 & -0.10 \\ 0 & 1.18 & -0.15 \\ 0 & 0 & 0.40 \end{bmatrix}, \quad \hat{\mathbf{x}} = \begin{bmatrix} 0.85 \\ -1.05 \\ -0.01 \end{bmatrix}. \tag{10.25}$$

Observe that the direct slicing of the MMSE estimate $\hat{\mathbf{x}}$ will result in an erroneously decided signal $\hat{\boldsymbol{s}} = \begin{bmatrix} 1 & -1 & -1 \end{bmatrix}^{\mathrm{T}}$. Subsequently, following the philosophy outlined in Section 10.4.1, for each legitimate candidate $\check{\mathbf{s}} \in \mathcal{M}^{m_{\mathrm{t}}}$ of the m_{t}-antenna-based composite transmitted signal vector $\mathbf{s}$ we calculate the corresponding value of the cost function $J(\check{\mathbf{s}})$ of Equation (10.20) using the recursive method described by Equation (10.22). The search process performed is illustrated in Figure 10.6(a). Each evaluation step, namely each evaluation of the CSC function $J_i(\check{\mathbf{s}}_i)$ of Equation (10.22b) is indicated by an elliptic node in Figure 10.6(a). The label inside each node indicates the order of evaluation as well as the corresponding value $J_i(\check{\mathbf{s}}_i)$ of the CSC function inside the brackets. Furthermore, the branches corresponding to the two legitimate values of $\check{s}_i = -1$ and 1 are indicated using the dashed and solid edges and nodes, respectively.

More specifically, commencing from the top of Figure 10.6(a), at recursive step $i = 3$ we calculate the CSC function of Equation (10.22a) associated with all legitimate values of the last element of the signal vector $\mathbf{s}$, where we have

$$J_3(\check{s}_3 = -1) = |u_{33}(\check{s}_3 - \hat{x}_3)|^2 = (0.40(-1 - (-0.01)))^2 = 0.15 \tag{10.26}$$

and

$$J_3(\check{s}_3 = 1) = (0.40(1 - (-0.01)))^2 = 0.16. \tag{10.27}$$

The corresponding values of $J_3(\check{s}_3 = -1) = 0.15$ and $J_3(\check{s}_3 = 1) = 0.16$ are indicated by the nodes 1 and 8 in Figure 10.6(a). Observe that the *recursive* nature of the search process considered suggests that the latter value of $J_3(\check{s}_3 = 1)$ is not considered until the entire search branch originating from the more promising node 1 associated with the lower CSC value of 0.15 is completed. Consequently, the value $J_3(\check{s}_3 = 1)$ is the 8th value of the CSC function to be evaluated, which is indicated by the corresponding node's index 8.

Furthermore, at recursive step $i = 2$ for each hypothesised value $\check{s}_3$ we calculate both the

quantity a_2 of Equation (10.21) as well as the sub-cost function of Equation (10.21) and the corresponding CSC function of Equation (10.22b) associated with all legitimate values of the last-but-one element of the signal vector $\mathbf{s}$. Explicitly, for $\check{s}_3 = -1$ we have

$$a_2 = u_{23}(\check{s}_3 - \hat{x}_3) = -0.15(-1 - (-0.01)) = 0.15 \tag{10.28}$$

and

$$\begin{aligned} J_2(\check{s}_2 = -1, \check{s}_3 = -1) &= J_3(\check{s}_3 = -1) + \phi_2(\check{s}_2 = -1, \check{s}_3 = -1) \\ &= J_3(\check{s}_3 = -1) + |u_{22}(\check{s}_2 - \hat{x}_2)) + a_2|^2 \\ &= 0.15 + (1.18(-1 - (-1.05)) + 0.15) = 0.20 \\ J_2(\check{s}_2 = 1, \check{s}_3 = -1) &= J_3(\check{s}_3 = -1) + \phi_2(\check{s}_2 = 1, \check{s}_3 = -1) \\ &= 0.15 + (1.18(1 - (-1.05)) + 0.15) = 6.79. \end{aligned} \tag{10.29}$$

The corresponding values of $J_2(\check{\mathbf{s}}_2 = [-1, -1]) = 0.20$ and $J_2(\check{\mathbf{s}}_2 = [1, -1]) = 6.79$ are indicated by the nodes 2 and 5 in Figure 10.6(a).

Finally, at recursive index $i = 1$ we calculate the quantity $a_1(\check{\mathbf{s}}_2)$ for each hypothesised subvector $\check{\mathbf{s}}_2$ and the sub-cost function $\phi_1(\check{\mathbf{s}}_1)$ of Equation (10.21) as well as the corresponding *total* cost function $J(\check{s}_1 = -1, \check{\mathbf{s}}_2)$ and $J(\check{s}_1 = 1, \check{\mathbf{s}}_2)$ of Equation (10.20) associated with all legitimate values of the first element of the signal vector $\mathbf{s}$. Specifically, for the left-most search branch of Figure 10.6(a) corresponding to the *a priori* candidate $\check{\mathbf{s}}_2 = [-1, -1]$ we have

$$\begin{aligned} a_1 &= u_{12}(\check{s}_2 - \hat{x}_2) + u_{13}(\check{s}_3 - \hat{x}_3) \\ &= 1.48(-1 - -1.05) + -0.10(-1 - -0.01) = 0.17 \end{aligned} \tag{10.30}$$

and

$$\begin{aligned} J_1(\check{s}_1 = -1, \check{s}_2 = -1, \check{s}_3 = -1) &= J_2(\check{s}_2 = -1, \check{s}_3 = -1) + \phi_1(\check{s}_1 = -1, \check{s}_2 = -1, \check{s}_3 = -1) \\ &= J_2(\check{s}_2 = -1, \check{s}_3 = -1) + |u_{11}(\check{s}_1 - \hat{x}_1)) + a_1|^2 \\ &= 0.20 + (1.15(-1 - 0.85) + 0.17) = 4.03, \\ J_1(\check{s}_1 = 1, \check{s}_2 = -1, \check{s}_3 = 1) &= J_2(\check{s}_2 = -1, \check{s}_3 = -1) + \phi_2(\check{s}_1 = 1, \check{s}_2 = -1, \check{s}_3 = -1) \\ &= 0.20 + (1.15(1 - 0.85) + 0.17) = 0.31. \end{aligned} \tag{10.31}$$

Upon completing the entire search process outlined above we arrive at eight different values of the total cost function $J(\check{\mathbf{s}})$ associated with the eight legitimate 3-bit solutions of the detection problem considered. The eight different candidate solutions are indicated by the eight bottom-most elliptic nodes in Figure 10.6(a). Clearly, the ML solution is constituted by the search branch terminating at node 11 of Figure 10.6(a) and having the minimum value $J(\check{\mathbf{s}}) = 0.19$ of the total cost function.

Observe that the difference between the values of $J_3(\check{s}_3 = -1)$ and $J_3(\check{s}_3 = 1)$ associated

with nodes 1 and 8 in Figure 10.6(a) is quite small and thus the ML solution along either of the search branches commencing at nodes 1 and 8 in Figure 10.6(a) may not be recognised with a high degree of confidence. On the other hand, the difference between the values of the CSC function along two complementary search branches commencing at nodes 1 and 8 becomes substantially more evident, if we apply the *best-first* detection strategy suggested in [373]. More specifically, we sort the columns of the channel matrix $\mathbf{H}$ in the increasing order of their Euclidean or square norm. The resultant reordered channel matrix $\mathbf{H}'$ as well as the corresponding triangular matrix $\mathbf{U}$ and the unconstrained MMSE estimate $\hat{\mathbf{x}}'$ may be expressed as

$$\mathbf{H}' = \begin{bmatrix} -0.2 & 0.5 & 0.4 \\ 0.2 & 0.4 & -0.3 \\ -0.1 & 0.9 & 1.8 \end{bmatrix}, \mathbf{U}' = \begin{bmatrix} 0.44 & -0.25 & -0.73 \\ 0 & 1.12 & 1.35 \\ 0 & 0 & 1.11 \end{bmatrix}, \hat{\mathbf{x}}' = \begin{bmatrix} -0.01 \\ 0.85 \\ -1.05 \end{bmatrix}. \tag{10.32}$$

The search tree generated by applying the aforementioned search process and using the modified quantities $\mathbf{H}', \mathbf{U}'$ and $\hat{\mathbf{x}}'$ is depicted in Figure 10.6(b). Note the substantial difference between the values of the CSC function $J_3(\check{s}_3 = -1)$ and $J_3(\check{s}_3 = 1)$ associated with the nodes 1 and 8. Moreover, by comparing the value of the CSC function $J_3(\check{s}_3)$ of node 8 to that of the total cost function $J(\check{\mathbf{s}})$ of node 7 we can conclude that the search along the branch commencing at node 8 is in fact redundant.

In order to further optimise our search process, at recursive steps of $i = 3$ and 2 we first calculate the sub-cost functions $\phi_3(\check{s}_3 = \{-1, 1\})$ and $\phi_2(\check{s}_3, \check{s}_2 = \{-1, 1\})$ of Equation (10.21). We then compare the values obtained and continue with the processing of the specific search branch corresponding to the smaller value of the sub-cost function $\phi_i(\check{\mathbf{s}}_i)$ first. The resultant search tree is depicted in Figure 10.6(c). Observe that in Figure 10.6(c) the minimum value of the total cost function $J(\check{\mathbf{s}}) = 0.19$ is obtained faster, namely in three evaluation steps in comparison to seven steps required by the search tree of Figure 10.6(b).

Finally, we discard all the search branches commencing at nodes having an associated value of the CSC function, which is in excess of the minimum total cost function value obtained. Specifically, we discontinue the search branches commencing at nodes 5 and 8 having the CSC function values in excess of 0.19, namely 4.03 and 5.15, respectively. The resultant reduced search tree is depicted in Figure 10.6(d). Note that the ML solution is obtained in six evaluation steps in comparison to the 14 steps required in the case of the exhaustive search of Figure 10.6(a). In conclusion, upon performing the appropriate reordering of the obtained ML estimate, we arrive at the correct value of the transmitted signal vector $\hat{\mathbf{s}} = \begin{bmatrix} 1 & -1 & 1 \end{bmatrix}^{\mathrm{T}}$.

10.4.2.1 Generalisation of the OHRSA-ML SDM Detector

Let us now generalise and substantiate further the detection paradigm derived in Example 1. Firstly, we commence the recursive search process with the evaluation of the CSC function value $J_{m_{\mathrm{t}}}(\check{s}_{m_{\mathrm{t}}})$ of Equation (10.22a). Secondly, at each recursive step i of the search algorithm proposed we stipulate a series of hypotheses concerning the value of the M-ary transmitted symbol s_i associated with the ith transmit antenna element and subsequently calculate the conditioned sub-cost function $J_i(\check{\mathbf{s}}_i)$ of Equation (10.22b), where $\check{\mathbf{s}}_i = (\check{s}_i, \cdots, \check{s}_{m_{\mathrm{t}}})^{\mathrm{T}}$

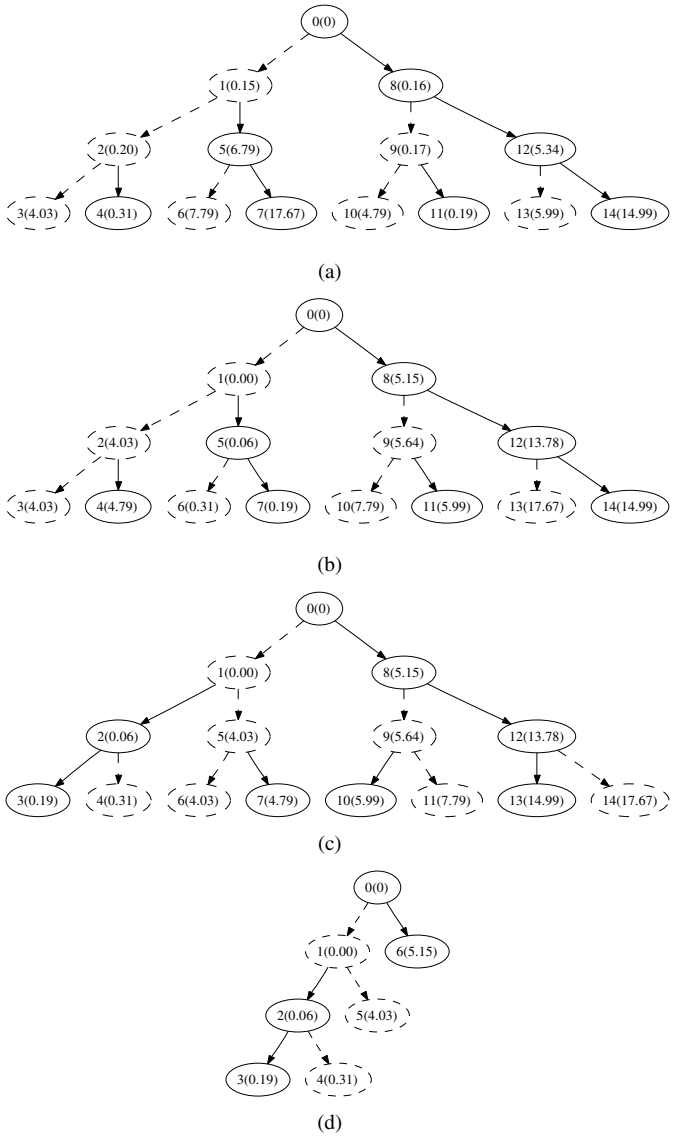


Figure 10.6: Examples of a search tree formed by the OHRSA-ML SDM detector in the scenario of a system employing BPSK modulation, $m_{\mathrm{t}} = n_{\mathrm{r}} = 3$ transmit and receive antennas and encountering average SNRs of 10dB. The labels indicate the order of evaluation, as well as the corresponding value $J_i(\check{\mathbf{s}}_i)$ of the CSC function of Equation (10.22), as seen in the brackets. The dashed and solid arrows indicate the values of $\check{s}_i = -1$ and 1, respectively.

denotes the subvector of the $m_{\rm t}$-antenna-based candidate vector $\check{\mathbf{s}}$ comprising only the indices higher than or equal to i. Furthermore, for each tentatively assumed value of $\check{s}_i$ we execute a successive recursive search step $i-1$, which is conditioned on the hypotheses made in all preceding recursive steps $j = i, \cdots, m_{\rm t}$. As substantiated by Equations (10.21) and (10.22b), the value of the CSC function $J_i(\check{\mathbf{s}}_i)$ is dependent only on the values of the elements $\{\check{s}_j\}_{j=i,\cdots,m_{\rm t}}$ of the *a priori* candidate signal vector $\check{\mathbf{s}}$, which are hypothesised from step $j = m_{\rm t}$ up to the present step i of our recursive process. At each arrival at the step $i = 1$ of the recursive process, a complete candidate vector $\check{\mathbf{s}}$ is hypothesised and the corresponding value of the cost function $J(\check{\mathbf{s}})$ formulated in Equation (10.20) is evaluated.

Observe that the recursive hierarchical search procedure described above may be employed to perform an exhaustive search through all possible values of the transmitted signal vector $\check{\mathbf{s}}$, and the resultant search process is guaranteed to arrive at the ML solution $\check{\mathbf{s}}_{\rm ML}$, which minimises the value of the cost function $J(\check{\mathbf{s}})$ of Equation (10.20). Fortunately however, as opposed to other ML search schemes, the search process described above can be readily optimised, resulting in a dramatic reduction of the associated computational complexity. Specifically, the potential optimisation complexity gain originates from the fact that most of the hierarchical search branches can be discarded at an early stage of the recursive search process. The corresponding optimisation rules proposed may be outlined as follows.

Rule 1. We reorder the system model of Equation (10.7) as suggested in [373]. Specifically, we apply the *best-first* detection strategy outlined in [90, pp.754-756] , which implies that the transmitted signal vector components are detected in the decreasing order of the associated channel quality. As it was advocated in [90, pp.754-756] , the quality of the channel associated with the ith element of the transmitted signal vector $\mathbf{s}$ is determined by the norm of the ith column of the channel matrix $\mathbf{H}$. Consequently, for the sake of applying the *best-first* detection strategy, the columns of the channel matrix $\mathbf{H}$ are sorted in the increasing order of their norm. Thus, the resultant, column-reordered channel matrix $\mathbf{H}$ complies with the following criterion

$$\|(\mathbf{H})_1\|^2 \leq \|(\mathbf{H})_2\|^2 \leq \cdots \leq \|(\mathbf{H})_{m_{\rm t}}\|^2, \tag{10.33}$$

where $(\mathbf{H})_i$ denotes the ith column of the channel matrix $\mathbf{H}$. Note that the elements of the transmitted signal vector $\mathbf{s}$ are reordered correspondingly, but their original order has to be reinstated in the final stage of the detection process.

Rule 2. At each recursive detection step $i = m_{\rm t}, \cdot, 1$, the potential candidate values $\{c_m\}_{m=1,\cdots,M} \in \mathcal{M}$ of the transmitted signal component s_i are considered in the increasing order of the corresponding value of the sub-cost function $\phi_i(\check{\mathbf{s}}_i) = \phi_i(c_m, \check{\mathbf{s}}_{i+1})$ of Equation (10.21), where we have

$$\phi_i(c_1, \check{\mathbf{s}}_{i+1}) < \cdots < \phi_i(c_m, \check{\mathbf{s}}_{i+1}) < \cdots \phi_i(c_M, \check{\mathbf{s}}_{i+1}),$$

and according to Equation (10.21)

$$\begin{aligned}\phi_i(c_m, \check{\mathbf{s}}_{i+1}) &= |u_{ii}(c_m - \hat{x}_i) + a_i|^2 \\ &= u_{ii}|c_m - \hat{x}_i + \frac{a_i}{u_{ii}^2}|^2. \end{aligned} \tag{10.34}$$

Consequently, the more likely candidates c_m of the ith element of the transmitted signal vector $\mathbf{s}$ are examined first. Observe that the sorting criterion of Equation (10.34) may also be interpreted as a biased Euclidean distance of the candidate constellation point c_m from the unconstrained MMSE estimate $\hat{x}_i$ of the transmitted signal component s_i.

Rule 3. We define a *cut-off* value of the cost function $J_{\min} = \min\{J(\check{\mathbf{s}})\}$ as the minimum value of the total cost function obtained up to the present point of the search process. Consequently, at each arrival at step $i = 1$ of the recursive search process, the *cut-off* value of the cost function is updated as follows

$$J_{\min} = \min\{J_{\min}, J(\check{\mathbf{s}})\} \tag{10.35}$$

Rule 4. Finally, at each recursive detection step i, only the high probability search branches corresponding to the highly likely symbol candidates c_m resulting in a value of the CSC function obeying $J_i(c_m) < J_{\min}$ are pursued. Furthermore, as follows from the sorting criterion of the optimisation Rule 2, as soon as the inequality $J_i(c_m) > J_{\min}$ is encountered, the search loop at the ith detection step is discontinued.

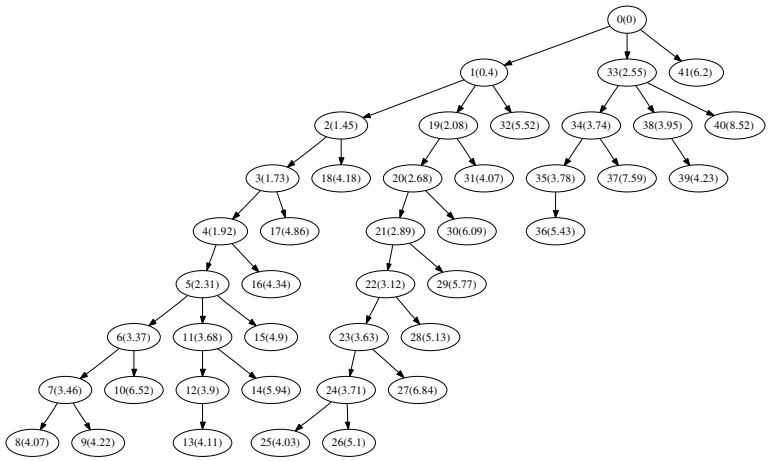
An example of the search tree generated by the algorithm invoking the Rules 1-4 described above is depicted in Figure 10.7. The search trees shown correspond to the scenario of using QPSK modulation and employing $m_{\rm t} = n_{\rm r} = 8$ antenna elements at both the transmitter and the receiver. Encountering the average SNRs of (a) 10 and (b) 20 dB was considered. Each step of the search procedure is depicted as an ellipsoidal-shaped node. The label associated with each node indicates the order of visitation, as well as the corresponding value of the CSC function $J_i(\check{\mathbf{s}}_i)$ formulated in Equation (10.22), as seen in the brackets. As suggested by the fact that QPSK modulation is considered, at each recursive step i, *four* legitimate search branches are possible. However, as can be seen in Figure 10.7(a), only a small fraction of the potential search branches are actually pursued. Observe that the rate of convergence of the algorithm proposed is particularly rapid at high values of SNR. In the case of encountering low SNR values, the convergence rate decreases. Nevertheless, the associated computational complexity is dramatically lower than that associated with an exhaustive ML search.

The pseudo-code summarising the recursive implementation of the OHRSA-based ML SDM detector proposed is depicted in Algorithm 3.

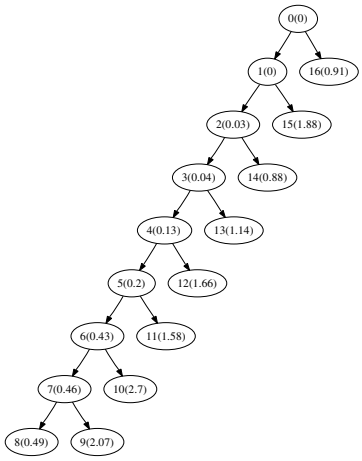
10.4.3 Bitwise OHRSA ML SDM Detection

Example 2 (OHRSA-ML QPSK 2x2)

Let us now consider a QPSK system having $n_{\rm r} = m_{\rm t} = 3$ transmit and receive antennas, which is described by Equation (10.7). The transmitted signal $\mathbf{s}$, the received signal $\mathbf{y}$ as



(a)



(b)

Figure 10.7: Examples of a search tree formed by the OHRSA-ML SDM detector in the scenario of a system employing QPSK modulation, $m_{\mathrm{t}} = n_{\mathrm{r}} = 8$ transmit and receive antennas and encountering average SNRs of (a) 10dB and (b) 20dB. The labels indicate the order of visitation, as well as the corresponding value $J_i(\check{\mathbf{s}}_i)$ of the CSC function of Equation (10.22), as seen in the brackets. The ML solution is attained in (a) 41 and (b) 16 evaluation steps in comparison to the $4^8 = 65536$ evaluation steps required in the case of the exhaustive ML search.

Algorithm 3 OH-RSA-aided ML SDM Detector

$$\texttt{Sort}\{\mathbf{H}\},\ \texttt{such that}\ \|(\mathbf{H})_1\|^2 \leq \cdots \leq \|(\mathbf{H})_{m_{\rm t}}\|^2 \tag{10.36a}$$
$$\mathbf{G} = (\mathbf{H}^{\rm H}\mathbf{H} + \sigma_w^2\mathbf{I}) \tag{10.36b}$$
$$\mathbf{U} = \texttt{CholeskyDecomposition}(\mathbf{G}) \tag{10.36c}$$
$$\hat{\mathbf{x}} = \mathbf{G}^{-1}\mathbf{H}^{\rm H}\mathbf{y} \tag{10.36d}$$
$$\texttt{Calculate}\quad J_{m_{\rm t}} \tag{10.36e}$$
$$\texttt{Unsort}\{\hat{\mathbf{s}}\} \tag{10.36f}$$

$$\texttt{function}\quad \texttt{Calculate}\quad J_i(\check{\mathbf{s}}_i) \tag{10.36g}$$
$$a_i = \sum_{j=i+1}^{m_{\rm t}} u_{ij}(\check{s}_j - \hat{x}_j) \tag{10.36h}$$
$$\texttt{Sort}\{c_m\},\ \texttt{such that}\ \phi_i(c_1) < \cdots < \phi_i(c_M), \tag{10.36i}$$
$$\texttt{where}\quad \phi_i(c_m) = |u_{ii}(c_m - \hat{x}_i) + a_i|^2 \tag{10.36j}$$
$$\texttt{for}\quad m = 1, 2, \ldots, M\quad \texttt{do}$$
$$\check{s}_i = c_m \tag{10.36k}$$
$$J_i(\check{\mathbf{s}}_i) = J_{i+1}(\check{\mathbf{s}}_{i+1}) + \phi_i(\check{s}_i) \tag{10.36l}$$
$$\texttt{if}\quad J_i(\check{\mathbf{s}}_i) < J_{\min}\quad \texttt{then} \tag{10.36m}$$
$$\texttt{if}\quad i > 0\quad \texttt{then}\quad \texttt{Calculate}\quad J_{i-1} \tag{10.36n}$$
$$\texttt{else}$$
$$J_{\min} = J(\check{\mathbf{s}}) \tag{10.36o}$$
$$\hat{\mathbf{s}} = \check{\mathbf{s}} \tag{10.36p}$$
$$\texttt{end}\quad \texttt{if}$$
$$\texttt{end}\quad \texttt{if}$$
$$\texttt{end}\quad \texttt{for}$$
$$\texttt{end}\quad \texttt{function}$$

well as the *best-first* reordered channel matrix $\mathbf{H}$ of Equation (10.7) are exemplified by the following values

$$\mathbf{s} = \begin{bmatrix} 1-1\jmath \\ -1-1\jmath \end{bmatrix}, \quad \mathbf{y} = \begin{bmatrix} 0.2+1.1\jmath \\ 1.4+1.7\jmath \end{bmatrix},$$
$$\mathbf{H} = \begin{bmatrix} 0.1-0.2\jmath & -0.7-0.6\jmath \\ 0.3+0.4\jmath & -1.3-0.5\jmath \end{bmatrix}. \tag{10.37}$$

As before, our task is to obtain the ML estimate of the transmitted signal vector $\mathbf{s}$. Firstly, we

apply the OHRSA-ML method of Algorithm 3.

As suggested by Algorithm 3, we commence the detection process by evaluating the quantities $\mathbf{U}$ and $\hat{\mathbf{x}}$ of Equations (10.36c) and (10.36d) respectively, which yields

$$\mathbf{U} = \begin{bmatrix} 0.63 & -0.85 + 0.27\jmath \\ 0 & 1.45 \end{bmatrix}, \quad \hat{\mathbf{x}} = \begin{bmatrix} 0.43 - 0.34\jmath \\ -1.10 - 0.79\jmath \end{bmatrix}. \tag{10.38}$$

Furthermore, we proceed by calculating *four* values of the CSC function $J_2(\check{s}_2 = c_m),\ m = 1, \cdots, 4$ of Equation (10.36l) associated with the *four* different points c_m of the QPSK constellation. For instance, we have

$$\begin{aligned} J_2(\check{s}_2 = -1 - 1\jmath) &= \phi_2(\check{s}_2 = -1 - 1\jmath) = |u_{22}(\check{s}_2 - \hat{x}_2)|^2 \\ &= |1.45(-1 - 1\jmath - (-1.10 - 0.79\jmath))|^2 = 0.12. \end{aligned} \tag{10.39}$$

Subsequently, four QPSK symbol candidates c_m are sorted in the order of increasing sub-cost function $\phi_2(c_m)$, as described by Equation (10.36i) of Algorithm 3. For each hypothesised symbol value $\check{s}_2 = c_m$ we can now obtain *four* values of the total cost function $J(\check{\mathbf{s}}) = J_1(\check{s}_1, \check{s}_2)$ of Equation (10.36l) associated with *four* legitimate values of $\check{s}_1 = c_m$. For instance, we have

$$\begin{aligned} &J(\check{s}_1 = 1 - 1\jmath, \check{s}_2 = -1 - 1\jmath) \\ &\quad = J_2(\check{s}_2 = -1 - 1\jmath) + \phi_1(\check{s}_1 = 1 - 1\jmath, \check{s}_2 = -1 - 1\jmath) \\ &\quad = J_2(\check{s}_2 = -1 - 1\jmath) + |u_{11}(\check{s}_1 - \hat{x}_1)) + a_1|^2 \\ &\quad = 0.12 + |0.63[1 - 1\jmath - (0.43 - 0.34\jmath)] + (-0.03 + 0.21\jmath)|^2 = 0.27, \end{aligned} \tag{10.40}$$

where the quantity a_1 is given by Equation (10.36h) of Algorithm 3 as follows

$$\begin{aligned} a_1(\check{s}_2 = -1 - 1\jmath) &= u_{12}(\check{s}_2 - \hat{x}_2) \\ &= (-0.85 + 0.27\jmath)[-1 - 1\jmath - (-1.10 - 0.79\jmath)] = -0.03 + 0.21\jmath. \end{aligned} \tag{10.41}$$

As further detailed in Algorithm 3, we calculate the values of the total cost function $J(\check{s}_1, \check{s}_2)$ only for the specific hypothesis $\check{s}_2$, for which the value of the CSC function $J_2(\check{s}_2)$ is lower than the minimum value $J_{\min}$ obtained.

The resultant search tree is depicted in Figure 10.8(a), where as before, each evaluation step, namely each evaluation of the CSC function $J_i(\check{\mathbf{s}}_i)$ of Equation (10.36l) is indicated by an elliptic node. Moreover, the label inside each node indicates the order of evaluation as well as the corresponding value $J_i(\check{\mathbf{s}}_i)$ of the CSC function inside the brackets. The branches corresponding to *four* legitimate values of the QPSK symbol are indicated by the specific type of the edges and nodes. Specifically, the *gray* and *black* lines indicate the value of the real part of the QPSK symbol $\mathcal{R}\{\check{s}_i\} = -1$ and 1, while the *dashed* and *solid* lines indicate the value of the imaginary part $\mathcal{I}\{\check{s}_i\} = -1$ and 1.

Example 3 (Bitwise OHRSA-ML QPSK 2x2)

Let us consider a QPSK system identical to that described in Example 2 and attempt to derive an alternative way of finding the ML estimate of the transmitted signal vector $\mathbf{s}$ using the bit-based representation of the QPSK symbols. In order to describe this bit-based multi-user

phasor constellation, let us develop a matrix- and vector-based mathematical model. Firstly, observe that each point of the QPSK constellation $c_m \in \mathcal{M}$ may be represented as the inner product $c_m = \boldsymbol{q}^{\mathrm{T}}\boldsymbol{d}_m$ of a unique bit-based vector $\boldsymbol{d}_m = [d_{m1}, d_{m2}]^{\mathrm{T}},\ d_{ml} = \{-1, 1\}$ and the vector $\boldsymbol{q} = [1, 1\jmath]^{\mathrm{T}}$. For instance we have

$$c_1 = -1 - 1\jmath = \boldsymbol{q}^{\mathrm{T}}\boldsymbol{d}_1 = \begin{bmatrix} 1 & 1\jmath \end{bmatrix} \cdot \begin{bmatrix} -1 \\ -1 \end{bmatrix}. \tag{10.42}$$

Furthermore, let us define a (4×2)-dimensional matrix

$$\mathbf{Q} = \mathbf{I} \otimes \boldsymbol{q} = \begin{bmatrix} 1 & 1\jmath & 0 & 0 \\ 0 & 0 & 1 & 1\jmath \end{bmatrix}, \tag{10.43}$$

where $\mathbf{I}$ is (2×2)-dimensional identity matrix, while $\otimes$ denotes the *matrix direct product* [374]. Consequently, the QPSK-modulated signal vector $\mathbf{s}$ may be represented as

$$\mathbf{s} = \begin{bmatrix} 1 - 1\jmath \\ -1 - 1\jmath \end{bmatrix} = \mathbf{Q}\mathbf{t} = \begin{bmatrix} 1 & 1\jmath & 0 & 0 \\ 0 & 0 & 1 & 1\jmath \end{bmatrix} \begin{bmatrix} 1 \\ -1 \\ -1 \\ -1 \end{bmatrix}, \tag{10.44}$$

where $\mathbf{t} = [\boldsymbol{t}_1^{\mathrm{T}}, \boldsymbol{t}_2^{\mathrm{T}}]^{\mathrm{T}}$ is a column supervector comprising the two bit-based vectors $\boldsymbol{t}_1$ and $\boldsymbol{t}_2$ associated with the QPSK-modulated symbols s_1 and s_2, respectively.

Substituting Equation (10.44) into the system model of Equation (10.7) yields

$$\mathbf{y} = \mathbf{H}\mathbf{Q}\mathbf{t} + \mathbf{w}. \tag{10.45}$$

Moreover, since $\mathbf{t}$ is a real-valued vector, we can elaborate a bit further and deduce a real-valued system model as follows

$$\begin{bmatrix} \mathcal{R}\{\mathbf{y}\} \\ \mathcal{I}\{\mathbf{y}\} \end{bmatrix} = \begin{bmatrix} \mathcal{R}\{\mathbf{H}\mathbf{Q}\} \\ \mathcal{I}\{\mathbf{H}\mathbf{Q}\} \end{bmatrix} \mathbf{t} + \begin{bmatrix} \mathcal{R}\{\mathbf{w}\} \\ \mathcal{I}\{\mathbf{w}\} \end{bmatrix} = \tilde{\mathbf{H}}\mathbf{t} + \tilde{\mathbf{w}}, \tag{10.46}$$

where $\tilde{\mathbf{H}}$ is a real-valued (4×4)-dimensional bitwise channel matrix, which may be expressed as

$$\tilde{\mathbf{H}} = \begin{bmatrix} \mathcal{R}\{\mathbf{H}\mathbf{Q}\} \\ \mathcal{I}\{\mathbf{H}\mathbf{Q}\} \end{bmatrix} = \begin{bmatrix} 0.1 & 0.2 & -0.7 & 0.6 \\ 0.3 & -0.4 & -1.3 & 0.5 \\ -0.2 & 0.1 & -0.6 & -0.7 \\ 0.4 & 0.3 & -0.5 & -1.3 \end{bmatrix}. \tag{10.47}$$

Thus, we arrive at the new system model of Equation (10.46), which may be interpreted as a (4×4)-dimensional BPSK-modulated SDM system. By applying the OHRSA-ML method

of Algorithm 3 we have

$$\mathbf{U} = \begin{bmatrix} 0.63 & 0 & -0.85 & -0.27 \\ 0 & 0.63 & 0.27 & -0.85 \\ 0 & 0 & 1.45 & 0 \\ 0 & 0 & 0 & 1.45 \end{bmatrix}, \quad \hat{\mathbf{x}} = \begin{bmatrix} 0.43 \\ -0.34 \\ -1.10 \\ -0.79 \end{bmatrix}. \tag{10.48}$$

Furthermore, the first two steps of the recursive search process of Algorithm 3 are given by

$$\begin{aligned} J_4(\check{t}_4 = -1) &= |u_{44}(\check{t}_4 - \hat{x}_4)|^2 \\ &= |1.45(-1 - (-0.79))|^2 = 0.10 \end{aligned} \tag{10.49}$$

and

$$\begin{aligned} a_3(\check{t}_4 = -1) &= u_{34}(\check{t}_4 - \hat{x}_4) \\ &= 0(-1 - (-0.79)) = 0, \\ J_3(\check{t}_3 = -1, \check{t}_4 = -1) &= |u_{33}(\check{t}_3 - \hat{x}_3) + a_3|^2 \\ &= |1.45(-1 - (-1.10)) + (0)|^2 = 0.12. \end{aligned} \tag{10.50}$$

Upon completing the recursive search process of Algorithm 3 we arrive at the search tree depicted in Figure 10.8(b). As before, each evaluation step, namely each evaluation of the CSC function $J_i(\check{\mathbf{t}}_i)$ of Equation (10.36l) is indicated by an elliptic node. Moreover, the label inside each node indicates the order of evaluation as well as the corresponding value $J_i(\check{\mathbf{t}}_i)$ of the CSC function inside the brackets. The branches corresponding to two legitimate values $\check{t}_i = -1$ and 1 are indicated using the *dashed* and *solid* edges and nodes, respectively.

Observe that the ML estimates $\hat{\mathbf{s}}$ and $\hat{\mathbf{t}}$ of Figures 10.8 (a) and (b) are obtained within the same number of evaluation steps. Nevertheless, the latter search procedure is constituted by lower-complexity real-valued operations. Furthermore, in contrast to the detection method considered in Example 2, the search method outlined in this QPSK-based example can be readily generalised for the scenario of M-QAM SDM systems, as demonstrated in the forthcoming section.

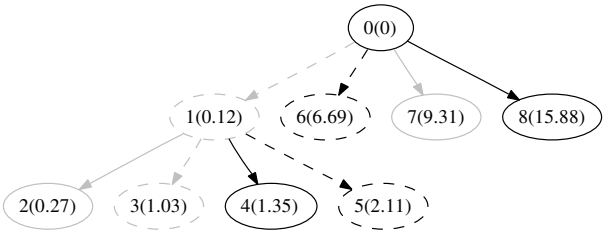
10.4.3.1 Generalisation of the BW-OHRSA-ML SDM Detector

In this section we generalise the result obtained in Section 10.4.1 to the case of systems employing hyper-rectangular modulation schemes, namely M-QAM, where each modulated symbol belongs to a discrete phasor constellation $\mathcal{M} = \{c_m\}_{m=1,\cdots,M}$. It is evident that each phasor point c_m of an M-QAM constellation map may be represented as the inner product of a unique bit-based vector $\boldsymbol{d}_m = \{d_{ml} = -1, 1\}_{l=1,\cdots,b}$ and the corresponding *quantisation vector* $\boldsymbol{q}$. Specifically, we have

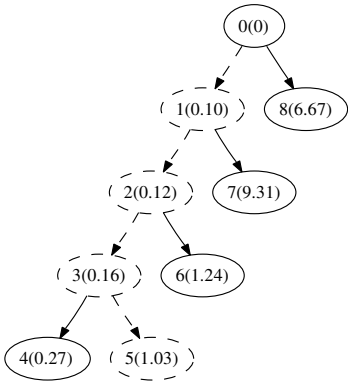
$$c_m = \boldsymbol{q}^{\mathrm{T}} \boldsymbol{d}_m. \tag{10.51}$$

Some examples of quantisation vectors corresponding to the modulation schemes of QPSK, 16-QAM and 64-QAM are portrayed in Table 10.2.

Furthermore, we define a $(bm_{\mathrm{t}} \times m_{\mathrm{t}})$-dimensional *quantisation matrix* $\mathbf{Q} = \mathbf{I} \otimes \boldsymbol{q}$, where $\mathbf{I}$



(a)



(b)

Figure 10.8: Examples of a search tree formed by the (a) OHRSA-ML and (b) BW-OHRSA-ML SDM detectors in the scenario of a system employing QPSK modulation, $m_{\rm t} = n_{\rm r} = 3$ transmit and receive antennas and encountering average SNRs of 10dB. The labels indicate the order of execution, as well as the corresponding value $J_i(\check{\mathbf{s}}_i)$ of the CSC function of Equation (10.22), as seen in the brackets.

Table 10.2: Examples of quantization vectors.

Modulation scheme	$\boldsymbol{q}^{\rm T}$
BPSK	$[1]$
QPSK	$\frac{1}{\sqrt{2}}[1,\ \jmath]$
16QAM	$\frac{1}{\sqrt{10}}[1,\ 1\jmath,\ 2,\ 2\jmath]$
64QAM	$\frac{1}{\sqrt{42}}[1,\ 1\jmath,\ 2,\ 2\jmath,\ 4,\ 4\jmath]$

is an $(m_{\rm t} \times m_{\rm t})$-dimensional identity matrix and $\boldsymbol{q}$ is the aforementioned *quantisation vector*, while $\otimes$ denotes the *matrix direct product* [374]. Consequently the M-QAM-modulated signal vector $\mathbf{s}$ may be represented as

$$\mathbf{s} = \mathbf{Q}\mathbf{t}, \tag{10.52}$$

where $\mathbf{t} = [\boldsymbol{t}_1^{\mathrm{T}}, \cdots, \boldsymbol{t}_{m_{\mathrm{t}}}^{\mathrm{T}}]^{\mathrm{T}}$ is a column supervector comprising the bit-based vectors $\boldsymbol{t}_i$ associated with each transmitted signal vector component s_i. Substituting Equation (10.52) into the system model of Equation (10.7) yields

$$\mathbf{y} = \mathbf{HQt} + \mathbf{w} = \tilde{\mathbf{H}}\mathbf{t} + \mathbf{w}, \tag{10.53}$$

where $\tilde{\mathbf{H}}$ is a $(n_{\mathrm{r}} \times bm_{\mathrm{t}})$-dimensional bitwise channel matrix. Observe in Equation (10.53) the requirement of having constant-envelope symbols is satisfied by the modified system model of Equation (10.53), since we have $|t_i|^2 = 1$ and thus the method described in Section 10.4.1 and summarised in Algorithm 3 is applicable to the evaluation of the bitwise ML estimate $\hat{\mathbf{t}}$ of Equation (10.53). Consequently, we apply the following changes to Algorithm 3:

1) Include the evaluation of the bitwise channel matrix $\tilde{\mathbf{H}}$ in (10.54a) and

2) Adjust the number of candidate bit values of t_i to $d_m = \{-1, 1\}$ in (10.54l).
Hence we arrive at a new detection technique, namely the Bitwise OHRSA-aided ML SDM detector, which is summarised in Algorithm 4

The operation of Algorithm 4 is illustrated by the search tree diagram depicted in Figure 10.9. Each circular node in the diagram represents a subvector candidate $\check{\mathbf{t}}_i = \{\check{t}_j\}_{j=i,\cdots,r}$ of the transmitted bit-based signal vector $\mathbf{t}$. The bold and hollow nodes denote the binary values of the bit $\check{t}_i = \{-1, 1\}$ assumed in the current step of the recursive search process. The corresponding values of the CSC function $J_i(\check{\mathbf{t}}_i)$ are indicated by both the colour and thickness of the transitions connecting each *child* or *descendant* node $\check{\mathbf{t}}_i$ with the corresponding *parent* node $\check{\mathbf{t}}_{i+1}$. The search-tree diagram depicted in Figure 10.9 corresponds to the system scenario employing QPSK modulation, m_{t}=n_{r}=8 operating at the average SNR of 6 dB. Observe that the ML solution is attained in 139 evaluation steps in comparison to the $2^{16} = 65536$ evaluation steps required by the exhaustive ML search.

10.4.4 OHRSA-Aided Log-MAP SDM Detection

It is evident [90] that the BER associated with the process of communicating over a fading noisy MIMO channel can be dramatically reduced by means of channel coding. A particularly effective channel coding scheme is constituted by the *soft-input soft-output* turbo coding method [216]. Turbo coding, however, requires *soft* information concerning the bit decisions at the output of the SDM detector, in other words, the *a posteriori* soft information regarding the confidence of the bit-decision is required.

The derivation of an expression for the low-complexity evaluation of the soft-bit information associated with the bit estimates of the SDM detector's output characterised by Equation (10.11) is given in [90]. Here, we present a brief summary of the results deduced in [90].

Algorithm 4 Bit-Wise OHRSA-aided ML SDM Detector

$$\tilde{\mathbf{H}} = \begin{bmatrix} \mathcal{R}\{\mathbf{HQ}\} \\ \mathcal{I}\{\mathbf{HQ}\} \end{bmatrix} \tag{10.54a}$$

$$\texttt{Sort}\{\tilde{\mathbf{H}}\},\ \texttt{such that}\ \|(\tilde{\mathbf{H}})_1\|^2 \leq \cdots \leq \|(\tilde{\mathbf{H}})_{m_\mathrm{t}}\|^2 \tag{10.54b}$$

$$\mathbf{G} = (\tilde{\mathbf{H}}^{\mathrm{H}}\tilde{\mathbf{H}} + \sigma_w^2\mathbf{I}) \tag{10.54c}$$

$$\mathbf{U} = \texttt{CholeskyDecomposition}(\mathbf{G}) \tag{10.54d}$$

$$\hat{\mathbf{x}} = \mathbf{G}^{-1}\tilde{\mathbf{H}}^{\mathrm{H}}\tilde{\mathbf{y}} \tag{10.54e}$$

$$\texttt{Calculate}\ \ J_r \tag{10.54f}$$

$$\texttt{Unsort}\{\hat{\mathbf{t}}\} \tag{10.54g}$$

$$\texttt{function}\ \ \texttt{Calculate}\ \ J_i \tag{10.54h}$$

$$a_i = \sum_{j=i+1}^{m_\mathrm{t}} u_{ij}(\check{t}_j - \hat{x}_j) \tag{10.54i}$$

$$\texttt{Sort}\{d_m\},\ \texttt{such that}\ \phi_i(d_0) < \phi_i(d_1), \tag{10.54j}$$

$$\texttt{where}\ \ \phi_i(b_m) = |u_{ii}(d_m - \hat{x}_i) + a_i|^2 \tag{10.54k}$$

$$\texttt{for}\ \ m = 0, 1\ \ \texttt{do} \tag{10.54l}$$

$$\check{t}_i = d_m \tag{10.54m}$$

$$J_i = J_{i+1} + \phi_i(\check{t}_i) \tag{10.54n}$$

$$\texttt{if}\ \ J_i < J_{\min}\ \ \texttt{then} \tag{10.54o}$$

$$\texttt{if}\ \ i > 0\ \ \texttt{then}\ \ \texttt{Calculate}\ \ J_{i-1} \tag{10.54p}$$

$$\texttt{else}$$

$$J_{\min} = J_0 \tag{10.54q}$$

$$\hat{\mathbf{t}} = \check{\mathbf{t}} \tag{10.54r}$$

$$\texttt{end if}$$

$$\texttt{end if}$$

$$\texttt{end for}$$

$$\texttt{end function}$$

The soft-bit value associated with the mth bit of the QAM symbol transmitted from the ith transmit antenna element is determined by the log-likelihood function defined in [109] as

$$L_{im} = \log \frac{\sum_{\check{\mathbf{s}} \in \mathcal{M}_{im}^{1;m_\mathrm{t}}} \mathtt{P}\left\{\mathbf{y}|\check{\mathbf{s}}, \mathbf{H}\right\}}{\sum_{\check{\mathbf{s}} \in \mathcal{M}_{im}^{0;m_\mathrm{t}}} \mathtt{P}\left\{\mathbf{y}|\check{\mathbf{s}}, \mathbf{H}\right\}}, \tag{10.55}$$

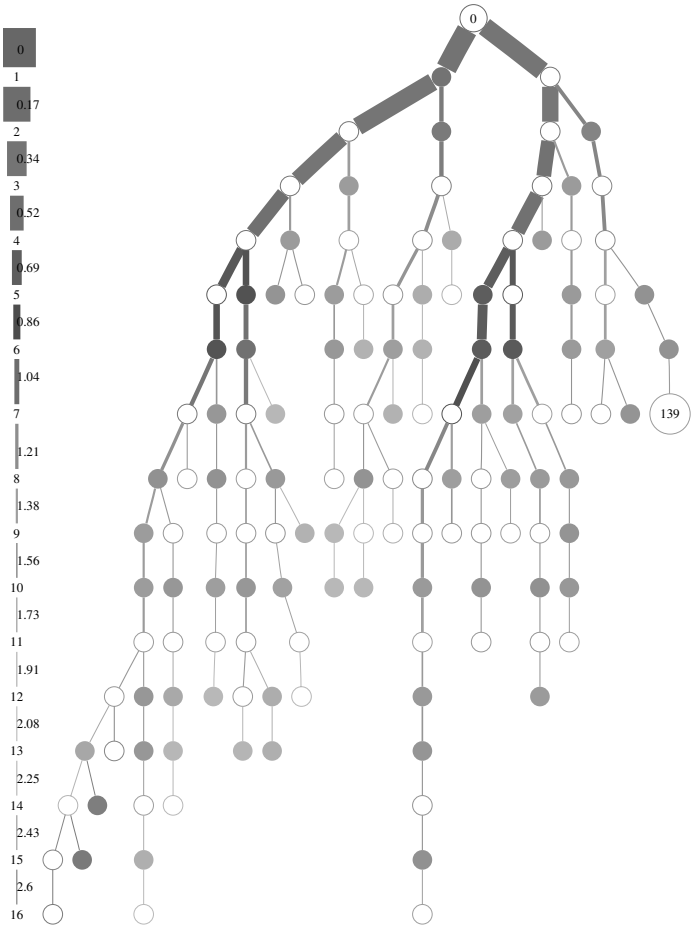


Figure 10.9: Example of a search tree formed by the BW-OHRSA method of Algorithm 4 in the scenario of QPSK, $m_{\rm t}$=$n_{\rm r}$=8 and an average SNR of 6 dB. Each circular node in the diagram represents a subvector candidate $\check{\mathbf{t}}_i = \{\check{t}_j\}_{j=i,\cdots,r}$ of the transmitted bit-based signal vector $\mathbf{t}$. The bold and hollow nodes denote the duo-binary values of the bit $\check{t}_i = \{-1, 1\}$ assumed. The corresponding value of the CSC function $J_i(\check{\mathbf{t}}_i)$ quantified in Equation (10.23b) is indicated by both the color and the thickness of the transitions connecting each child node $\check{\mathbf{t}}_i$ with the corresponding parent node $\check{\mathbf{t}}_{i+1}$. The ML solution is attained in 139 evaluation steps in comparison to the $2^{16} = 65536$ evaluation steps required by the exhaustive ML search.

where we define

$$\mathcal{M}_{im}^{b;m_{\rm t}} = \left\{\check{\mathbf{s}} = (\check{s}_1, \cdots, \check{s}_{m_{\rm t}})^{\rm T};\ \check{s}_j \in \mathcal{M} \text{ for } j \neq i,\ \check{s}_i \in \mathcal{M}_m^b\right\} \tag{10.56}$$

and $\mathcal{M}_m^b$ denotes the specific subset of the entire set $\mathcal{M}$ of modulation constellation points, which comprises the bit value $b = \{0, 1\}$ at the mth bit position.

However, the direct calculation of the accumulated *a posteriori* conditional probabilities

in nominator and denominator of Equation (10.55) may have an excessive complexity in practice. Fortunately, as advocated in [90], the expression in Equation (10.55) can be closely approximated as follows

$$L_{im} \approx \log \frac{\mathtt{P}\left\{\mathbf{y}|\check{\mathbf{s}}_{im}^{1}, \mathbf{H}\right\}}{\mathtt{P}\left\{\mathbf{y}|\check{\mathbf{s}}_{im}^{0}, \mathbf{H}\right\}}, \tag{10.57}$$

where we define

$$\check{\mathbf{s}}_{im}^{b} = \arg \max_{\check{\mathbf{s}} \in \mathcal{M}_{im}^{b;m_{\mathrm{t}}}} \mathtt{P}\left\{\mathbf{y}|\check{\mathbf{s}}, \mathbf{H}\right\}, \quad b = 0, 1. \tag{10.58}$$

As suggested by the nature of Equation (10.57), the detection process employing the objective function determined by Equations (10.57) and (10.58) is usually referred to as Logarithmic Maximum *A Posteriori* (Log-MAP) probability detector.

A practical version of the Log-MAP detector may be derived as follows. Substituting Equation (10.10) into (10.55) yields

$$L_{im} = \log \frac{\sum_{\check{\mathbf{s}} \in \mathcal{M}_{im}^{1;m_{\mathrm{t}}}} \exp\left(-\frac{1}{\sigma_w^2}\|\mathbf{y} - \mathbf{H}\check{\mathbf{s}}\|^2\right)}{\sum_{\check{\mathbf{s}} \in \mathcal{M}_{im}^{0;m_{\mathrm{t}}}} \exp\left(-\frac{1}{\sigma_w^2}\|\mathbf{y} - \mathbf{H}\check{\mathbf{s}}\|^2\right)}. \tag{10.59}$$

Note that Equation (10.59) involves summation over $2^{rm_{\mathrm{t}}-1}$ exponential functions. This operation may potentially impose an excessive computational complexity for large values of m_{t} and/or r. However, as demonstrated in [90], the expression in (10.59) may be closely approximated by a substantially simpler expression, namely by

$$L_{im} \approx \frac{1}{\sigma_w^2}\left[\|\mathbf{y} - \mathbf{H}\check{\mathbf{s}}_{im}^{0}\|^2 - \|\mathbf{y} - \mathbf{H}\check{\mathbf{s}}_{im}^{1}\|^2\right], \tag{10.60}$$

where we have

$$\check{\mathbf{s}}_{im}^{b} = \arg \min_{\check{\mathbf{s}} \in \mathcal{M}_{im}^{b;m_{\mathrm{t}}}} \|\mathbf{y} - \mathbf{H}\check{\mathbf{s}}\|^2, \quad b = 0, 1, \tag{10.61}$$

and again, $\mathcal{M}_{im}^{b;m_{\mathrm{t}}}$ denotes the specific subset of the entire set $\mathcal{M}^{m_{\mathrm{t}}}$ of signal vector candidates associated with the modulation scheme employed, which comprises the bit value $b = \{0, 1\}$ at the mth bit position of the ith signal vector component.

The Log-MAP detector defined by Equations (10.60) and (10.61) may be applied for the sake of obtaining the soft-bit information associated with the bitwise OHRSA ML SDM detector derived in Section 10.4.3. Consequently, substituting the bitwise system model of Equation (10.53) into (10.60) and (10.61) yields

$$L_i \approx \frac{1}{\sigma_w^2}\left[\|\mathbf{y} - \tilde{\mathbf{H}}\check{\mathbf{t}}_{i;\min}^{0}\|^2 - \|\mathbf{y} - \tilde{\mathbf{H}}\check{\mathbf{t}}_{i;min}^{1}\|^2\right], \tag{10.62}$$

where we have

$$\check{\mathbf{t}}^m_{i;\min} = \arg \min_{\check{\mathbf{t}} \in \mathcal{D}_i^{m;r}} \|\mathbf{y} - \tilde{\mathbf{H}}\check{\mathbf{t}}\|^2, \quad b = 0, 1 \tag{10.63}$$

and $\mathcal{D}_i^{m;r}$ denotes the subset of the entire set $\mathcal{D}^r$ of $(r = m_{\rm t} \log_2 M)$-dimensional bitwise vectors, which comprise the binary value $\check{t}_i = d_m = \{-1, 1\}$ at the ith bit position.

Furthermore, substituting the bitwise objective function of Equation (10.60) into (10.62) yields

$$\begin{aligned} L_i \approx & \frac{1}{\sigma_w^2} \left[J(\check{\mathbf{t}}^0_{i;\min}) + \phi - J(\check{\mathbf{t}}^1_{i;\min}) - \phi \right] \\ = & \frac{1}{\sigma_w^2} \left[J(\check{\mathbf{t}}^0_{i;\min}) - J(\check{\mathbf{t}}^1_{i;\min}) \right], \end{aligned} \tag{10.64}$$

where $\check{\mathbf{t}}^m_{i;\min}$ and the corresponding cost function value $J(\check{\mathbf{t}}^m_{i;\min})$ may be obtained by applying the constrained OHRSA-aided ML detection method derived in Section 10.4.3.

Consequently, the evaluation of the bitwise Log-MAP estimates of the transmitted bitwise signal vector $\mathbf{t}$ involves repetitive evaluation of $2r$ constrained ML estimates $\check{\mathbf{t}}^m_{i;\min}$ along with the associated $2r$ values of the objective function $J(\check{\mathbf{t}}^m_{i;\min})$.

The pseudo-code describing the implementation of the bitwise OHRSA-aided Log-MAP SDM detector is summarised in Algorithm 5.

Clearly, the repetitive nature of the search process entailing Equations (10.65f,i-r) in Algorithm 5 imposes a substantial increase in the associated computational complexity. Hence, in the next section we derive an OHRSA-aided approximate Log-MAP method, which is capable of approaching the optimum Log-MAP performance, while avoiding the repetitive evaluation of Equation (10.65f) in Algorithm 5 and therefore imposes considerably reduced complexity requirements.

Example 4 (OHRSA-Log-MAP BPSK 3x3)

Consider a BPSK system having $n_{\rm r} = m_{\rm t} = 3$ transmit and receive antennas, which is described by Equation (10.7). The transmitted signal $\mathbf{s}$, received signal $\mathbf{y}$ as well as the channel matrix $\mathbf{H}$ of Equation (10.7) are exemplified by the following values

$$\mathbf{s} = \begin{bmatrix} -1 \\ 1 \\ 1 \end{bmatrix}, \quad \mathbf{y} = \begin{bmatrix} 0.2 \\ 0.3 \\ -0.5 \end{bmatrix}, \quad \mathbf{H} = \begin{bmatrix} 0.1 & -1 & 1.1 \\ -0.2 & 0.7 & -0.7 \\ 0.4 & 0.5 & -0.5 \end{bmatrix}. \tag{10.66}$$

Observe that the channel matrix $\mathbf{H}$ of Equation (10.66) happens to be *best-first* ordered and does not require any further reordering. Furthermore, in our scenario of BPSK modulation the channel matrix $\mathbf{H}$ of Equation (10.66) is equivalent to the bitwise channel matrix $\tilde{\mathbf{H}}$ of Algorithm 5.

Subsequently, our task is to obtain the Log-MAP estimate of the transmitted signal vector $\mathbf{t} = \mathbf{s}$. We apply the OHRSA-Log-MAP method of Algorithm 5. Firstly, we evaluate the triangular matrix $\mathbf{U}$ of Equation (10.65d) as well as the unconstrained MMSE estimate $\hat{\mathbf{x}}$ of

Algorithm 5 BW-OHRSA-aided LogMAP SDM Detector

$$\tilde{\mathbf{H}} = \begin{bmatrix} \mathcal{R}\{\mathbf{HQ}\} \\ \mathcal{I}\{\mathbf{HQ}\} \end{bmatrix} \tag{10.65a}$$

$$\texttt{Sort}\{\tilde{\mathbf{H}}\},\ \texttt{such that}\ \|(\tilde{\mathbf{H}})_1\|^2 \leq \cdots \leq \|(\tilde{\mathbf{H}})_{m_t}\|^2 \tag{10.65b}$$

$$\mathbf{G} = (\tilde{\mathbf{H}}^{\mathrm{H}}\tilde{\mathbf{H}} + \sigma_w^2\mathbf{I}) \tag{10.65c}$$

$$\mathbf{U} = \texttt{CholeskyDecomposition}(\mathbf{G}) \tag{10.65d}$$

$$\hat{\mathbf{x}} = \mathbf{G}^{-1}\tilde{\mathbf{H}}^{\mathrm{H}}\tilde{\mathbf{y}} \tag{10.65e}$$

$$\texttt{for}\quad i = 1, \cdots, r$$

$$L_{im} = \frac{1}{\sigma_w^2}\left[J_{i;\min}^0 - J_{i;\min}^1\right] \tag{10.65f}$$

$$\texttt{end for}$$

$$\texttt{Unsort}\{L_i\}_{i=1,\cdots,r} \tag{10.65g}$$

$$\texttt{function Calculate}\ J_{k;i}^b \tag{10.65h}$$

$$a_i = \sum_{j=i+1}^{m_t} u_{ij}(\check{t}_j - \hat{x}_j) \tag{10.65i}$$

$$\texttt{if}\quad i = k\quad \texttt{then}$$

$$d_0 = \{-1, 1\}_b \tag{10.65j}$$

$$\texttt{else}$$

$$\texttt{Sort}\{d_m = -1, 1\}, \tag{10.65k}$$

$$\texttt{such that}\ \phi_i(d_0) < \phi_i(d_1), \tag{10.65l}$$

$$\texttt{where}\quad \phi_i(d_m) = |u_{ii}(d_m - \hat{x}_i) + a_i|^2 \tag{10.65m}$$

$$\texttt{end if}$$

$$\texttt{for}\quad m = 0, 1\quad \texttt{do}$$

$$\check{t}_i = d_m \tag{10.65n}$$

$$J_{k;i} = J_{k;i+1} + \phi_i(d_m) \tag{10.65o}$$

$$\texttt{if}\quad J_i < J_{\min}\quad \texttt{then} \tag{10.65p}$$

$$\texttt{if}\quad i > 0\quad \texttt{then Calculate}\quad J_{k;i-1}^b \tag{10.65q}$$

$$\texttt{else}$$

$$J_{\min} = J_{k;\min}^b = J_{k;0}^b \tag{10.65r}$$

$$\texttt{end if}$$

$$\texttt{end if}$$

$$\texttt{if}\quad i = k\quad \texttt{then break for loop}$$

$$\texttt{end for}$$

$$\texttt{end function}$$

Equation (10.65e). The resultant quantities are given by

$$\mathbf{U} = \begin{bmatrix} 0.56 & -0.07 & 0.09 \\ 0 & 1.35 & -1.35 \\ 0 & 0 & 0.46 \end{bmatrix}, \quad \hat{\mathbf{x}} = \begin{bmatrix} -0.80 \\ -0.01 \\ 0.13 \end{bmatrix}. \tag{10.67}$$

Secondly, as further suggested by Algorithm 5, for each transmitted bitwise symbol t_i we calculate the quantities $J(\check{\mathbf{t}}^{-1}_{i;\min})$ and $J(\check{\mathbf{t}}^{1}_{i;\min})$ corresponding to the values of the cost function $J(\check{\mathbf{t}})$ of Equation (10.65o) associated with the constrained ML estimates of the transmitted bitwise vector $\mathbf{t}$ with the ith bit-component assuming values of -1 and 1, respectively.

For instance, the cost function value $J(\check{\mathbf{t}}^{-1}_{1;\min})$ associated with the ML estimate of the bitwise signal vector $\mathbf{t}$ constrained by bit-component value $\check{t}_1 = -1$ may be calculated as follows

$$\begin{aligned} J_3(\check{t}_3 = 1) &= |u_{33}(\check{t}_3 - \hat{x}_3)|^2 = (0.46(1 - (0.13)))^2 = 0.16, \\ a_2(\check{t}_3 = 1) &= u_{23}(\check{t}_3 - \hat{x}_3) = -1.35(1 - (0.13)) = -1.17, \\ J_2(\check{t}_2 = 1, \check{t}_3 = 1) &= J_3(\check{t}_3 = 1) + |u_{22}(\check{t}_2 - \hat{x}_2) + a_2|^2 \\ &= 0.16 + |1.35(1 - (-0.01)) + (-1.17)|^2 = 0.20. \end{aligned} \tag{10.68}$$

Furthermore, we have

$$\begin{aligned} a_1(\check{t}_2 = 1, \check{t}_3 = 1) &= u_{12}(\check{t}_2 - \hat{x}_2) + u_{13}(\check{t}_3 - \hat{x}_3) \\ &= -0.07(1 - (-0.01)) + 0.09(1 - (0.13)) = 0.00, \\ J(\check{\mathbf{t}}^{-1}_{1;\min}) &= J_1(\check{t}_1 = -1, \check{t}_2 = 1, \check{t}_3 = 1) \\ &= J_2(\check{t}_2 = 1, \check{t}_3 = 1) + |u_{11}(\check{t}_1 - \hat{x}_1) + a_1|^2 \\ &= 0.20 + |0.56(-1 - (-0.80)) + (0.00)|^2 = 0.21. \end{aligned} \tag{10.69}$$

Observe that for the sake of brevity we omit the calculation of the CSC values outside the major search branch of Algorithm 5, *i. e.* outside the search branch leading to the constrained ML estimate. The corresponding search tree formed by the evaluation of the value of $J(\check{\mathbf{s}}^{-1}_{1;\min})$ using Algorithm 5 is depicted in Figure 10.10(a). Furthermore, Figures 10.10 (b)-(f) illustrate the search trees formed by the search sub-processes of Algorithm 5 corresponding to the remaining *five* values $\left\{J(\check{\mathbf{s}}^{b}_{i;\min})\right\}^{b=-1,1}_{i=1,\cdots,3}$.

Finally, upon completing the calculation of all *six* values $\left\{J(\check{\mathbf{s}}^{b}_{i;\min})\right\}^{b=-1,1}_{i=1,\cdots,3}$ we arrive at the following matrix

$$\hat{\mathbf{J}} = \left\{J(\check{\mathbf{s}}^{b}_{i;\min})\right\}^{b=-1,1}_{i=1,\cdots,3} = \begin{bmatrix} 0.21 & 1.21 \\ 0.33 & 0.21 \\ 0.33 & 0.21 \end{bmatrix}, \tag{10.70}$$

where the elements of the matrix $\hat{\mathbf{J}}$, which we refer to as Minimum Cost Function (MCF) matrix, are defined as $\hat{J}_{ij} = J(\check{\mathbf{s}}^{b_j}_{i;\min})$. Consequently, the *soft-bit* vector representing the

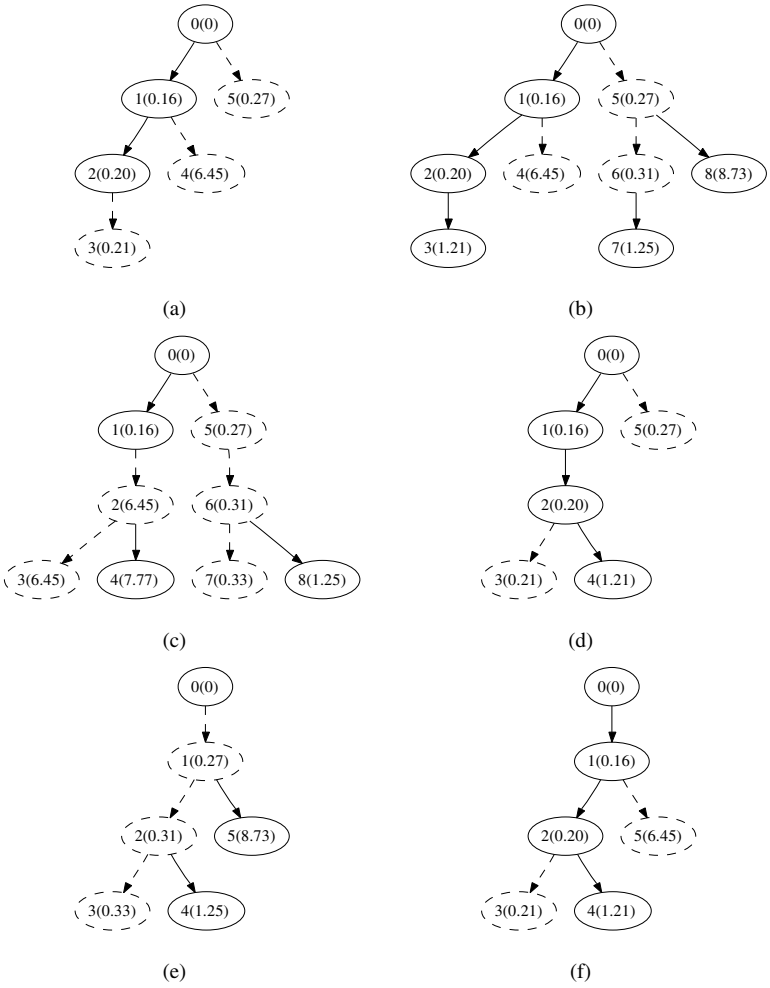


Figure 10.10: Example of search trees formed by the OHRSA-Log-MAP SDM detector of Algorithm 5 in the scenario of a system employing BPSK modulation, $m_{\mathrm{t}} = n_{\mathrm{r}} = 3$ transmit and receive antennas and encountering average SNRs of 10dB. The labels indicate the order of visitation, as well as the corresponding value $J_i(\check{\mathbf{t}}_i)$ of the CSC function of Equation (10.65o), as seen in the brackets.

Log-MAP estimate of the transmitted bitwise signal vector $\mathbf{t}$ may be expressed as

$$\mathbf{L} = \frac{1}{\sigma_w^2}\left[(\hat{\mathbf{J}})_1 - (\hat{\mathbf{J}})_2\right] = \begin{bmatrix} -9 \\ 1.2 \\ 1.2 \end{bmatrix}, \tag{10.71}$$

where $(\hat{\mathbf{J}})_j$ denotes the jth column of the MCF matrix $\hat{\mathbf{J}}$ defined in Equation (10.70).

Example 5 (OHRSA Approximate Log-MAP BPSK 3x3)

Again, consider a BPSK system identical to that described in Example 4. Specifically, we have a (3×3)-dimensional real-valued linear system described by Equation (10.7) with the corresponding transmitted signal $\mathbf{s}$, the received signal $\mathbf{y}$ and the channel matrix $\mathbf{H}$ described in Equation (10.66). In this example we would like to demonstrate an alternative search paradigm, which avoids the repetitive process characterised by Algorithm 5 and exemplified in Figure 10.10 of Example 4, while obtaining a similar result.

Firstly, we apply the OHRSA-ML method of Algorithm 4. The triangular matrix $\mathbf{U}$ of Equation (10.54d) as well as the unconstrained MMSE estimate $\hat{\mathbf{x}}$ of Equation (10.54e) are similar to those evaluated in Example 4 and are characterised by Equation (10.67). The resultant search process is characterised by the search tree diagram portrayed in Figure 10.11(a).

Additionally, however, we define a (3×2)-dimensional Minimum Cost Function (MCF) matrix $\hat{\mathbf{J}}$, which will be used for the evaluation of the soft-bit information, and we assign an initial value of $\hat{\mathbf{J}} = J_0\,\mathbf{1}$, where $\mathbf{1}$ is a (3×2)-dimensional matrix of ones and $J_0 \gg \gamma$ is some large constant, which should be greater than the average SNR of $\gamma = 10$ encountered. For instance let us assume $J_0 = 100$. Subsequently, the cost-function-related matrix $\hat{\mathbf{J}}$ is updated according to a procedure to be outlined below each time when the search branch forming the search tree portrayed in Figure 10.11(a) is terminated, regardless whether its termination occured due to reaching the final recursive index value of $i = 1$, or owing to exceeding the minimum value of the cost function $J_{\min}$. More specifically, we update the elements of the matrix $\hat{\mathbf{J}}$ corresponding to the bitwise symbols $\check{t}_j,\ j = i, \cdots, 3$ constituting the bitwise subvector candidate $\check{\mathbf{t}}_i$ associated with the particular search branch, as outlined below

$$\hat{J}_{jb_j} = \min\left\{\hat{J}_{jb_j}, J_i(\check{\mathbf{t}}_i)\right\}, \quad j = i, \cdots, 3, \quad \check{t}_j = \{-1, 1\}_{b_j}. \tag{10.72}$$

For instance, upon completing the first, left-most search branch depicted in Figure 10.11(a) and associated with the transmitted signal candidate $\check{\mathbf{t}} = \begin{bmatrix} -1 & 1 & 1 \end{bmatrix}^{\mathrm{T}}$, namely upon reaching node 3 of the search tree, the following update of the MCF matrix $\hat{\mathbf{J}}$ is performed

$$\begin{aligned} \hat{J}_{11} &= \min\left\{\hat{J}_{11}, J(\check{\mathbf{t}})\right\} = \min\{100, 0.21\} = 0.21 \\ \hat{J}_{22} &= \hat{J}_{32} = \min\{100, 0.21\} = 0.21. \end{aligned} \tag{10.73}$$

Consequently, the matrix $\hat{\mathbf{J}}$ becomes

$$\hat{\mathbf{J}}(3) = \begin{bmatrix} 0.21 & 100 \\ 100 & 0.21 \\ 100 & 0.21 \end{bmatrix}. \tag{10.74}$$

Furthermore, the states of the MCF matrix corresponding to the search steps 4, 5 and 6 of Figure 10.11(a) are

$$\hat{\mathbf{J}}(4) = \begin{bmatrix} 0.21 & 1.21 \\ 100 & 0.21 \\ 100 & 0.21 \end{bmatrix}, \quad \hat{\mathbf{J}}(5) = \begin{bmatrix} 0.21 & 1.21 \\ 6.45 & 0.21 \\ 100 & 0.21 \end{bmatrix}, \quad \hat{\mathbf{J}}(6) = \begin{bmatrix} 0.21 & 1.21 \\ 6.45 & 0.21 \\ 0.27 & 0.21 \end{bmatrix}. \tag{10.75}$$

Finally, by substituting the resultant value of the MCF matrix $\hat{\mathbf{J}}(6)$ of Equation (10.75) into (10.71) we obtain the following soft-bit estimate of the transmitted bitwise signal vector $\mathbf{t}$

$$\mathbf{L}_a = \begin{bmatrix} -9 \\ 62.39 \\ 0.60 \end{bmatrix}. \tag{10.76}$$

Observe that the soft-bit estimate $\mathbf{L}_a$ of Equation (10.76) appears to be considerably more reliable than the MMSE estimate $\hat{\mathbf{x}}$ of Equation (10.67). Specifically, as opposed to the MMSE estimate $\hat{\mathbf{x}}$ in Equation (10.25) the direct slicing of the soft-bit estimate $\mathbf{L}_a$ results in the correct signal vector $\mathbf{s}$ of Equation (10.66). Moreover, the soft-bit estimate $\mathbf{L}_a$ provides further information concerning the reliability of each estimated bit, albeit the resultant soft-bit information of Equation (10.76) substantially deviates from the more reliable exact Log-MAP estimate $\mathbf{L}$ given by Equation (10.71).

Fortunately, however, the precision of the soft-bit estimate $\mathbf{L}_a$ may be readily improved. Specifically, we introduce an additional parameter ρ, which will allow us to control the rate of convergence in the search process of Algorithm 4 by increasing the threshold value of the CSC function, which controls the passage of the recursive search process through *low-likelihood* search branches having CSC function values $J_i(\check{\mathbf{t}}_i)$ in excess of $\rho J_{\min}$, as opposed to $J_{\min}$ of Equation (10.54o) in Algorithm 4. Let us now execute the modified OHRSA-ML method of Algorithm 4, where the condition $J_i < J_{\min}$ of Equation (10.54o) is replaced by the corresponding condition of $J_i < \rho J_{\min}$.

The search trees formed by the execution of the modified Algorithm 4 in the scenarios of setting (b) $\rho = 1.3$ and (c) $\rho = 2.0$ are depicted in Figures 10.10 (b) and (c), respectively. Furthermore, the convergence of the MCF matrix $\hat{\mathbf{J}}$ as well as the resultant soft-bit estimate $\mathbf{L}$ of both scenarios may be characterised as follows

$$(b) \quad \hat{\mathbf{J}}(7) = \begin{bmatrix} 0.21 & 1.21 \\ 0.31 & 0.21 \\ 0.31 & 0.21 \end{bmatrix}, \hat{\mathbf{J}}(8) = \begin{bmatrix} 0.21 & 1.21 \\ 0.31 & 0.21 \\ 0.31 & 0.21 \end{bmatrix}, \mathbf{L}_b = \begin{bmatrix} -9 \\ 0.99 \\ 0.99 \end{bmatrix} \tag{10.77}$$

and

$$(c) \quad \hat{\mathbf{J}}(8) = \begin{bmatrix} 0.21 & 1.21 \\ 0.33 & 0.21 \\ 0.33 & 0.21 \end{bmatrix}, \hat{\mathbf{J}}(10) = \begin{bmatrix} 0.21 & 1.21 \\ 0.33 & 0.21 \\ 0.33 & 0.21 \end{bmatrix}, \mathbf{L}_c = \begin{bmatrix} -9 \\ 1.2 \\ 1.2 \end{bmatrix}, \tag{10.78}$$

where as before, $\hat{\mathbf{J}}(n)$ denotes the state of the MCF matrix at search step n corresponding to the nth node of the search tree in Figures 10.10 (b) and (c). Note that the search processes characterised by Figures 10.10 (b) and (c) merely expand the search process portrayed in Figure 10.10(a). Consequently, for the sake of brevity, the corresponding Equations (10.77) and (10.78) depict only the extra states of the MCF matrix introduced by the expanded search procedure. For instance, the states $\hat{\mathbf{J}}(10)$ and $\hat{\mathbf{J}}(8)$ of Equation (10.78) complement the state $\hat{\mathbf{J}}(7)$ of Equation (10.77), as well as the states $\hat{\mathbf{J}}(6), \hat{\mathbf{J}}(5), \hat{\mathbf{J}}(4)$ and $\hat{\mathbf{J}}(3)$ of Equations (10.74) and (10.75), respectively.

Finally, by comparing the resultant soft-bit estimates $\mathbf{L}_a, \mathbf{L}_b$ and $\mathbf{L}_c$ of Equations (10.76), (10.77) and (10.78) corresponding to the scaling values of $\rho = 1.0, 1.3$ and 2.0 to the cor-

responding Log-MAP estimate $\mathbf{L}$ of Equation (10.71), we may hypothesise that the value of the soft-bit estimate obtained by the modified OHRSA-ML method of Algorithm 4 rapidly converges to the Log-MAP estimate of the OHRSA-Log-MAP method of Algorithm 5 upon increasing the value of the parameter ρ. As expected, there is a tradeoff between the accuracy of the soft-bit information obtained and the corresponding computational complexity associated with the particular choice of ρ. In the next section we will generalise the results obtained in this example and substantiate the aforementioned convergence-related hypothesis, as well as deduce the optimal value of the associated scaling parameter ρ.

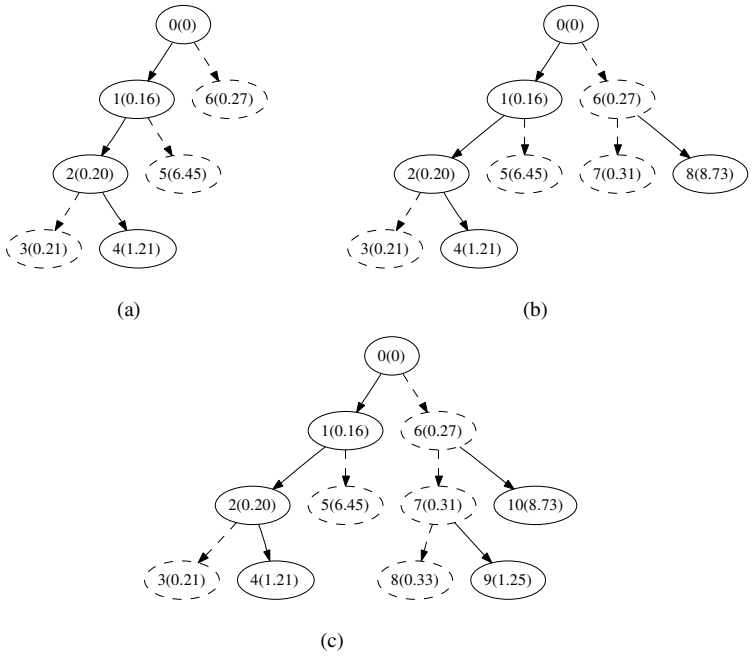


Figure 10.11: Example of the search trees formed by the modified OHRSA-ML SDM detector of Algorithm 4 using different values of the parameter ρ, namely, (a) $\rho = 1.0$, (b) 1.3 and (c) 2.0. We consider a system employing BPSK modulation, $m_{\rm t} = n_{\rm r} = 3$ transmit and receive antennas and encountering an average SNR of 10dB. The labels indicate the order of evaluation, as well as the corresponding value $J_i(\check{\mathbf{s}}_i)$ of the CSC function of Equation (10.22), as seen in the brackets.

Clearly, the repetitive nature of the search process entailing Equations (10.65f,i-r) in Algorithm 5 and exemplified by Example 4 imposes a substantial increase in the associated computational complexity. Hence, in the next section we derive an OHRSA-aided approximate Log-MAP method, which is capable of approaching the optimum Log-MAP performance, while avoiding the repetitive evaluation of Equation (10.65f) in Algorithm 5 and therefore imposes considerably reduced complexity requirements.

10.4.5 Soft-Output OHRSA-Aided Approximate Log-MAP Detection

Let us define the $(r \times 2)$-dimensional Bitwise Minimum Cost (BMC) function matrix $\hat{\mathbf{J}}$ having elements as follows

$$\hat{J}_{ib} = J(\hat{\mathbf{t}}_i^b),\ i = 1, \cdots, r,\ b = -1, 1, \tag{10.79}$$

where $\hat{\mathbf{t}}_i^b$ is defined by Equation (10.61). Using the BMC matrix of Equation (10.79), Equation (10.64) may also be expressed in a vectorial form as

$$\mathbf{L} = \frac{1}{\sigma_w^2}\left[(\hat{\mathbf{J}})_1 - (\hat{\mathbf{J}})_2\right], \tag{10.80}$$

where, as before, $(\hat{\mathbf{J}})_b$ denotes the bth column of the matrix $\hat{\mathbf{J}}$ having elements defined by Equation (10.79).

Consequently, in order to evaluate the bit-related soft information we have to populate the BMC matrix $\hat{\mathbf{J}}$ of Equation (10.79) with the corresponding values of the cost function of Equation (10.79). Observe, that the evaluation of the ML estimate $\hat{\mathbf{t}}$ will situate half elements of the cost matrix $\hat{\mathbf{J}}$ with the corresponding minimum value of the cost function associated with the ML estimate, such that we have

$$J_{ib} = J(\hat{\mathbf{t}}),\ i = 1, \cdots, r,\ b = \hat{t}_i. \tag{10.81}$$

Subsequently, let us introduce the following adjustments to Algorithm 4. Firstly, we introduce an additional parameter ρ, which we refer to as the *search radius factor*. More specifically, the parameter ρ allows us to control the rate of convergence for the tree search process of Algorithm 4 and affects the cut-off value of a CSC function, which limits the passage of the recursive search process through *low-likelihood* search branches having the a CSC function value $J_i(\check{\mathbf{t}}_i)$ in excess of $\rho J_{\min}$, as opposed to $J_{\min}$. Thus, the following rule replaces Rule 4 of Section 10.4.2.

Rule 4a At each recursive detection level i, only the high-probability search branches corresponding to the highly likely symbol candidates c_m resulting in low values of the CSC function obeying $J_i(c_m) < \rho J_{\min}$ are pursued. Furthermore, as follows from the sorting criterion of the optimisation Rule 2, as soon as the inequality $J_i(c_m) > \rho J_{\min}$ is satisfied, the search loop at the ith recursive detection level is discontinued.

Secondly, we introduce an additional rule, which facilitates the evaluation of the elements of the BMC matrix $\hat{\mathbf{J}}$ of Equation (10.79). Explicitly, we postulate Rule 5.

Rule 5 At each arrival at the bottom of the search tree, which corresponds to search level 1, the resultant value of the branch cost function $J(\check{\mathbf{t}})$ is utilized to populate the elements of the BMC matrix $\hat{\mathbf{J}}$, which correspond to the bitwise signal components $\check{t}_i$ comprising the obtained signal candidate $\check{\mathbf{t}}$. Namely, we have

$$\hat{J}_{ib} = \min\{\hat{J}_{ib}, J(\check{\mathbf{t}})\},\ i = 1, \cdots, r,\ b = \check{t}_i. \tag{10.82}$$

Subsequently, we suggest that the evaluation of the BMC matrix $\hat{\mathbf{J}}$, which is performed

in the process of the ML search of Algorithm 4 extended by Rule 4a and using Rule 5 will allow us to provide reliable soft-bit information, while imposing a relatively low computational complexity. The main rationale of this assumption will be outlined in our quantitative complexity and performance analysis portrayed in Section 10.4.5.1.

As we will further demonstrate in Section 10.4.5.1, the resultant approximate Log-MAP SDM detector exhibits a particularly low complexity at high SNR values. On the other hand, at low SNR values the associated complexity substantially increases. Consequently, in order to control the computational complexity at low SNR values, we introduce the additional complexity-control parameter γ. Our aim is to avoid the computationally demanding and yet inefficient detection of the specific signal components, which have their signal energy well below the noise floor. More specifically, we modify Equation (10.54p) of Algorithm 4 according to Rule 6.

Rule 6 The branching of the tree search described by Algorithm 4 is truncated, if the SNR associated with the corresponding signal component is lower than the value of the complexity-control parameter γ. In other words, the search along a given branch is truncated if we have $\frac{\|\mathbf{H}_i\|^2}{\sigma_w^2} < \gamma$.

Upon applying Rules 4, 5 and 6 in the context of the OHRSA-ML method of Algorithm 4, we arrive at an *approximate* OHRSA-Log-MAP SDM detector, which avoids the repetitive search required by the OHRSA-Log-MAP SDM detector of Section 10.4.4.

The resultant OHRSA-aided approximate Log-MAP SDM detector, which we refer to as the Soft-output OPtimised HIErarchy (SOPHIE) SDM detector is summarised in Algorithm 6.

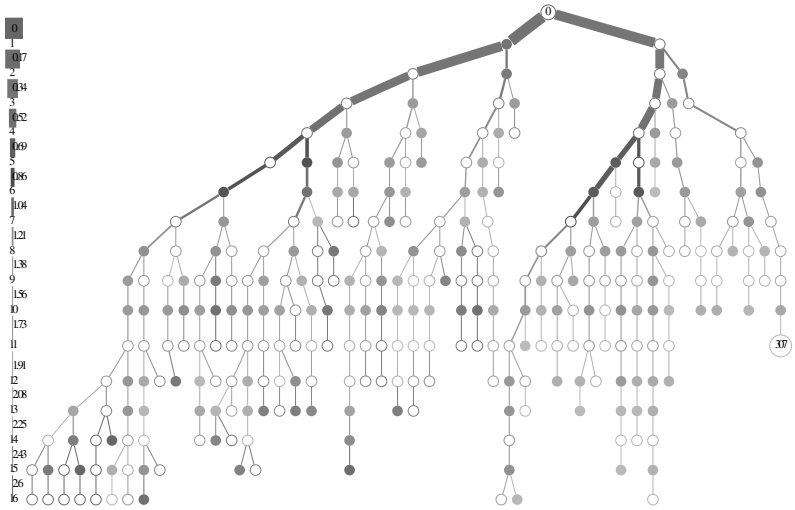


Figure 10.12: Example of a search tree formed by the SOPHIE SDM detector of Algorithm 4 in the scenario of QPSK, $m_{\rm t} = n_{\rm r} = 8$ and an average SNR of 6 dB. The approximate Log-MAP solution is attained in 307 evaluation steps in comparison to $32 \cdot 2^{15} = 1,048,576$ evaluation steps required by the exhaustive Log-MAP search. For more details on the notations employed in the diagram see the caption of Figure 10.9.

Algorithm 6 SOPHIE Approximate Log-MAP SDM Detector

$$\tilde{\mathbf{H}} = \begin{bmatrix} \mathcal{R}\{\mathbf{HQ}\} \\ \mathcal{I}\{\mathbf{HQ}\} \end{bmatrix} \tag{10.83a}$$

$$\texttt{Sort}\{\tilde{\mathbf{H}}\},\ \texttt{such that}\ \|(\tilde{\mathbf{H}})_1\|^2 \leq \cdots \leq \|(\tilde{\mathbf{H}})_r\|^2 \tag{10.83b}$$

$$\mathbf{G} = (\tilde{\mathbf{H}}^{\mathrm{H}}\tilde{\mathbf{H}} + \sigma_w^2\mathbf{I}) \tag{10.83c}$$

$$\mathbf{U} = \texttt{CholeskyDecomposition}(\mathbf{G}) \tag{10.83d}$$

$$\hat{\mathbf{x}} = \mathbf{G}^{-1}\tilde{\mathbf{H}}^{\mathrm{H}}\tilde{\mathbf{y}} \tag{10.83e}$$

$$\texttt{Calculate}\quad J_r \tag{10.83f}$$

$$\mathbf{L} = \frac{1}{\sigma_w^2}\left[(\hat{\mathbf{J}})_0 - (\hat{\mathbf{J}})_1\right] \tag{10.83g}$$

$$\texttt{Unsort}\{L_i\}_{i=1,\cdots,r} \tag{10.83h}$$

$$\texttt{function}\quad \texttt{Calculate}\quad J_i \tag{10.83i}$$

$$a_i = \sum_{j=i+1}^{m_{\mathrm{t}}} u_{ij}(\check{t}_j - \hat{x}_j) \tag{10.83j}$$

$$\texttt{Sort}\{\boldsymbol{b}\},\ \texttt{such that}\ \phi_i(b_1) < \phi_i(b_2), \tag{10.83k}$$

$$\texttt{where}\quad \phi_i(b) = |u_{ii}(b - \hat{x}_i) + a_i|^2 \tag{10.83l}$$

$$\texttt{for}\quad m = 1, 2\quad \texttt{do} \tag{10.83m}$$

$$\check{t}_i = b_m \tag{10.83n}$$

$$J_i = J_{i+1} + \phi_i(\check{t}_i) \tag{10.83o}$$

$$\texttt{if}\quad J_i < \rho J_{\min}\quad \texttt{then} \tag{10.83p}$$

$$\texttt{if}\quad i > 0\ \texttt{and}\ \frac{\|(\tilde{\mathbf{H}})_i\|^2}{\sigma_w^2} > \gamma\quad \texttt{then} \tag{10.83q}$$

$$\texttt{Calculate}\quad J_{i-1} \tag{10.83r}$$

$$\texttt{else}$$

$$J_{\min} = \min(J_i, J_{\min}) \tag{10.83s}$$

$$\texttt{for}\quad j = 1, \cdots, r \tag{10.83t}$$

$$\hat{J}_{j\check{t}_j} = \min\{\hat{J}_{j\check{t}_j}, J(\check{\mathbf{t}})\},\ j = 1, \cdots, r \tag{10.83u}$$

$$\texttt{end}\quad \texttt{for} \tag{10.83v}$$

$$\texttt{end}\quad \texttt{if}$$

$$\texttt{end}\quad \texttt{if}$$

$$\texttt{end}\quad \texttt{for}$$

$$\texttt{end}\quad \texttt{function}$$

Example 6 (SOPHIE 16QAM 1x1)

In this example we would like to demonstrate two major points, namely

1) the applicability of the SOPHIE detection method of Algorithm 6 in the context of systems employing high-throughput modulation schemes, such as M-QAM, as well as

2) the advantage of employing SOPHIE detection in the SISO M-QAM scenario.

Consider a 16-QAM SISO-OFDM system. Specifically, we have a scalar complex-valued linear system described by Equation (10.7), where the corresponding transmitted signal $\mathbf{s}$, the received signal $\mathbf{y}$ and the (1×1)-dimensional channel matrix $\mathbf{H}$ are exemplified by the values

$$\mathbf{s} = -3 + 1\jmath, \quad \mathbf{y} = -0.57 + 4.08\jmath \quad \text{and} \quad \mathbf{H} = [0.8 - 1.2\jmath]. \tag{10.84}$$

Observe that the transmitted symbol s belongs to the unnormalised 16-QAM constellation obtained by multiplying the transmitted bit-vector $\mathbf{t}$ to the corresponding quantisation vector $\mathbf{q}$ depicted in Table 10.2. Firstly, we apply the brute-force Log-MAP QAM demodulation technique. Namely, for each transmitted bit t_i we calculate the log-likelihood ratio (LLR) value

$$\log\left(\frac{p(t_i = 0|y, H)}{p(t_i = 0|y, H)}\right) = \log\left(\frac{\sum_{\check{s}\in\mathcal{M}_0}\left(\frac{|y-H\check{s}|^2}{\sigma_w^2}\right)}{\sum_{\check{s}\in\mathcal{M}_1}\left(\frac{|y-H\check{s}|^2}{\sigma_w^2}\right)}\right) \tag{10.85}$$

for each of the 16 legitimate signal candidates $\check{s}$. Then we calculate the corresponding value of the objective function as follows

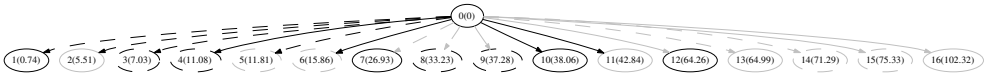
$$J(\check{s}) = \|y - H\check{s}\|^2. \tag{10.86}$$

10.4.5.1 Complexity Analysis.

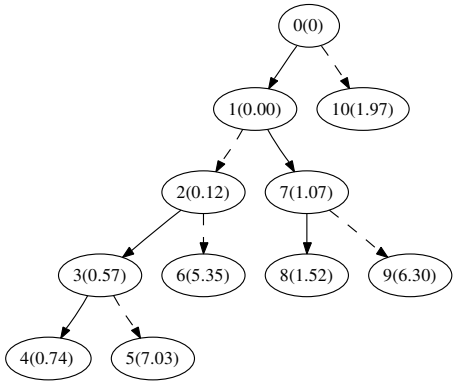
As pointed out in [90] , "the brute-force" ML SDM detection method does not provide a feasible solution to the generic SDM detection problem, as a result of the excessive associated computational complexity. More explicitly, the ML SDM detector advocated in [90] has a computational complexity, which is of the order of

$$\mathcal{C}_{\mathrm{ML}} = O\{M^{m_{\mathrm{t}}} \cdot (3n_{\mathrm{r}} + 2n_{\mathrm{r}}m_{\mathrm{t}})\}, \tag{10.87}$$

where $3n_{\mathrm{r}} + 2n_{\mathrm{r}}m_{\mathrm{t}}$ is the complexity associated with a single search step, namely the evaluation of the objective function value $\|\mathbf{H}\check{\mathbf{s}} - \mathbf{y}\|^2$, while $M^{m_{\mathrm{t}}}$ is the number of legitimate candidates of the transmitted signal vector $\mathbf{s}$. Clearly, the order of complexity imposed by Equation (10.87) becomes excessive for a large number of transmit antennas, for example in the case of employing 16QAM and $m_{\mathrm{t}} = n_{\mathrm{r}} = 8$ transmit and receive antennas, where the computational complexity associated with ML detection is of the order of 10^7 complex operations per channel use, or 10^9 complex operations per OFDM symbol formed by $K = 128$ subcarriers. Furthermore, the evaluation of the soft-bit information required by



(a)



(b)

Figure 10.13: Examples of a search tree formed by the (a) OHRSA-ML and (b) BW-OHRSA-ML SDM detectors in the scenario of a system employing QPSK modulation, $m_{\rm t} = n_{\rm r} = 3$ transmit and receive antennas and encountering average SNRs of 10dB. The labels indicate the order of execution, as well as the corresponding value $J_i(\check{\mathbf{s}}_i)$ of the CSC function of Equation (10.22), as seen in the brackets.

an efficient turbo-decoder implementation imposes a further substantial increase of the associated computational complexity. Specifically, the soft-output Log-MAP SDM detector advocated in [90] has a computational complexity, which is of the order of

$$\mathcal{C}_{\rm LM} = O\{m_{\rm t} \log_2 M \cdot 2^{m_{\rm t} \log_2 M - 1} \cdot (3n_{\rm r} + 2n_{\rm r} m_{\rm t})\}. \tag{10.88}$$

On the other hand, the MMSE SDM detector derived in [90] constitutes the low-complexity SDM detector. The complexity imposed by the MMSE SDM detector of [90] may be shown to be of the order of

$$\mathcal{C}_{\rm MMSE} = O\{m_{\rm t}^3 + m_{\rm t} n_{\rm r}^2 + m_{\rm t}^2 n_{\rm r} + m_{\rm t} n_{\rm r}\}. \tag{10.89}$$

Clearly, the MMSE SDM detector's complexity is substantially lower than that associated with the ML or Log-MAP SDM detectors. Specifically, for example only 1600 complex operations are required for detecting 16QAM signals transmitted and received by $m_{\rm t} = n_{\rm r} = 8$ transmit and receive antennas. Unfortunately, however, as demonstrated in [90] , the achievable performance exhibited by the linear MMSE SDM detector is considerably lower than that attained by the optimal Log-MAP SDM detector advocated in [90] . Moreover, linear SDM detectors, such as the MMSE detector do not allow the high-integrity detection of signals in the over-loaded scenario, where the number of the transmit antennas exceeds that of the receive antennas.

Consequently, in Sections 10.4.3, 10.4.4 and 10.4.5 we derived a family of methods which combine the advantageous properties of the ML and Log-MAP detection, while imposing a substantially lower complexity. In this section we demonstrate that the computational complexity associated with the SOPHIE-aided Log-MAP SDM detector of Algorithm 6 is in fact only slightly higher than that imposed by the low-complexity MMSE SDM detector advocated in [90] , while its performance is virtually identical to the performance of the Log-MAP SDM detector [90] .

The direct calculation of the complexity associated with the OHRSA methods of Algorithms 4, 5 and 6 is infeasible, since the complexity is not a constant, but rather a random variable, which is a function of several parameters, such as the number $m_{\rm t}$ and $n_{\rm r}$ of transmit and receive antennas, the average SNR encountered as well as the value of the parameter ρ in Algorithm 6. Therefore, we perform the corresponding complexity analysis using computer simulations. Figure 10.14(a) illustrates our comparison between the computational complexity required by different SDM detection methods, namely the linear MMSE detector advocated in [90] , the SIC detector of [90, pp.754-756] , the exhaustive search-based ML and Log-MAP detectors of [90] as well as the OHRSA-aided ML, Log-MAP and SOPHIE SDM detectors of Algorithms 4, 5 and 6, respectively. The results depicted in Figure 10.14(a) correspond to the *fully-loaded* scenario, where we have $m_{\rm t} = n_{\rm r}$ transmit and receive antennas. Observe that the complexity associated with both the OHRSA-ML and SOPHIE SDM detectors is only slightly higher than that imposed by the MMSE SDM detector and is in fact lower than the complexity imposed by the SIC SDM detector.

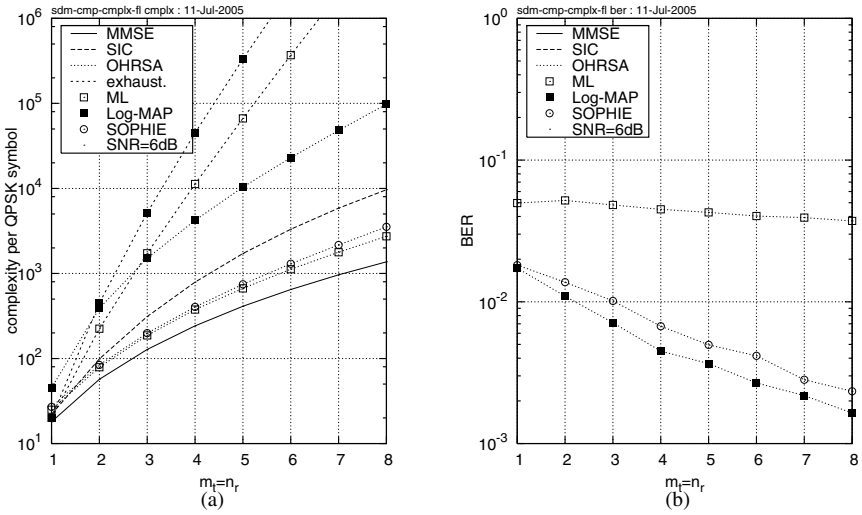


Figure 10.14: (a) **Computational complexity** quantified in terms of the total number of real multiplications and additions per detected QPSK symbol and (b) the corresponding **BER** exhibited by the rate half turbo-coded **SDM-QPSK-OFDM** system employing the different SDM detection methods considered at SNR=6dB. The abscissa represents the number $m_{\rm t} = n_{\rm r} = 1, \cdots, 8$ of transmit and receive antenna elements. The corresponding system parameters are summarized in Table 10.3.

Furthermore, the achievable performance of the SDM-OFDM system employing the different SDM detection methods considered is depicted in Figure 10.14(b). Observe that both the OHRSA-Log-MAP and SOPHIE SDM detectors considerably outperform the linear MMSE detector. Moreover, the associated BER decreases upon increasing the number of transmit and receive antennas $m_{\rm t} = n_{\rm r}$, which suggests that as opposed to both the MMSE and the SIC SDM detectors, the OHRSA-Log-MAP SDM detector is capable of achieving spatial diversity even in the *fully-loaded* system. In other words, it is capable of achieving both multiplexing and diversity gains simultaneously, while maintaining a low computational complexity.

The relatively low performance of the OHRSA-ML SDM detector may be attributed to the fact that it produces no soft-bit information and therefore the efficiency of the turbo code employed is substantially degraded. Moreover, observe that while the SIC SDM detector outperforms its MMSE counterpart at high SNR values [90], the achievable performance of the two methods is fairly similar at low SNR values, such as 6dB.

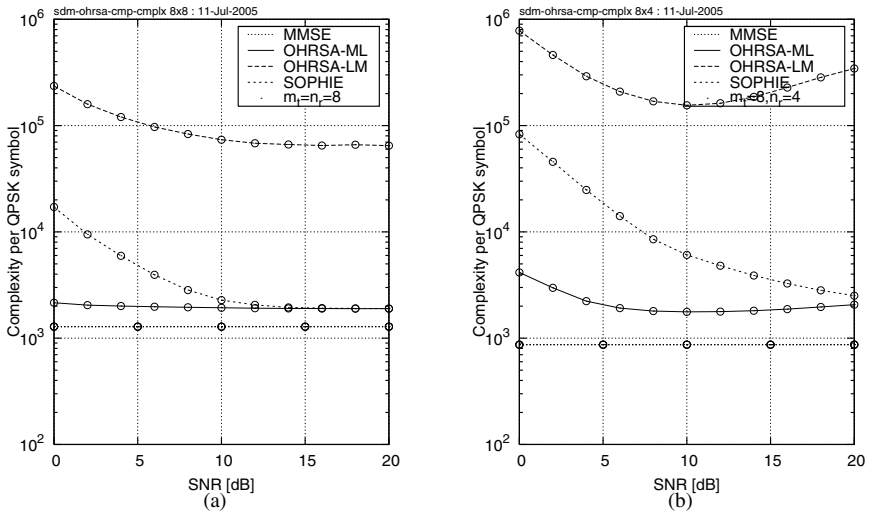


Figure 10.15: Computational complexity quantified in terms of the total number of real multiplications and additions per detected QPSK symbol. We consider the **OHRSA-ML, OHRSA-Log-MAP** and **SOPHIE** SDM detection methods of Algorithms 4, 5 and 6, respectively. Additionally, we show the corresponding computational complexity required by the low-complexity linear MMSE SDM detector. The abscissa represents the average SNR encountered.

Additionally, Figure 10.15 illustrates the complexity imposed by the OHRSA methods of Algorithms 4, 5 and 6 as a function of the average SNR encountered. Figures 10.15 (a) and (b) portray the average complexity encountered in the scenarios of $m_{\rm t} = n_{\rm r} = 8$ and $m_{\rm t} = 8, n_{\rm r} = 4$ transmit and receive antennas, respectively. Observe that the complexity associated with both the OHRSA-ML and SOPHIE methods of Algorithms 5 and 6 is mainly determined by the number $m_{\rm t}$ of transmit antennas employed. Furthermore, the complexity associated with the SOPHIE method closely matches that exhibited by the OHRSA-ML method at high

Table 10.3: System parameters.

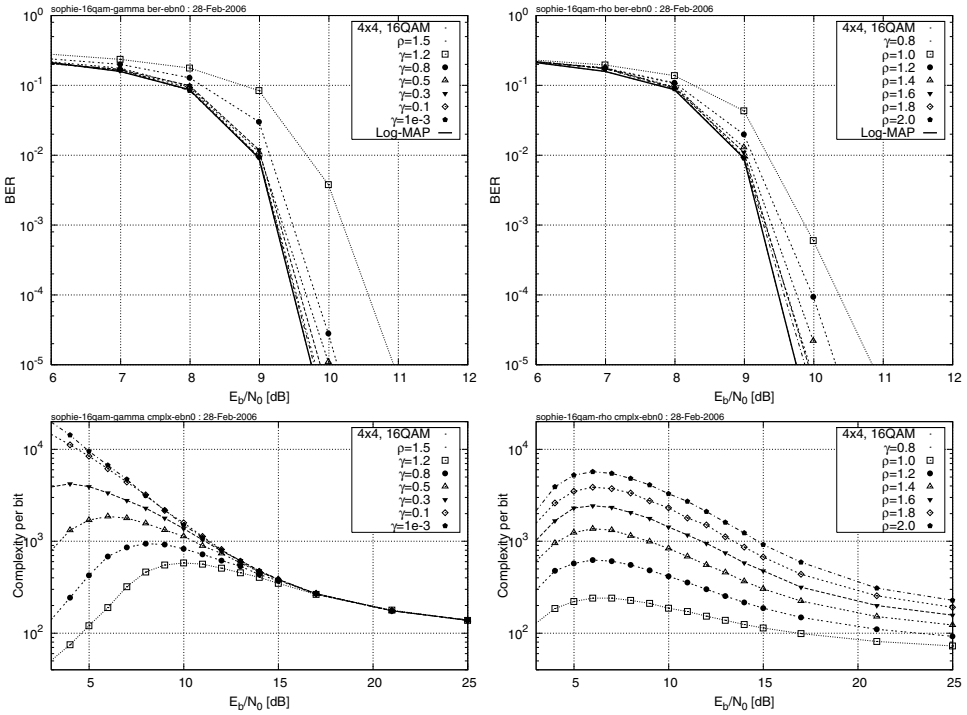
Parameter	OFDM	MC-CDMA
Channel bandwidth	800 kHz	
Number of carriers K	128	
Symbol duration T	160 μs	
Max. delay spread τ_{max}	40 μs	
Channel interleaver	WCDMA [375] 248 bit	–
Modulation	QPSK	
Spreading scheme	–	WH
FEC component codes code interleaver	Turbo code [216] , rate 1/2 RSC, K=3(7,5) WCDMA (124 bit)	

SNR values and the complexity exhibited by both methods is only slightly higher than the complexity exhibited by the low-complexity MMSE SDM detector.

10.4.5.2 Performance Analysis

In this section we present our simulation results characterising the SDM-OFDM system employing the OHRSA-aided SDM detection schemes described in Section 10.4. Our simulations were performed in the base-band frequency domain and the system configuration characterised in Table 10.3 is to a large extent similar to that used in [361]. We assume having a total bandwidth of 800kHz. The OFDM system utilises 128 orthogonal subcarriers. For forward error correction (FEC) we use 1/2-rate turbo coding [216] employing two constraint-length $K = 3$ Recursive Systematic Convolutional (RSC) component codes [375]. The octally represented RCS generator polynomials of (7,5) were used. Finally, throughout this chapter we stipulate the assumption of perfect channel knowledge, where the knowledge of the frequency-domain subcarrier-related coefficients $H[n, k]$ is deemed to be available in the receiver. Figure 10.16 characterises the achievable performance as well as the associated computational complexity exhibited by the 4×4 16QAM-SDM-OFDM system employing the SOPHIE SDM detector of Algorithm 6. More specifically, we analyse the associated performance versus complexity trade-offs of using various values of the complexity-control parameters ρ and γ. In Figure 10.16(a) we can observe how the achievable BER performance (top) and the corresponding computational complexity depend on the value of the parameter γ. Using the results depicted in Figure 10.16(a) we may conclude that the optimum choice of the complexity-control parameter γ lies in the range $0.5 - 0.8$, where we have a minor BER performance degradation of less than 0.5 dB, while achieving up to two orders of magnitude complexity reduction at low SNR values, when compared to the full-complexity SOPHIE algorithm assuming $\gamma = 0$.

On the other hand, Figure 10.16(b) portrays both the achievable BER performance and the associated complexity of the 4×4 16QAM-SDM-OFDM system for different values of

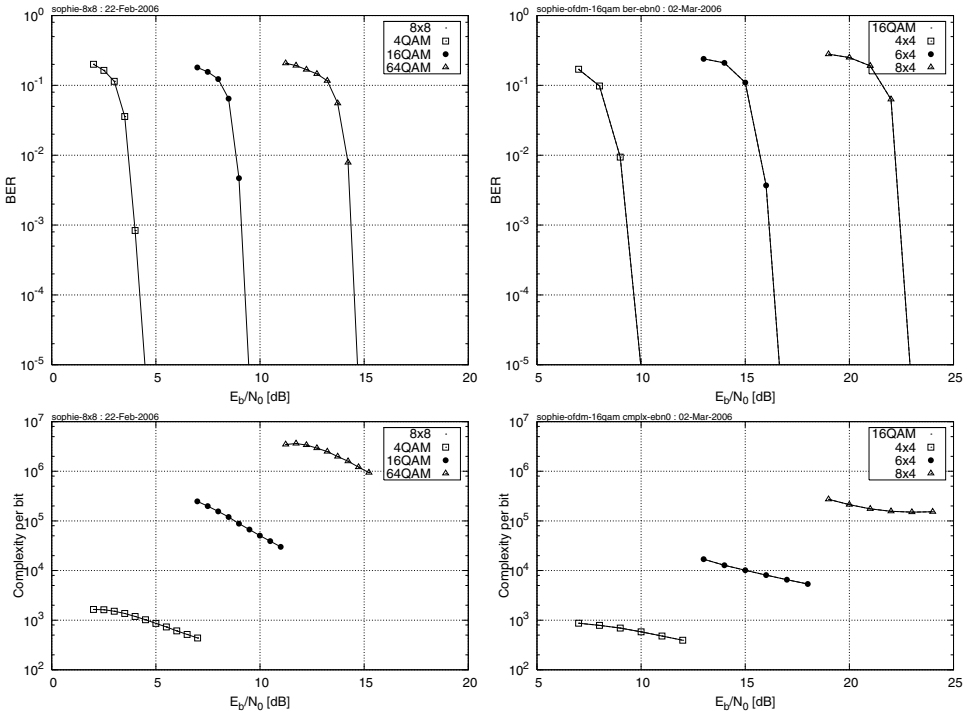


(a) (b)

Figure 10.16: Bit Error Rate (top) and the associated **computational complexity per detected bit** (bottom) exhibited by the 4×4 **16QAM-SDM-OFDM** system employing a **SOPHIE** SDM detector of Algorithm 6. (a) assuming different values of parameters (a) γ and (b) ρ. The abscissa represents the average E_b/N_0 recorded at the receive antenna elements.

the complexity-control parameter ρ. We may conclude that the optimum trade-off between the attainable BER performance and the associated complexity is achieved, when the value of the complexity-control parameter ρ lies in the range of $1.3 - 1.5$, where the BER performance degradation imposed does not exceed 0.5 dB, while the associated computational complexity is reduced by more than an order of magnitude, when compared to large values of ρ, such as for instance $\rho = 2.0$.

Furthermore, Figure 10.17(a) demonstrates both the BER performance (top) and the associated computational complexity exhibited by the (8×8) 4, 16 and 64QAM SDM-OFDM systems employing the SOPHIE SDM detector of Algorithm 6. Figure 10.17(b) characterises the 16QAM-SDM-OFDM system employing the SOPHIE SDM detector of Algorithm 6 and having a constant number of $n_{\rm r} = 4$ receive antenna elements in terms of its ability to detect the multiplexed signals arriving from various numbers of transmit antenna elements. Specifically, we aim for exploring the performance of the SOPHIE SDM detector in the overloaded system scenario, where the number of transmit antenna elements exceeds that of the receiver elements and thus we have $m_{\rm t} > n_{\rm r}$. Indeed, the BER curves portrayed in Figure 10.17 (top)



(a) (b)

Figure 10.17: Bit Error Rate (top) and the associated **computational complexity per detected bit** (bottom) exhibited by the **SDM-OFDM** system employing a **SOPHIE** SDM detector of Algorithm 6 assuming different values of parameters (a) γ and (b) ρ. The abscissa represents the average E_b/N_0 recorded at the receive antenna elements.

confirm the near-Log-MAP performance of the SOPHIE SDM detector of Algorithm 6 in both systems employing high-throughput modulation schemes as well as in the overloaded system scenario.

Figure 10.18(a) demonstrates that the SDM-OFDM system employing the SOPHIE SDM detector of Algorithm 6 is capable of exploiting the available MIMO channel's multiplexing gain in the fully loaded system scenario, when the number of the transmit antenna elements $m_{\rm t}$ is equal to that of the receiver antenna elements $n_{\rm r}$. More specifically, the results depicted in Figure 10.18(a) suggest that the SDM-OFDM SOPHIE SDM detector having $m_{\rm t} = n_{\rm r} = 8$ transmit and receive antennas exhibits an SNR-related diversity gain of 2dB at the target BER of 10^{-4}, as well as a factor four higher throughput, when compared to the same system employing two antennas at both the transmitter and receiver.

Additionally, Figure 10.18(b) characterises the SDM-OFDM system employing the SOPHIE SDM detector of Algorithm 6 and having a constant number of $n_{\rm r} = 4$ receive antenna elements in terms of its ability to detect the multiplexed signals arriving from various numbers of transmit antenna elements. Specifically, we aim for exploring the performance of the

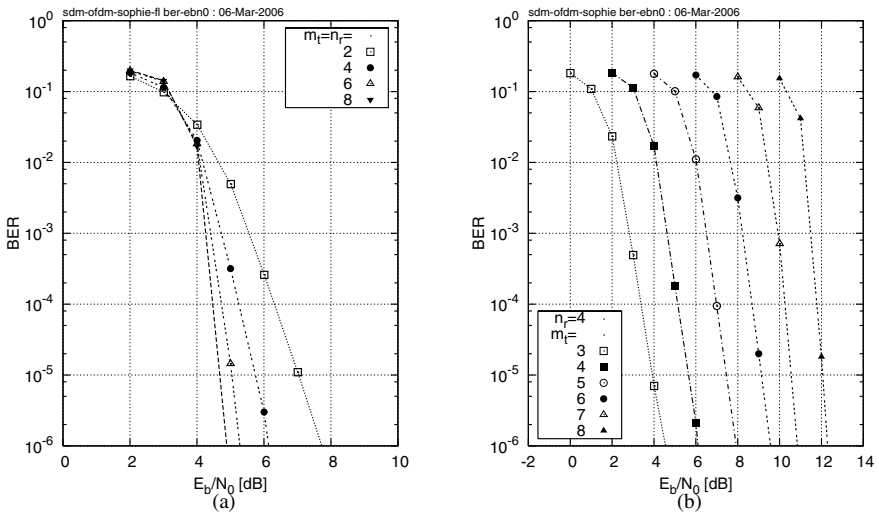


Figure 10.18: Bit Error Rate exhibited by the **SDM-QPSK-OFDM** system employing **SOPHIE** SDM detector of Algorithm 6 in (a) fully-loaded scenario with $m_{\rm t} = n_{\rm r} = 2, 4, 6$ and 8 transmit and receive antennas, as well as (b) overloaded scenario with fixed number of $n_{\rm r} = 4$ receive antennas and $m_{\rm t} = 3, 4, \cdots, 8$ transmit antennas. The abscissa represents the average value of E_b/N_0 recorded at the receive antenna elements.

SOPHIE SDM detector in the over-loaded system scenario, where the number of transmit antenna elements exceeds that of the receiver elements and thus we have $m_{\rm t} > n_{\rm r}$. We can see that as opposed to the MMSE SDM detector [90] , the SOPHIE SDM detector exhibits a good performance both when we have $m_{\rm t} \leq n_{\rm r}$, as well as in the over-loaded system scenario, when the number of transmit antenna elements exceeds the number of the receive antenna elements, i.e. when we have $m_{\rm t} > n_{\rm r}$.

10.5 Chapter Summary and Conclusion

In this chapter we proposed a novel OHRSA-aided SDM detection method, which may be regarded as an advanced extension of the CSD method. The algorithm proposed extends the potential range of applications of the CSD methods, as well as reducing the associated computational complexity, rendering the algorithm proposed a feasible solution for implementation in high-throughput practical systems.

Furthermore, we have shown that the OHRSA-aided SDM detector proposed combines the advantageous properties of both the optimum-performance Log-MAP SDM detector and that of the low-complexity linear MMSE SDM detector, which renders it an attractive alternative for implementation in practical systems. More specifically, we have shown that the OHRSA-aided SDM detector proposed exhibits the following advantageous properties.

The method can be employed in the over-loaded scenario, where the number of transmit antenna elements exceeds that of the receive antenna elements, while the associated compu-

tational complexity increases only moderately even in heavily over-loaded scenarios and is almost independent of the number of receive antennas. Furthermore, as opposed to standard CSD schemes [176], no calculation of the sphere radius is required and therefore the method proposed is robust to the particular choice of the initial parameters both in terms of the achievable performance and the associated computational complexity. The overall computational complexity required is only slightly higher than that imposed by the linear MMSE multi-user detector designed for detecting a similar number of users. Specifically, the computational complexity per detected QAM symbol associated with both the MMSE and SOPHIE SDM detectors is of the order of $O\{m_{\rm t}^3\}$, where $m_{\rm t}$ is the number of transmit antennas. Finally, the associated computational complexity is fairly independent of the channel conditions quantified in terms of the SNR encountered.

In our future work the achievable performance of the SDM detection schemes proposed will be explored in the presence of imperfect channel state information. More explicitly, we will characterise and analyse the performance of a range of channel estimation methods suitable for employment in the SDM-OFDM system considered in this chapter. Subsequently, we will analyse the achievable performance of the SDM detection methods portrayed in this chapter in the context of the SDM-OFDM system employing our channel estimation schemes.

Additionally, an iterative joint SDM detection and decoding scheme, which can potentially approach the information-theoretic capacity bound will be designed. Furthermore, joint iterative turbo-structured SDM detection, decoding and channel estimation methods will be explored.

Chapter 11

Genetic Algorithm Aided Joint Channel Estimation and MUD for SDMA OFDM[1]

M. Jiang, J. Akhtman and L. Hanzo

11.1 Introduction

As argued in Chapter 10, Multiple-Input-Multiple-Output (MIMO) Orthogonal Frequency Division Multiplexing (OFDM) systems have recently attracted substantial research interest [90]. The various applications of MIMO systems were briefly summarised in Table 10.1. On one hand, the employment of multiple antennas offers an opportunity to exploit both transmitter and receiver diversity, hence significantly increasing the system's transmission integrity [357]. On the other hand, as a further benefit, OFDM exhibits robustness against both frequency-selective fading as well as the Inter-Symbol-Interference (ISI) imposed by multi-path propagation. Specifically, intensive research efforts have been invested both in Bell Labs Layered Space-Time architecture (BLAST) [123] and in Space Division Multiple Access (SDMA) based MIMO OFDM [90]. More specifically, in SDMA-OFDM systems the transmitted signals of L simultaneous uplink mobile users - each equipped with a single transmit antenna - are received by the P different receiver antennas of the Base Station (BS). At the BS Multi-User Detection (MUD) [321] techniques are invoked for detecting the different users' transmitted signals with the aid of their unique, user-specific spatial signature constituted by their Frequency-Domain CHannel Transfer Functions (FD-CHTFs) or, equiva-

[1] Acknowledgements: The work reported in this paper has formed part of the Wireless Enabling Techniques work area of the Core 3 Research Programme of the Virtual Centre of Excellence in Mobile and Personal Communications, Mobile VCE, www.mobilevce.com, whose funding support, including that of EPSRC, is gratefully acknowledged. Fully detailed technical reports on this research are available to Industrial Members of Mobile VCE.

© 2006 John Wiley & Sons, Ltd

lently, Channel Impulse Responses (CIRs). Since the same time-frequency resource is shared by simultaneous users, a higher bandwidth efficiency can be achieved by SDMA systems in comparison to conventional multiplexing techniques, such as for example Time Division Multiple Access (TDMA) or Frequency Division Multiple Access (FDMA).

However, in these systems accurate channel estimation is required at the receiver for the sake of invoking both coherent demodulation and interference cancellation. Compared to Single-Input-Single-Output (SISO) systems, channel estimation in the MIMO scenario becomes more challenging, since a significantly increased number of independent transmitter-receiver channel links have to be estimated simultaneously for each subcarrier. Moreover, the interfering signals of the other transmit antennas have to be suppressed. All these factors render channel estimation for MIMO OFDM systems a new challenge.

In the literature, a number of blind channel estimation techniques have been proposed for MIMO-OFDM systems [376–381]. However, most of these approaches suffer from either a slow convergence rate or a performance degradation, owing to the inherent limitations of blind search mechanisms. By contrast, the techniques benefiting from explicit training with the aid of known reference/pilot signals, are typically capable of achieving a better performance at the cost of a reduced effective system throughput. For example, Li *et al.* [382] proposed an approach exploiting both transmitter diversity and the delay profile characteristics of typical mobile channels, which was further simplified and enhanced in [118, 120] and [383], respectively. Other schemes employed Minimum Mean Square Error (MMSE) [116], Constrained Least Squares (CLS) [384], iterative Least Squares (LS) [385], Second-Order Statistics (SOS) based SubSpace (SS) [386] estimation algorithms as well as the QR Decomposition combined with the M-algorithm (QRD-M) [387, 388] or techniques based on Time Of Arrivals (TOAs) [389], etc. Some researchers have focused their attention on designing optimum training patterns or structures [118, 390, 391]. Furthermore, various joint approaches combining channel estimation with data symbol detection at the receiver were also proposed for Code Division Multiple Access (CDMA) [381, 387], SISO OFDM [392] and MIMO OFDM [388, 393] systems. *However, in the context of BLAST or SDMA type multi-user MIMO OFDM systems, all channel estimation techniques found in the literature were developed under the assumption that the number of users L is lower than [116, 376–378, 386, 394] or equal to [379, 384, 388–390, 393] the number of receiver antennas P.* This assumption is critical for the following reasons. When we have $L > P$, which we refer to as an *over-loaded* scenario, the $(P \times L)$-dimensional MIMO channel matrix representing the $P \times L$ number of channel links becomes singular, thus rendering the degree of freedom of the detector insufficient. This will catastrophically degrade the performance of numerous known detection approaches, such as, for example, the MMSE algorithm of [90, 321] and the QRD-M algorithm of [388]. Furthermore, the associated significant degradation of the MUD's performance in this over-loaded scenario will inevitably result in severe error propagation in decision-directed type channel estimators [90].

Against this background, in this chapter we propose a new Genetic Algorithm (GA) assisted [323, 359] iterative Joint Channel Estimation and Multi-User Detection (GA-JCEMUD) approach for multi-user MIMO SDMA-OFDM systems, which provides an effective solution to the multi-user MIMO channel estimation problem in the above-mentioned over-loaded scenario. Our ambitious goal of supporting a high number of users is physically possible, because the proposed GA-based technique dispenses with any constraints concerning the rank of the channel matrix. In the literature, only a few channel estimation schemes

have been proposed based on GAs. More specifically, Yen *et al.* [395] proposed a GA-aided multi-user CDMA single-antenna receiver, which jointly estimates the transmitted symbols and fading channel coefficients of all the users. A batch blind equalisation scheme based on Maximum Likelihood (ML) concatenated channel and data estimation employing a micro genetic algorithm (μGA) and the Viterbi Algorithm (VA) was proposed in [396]. In [397, 398], GA-based approaches were used for finding optimum training sequences for channel estimation in OFDM systems. *However, to the best of our knowledge, no techniques employing GAs for joint channel and data optimisation can be found in the literature in the context of multi-user MIMO OFDM. Furthermore, at the time of writing the GAs invoked in the data detection literature [323, 395, 399–402] can only provide a hard-decision output for the Forward Error Correction (FEC) or channel decoder, which inevitably limits the system's achievable performance. By contrast, our proposed GA is capable of providing "soft" outputs and hence it becomes capable of achieving an improved performance with the aid of FEC decoders.*

The structure of this chapter is as follows. The SDMA MIMO channel model used is described in Section 11.2, while an overview of the proposed scheme is provided in Section 11.3, followed by our detailed analysis in Section 11.4. The numerical results are presented in Section 11.5, while our final conclusions are offered in Section 11.6.

11.2 SDMA MIMO Channel Model

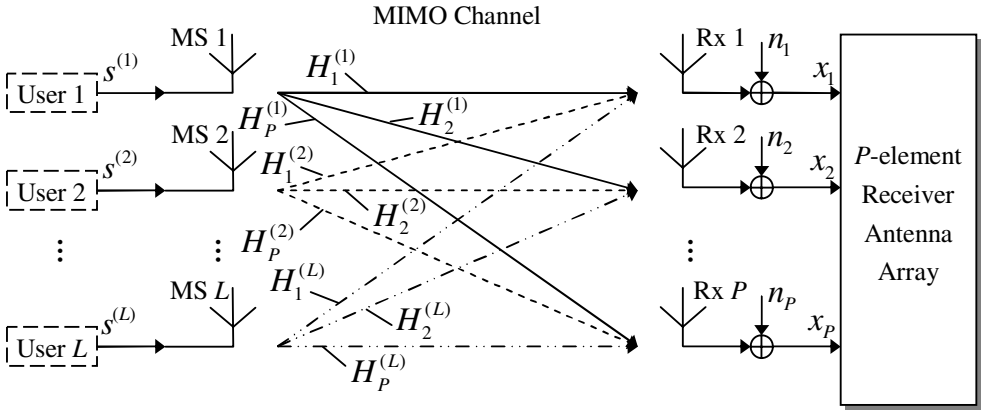


Figure 11.1: Schematic of the SDMA uplink MIMO channel model [90], where each of the L mobile users has a single transmit antenna and the BS's receiver is assisted by a P-element antenna front-end.

Figure 11.1 shows the SDMA uplink MIMO channel model, where each of the L simultaneous mobile users employs a single transmit antenna at the mobile station (MS), while the BS's receiver exploits P antennas. At the k^{th} subcarrier of the n^{th} OFDM symbol received by the P-element receiver antenna array we have the complex-valued received signal vector $\mathbf{x}[n,k]$, which is constituted by the superposition of the independently faded signals associated with the L mobile users and contaminated by the Additive White Gaussian Noise

(AWGN), expressed as:

$$\mathbf{x} = \mathbf{H}\mathbf{s} + \mathbf{n}, \tag{11.1}$$

where the $(P \times 1)$-dimensional vector $\mathbf{x}$, the $(L \times 1)$-dimensional vector $\mathbf{s}$ and the $(P \times 1)$-dimensional vector $\mathbf{n}$ are the received, transmitted and noise signals, respectively. Here we have omitted the indices $[n, k]$ for each vector for the sake of notational convenience. Specifically, the vectors $\mathbf{x}$, $\mathbf{s}$ and $\mathbf{n}$ are given by:

$$\mathbf{x} = (x_1, x_2, \cdots, x_P)^T, \tag{11.2}$$
$$\mathbf{s} = (s^{(1)}, s^{(2)}, \cdots, s^{(L)})^T, \tag{11.3}$$
$$\mathbf{n} = (n_1, n_2, \cdots, n_P)^T. \tag{11.4}$$

The $(P \times L)$-dimensional matrix $\mathbf{H}$ contains the FD-CHTFs of the L users and is given by:

$$\mathbf{H} = (\mathbf{H}^{(1)}, \mathbf{H}^{(2)}, \cdots, \mathbf{H}^{(L)}), \tag{11.5}$$

where $\mathbf{H}^{(l)}$ $(l = 1, \cdots, L)$ is the vector of the FD-CHTFs associated with the transmission paths from the l^{th} user's transmit antenna to each element of the P-element receiver antenna array, expressed as:

$$\mathbf{H}^{(l)} = (H_1^{(l)}, H_2^{(l)}, \cdots, H_P^{(l)})^T, \quad l = \{1, \cdots, L\}, \tag{11.6}$$

where $\mathbf{H}^{(l)}$ $(l = 1, \cdots, L)$ are independent for the different users.

11.3 System Overview

Figure 11.2 shows the schematic of an SDMA-OFDM uplink system using the proposed iterative GA-JCEMUD. As shown in the upper half of Figure 11.2, the binary information bit blocks $\mathbf{b}^{(l)}$ $(l = 1, \cdots, L)$ of the L number of mobile users are first encoded by the L independent FEC encoders. The resultant coded bits $\mathbf{b}_s^{(l)}$ are then mapped to Quadrature Amplitude Modulation (QAM) or Phase-Shift Keying (PSK) symbols $\mathbf{s}^{(l)}$, which are modulated by the Inverse Fast Fourier Transform (IFFT) based OFDM modulators and transmitted over the SDMA MIMO channel seen in Figure 11.1. At the BS illustrated at the lower half of Figure 11.2, the received signal constituted by the noise-contaminated superposition of all users' transmitted signals is OFDM-demodulated at the P number of receiver antenna elements and forwarded to the iterative GA-JCEMUD for joint channel estimation and symbol detection, as we will detail in Section 11.4. Then the detected soft bits $\hat{\mathbf{b}}_s^{(l)}$ are generated, which are forwarded to the L independent FEC decoders for channel decoding.

11.4 GA-Aided Iterative Joint Channel Estimation and Multi-User Detection

In this section, we will elaborate on the philosophy of the proposed iterative GA-JCEMUD, which is illustrated in Figure 11.3. We assume that each OFDM symbol consists of K sub-

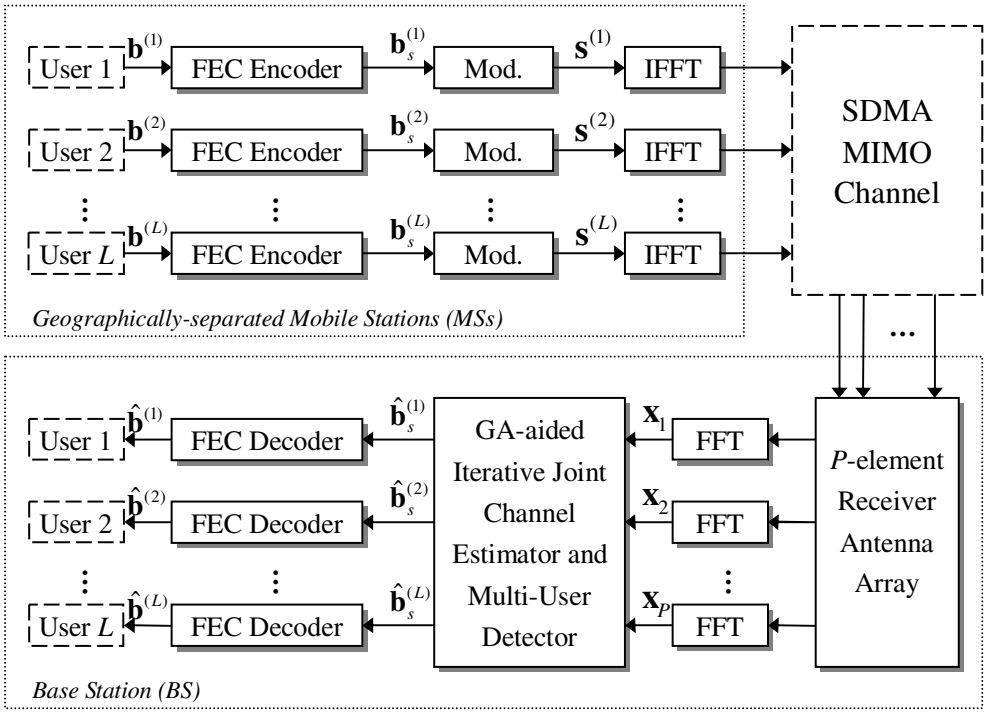


Figure 11.2: Schematic of the SDMA-OFDM uplink system employing the proposed GA-aided iterative joint channel estimator and multi-user detector.

carriers. All subcarriers of the first transmitted OFDM symbol of all the L users carry known pilot QAM symbols. Within the first OFDM symbol duration ($n = 0$), the BS pilot controller seen in the middle of Figure 11.3 feeds the pilots to the GA-JCEMUD printed in grey, which simultaneously processes the received signals $x_p[0,k]$ $(p = 1, \cdots, P;\ k = 1, \cdots, K)$ at the P receiver antenna elements. In order to simplify the analysis, we now focus our attention on the p^{th} receiver. Based on the pilots and the corresponding received signals, the initial estimates of the FD-CHTFs $\tilde{H}_p^{(l)}[0,k]$ $(l = 1, \cdots, L;\ k = 1, \cdots, K)$ can be generated, which will be subject to time-domain filtering invoked at the p^{th} receiver, as plotted at the top of Figure 11.3.

The time-domain filtering is invoked for each of the L users on an OFDM symbol basis. More specifically, for the l^{th} user, the K initial FD-CHTF estimates $\tilde{H}_p^{(l)}[n,k]$ $(k = 1, \cdots, K)$ associated with the current, i.e. the n^{th} OFDM symbol are processed by a K-length IFFT, resulting in the set of K uncorrelated CIR-related taps $\tilde{h}_p^{(l)}[n,k]$. Then, only the first K_0 CIR tap coefficients are retained with the rest set to zero. The value of K_0 depends on the delay profile of the channel, which is not known *a priori* at the receiver. However, in many application scenarios it is possible to appropriately over-estimate K_0 on the basis of previous field experiments [377]. Hence, in our system the value of K_0 is set to a sufficiently large number so that it sufficiently exceeds the actual maximum delay spread of the chan-

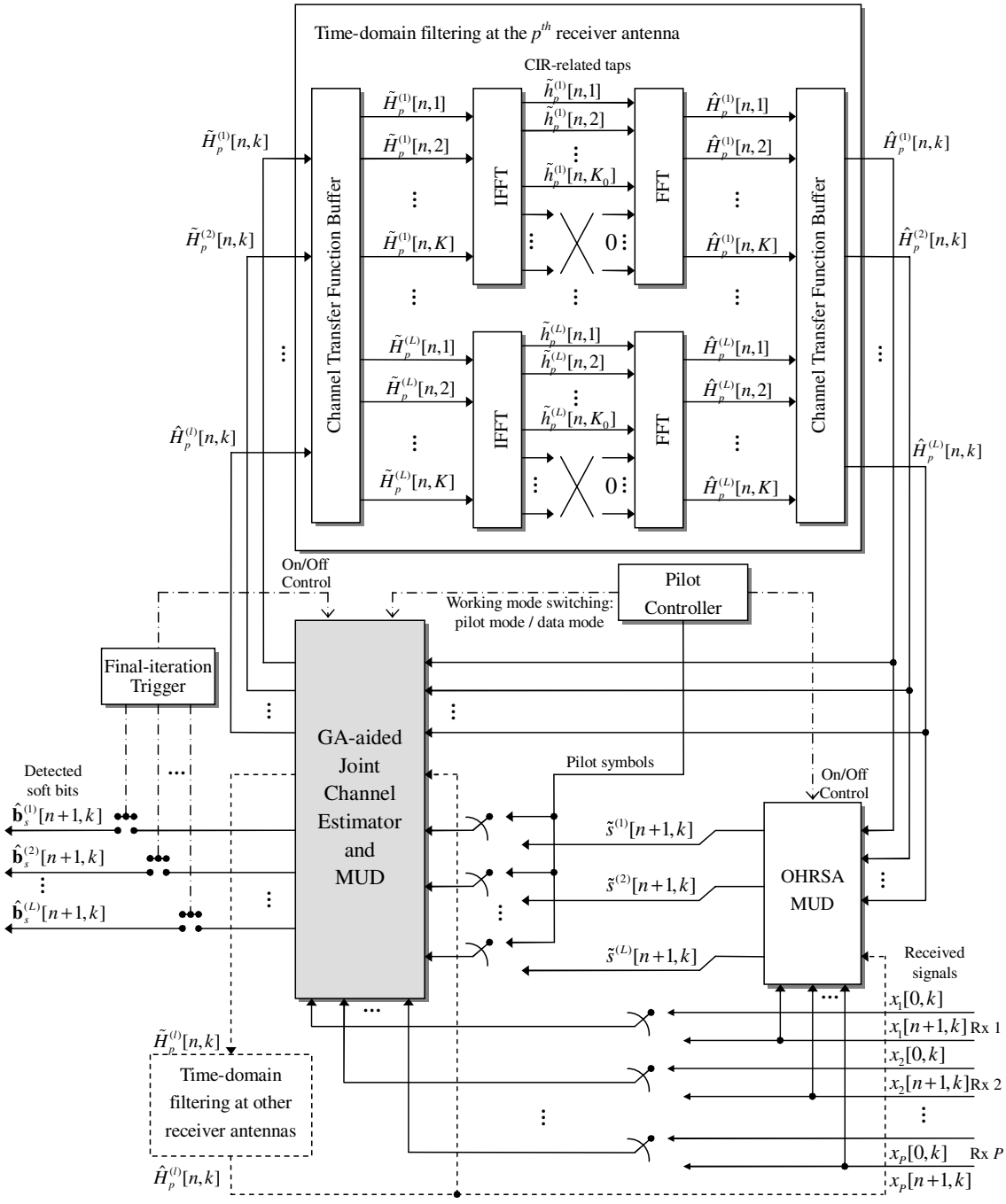


Figure 11.3: Structure of the proposed GA-aided iterative joint channel estimator and multi-user detector.

nel. Nonetheless, we point out that the 'significant-tap catching' approaches of [118, 382] can be employed for improving the channel estimator's performance by further removing the low-power taps within the range of $[1, \cdots, K_0]$ according to a pre-defined threshold. The retained CIR-related coefficients $\tilde{h}_p^{(l)}[n,k]$ $(k = 1, \cdots, K_0)$ are then converted to the improved *a posteriori* FD-CHTF estimates $\hat{H}_p^{(l)}[n,k]$ $(k = 1, \cdots, K)$ by the Fast Fourier Transform (FFT). For more detailed discussions on these processes we refer to Chapters 15 and 16 of [90].

If in the $(n+1)^{th}$ OFDM symbol duration a data symbol rather than a pilot symbol was transmitted, the pilot controller will carry out the following actions:

- Enable a first-stage MUD for generating reference symbol estimates, and
- Switch the operating mode of the GA-JCEMUD from *pilot-aided channel estimation* mode to *joint channel estimation and data detection* mode.

More specifically, the Optimised Hierarchy Reduced Search Algorithm (OHRSA) aided MUD of [403, 404] is employed as the first-stage MUD, as shown in Figure 11.3. It exploits the *a posteriori* FD-CHTF estimates $\hat{H}_p^{(l)}[n,k]$ associated with the previous OFDM symbol to invoke subcarrier-by-subcarrier based detection, yielding an initial guess of the L users' transmitted symbols $s^{(l)}[n+1,k]$ $(l = 1, \cdots, L;\ k = 1, \cdots, K)$. The resultant symbol estimates $\tilde{s}^{(l)}[n+1,k]$, the FD-CHTF estimates $\hat{H}_p^{(l)}[n,k]$ as well as the corresponding received signals $x_p[n+1,k]$ $(p = 1, \cdots, P;\ k = 1, \cdots, K)$ are then forwarded to the GA-JCEMUD, where the FD-CHTFs and data symbols associated with the $(n+1)^{th}$ OFDM symbol are jointly optimised on a subcarrier-by-subcarrier basis. The GA-optimised FD-CHTF estimates $\tilde{H}_p^{(l)}[n+1,k]$ are then forwarded to the time-domain filters for further enhancement, as mentioned earlier in this section. Now the cleansed *a posteriori* channel estimates $\hat{H}_p^{(l)}[n+1,k]$ are expected to be closer to their true values of $H_p^{(l)}[n+1,k]$ than the initially used estimates, i.e. $\hat{H}_p^{(l)}[n,k]$, which are associated with the previous OFDM symbol. Thus, based on the improved channel estimates, the OHRSA MUD is capable of providing a better initial guess of the transmitted symbols for the GA-JCEMUD. This decision-directed process can be invoked for a number of iterations for attaining a further performance enhancement. After the final iteration, the final-iteration trigger portrayed on the left-hand side of Figure 11.3 terminates the GA-JCEMUD's operation and enables the output links, generating the L users' detected soft bits $\hat{b}_s^{(l)}[n+1,k]$ $(l = 1, \cdots, L;\ k = 1, \cdots, K)$ corresponding to the $(n+1)^{th}$ OFDM symbol.

In the following sections, we will further detail the processes of obtaining initial FD-CHTF estimates with the aid of pilots, generating initial symbol estimates by the OHRSA MUD as well as jointly optimising the FD-CHTFs and the data symbols using the GA, respectively.

11.4.1 Pilot-Aided Initial Channel Estimation

In order to obtain an initial estimate of the FD-CHTFs, each user's pilot OFDM symbol is multiplied by a user-specific spreading code before it is transmitted.[2] With the aid of the

[2]Note that no spreading is applied to the data OFDM symbols.

spread pilot OFDM symbols, an initial FD-CHTF estimate is attainable at the receivers, where the Multi-User Interference (MUI) is effectively reduced proportionately to the spreading factor.

More specifically, the orthogonal Walsh-Hadamard-Transform (WHT) [90] based codes of length L are chosen. The received symbol at the p^{th} receiver antenna element associated with the k^{th} subcarrier of the $n = 0^{th}$ OFDM symbol duration can be formulated as:

$$x_p[0,k] \;=\; \mathbf{c}\bar{\mathbf{H}}_p[0,k]\mathbf{s}[0,k] + n_p[0,k], \quad p = 1, \cdots, P, \tag{11.7}$$

where the pilot signal vector $\mathbf{s}[0,k]$ and the diagonal FD-CHTF matrix $\bar{\mathbf{H}}_p[0,k]$ are given by:

$$\mathbf{s}[0,k] \;=\; \Big[\, s^{(1)}[0,k],\; s^{(2)}[0,k],\; \cdots,\; s^{(L)}[0,k] \,\Big]^T, \tag{11.8}$$

$$\bar{\mathbf{H}}_p[0,k] \;=\; \mathrm{diag}\Big[\, H_p^{(1)}[0,k],\; H_p^{(2)}[0,k],\; \cdots,\; H_p^{(L)}[0,k] \,\Big], \tag{11.9}$$

respectively, and the user signature vector $\mathbf{c}$ is formulated as:

$$\mathbf{c} \;=\; [\, \mathbf{c}^{(1)},\; \mathbf{c}^{(2)},\; \cdots,\; \mathbf{c}^{(L)} \,], \tag{11.10}$$

where $\mathbf{c}^{(l)}$ $(l = 1, \cdots, L)$ represents the l^{th} user's WHT code sequence, which is the l^{th} row of the L-order recursive WHT matrix given by [90]:

$$\mathbf{U}_{\mathrm{WHT}_L} \;=\; \frac{1}{\sqrt{2}} \begin{bmatrix} 1 \cdot \mathbf{U}_{\mathrm{WHT}_{L/2}} & 1 \cdot \mathbf{U}_{\mathrm{WHT}_{L/2}} \\ 1 \cdot \mathbf{U}_{\mathrm{WHT}_{L/2}} & -1 \cdot \mathbf{U}_{\mathrm{WHT}_{L/2}} \end{bmatrix}, \tag{11.11}$$

while the lowest-order WHT unitary matrix is defined as:

$$\mathbf{U}_{\mathrm{WHT}_2} \;=\; \frac{1}{\sqrt{2}} \begin{bmatrix} 1 & 1 \\ 1 & -1 \end{bmatrix}. \tag{11.12}$$

Note that the pilot symbol vector $\mathbf{s}[0,k]$ of Equation 11.7 is known at the receivers. Furthermore, we can use the same unspread pilot QAM symbol for all users, i.e. $s^{(l)}[0,k] = s_0$ $(l = 1, \cdots, L)$. Hence, it directly follows from Equation 11.7 that:

$$\begin{aligned} \check{x}_p[0,k] \;&=\; \frac{s_0^*}{|s_0|^2} x_p[0,k] \\ &=\; \mathbf{c}\mathbf{H}_p^T[0,k] + \frac{s_0^*}{|s_0|^2} n_p[0,k], \quad p = 1, \cdots, P, \end{aligned} \tag{11.13}$$

where $(\cdot)^*$ denotes complex conjugate and $\mathbf{H}_p[0,k]$ is the p^{th} row of the FD-CHTF matrix $\mathbf{H}$, given by:

$$\mathbf{H}_p[0,k] \;=\; \Big[\, H_p^{(1)}[0,k],\; H_p^{(2)}[0,k],\; \cdots,\; H_p^{(L)}[0,k] \,\Big]. \tag{11.14}$$

Thus, the initial FD-CHTF estimates can be obtained as follows:

$$\begin{aligned}\tilde{\mathbf{H}}_p^T[0,k] &= \mathbf{c}^T \breve{x}_p[0,k] \\ &= \mathbf{H}_p^T[0,k] + \underbrace{\frac{s_0^*}{|s_0|^2} n_p[0,k]\mathbf{c}^T}_{n'_p[0,k]}, \quad p = 1, \cdots, P. \end{aligned} \tag{11.15}$$

After the time-domain CIR tap filtering operation shown in Figure 11.3, the refined channel estimates can then be used to assist the OHRSA MUD for detecting the unknown transmitted symbols within the next OFDM symbol duration. Afterwards, the GA-JCEMUD will be set to joint channel estimation and data detection mode, providing the FD-CHTF estimates associated with the forthcoming OFDM symbols.

Depending on the specific performance-versus-throughput design tradeoff targeted, this process of generating initial channel estimates can be invoked at pre-defined time intervals. Here we denote the pilot overhead as ϵ, which is defined by the ratio of the number of pilot OFDM symbols to the total number of transmitted OFDM symbols. We will show in Section 11.5 that a good performance is achievable by the proposed scheme with a small value of ϵ.

11.4.2 Generating Initial Symbol Estimates

As mentioned earlier, for each subcarrier, an initial symbol estimate is first obtained with the aid of the first-stage Optimised Hierarchy Reduced Search Algorithm (OHRSA) assisted MUD [403, 404] shown in Figure 11.3, which exploits the *a posteriori* FD-CHTF estimates generated within the previous OFDM symbol duration. For the sake of notational convenience, in this section the index of $[n, k]$ is omitted. However, we note that the following analysis is conducted on a subcarrier basis.

As an extension of the Complex Sphere Decoder (CSD) method [176, 367], the OHRSA MUD is capable of achieving a near-optimum performance at a significantly reduced computational complexity. It is well known that the optimum ML MUD [90] employs an exhaustive search for finding the most likely transmitted signals. More explicitly, the L-user symbol vector estimate $\hat{\mathbf{s}}_{\text{ML}}$ can be obtained by minimising the following metric:

$$\hat{\mathbf{s}}_{\text{ML}} = \arg\left\{ \min_{\check{\mathbf{s}} \in \mathcal{M}^L} ||\mathbf{x} - \mathbf{H}\check{\mathbf{s}}||^2 \right\}, \tag{11.16}$$

where $\check{\mathbf{s}}$ is an *a priori* candidate vector of the set $\mathcal{M}^L$, which is constituted by 2^{mL} number of trial-vectors, where m denotes the number of Bits Per Symbol (BPS). More specifically, $\mathcal{M}^L$ is formulated as:

$$\mathcal{M}^L = \left\{ \check{\mathbf{s}} = (\check{s}^{(1)}, \check{s}^{(2)}, \cdots, \check{s}^{(L)})^T \middle| \check{s}^{(1)}, \check{s}^{(2)}, \cdots, \check{s}^{(L)} \in \mathcal{M}_c \right\}, \tag{11.17}$$

where $\mathcal{M}_c$ denotes the set containing the 2^m number of legitimate complex constellation points associated with the specific modulation scheme employed. Furthermore, it can be

shown that Equation 11.16 is equivalent to [403, 404]:

$$\hat{\mathbf{s}} = \arg\left\{ \min_{\check{\mathbf{s}} \in \mathcal{M}^L} ||\mathbf{V}(\check{\mathbf{s}} - \hat{\mathbf{s}}_{\text{MMSE}})||^2 \right\}, \tag{11.18}$$

where $\mathbf{V}$ is an upper-triangular matrix having positive real-valued elements on the main diagonal and satisfying

$$\mathbf{V}^H\mathbf{V} = \mathbf{H}^H\mathbf{H} + \sigma_n^2\mathbf{I}, \tag{11.19}$$

while

$$\hat{\mathbf{s}}_{\text{MMSE}} = (\mathbf{H}^H\mathbf{H} + \sigma_n^2\mathbf{I})^{-1}\mathbf{H}^H\mathbf{x} \tag{11.20}$$

is the unconstrained MMSE-based estimate[3] of the transmitted signal vector $\mathbf{s}$, with $\mathbf{I}$ and σ_n^2 are the identity matrix and the AWGN noise variance, respectively. The superscript of $(\cdot)^H$ denotes the Hermitian transpose. Since $\mathbf{V}$ is an upper-triangular matrix, a specific cost function can be derived:

$$\begin{aligned}
\Phi(\check{\mathbf{s}}) &= ||\mathbf{V}(\check{\mathbf{s}} - \hat{\mathbf{s}}_{\text{MMSE}})||^2 \\
&= (\check{\mathbf{s}} - \hat{\mathbf{s}}_{\text{MMSE}})^H\mathbf{V}^H\mathbf{V}(\check{\mathbf{s}} - \hat{\mathbf{s}}_{\text{MMSE}}) \\
&= \sum_{i=1}^{L}\Big|\sum_{j=i}^{L} v_{ij}(\check{s}^{(j)} - \hat{s}_{\text{MMSE}}^{(j)})\Big|^2 \\
&= \sum_{i=1}^{L}\phi_i(\check{\mathbf{s}}_i),
\end{aligned} \tag{11.21}$$

where $\phi(\check{\mathbf{s}}_i)$ is a set of sub-cost functions. Note that the outputs of both $\Phi(\check{\mathbf{s}})$ and $\phi(\check{\mathbf{s}}_i)$ are real-valued. Furthermore, we have:

$$\begin{aligned}
\phi_i(\check{\mathbf{s}}_i) &= \Big|\sum_{j=i}^{L} v_{ij}(\check{s}^{(j)} - \hat{s}_{\text{MMSE}}^{(j)})\Big|^2 \\
&= \Big|v_{ii}(\check{s}^{(i)} - \hat{s}_{\text{MMSE}}^{(i)}) + \sum_{j=i+1}^{L} v_{ij}(\check{s}^{(j)} - \hat{s}_{\text{MMSE}}^{(j)})\Big|^2.
\end{aligned} \tag{11.22}$$

Based on Equation 11.22, $\Phi(\check{\mathbf{s}})$ can be re-defined as the Cumulative Sub-Cost (CSC) function:

$$\Phi_L(\check{\mathbf{s}}_L) = \phi_L(\check{\mathbf{s}}_L) = \Big|v_{LL}(\check{s}^{(L)} - \hat{s}_{\text{MMSE}}^{(L)})\Big|^2, \quad i = L; \tag{11.23a}$$

$$\Phi_i(\check{\mathbf{s}}_i) = \Phi_{i+1}(\check{\mathbf{s}}_{i+1}) + \phi_i(\check{\mathbf{s}}_i), \quad i = L-1, \cdots, 1, \tag{11.23b}$$

where $\check{\mathbf{s}}_i$ represents the sub-vectors of $\check{\mathbf{s}}$, formulated as:

$$\check{\mathbf{s}}_i = \left[\ \check{s}^{(i)},\ \check{s}^{(i+1)},\ \cdots,\ \check{s}^{(L)}\ \right], \quad i \in \{1, \cdots, L\}. \tag{11.24}$$

[3]The unconstrained MMSE-based estimate denotes the resultant complex value calculated from Equation 11.20, as opposed to the constrained estimate, which is the hard-decoded version of the unconstrained estimate.

In physically tangible terms, the Euclidean norm of Equation 11.23 can be interpreted as a weighted Euclidean distance between the candidate constellation point $\check{s}^{(l)}$ and the unconstrained MMSE estimate $\hat{s}^{(l)}_{\text{MMSE}}$ of the transmitted signal component $s^{(l)}_{\text{MMSE}}$. Explicitly, the CSC functions obey the property:

$$\Phi(\check{\mathbf{s}}) = \Phi_1(\check{\mathbf{s}}_1) > \Phi_2(\check{\mathbf{s}}_2) > \cdots > \Phi_L(\check{\mathbf{s}}_L) > 0 \tag{11.25}$$

for all possible combinations of $\check{\mathbf{s}} \in \mathcal{M}^L$ and $\hat{\mathbf{s}}_{\text{MMSE}} \in \mathbb{C}^L$, where the L-dimensional complex space $\mathbb{C}^L$ contains all possible unconstrained MMSE estimates $\hat{\mathbf{s}}_{\text{MMSE}}$ of the transmitted signal vector $\mathbf{s}$.

Exploiting the monotonously increasing nature of the non-binary, i.e. multi-bit symbol-based CSC functions of Equation 11.25, a bit-based recursive search algorithm can be developed [403, 404], where the $(L_b = mL)$-dimensional bit vectors $\check{\mathbf{b}}$ constituting the L users' bits, rather than the symbol vectors $\check{\mathbf{s}}$ are used as the candidates for the CSC functions given by Equations 11.21 and 11.23. More specifically, two legitimate hypotheses of -1 and 1 are stipulated at each recursive step i of the search algorithm, concerning one of the bits of the bit-based trial vector $\check{\mathbf{b}}_i$. This allows us now to physically interpret the CSC functions as the Euclidian distance contribution of the specific $\check{\mathbf{b}}_i$, when considering a specific bit of a given symbol of a given user. The recursive search process commences with the evaluation of the CSC function of Equation 11.23a, followed by the calculation of the conditioned CSC function values of Equation 11.23b. Moreover, for each tentatively assumed value of $\check{\mathbf{b}}_i$ a successive recursive search step $(i-1)$ is invoked, which is conditioned on the hypotheses made in all preceding recursive steps $j = i, \cdots, L_b = mL$. Upon each arrival at the index $i = 1$ of the recursive process, a complete bit-based candidate vector $\check{\mathbf{b}}$ associated with a certain symbol vector $\check{\mathbf{s}}$ is hypothesised and the corresponding value of the cost function $\Phi(\check{\mathbf{b}})$ formulated in Equation 11.21 is evaluated. Furthermore, with the aid of a carefully-designed search strategy [403, 404], the OHRSA is capable of arriving at the optimum ML estimate at a significantly reduced complexity. For more details on the OHRSA MUD, the interested reader is referred to [403, 404].

11.4.3 GA-Aided Joint FD-CHTF and Data Optimisation Providing Soft Outputs

With the aid of the initial FD-CHTF estimates of Section 11.4.1 and the initial symbol estimates of Section 11.4.2, the proposed GA-JCEMUD printed in the grey block of Figure 11.3 is employed for jointly optimising the estimates of the FD-CHTFs and multi-user data symbols.

11.4.3.1 Extended GA Individual Structure for MIMO Systems

In comparison to the pure GA-based MUDs [399–401, 405], which optimise the multi-user data symbols only, the joint optimisation work requires the FD-CHTFs to be simultaneously optimised along with the data symbols, as in [323, 395]. Furthermore, concerning the MIMO

channel's structure, the GA *individuals*' representation of [323, 395] is extended to:

$$\begin{cases} \tilde{\mathbf{s}}_{(y,x)}[n,k] &= \left[\tilde{s}^{(1)}_{(y,x)}[n,k],\ \tilde{s}^{(2)}_{(y,x)}[n,k],\ \cdots,\ \tilde{s}^{(L)}_{(y,x)}[n,k] \right] \\ \tilde{\mathbf{H}}_{(y,x)}[n,k] &= \begin{bmatrix} \tilde{H}^{(1)}_{1,(y,x)}[n,k] & \tilde{H}^{(2)}_{1,(y,x)}[n,k] & \cdots & \tilde{H}^{(L)}_{1,(y,x)}[n,k] \\ \tilde{H}^{(1)}_{,(y,x)2}[n,k] & \tilde{H}^{(2)}_{2,(y,x)}[n,k] & \cdots & \tilde{H}^{(L)}_{2,(y,x)}[n,k] \\ \vdots & \vdots & \ddots & \vdots \\ \tilde{H}^{(1)}_{P,(y,x)}[n,k] & \tilde{H}^{(2)}_{P,(y,x)}[n,k] & \cdots & \tilde{H}^{(L)}_{P,(y,x)}[n,k] \end{bmatrix} \end{cases} \quad (11.26)$$

in the context of the k^{th} subcarrier of the n^{th} OFDM symbol, where the subscript (y,x) denotes the x^{th} $(x = 1, \cdots, X)$ individual at the y^{th} $(y = 1, \cdots, Y)$ *generation*. In compliance with classic GA terminology, any combination of a symbol vector $\tilde{\mathbf{s}}_{(y,x)}[n,k]$ and a FD-CHTF matrix $\tilde{\mathbf{H}}_{(y,x)}[n,k]$ represents a GA individual, where $\tilde{\mathbf{s}}_{(y,x)}[n,k]$ is referred to as the individual's *symbol chromosome* and $\tilde{\mathbf{H}}_{(y,x)}[n,k]$ as the associated *FD-CHTF chromosome*, respectively, while each element of a chromosome is termed as a *gene*. Note that the symbol genes and the channel genes belong to different sets. More specifically, we have $\tilde{s}^{(l)}_{(y,x)}[n,k] \in \mathcal{M}_c$ and $\tilde{H}^{(l)}_{p,(y,x)}[n,k] \in \mathbb{C}$,[4] respectively. This particular association of a pair of hypothesised channel and data estimates is reminiscent of the so-called Per-Survivor-Processing (PSP) based blind detection techniques of [406, 407], however, it distinguished itself by invoking a genetically guided efficient search strategy.

11.4.3.2 Initialisation

During the stage of initialisation, the GA generates a *population* of X individuals represented by Equation 11.26, based on the initial FD-CHTF estimates of Section 11.4.1 and the initial symbol estimates of Section 11.4.2. More explicitly, at the k^{th} subcarrier in the $(n+1)^{th}$ OFDM symbol duration, the genes of the $(y,x) = (1,1)^{st}$ individual are generated as:

$$\begin{cases} \tilde{s}^{(l)}_{(1,1)}[n+1,k] &= \tilde{s}^{(l)}[n+1,k] \\ \tilde{H}^{(l)}_{p,(1,1)}[n+1,k] &= \tilde{H}^{(l)}_{p}[n,k] \end{cases}, \quad l = 1, \cdots, L;\ p = 1, \cdots, P, \quad (11.27)$$

where $\tilde{s}^{(l)}[n+1,k]$ represents the initial symbol estimates provided by the OHRSA MUD, while $\tilde{H}^{(l)}_{p}[n,k]$ denotes the initial FD-CHTF estimates associated with the previous, i.e. the n^{th} OFDM symbol. The other $X-1$ individuals are then created by the GA's *mutation* operator:

$$\begin{cases} \tilde{s}^{(l)}_{(y,x)}[n+1,k] &= \text{MUTATION}\left[\tilde{s}^{(l)}_{(1,1)}[n+1,k] \right] \\ \tilde{H}^{(l)}_{p,(y,x)}[n+1,k] &= \text{MUTATION}\left[\tilde{H}^{(l)}_{p,(1,1)}[n+1,k] \right] \end{cases}, \\ x = 2, \cdots, X;\ y = 1, \cdots, Y;\ l = 1, \cdots, L;\ p = 1, \cdots, P. \quad (11.28)$$

The details of the mutation process are discussed in Section 11.4.3.3.2. After the creation of the $y = 1^{st}$ generation, which consists of the population of the initially generated X

[4] $\mathbb{C}$ denotes the set of all complex numbers.

individuals, the GA-based search process can be invoked for jointly optimising the estimates of the multi-user symbols and FD-CHTFs.

11.4.3.3 Joint Genetic Optimisation

The basic idea of the GA-based optimisation is to find the optimum or a near-optimum solution according to a pre-defined *objective function (OF)*. In the context of the joint detection problem in SDMA-OFDM systems, the GA's OF can be based on the ML metric of Equation 11.16, formulated as:

$$\Omega\left(\tilde{\mathbf{H}}[n,k],\ \tilde{\mathbf{s}}[n,k]\right) = \left|\left|\ \mathbf{x}[n,k] - \tilde{\mathbf{H}}[n,k]\cdot\tilde{\mathbf{s}}[n,k]\ \right|\right|^2, \tag{11.29}$$

where each combination of the trial data vector $\tilde{\mathbf{s}}[n,k]$ and trial FD-CHTF matrix $\tilde{\mathbf{H}}[n,k]$ constitutes a GA individual defined in Equation 11.26. The output of the OF is referred to as the *objective score (OS)*, and the individual having a lower OS is considered to have a higher *fitness* value. Explicitly, the GA's ultimate aim is to find the individual that has the highest fitness value. This is achieved with the aid of the genetic operators invoked during the evolution process, such as *cross-over* and *mutation* [323, 408], where specific genes of the different individuals are exchanged and mutated to produce the corresponding *offspring*. The X number of resultant offspring individuals then constitute a new population, which forms the GA's next generation and is expected to have a statistically improved average fitness value in comparison to the parent population. Finally, the GA terminates, when the generation index reaches a pre-defined value Y. Conventionally, the highest-fitness individual of the final population will be considered the GA's final solution, which consists of the genetically-improved FD-CHTF and data symbol estimates. For more details about the genetic optimisation process, we refer to [323, 395, 399–401, 405].

Recall that the elements of the symbol chromosome $\tilde{\mathbf{s}}[n,k]$ of an individual belong to $\mathcal{M}_c$, i.e. to the legitimate constellation symbol set. Thus, the symbol mutation space is discrete and is limited by the 2^m number of constellation points in $\mathcal{M}_c$. By contrast, the mutation space of the FD-CHTFs is continuous and infinite, simply because the value of a FD-CHTF sample can be an arbitrary value on the complex plane $\mathbb{C}$. Therefore, different cross-over/mutation operators have to be employed for the symbol chromosome and channel chromosome, respectively.

11.4.3.3.1 Cross-Over Operator In our system, the Uniform Cross-over [323, 409] is used for mutating the symbol chromosomes. As discussed in [323, 409], the uniform cross-over exchanges specific symbol genes of two parent individuals in order to generate the offspring. Theoretically, this cross-over method may also be applied to the FD-CHTF mutation process, where the channel chromosomes of parent individuals are swapped. However, this "exchange-only" mechanism neglects the continuous nature of the complex-valued FD-CHTFs, thus imposing a limitation during the cross-over process, when the genetic information is delivered from parents to offspring.

For the sake of improving the cross-over efficiency, the Blend Cross-over [410, 411] is invoked for combining the channel chromosomes from each of the two parent individuals into new channel chromosomes of the two offspring. More specifically, the offspring's channel

chromosomes can be formulated as:

$$\begin{cases} \tilde{H}^{(l)}_{p,(y+1,1)}[n,k] &= \beta_1 \tilde{H}^{(l)}_{p,(y,1)}[n,k] + \beta_2 \tilde{H}^{(l)}_{p,(y,2)}[n,k] \\ \tilde{H}^{(l)}_{p,(y+1,2)}[n,k] &= \beta_2 \tilde{H}^{(l)}_{p,(y,1)}[n,k] + \beta_1 \tilde{H}^{(l)}_{p,(y,2)}[n,k] \end{cases}, \quad y = 1, \cdots, Y, \tag{11.30}$$

where the random weight factors $\beta_i \in [0,\ 1]$ $(i = 1, 2)$ satisfy:

$$\beta_1 + \beta_2 = 1. \tag{11.31}$$

Similar to the uniform cross-over operator invoked for symbol chromosomes, in the blend cross-over operator a random binary cross-over mask is also created for identifying the specific channel genes to be combined. Observing Equation 11.30, we note that the genes of the new channel chromosomes are actually the linearly biased/weighted results averaged between the two parents in the context of the $(P \times L)$-dimensional complex space. When we have $\beta_1 = \beta_2 = 0.5$, the result becomes an unbiased average of the channel chromosomes of the two parents. Explicitly, the blend cross-over operator exploits the continuous and infinite nature of the FD-CHTFs and hence it is capable of amalgamating the parental genetic information in a more meritorious manner.

11.4.3.3.2 Mutation Operator Similar to the cross-over operator, the mutation operator also requires the employment of different methods for the symbol and channel chromosomes, respectively. Explicitly, the mutation schemes based on discrete character sets, for example, the classic Uniform Mutation [323], can be applied to the symbol chromosomes. On the other hand, the approach of [395], which is referred to here as Step Mutation, can be employed for mutating the channel chromosomes. To elaborate a little further, the offspring's channel chromosomes can be generated by:

$$\begin{cases} \Re\left(\tilde{H}^{(l)}_{p,(y+1,x)}[n,k]\right) &= \Re\left(\tilde{H}^{(l)}_{p,(y,x)}[n,k]\right) + \theta_{\Re}\Delta^{(l)}_{p,(y,x)}[n,k] \\ \Im\left(\tilde{H}^{(l)}_{p,(y+1,x)}[n,k]\right) &= \Im\left(\tilde{H}^{(l)}_{p,(y,x)}[n,k]\right) + \theta_{\Im}\Delta^{(l)}_{p,(y,x)}[n,k] \end{cases}, \\ x = 1, \cdots, X;\ y = 1, \cdots, Y;\ l = 1, \cdots, L;\ p = 1, \cdots, P, \tag{11.32}$$

where $\Delta^{(l)}_{p,(y,x)}[n,k]$ is a random number within $(0,\ \lambda_{max}]$, while $\Re$ and $\Im$ respectively, denote the real and imaginary components of the specific channel gene $\tilde{H}^{(l)}_{p,(y+1,x)}[n,k]$ to be mutated. The sign factors $\theta_{\Re}$ and $\theta_{\Im}$ of Equation 11.32 are uniformly and randomly generated, assuming values of $+1$ or -1.

We point out that the value of the maximum mutation step size λ_{max} is critical for the system's attainable performance, since it directly affects the convergence of the GA's optimisation process. A low system performance will be expected, when λ_{max} is insufficiently high, where the GA may get trapped in local rather than global minima. However, an excessively high value of λ_{max} will result in a slow convergence rate. Hence, the value of λ_{max} should be adjusted according to the Doppler frequency encountered. More specifically, when we have a higher Doppler frequency, the consecutive channel fades in the time domain experienced by each of the subcarriers become faster, thus requiring a higher λ_{max} value for assisting the GA in capturing the rapid changes of the channel fades. In low-Doppler scenarios, the situation is inverse. Therefore, it is desirable that the value of λ_{max} is adjusted as a

function of the Doppler frequency. However, in this case it is a challenging task to develop a close-form function for quantifying the effects of the Doppler frequency, owing to the inherently nonlinear nature of the GA-based optimisation process. Nonetheless, with the aid of computer simulations we can identify the appropriate values of λ_{max} for different Doppler frequencies, as will be discussed in Section 11.5.1.

11.4.3.3.3 Comments on the Joint Optimisation Process Note that since the FD-CHTFs and data symbols are jointly optimised within the same genetic process, the individuals having better FD-CHTF estimates will have a higher probability of producing better symbol estimates and vice versa. Thus, this joint optimisation is a "self-adaptive" process with its native intuition leading towards the optimum solution. Furthermore, comparing to other techniques, for example, that of [396], where the channel estimation and symbol detection are completed by the GA and the VA separately, the proposed joint scheme is capable of reducing the associated complexity, since the channel estimation is simultaneously achieved with the aid of the same GA process, thus incurring no additional complexity.

Moreover, it is worth pointing out that at the time of writing the GA-aided detection schemes found in the literature [323, 395, 399–401, 405] are only capable of providing single-individual based hard-decoded symbol estimates, which inevitably limits the GA-aided system's attainable performance. In Section 11.4.3.4, we will introduce a method, which enables the GA to provide soft outputs based on the entire population.

11.4.3.4 Generating the GA's Soft Outputs

In this section we derive an algorithm that enables the GA to output soft information. For the sake of simplicity, again, we omit the index $[n, k]$ in this section.

The soft-bit value or Log-Likelihood Ratio (LLR) associated with the $(m_B)^{th}$ bit position of the l^{th} $(l = 1, \cdots, L)$ user's transmitted symbol $s^{(l)}$ can be formulated as [109]:

$$\mathcal{L}_{l,m_B} = \ln \frac{P(b_{l,m_B} = 1|\mathbf{x}, \mathbf{H})}{P(b_{l,m_B} = 0|\mathbf{x}, \mathbf{H})}, \tag{11.33}$$

which is the natural logarithm of the quotient of probabilities that the bit considered has a value of $b_{l,m_B} = 1$ or $b_{l,m_B} = 0$. Note that the probability $P(b_{l,m_B} = b|\mathbf{x}, \mathbf{H})$ that the symbol transmitted by the l^{th} user has the $(m_B)^{th}$ bit value of $b_{l,m_B} = b \in \{0, 1\}$, is given by the sum of all the probabilities of the symbol combinations which assume that $b_{l,m_B} = b$. Hence, Equation 11.33 can be equivalently rewritten as:

$$\mathcal{L}_{l,m_B} = \ln \frac{\sum_{\check{\mathbf{s}} \in \mathcal{M}^L_{l,m_B,1}} P(\check{\mathbf{s}}|\mathbf{x}, \mathbf{H})}{\sum_{\check{\mathbf{s}} \in \mathcal{M}^L_{l,m_B,0}} P(\check{\mathbf{s}}|\mathbf{x}, \mathbf{H})}, \tag{11.34}$$

where $\mathcal{M}^L_{l,m_B,b}$ denotes the specific subset associated with the l^{th} user, which is constituted by those specific trial vectors, whose l^{th} element's $(m_B)^{th}$ bit has a value of b, which is

expressed as:

$$\mathcal{M}_{l,m_B,b}^{L} = \left\{ \check{\mathbf{s}} = [\ \check{s}^{(1)},\ \check{s}^{(2)},\ \cdots,\ \check{s}^{(L)}\ ]^T \;\middle|\; \{\ \check{s}^{(1)},\ \check{s}^{(2)},\ \cdots,\ \check{s}^{(L)} \in \mathcal{M}_c\ \} \wedge \{\ b_{l,m_B} = b\ \} \right\}. \tag{11.35}$$

With the aid of Bayes' theorem [109], we have:

$$P(\check{\mathbf{s}}|\mathbf{x},\mathbf{H}) = P(\mathbf{x}|\check{\mathbf{s}},\mathbf{H})\frac{P(\check{\mathbf{s}})}{P(\mathbf{x})}. \tag{11.36}$$

Upon substituting Equation 11.36 into Equation 11.34, we arrive at:

$$\mathcal{L}_{l,m_B} = \ln \frac{\sum_{\check{\mathbf{s}}\in\mathcal{M}_{l,m_B,1}^{L}} P(\mathbf{x}|\check{\mathbf{s}},\mathbf{H})}{\sum_{\check{\mathbf{s}}\in\mathcal{M}_{l,m_B,0}^{L}} P(\mathbf{x}|\check{\mathbf{s}},\mathbf{H})}. \tag{11.37}$$

Note that here we have assumed that the different (2^m)-ary symbol combination vectors $\check{\mathbf{s}}$ have the same probability, namely that $P(\check{\mathbf{s}}), \check{\mathbf{s}} \in \mathcal{M}_c$ is a constant. On the other hand, it can be observed from Equation 11.1 that $\mathbf{x}$ is a random sample of the L-dimensional multi-variate complex Gaussian distribution, where the mean vector is $\mathbf{Hs}$, while the $(P \times P)$-dimensional covariance matrix $\mathbf{R_n}$ is given by:

$$\mathbf{R_n} = E\{\mathbf{n}\mathbf{n}^H\} = \sigma_n^2\mathbf{I}, \tag{11.38}$$

and the noise encountered at the P number of receiver antennas is assumed to be uncorrelated. Hence, the above-mentioned multi-variate complex Gaussian distribution can be described by [412]:

$$f(\mathbf{x}|\mathbf{s},\mathbf{H}) = \frac{1}{\pi^P|\mathbf{R_n}|}\exp\Big\{ -(\mathbf{x}-\mathbf{Hs})^H\mathbf{R_n^{-1}}(\mathbf{x}-\mathbf{Hs})\Big\}. \tag{11.39}$$

When substituting Equation 11.38 into Equation 11.39, we have:

$$f(\mathbf{x}|\mathbf{s},\mathbf{H}) = \frac{1}{\pi^P\sigma_n^2}\exp\Big\{ -\frac{1}{\sigma_n^2}||\mathbf{x}-\mathbf{Hs}||^2\Big\}. \tag{11.40}$$

Note that $f(\mathbf{x}|\mathbf{s},\mathbf{H}) = P(\mathbf{x}|\mathbf{s},\mathbf{H})$ is the *a priori* probability that the vector $\mathbf{x}$ has been received under the condition that the vector $\mathbf{s}$ was transmitted over the MIMO channel characterised by the FD-CHTF matrix $\mathbf{H}$. Thus, Equation 11.37 can be further developed with the aid of Equation 11.40, yielding:

$$\mathcal{L}_{l,m_B} = \ln \frac{\sum_{\check{\mathbf{s}}\in\mathcal{M}_{l,m_B,1}^{L}} \frac{1}{\pi^P\sigma_n^2}\exp\Big\{ -\frac{1}{\sigma_n^2}||\mathbf{x}-\mathbf{H}\check{\mathbf{s}}||^2\Big\}}{\sum_{\check{\mathbf{s}}\in\mathcal{M}_{l,m_B,0}^{L}} \frac{1}{\pi^P\sigma_n^2}\exp\Big\{ -\frac{1}{\sigma_n^2}||\mathbf{x}-\mathbf{H}\check{\mathbf{s}}||^2\Big\}}. \tag{11.41}$$

In order to avoid the exponential computation imposed by Equation 11.41, the maximum-approximation [90] can be applied, yielding:

$$\mathcal{L}_{l,m_B} \approx -\frac{1}{\sigma_n^2}\Big[||\mathbf{x}-\mathbf{H}\check{\mathbf{s}}_{l,m_B,1}||^2 - ||\mathbf{x}-\mathbf{H}\check{\mathbf{s}}_{l,m_B,0}||^2\Big], \tag{11.42}$$

where

$$\check{\mathbf{s}}_{l,m_B,b} = \arg\left\{ \min_{\check{\mathbf{s}} \in \mathcal{M}^L_{l,m_B,b}} \left[||\mathbf{x} - \mathbf{H}\check{\mathbf{s}}||^2 \right] \right\}, \quad b = 0, 1. \tag{11.43}$$

Furthermore, concerning the fact that the true FD-CHTF matrix $\mathbf{H}$ is unknown and using Equation 11.29, Equation 11.42 can be represented as:

$$\mathcal{L}_{l,m_B} \approx -\frac{1}{\sigma_n^2}\left[\overline{\Omega}_{l,m_B,1} - \overline{\Omega}_{l,m_B,0}\right], \tag{11.44}$$

where

$$\overline{\Omega}_{l,m_B,b} = \min\left[\ \Omega\left(\tilde{\mathbf{H}},\ \check{\mathbf{s}}_{l,m_B,b}\right),\ \omega\ \right], \quad b = 0, 1, \tag{11.45}$$

and $\omega = P \cdot L$ is a normalisation factor. Equation 11.44 suggests that the LLRs can be obtained by evaluating the GA's OF. More explicitly, in order to calculate the LLR of the $(m_B)^{th}$ bit of the l^{th} $(l = 1, \cdots, L)$ user at the specific subcarrier considered, the X number of individuals in the GA's final generation are divided into two groups, where the first (or second) group is constituted by those individuals that have a value of one (or zero) at the $(m_B)^{th}$ bit of the l^{th} user's estimated transmitted symbol. The resultant lowest OS calculated in each of the two groups is then compared to ω, and the smaller of the two will be used in Equation 11.44 for calculating the corresponding LLR, which can therefore assist the channel decoder in improving the SDMA-OFDM system's performance.

It is worth pointing out that the proposed GA generating the above-mentioned population-based soft outputs only imposes a modest complexity increase in comparison to the conventional hard-decision aided individual-based GAs [323,395,399–401,405]. This is because the only additional operation required by the proposed scheme is to compare ω to the OSs, which are already available, since the results of the OF evaluation carried out by the conventional GAs can be readily used.

11.5 Simulation Results

In this section, we will quantify the performance of the MIMO SDMA-OFDM system using the proposed GA-aided iterative joint channel estimation and multi-user detection technique. Due to space limitations, we only show the results achieved by the proposed scheme in the over-loaded scenario, although we point out that it performs equally well in the scenarios, where the number of users L is less than or equal to the number of receiver antenna elements P.

More specifically, an over-loaded scenario where $L = 4$ users were supported by $P = 2$ receiver antenna elements was considered. As an example, a simple two-path Rayleigh fading channel model was employed, where the associated delay profile was $(0.7740 \cdot z^0 + 0.6332 \cdot z^{-1})$. The value of the parameter K_0 was set to $8 \gg 2$, which is potentially capable of tolerating an increase of the actual dispersion up to eight CIR taps. Each of the paths experienced independent Rayleigh fading having the same Doppler frequency of $F_D = f_d T_s$ normalized to the OFDM symbol rate, where f_d and T_s are the maximum Doppler frequency and the OFDM symbol duration including the cyclic prefix, respectively. The channel was assumed to be OFDM symbol-invariant, implying that the CIR taps were assumed to be

constant for the duration of one OFDM symbol, but they were faded at the beginning of each symbol. Furthermore, the fading envelope of the $(P \times L)$ number of user-receiver channel links were assumed to be uncorrelated. Each user's associated transmit power or signal variance was assumed to be unity.

Both scenarios with and without FEC coding were investigated. In the FEC-coded scenario, as an example, a half-rate binary Low Density Parity Check (LDPC) [413, 414] code was employed. However, other FEC codes, for example, Turbo Convolutional (TC) [216, 415, 416] codes are also applicable to the proposed system. For the reader's convenience, the simulation parameters are summarised in Table 11.1. For more details on the GA's configuration, the interested reader is referred to Section 11.4.3.3 and [323, 405, 417].

11.5.1 Effects of the Maximum Mutation Step Size

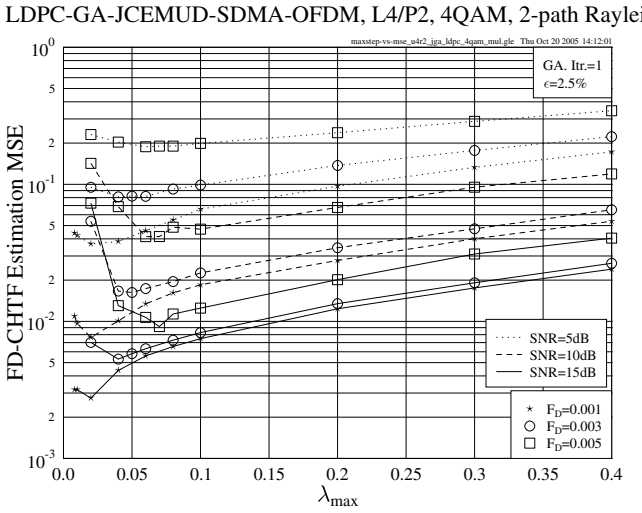


Figure 11.4: FD-CHTF estimation MSE versus λ_{max} performance of the LDPC-coded iterative GA-JCEMUD assisted SDMA-OFDM system in the over-loaded scenario, where $L = 4$ users were supported with the aid of $P = 2$ receiver antenna elements, while assuming different values of the OFDM symbol normalized Doppler frequency F_D. The basic simulation parameters are given in Table 11.1.

As a preliminary investigation, in this section we attempt to identify the appropriate choices of the maximum mutation step size λ_{max} in conjunction with different Doppler frequencies. Firstly, we characterise the average FD-CHTF estimation Mean Square Error (MSE) performance of the GA-JCEMUD/SDMA-OFDM system using various values of λ_{max}, as shown in Figure 11.4, where the GA-JCEMUD invoked a single iteration and used a pilot overhead of $\epsilon = 2.5\%$. The average FD-CHTF estimation MSE is defined by:

$$\overline{\text{MSE}} = \frac{1}{N_T} \sum_{n=1}^{N_T} \overline{\text{MSE}}[n], \tag{11.46}$$

LDPC parameters	Modem		4QAM
	Code rate		0.5
	Column weight		2.5
	Maximum iterations		10
	Block length of input bits		640 bits
GA-JCEMUD parameters	Symbol initialisation		OHRSA [403, 404]
	Mating pool creation strategy		Pareto-Optimality [359]
	Selection method		Fitness-Proportionate
	Cross-over scheme	FD-CHTF	Blend cross-over
		Symbol	Uniform cross-over
	Mutation scheme	FD-CHTF	Step mutation [323, 395]
		Symbol	Uniform mutation
	Mutation probability	FD-CHTF	0.20
		Symbol	0.15
	Maximum mutation step size λ_{max}		Varied (dependent on F_D)
	Elitism percentage		10%
	Incest prevention		Enabled
	Population size X		160
	Generations Y		5
	GA's output		Population-based
	Iterations		1 (unless specified)
	Pilot overhead ϵ		2.5% (unless specified)
Channel parameters	Paths		2
	Delay profile		$0.7740 \cdot z^0 + 0.6332 \cdot z^{-1}$
	K_0		8
	Subcarriers K		64
	Cyclic prefix		8
	F_D		0.003 (unless specified)

Table 11.1: Basic simulation parameters used in Section 11.5.

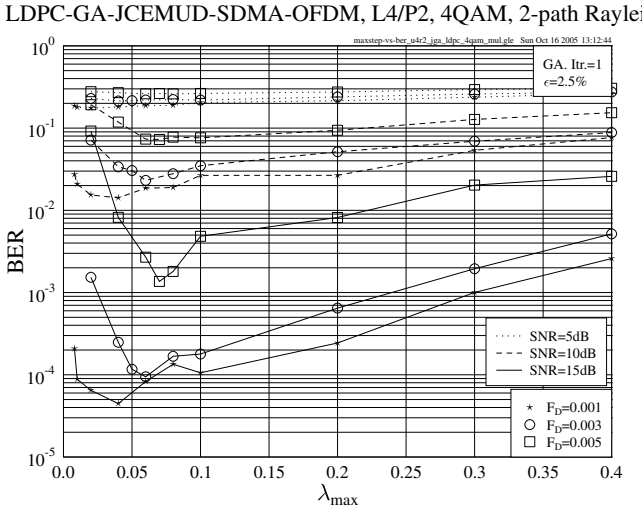


Figure 11.5: BER versus λ_{max} performance of the LDPC-coded iterative GA-JCEMUD assisted SDMA-OFDM system in the over-loaded scenario, where $L = 4$ users were supported with the aid of $P = 2$ receiver antenna elements, while assuming different values of the OFDM symbol normalized Doppler frequency F_D. The basic simulation parameters are given in Table 11.1.

where N_T is the total number of OFDM symbols transmitted, while $\overline{\text{MSE}}[n]$ is the average FD-CHTF estimation MSE associated with the n^{th} OFDM symbol, given by:

$$\overline{\text{MSE}}[n] = \frac{1}{PLK} \sum_{p=1}^{P} \sum_{l=1}^{L} \sum_{k=1}^{K} \left| \hat{H}_p^{(l)}[n,k] - H_p^{(l)}[n,k] \right|^2. \tag{11.47}$$

Here we point out that the FD-CHTF estimation MSE performance of the GA-JCEMUD is the same both with and without employing FEC coding. This is because the GA-aided joint optimisation process has no direct interaction with the outer FEC code and thus it becomes independent of the codec. Explicitly, we can see in Figure 11.4 that the choice of λ_{max} has a substantial effect on the system's FD-CHTF estimation MSE performance, regardless of both F_D as well as of Signal-to-Noise Ratio (SNR).

In Figure 11.5, the Bit Error Ratio (BER) versus λ_{max} performance of the LDPC-coded GA-JCEMUD aided SDMA-OFDM system is portrayed. It can be found that in scenarios associated with a higher SNR the effect of λ_{max} becomes more significant in terms of the achievable BER performance. The reason for this phenomenon is that at low SNRs the BER performance of the system is mainly dominated by the noise signal, while at high SNRs by the choice of λ_{max}, provided that the Doppler frequency is the same. Furthermore, a higher F_D value typically requires a higher λ_{max} for attaining the best achievable BER performance, as discussed in Section 11.4.3.3.2. According to Figure 11.5, the recommended values of λ_{max}

in terms of achieving the best possible BER performance[5] are 0.4, 0.6 and 0.7 in conjunction with F_D values of 0.001, 0.003 and 0.005, respectively. These values of λ_{max} corresponding to the specific F_D values encountered were used for generating all the simulation results to be discussed in the rest of the chapter.

11.5.2 Effects of the Doppler Frequency

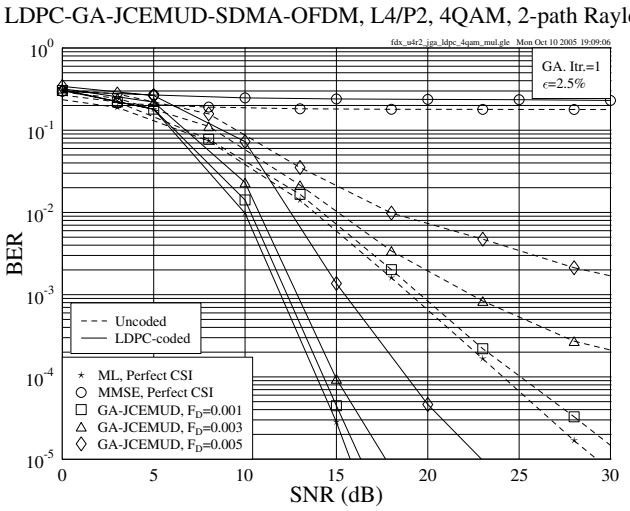


Figure 11.6: BER versus SNR performances of the uncoded and LDPC-coded iterative GA-JCEMUD assisted SDMA-OFDM systems in the over-loaded scenario, where $L = 4$ users were supported with the aid of $P = 2$ receiver antenna elements, while assuming different values of the OFDM symbol normalized Doppler frequency F_D. The basic simulation parameters are given in Table 11.1.

In Figure 11.6 we compare the BER versus SNR performance of both the uncoded and LDPC-coded GA-JCEMUD/SDMA-OFDM systems in conjunction with different values of F_D. The performances of the systems employing the linear MMSE MUD or the optimum ML MUD are also provided as references, both assuming perfect Channel State Information (CSI). A pilot overhead of $\epsilon = 2.5\%$ was assumed and the GA-JCEMUD used a single iteration. As shown in Figure 11.6, unsurprisingly, the performances of both the uncoded and coded GA-JCEMUD aided systems degraded, when F_D was increased, since a higher Doppler frequency implies that the channel fades more rapidly, which renders channel estimation more challenging. This is especially true for MIMO systems, even more so for over-loaded MIMO systems, as discussed in Section 11.1. Nonetheless, with only a 2.5% pilot overhead, the proposed GA-JCEMUD/SDMA-OFDM system was capable of achieving

[5]Note that the best choice of λ_{max} for achieving the best BER performance may be similar to, but may not necessarily be the best choice for attaining the best FD-CHTF estimation MSE performance. This effect can be observed from Figures 11.4 and 11.5.

a performance close to the perfect-CSI aided optimum ML MUD at $F_D = 0.001$. By contrast, the system employing the MMSE MUD completely failed even with the aid of perfect CSI, owing to the insufficient degree of detection freedom experienced in over-loaded scenarios. Furthermore, compared to the uncoded scenario, the performance degradation of the LDPC-coded GA-JCEMUD incurred by higher Doppler frequencies was much less dramatic, as observed in Figure 11.6.

11.5.3 Effects of the Number of GA-JCEMUD Iterations

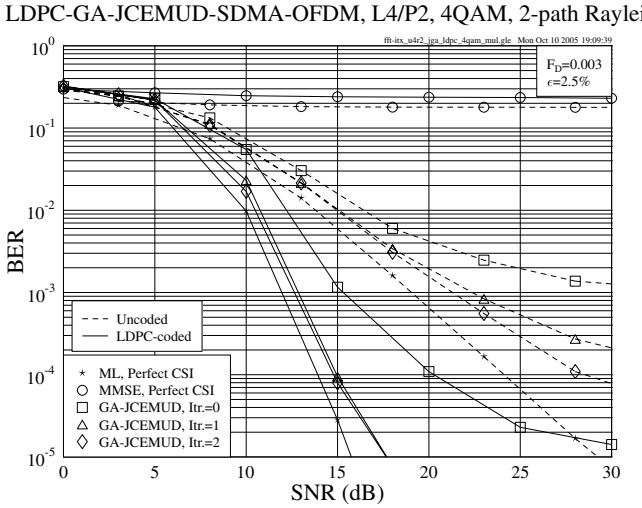


Figure 11.7: BER versus SNR performances of the uncoded and LDPC-coded iterative GA-JCEMUD assisted SDMA-OFDM systems in the over-loaded scenario, where $L = 4$ users were supported with the aid of $P = 2$ receiver antenna elements, while invoking different numbers of GA-JCEMUD iterations. The basic simulation parameters are given in Table 11.1.

Figure 11.7 shows the achievable performance of the proposed system invoking different numbers of GA-JCEMUD iterations. It was assumed that we had $\epsilon = 2.5\%$ and $F_D = 0.003$. As seen in Figure 11.7, a significant iteration gain was achieved, when the GA-JCEMUD invoked additional iterations. Furthermore, the performance of the uncoded system consistently improved as the number of iterations was increased, while in the LDPC-coded system most of the gain was attained by the first GA-JCEMUD iteration. In Figure 11.8, the average FD-CHTF estimation MSE performance of the GA-JCEMUD/SDMA-OFDM system and the performance of the reference system employing $\epsilon = 100\%$ pilot overhead are compared. Observe from Figure 11.8 that, as expected, the FD-CHTF estimation MSE performance was improved, when the number of GA-JCEMUD iterations was increased. Moreover, when the SNR exceeded about 13dB, the GA-JCEMUD using $\epsilon = 2.5\%$ pilot overhead approached the best-case FD-CHTF estimation MSE performance associated with $\epsilon = 100\%$.

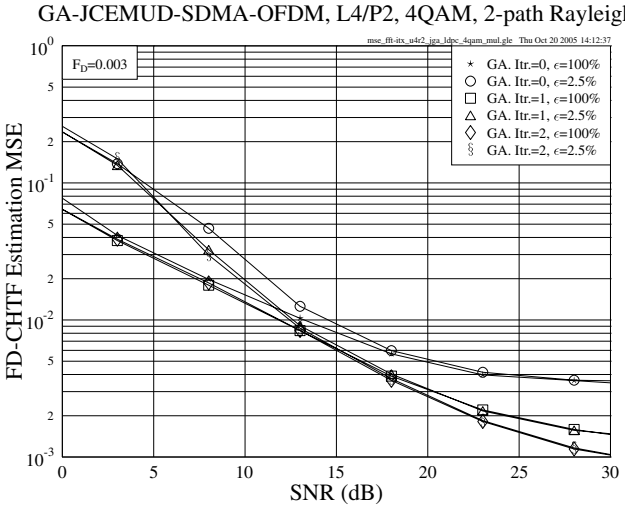


Figure 11.8: FD-CHTF estimation MSE versus SNR performance of the iterative GA-JCEMUD assisted SDMA-OFDM system in the over-loaded scenario, where $L = 4$ users were supported with the aid of $P = 2$ receiver antenna elements, while invoking different numbers of iterations. The basic simulation parameters are given in Table 11.1.

11.5.4 Effects of the Pilot Overhead

In Figure 11.9 the BER performance of the proposed system using different pilot overheads is investigated. In most cases, the GA-JCEMUD was capable of achieving a good performance using a pilot overhead as low as $\epsilon = 1.5 \sim 2.5\%$. Furthermore, the increase of pilot OFDM symbol overhead brings about more substantial benefits at the higher Doppler frequencies than at the lower ones, especially in the scenarios associated with higher SNRs, where an increasing fraction of the residual detection errors was inflicted by the inaccurate channel estimation.

11.5.5 Joint Optimisation versus Separate Optimisation

In order to further characterise the advantages of the proposed GA-aided joint optimisation scheme, in Figure 11.10 we compare the performances of the GA-JCEMUD and its counterpart, referred to as the GA-based channel estimator assisted OHRSA MUD (GACE-OHRSA-MUD), where the OHRSA MUD is serially concatenated with the stand-alone GA-aided channel estimator. More specifically, in the GACE-OHRSA-MUD, channel estimation and symbol detection are separately accomplished by the GA-aided channel estimator and the OHRSA MUD, respectively. In other words, the symbol estimates offered by the OHRSA MUD are fixed during the GA-aided optimisation process of the FD-CHTF estimates. Explicitly, in this case the effect of error propagation due to inaccurate symbol and/or channel estimates will become more severe, thus resulting in a dramatic BER performance degradation in comparison to the proposed joint optimisation scheme, as evidenced in Figure 11.10.

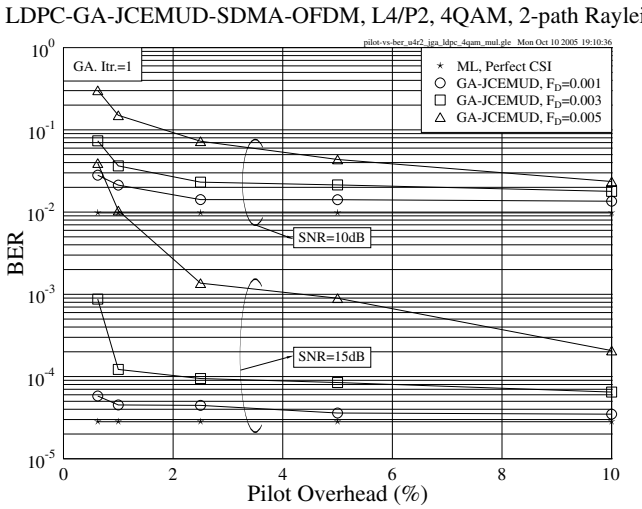


Figure 11.9: BER versus pilot overhead performance of the LDPC-coded iterative GA-JCEMUD assisted SDMA-OFDM system in the over-loaded scenario, where $L = 4$ users were supported with the aid of $P = 2$ receiver antenna elements, while assuming different values of the OFDM symbol normalized Doppler frequency F_D. The basic simulation parameters are given in Table 11.1.

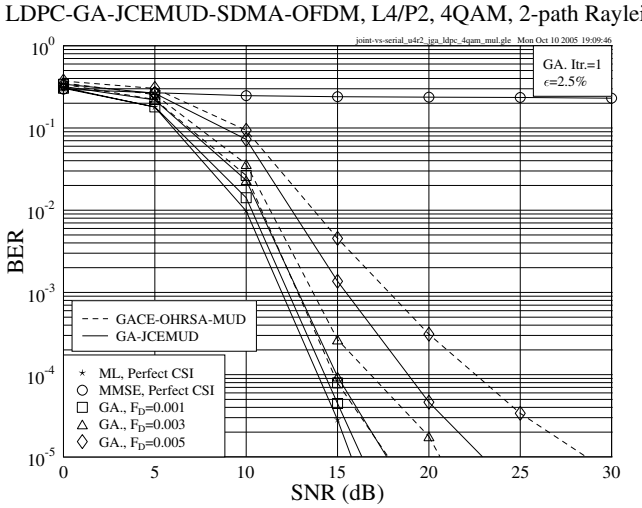


Figure 11.10: Performance comparison of the LDPC-coded SDMA-OFDM system using either the iterative GA-JCEMUD or the GACE-OHRSA-MUD in the over-loaded scenario, where $L = 4$ users were supported with the aid of $P = 2$ receiver antenna elements, while assuming different values of the OFDM symbol normalized Doppler frequency F_D. The basic simulation parameters are given in Table 11.1.

Furthermore, the superiority of the GA-JCEMUD becomes even more conspicuous in high-Doppler scenarios.

11.5.6 Comparison of GA-JCEMUDs Having Soft and Hard Outputs

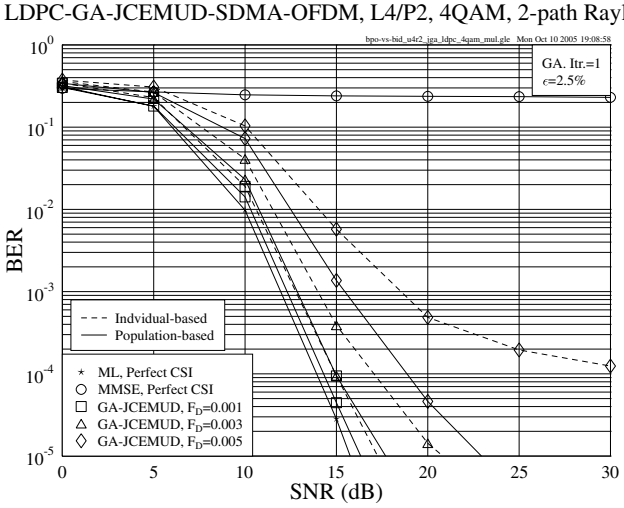


Figure 11.11: Performance comparison of the LDPC-coded SDMA-OFDM system using either the conventional individual-based or the proposed population-based GA-JCEMUD in the over-loaded scenario, where $L = 4$ users were supported with the aid of $P = 2$ receiver antenna elements, while assuming different values of the OFDM symbol normalized Doppler frequency F_D. The basic simulation parameters are given in Table 11.1.

In this section, we present the performance comparison of the GA-JCEMUD providing either the conventional individual-based hard outputs [323,395,399–401,405] or the proposed population-based soft outputs, as shown in Figure 11.11. As expected, with the advent of FEC codes, the proposed soft GA is capable of significantly outperforming the conventional arrangement, especially when the channel fades more rapidly. This result implies that the proposed GA exhibited a higher robustness against fast fading channels than the conventional GAs [323, 395, 399–401, 405].

11.5.7 MIMO Robustness

As a further investigation, a visual comparison of the true and estimated FD-CHTFs is portrayed in Figure 11.12. More specifically, the L users' FD-CHTFs associated with a specific receiver antenna element during a block of 40 consecutive OFDM symbols are plotted at a SNR value of 20dB. Each dot of the curves plotted in Figure 11.12 represents a complex-valued FD-CHTF at a specific subcarrier. By observing the perfect channel-knowledge based illustration at the top of Figure 11.12, we can see that the FD-CHTF at each subcarrier evolves

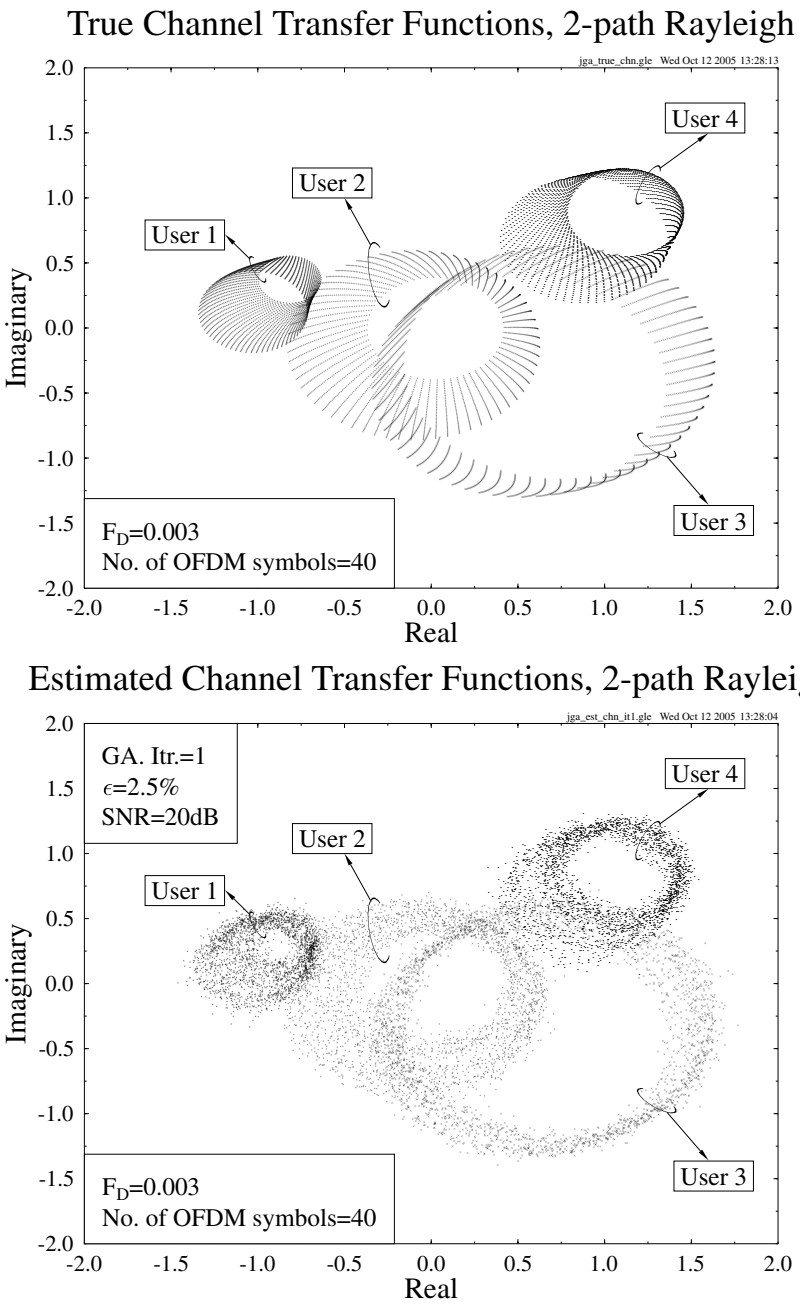


Figure 11.12: Channel estimation performance of the iterative GA-JCEMUD assisted SDMA-OFDM system in the over-loaded scenario, where $L = 4$ users were supported with the aid of $P = 2$ receiver antenna elements. The estimated FD-CHTFs $\hat{H}_1^{(l)}[n,k]$ $(l = 1,\cdots,L;\ k = 1,\cdots,K)$ associated with $n = 1,\cdots,40$ consecutive OFDM symbols at the $p = 1^{st}$ receiver antenna are plotted at a SNR value of 20dB, and compared with the true FD-CHTFs. The basic simulation parameters are given in Table 11.1.

over the duration of the 40 OFDM symbols, where the thickness of the ring-shaped formations indicates the amount of FD-CHTF change during this time interval. The full perimeter of the ring is constituted by the $K = 64$ spoke-like formations corresponding to the 64 OFDM subcarriers. Explicitly, the radii of the FD-CHTF rings associated with the four user-receiver channel links are significantly different. This is because each individual link is subject to independent fading, and although the Doppler frequency encountered at the four links is identical, their short-term envelope fluctuation observed over the 40 OFDM symbol durations is different. However, by comparing the subfigures at the top and bottom of Figure 11.12, we can see that the FD-CHTF estimates closely match their true values, resulting in a similar FD-CHTF contour for each of the four channel links. This implies that the proposed GA-JCEMUD is capable of *simultaneously* capturing the fading envelope changes of *each* individual user-receiver link, regardless of the near-instantaneous fading fluctuations encountered. Since an equally good performance was attained over all the user-receiver links, this demonstrates the global robustness of the proposed approach in MIMO scenarios.

11.6 Chapter Summary and Conclusion

From the investigations and discussions conducted in the previous sections, we conclude that the proposed GA-aided iterative joint channel estimation and multi-user detection scheme generating soft outputs constitutes an effective solution to the channel estimation problem in multi-user MIMO SDMA-OFDM systems. Furthermore, the GA-JCEMUD is capable of exhibiting a robust performance in over-loaded scenarios, where the number of users is higher than the number of receiver antenna elements, either with or without FEC coding. This attractive property enables the SDMA-OFDM system to potentially support an increased number of users. Our future research will consider the design of similar downlink systems.

Chapter 12

Multi-User OFDM Employing Genetic Algorithm Aided Minimum Bit Error Rate Multi-User Detection[1]

M. Y. Alias, S. Chen and L. Hanzo

12.1 Introduction

In an effort to increase the achievable system capacity of an OFDM system, antenna arrays can be employed for supporting multiple users in a Space Division Multiple Access (SDMA) communications scenario [29, 90]. A variety of linear multi-user detectors (MUD) have been proposed for performing the separation of OFDM users based on their unique, user-specific, spatial signature, provided that their channel impulse response (CIR) was accurately estimated [29, 90]. The most popular SDMA-receiver design strategy is constituted by the minimum mean-squared-error (MMSE) MUD, which was mentioned in Chapters 10 and 11 and was more extensively characterised in Chapter 12 of [90] along with numerous other MUDs.

However, as recognised in [418–420] in a CDMA context, a better strategy is to choose the linear detector's coefficients so as to directly minimise the error-probability or bit-error ratio (BER), rather than the mean-squared error (MSE). This is because minimising the MSE does not necessarily guarantee that the BER of the system is also minimised. The family of detectors that directly minimises the BER is referred to as the minimum bit-error rate (MBER) detector class [418–421]. The MBER criterion has been successfully applied in the linear equalisation of binary signalling [419], for decision feedback equalisation (DFE) [422] and in linear MIMO receivers [421]. It has also been shown that the MBER detector can be

[1] M. Y. Alias, S. Chen and L. Hanzo "Multiple-Antenna-Aided OFDM Employing Genetic-Algorithm-Assisted Minimum Bit Error Rate Multiuser Detection Vehicular Technology," *IEEE Transactions on Vehicular Technology*, Volume 54, Issue 5, pp. 1713–1721, September 2005.

© 2006 John Wiley & Sons, Ltd

effectively used for linear multi-user detection in CDMA systems [418, 420].

12.1.1 Minimum Bit Error Ratio Detection of OFDM

As discussed in the previous subsection, a variety of linear multi-user detectors have been proposed in the literature for performing the SDMA-based separation of OFDM users upon exploiting their unique, user-specific, spatial signature, provided that their channel impulse response was accurately estimated [90]. The most popular design strategy is constituted by the MMSE MUD mentioned amongst other now classic solutions listed in Table 1.5. By contrast, the range of recent contributions on the more unorthodox design of various MBER detectors is summarised in Table 12.1.

In a CDMA system, each user is separated by a unique user-specific spreading code. However, given a certain bandwidth, the effective data rate is determined by the ratio of the chip-rate and the spreading factor. As opposed to a CDMA system, an SDMA system differentiates each user by the associated unique, user-specific CIR encountered at the receiver antenna. Therefore each user will be able to transmit in a multi-user environment without reducing the data rate by the spreading factor (SF). Hence, the combination of SDMA and OFDM is attractive, especially for high-rate transmission. In a rather simplistic, but conceptually appealing interpretation one could argue that the unique user-specific CIR plays the role of a user-specific CDMA signature, without reducing the data rate according to the Spreading Factor (SF) of a hypothetical CDMA system. In this analogy the CIR-signatures are not orthogonal to each other, but this is not a serious impediment, because even orthogonal spreading codes become non-orthogonal upon convolution by the CIR. However, owing to the non-orthogonal nature of the CIRs an efficient multi-user receiver is required for separating the users.

In [440] we have provided a formula for the exact MBER MUD weight calculation of an uplink SDMA OFDM system. We have also shown that the MBER MUD may significantly outperform the MMSE MUD in terms of the achievable BER in a two-user OFDM scenario. *The novelty of this chapter is that we propose a new Genetic Algorithm (GA) assisted MBER MUD-aided OFDM system*, as a design alternative to the simplified conjugate gradient (CG) algorithm of [440]. Our complexity comparisons show that the GA-based MBER MUD is capable of achieving the MBER performance at a lower number of objective function evaluations than the CG MBER MUD. We will also show that unlike the MMSE MUD, the MBER MUD has the capability of supporting more users than the number of receivers at the base-station.

The outline of the chapter is as follows. Section 12.2 describes our system model, while Section 12.3 proposes a new GA-aided SDMA MUD. Section 12.4 characterises the achievable performance, while Section 12.5 quantifies the attainable complexity reduction. Finally, Section 12.6 offers our conclusions.

12.2 System Model

12.2.1 Space Division Multiple Access

Figure 12.1 portrays the antenna array-aided uplink transmission scenario considered. In this figure, each of the L simultaneous users is equipped with a single transmission antenna, while

Year	Author	Contribution
'66	Aaron and Tufts [423]	A paper relating intersymbol interference and error probability.
'74	Shamash and Yao [424]	Structure and performance of a linear decision feedback equaliser (DFE) based on the minimum error probability criterion.
'82	Galko and Pasupathy [425]	Linear receivers for binary digital signals.
'96	Chen, Chng, Mulgrew and Gibson [426]	Minimum-BER linear-combiner DFE
'97	Yeh and Barry [427]	Approximate minimum bit-error rate equalisation for binary signalling.
	Mandayam and Aazhang [428]	A non-adaptive MBER linear multi-user detector based on gradient optimisation for narrow-band Gaussian CDMA channels which do not introduce ISI.
'98	Yeh and Barry [429]	Approximate minimum bit-error rate equalisation for pulse-amplitude and quadrature amplitude modulation.
	Yeh, Lopes and Barry [430]	Approximate minimum bit-error rate multi-user detection.
	Chen, Mulgrew, Chng and Gibson [431]	Space translation properties and the minimum-BER linear combiner DFE.
'99	Chen and Mulgrew [432]	The minimum-SER linear-combiner decision feedback equaliser.
	Psaromiligkos, Batalama and Pados [433]	Adaptive minimum probability of error linear filter receivers for DS-CDMA channels.
'00	Yeh and Barry [419]	Adaptive minimum bit error rate equalisation for binary signalling.
	Mulgrew and Chen [434]	Stochastic gradient MBER DFEs.
	Wang, Lu and Antoniou [435]	Another type of MBER MUD called constrained MBER MUD.
'01	Chen, Samingan, Mulgrew and Hanzo [420, 436]	Adaptive minimum BER linear multi-user detection for DS-CDMA signals in multipath fading channels.
	Mulgrew and Chen [422]	Adaptive MBER DFEs for binary signalling
	Samingan, Chen and Hanzo [437]	Adaptive MBER linear MUD for CDMA signals in multipath channels with 4-QAM constellation.
'03	Chen, Mulgrew and Hanzo [438]	Least bit-error rate adaptive nonlinear equalisers for binary signalling.
	de Lamare and Sampaio-Neto [418]	Adaptive MBER decision feedback multi-user receivers in frequency selective fading channels.
	Chen, Hanzo and Ahmad [439]	Adaptive MBER beamforming assisted receiver for wireless communications.

Table 12.1: Contributions on MBER receivers

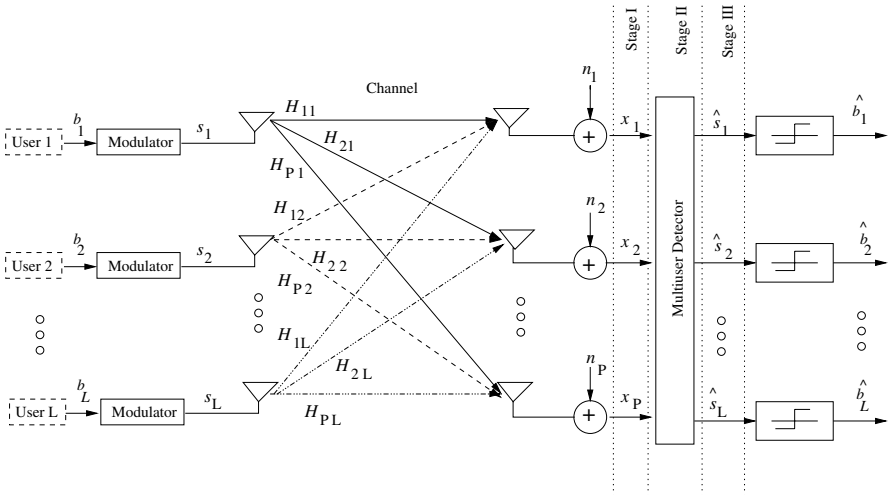


Figure 12.1: Schematic of an antenna array aided OFDM uplink scenario, where each of the L users is equipped with a single transmit antenna and the BS's receiver is assisted by a P-element antenna front-end

the base-station's receiver capitalises on a P-element antenna front-end. The set of complex signals, $x_p[n,k], p \in 1,\ldots,P$ received by the P-element antenna array in the k-th subcarrier of the n-th OFDM symbol is constituted by the superposition of the independently faded signals associated with the L users sharing the same space-frequency resource, as argued in Chapters 10 and 11, as well as in Chapter 12 of [90]. The received signal was corrupted by the Gaussian noise at the array elements. The indices $[n,k]$ have been omitted for notational convenience during our forthcoming discourse, yielding [90]:

$$\mathbf{x} \;=\; \mathbf{Hs} + \mathbf{n} \;=\; \bar{\mathbf{x}} + \mathbf{n}, \tag{12.1}$$

where $\mathbf{x}$ is the $(P \times 1)$-dimensional vector of the received signals, $\mathbf{s}$ is the $(L \times 1)$-dimensional vector of transmitted signals, $\mathbf{n}$ is the $(P \times 1)$-dimensional noise vector and $\bar{\mathbf{x}}$ represents the noiseless component of $\mathbf{x}$. The complex data signal, s_l, transmitted by the l-th user, $l \in 1,\ldots,L$ and the AWGN noise process, n_p, at any antenna array element p, $p \in 1,\ldots,P$ are assumed to exhibit a zero mean and a variance of σ_l^2 and $2\sigma_n^2$ for the data signal and AWGN noise process, respectively.

The frequency domain channel transfer function (FDCHTF) matrix $\mathbf{H}$ of dimension $P \times L$ is constituted by the set of channel transfer function vectors of the L users, each of which describes the FDCHTF between the single transmitter antenna associated with a particular user l and the reception array elements $p \in 1,\ldots,P$. The FDCHTFs, H_{pl} of the different array elements $p \in 1,\ldots,P$ for users $l \in 1,\ldots,L$ are independent, stationary, and complex Gaussian distributed processes with zero-mean and unit variance. The users are assumed to be at a sufficiently high distance from each other, namely at a distance of more than a typical spacing of 10λ [441], so that the transmitted signals of the different antennas experience independent fading, when they reach the receiver. By contrast, in the scenario, where the users

are in each other's proximity, methods such as beamforming [442] exploiting the difference in the angle of arrival amongst the users may be applied for differentiating the users.

The estimate $\hat{\mathbf{s}}$ of the transmitted signal vector $\mathbf{s}$ of the L simultaneous users is generated by the MUD upon linearly combining the signals received by the P different antenna elements at the BS with the aid of the array weight matrix $\mathbf{W}$, resulting in:

$$\hat{\mathbf{s}} = \mathbf{W}^H \mathbf{x}. \tag{12.2}$$

By substituting $\mathbf{x}$ from Equation 12.1 into Equation 12.2 and considering the l-th user's associated vector component, we will arrive at:

$$\begin{aligned} \hat{s}_l &= \mathbf{w}_l^H \mathbf{x} = \mathbf{w}_l^H \mathbf{H}\mathbf{s} + \mathbf{w}_l^H \mathbf{n} \\ &= \bar{s}_l + \mathbf{w}_l^H \mathbf{n}, \end{aligned} \tag{12.3}$$

where the weight vector $\mathbf{w}_l$ is the l-th column of the weight matrix $\mathbf{W}$. At the current state-of-the-art, the most popular MUD strategy is the MMSE design, where $\mathbf{w}_l$ is chosen as the unique vector minimising the MSE expressed as MSE $= E[|\hat{s}_l - s_l|^2]$, namely as [90]:

$$\mathbf{w}_{l(MMSE)} = (\mathbf{H}\mathbf{H}^H + 2\sigma_n^2 \mathbf{I})^{-1} \mathbf{H}_l, \tag{12.4}$$

where $\mathbf{H}_l$ is the l-th column of the FDCHTF matrix $\mathbf{H}$.

12.2.2 Error Probability of a BPSK System

In this chapter, the term BER and probability of error P_E are used interchangeably. In a BPSK system we have $b_l \in \{+1, -1\}$. Then the BER encountered at the output of the SDMA MUD characterised by the combiner weight vector $\mathbf{w}_l$ of user l may be expressed as [420]:

$$\begin{aligned} P(\mathbf{w}_l) &= Pr[\text{sgn}(b_l) \cdot \Re\{\bar{s}_l(\mathbf{w}_l)\} < 0], \\ &= Pr[z_l < 0], \end{aligned} \tag{12.5}$$

where z_l is the signed decision variable given by:

$$z_l = \text{sgn}(b_l) \cdot \Re\{\bar{s}_l(\mathbf{w}_l)\}, \tag{12.6}$$

while as before, b_l represents the transmitted bit of user l, $\bar{s}_l$ is the noiseless signal at the output of the MUD related to the l-th user and $\Re\{x\}$ is the real part of the complex-valued x.

The Probability Density Function (PDF) of the decision variable z_l is constituted by a mixture of the Gaussian distributions associated with each possible combination of the transmitted data symbols of all users. Under the assumption that all the noise-free signal states are equiprobable, the PDF of z_l is given by [420]:

$$p_{z_l}(z_l; \mathbf{w}_l) = \frac{1}{N_b \sqrt{2\pi}\sigma_n \sqrt{\mathbf{w}_l^H \mathbf{w}_l}} \sum_{j=1}^{N_b} e^{\left(-\frac{(z_l - \text{sgn}(b_l^{(j)})\bar{s}_l^{(j)})^2}{2\sigma_n^2 \mathbf{w}_l^H \mathbf{w}_l} \right)}, \tag{12.7}$$

where N_b is the number of equiprobable combinations of the binary vectors of the L users, i.e.

we have $N_b = 2^L$. Furthermore, $\bar{s}_l^{(j)},\ j \in 1, \ldots, N_b$, denotes the real part of the noiseless signal at the output of the MUD related to the l-th user, while $b_l^{(j)},\ j \in 1, \ldots, N_b$, is the transmitted bit of user l.

The erroneous decision events are associated with the area under the PDF curve in the interval $(-\infty, 0)$, which is quantified as:

$$P_E(\mathbf{w}_l) = \int_{-\infty}^{0} p_{z_l}(z_l; \mathbf{w}_l) dz_l. \tag{12.8}$$

Upon using the integration by substitution technique and introducing the shorthand of

$$y_j = \frac{(z_l - \text{sgn}(b_l^{(j)})\bar{s}_l^{(j)})}{\sigma_n \sqrt{\mathbf{w}_l^H \mathbf{w}_l}}, \tag{12.9}$$

the probability of error in Equation 12.8 becomes:

$$\begin{aligned} P_E(\mathbf{w}_l) &= \frac{1}{N_b\sqrt{2\pi}} \sum_{j=1}^{N_b} \int_{-\infty}^{c_j(\mathbf{w}_l)} \exp\left(-\frac{(y_j)^2}{2}\right) dy_j \\ &= \frac{1}{N_b} \sum_{j=1}^{N_b} Q[c_j(\mathbf{w}_l)], \end{aligned} \tag{12.10}$$

where $c_j(\mathbf{w}_l)$ is given by:

$$c_j(\mathbf{w}_l) = \frac{\text{sgn}(b_l^{(j)}) \cdot \bar{s}_l^{(j)}}{\sigma_n \sqrt{\mathbf{w}_l^H \mathbf{w}}} = \frac{\text{sgn}(b_l^{(j)}) \cdot \Re\{\mathbf{w}_l^H \bar{\mathbf{x}}_j\}}{\sigma_n \sqrt{\mathbf{w}_l^H \mathbf{w}}}, \tag{12.11}$$

and $\bar{\mathbf{x}}_j,\ j \in 1, \ldots, N_b$ constitutes a possible value of $\bar{\mathbf{x}}$ defined in the context of Equation 12.1.

12.2.3 Exact MBER Multi-User Detection

In our initial discourse we assumed the explicit knowledge of the FDCHTF matrix **H** defined in Equation 12.1. However, in practice **H** has to be determined on the basis of the channel-impaired noisy value of **x** and hence a number of adaptive techniques have been proposed in references [419,420] to this effect. The FDCHTF can also be estimated using various channel estimation methods as outlined in great detail in [90], which will hence not be investigated in this chapter. The MBER solution is defined as [420]:

$$\mathbf{w}_{l(MBER)} = \arg\min_{\mathbf{w}_l} P_E(\mathbf{w}_l). \tag{12.12}$$

However, the complex, irregular shape of the BER cost function, for example as shown in Figure 12.2, prevents us from deriving a closed-form solution for the MBER MUD weights. Therefore, in practice, an iterative strategy based on the steepest-descent gradient method may be used for finding the MBER solution [420]. According to this method, the linear

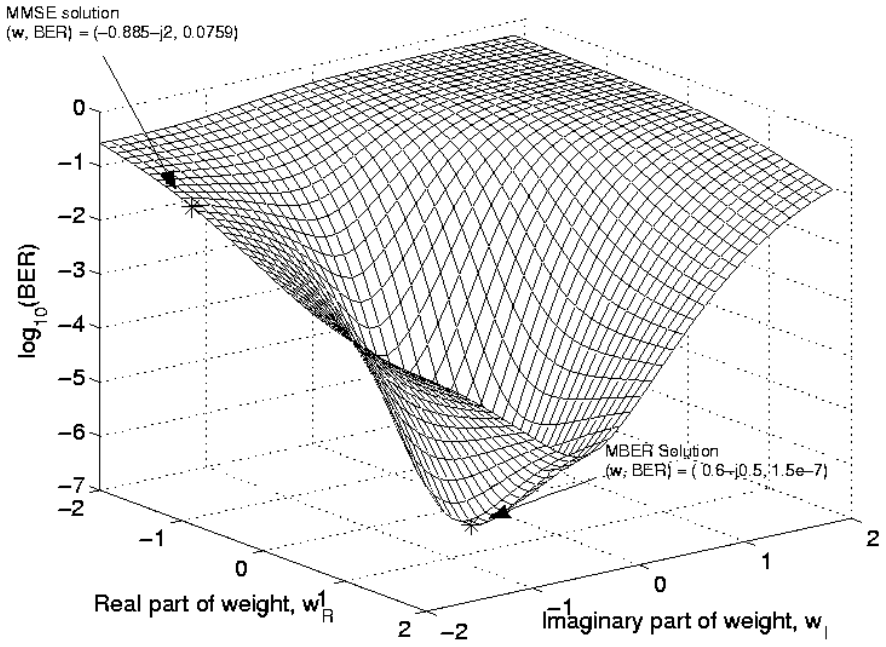


Figure 12.2: An example of the BER cost function surface for subcarrier 62 in the P=2, L=2 OFDM SDMA system employing 128-subcarrier in the symbol-invariant dispersive Gaussian channel given in Table 12.2 at SNR $=$ 10 dB

SDMA MUD's weight vector $\mathbf{w}_l$ is iteratively updated, commencing, for example, from the MMSE weights, until the specific SDMA MUD weight vector that exhibits the lowest BER is arrived at. In each step, the weight vector is updated according to a specific step-size, μ, in the vectorial direction in which the BER cost function decreases most rapidly, namely in the direction opposite to the gradient of the BER cost function, which is given by:

$$\nabla_{\mathbf{w}_l} P_E(\mathbf{w}_l) = \frac{1}{N_b\sqrt{2\pi}\sigma_n}\left(\frac{\mathbf{w}_l\mathbf{w}_l^H - \mathbf{w}_l^H\mathbf{w}_l\mathbf{I}}{(\mathbf{w}_l^H\mathbf{w}_l)^{\frac{3}{2}}}\right) \cdot \sum_{j=1}^{N_b} e^{\left(-\frac{(\bar{s}_l^{(j)})^2}{2\sigma_n^2\mathbf{w}_l^H\mathbf{w}_l}\right)} \cdot \mathrm{sgn}(b_l^{(j)}) \cdot \bar{\mathbf{x}}_j, \quad (12.13)$$

where $\bar{s}_l^{(j)} = \Re\{\mathbf{w}_l^H\bar{\mathbf{x}}_j\}$.

The BER is independent of the magnitude of the MUD's weight vector [440], and hence the knowledge of the orientation of the detector's weight vector is sufficient for defining the decision boundary of the linear MBER OFDM/SDMA detector. Therefore, the MBER detector has an infinite number of MUD weight solutions, although with the aid of appropriate weight-vector normalisation, it is possible to reduce the infinite number of MBER solutions to a single solution.

Parameter	Value or type
OFDM	
Number of subcarriers	128
Length of cyclic prefix	32
GA	
GA type	Non-overlapping
Population size	100
Number of generations	100
Mutation type	Flip mutator
Probability of mutation	0.01
Cross-over type	Single-point cross-over
Probability of cross-over	0.6
Scaling	Sigma truncation
Genome type	Binary string
Initialisation	Uniform
Comparison	Bit comparator
Encoding/decoding	Binary encoding and decoding
Selection	Roulette wheel
Elitism	On
Others	
Receiver antennas	4
MBER detector algorithm	Exact MBER
Channel impulse response	Dispersive Gaussian channel [90], which is specified for each user in Table 12.3.

Table 12.2: Parameters for the GA simulations

In [440], we employed the simplified conjugate gradient (CG) algorithm for arriving at the minimum solution of the BER cost function, and the step size, μ, is fixed for every iteration.

12.3 Genetic Algorithm

Even though the MBER detector of [440] is capable of maintaining a good performance, the convergence of the algorithm is sensitive to the choice of the algorithm's parameters. For example, the choice of the initial condition for the MBER MUD is critical in order for the solution to converge to the minimum of the BER surface seen in Figure 12.2. In [440], the MMSE SDMA MUD weight solution has been used for initialising the CG algorithm based MUD, which is also exemplified in Figure 12.2. However, this choice of initial conditions does not necessarily guide the algorithm's convergence to the required MBER solution, if the BER surface exhibits local minima, although this is not the case in Figure 12.2. Another parameter that affects the performance of the MBER detector is the step size μ used for updating the array weights in the direction opposite to the BER gradient. The choice of this step size must be based on a compromise, since a step-size that is too high might not allow

User	Antenna	CIR
User 1	Antenna 1	$(-0.097 - j0.062) - (0.56 + j0.40)z^{-6} - (0.30 - j0.014)z^{-11}$
	Antenna 2	$(-0.50 - j0.51) - (0.116334 + j0.50)z^{-6} + (0.37 - j0.12)z^{-11}$
	Antenna 3	$(-0.13 - j0.20) + (0.19 + j0.31)z^{-6} + (0.21 - j0.16)z^{-11}$
	Antenna 4	$(-1.41 + j0.17) - (0.88 - j0.13)z^{-6} + (0.71 + j0.25)z^{-11}$
User 2	Antenna 1	$(-0.24 - j0.32) + (0.24 + j0.18)z^{-6} + (0.25 + j0.38)z^{-11}$
	Antenna 2	$(0.48 - j0.27) - (0.16 + j0.27)z^{-6} - (0.041 + j0.24)z^{-11}$
	Antenna 3	$(0.84 + j0.57) + (0.10 - j0.15)z^{-6} + (0.61 + j0.018)z^{-11}$
	Antenna 4	$(-0.57 - j0.43) - (0.17 + j0.090)z^{-6} + (0.11 + j0.15)z^{-11}$
User 3	Antenna 1	$(-0.79 + j1.43) + (0.082 + j0.35)z^{-6} + (0.16 - j0.59)z^{-11}$
	Antenna 2	$(0.53 - j0.52) + (0.37 + j0.11)z^{-6} + (0.29 + j0.29)z^{-11}$
	Antenna 3	$(0.76 - j0.070) - (0.032 - j0.62)z^{-6} + (0.43 - j0.11)z^{-11}$
	Antenna 4	$(0.85 + j0.104) - (0.068 - j0.42)z^{-6} + (0.080 - j0.46)z^{-11}$
User 4	Antenna 1	$(1.92 + j0.12) - (0.10 + j0.60)z^{-6} - (0.17 + j0.0049)z^{-11}$
	Antenna 2	$(0.42 - j0.47) + (0.0095 + j0.097)z^{-6} - (0.21 + j0.23)z^{-11}$
	Antenna 3	$(-0.022 + j0.21) + (0.059 - j0.069)z^{-6} + (0.21 - j0.11)z^{-11}$
	Antenna 4	$(0.45 - j0.12) - (0.12 - j0.57)z^{-6} - (0.30 + j0.21)z^{-11}$

Table 12.3: CIR of the different users at the different antennas for the P=4,L=4 system

convergence to the minimum BER point, whereas the opposite scenario will require a high number of iterations for attaining convergence to the MBER solution. An attractive method that might be able to assist the MBER MUD in circumventing the above-mention problems is constituted by the family of genetic algorithms [443], which were extensively used in various CDMA and MC-CDMA MUD problems in [444].

12.3.1 Overview of GAs

The philosophy of GA-based search methods is reminiscent of the rules of evolution and survival in nature, where a group of the fittest individuals in a population will survive. These individuals will then 'mate' and 'mutate' for the sake of developing a new set of individuals for the next generation. GAs were proposed by John Holland at the University of Michigan in the early 1970s [445]. His original target was to study the adaptive process of a natural system and later to adapt this natural system in the context of an artificial system software. Holland's research was further developed by one of his students, Goldberg [443]. Since then, GAs have been employed in numerous applications, such as machine learning [446–448] and in modelling adaptive processes [449, 450], but the most frequent application of GAs may be found in the domain of function optimisation [443, 445, 451]. GAs have also been successfully applied in CDMA [444, 452–459] , beamforming [460] and space-time block coding (STBC) [461] aided multi-user detection scenarios. These contributions developing the field of GAs are summarised at a glance in Table 12.4.

GAs are different from traditional optimisation algorithms, because they do not directly attempt to optimise the desired decision variable [443]. Instead, they encode the decision variables to be optimised such as, for example, the SDMA MUD's weight vectors into finite-

Year	Author	Contribution
'75	Holland [445]	Originally proposed GAs for studying the adaptive process of natural evolution in an artificial system software.
'89	Goldberg [443]	Goldberg further developed GAs in the context of optimisation and machine learning.
'96	Mitchell [462]	A further advancement of GAs in machine learning.
'97	Juntti, Schlosser and Lilleberg [452]	First known study of the application of GAs in MUDs.
'98	Wang, Lu and Antoniou [453]	Proposed a detector for multi-user communications, which is based on the maximum-likelihood decision rule and employs a GA for detecting the user bits sequentially.
'00	Ergun and Hacioglu [454]	Suggested a hybrid approach that combines GAs with a multistage multi-user detector (MSD) in the context of a CDMA system.
'01	Yen and Hanzo [457]	Employed a novel CDMA multi-user receiver based on GAs, for jointly estimating the transmitted symbols and the fading channel coefficients of all users.
	Abedi and Tafazolli [455]	Proposed and characterised a genetic implementation of the optimal MUD.
'02	Ng, Yen and Hanzo [459]	Advocated a turbo trellis coded modulation assisted GA-aided reduced complexity MUD (TTCM-GA-MUD) that is capable of providing a considerable coding gain without any bandwidth expansion, while maintaining a low complexity compared to the optimum MUD.
	Chiang and Chang [463]	Improved the GA and MSD using eugenic population. Unlike the elitist selection which ensures that only the fittest member of the parents' population is retained in the next generation, the eugenic GA combines the offspring and members of the parents' population into a joint population. Then, the fitness values of all the elements in the joint population are evaluated and the high-fitness chromosomes are selected to produce the eugenic population.
'03	Shayesteh, Menhaj and Nobary [456]	Proposed a modified genetic algorithm for multi-user detection in DS/CDMA systems, which attains a performance comparable to that of the optimum detector with at a lower complexity.
	Yen and Hanzo [458]	Advocated a spatial diversity reception-assisted CDMA multi-user detector based on GAs.
	Du and Chan [461]	Invoked a GA for sub-optimal detection in space-time block coding (STBC) aided multi-user detection systems.
'04	Wolfgang, Ahmad, Chen and Hanzo [464]	Introduced a novel GA-assisted Minimum Bit Error Ratio (MBER) beamforming technique.
	Alias, Chen and Hanzo [465]	Employed GAs to determine the MUD's weights for an SDMA OFDM system directly optimizing the MBER criterion.

Table 12.4: Contributions towards the development of GA-aided MUDs

length strings or GA individuals, which are then optimised. In the case of SDMA-MUDs, both the real and imaginary part of a complex-valued weight have to be represented by a single GA string to create an individual. A GA does not commence its optimisation process from a single point in the search space, but rather from an entire set of individuals, which form the initial population. In other words, GAs may be invoked in robust global search and optimisation procedures that do not require any knowledge of the objective function's derivatives or any gradient-related information concerning the search space. Hence, non-differentiable functions as well as functions with multiple local minima, such as the BER surface of the SDMA-MUD, represent classes of problems, where GAs can be efficiently applied. For further details on the origin of GAs and its applications, interested readers are referred to the impressive compilation of ideas in [443, 445, 462]. The most detailed portrayal of the GA-aided CDMA MUDs may be found in [444].

12.3.2 Employing GAs in the MBER MUD Aided SDMA OFDM System

In the proposed system a GA is used for finding the best SDMA-MUD weight vectors that will minimise the probability of error in Equation 12.10. Figure 12.3 shows the flow chart of a GA invoked for the optimisation of the MBER MUD's weights. The basic approach of a GA system is quite simple. Firstly, the probability of error is used as the objective function to be solved by the GA. To begin the GA process, an initial population consisting of Y number of so-called individuals is created in the 'Initialisation' block, where Y is known as the population size. Each individual represents a legitimate solution to the given optimisation problem. An individual can be considered as a vector consisting of the decision variables to be optimised. Traditionally, the individuals in a GA population take the form of binary bit vectors, but they can also be represented by real values. In our specific problem, each individual in a population is represented by the two-dimensional binary arrays, which store the real and imaginary part of the SDMA-MUD's weight values. An example of the GA's individual is shown in Figure 12.4. The initial population may be generated randomly, optionally including as one of the individuals the MMSE solution for the sake of expediting the search as well as for reducing the complexity of the search.

Each individual in the population is evaluated according to the so-called *fitness* value associated with it. This fitness value is calculated by substituting the individual into the objective function in the 'Evaluation' block seen in Figure 12.3. Following the fitness evaluation process, the termination criterion will be checked, which may be either a certain convergence accuracy, a certain number of generations or various other criteria. We opted for terminating the evaluations after G number of generations. If the stopping criterion is not met, a group of the highest-fitness individuals is selected for creating a generation in the 'Selection' block of Figure 12.3. This group of individuals, referred to as *parents*, will be subjected to various genetically-inspired operators, such as the so-called *cross-over* and *mutation*, for the sake of creating new individuals. The fitness of these new individuals will then be re-evaluated and the termination criterion is examined again.

This process will continue, until the termination criterion is finally met. After this stage, the best individual having the highest fitness encountered will be chosen as the solution to the optimisation problem.

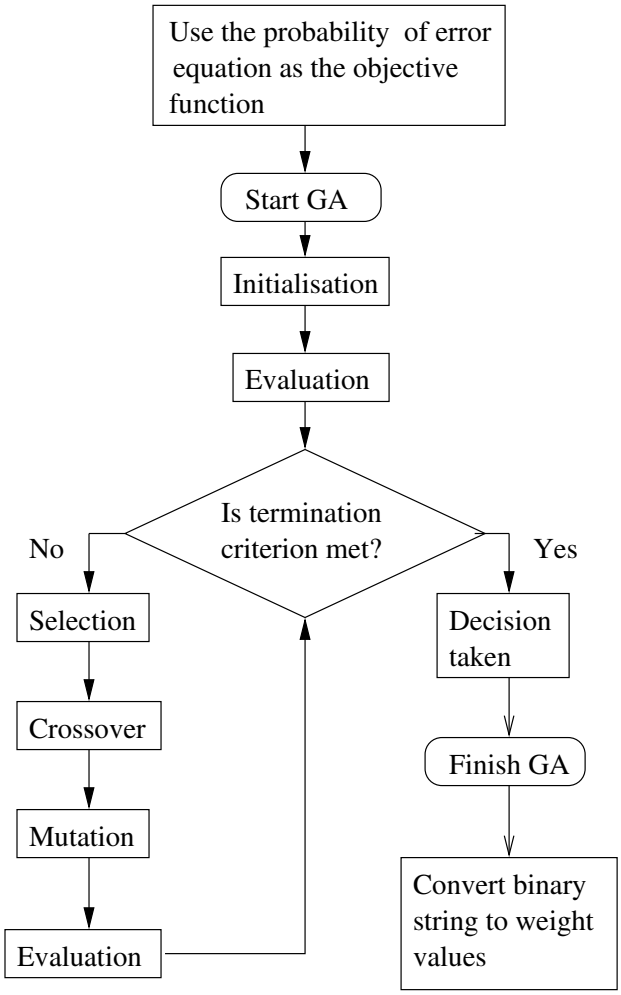


Figure 12.3: Flowchart for the probability error optimisation using GA

12.4 Simulation Results

12.4.1 Performance of a Four-User and Four-Receiver Antenna Scenario

The parameters used in our simulations are outlined in Table 12.2. The channel that we used in these investigations was the unfaded dispersive Gaussian channel, where the z-domain transfer function associated with the CIR of all four users and four antennas are summarised in Table 12.3. Since the different users experienced different CIR taps at each receiver antennas, we also had unique FDCHTFs for the various users. As a starting point, we used binary type genomes [443] for representing the GA's individuals. Therefore each real and imaginary part of each of the SDMA MUD weights is represented by a 16-bit binary string. The GA's

w_{1R}	1 0 0 1 1 1 0 1 0 1 0 0 1 1 0 1
w_{1I}	1 1 0 0 1 1 0 0 1 1 0 0 1 1 0 0
w_{2R}	0 1 1 1 1 1 1 1 0 0 0 0 1 0 1 0
w_{2I}	0 0 0 1 1 0 0 1 0 1 0 1 1 1 0 0
⋮	⋮
w_{PR}	1 0 0 1 0 0 0 1 1 1 1 0 1 1 0 1
w_{PI}	0 1 0 0 1 1 1 1 0 1 0 0 1 1 0 1

Figure 12.4: An example of an individual in the GA system represented by the two-dimensional binary arrays where P is the number of antennas at the receiver, R is the real part of the weight and I is the imaginary part of the weight

termination criterion is constituted by the maximum affordable number of generations. Following the termination of the optimisation process, the best individual encountered is deemed to be the best MBER MUD weight solution and hence it is converted to the corresponding real and imaginary values of the weight vectors. Our results derived for four different users employing the parameters summarised in Table 12.2 are presented in Figure 12.6. In these investigations we imposed the same complexity, as quantified explicitly in Section 12.5 for both the CG and GA-aided MBER MUDs. It may be observed from the figure that the GA-aided MBER MUD and the CG MBER MUD perform similarly for the same complexity. We can also see from the figure that the MMSE MUD's BER performance is different for each user due to their different CIR experienced at the base station antennas. On the other hand, the results of both types of MBER MUDs differs only slightly for the different users, and the achievable BER of the different users is close to that of the single-user single-antenna scenario recorded for a non-dispersive AWGN channel. We have also derived the average of the achievable BER of all the users determined for the CIRs summarised in Table 12.3 and the corresponding results are portrayed in Figure 12.5.

12.4.2 Performance of the Four-Antenna Scenario versus the Number of Users

So far, we have been supporting the same number of users as the number of receiver antennas in our simulations. By contrast, Figure 12.7 shows the BER results for User 1, when supporting different number of users in the four receiver antenna scenario. For the MBER MUD, we used the GA-aided system introduced in Section 12.3.2, employing the simulation parameters specified in Table 12.2. We can see from the figure that as the number of users increases, the BER performance degrades, owing to the increased multi-user interference imposed. In the absence of multi-user interference when only one user is communicating, both MUDs have similar BER curves. As expected, this is because no multi-user interference is inflicted and hence the MMSE MUD is also capable of minimising the BER. However, the MMSE MUDs

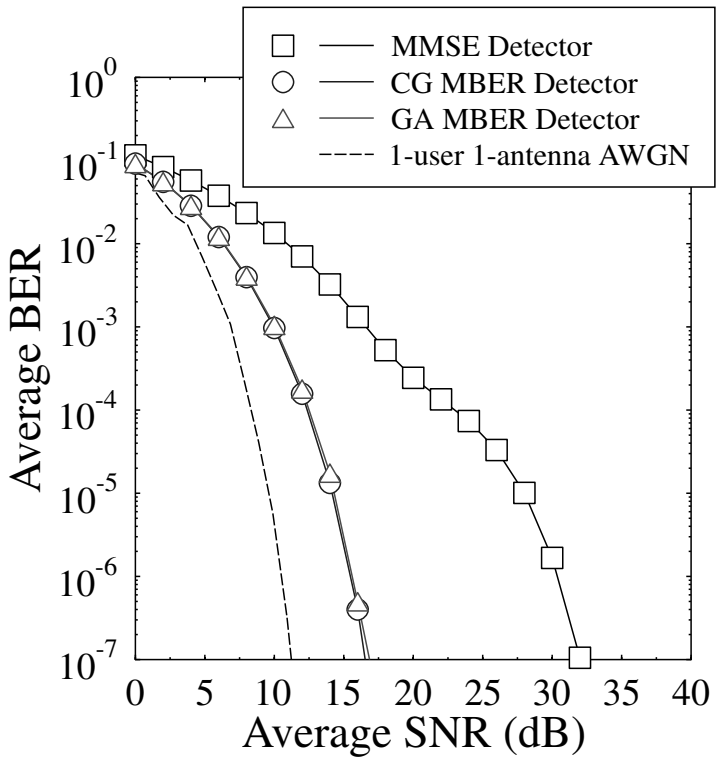


Figure 12.5: The *average BER* performance of the four different users characterised in Figure 12.6 and encountering the CIRs of Table 12.3 in an SDMA system employing four receiver antennas and 128-subcarrier OFDM for communicating over the OFDM symbol-invariant dispersive Gaussian channel given in Table 12.2

characterised in Figure 12.7(a) can only support a maximum number of users that is equal to the number of receiver antennas, which is four in this case. Once the number of users exceeds the number of receiver antennas, the MMSE MUD becomes incapable of differentiating the users and this results in the high residual BER seen in Figure 12.7(a). By contrast, we observed in Figure 12.7(b) that the MBER MUD performs significantly better. Furthermore, by comparing Figure 12.7(a) and Figure 12.7(b) we may conclude that the MBER MUD is capable of supporting more users than the number of receiver antennas employed.

These performance trends may be more explicitly interpreted with the aid of Figure 12.8, where the composition of User 1's noiseless received phasors are illustrated when transmitting $s_1 = +1$ in the six user scenario employing four receiver antennas. In this figure, the different processing stages are defined in Figure 12.1. In short, Stage I represents the composite multi-user received signals, $x_1, \ldots, x_P$ at the different antennas. The MUD Stage II outputs the product of the Hermitian of the MUD's weight value, $w_p,\ p \in 1, \ldots, P$, of the individual antenna elements and the corresponding $x_p,\ p \in 1, \ldots, P$, value, i.e. $w^H x$.

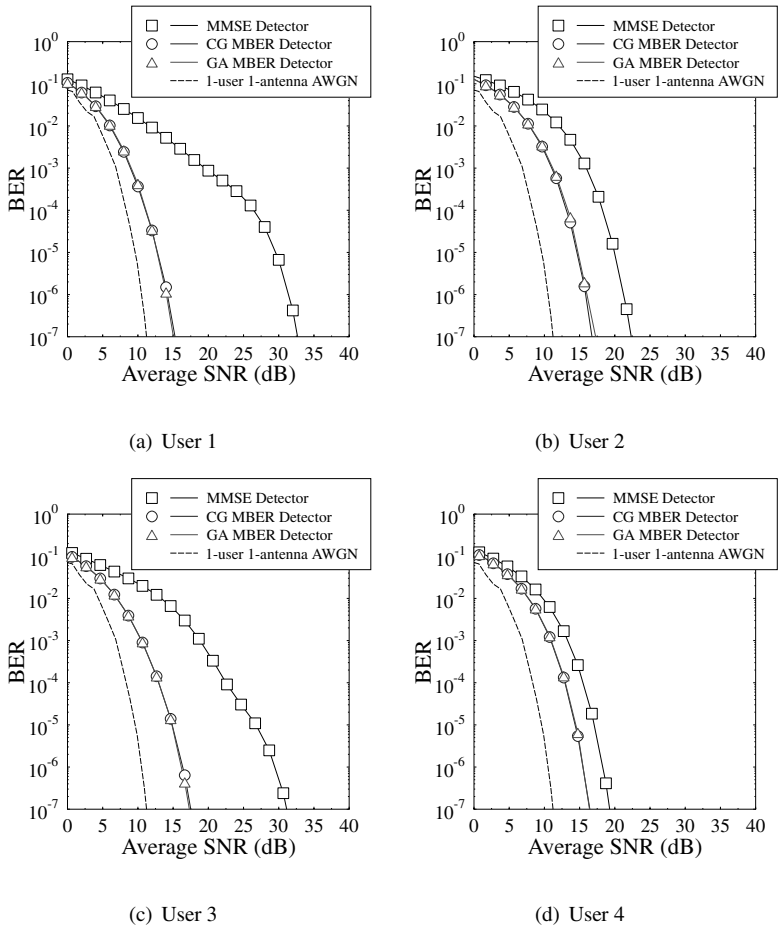


Figure 12.6: The BER performance of the four different users in an SDMA system employing four receiver antennas and 128-subcarrier OFDM for communicating over the OFDM symbol-invariant dispersive Gaussian channel given in Table 12.3. The other parameters are summarised in Table 12.2

Finally, Stage III represents the combination of the outputs of each antenna. Explicitly, the MMSE MUD attempts to minimise the Euclidean distance between the estimated received symbol, $\hat{s}_1$ and the original transmitted symbol s_1. However, as can be observed at Stage III of Figure 12.8, some of the $\hat{s}_{1,MMSE}$ points are either on the wrong half-plane of the BPSK phasor constellation or exactly on the decision boundary, at $y_R = 0$. As a consequence, the associated residual BER experienced in the absence of noise can be calculated by taking into account the relative frequency of these points. On the other hand, since the MBER MUD is directly minimising the BER, the MUD's weight values are adjusted for the sake of ensuring that the estimated phasors are as far away from the decision boundary as possible. Therefore, we can see from Figure 12.8 that the estimated received phasors $\hat{s}_{1,MBER}$ are

significantly further from the BPSK decision boundary of $y_R = 0$, than for the MMSE MUD hence avoiding the MMSE-specific residual BER.

12.5 Complexity Comparison

The advantage of using GAs for determining the MBER MUD's weight values compared to the CG method [440] is that the GA does not necessarily require a good initial MUD weight guess for exhibiting a rapid convergence. In this section, we will estimate the complexity of these two methods. In this chapter the complexity refers to the number objective function evaluations or the gradient evaluations for the GA and the CG methods, respectively.

The complexity of the CG algorithm is proportional to the number of iterations used for finding the MBER solution on the BER surface. In each iteration the gradient expression of Equation 12.13 will have to be calculated and the SDMA-MUD weight values will be updated accordingly. Therefore the complexity of the CG method may be estimated as:

$$Compl\{CG\} \simeq \text{Maximum number of iterations.} \tag{12.14}$$

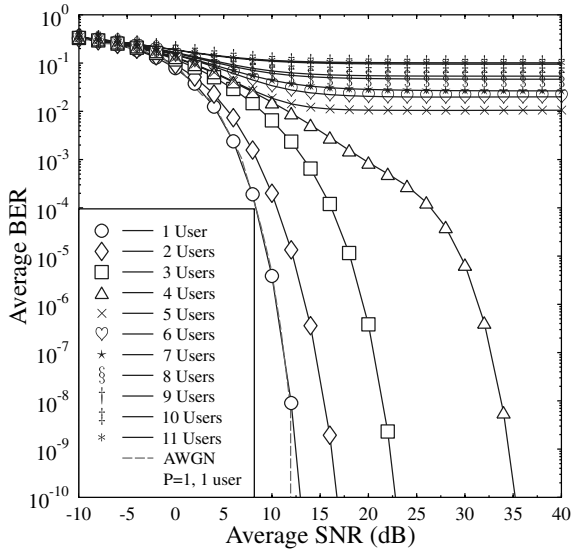
On the other hand, if we used the maximum number of generations as the termination criterion in the GA, each generation of the population contains a certain number of individuals, thus the complexity of the GA-aided MUD is proportional to the product of the population size and to the number of generations used, which is given by:

$$\begin{aligned} Compl\{GA\} &\simeq \text{Population size} \times \text{Number of generations} \\ &= Y \times G. \end{aligned} \tag{12.15}$$

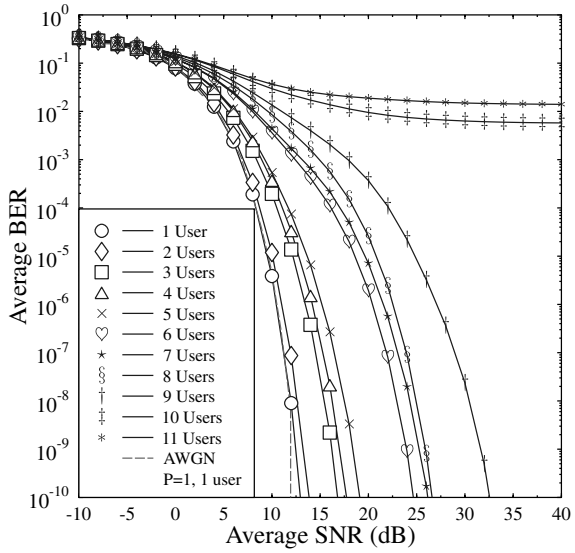
By using Equation 12.14 and Equation 12.15, we can compare the complexity of the two methods. Figure 12.9 shows the probability of error for User 1 at SNR = 15 dB for the P = 4 and L = 4 system configuration. We can see from the figure that the GA-aided SDMA-MUD will reach the minimum BER at a lower complexity compared to the CG method.

12.6 Chapter Summary and Conclusion

In this chapter we have shown that GAs may be applied in the context of an SDMA OFDM system for determining the MBER MUD's weight vectors. The GA-aided system has an edge over the CG-based system, because it does not require an initial weight solution. Unlike the MMSE MUD, the MBER MUD is capable of supporting more users than the number of receiver antennas. It was also shown that the GA is capable of approaching the MBER solution at a lower complexity than the CG algorithm. Our future work will aim for finding more efficient adaptive weight optimisation algorithms in the context of LDPC-coded SDMA OFDM systems.



(a) MMSE MUD



(b) MBER MUD

Figure 12.7: The BER performance of User 1 employing both the MMSE and MBER MUD in an SDMA system equipped with four receiver antennas for a different number of users employing 128-subcarrier OFDM communicating over the OFDM symbol-invariant dispersive Gaussian channel given in Table 12.2

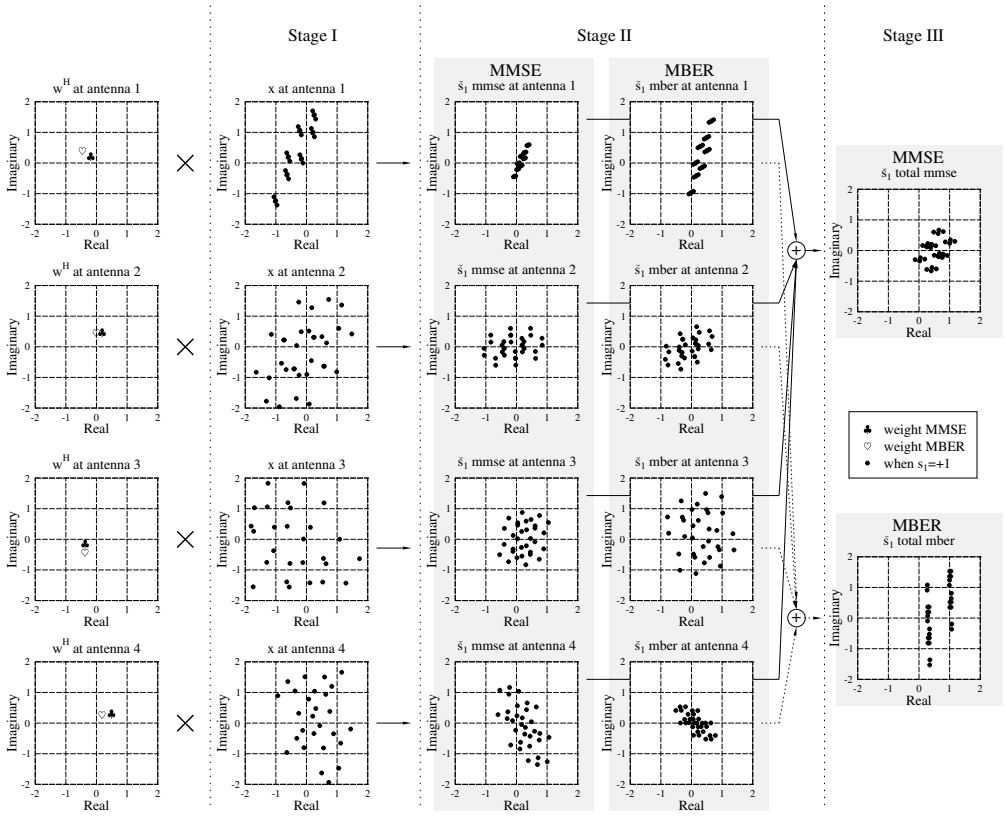


Figure 12.8: An example composition of the likely noiseless received signals for User 1 for the case of $P = 4$, $L = 6$ when transmitting $s_1 = +1$. The consecutive processing stages correspond to those depicted in Figure 12.1. The remaining parameters are given in Table 12.2. *The striking difference of the MMSE and MBER phasor constellations manifests itself in the fact that the MBER receiver attempts to align all phasor points equi-distantly from the decision boundary, which indeed, minimises the BER. By contrast, the MMSE solution indeed, minimises the MSE between the legitimate and processed phasor points, while allowing some of the phasors to become more prone to decision errors*

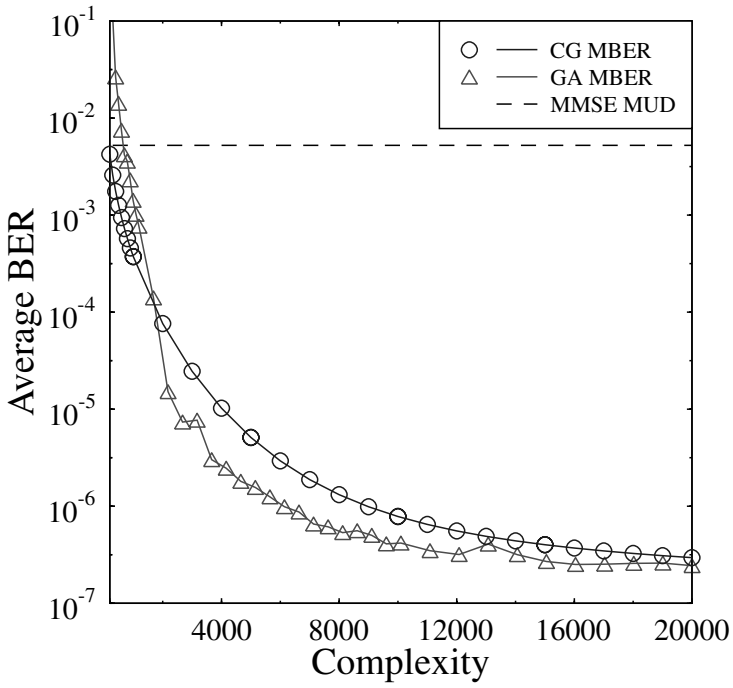


Figure 12.9: The BER performance of User 1 versus complexity for the GA and CG MBER MUD invoked in the OFDM/SDMA system employing P = 4, L = 4 and 128-subcarrier OFDM for communicating over the OFDM-symbol invariant dispersive Gaussian channel given in Table 12.2 at SNR = 15 dB. The complexity calculations were described in Section 12.5

Chapter 13

Conclusion and Further Research Problems

13.1 Summary and Conclusions of Part I

13.1.1 Summary of Part I

In Chapters 2 - 4 we discussed the basic implementational, algorithmic and performance aspects of orthogonal frequency division multiplexing in predominantly duplex mobile communications environments. Specifically, following a rudimentary introduction to OFDM in Chapter 2, in Chapter 3 we further studied the structure of an OFDM modem and we investigated the problem of the high peak-to-mean power ratio observed for OFDM signals, and that of clipping amplification caused by insufficient amplifier back-off. We investigated the BER performance and the spectrum of the OFDM signal in the presence of clipping, and we have seen that for an amplifier back-off of 6 dB the BER performance was indistinguishable from the perfectly amplified case. We investigated the effects of quantisation of the time domain OFDM signal. The effects of phase noise on the OFDM transmission were studied, and two-phase noise models were suggested. One model was based on white phase noise, only relying on the integrated phase jitter, while a second model used coloured noise, which was generated from the phase noise mask.

In Chapter 4 we studied OFDM transmissions over time-dispersive channels. The spectrum of the transmitted frequency domain symbols is multiplied with the channel's frequency domain channel transfer function, hence the amplitude and phase of the received subcarriers are distorted. If the channel is varying significantly during each OFDM symbol's duration, then additional inter-subcarrier interference occurs, affecting the modem's performance. We have seen the importance of channel estimation on the performance of coherently detected OFDM, and we have studied two simple pilot-based channel estimation schemes. Differentially detected modulation can operate without channel estimation, but exhibits lower BER performance than coherent detection. We have seen that the signal-to-noise ratio is not con-

© 2006 John Wiley & Sons, Ltd

stant across the OFDM symbol's subcarriers, and that this translates into a varying bit error probability across the different subcarriers.

The effects of timing and frequency errors between transmitter and receiver were studied in Chapter 5. We saw that a timing error results in a phase rotation of the frequency domain symbols, and possibly inter-OFDM-symbol interference, while a carrier frequency error leads to inter-subcarrier interference. We suggested the introduction of a cyclic postamble, in order to suppress inter-OFDM-symbol interference for small timing errors, but we saw that frequency errors higher than 5% of the subcarrier separation lead to severe performance losses. In order to combat this, we investigated a set of frequency- and timing-error estimation algorithms. We suggested a time domain-based joint time and frequency error acquisition algorithm, and studied the performance of the resulting system over fading time-dispersive channels.

Based on the findings of Chapter 4 we investigated adaptive modulation techniques to exploit the frequency diversity of the channel. Specifically, in Chapter 6, three adaptive modulation algorithms were proposed and their performance was investigated. The issue of signalling was discussed, and we saw that adaptive OFDM systems require a significantly higher amount of signalling information than adaptive serial systems. In order to limit the amount of signalling overhead, a sub-band adaptive scheme was suggested, and the performance trade-offs against a subcarrier-by-subcarrier adaptive scheme were discussed. Blind modulation mode detection schemes were investigated, and combined with an error correction decoder. We saw that by combining adaptive modulation techniques with a strong convolutional turbo channel codec significant system throughput improvements were achieved for low SNR values. Finally, frequency domain pre-distortion techniques were investigated in order to pre-equalise the time-dispersive channel's transfer function. We saw that by incorporating pre-distortion in adaptive modulation, significant throughput performance gains were achieved compared to adaptive modems without pre-equalisation.

13.1.2 Conclusions of Part I

(1) Based on the implementation-oriented characterisation of OFDM modems, leading to a real-time testbed implementation and demonstration at 34 Mbps we concluded that OFDM is amenable to the implementation of high bit rate wireless ATM networks, which is underlined by the recent ratification of the HIPERLAN II standard.

(2) The range of proposed joint time and frequency synchronisation algorithms efficiently supported the operation of OFDM modems in a variety of propagation environments, resulting in virtually no BER degradation in comparison to the perfectly synchronised modems. For implementation in the above-mentioned 34 Mbps, real-time testbed simplified versions of these algorithms were invoked.

(3) Symbol-by-symbol adaptive OFDM substantially increases the BPS throughput of the system at the cost of moderately increased complexity. It was demonstrated in the context of an adaptive real-time audio system that this increased modem throughput can be translated into improved audio quality at a given channel quality.

(4) The proposed blind symbol-by-symbol adaptive OFDM modem mode detection algorithms were shown to be robust against channel impairments in conjunction with

twin-mode AOFDM. However, it was necessary to combine it with higher-complexity channel coding based mode detection techniques, in order to maintain sufficient robustness, when using quadruple-mode AOFDM.

(5) The combination of frequency domain pre-equalisation with AOFDM resulted in further performance benefits at the cost of a moderate increase in the peak-to-mean envelope fluctuation and system complexity.

13.2 Summary and Conclusions of Part II

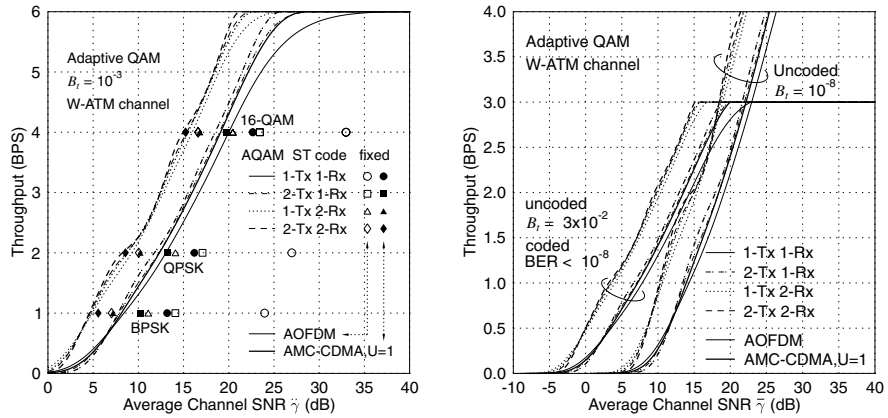
13.2.1 Summary of Part II

Since their initial introduction in 1993 [70, 73, 263, 264], multi-carrier spread-spectrum systems have attracted significant research interest. Existing advanced techniques originally developed for DS-CDMA and OFDM have also been applied to MC-CDMA, while a range of new unique techniques have been proposed for solving various problems specific to multi-carrier CDMA systems. The first two chapters of Part II, namely Chapters 7 and 8, reviewed the basic concepts of MC-CDMA and the various spreading sequences applicable to MC-CDMA transmissions. Chapter 9 characterised the achievable performance of MC-CDMA schemes employing various detectors. A number of further topics closely related to MC-CDMA based communications were also investigated in depth.

Part II of the book concentrated on investigating the MC-CDMA scheme of [70, 71, 73], which constitutes a specific family of the three different multi-carrier CDMA types often used in the literature [90]. This technique was advocated, because MC-CDMA results in the lowest BER among the three schemes investigated in a similar scenario [312]. Our investigations concentrated on the downlink, because in the uplink stringent synchronisation of the mobile terminals has to be met. Future research should extend the results of Chapter 6 to both multi-carrier DS-CDMA [263] and to multi-tone (MT) CDMA [264], as well as to the family of more sophisticated adaptive MC-CDMA schemes [300].

13.2.2 Conclusions of Part II

The main contributions and conclusions of Part II of the book emerge from Section 9.4.3, where the performance of Space-Time (ST) block coded constant-power adaptive multi-carrier modems employing the optimum SNR-dependent modem mode switching levels derived in Chapter 12 of [90] were investigated [334, 466]. As expected, it was found that ST block coding reduces the relative performance advantage of adaptive modulation, since it increases the diversity order and eventually reduces the channel quality variations, as it can be observed in Figure 13.1(a).*Having observed that 1-Tx aided AOFDM and 2-Tx ST coding aided fixed-mode MC-CDMA resulted in a similar BPS throughput performance, we concluded that fixed-mode MC-CDMA in conjunction with 2-Tx ST coding could be employed, provided that we could afford the associated complexity. By contrast, AOFDM could be a low complexity alternative of counteracting the near-instantaneous channel quality variations.* When turbo convolutional coding was concatenated to the ST block codes, near-error-free transmission was achieved at the expense of halving the average throughput, as seen in Figure 13.1(b) . Compared to the uncoded system, the turbo coded system was capable



(a) With ST coding

(b) With ST and turbo coding

Figure 13.1: The BPS throughput performance of five-mode AOFDM and AMC-CDMA for communicating over the W-ATM channel [2, pp.474]. (a) The SNR gain of the adaptive modems decreases, as the diversity of the ST coding increases. The BPS curves appear in pairs, corresponding to AOFDM and AMC-CDMA - indicated by the thin and thick lines, respectively - for each of the four different ST code configurations. The markers represent the SNRs required by the fixed-mode OFDM and MC-CDMA schemes for maintaining the target BER of 10^{-3} in conjunction with the four ST-coded schemes considered. (b) The turbo convolutional coding assisted adaptive modems have SNR gains up to 7dB compared to their uncoded counterparts achieving a comparable average BER.

of achieving a higher throughput in the low SNR region at the cost of a higher complexity. Our study of the relationship between the uncoded BER and the corresponding coded BER showed that adaptive modems obtain higher coding gains, than that of fixed modems. This was due to the fact that the adaptive modem avoids burst errors even in deep channel fades by reducing the number of bits per modulated symbol eventually to zero.

13.3 Summary and Conclusions of Part III

13.3.1 Near-ML Enhanced Sphere Detection of MIMO-OFDM

In Chapter 10 we proposed a novel OHRSA-aided SDM detection method, which may be regarded as an advanced extension of the Complex Sphere Detector. The algorithm proposed extends the potential range of applications of the CSD methods, as well as reducing the associated computational complexity, rendering the algorithm proposed a feasible solution for implementation in practical systems.

Furthermore, we demonstrated that the OHRSA-aided SDM detector proposed combines the advantageous properties of both the optimum-performance Log-MAP SDM detector and the minimum-complexity linear MMSE SDM detector, which renders it an attractive alternative for implementation in practical systems. More specifically, we have shown that the OHRSA-aided SDM detector proposed exhibits the following advantageous properties.

The method can be employed in the over-loaded scenario, where the number of transmit antenna elements exceeds that of the receive antenna elements, while the associated computational complexity increases only moderately even in heavily overloaded scenarios and is almost independent of the number of receive antennas. Furthermore, as opposed to standard CSD schemes [176], no calculation of the sphere radius is required and therefore the method proposed is robust to the particular choice of the initial parameters both in terms of the achievable performance and the associated computational complexity. The overall computational complexity required is only slightly higher than that imposed by the linear MMSE multiuser detector designed for detecting a similar number of users. Specifically, the computational complexity per detected QAM symbol associated with both the MMSE and SOPHIE SDM detectors is of the order of $O\{m_{\rm t}^3\}$, where $m_{\rm t}$ is the number of transmit antennas. Finally, the associated computational complexity is fairly independent of the channel conditions quantified in terms of the SNR encountered.

In our future work the achievable performance of the SDM detection schemes proposed will be explored in the presence of imperfect channel state information. More explicitly, we will characterize and analyse the performance of a range of channel estimation methods suitable for employment in the SDM-OFDM system considered in this chapter. Subsequently, we will analyse the achievable performance of the SDM detection methods portrayed in this chapter in the context of the SDM-OFDM system employing our channel estimation schemes.

Additionally, an iterative joint SDM detection and decoding scheme, which can potentially approach the information-theoretic capacity bound will be designed. Furthermore, joint iterative turbo-structured SDM detection, decoding and channel estimation methods will be explored.

13.3.2 GA-Aided Joint MUD and Channel Estimation

From the investigations and discussions conducted in Chapter 11 we conclude that the proposed GA-aided iterative joint channel estimation and multi-user detection scheme generating soft outputs constitutes an effective solution to the channel estimation problem in multi-user MIMO SDMA-OFDM systems. Furthermore, the GA-JCEMUD is capable of exhibiting a robust performance in overloaded scenarios, where the number of users is higher than the number of receiver antenna elements, either with or without FEC coding. This attractive property enables the SDMA-OFDM system to potentially support an increased number of users. Our future research will consider the design of similar downlink systems.

13.3.3 GA-Aided MBER MUD

In Chapter 12 we demonstrated that GAs may be applied in the context of an SDMA-OFDM system for determining the MBER MUD's weight vectors. The GA-aided system has an edge over the conjugate gradient algorithm based system, because it does not require an initial SDMA array weight solution. Unlike the MMSE MUD of Chapter 12 in [90], the MBER MUD is capable of supporting more users than the number of receiver antennas. It was also shown that the GA is capable of approaching the exact MBER solution at a lower complexity than the conjugate gradient algorithm. Our future work will aim for finding more efficient adaptive weight optimisation algorithms in the context of LDPC-coded SDMA-OFDM systems.

13.4 Closing Remarks

This monograph has considered a range of OFDM and MC-CDMA-related topics applicable to both single-user and multi-user communications. However, a whole host of further recent advances in the field of communications research are applicable also to OFDM. Specifically, the family of classification and learning-based neural network-assisted receivers investigated in the context of conventional single-carrier systems provides a rich set of further research topics. Partial response modulation techniques also promise performance advantages in OFDM schemes. The joint optimisation of adaptive subcarrier bit-allocation and crest-factor reduction techniques constitutes a further research challenge in the context of multi-user OFDM and MC-CDMA systems. All the above-mentioned techniques have the potential of improving the complexity versus performance balance of the system. The design of joint coding and modulation schemes is particularly promising in the context of OFDM and MC-CDMA. Finally, the use of OFDM in ultra-wide band systems invoking various frequency-hopping and multiple access techniques is likely to grow in popularity as an exciting research area.

These enabling techniques along with those detailed in the book are expected to find their way into future standards, such as the successors of the 802.11, the High Performance Local Area Network standard known as HiPerLAN, the European Digital Audio Broadcast (DAB) and Digital Video Broadcast (DVB) arrangements and their descendants. They are also likely to be adopted by the standardisation bodies in future generations of personal communications systems.

It is expected that wireless systems of the near future are likely to witness the coexistence of space-time-coded transmit diversity arrangements and near-instantaneously adaptive OFDM as well as MC-CDMA schemes for years to come. Intelligent learning algorithms will configure the transceivers in the appropriate mode that ultimately provides the best trade-off in terms of satisfying the user's preference in the context of the service requested [7, 215, 217].

A further advantage of the near-instantaneously adaptive OFDM and MC-CDMA transceivers is that they allow the system to instantaneously drop its transmission rate, when the channel quality is reduced, for example, as a consequence of the instantaneously peaking co-channel interference. By contrast, a conventional fixed-mode transceiver would drop the call and hence degrade both the quality of service and the network's teletraffic capacity. The achievable teletraffic performance of adaptive CDMA systems was documented in depth in conjunction with adaptive antenna-assisted dynamic channel allocation schemes in [217].[1]

* *

Throughout this monograph we endeavoured to depict the range of contradictory system design trade-offs associated with the conception of OFDM and MC-CDMA systems. Our

[1] A range of related research papers and book chapters can be found at http://www-mobile.ecs.soton.ac.uk.

intention was to present the material in an unbiased fashion and sufficiently richly illustrated in terms of the associated design trade-offs so that readers will be able to find recipes and examples for solving their own particular wireless communications problems. In this rapidly evolving field it is a challenge to complete a timely, yet self-contained treatise, since new advances are being discovered at an accelerating pace, which the authors would like to report on. Our sincere hope is that you, dear readers, have found the book a useful source of information, but above all a catalyst for further research.

Glossary

ACF	Auto-correlation Function
ACTS	Advanced Communications Technologies and Services - a European research programme
ADSL	Asynchronous Digital Subscriber Loop
AOFDM	Adaptive Orthogonal Frequency Division Multiplexing
APR	A Priori
APT	A Posteriori
AWGN	Additive White Gaussian Noise
BER	Bit-Error Ratio
BLAST	Bell Labs Space-Time architecture
BPOS	Bit Per OFDM Symbol
BPSK	Binary Phase-Shift Keying
BS	Base Station
CDF	Cumulative Distribution Function
CDMA	Code-Division Multiple Access
CE	Channel Estimation
CIR	Channel Impulse Response
DAB	Digital Audio Broadcasting
DDCE	Decision-Directed Channel Estimation

© 2006 John Wiley & Sons, Ltd

DDCP	Decision-Directed Channel Prediction
DFT	Discrete Fourier Transform
DMUX	Demultiplexer
DTTB	Digital Terrestrial Television Broadcast
D-BLAST	Diagonal BLAST
EM	Expectation Maximisation
EVD	EigenValue Decomposition
FDM	Frequency Division Multiplexing
FDMA	Frequency Division Multiple Access
FEC	Forward Error Correction
FFT	Fast Fourier Transform
FIR	Finite Impulse Response
HF	High-Frequency
ICI	Inter-subCarrier Interference
IDFT	Inverse Discrete Fourier Transform
IFFT	Inverse Fast Fourier Transform
IIR	Infinite Impulse Response
ISI	Inter-Symbol Interference
IWHT	Inverse Walsh Hadamard Transform
KLT	Karhunen-Loeve Transform
LLR	Log-Likelihood Ratio
LS	Least-Squares
LSE	Least-Squares Error
MA	Multiple Access
MC	Multi-Carrier
MIMO	Multiple-Input Multiple-Output
ML	Maximum Likelihood

MLSE	Maximum Likelihood Sequence Estimation
MMSE	Minimum Mean-Square Error
MSE	Mean-Square Error
MU	Multi-User
MUD	Multi-User Detection
MUI	Multi-User Interference
MUX	Multiplexer
MV	Minimum Variance
MVDR	Minimum Variance Distortionless Response
OFDM	Orthogonal Frequency Division Multiplexing
PAPR	Peak-to-Average Power Ratio
PDF	Probability Density Function
PIC	Parallel Interference Cancellation
PSAM	Pilot Symbol Aided Modulation
PSD	Power Spectral Density
PSK	Phase-Shift Keying
QAM	Quadrature Amplitude Modulation
QPSK	Quadrature Phase-Shift Keying
RLS	Recursive Least-Squares
RNS	Residue Number System
SB	Subband
SDM	Space Division Multiplexing
SDMA	Space Division Multiple Access
SDI	Selective Decision Insertion
SER	Symbol Error Ratio
SIC	Successive Interference Cancellation
SINR	Signal-to-Interference-plus-Noise Ratio

SIR	Signal-to-Interference Ratio
SMI	Sample Matrix Inversion
SNR	Signal-to-Noise Ratio
STC	Space-Time Coding
SVD	Singular-Value Decomposition
TCM	Trellis-Coded Modulation
TDD	Time-Division Duplexing
TDMA	Time-Division Multiple Access
TTCM	Turbo-Trellis Coded Modulation
V-BLAST	Vertical BLAST
WATM	Wireless Asynchronous Transfer Mode
WHT	Walsh-Hadamard Transform
WHTS	Walsh-Hadamard Transform Spreading
ZF	Zero-Forcing
1D	One-Dimensional
2D	Two-Dimensional

Bibliography

[1] R. W. Chang, "Synthesis of band-limited orthogonal signals for multichannel data transmission," *Bell Systems Technical Journal*, vol. 46, pp. 1775–1796, December 1966.

[2] L. Hanzo, W. Webb, and T. Keller, *Single- and Multi-carrier Quadrature Amplitude Modulation*. New York, USA: John Wiley and IEEE Press, April 2000.

[3] W. Webb and R. Steele, "Variable rate QAM for mobile radio," *IEEE Transactions on Communications*, vol. 43, pp. 2223–2230, July 1995.

[4] L. Hanzo, "Bandwidth-efficient wireless multimedia communications," *Proceedings of the IEEE*, vol. 86, pp. 1342–1382, July 1998.

[5] S. Nanda, K. Balachandran, and S. Kumar, "Adaptation techniques in wireless packet data services," *IEEE Communications Magazine*, vol. 38, pp. 54–64, January 2000.

[6] L. Hanzo, F. Somerville, and J. Woodard, *Voice Compression and Communications: Principles and Applications for Fixed and Wireless Channels*. IEEE Press and John Wiley, 2001. (For detailed contents and sample chapters please refer to http://www-mobile.ecs.soton.ac.uk.).

[7] L. Hanzo, P. Cherriman, and J. Streit, *Wireless Video Communications: From Second to Third Generation Systems, WLANs and Beyond*. IEEE Press and John Wiley, 2001. (For detailed contents please refer to http://www-mobile.ecs.soton.ac.uk.).

[8] M. Zimmermann and A. Kirsch, "The AN/GSC-10/KATHRYN/variable rate data modem for HF radio," *IEEE Transactions on Communication Technology*, vol. CCM–15, pp. 197–205, April 1967.

[9] S. B. Weinstein and P. M. Ebert, "Data transmission by frequency division multiplexing using the discrete Fourier transform," *IEEE Transactions on Communication Technology*, vol. COM–19, pp. 628–634, October 1971.

[10] L. Cimini, "Analysis and simulation of a digital mobile channel using orthogonal frequency division multiplexing," *IEEE Transactions on Communications*, vol. 33, pp. 665–675, July 1985.

[11] M. Alard and R. Lassalle, "Principles of modulation and channel coding for digital broadcasting for mobile receivers," *EBU Review, Technical No. 224*, pp. 47–69, August 1987.

© 2006 John Wiley & Sons, Ltd

[12] *Proceedings of 1st International Symposium,DAB*, (Montreux, Switzerland), June 1992.

[13] A. Peled and A. Ruiz, "Frequency domain data transmission using reduced computational complexity algorithms," in *Proceedings of International Conference on Acoustics, Speech, and Signal Processing, ICASSP'80*, vol. 3, (Denver, CO, USA), pp. 964–967, IEEE, 9–11 April 1980.

[14] B. Hirosaki, "An orthogonally multiplexed QAM system using the discrete Fourier transform," *IEEE Transactions on Communications*, vol. COM-29, pp. 983–989, July 1981.

[15] H. Kolb, "Untersuchungen über ein digitales Mehrfrequenzverfahren zur Datenübertragung," in *Ausgewählte Arbeiten über Nachrichtensysteme*, no. 50, Universität Erlangen-Nürnberg, 1982.

[16] H. Schüssler, "Ein digitales Mehrfrequenzverfahren zur Datenübertragung," in *Professoren-Konferenz, Stand und Entwicklungsaussichten der Daten und Telekommunikation*, (Darmstadt, Germany), pp. 179–196, 1983.

[17] K. Preuss, "Ein Parallelverfahren zur schnellen Datenübertragung im Ortsnetz," in *Ausgewählte Arbeiten über Nachrichtensysteme*, no. 56, Universität Erlangen-Nürnberg, 1984.

[18] R. Rückriem, "Realisierung und messtechnische Untersuchung an einem digitalen Parallelverfahren zur Datenübertragung im Fernsprechkanal," in *Ausgewählte Arbeiten über Nachrichtensysteme*, no. 59, Universität Erlangen-Nürnberg, 1985.

[19] I. Kalet, "The multitone channel," *IEEE Transactions on Communications*, vol. 37, pp. 119–124, February 1989.

[20] B. Hirosaki, "An analysis of automatic equalizers for orthogonally multiplexed QAM systems," *IEEE Transactions on Communications*, vol. COM-28, pp. 73–83, January 1980.

[21] P. Bello, "Selective fading limitations of the KATHRYN modem and some system design considerations," *IEEE Transactions on Communications Technology*, vol. COM–13, pp. 320–333, September 1965.

[22] E. Powers and M. Zimmermann, "A digital implementation of a multichannel data modem," in *Proceedings of the IEEE International Conference on Communications*, (Philadelphia, USA), 1968.

[23] R. Chang and R. Gibby, "A theoretical study of performance of an orthogonal multiplexing data transmission scheme," *IEEE Transactions on Communication Technology*, vol. COM–16, pp. 529–540, August 1968.

[24] B. R. Saltzberg, "Performance of an efficient parallel data transmission system," *IEEE Transactions on Communication Technology*, pp. 805–813, December 1967.

[25] K. Fazel and G. Fettweis, eds., *Multi-Carrier Spread-Spectrum*. Dordrecht: Kluwer, 1997. ISBN 0-7923-9973-0.

[26] F. Classen and H. Meyr, "Synchronisation algorithms for an OFDM system for mobile communications," in *Codierung für Quelle, Kanal und Übertragung*, no. 130 in ITG Fachbericht, (Berlin), pp. 105–113, VDE–Verlag, 1994.

[27] F. Classen and H. Meyr, "Frequency synchronisation algorithms for OFDM systems suitable for communication over frequency selective fading channels," in *Proceedings of IEEE VTC '94*, (Stockholm, Sweden), pp. 1655–1659, IEEE, 8–10 June 1994.

[28] R. van Nee and R. Prasad, *OFDM for Wireless Multimedia Communications*. London: Artech House Publishers, 2000.

[29] P. Vandenameele, L. van der Perre, and M. Engels, *Space Division Multiple Access for Wireless Local Area Networks*. Kluwer, 2001.

[30] R. W. Chang, *U.S. Patent No. 3,488,445: Orthogonal Frequency Division Multiplexing*, filed November 14, 1966, issued January 6, 1970.

[31] W. E. Keasler, D. L. Bitzer, and P. T. Tucker, *U.S. Patent No. 4,206,320: High-speed Modem Suitable for Operating with a Switched Network*, filed August 21, 1978, issued June 3, 1980.

[32] M. Alard and R. Lassalle, "Principles of modulation and channel coding for digital broadcasting for mobile receivers," *EBU Technical Review*, pp. 168–190, August 1987.

[33] J. M. Cioffi, *A Multicarrier Primer*, November 1991. ANSI T1E1.4/91-157.

[34] ANSI Committee T1-Telecommunications, *A Technical Report on High-Bit-Rate Digital Subscriber Lines (HDSL)*, February 1994. Technical Report No. 28.

[35] European Telecommunication Standard Institute, *Digital Audio Broadcasting (DAB);DAB to mobile, portable and fixed Receivers*, February 1995. ETSI ETS 300 401 ed.1.

[36] European Telecommunication Standard Institute, *Radio Equipment and Systems (RES);HIgh PErformance Radio Local Area Network (HIPERLAN) Type 1;Functional specification*, October 1996. ETSI ETS 300 652 ed.1.

[37] European Telecommunication Standard Institute, *Digital Video Broadcasting (DVB);Framing structure, channel coding and modulation for digital terrestrial television (DVB-T)*, March 1997. ETSI ETS 300 744 ed.1.

[38] *Very-high-speed Digital Subscriber Lines: System Requirements*, September 1998. ANSI T1E1.4 VDSL SR: 98-043R5.

[39] European Telecommunication Standard Institute, *Transmission and Multiplexing (TM);Access transmission systems on metallic access cables;Very high speed Digital Subscriber Line (VDSL);Part 1: Functional requirements*, June 1998. ETSI TS 101 270-1 V1.1.2.

[40] European Telecommunication Standard Institute, *Broadband Radio Access Networks (BRAN);Inventory of broadband radio technologies and techniques*, May 1998. ETSI TR 101 173 V1.1.1.

[41] Institute of Electrical and Electronics Engineers, *IEEE Standard 802.11a: Wireless LAN Medium Access Control (MAC) and Physical Layer (PHY) specifications: high-speed physical layer in the 5 GHz band*, 1999.

[42] Institute of Electrical and Electronics Engineers, *IEEE Standard 802.11g: Wireless LAN Medium Access Control (MAC) and Physical Layer (PHY) specifications*, 2003.

[43] European Telecommunication Standard Institute, *Digital Video Broadcasting (DVB);Transmission System for Handheld Terminals (DVB-H)*, November 2004. ETSI EN 302 304 V1.1.1.

[44] Institute of Electrical and Electronics Engineers, *IEEE Standard 802.16: Air Interface for Fixed Broadband Wireless Access Systems*, 2004.

[45] Institute of Electrical and Electronics Engineers, *IEEE Candidate Standard 802.11n: Wireless LAN Medium Access Control (MAC) and Physical Layer (PHY) specifications*, 2004. http://grouper.ieee.org/groups/802/11/Reports/tgn_update.htm.

[46] Institute of Electrical and Electronics Engineers, *IEEE Candidate Standard 802.15.3a: Wireless Medium Access Control (MAC) and Physical Layer (PHY) specifications for high rate Wireless Personal Area Networks (WPANs) involving imaging and multimedia*, 2004. http://www.ieee802.org/15/pub/TG3a.html.

[47] M. Yabusaki, "Asia Pacific Viewpoint and Activities: Introduction." 4G Forum, 27 May 2003.

[48] S. Shepherd, P. van Eetvelt, C. Wyatt-Millington, and S. Barton, "Simple coding scheme to reduce peak factor in QPSK multicarrier modulation," *Electronics Letters*, vol. 31, pp. 1131–1132, July 1995.

[49] A. E. Jones, T. A. Wilkinson, and S. K. Barton, "Block coding scheme for reduction of peak to mean envelope power ratio of multicarrier transmission schemes," *Electronics Letters*, vol. 30, pp. 2098–2099, December 1994.

[50] D. Wulich, "Reduction of peak to mean ratio of multicarrier modulation by cyclic coding," *Electronics Letters*, vol. 32, pp. 432–433, 1996.

[51] S. Müller and J. Huber, "Vergleich von OFDM–Verfahren mit reduzierter Spitzenleistung," in *2. OFDM–Fachgespräch in Braunschweig*, 1997.

[52] M. Pauli and H.-P. Kuchenbecker, "Neue Aspekte zur Reduzierung der durch Nicht-linearitäten hervorgerufenen Außerbandstrahlung eines OFDM–Signals," in *2. OFDM–Fachgespräch in Braunschweig*, 1997.

[53] T. May and H. Rohling, "Reduktion von Nachbarkanalstörungen in OFDM–Funkübertragungssystemen," in *2. OFDM–Fachgespräch in Braunschweig*, 1997.

[54] D. Wulich, "Peak factor in orthogonal multicarrier modulation with variable levels," *Electronics Letters*, vol. 32, no. 20, pp. 1859–1861, 1996.

[55] H. Schmidt and K. Kammeyer, "Adaptive Subträgerselektion zur Reduktion des Crest faktors bei OFDM," in *3. OFDM Fachgespräch in Braunschweig*, 1998.

[56] R. Dinis and A. Gusmao, "Performance evaluation of OFDM transmission with conventional and 2-branch combining power amplification schemes," in *Proceeding of IEEE Global Telecommunications Conference, Globecom 96*, (London, UK), pp. 734–739, IEEE, 18–22 November 1996.

[57] R. Dinis, P. Montezuma, and A. Gusmao, "Performance trade-offs with quasi-linearly amplified OFDM through a 2-branch combining technique," in *Proceedings of IEEE VTC'96*, (Atlanta, GA, USA), pp. 899–903, IEEE, 28 April–1 May 1996.

[58] R. Dinis, A. Gusmao, and J. Fernandes, "Adaptive transmission techniques for the mobile broadband system," in *Proceeding of ACTS Mobile Communication Summit '97*, (Aalborg, Denmark), pp. 757–762, ACTS, 7–10 October 1997.

[59] B. Daneshrad, L. Cimini Jr., and M. Carloni, "Clustered-OFDM transmitter implementation," in *Proceedings of IEEE International Symposium on Personal, Indoor, and Mobile Radio Communications (PIMRC'96)*, (Taipei, Taiwan), pp. 1064–1068, IEEE, 15–18 October 1996.

[60] M. Okada, H. Nishijima, and S. Komaki, "A maximum likelihood decision based nonlinear distortion compensator for multi-carrier modulated signals," *IEICE Transactions on Communications*, vol. E81B, no. 4, pp. 737–744, 1998.

[61] R. Dinis and A. Gusmao, "Performance evaluation of a multicarrier modulation technique allowing strongly nonlinear amplification," in *Proceedings of ICC 1998*, pp. 791–796, IEEE, 1998.

[62] T. Pollet, M. van Bladel, and M. Moeneclaey, "BER sensitivity of OFDM systems to carrier frequency offset and wiener phase noise," *IEEE Transactions on Communications*, vol. 43, pp. 191–193, February/March/April 1995.

[63] H. Nikookar and R. Prasad, "On the sensitivity of multicarrier transmission over multipath channels to phase noise and frequency offset," in *Proceedings of IEEE International Symposium on Personal, Indoor, and Mobile Radio Communications (PIMRC'96)*, (Taipei, Taiwan), pp. 68–72, IEEE, 15–18 October 1996.

[64] W. Warner and C. Leung, "OFDM/FM frame synchronization for mobile radio data communication," *IEEE Transactions on Vehicular Technology*, vol. 42, pp. 302–313, August 1993.

[65] H. Sari, G. Karam, and I. Jeanclaude, "Transmission techniques for digital terrestrial TV broadcasting," *IEEE Communications Magazine*, pp. 100–109, February 1995.

[66] P. Moose, "A technique for orthogonal frequency division multiplexing frequency offset correction," *IEEE Transactions on Communications*, vol. 42, pp. 2908–2914, October 1994.

[67] K. Brüninghaus and H. Rohling, "Verfahren zur Rahmensynchronisation in einem OFDM-System," in *3. OFDM Fachgespräch in Braunschweig*, 1998.

[68] F. Daffara and O. Adami, "A new frequency detector for orthogonal multicarrier transmission techniques," in *Proceedings of IEEE Vehicular Technology Conference (VTC'95)*, (Chicago, USA), pp. 804–809, IEEE, 15–28 July 1995.

[69] M. Sandell, J.-J. van de Beek, and P. Börjesson, "Timing and frequency synchronisation in OFDM systems using the cyclic prefix," in *Proceedings of International Symposium on Synchronisation*, (Essen, Germany), pp. 16–19, 14–15 December 1995.

[70] N. Yee, J.-P. Linnartz, and G. Fettweis, "Multicarrier CDMA in indoor wireless radio networks," in *PIMRC'93*, pp. 109–113, 1993.

[71] A. Chouly, A. Brajal, and S. Jourdan, "Orthogonal multicarrier techniques applied to direct sequence spread spectrum CDMA systems," in *Proceedings of the IEEE Global Telecommunications Conference 1993*, (Houston, TX, USA), pp. 1723–1728, 29 November - 2 December 1993.

[72] G. Fettweis, A. Bahai, and K. Anvari, "On multi-carrier code division multiple access (MC-CDMA) modem design," in *Proceedings of IEEE VTC '94*, (Stockholm, Sweden), pp. 1670–1674, IEEE, 8–10 June 1994.

[73] K. Fazel and L. Papke, "On the performance of convolutionally-coded CDMA/OFDM for mobile communication system," in *PIMRC'93*, pp. 468–472, 1993.

[74] R. Prasad and S. Hara, "Overview of multicarrier CDMA," *IEEE Communications Magazine*, pp. 126–133, December 1997.

[75] B.-J. Choi, E.-L. Kuan, and L. Hanzo, "Crest–factor study of MC-CDMA and OFDM," in *Proceeding of VTC'99 (Fall)*, vol. 1, (Amsterdam, Netherlands), pp. 233–237, IEEE, 19–22 September 1999.

[76] P. Höher, "TCM on frequency-selective land-mobile fading channels," in *International Workshop on Digital Communications*, (Tirrenia, Italy), pp. 317–328, September 1991.

[77] J. Chow, J. Cioffi, and J. Bingham, "Equalizer training algorithms for multicarrier modulation systems.," in *International Conference on Communications*, (Geneva, Switzerland), pp. 761–765, IEEE, May 1993.

[78] S. Wilson, R. E. Khayata, and J. Cioffi, "16QAM Modulation with Orthogonal Frequency Division Multiplexing in a Rayleigh-Fading Environment," in *Vehicular Technology Conference*, vol. 3, (Stockholm, Sweden), pp. 1660–1664, IEEE, June 1994.

[79] J.-J. van de Beek, O. Edfors, M. Sandell, S. Wilson, and P. Börjesson, "On channel estimation in OFDM systems," in *Proceedings of Vehicular Technology Conference*, vol. 2, (Chicago, IL USA), pp. 815–819, IEEE, July 1995.

[80] O. Edfors, M. Sandell, J. van den Beek, S. K. Wilson, and P. Börjesson, "OFDM Channel Estimation by Singular Value Decomposition," in *Proceedings of Vehicular Technology Conference*, vol. 2, (Atlanta, GA USA), pp. 923–927, IEEE, April 28 - May 1 1996.

[81] P. Frenger and A. Svensson, "A Decision Directed Coherent Detector for OFDM," in *Proceedings of Vehicular Technology Conference*, vol. 3, (Atlanta, GA USA), pp. 1584–1588, IEEE, April 28 - May 1 1996.

[82] V. Mignone and A. Morello, "CD3-OFDM: A Novel Demodulation Scheme for Fixed and Mobile Receivers," *IEEE Transactions on Communications*, vol. 44, pp. 1144–1151, September 1996.

[83] F. Tufvesson and T. Maseng, "Pilot Assisted Channel Estimation for OFDM in Mobile Cellular Systems," in *Proceedings of Vehicular Technology Conference*, vol. 3, (Phoenix, Arizona), pp. 1639–1643, IEEE, May 4-7 1997.

[84] P. Höher, S. Kaiser, and P. Robertson, "Two-dimensional pilot-symbol-aided channel estimation by Wiener filtering," in *International Conference on Acoustics, Speech and Signal Processing*, (Munich, Germany), pp. 1845–1848, IEEE, April 1997.

[85] P. Höher, S. Kaiser, and P. Robertson, "Pilot–symbol–aided channel estimation in time and frequency," in *Proceedings of Global Telecommunications Conference: The Mini–Conf.*, (Phoenix, AZ), pp. 90–96, IEEE, November 1997.

[86] Y. Li, L. Cimini, and N. Sollenberger, "Robust Channel Estimation for OFDM Systems with Rapid Dispersive Fading Channels," *IEEE Transactions on Communications*, vol. 46, pp. 902–915, April 1998.

[87] O. Edfors, M. Sandell, J.-J. van den Beek, S. Wilson, and P. Börjesson, "OFDM Channel Estimation by Singular Value Decomposition," *IEEE Transactions on Communications*, vol. 46, pp. 931–939, July 1998.

[88] F. Tufvesson, M. Faulkner, and T. Maseng, "Pre-Compensation for Rayleigh Fading Channels in Time Division Duplex OFDM Systems," in *Proceedings of 6th International Workshop on Intelligent Signal Processing and Communications Systems*, (Melbourne, Australia), pp. 57–33, IEEE, November 5-6 1998.

[89] M. Itami, M. Kuwabara, M. Yamashita, H. Ohta, and K. Itoh, "Equalization of Orthogonal Frequency Division Multiplexed Signal by Pilot Symbol Assisted Multipath Estimation," in *Proceedings of Global Telecommunications Conference*, vol. 1, (Sydney, Australia), pp. 225–230, IEEE, November 8-12 1998.

[90] L. Hanzo, M. Münster, B. Choi, and T. Keller, *OFDM and MC-CDMA for Broadband Multi-user Communications, WLANs and Broadcasting*. John Wiley and IEEE Press, 2003. 992 pages.

[91] E. Al-Susa and R. Ormondroyd, "A Predictor-Based Decision Feedback Channel Estimation Method for COFDM with High Resilience to Rapid Time-Variations," in *Proceedings of Vehicular Technology Conference*, vol. 1, (Amsterdam, Netherlands), pp. 273–278, IEEE, September 19-22 1999.

[92] B. Yang, K. Letaief, R. Cheng, and Z. Cao, "Robust and Improved Channel Estimation for OFDM Systems in Frequency Selective Fading Channels," in *Proceedings of Global Telecommunications Conference*, vol. 5, (Rio de Janeiro, Brazil), pp. 2499–2503, IEEE, December 5-9 1999.

[93] Y. Li, "Pilot-Symbol-Aided Channel Estimation for OFDM in Wireless Systems," *IEEE Transactions on Vehicular Technology*, vol. 49, pp. 1207–1215, July 2000.

[94] B. Yang, K. Letaief, R. Cheng, and Z. Cao, "Channel Estimation for OFDM Transmission in Multipath Fading Channels Based on Parametric Channel Modeling," *IEEE Transactions on Communications*, vol. 49, pp. 467–479, March 2001.

[95] S. Zhou and G. Giannakis, "Finite-Alphabet Based Channel Estimation for OFDM and Related Multicarrier Systems," *IEEE Transactions on Communications*, vol. 49, pp. 1402–1414, August 2001.

[96] X. Wang and K. Liu, "OFDM Channel Estimation Based on Time-Frequency Polynomial Model of Fading Multipath Channel," in *Proceedings of Vehicular Technology Conference*, vol. 1, (Atlantic City, NJ USA), pp. 460–464, IEEE, October 7-11 2001.

[97] B. Yang, Z. Cao, and K. Letaief, "Analysis of Low-Complexity Windowed DFT-Based MMSE Channel Estimator for OFDM Systems," *IEEE Transactions on Communications*, vol. 49, pp. 1977–1987, November 2001.

[98] B. Lu and X. Wang, "Bayesian Blind Turbo Receiver for Coded OFDM Systems with Frequency Offset and Frequency-Selective Fading," *IEEE Journal on Selected Areas in Communications*, vol. 19, pp. 2516–2527, December 2001.

[99] Y. Li and N. Sollenberger, "Clustered OFDM with Channel Estimation for High Rate Wireless Data," *IEEE Transactions on Communications*, vol. 49, pp. 2071–2076, December 2001.

[100] M. Morelli and U. Mengali, "A Comparison of Pilot-Aided Channel Estimation Methods for OFDM Systems," *IEEE Transactions on Signal Processing*, vol. 49, pp. 3065–3073, December 2001.

[101] M.-X. Chang and Y. Su, "Model-Based Channel Estimation for OFDM Signals in Rayleigh Fading," *IEEE Transactions on Communications*, vol. 50, pp. 540–544, April 2002.

[102] M. Necker and G. Stüber, "Totally Blind Channel Estimation for OFDM over Fast Varying Mobile Channels," in *Proceedings of International Conference on Communications*, (New York, NY USA), IEEE, April 28 - May 2 2002.

[103] B. Yang, Z. Cao, and K. Letaief, "Low Complexity Channel Estimator Based on Windowed DFT and Scalar Wiener Filter for OFDM Systems," in *Proceedings of International Conference on Communications*, vol. 6, (Helsinki, Finland), pp. 1643–1647, IEEE, June 11-14 2001.

[104] J. Deller, J. Proakis, and J. Hansen, *Discrete-Time Processing of Speech Signals*. Macmillan Publishing Company, 1993.

[105] L. Hanzo, F. Somerville, and J. Woodard, *Voice Compression and Communications*. IEEE Press Wiley Inter-Science, 2001.

[106] A. Duel-Hallen, S. Hu, and H. Hallen, "Long Range Prediction of Fading Signals," *IEEE Signal Processing Magazine*, vol. 17, pp. 62–75, May 2000.

[107] F. Tufvesson, *Design of Wireless Communication Systems - Issues on Synchronization, Channel Estimation and Multi-Carrier Systems,*. Department of Applied Electronics, Lund University, Sweden, 2000.

[108] W. Press, S. Teukolshy, W. Vetterling, and B. Flannery, *Numerical Recipes in C*. Cambridge University Press, 1992.

[109] T. Moon and W. Stirling, *Mathematical Methods and Algorithms for Signal Processing*. Prentice Hall, 2000.

[110] Y. Li, N. Seshadri, and S. Ariyavisitakul, "Channel Estimation for OFDM Systems with Transmitter Diversity in Mobile Wireless Channels," *IEEE Journal on Selected Areas in Communications*, vol. 17, pp. 461–471, March 1999.

[111] W. Jeon, K. Paik, and Y. Cho, "An Efficient Channel Estimation Technique for OFDM Systems with Transmitter Diversity," in *Proceedings of International Symposium on Personal, Indoor and Mobile Radio Communications*, vol. 2, (Hilton London Metropole Hotel, London, UK), pp. 1246–1250, IEEE, September 18-21 2000.

[112] Y. Li, "Optimum Training Sequences for OFDM Systems with Multiple Transmit Antennas," in *Proc. of Global Telecommunications Conference*, vol. 3, (San Francisco, United States), pp. 1478–1482, IEEE, November 27 - December 1 2000.

[113] A. Mody and G. Stüber, "Parameter Estimation for OFDM with Transmit Receive Diversity," in *Proceedings of Vehicular Technology Conference*, vol. 2, (Rhodes, Greece), pp. 820–824, IEEE, May 6-9 2001.

[114] Y. Gong and K. Letaief, "Low Rank Channel Estimation for Space-Time Coded Wideband OFDM Systems," in *Proceedings of Vehicular Technology Conference*, vol. 2, (Atlantic City Convention Center, Atlantic City, NJ USA), pp. 772–776, IEEE, October 7-11 2001.

[115] W. Jeon, K. Paik, and Y. Cho, "Two-Dimensional MMSE Channel Estimation for OFDM Systems with Transmitter Diversity," in *Proceedings of Vehicular Technology Conference*, vol. 3, (Atlantic City Convention Center, Atlantic City, NJ USA), pp. 1682–1685, IEEE, October 7-11 2001.

[116] F. Vook and T. Thomas, "MMSE Multi-User Channel Estimation for Broadband Wireless Communications," in *Proceedings of Global Telecommunications Conference*, vol. 1, (San Antonio, Texas, USA), pp. 470–474, IEEE, November 25-29 2001.

[117] Y. Xie and C. Georghiades, "An EM-based Channel Estimation Algorithm for OFDM with Transmitter Diversity," in *Proceedings of Global Telecommunications Conference*, vol. 2, (San Antonio, Texas, USA), pp. 871–875, IEEE, November 25-29 2001.

[118] Y. Li, "Simplified Channel Estimation for OFDM Systems with Multiple Transmit Antennas," *IEEE Transactions on Wireless Communications*, vol. 1, pp. 67–75, January 2002.

[119] H. Bölcskei, R. Heath, and A. Paulraj, "Blind Channel Identification and Equalization in OFDM-Based Multi-Antenna Systems," *IEEE Transactions on Signal Processing*, vol. 50, pp. 96–109, January 2002.

[120] H. Minn, D. Kim, and V. Bhargava, "A Reduced Complexity Channel Estimation for OFDM Systems with Transmit Diversity in Mobile Wireless Channels," *IEEE Transactions on Wireless Communications*, vol. 50, pp. 799–807, May 2002.

[121] S. Slimane, "Channel Estimation for HIPERLAN/2 with Transmitter Diversity," in *International Conference on Communications*, (New York, NY USA), IEEE, April 28 - May 2 2002.

[122] C. Komninakis, C. Fragouli, A. Sayed, and R. Wesel, "Multi-Input Multi-Output Fading Channel Tracking and Equalization Using Kalman Estimation," *IEEE Transactions on Signal Processing*, vol. 50, pp. 1065–1076, May 2002.

[123] G. Foschini, "Layered Space-Time Architecture for Wireless Communication in a Fading Environment when using Multi-Element Antennas"," *Bell Labs Technical Journal*, vol. Autumn, pp. 41–59, 1996.

[124] F. Vook and K. Baum, "Adaptive antennas for OFDM," in *Proceedings of IEEE Vehicular Technology Conference (VTC'98)*, vol. 2, (Ottawa, Canada), pp. 608–610, IEEE, 18–21 May 1998.

[125] X. Wang and H. Poor, "Robust Adaptive Array for Wireless Communications," *IEEE Transactions on Communications*, vol. 16, pp. 1352–1366, October 1998.

[126] K.-K. Wong, R.-K. Cheng, K. Letaief, and R. Murch, "Adaptive Antennas at the Mobile and Base Station in an OFDM/TDMA System," in *Proceedings of Global Telecommunications Conference*, vol. 1, (Sydney, Australia), pp. 183–190, IEEE, November 8-12 1998.

[127] Y. Li and N. Sollenberger, "Interference Suppression in OFDM Systems using Adaptive Antenna Arrays," in *Proceedings of Global Telecommunications Conference*, vol. 1, (Sydney, Australia), pp. 213–218, IEEE, November 8-12 1998.

[128] G. Golden, G. Foschini, R. Valenzuela, and P. Wolniansky, "Detection Algorithms and Initial Laboratory Results using V-BLAST Space-Time Communication Architecture," *IEE Electronics Letters*, vol. 35, pp. 14–16, January 1999.

[129] Y. Li and N. Sollenberger, "Adaptive Antenna Arrays for OFDM Systems with Cochannel Interference," *IEEE Transactions on Communications*, vol. 47, pp. 217–229, February 1999.

[130] P. Vandenameele, L. Van der Perre, M. Engels, and H. Man, "A novel class of uplink OFDM/SDMA algorithms for WLAN," in *Proceedings of Global Telecommunications Conference — Globecom'99*, vol. 1, (Rio de Janeiro, Brazil), pp. 6–10, IEEE, 5–9 December 1999.

[131] M. Speth, A. Senst, and H. Meyr, "Low complexity space-frequency MLSE for multi-user COFDM," in *Proceedings of Global Telecommunications Conference — Globecom'99*, vol. 1, (Rio de Janeiro, Brazil), pp. 2395–2399, IEEE, 5–9 December 1999.

[132] C. H. Sweatman, J. Thompson, B. Mulgrew, and P. Grant, "A Comparison of Detection Algorithms including BLAST for Wireless Communication using Multiple Antennas," in *Proceedings of International Symposium on Personal, Indoor and Mobile Radio Communications*, vol. 1, (Hilton London Metropole Hotel, London, UK), pp. 698–703, IEEE, September 18-21 2000.

[133] R. van Nee, A. van Zelst, and G. Awater, "Maximum Likelihood Decoding in a Space-Division Multiplexing System," in *Proceedings of Vehicular Technology Conference*, vol. 1, (Tokyo, Japan), pp. 6–10, IEEE, May 15-18 2000.

[134] G. Awater, A. van Zelst, and R. van Nee, "Reduced Complexity Space Division Multiplexing Receivers," in *Proceedings of Vehicular Technology Conference*, vol. 1, (Tokyo, Japan), pp. 11–15, IEEE, May 15-18 2000.

[135] A. van Zelst, R. van Nee, and G. Awater, "Space Division Multiplexing (SDM) for OFDM systems," in *Proceedings of Vehicular Technology Conference*, vol. 2, (Tokyo, Japan), pp. 1070–1074, IEEE, May 15-18 2000.

[136] P. Vandenameele, L. V. D. Perre, M. Engels, B. Gyselinckx, and H. D. Man, "A Combined OFDM/SDMA Approach," *IEEE Journal on Selected Areas in Communications*, vol. 18, pp. 2312–2321, November 2000.

[137] X. Li, H. Huang, A. Lozano, and G. Foschini, "Reduced-Complexity Detection Algorithms for Systems Using Multi-Element Arrays," in *Proc. of Global Telecommunications Conference*, vol. 2, (San Francisco, United States), pp. 1072–1076, IEEE, November 27 - December 1 2000.

[138] C. Degen, C. Walke, A. Lecomte, and B. Rembold, "Adaptive MIMO Techniques for the UTRA-TDD Mode," in *Proceedings of Vehicular Technology Conference*, vol. 1, (Rhodes, Greece), pp. 108–112, IEEE, May 6-9 2001.

[139] X. Zhu and R. Murch, "Multi-Input Multi-Output Maximum Likelihood Detection for a Wireless System," in *Proceedings of Vehicular Technology Conference*, vol. 1, (Rhodes, Greece), pp. 137–141, IEEE, May 6-9 2001.

[140] J. Li, K. Letaief, R. Cheng, and Z. Cao, "Joint Adaptive Power Control and Detection in OFDM/SDMA Wireless LANs," in *Proceedings of Vehicular Technology Conference*, vol. 1, (Rhodes, Greece), pp. 746–750, IEEE, May 6-9 2001.

[141] F. Rashid-Farrokhi, K. Liu, and L. Tassiulas, "Transmit Beamforming and Power Control for Cellular Wireless Systems," *IEEE Journal on Selected Areas in Communications*, vol. 16, pp. 1437–1450, October 1998.

[142] A. van Zelst, R. van Nee, and G. Awater, "Turbo-BLAST and its Performance," in *Proceedings of Vehicular Technology Conference*, vol. 2, (Rhodes, Greece), pp. 1282–1286, IEEE, May 6-9 2001.

[143] A. Benjebbour, H. Murata, and S. Yoshida, "Performance of Iterative Successive Detection Algorithm with Space-Time Transmission," in *Proceedings of Vehicular Technology Conference*, vol. 2, (Rhodes, Greece), pp. 1287–1291, IEEE, May 6-9 2001.

[144] M. Sellathurai and S. Haykin, "A Simplified Diagonal BLAST Architecture with Iterative Parallel-Interference Cancellation Receivers," in *Proceedings of International Conference on Communications*, vol. 10, (Helsinki, Finland), pp. 3067–3071, IEEE, June 11-14 2001.

[145] A. Bhargave, R. Figueiredo, and T. Eltoft, "A Detection Algorithm for the V-BLAST System," in *Proceedings of Global Telecommunications Conference*, vol. 1, (San Antonio, Texas, USA), pp. 494–498, IEEE, November 25-29 2001.

[146] S. Thoen, L. Deneire, L. V. D. Perre, and M. Engels, "Constrained Least Squares Detector for OFDM/SDMA-based Wireless Networks," in *Proceedings of Global Telecommunications Conference*, vol. 2, (San Antonio, Texas, USA), pp. 866–870, IEEE, November 25-29 2001.

[147] Y. Li and Z.-Q. Luo, "Parallel Detection for V-BLAST System," in *Proceedings of International Conference on Communications*, (New York, NY USA), IEEE, April 28 - May 2 2002.

[148] Y. Li and N. Sollenberger, "Interference suppression in OFDM systems using adaptive antenna arrays," in *Proceeding of Globecom'98*, (Sydney, Australia), pp. 213–218, IEEE, 8–12 November 1998.

[149] Y. Li and N. Sollenberger, "Adaptive antenna arrays for OFDM systems with cochannel interference," *IEEE Transactions on Communications*, vol. 47, pp. 217–229, February 1999.

[150] Y. Li, L. Cimini, and N. Sollenberger, "Robust channel estimation for OFDM systems with rapid dispersive fading channels," *IEEE Transactions on Communications*, vol. 46, pp. 902–915, April 1998.

[151] C. Kim, S. Choi, and Y. Cho, "Adaptive beamforming for an OFDM system," in *Proceeding of VTC'99 (Spring)*, (Houston, TX, USA), IEEE, 16–20 May 1999.

[152] L. Lin, L. Cimini Jr., and J.-I. Chuang, "Turbo codes for OFDM with antenna diversity," in *Proceeding of VTC'99 (Spring)*, (Houston, TX, USA), IEEE, 16–20 May 1999.

[153] M. Münster, T. Keller, and L. Hanzo, "Co–channel interference suppression assisted adaptive OFDM in interference limited environments," in *Proceeding of VTC'99 (Fall)*, vol. 1, (Amsterdam, Netherlands), pp. 284–288, IEEE, 19–22 September 1999.

[154] S. Verdu, *Multiuser Detection*. Cambridge University Press, 1998.

[155] J. Litva and T.-Y. Lo, *Digital Beamforming in Wireless Communications*. London: Artech House Publishers, 1996.

[156] P. Vandenameele, L. Van der Perre, M. Engels, B. Gyselinckx, and H. Man, "A novel class of uplink OFDM/SDMA algorithms: A statistical performance analysis," in

Proceedings of Vehicular Technology Conference, vol. 1, (Amsterdam, Netherlands), pp. 324–328, IEEE, 19–22 September 1999.

[157] F. Mueller-Roemer, "Directions in audio broadcasting," *Journal of the Audio Engineering Society*, vol. 41, pp. 158–173, March 1993.

[158] G. Plenge, "DAB — a new radio broadcasting system — state of development and ways for its introduction," *Rundfunktech. Mitt.*, vol. 35, no. 2, 1991.

[159] ETSI, *Digital Audio Broadcasting (DAB)*, 2nd ed., May 1997. ETS 300 401.

[160] ETSI, *Digital Video Broadcasting (DVB); Framing structure, channel coding and modulation for digital terrestrial television*, August 1997. EN 300 744 V1.1.2.

[161] P. Chow, J. Tu, and J. Cioffi, "A discrete multitone transceiver system for HDSL applications," *IEEE Journal on Selected Areas in Communications*, vol. 9, pp. 895–908, August 1991.

[162] P. Chow, J. Tu, and J. Cioffi, "Performance evaluation of a multichannel transceiver system for ADSL and VHDSL services," *IEEE Journal on Selected Areas in Communications*, vol. 9, pp. 909–919, August 1991.

[163] K. Sistanizadeh, P. Chow, and J. Cioffi, "Multi-tone transmission for asymmetric digital subscriber lines (ADSL)," in *Proceedings of ICC'93*, pp. 756–760, IEEE, 1993.

[164] ANSI, *ANSI/T1E1.4/94-007, Asymmetric Digital Subscriber Line (ADSL) Metallic Interface.*, August 1997.

[165] A. Burr and P. Brown, "Application of OFDM to powerline telecommunications," in *3rd International Symposium on Power-Line Communications*, (Lancaster, UK), 30 March – 1 April 1999.

[166] M. Deinzer and M. Stoger, "Integrated PLC-modem based on OFDM," in *3rd International Symposium on Power-Line Communications*, (Lancaster, UK), 30 March – 1 April 1999.

[167] R. Prasad and H. Harada, "A novel OFDM based wireless ATM system for future broadband multimedia communications," in *Proceeding of ACTS Mobile Communication Summit '97*, (Aalborg, Denmark), pp. 757–762, ACTS, 7–10 October 1997.

[168] C. Ciotti and J. Borowski, "The AC006 MEDIAN project — overview and state–of–the–art," in *Proc. ACTS Summit '96*, (Granada, Spain), pp. 362–367, 27–29 November 1996.

[169] J. Borowski, S. Zeisberg, J. Hübner, K. Koora, E. Bogenfeld, and B. Kull, "Performance of OFDM and comparable single carrier system in MEDIAN demonstrator 60GHz channel," in *Proceeding of ACTS Mobile Communication Summit '97*, (Aalborg, Denmark), pp. 653–658, ACTS, 7–10 October 1997.

[170] M. D. Benedetto, P. Mandarini, and L. Piazzo, "Effects of a mismatch in the in–phase and in–quadrature paths, and of phase noise, in QDCPSK-OFDM modems," in *Proceeding of ACTS Mobile Communication Summit '97*, (Aalborg, Denmark), pp. 769–774, ACTS, 7–10 October 1997.

[171] T. Rautio, M. Pietikainen, J. Niemi, J. Rautio, K. Rautiola, and A. Mammela, "Architecture and implementation of the 150 Mbit/s OFDM modem (invited paper)," in *IEEE*

Benelux Joint Chapter on Communications and Vehicular Technology, 6th Symposium on Vehicular Technology and Communications, (Helsinki, Finland), p. 11, 12–13 October 1998.

[172] J. Ala-Laurila and G. Awater, "The magic WAND — wireless ATM network demonstrator system," in *Proceeding of ACTS Mobile Communication Summit '97*, (Aalborg, Denmark), pp. 356–362, ACTS, 7–10 October 1997.

[173] J. Aldis, E. Busking, T. Kleijne, R. Kopmeiners, R. van Nee, R. Mann-Pelz, and T. Mark, "Magic into reality, building the WAND modem," in *Proceeding of ACTS Mobile Communication Summit '97*, (Aalborg, Denmark), pp. 775–780, ACTS, 7–10 October 1997.

[174] E. Hallmann and H. Rohling, "OFDM-Vorschläge für UMTS," in *3. OFDM Fachgespräch in Braunschweig*, 1998.

[175] "Universal mobile telecommunications system (UMTS); UMTS terrestrial radio access (UTRA); concept evaluation," tech. rep., ETSI, 1997. TR 101 146.

[176] B. M. Hochwald and S. ten Brink, "Achieving near-capacity on a multiple-antenna channel," *IEEE Transactions on Communications*, vol. 51, pp. 389–399, March 2003.

[177] L. Hanzo, W. Webb, and T. Keller, *Single- and Multi-Carrier Quadrature Amplitude Modulation: Principles and Applications for Personal Communications, WLANs and Broadcasting*. John Wiley and IEEE Press, 2000.

[178] H. Kolb Private Communications.

[179] J. Lindner Private Communications.

[180] W. Webb and L. Hanzo, *Modern Quadrature Amplitude Modulation: Principles and Applications for Wireless Communications*. IEEE Press-Pentech Pressm, 1994.

[181] J. K. Cavers, "An Analysis of Pilot Symbol Assisted Modulation for Rayleigh Fading Channels," *IEEE Transactions on Vehicular Technology*, vol. 40, pp. 686–693, November 1991.

[182] H. Harmuth, *Transmission of Information by Orthogonal Time Functions*. Berlin: Springer Verlag, 1969.

[183] H. Harmuth, "On the transmission of information by orthogonal time functions," *AIEE*, July 1960.

[184] J. Proakis, *Digital Communications*. McGraw-Hill, 1995.

[185] R. O'Neill and L. Lopes, "Performance of amplitude limited multitone signals," in *Proceedings of IEEE VTC '94*, (Stockholm, Sweden), IEEE, 8–10 June 1994.

[186] X. Li and L. Cimini, "Effects of clipping and filtering on the performance of OFDM," in *Proceedings of IEEE VTC'97*, (Phoenix, AZ, USA), pp. 1634–1638, IEEE, 4–7 May 1997.

[187] A. Garcia and M. Calvo, "Phase noise and sub–carrier spacing effects on the performance of an OFDM communications system," *IEEE Communications Letters*, vol. 2, pp. 11–13, January 1998.

[188] W. Robins, *Phase Noise in Signal Sources*, vol. 9 of *IEE Telecommunication series*. Peter Peregrinus Ltd., 1982.

[189] C. Tellambura, Y. Guo, and S. Barton, "Equaliser performance for HIPERLAN in indoor channels," *Wireless Personal Communications*, vol. 3, no. 4, pp. 397–410, 1996.

[190] T. Ojanperä, M. Gudmundson, P. Jung, J. Sköld, R. Pirhonen, G. Kramer, and A. Toskala, "FRAMES: - hybrid multiple access technology," in *Proceedings of IEEE ISSSTA'96*, (Mainz, Germany), pp. 334–338, IEEE, September 1996.

[191] M. Failli, "Digital land mobile radio communications COST 207," tech. rep., European Commission, 1989.

[192] J. Torrance and L. Hanzo, "Comparative study of pilot symbol assisted modem schemes," in *Proceedings of IEE Conference on Radio Receivers and Associated Systems (RRAS'95)*, (Bath, UK), pp. 36–41, IEE, 26–28 September 1995.

[193] R. Hasholzner, C. Drewes, and A. Hutter, "Untersuchungen zur linearen ICI-Kompensation bei OFDM," in *3.OFDM Fachgespräch*, Technische Universität Braunschweig, Germany, Sept. 1998.

[194] W. Jeon, K. Chang, and Y. Cho, "An Equalization Technique for Orthogonal Frequency-Division Multiplexing Systems in Time-Variant Multipath Channels," *IEEE Transactions on Communications*, vol. 47, pp. 27–32, January 1999.

[195] A. Hutter and R. Hasholzner, "Determination of Intercarrier Interference Covariance Matrices and their Application to Advanced Equalization for Mobile OFDM," in 5^{th} *International OFDM-Workshop 2000*, pp. 33/1–33/5, Technische Universität Hamburg-Harburg, Sept. 2000.

[196] M. Ruessel and G. Stüber, "Terrestrial digital video broadcasting for mobile reception using OFDM," *Wireless Pers. Commun.*, vol. 2, no. 3, pp. 45–66, 1995.

[197] M. Münster and L. Hanzo, "MMSE Channel Prediction for Symbol-by-symbol Adaptive OFDM Systems," in 5^{th} *International OFDM-Workshop 2000*, pp. 35/1–35/6, Technische Universität Hamburg-Harburg, September 2000.

[198] K. Fazel, S. Kaiser, P. Robertson, and M. Ruf, "A concept of digital terrestrial television broadcasting," *Wireless Personal Communications*, vol. 2, pp. 9–27, 1995.

[199] J. Kuronen, V.-P. Kaasila, and A. Mammela, "An all-digital symbol tracking algorithm in an OFDM system by using the cyclic prefix," in *Proc. ACTS Summit '96*, (Granada, Spain), pp. 340–345, 27–29 November 1996.

[200] M. Kiviranta and A. Mammela, "Coarse frame synchronization structures in OFDM," in *Proc. ACTS Summit '96*, (Granada, Spain), pp. 464–470, 27–29 November 1996.

[201] Z. Li and A. Mammela, "An all digital frequency synchronization scheme for OFDM systems," in *Proceedings of the IEEE International Symposium on Personal, Indoor and Mobile Radio Communications (PIMRC)*, (Helsinki, Finland), pp. 327–331, 1–4 September 1997.

[202] J. Bingham, "Method and apparatus for correcting for clock and carrier frequency offset, and phase jitter in multicarrier modems." U.S. Patent No. 5206886, 27 April 1993.

[203] T. de Couasnon, R. Monnier, and J. Rault, "OFDM for digital TV broadcasting," *Signal Processing*, vol. 39, pp. 1–32, 1994.

[204] P. Mandarini and A. Falaschi, "SYNC proposals." MEDIAN Design Note, January 1996.

[205] T. Keller and L. Hanzo, "Orthogonal frequency division multiplex synchronisation techniques for wireless local area networks," in *Proceedings of IEEE International Symposium on Personal, Indoor, and Mobile Radio Communications (PIMRC'96)*, vol. 3, (Taipei, Taiwan), pp. 963–967, IEEE, 15–18 October 1996.

[206] R. Steele and W. Webb, "Variable rate QAM for data transmission over Rayleigh fading channels," in *Proceedings of Wireless '91*, (Calgary, Alberta), pp. 1–14, IEEE, 1991.

[207] H. Matsuoka, S. Sampei, N. Morinaga, and Y. Kamio, "Adaptive modulation system with variable coding rate concatenated code for high quality multi-media communications systems," in *Proceedings of IEEE VTC'96*, vol. 1, (Atlanta, GA, USA), pp. 487–491, IEEE, 28 April–1 May 1996.

[208] S.-G. Chua and A. Goldsmith, "Variable-rate variable-power mQAM for fading channels," in *Proceedings of IEEE VTC'96*, (Atlanta, GA, USA), pp. 815–819, IEEE, 28 April–1 May 1996.

[209] D. Pearce, A. Burr, and T. Tozer, "Comparison of counter-measures against slow Rayleigh fading for TDMA systems," in *IEE Colloquium on Advanced TDMA Techniques and Applications*, (London, UK), pp. 9/1–9/6, IEE, 28 October 1996. Digest 1996/234.

[210] V. Lau and M. Macleod, "Variable rate adaptive trellis coded QAM for high bandwidth efficiency applications in Rayleigh fading channels," in *Proceedings of IEEE Vehicular Technology Conference (VTC'98)*, (Ottawa, Canada), pp. 348–352, IEEE, 18–21 May 1998.

[211] J. Torrance and L. Hanzo, "Latency and networking aspects of adaptive modems over slow indoors Rayleigh fading channels," *IEEE Transactions on Vehicular Technology*, vol. 48, no. 4, pp. 1237–1251, 1998.

[212] J. Torrance, L. Hanzo, and T. Keller, "Interference aspects of adaptive modems over slow Rayleigh fading channels," *IEEE Transactions on Vehicular Technology*, vol. 48, pp. 1527–1545, September 1999.

[213] A. Czylwik, "Adaptive OFDM for wideband radio channels," in *Proceeding of IEEE Global Telecommunications Conference, Globecom 96*, (London, UK), pp. 713–718, IEEE, 18–22 November 1996.

[214] P. Chow, J. Cioffi, and J. Bingham, "A practical discrete multitone transceiver loading algorithm for data transmission over spectrally shaped channels," *IEEE Transactions on Communications*, vol. 48, pp. 772–775, 1995.

[215] L. Hanzo, C. Wong, and M. Yee, *Adaptive Wireless Transceivers*. John Wiley, IEEE Press, 2002. (For detailed contents, please refer to http://www-mobile.ecs.soton.ac.uk.).

[216] L. Hanzo, T. H. Liew, and B. L. Yeap, *Turbo Coding, Turbo Equalisation and Space-Time Coding*. Chichester, UK; Piscataway, NJ, USA: John Wiley, IEEE Press, 2002. 766 pages. (For detailed contents, please refer to http://www-mobile.ecs.soton.ac.uk.).

[217] J. Blogh and L. Hanzo, *Third-Generation Systems and Intelligent Networking*. John Wiley and IEEE Press, 2002. (For detailed contents, please refer to http://www-mobile.ecs.soton.ac.uk.).

[218] J. Torrance, *Adaptive Full Response Digital Modulation for Wireless Communications Systems*. PhD thesis, Department of Electronics and Computer Science, University of Southampton, UK, 1997.

[219] K. Miya, O. Kato, K. Homma, T. Kitade, M. Hayashi, and T. Ue, "Wideband CDMA systems in TDD-mode operation for IMT-2000," *IEICE Transactions on Communications*, vol. E81-B, pp. 1317–1326, July 1998.

[220] O. Kato, K. Miya, K. Homma, T. Kitade, M. Hayashi, and M. Watanabe, "Experimental performance results of coherent wideband DS-CDMA with TDD scheme," *IEICE Transactions on Communications.*, vol. E81-B, pp. 1337–1344, July 1998.

[221] T. Keller and L. Hanzo, "Blind-detection assisted sub-band adaptive turbo-coded OFDM schemes," in *Proceeding of VTC'99 (Spring)*, (Houston, TX, USA), pp. 489–493, IEEE, 16–20 May 1999.

[222] J. Torrance and L. Hanzo, "Optimisation of switching levels for adaptive modulation in a slow Rayleigh fading channel," *Electronics Letters*, vol. 32, pp. 1167–1169, 20 June 1996.

[223] C. Berrou, A. Glavieux, and P. Thitimajshima, "Near shannon limit error-correcting coding and decoding: Turbo codes," in *Proceedings of the International Conference on Communications*, (Geneva, Switzerland), pp. 1064–1070, May 1993.

[224] L. Bahl, J. Cocke, F. Jelinek, and J. Raviv, "Optimal decoding of linear codes for minimising symbol error rate," *IEEE Transactions on Information Theory*, vol. 20, pp. 284–287, March 1974.

[225] T. Keller, M. Muenster, and L. Hanzo, "A burst–by–burst adaptive OFDM wideband speech transceiver." submitted to IEEE JSAC, 1999.

[226] T. Keller, J. Woodard, and L. Hanzo, "Turbo-coded parallel modem techniques for personal communications," in *Proceedings of IEEE VTC'97*, (Phoenix, AZ, USA), pp. 2158–2162, IEEE, 4–7 May 1997.

[227] T. Keller and L. Hanzo, "Adaptive orthogonal frequency division multiplexing schemes," in *Proceeding of ACTS Mobile Communication Summit '98*, (Rhodes, Greece), pp. 794–799, ACTS, 8–11 June 1998.

[228] C. E. Shannon, "Communication in the presence of noise," *Proceedings of the I.R.E.*, vol. 37, pp. 10–22, January 1949.

[229] L. Piazzo, "A fast algorithm for near-optimum power and bit allocation in OFDM systems." Electronics Letters, December 1999.

[230] T. Willink and P. Wittke, "Optimization and performance evaluation of multicarrier transmission," *IEEE Transactions on Information Theory*, vol. 43, pp. 426–440, March 1997.

[231] R. Fischer and J. Huber, "A new loading algorithm for discrete multitone transmission," in *Proceeding of IEEE Global Telecommunications Conference, Globecom 96*, (London, UK), pp. 713–718, IEEE, 18–22 November 1996.

[232] S. Lai, R. Cheng, K. Letaief, and R. Murch, "Adaptive trellis coded MQAM and power optimization for OFDM transmission," in *Proceedings of VTC'99 (Spring)*, (Houston, TX, USA), IEEE, 16–20 May 1999.

[233] D. Hughes-Hartogs, "Ensemble modem structure for imperfect transmission media." U.S Patents Nos. 4,679,227 (July 1988) 4,731,816 (March 1988) and 4,833,796 (May 1989).

[234] J. Bingham, "Multicarrier modulation for data transmission: an idea whose time has come," *IEEE Communications Magazine*, pp. 5–14, May 1990.

[235] L. Godara, "Applications of antenna arrays to mobile communications, part II: Beamforming and direction-of-arrival considerations," *Proceedings of the IEEE*, vol. 85, pp. 1193–1245, August 1997.

[236] Y. Li, "Pilot-symbol-aided channel estimation for OFDM in wireless systems," in *Proceedings of VTC'99 (Spring)*, (Houston, TX, USA), IEEE, 16–20 May 1999.

[237] A. Viterbi, *CDMA: Principles of Spread Spectrum Communication*. Reading MA, USA: Addison-Wesley, June 1995. ISBN 0201633744.

[238] L. Miller and J. Lee, *CDMA Systems Engineering Handbook*. London, UK: Artech House, 1998.

[239] R. A. Scholtz, "The origins of spread spectrum communications," *IEEE Transactions on Communications*, vol. 30, no. 5, pp. 822–854, 1982.

[240] G. R. Cooper and R. W. Nettleton, "A spread-spectrum technique for high-capacity mobile communications," *IEEE Transactions on Vehicular Technology*, vol. 27, pp. 264–275, November 1978.

[241] O. C. Yue, "Spread spectrum mobile radio, 1977-1982," *IEEE Transactions on Vehicular Technology*, vol. 32, pp. 98–105, February 1983.

[242] M. Simon, J. Omura, R. Scholtz, and B. Levitt, *Spread Spectrum Communications Handbook*. New York, USA: McGraw-Hill, 1994.

[243] Y. Yoon, R. Kohno, and H. Imai, "A SSMA system with cochannel interference cancellation with multipath fading channels," *IEEE Journal on Selected Areas in Communications*, vol. 11, pp. 1067–1075, September 1993.

[244] K. Gilhousen, I. Jacobs, R. Padovani, A. Viterbi, L. Weaver Jr., and C. Wheatley III, "On the capacity of a cellular CDMA system," *IEEE Transactions on Vehicular Technology*, vol. 40, pp. 303–312, May 1991.

[245] P. Patel and J. Holtzman, "Analysis of a simple successive interference cancellation scheme in a DS/CDMA system," *IEEE Journal on Selected Areas in Communications*, vol. 12, pp. 796–807, June 1994.

[246] R. Lupas and S. Verdú, "Linear multiuser detectors for synchronous code division multiple access channels," *IEEE Transactions on Information Theory*, vol. 35, pp. 123–136, January 1989.

[247] P. Jung and J. Blanz, "Joint detection with coherent receiver antenna diversity in CDMA mobile radio systems," *IEEE Transactions on Vehicular Technology*, vol. 44, pp. 76–88, February 1995.

[248] J. Thompson, P. Grant, and B. Mulgrew, "Smart antenna arrays for CDMA systems," *IEEE Personal Communications Magazine*, vol. 3, pp. 16–25, October 1996.

[249] R. Steele and L. Hanzo, eds., *Mobile Radio Communications*. New York, USA: John Wiley and IEEE Press, 2nd ed., 1999. 1090 pages.

[250] K. Feher, *Wireless Digital Communications: Modulation and Spread Spectrum*. Englewood Cliffs, NJ: Prentice-Hall, 1995.

[251] R. Kohno, R. Meidan, and L. Milstein, "Spread spectrum access methods for wireless communication," *IEEE Communications Magazine*, vol. 33, pp. 58–67, January 1995.

[252] R. Price and E. Green Jr., "A communication technique for multipath channels," *Proceedings of the IRE*, vol. 46, pp. 555–570, March 1958.

[253] U. Grob, A. L. Welti, E. Zollinger, R. Kung, and H. Kaufmann, "Microcellular direct-sequence spread-spectrum radio system using n-path rake receiver," *IEEE Journal on Selected Areas in Communications*, vol. 8, no. 5, pp. 772–780, 1990.

[254] P. W. Baier, "A critical review of CDMA," in *Proceedings of the IEEE Vehicular Technology Conference (VTC)*, (Atlanta, GA, USA), pp. 6–10, 28 April–1 May 1996.

[255] Telcomm. Industry Association (TIA), Washington, DC, USA, *Mobile station — Base station compatibility standard for dual-mode wideband spread spectrum cellular system, EIA/TIA Interim Standard IS-95*, July 1993.

[256] A. J. Viterbi, A. M. Viterbi, and E. Zehavi, "Performance of power-controlled wideband terrestrial digital communication," *IEEE Transactions on Communications*, vol. 41, no. 4, pp. 559–569, 1993.

[257] F. Simpson and J. Holtzman, "Direct sequence CDMA power control, interleaving, and coding," *IEEE Journal on Selected Areas in Communications*, vol. 11, pp. 1085–1095, September 1993.

[258] S. Ariyavisitakul and L. Chang, "Signal and interference statistics of a CDMA system with feedback power control," *IEEE Transactions on Communications*, vol. 41, pp. 1626–1634, November 1993.

[259] S. Ariyavisitakul, "Signal and interference statistics of a CDMA system with feedback power control - Part II," *IEEE Transactions on Communications*, vol. 42, no. 2/3/4, pp. 597–605, 1994.

[260] J. G. Proakis, *Digital Communications*. Mc-Graw Hill International Editions, 3rd ed., 1995.

[261] R. W. Chang and R. A. Gibby, "A theoretical study of performance of an orthogonal multiplexing data transmission scheme," *IEEE Transactions on Communication Technology*, vol. 16, no. 4, pp. 529–540, 1968.

[262] P. V. Eetvelt, S. J. Shepherd, and S. K. Barton, "The distribution of peak factor in QPSK multi-carrier modulation," *Wireless Personal Communications*, vol. 2, pp. 87–96, 1995.

[263] V. M. DaSilva and E. S. Sousa, "Performance of orthogonal CDMA codes for quasi-synchronous communication systems," in *Proceedings of IEEE ICUPC 1993*, (Ottawa, Canada), pp. 995–999, October 1993.

[264] L. Vandendorpe, "Multitone direct sequence CDMA system in an indoor wireless environment," in *Proceedings of IEEE SCVT 1993*, (Delft, The Netherlands), pp. 4.1:1–8, October 1993.

[265] R. Prasad and S. Hara, "Overview of multi-carrier CDMA," in *Proceedings of the IEEE International Symposium on Spread Spectrum Techniques and Applications (ISSSTA)*, (Mainz, Germany), pp. 107–114, 22–25 September 1996.

[266] D. Scott, P. Grant, S. McLaughlin, G. Povey, and D. Cruickshank, "Research in reconfigurable terminal design for mobile and personal communications," tech. rep., Department of Electrical Engineering, The University of Edinburgh, March 1997.

[267] N. Yee and J. P. Linnartz, "MICRO 93-101: Multi-carrier CDMA in an indoor wireless radio channel," tech. rep., University of California at Berkeley, 1994.

[268] L.-L. Yang and L. Hanzo, "Performance of generalized multicarrier DS-CDMA over Nakagami-m fading channels," *IEEE Transactions on Communications, (http://www-mobile.ecs.soton.ac.uk/lly)*, vol. 50, pp. 956–966, June 2002.

[269] L.-L. Yang and L. Hanzo, "Slow frequency-hopping multicarrier DS-CDMAfor transmission over Nakagami multipath fading channels," *IEEE Journal on Selected Areas in Communications*, vol. 19, no. 7, pp. 1211–1221, 2001.

[270] E. A. Sourour and M. Nakagawa, "Performance of orthogonal multicarrier CDMA in a multipath fading channel," *IEEE Transactions on Communications*, vol. 44, pp. 356–367, March 1996.

[271] L.-L. Yang and L. Hanzo, "Slow frequency-hopping multicarrier DS-CDMA," in *International Symposium on Wireless Personal Multimedia Communications (WPMC'99)*, (Amsterdam, The Netherlands), pp. 224–229, September:21–23 1999.

[272] L.-L. Yang and L. Hanzo, "Blind soft-detection assisted frequency-hopping multicarrier DS-CDMA systems," in *Proceedings of IEEE GLOBECOM'99*, (Rio de Janeiro, Brazil), pp. 842–846, December:5-9 1999.

[273] S. Slimane, "MC-CDMA with quadrature spreading for wireless communication systems," *European Transactions on Telecommunications*, vol. 9, pp. 371–378, July–August 1998.

[274] I. Kalet, "The multitone channel," *IEEE Transactions on Communications*, vol. 37, pp. 119–124, February 1989.

[275] R.-Y. Li and G. Stette, "Time-limited orthogonal multicarrier modulation schemes," *IEEE Transactions on Communications*, vol. 43, pp. 1269–1272, February/March/April 1995.

[276] L. Goldfeld and D. Wulich, "Multicarrier modulation system with erasures-correcting decoding for Nakagami fading channels," *European Trans. on Telecommunications*, vol. 8, pp. 591–595, November–December 1997.

[277] E. Sousa, "Performance of a direct sequence spread spectrum multiple access system utilizing unequal carrier frequencies," *IEICE Transactions on Communications*, vol. E76-B, pp. 906–912, August 1993.

[278] B. Saltzberg, "Performance of an efficient parallel data transmission system," *IEEE Transactions on Communication Technology*, vol. 15, pp. 805–811, December 1967.

[279] C. Baum and K. Conner, "A multicarrier transmission scheme for wireless local communications," *IEEE Journal on Selected Areas in Communications*, vol. 14, pp. 512–529, April 1996.

[280] V. Dasilva and E. Sousa, "Multicarrier orthogonal CDMA signals for quasi-synchronous communication systems," *IEEE Journal on Selected Areas in Communications*, vol. 12, pp. 842–852, June 1994.

[281] L. Vandendorpe and O. V. de Wiel, "MIMO DEF equalization for multitone DS/SS systems over multipath channels," *IEEE Journal on Selected Areas in Communications*, vol. 14, pp. 502–511, April 1996.

[282] N. Al-Dhahir and J. Cioffi, "A bandwidth-optimized reduced-complexity equalized multicarrier transceiver," *IEEE Transactions on Communications*, vol. 45, pp. 948–956, August 1997.

[283] P. Jung, F. Berens, and J. Plechinger, "A generalized view on multicarrier CDMA mobile radio systems with joint detection (Part i)," *FREQUENZ*, vol. 51, pp. 174–184, July–August 1997.

[284] S. Hara and R. Prasad, "Design and performance of multicarrier CDMA system in frequency-selective Rayleigh fading channels," *IEEE Transactions on Vehicular Technology*, vol. 48, pp. 1584–1595, September 1999.

[285] V. Tarokh and H. Jafarkhani, "On the computation and reduction of the peak-to-average power ratio in multicarrier communications," *IEEE Transactions on Communications*, vol. 48, pp. 37–44, January 2000.

[286] D. Wulich and L. Goldfield, "Reduction of peak factor in orthogonal multicarrier modulation by amplitude limiting and coding," *IEEE Transactions on Communications*, vol. 47, pp. 18–21, January 1999.

[287] H.-W. Kang, Y.-S. Cho, and D.-H. Youn, "On compensating nonlinear distortions of an OFDM system using an efficient adaptive predistorter," *IEEE Transactions on Communications*, vol. 47, pp. 522–526, April 1999.

[288] Y.-H. Kim, I. Song, Seokho, and S.-R. Park, "A multicarrier CDMA system with adaptive subchannel allocation for forward links," *IEEE Transactions on Vehicular Technology*, vol. 48, pp. 1428–1436, September 1999.

[289] X. Gui and T.-S. Ng, "Performance of asynchronous orthogonal multicarrier CDMA system in frequency selective fading channel," *IEEE Transactions on Communications*, vol. 47, pp. 1084–1091, July 1999.

[290] T.-M. Lok, T.-F. Wong, and J. Lehnert, "Blind adaptive signal reception for MC-CDMA systems in Rayleigh fading channels," *IEEE Transactions on Communications*, vol. 47, pp. 464–471, March 1999.

[291] B. Rainbolt and S. Miller, "Multicarrier CDMA for cellular overlay systems," *IEEE Journal on Selected Areas in Communications*, vol. 17, pp. 1807–1814, October 1999.

[292] S.-M. Tseng and M. Bell, "Asynchronous multicarrier DS-CDMA using mutually orthogonal complementary sets of sequences," *IEEE Transactions on Communications*, vol. 48, pp. 53–59, January 2000.

[293] D. Rowitch and L. Milstein, "Convolutionally coded multicarrier DS-CDMA systems in a multipath fading channel – Part I: Performance analysis," *IEEE Transactions on Communications*, vol. 47, pp. 1570–1582, October 1999.

[294] D. Rowitch and L. Milstein, "Convolutionally coded multicarrier DS-CDMA systems in a multipath fading channel – Part II: Narrow-band interference suppression," *IEEE Transactions on Communications*, vol. 47, pp. 1729–1736, November 1999.

[295] D.-W. Lee and L. Milstein, "Comparison of multicarrier DS-CDMA broadcast systems in a multipath fading channel," *IEEE Transactions on Communications*, vol. 47, pp. 1897–1904, December 1999.

[296] N. Yee, J.-P. Linnartz, and G. Fettweis, "Multi-carrier CDMA in indoor wireless radio network," *IEICE Transactions on Communications*, vol. E77-B, pp. 900–904, July 1994.

[297] S. Kondo and L. Milstein, "On the use of multicarrier direct sequence spread spectrum systems," in *Proceedings of IEEE MILCOM'93*, (Boston, MA), pp. 52–56, Oct. 1993.

[298] V. M. DaSilva and E. S. Sousa, "Performance of orthogonal CDMA codes for quasi-synchronous communication systems," in *Proceedings of IEEE ICUPC'93*, (Ottawa, Canada), pp. 995–999, Oct. 1993.

[299] L. Vandendorpe, "Multitone direct sequence CDMA system in an indoor wireless environment," in *Proceedings of IEEE First Symposium of Communications and Vehicular Technology in the Benelux, Delft, The Netherlands*, pp. 4.1–1–4.1–8, Oct. 1993.

[300] L. L. Yang and L. Hanzo, "Blind joint soft-detection assisted slow frequency-hopping multi-carrier DS-CDMA," *IEEE Transactions on Communication*, vol. 48, no. 9, pp. 1520–1529, 2000.

[301] D.-W. Lee and L. Milstein, "Analysis of a multicarrier DS-CDMA code-acquisition system," *IEEE Transactions on Communications*, vol. 47, pp. 1233–1244, August 1999.

[302] B. Steiner, "Time domain uplink channel estimation in multicarrier-CDMA mobile radio system concepts," in *Multi-Carrier Spread-Spectrum* (K. Fazel and G. Fettweis, eds.), pp. 153–160, Kluwer Academic Publishers, 1997.

[303] K. W. Yip and T. S. Ng, "Tight error bounds for asynchronous multicarrier CDMA and their application," *IEEE Communications Letters*, vol. 2, pp. 295–297, November 1998.

[304] S. Kondo and L. Milstein, "Performance of multicarrier DS CDMA systems," *IEEE Transactions on Communications*, vol. 44, pp. 238–246, February 1996.

[305] B. M. Popovic, "Spreading sequences for multicarrier CDMA systems," *IEEE Transactions on Communications*, vol. 47, no. 6, pp. 918–926, 1999.

[306] P. Jung, P. Berens, and J. Plechinger, "Uplink spectral efficiency of multicarrier joint detection code division multiple access based cellular radio systems," *Electronics Letters*, vol. 33, no. 8, pp. 664–665, 1997.

[307] D.-W. Lee, H. Lee, and J.-S. Kim, "Performance of a modified multicarrier direct sequence CDMA system," *Electronics and Telecommunications Research Institute Journal*, vol. 19, pp. 1–11, April 1997.

[308] L. Rasmussen and T. Lim, "Detection techniques for direct sequence and multicarrier variable rate for broadband CDMA," in *Proceedings of the ICCS/ISPACS '96*, pp. 1526–1530, 1996.

[309] P. Jung, F. Berens, and J. Plechinger, "Joint detection for multicarrier CDMA mobile radio systems - Part II: Detection techniques," in *Proceedings of IEEE ISSSTA 1996*, vol. 3, (Mainz, Germany), pp. 996–1000, September 1996.

[310] Y. Sanada and M. Nakagawa, "A multiuser interference cancellation technique utilizing convolutional codes and multicarrier modulation for wireless indoor communications," *IEEE Journal on Selected Areas in Communications*, vol. 14, pp. 1500–1509, October 1996.

[311] Q. Chen, E. S. Sousa, and S. Pasupathy, "Multicarrier CDMA with adaptive frequency hopping for mobile radio systems," *IEEE Journal on Selected Areas in Communications*, vol. 14, pp. 1852–1857, December 1996.

[312] T. Ojanperä and R. Prasad, "An overview of air interface multiple access for IMT-2000/UMTS," *IEEE Communications Magazine*, vol. 36, pp. 82–95, September 1998.

[313] R. L. Peterson, R. E. Ziemer, and D. E. Borth, *Introduction to Spread Spectrum Communications*. Prentice Hall International Editions, 1995.

[314] S. W. Golomb, *Shift Register Sequences*. Holden-Day, 1967.

[315] F. Adachi, K. Ohno, A. Higashi, T. Dohi, and Y. Okumura, "Coherent multicode DS-CDMA mobile Radio Access," *IEICE Transactions on Communications*, vol. E79-B, pp. 1316–1324, September 1996.

[316] S. C. Bang, "ETRI wideband CDMA system for IMT-2000," in *Presentation material in 1st IMT-2000 Workshop*, (Seoul, Korea), pp. II–1–1 – II–1–21, KIET, August 1997.

[317] H. Rohling, K. Brüninghaus, and R. Grünheid, "Comparison of multiple access schemes for an OFDM downlink system," in *Multi-Carrier Spread-Spectrum* (K. Fazel and G. P. Fettweis, eds.), pp. 23–30, Kluwer Academic Publishers, 1997.

[318] R. Prasad, *CDMA for Wireless Personal Communications*. London: Artech House, May 1996. ISBN 0890065713.

[319] M. Schnell and S. Kaiser, "Diversity considerations forMC-CDMA systems in mobile communications," in *Proceedings of IEEE ISSSTA 1996*, pp. 131–135, 1996.

[320] W. H. Press, S. A. Teukolsky, W. T. Vetterling, and B. P. Flannery, *Numerical Recipes in C*. Cambridge University Press, 1992.

[321] S. Verdú, *Multiuser Detection*. Cambridge, UK: Cambridge University Press, 1998.

[322] E. Kuan and L. Hanzo, "Burst-by-burst adaptive multiuser detection cdma: A framework for existing and future wireless standards," *Proceedings of the IEEE*, December 2002.

[323] L. Hanzo, L.-L. Yang, E.-L. Kuan, and K. Yen, *Single- and Multi-Carrier DS-CDMA*. John Wiley and IEEE Press, 2003. 430 pages.

[324] R. Prasad, *Universal Wireless Personal Communications*. London, UK: Artech House Publishers, 1998.

[325] S. Glisic and B. Vucetic, *Spread Spectrum CDMA Systems for Wireless Communications*. London, UK: Artech House, April 1997. ISBN 0890068585.

[326] G. Woodward and B. Vucetic, "Adaptive detection for DS-CDMA," *Proceedings of the IEEE*, vol. 86, pp. 1413–1434, July 1998.

[327] S. Moshavi, "Multi-user detection for DS-CDMA communications," *IEEE Communications Magazine*, vol. 34, pp. 124–136, October 1996.

[328] A. Duel-Hallen, J. Holtzman, and Z. Zvonar, "Multiuser detection for CDMA systems," *IEEE Personal Communications*, vol. 2, pp. 46–58, April 1995.

[329] J. Laster and J. Reed, "Interference rejection in digital wireless communications," *IEEE Signal Processing Magazine*, vol. 14, pp. 37–62, May 1997.

[330] J. Thompson, P. Grant, and B. Mulgrew, "Performance of antenna array receiver algorithms for CDMA," in *Proceedings of the IEEE Global Telecommunications Conference (GLOBECOM)*, (London, UK), pp. 570–574, 18–22 November 1996.

[331] A. Naguib and A. Paulraj, "Performance of wireless CDMA with m-ary orthogonal modulation and cell site antenna arrays," *IEEE Journal on Selected Areas in Communications*, vol. 14, pp. 1770–1783, December 1996.

[332] L. Godara, "Applications of antenna arrays to mobile communications, part I: Performance improvement, feasibility, and system considerations," *Proceedings of the IEEE*, vol. 85, pp. 1029–1060, July 1997.

[333] R. Kohno, H. Imai, M. Hatori, and S. Pasupathy, "Combination of adaptive array antenna and a canceller of interference for direct-sequence spread-spectrum multiple-access system," *IEEE Journal on Selected Areas in Communications*, vol. 8, pp. 675–681, May 1998.

[334] B. J. Choi, T. H. Liew, and L. Hanzo, "Concatenated space-time block coded and turbo coded symbol-by-symbol adaptive OFDM and multi-carrier CDMA systems," in *Proceedings of IEEE VTC 2001-Spring*, p. P.528, IEEE, May 2001.

[335] W. T. Webb and R. Steele, "Variable rate QAM for mobile radio," *IEEE Transactions on Communications*, vol. 43, no. 7, pp. 2223–2230, 1995.

[336] B. Vucetic, "An adaptive coding scheme for time-varying channels," *IEEE Transactions on Communications*, vol. 39, no. 5, pp. 653–663, 1991.

[337] H. Imai and S. Hirakawa, "A new multi-level coding method using error correcting codes," *IEEE Transactions on Information Theory*, vol. 23, pp. 371–377, May 1977.

[338] G. Ungerboeck, "Channel coding with multilevel/phase signals," *IEEE Transactions on Information Theory*, vol. IT-28, pp. 55–67, January 1982.

[339] S. M. Alamouti and S. Kallel, "Adaptive trellis-coded multiple-phased-shift keying Rayleigh fading channels," *IEEE Transactions on Communications*, vol. 42, pp. 2305–2341, June 1994.

[340] S. Chua and A. Goldsmith, "Adaptive coded modulation for fading channels," *IEEE Transactions on Communications*, vol. 46, pp. 595–602, May 1998.

[341] K. J. Hole, H. Holm, and G. E. Oien, "Adaptive multidimensional coded modulation over flat fading channels," *IEEE Journal on Selected Areas in Communications*, vol. 18, pp. 1153–1158, July 2000.

[342] T. Keller, T. Liew, and L. Hanzo, "Adaptive rate RRNS coded OFDM transmission for mobile communication channels," in *Proceedings of VTC 2000 Spring*, (Tokyo, Japan), pp. 230–234, 15-18 May 2000.

[343] T. Keller, T. H. Liew, and L. Hanzo, "Adaptive redundant residue number system coded multicarrier modulation," *IEEE Journal on Selected Areas in Communications*, vol. 18, pp. 1292–2301, November 2000.

[344] T. Liew, C. Wong, and L. Hanzo, "Block turbo coded burst-by-burst adaptive modems," in *Proceedings of Microcoll'99*, (Budapest, Hungary), pp. 59–62, 21-24 March 1999.

[345] C. Wong, T. Liew, and L. Hanzo, "Turbo coded burst by burst adaptive wideband modulation with blind modem mode detection," in *ACTS Mobile Communications Summit*, (Sorrento, Italy), pp. 303–308, 8-11 June 1999.

[346] M. Yee, T. Liew, and L. Hanzo, "Radial basis function decision feedback equalisation assisted block turbo burst-by-burst adaptive modems," in *Proceedings of VTC '99 Fall*, (Amsterdam, Holland), pp. 1600–1604, 19-22 September 1999.

[347] V. Tarokh, N. Seshadri, and A. R. Calderbank, "Space-Time Codes for High Data Rate Wireless Communication: Performance Criterion and Code Construction," *IEEE Transactions on Information Theory*, vol. 44, pp. 744–765, March 1998.

[348] S. M. Alamouti, "A simple transmit diversity technique for wireless communications," *IEEE Journal on Selected Areas in Communications*, vol. 16, pp. 1451–1458, October 1998.

[349] V. Tarokh, H. Jafarkhani, and A. R. Calderbank, "Space-time block coding for wireless communications: Performance results," *IEEE Journal on Selected Areas in Communications*, vol. 17, pp. 451–460, March 1999.

[350] C. Berrou and A. Glavieux, "Near optimum error correcting coding and decoding: Turbo codes," *IEEE Transactions on Communications*, vol. 44, pp. 1261–1271, October 1996.

[351] J. Winters, "Smart antennas for wireless systems," *IEEE Personal Communications*, vol. 5, pp. 23–27, February 1998.

[352] R. Derryberry, S. Gray, D. Ionescu, G. Mandyam, and B. Raghothaman, "Transmit diversity in 3G CDMA systems," *IEEE Communications Magazine*, vol. 40, pp. 68–75, April 2002.

[353] A. Molisch, M. Win, and J. Winters, "Space-time-frequency (STF) coding for MIMO-OFDM systems," *IEEE Communications Letters*, vol. 6, pp. 370–372, September 2002.

[354] A. Molisch, M. Steinbauer, M. Toeltsch, E. Bonek, and R. Thoma, "Capacity of MIMO systems based on measured wireless channels," *IEEE Journal on Selected Areas in Communications*, vol. 20, pp. 561–569, April 2002.

[355] D. Gesbert, M. Shafi, D.-S. Shiu, P. Smith, and A. Naguib, "From theory to practice: an overview of MIMO space-time coded wireless systems," *IEEE Journal on Selected Areas in Communications*, vol. 21, pp. 281–302, April 2003.

[356] M. Shafi, D. Gesbert, D.-S. Shiu, P. Smith, and W. Tranter, "Guest editorial: MIMO systems and applications," *IEEE Journal on Selected Areas in Communications*, vol. 21, pp. 277–280, April 2003.

[357] G. Foschini Jr. and M. Gans, "On limits of wireless communication in a fading environment when using multiple antennas," *Wireless Personal Communications*, vol. 6, pp. 311–335, March 1998.

[358] S. X. Ng, B. L. Yeap, and L. Hanzo, "Full-rate, full-diversity adaptive space time block coding for transmission over Rayleigh fading channels," in *Proceedings of the IEEE VTC'05 Fall*, (Dallas, Texas), 25-28, September 2005.

[359] D. E. Goldberg, *Genetic Algorithms in Search, Optimization, and Machine Learning*. Reading, Massachusetts: Addison-Wesley, 1989.

[360] M. J. Juntti, T. Schlösser, and J. O. Lilleberg, "Genetic algorithms for multiuser detection in synchronous CDMA," in *IEEE International Symposium on Information Theory – ISIT'97*, (Ulm, Germany), p. 492, 1997.

[361] Y. Li, L. Cimini, and N. Sollenberger, "Robust channel estimation for OFDM systems with rapid dispersive fading channels," *IEEE Transactions on Communications*, vol. 46, pp. 902–915, April 1998.

[362] W. Jakes Jr., ed., *Microwave Mobile Communications*. New York, USA: John Wiley & Sons, 1974.

[363] M. C. Jeruchim, P. Balaban, and K. S. Shanmugan, *Simulation of Communication Systems*. Dordrecht; Kluwer Academic, 2000. 2nd edition.

[364] U. Fincke and M. Pohst, "Improved method for calculating vector of short length in a lattice, including a complexity analysis," *Math. Comput.*, vol. 44, pp. 463–471, April 1985.

[365] M. O. Damen, A. Chkeif, and J.-C. Belfiore, "Lattice code decoder for space-time codes," *IEEE Commun. Letters*, pp. 161–163, May 2000.

[366] M. O. Damen, H. E. Gamal, and G. Caier, "On maximum-likelihood detection and the search for closest lattice point," *IEEE Transactions on Information Theory*, vol. 49, pp. 2389–2402, October 2003.

[367] D. Pham, K. R. Pattipati, P. K. Willet, and J. Luo, "An improved complex sphere decoder for V-BLAST Systems," *IEEE Signal Processing Letters*, vol. 11, pp. 748–751, September 2004.

[368] T. Cui and C. Tellambura, "Joint channel estimation and data detection for OFDM systems via sphere decoding," in *IEEE Globcom 2004*, (Dallas, USA), pp. 3656–3660, November 2004.

[369] T. Cui and C. Tellambura, "Approximate ML detection for MIMO systems using multistage sphere decoding," *IEEE Signal Processing Letters*, vol. 12, pp. 222–225, March 2005.

[370] M. Damen, K. Abed-Meraim, and J.-C. Belfiore, "Generalised sphere decoder for asymmetrical space-time communication architecture," *Electronics Letters*, vol. 36, no. 2, pp. 166–167, 2000.

[371] T. Cui and C. Tellambura, "An efficient generalized sphere decoder for rank-deficient MIMO systems," *IEEE Communications Letters*, vol. 9, no. 5, pp. 423–425, 2005.

[372] J. E. Gentle, *Numerical Linear Algebra for Applications in Statistics*. Berlin: Springer-Verlag, 1998.

[373] M. K. Varanasi, "Decision feedback multiuser detection: A systematic approach," *IEEE Transactions on Information Theory*, vol. 45, pp. 219–240, January 1999.

[374] R. D. Schafer, *An Introduction to Nonassociative Algebras*. New York: Dover, 1996.

[375] H. Holma and A. Toskala, eds., *WCDMA for UMTS : Radio Access for Third Generation Mobile Communications*. John Wiley and Sons, Ltd., 2000.

[376] H. Liu and G. Xu, "Smart Antennas in Wireless Systems: Uplink Multiuser Blind Channel and Sequence Detection," *IEEE Transactions on Communications*, vol. 45, pp. 187–199, February 1997.

[377] J. Xavier, V. Barroso, and J. Moura, "Closed-form blind channel identification and source separation in SDMA systems through correlative coding," *International Journal on Selected Areas in Communications*, vol. 16, pp. 1506–1517, October 1998.

[378] J. Xavier, V. A. N. Barroso, and J. M. F. Moura, "Closed-form correlative coding (CFC2) blind identification of MIMO channels: isometry fitting to second order statistics," *IEEE Transactions on Signal Processing*, vol. 49, pp. 1073–1086, May 2001.

[379] I. Bradaric, A. P. Pertropulu, and K. I. Diamantaras, "Blind MIMO FIR Channel Identification Based on Second-order Spectra Correlations," *IEEE Transactions on Signal Processing*, vol. 51, pp. 1668–1674, June 2003.

[380] M. C. Necker and G. L. Stüber, "Totally blind channel estimation for OFDM on fast varying mobile radio channels," *IEEE Transactions on Wireless Communications*, vol. 3, pp. 1514–1525, September 2004.

[381] W. Nabhane and H. V. Poor, "Blind Joint Equalization and Multiuser Detection in Dispersive MC-CDMA/MC-DS-CDMA/MT-CDMA Channels," in *Proceedings MILCOM 2002*, vol. 2, pp. 814–819, 7-10 October 2002.

[382] Y. Li, N. Seshadri, and S. Ariyavisitakul, "Channel estimation for OFDM systems with transmitter diversity in mobile wireless channels," *IEEE Journal on Selected Areas in Communications*, vol. 17, pp. 461–471, March 1999.

[383] Y. Li, J. H. Winters, and N. R. Sollenberger, "MIMO-OFDM for Wireless Communications: Signal Detection with Enhanced Channel Estimation," *IEEE Transactions on Communications*, vol. 50, pp. 1471–1477, September 2002.

[384] S. Thoen, L. Deneire, L. V. der Perre, M. Engels, and H. D. Man, "Constrained Least Squares Detector for OFDM/SDMA-based Wireless Networks," *IEEE Transactions on Wireless Communications*, vol. 2, pp. 129–140, January 2003.

[385] Y. Qiao, S. Yu, P. Su, and L. Zhang, "Research on an Iterative Algorithm of LS Channel Estimation in MIMO OFDM Systems," *IEEE Transactions on Broadcasting*, vol. 51, pp. 149–153, March 2005.

[386] Y. Zeng and T. S. Ng, "A Semi-blind Channel Estimation Method for Multiuser Multiantenna OFDM Systems," *IEEE Transactions on Signal Processing*, vol. 52, pp. 1419–1429, May 2004.

[387] K. J. Kim and R. A. Iltis, "Joint Detection and Channel Estimation Algorithms for QS-CDMA Signals Over Time-varying Channels," *IEEE Transactions on Communications*, vol. 50, pp. 845–855, May 2002.

[388] K. J. Kim, J. Yue, R. A. Iltis, and J. D. Gibson, "A QRD-M/Kalman Filter-based Detection and Channel Estimation Algorithm for MIMO-OFDM Systems," *IEEE Transactions on Wireless Communications*, vol. 4, pp. 710–721, March 2005.

[389] Z. Wang, Z. Han, and K. J. R. Liu, "A MIMO-OFDM Channel Estimation Approach Using Time of Arrivals," *IEEE Transactions on Wireless Communications*, vol. 4, pp. 1207–1213, May 2005.

[390] M. Shin, H. Lee, and C. Lee, "Enhanced Channel-estimation Technique for MIMO-OFDM Systems," *IEEE Transactions on Vehicular Technology*, vol. 53, pp. 262–265, January 2004.

[391] F. Horlin and L. V. der Perre, "Optimal Training Sequences for Low Complexity ML Multi-channel Estimation in Multi-user MIMO OFDM-based Communications," in *2004 IEEE International Conference on Communications*, vol. 4, pp. 2427–2431, 20-24 June 2004.

[392] T. Cui and C. Tellambura, "Joint channel estimation and data detection for OFDM systems via sphere decoding," in *IEEE Global Telecommunications Conference, 2004 (GLOBECOM '04)*, vol. 6, pp. 3656–3660, 29 November-3 December 2004.

[393] H. Zhu, B. Farhang-Boroujeny, and C. Schlegel, "Pilot Embedding for Joint Channel Estimation and Data Detection in MIMO Communication Systems," *IEEE Communications Letters*, vol. 7, pp. 30–32, January 2003.

[394] J. Wang and K. Araki, "Pilot-symbol Aided Channel Estimation in Spatially Correlated Multiuser MIMO-OFDM Channels," in *2004 IEEE 60th Vehicular Technology Conference, 2004 (VTC 2004 Fall)*, vol. 1, pp. 33–37, 26-29 September 2004.

[395] K. Yen and L. Hanzo, "Genetic Algorithm Assisted Joint Multiuser symbol Detection and Fading Channel Estimation for Synchronous CDMA Systems," *IEEE Journal on Selected Areas in Communications*, vol. 19, pp. 985–998, June 2001.

[396] S. Chen and Y. Wu, "Maximum likelihood joint channel and data estimation using genetic algorithms," *IEEE Transactions on Signal Processing*, vol. 46, pp. 1469–1473, May 1998.

[397] Y. S. Zhang, Y. Du, W. Zhang, X. Z. Wang, and J. Li, "A data-aided time domain channel estimation method," in *Proceedings of the 2004 Joint Conference of the 10th Asia-Pacific Conference on Communications and the 5th International Symposium on Multi-Dimensional Mobile Communications*, vol. 1, pp. 469–473, 29 August-1 September 2004.

[398] C. E. Tan and I. J. Wassell, "Near-optimum training sequences for OFDM systems," in *The 9th Asia-Pacific Conference on Communications (APCC 2003)*, vol. 1, pp. 119–123, 21-24 September 2003.

[399] C. Ergün and K. Hacioglu, "Multiuser detection using a genetic algorithm in CDMA communications systems," *IEEE Transactions on Communications*, vol. 48, pp. 1374–1383, August 2000.

[400] K. Yen and L. Hanzo, "Antenna-diversity-assisted genetic-algorithm-based multiuser detection schemes for synchronous CDMA systems," *IEEE Transactions on Communications*, vol. 51, pp. 366–370, March 2003.

[401] K. Yen and L. Hanzo, "Genetic-algorithm-assisted multiuser detection in asynchronous CDMA communications," *IEEE Transactions on Vehicular Technology*, vol. 53, pp. 1413–1422, September 2004.

[402] X. Wu, T. C. Chuah, B. S. Sharif, and O. R. Hinton, "Adaptive robust detection for CDMA using a genetic algorithm," *IEE Proceedings Communications*, vol. 150, pp. 437–444, 10 December 2003.

[403] J. Akhtman and L. Hanzo, "Reduced-Complexity Maximum-Likelihood Detection in Multiple-Antenna-Aided Multicarrier Systems," in *Proceedings of the 5th International Workshop on Multi-Carrier Spread Spectrum Communications*, (Oberpfaffenhofen, Germany), 14-16 September 2005.

[404] J. Akhtman and L. Hanzo, "Novel Optimized-Hierarchy RSA-aided Space-Time Processing Method," Mobile VCE Core 3 Programme - Wireless Enablers 2.2: ICR-WE2.2.1, University of Southampton, Southampton, UK, May 2005.

[405] M. Jiang and L. Hanzo, "Improved Hybrid MMSE Detection for Turbo Trellis Coded Modulation Assisted Multi-User OFDM Systems," *IEE Electronics Letters*, vol. 40, pp. 1002–1003, August 2004.

[406] N. Seshadri, "Joint data and channel estimation using blind Trellis search techniques," *IEEE Transactions on Communications*, vol. 42, pp. 1000–1011, February–April 1994.

[407] R. Raheli, A. Polydoros, and C.-K. Tzou, "Per-survivor processing: A general approach to MLSE in uncertain environments," *IEEE Transactions on Communications*, vol. 43, pp. 354–364, February/March/April 1995.

[408] J. Holland, *Adaptation in Natural and Artificial Systems*. Ann Arbor, Michigan: University of Michigan Press, 1975.

[409] M. Jiang and L. Hanzo, "Novel MUD Techniques Designed for OFDM/MC-CDMA," Mobile VCE Core 3 Programme - Wireless Enablers 2.2: Deliverable D-WE2.2.2, University of Southampton, Southampton, UK, June 2004.

[410] R. L. Haupt and S. E. Haupt, *Practical Genetic Algorithms*. New Jersey, USA: John Wiley & Sons, Ltd, 2nd ed., 2004. ISBN 0-471-45565-2.

[411] Z. Michalewicz, *Genetic Algorithms + Data Structures = Evolution Programs*. New York, USA: Springer-Verlag, 2nd ed., 1994.

[412] S. M. Kay, *Fundamentals of Statistical Signal Processing, Estimation Theory*. Prentice Hall, New Jersey, 1993.

[413] R. Gallager, "Low-density parity-check codes," *IEEE Transactions on Information Theory*, pp. 21–28, 1962.

[414] M. C. Davey, *Error-Correction Using Low Density Parity Check Codes*. PhD thesis, University of Cambridge, UK, 1999.

[415] C. Berrou, A. Glavieux, and P. Thitimajshima, "Near shannon limit error-correcting coding and decoding: Turbo codes," in *Proc. of International Conference on Communications*, (Geneva, Switzerland), pp. 1064–1070, IEEE, May 1993.

[416] C. Berrou and A. Glavieux, "Near optimum error-correcting coding and decoding: Turbo codes," *IEEE Transactions on Communications*, vol. 44, pp. 1261–1271, October 1996.

[417] M. Jiang, S. X. Ng, and L. Hanzo, "Hybrid iterative multi-user detection for channel coded space division multiple access ofdm systems," *IEEE Transactions on Vehicular Technology*, vol. 55, pp. 115 – 127, January 2006.

[418] R. C. de Lamare and R. Sampaio-Neto, "Adaptive MBER Decision Feedback Multiuser Receivers in Frequency Selective Fading Channels," *IEEE Communications Letters*, vol. 7, no. 2, pp. 73–75, February 2003.

[419] C.-C. Yeh and J. R. Barry, "Adaptive Minimum Bit-Error Rate Equalization for Binary Signalling," *IEEE Transactions on Communications*, vol. 48, no. 7, pp. 1226–1235, July 2000.

[420] S. Chen, A. K. Samingan, B. Mulgrew, and L. Hanzo, "Adaptive Minimum-BER Linear Multiuser Detection for DS-CDMA Signals in Multipath Channels," *IEEE Transactions on Signal Processing*, vol. 49, no. 6, pp. 1240–1247, June 2001.

[421] D. Gesbert, "Robust Linear MIMO Receivers: A Minimum Error-Rate Approach," *IEEE Transactions on Signal Processing*, vol. 51, no. 11, pp. 2863–2871, November 2003.

[422] B. Mulgrew and S. Chen, "Adaptive Minimum-BER Decision Feedback Equalizers for Binary Signalling," *EURASIP Signal Processing Journal*, vol. 81, no. 7, pp. 1479–1489, 2001.

[423] M. R. Aaron and D. W. Tufts, "Intersymbol Interference and Error Probability," *IEEE Transactions on Information Theory*, vol. IT-12, pp. 26–34, January 1966.

[424] E. Shamash and K. Yao, "On the Structure and Performance of a Linear Decision Feedback Equalizer Based on the Minimum Error Probability Criterion," in *Proceedings of the International Conference on Communications (ICC)*, (Minneapolis, Minnesota, USA), pp. 25F1–25F5, 17-19 June 1974.

[425] P. Galko and S. Pasupathy, "Optimal Linear Receiver Filters for Binary Digital Signals," in *Proceedings of the International Conference on Communications (ICC)*, pp. 1H.6.1–1H.6.5, 1982.

[426] S. Chen, E. Chng, B. Mulgrew, and G. Gibson, "Minimum-BER Linear-Combiner DFE," in *Proceedings of International Conference on Communications (ICC)*, (Dallas, Texas, USA), pp. 1173–1177, 23-27 June 1996.

[427] C. C. Yeh and J. R. Barry, "Approximate Minimum Bit-Error Rate Equalization for Binary Signaling," in *Proceedings of International Conference on Communications (ICC)*, vol. 1, (Montreal, Canada), pp. 1095–1099, 8-12 June 1997.

[428] N. B. Mandayam and B. Aazhang, "Gradient Estimation for Sensitivity Analysis and Adaptive Multiuser Interference Rejection in Code-Division Multiple-Access Systems," *IEEE Transactions on Communications*, vol. 45, no. 6, pp. 848–858, July 1997.

[429] C. C. Yeh and J. R. Barry, "Approximate Minimum Bit-Error Rate Equalization for Pulse-Amplitude and Quadrature Amplitude Modulation," in *Proceedings of International Conference on Communications (ICC)*, vol. 1, (Atlanta, Georgia, USA), pp. 16–20, 7-11 June 1998.

[430] C. C. Yeh, R. R. Lopes, and J. R. Barry, "Approximate Minimum Bit-Error Rate Multiuser Detection," in *Proceedings of IEEE Global Telecommunications Conference (GLOBECOM)*, vol. 1, (Sydney, Australia), pp. 3590–3595, 8-12 November 1998.

[431] S. Chen, B. Mulgrew, E. S. Chng, and G. Gibson, "Space Translation Properties and the minimum-BER Linear-Combiner DFE," *IEE Proceedings on Communications*, vol. 145, no. 5, pp. 316–322, October 1998.

[432] S. Chen and B. Mulgrew, "The Minimum-SER Linear-Combiner Decision Feedback Equalizer," *IEE Proceedings on Communications*, vol. 146, no. 6, pp. 347–353, December 1999.

[433] I. N. Psaromiligkos, S. N. Batalama, and D. A. Pados, "On Adaptive Minimum Probability of Error Linear Filter Receivers for DS-CDMA Channels," *IEEE Transactions on Communications*, vol. 47, no. 7, pp. 1092–1102, July 1999.

[434] B. Mulgrew and S. Chen, "Stochastic Gradient Minimum-BER Decision Feedback Equalisers," in *Proceedings of IEEE Symposium on Adaptive Systems for Signal Processing, Communication and Control*, (Lake Louise, Alberta, Canada), pp. 93–98, 1-4 October 2000.

[435] X. Wang, W.-S. Lu, and A. Antoniou, "Constrained Minimum-BER Multiuser Detection," *IEEE Transactions on Signal Processing*, vol. 48, no. 10, pp. 2903–2909, October 2000.

[436] S. Chen, A. K. Samingan, B. Mulgrew, and L. Hanzo, "Adaptive Minimum-BER Linear Multiuser Detection," in *Proceedings of IEEE International Conference of Acoustics, Speech and Signal Processing (ICASSP)*, (Salt-Lake City, Utah, USA), pp. 2253–2256, 7-11 May 2001.

[437] A. K. Samingan, S. Chen, and L. Hanzo, "Adaptive Minimum-BER Linear Multiuser Detection for CDMA Signals in Multipath Channels with 4-QAM Constellation," *IEE Electronics Letters*, vol. 37, no. 11, pp. 721–723, 24 May 2001.

[438] S. Chen, B. Mulgrew, and L. Hanzo, "Least Bit Error Rate Adaptive Nonlinear Equalizers for Binary Signalling," *IEE Proceedings Communications*, vol. 150, no. 1, pp. 29–36, February 2003.

[439] S. Chen, L. Hanzo, and N. N. Ahmad, "Adaptive Minimum Bit Error Rate Beamforming Assisted Receiver for Wireless Communications," in *Proceedings of IEEE International Conference of Acoustics, Speech and Signal Processing (ICASSP)*, vol. IV, (Hong Kong, China), pp. 640–643, 6-10 April 2003.

[440] M. Y. Alias, A. K. Samingan, S. Chen, and L. Hanzo, "Multiple Antenna Aided OFDM Employing Minimum Bit Error Rate Multiuser Detection," *IEE Electronics Letters*, vol. 39, no. 24, pp. 1769–1770, 27 November 2003.

[441] J.H. Winters, "Smart Antennas for Wireless Systems," *IEEE Personal Communications*, vol. 5, no. 1, pp. 23–27, February 1998.

[442] J. Blogh and L. Hanzo, *3G Systems and Intelligent Networking*. John Wiley and IEEE Press, 2002.

[443] D. E. Goldberg, *Genetic Algorithms in Search, Optimization, and Machine Learning*. Reading, Massachusetts: Addison-Wesley, 1989.

[444] L. Hanzo, L-L. Yang, E-L. Kuan and K. Yen, *Single- and Multi-Carrier DS-CDMA: Multi-User Detection, Space-Time Spreading, Synchronisation, Networking and Standards*. Chichester, UK:: John Wiley and Sons, 2002.

[445] J. Holland, *Adaptation in Natural and Artificial Systems*. Ann Arbor, Michigan: University of Michigan Press, 1975.

[446] J. J. Grefenstette, *Genetic Algorithms for Machine Learning*. Kluwer academic Publishers, 1993.

[447] H. Adeli and S. L. Hung, *Machine Learning: Neural Networks, Genetic Algorithms and Fuzzy Systems*. John Wiley & Sons Inc., 1994.

[448] S. K. Pal and P. P. Wong, *Genetic Algorithms for Pattern Recognition*. CRC Press, 1996.

[449] M. D. Vose, *The Simple Genetic Algorithm: Foundations and Theory (Complex Adaptive Systems)*. Cambridge, Massachusetts: MIT Press, 1999.

[450] H. Dawid, *Adaptive Learning by Genetic Algorithms: Analytical Results and Applications to Economic Models (Lecture Notes in Economics and Mathematical Systems)*. Springer-Verlag Berlin and Heidelberg GmbH & Co. KG, 1996.

[451] M. Gen and R. Cheng, *Genetic Algorithms and Engineering Optimisation (Wiley Series in Engineering Design & Automation)*. John Wiley & Sons Inc., 2000.

[452] M. J. Juntti, T. Schlosser, and J. O. Lilleberg, "Genetic Algorithms for Multiuser Detection in Synchronous CDMA," in *Proceedings of IEEE Symposium on Information Theory*, (Ulm, Germany), p. 492, 29 June-4 July 1997.

[453] X. F. Wang, W.-S. Lu and A. Antoniou, "Genetic-algorithm-based Multiuser Detector for Multiple-access Communications," in *Proceedings of IEEE International Symposium on Circuits and Systems*, vol. 4, (Monterey, CA, USA), pp. 534–537, 31 May-3 June 1998.

[454] C. Ergun and K. Hacioglu, "Multiuser Detection Using a Genetic Algorithm in CDMA Communications Systems," *IEEE Transactions on Communications*, vol. 48, no. 8, pp. 1374–1383, August 2000.

[455] S. Abedi and R. Tafazolli, "A New CDMA Multiuser Detection Technique Using an Evolutionary Algorithm," *IEE Proceedings: Communications*, vol. 148, no. 6, pp. 393–399, December 2001.

[456] M. G. Shayesteh, M. B. Menhaj, and B. G. Nobary, "A Modified Genetic Algorithm for Multiuser Detection in DS/CDMA," *IEICE Transactions on Communications*, vol. E86-B, no. 8, pp. 2377–2388, August 2003.

[457] K. Yen and L. Hanzo, "Genetic Algorithm Assisted Joint Multiuser Detection and Fading Channel Estimation for Synchronous CDMA Systems," *IEEE Journal on Selected Areas in Communications*, vol. 19, no. 6, pp. 985–998, June 2001.

[458] K. Yen and L. Hanzo, "Antenna-diversity-assisted Genetic-algorithm-based Multiuser Detection Schemes for Synchronous CDMA Systems," *IEEE Transactions on Communications*, vol. 51, no. 3, pp. 366–370, March 2003.

[459] S. X. Ng, K. Yen, and L. Hanzo, "TTCM Assisted Genetic-algorithm Aided Reduced-Complexity Multiuser Detection," *Electronics Letters*, vol. 38, no. 14, pp. 722–724, 4 July 2002.

[460] A. Wolfgang, N. N. Ahmad, S. Chen and L. Hanzo, "Genetic Algorithm Assisted Error Probability Optimisation for Beamforming," *IEE Electronics Letters*, vol. 40, no. 5, pp. 320–322, 4 March 2004.

[461] Y. Du and K. T. Chan, "Feasibility of Applying Genetic Algorithms in Space-time Block Coding Multiuser Detection Systems," in *Proceedings of the IASTED International Conference on Wireless and Optical Communications*, vol. 3, (Banff, Canada), pp. 469–473, 2-4 July 2003.

[462] M. Mitchell, *An Introduction to Genetic Algorithm*. Cambridge, Massachusetts: MIT Press, 1996.

[463] C.-T. Chiang and C.-Y. Chang, "An Improved Genetic Algorithm Based on Eugenic Population for Multiuser Detection in DS-CDMA Systems," in *Proceedings of IEEE Region 10 Annual International Conference (TENCON)*, vol. 2, (Beijing, China), pp. 984–987, 28-31 October 2002.

[464] A. Wolfgang, N. N. Ahmad, S. Chen, and L. Hanzo, "Genetic Algorithm Assisted Minimum Bit Error Rate Beamforming," in *Proceedings of IEEE Vehicular Technology Conference (VTC-Spring)*, (Milan, Italy), pp. 142 – 146, 17-19 May 2004.

[465] M. Y. Alias, S. Chen and L. Hanzo, "Genetic Algorithm Assisted Minimum Bit Error Rate Multiuser Detection in Multiple Antenna Aided OFDM ," in *Proceedings of IEEE Vehicular Technology Conference (VTC-Fall)*, (Los Angeles, California, USA), p. To be published, September 2004.

[466] T. H. Liew, B. J. Choi, and L. Hanzo, "Space-time block coded and space-time trellis coded OFDM," in *Proceedings of IEEE VTC 2001-Spring*, p. P.533, IEEE, May 2001.

[467] J. Akhtman and L. Hanzo, "Channel estimation methods for OFDM and MC-CDMA systems," tech. rep., University of Southampton, July 2004. Mobile VCE Core 3 Programme - Wireless Enablers 2.2.

Subject Index

A

Adaptive
- blind detection . . 146, 149, 158, 160, 161
  - SNR estimator 159
  - trellis 161, 162
- channel estimation 167
- channel quality 146
  - estimation 147, 151
- closed-loop 147, 149
- delay 147, 164, 166
- modem 145
- modulation 150
  - BER estimator algorithm . . . 155, 156
  - constant throughput algorithm . . . 156, 157
  - fixed threshold algorithm . . . 152, 154, 155
  - fixed thresholds 153
  - with channel coding 164, 165
- modulation modes 152
- open-loop 147, 149
- parameter choice 146, 148
- scheme comparison 184
- signalling 146, 148, 158
  - error probability 158, 159
- sub-band 152
- with predistortion 181

ADC 50–52
- BER results 52
- clipping noise 50
- dynamic range 50
- noise 51, 52
- quantisation noise 51

Alternative Frequency Error Estimation for Frequency Domain Pilot Tones 131–133

Analogue-to-Digital Conversion 50–52

Appendix: OFDM Synchronisation Performance 139–144

ATM 61

Avalanche SNR 246

B

Bandlimited Channels 29

Basic OFDM Modem Implementations 32–35

BCH Code 244

BER Performance Using Clipping Amplifiers 46–47

BER Performance with Frequency Synchronisation 137–138

Bitwise OHRSA ML SDM Detection 274–279

Block Diagram of the Synchronisation Algorithms 122–123

Broadcasting 21

C

Cartesian Coordinates 139

Cavers 38

Chang 21

Channel
- bandlimited 29
- delay spread 41
- equalisation
  - adaptive 36
- estimation 70–78
- frequency selective 66
- impulse response 41, 61
- model 61–66
  - short WATM 64
  - UMTS 65

OFDM and MC-CDMA: A Primer L. Hanzo and T. Keller
© 2006 John Wiley & Sons, Ltd

WATM 62
WLAN 64
non stationary 68
stationary 67
Channel Model 61–66
Channel Transfer Function Estimation . 70–78
Chapter Summary and Conclusion . . 299–301, 329, 348
Chapter Summary and Conclusions 39–40, 60, 101–102, 138
Choice of the OFDM Modulation 42
Cimini 5
CIR 41
Classification of Smart Antennas 253–255
Clipping Amplification 43–50
Clipping Amplification - Summary 50
Clipping Amplifier Simulations 44–50
Coarse Frame and OFDM Symbol Synchronisation 115–116
Coherent Demodulation 110
Coherent Modulation 108
Coloured Phase Noise Model 57–59
Comments on the Joint Optimisation Process 317
Comparison of GA-JCEMUDs Having Soft and Hard Outputs 327
Comparison of the Frequency Acquisition Algorithms 133–137
Complexity Analysis. 294–296
Complexity Comparison 346
Correlation Functions 119
Cross-Over Operator 315–316
Cyclic Block Extension in OFDM 35
Cyclic OFDM Symbol Extension 35–36
Cyclic Prefix . . . . . *see* OFDM

D

Decision-Directed Adaptive Channel Equalisation 36–38
DFT 32, 209
Differential Modulation 109, 112–114
BER performance 81
Differential Modulation in OFDM 42
Differentially Coded Modulation 81–83
Digital Audio 21
Discrete Fourier Transform 209
Discrete Fourier Transform (DFT) 25
Doppler Frequency 61
frame normalised 164
normalised 61
OFDM symbol normalised 68
DS-CDMA
brief history 205
frequency reuse 206
overview 205–207
power control 207
closed loop 207
open loop 207
rake receiver 206
soft capacity 205
soft handoff 206

E

Effects of Frequency Mismatch on Different Modulation Schemes 108–109
Effects of Phase Noise 53–54
Effects of the Doppler Frequency . . . 323–324
Effects of the Maximum Mutation Step Size 320–323
Effects of the Number of GA-JCEMUD Iterations 324
Effects of the Pilot Overhead 325
Effects of the Stationary Time-Dispersive Channel 67
Effects of Time-Dispersive Channels on OFDM 66–70
EGC 239
Employing GAs in the MBER MUD Aided SDMA OFDM System . . . 340–342
Equal Gain Combining 239
Error Probability of a BPSK System . 335–336
European Digital Audio Broadcasting (DAB) 21
Exact MBER Multi-User Detection . . 336–337
Extended GA Individual Structure for MIMO Systems 313–314

F

Fading Channel
coherence bandwidth 231
frequency selective 231
impulse response 232
maximum diversity 232
multi-path spread 231
RMS delay spread 231
Fast Fourier Transform 25
FDM 208
FDMA 206
FEC 244
FFT 25, 32, 210

Filter
ideal rectangular 75
Fine Symbol Tracking 116
Fourier Transform 25
Frame Structure 117
Frame Synchronisation 122
Frequency Acquisition 116, 122, 124–126
Frequency Acquisition and Frame Synchronisation 122–123
Frequency Domain Channel Transfer Function Estimation 70–78
Frequency Error - Summary 109
Frequency Hopping 205
Frequency Shift 103–109
Frequency Synchronisation in an AWGN Channel 139–144
Frequency Tracking 116–117, 120–121
Frequency Tracking and OFDM Symbol Synchronisation 120–121

G

GA-Aided Iterative Joint Channel Estimation and Multi-User Detection 306–319
GA-Aided Joint FD-CHTF and Data Optimisation Providing Soft Outputs . 313
GA-aided Joint FD-CHTF and Data Optimisation Providing Soft Outputs . . . 319
Generalisation of the BW-OHRSA-ML SDM Detector 277–279
Generalisation of the OHRSA-ML SDM Detector 271–274
Generating Initial Symbol Estimates . 311–313
Generating the GA's Soft Outputs . . . 317–319
Genetic Algorithm 337–342
Gold Codes 221–222
generator 221
three valued cross-correlations 221

H

Hadamard Transform 223
Harmuth 38
Hirosaki 5, 32, 34
History of QAM / OFDM 6

I

Ideal Lowpass Interpolation for PSAM . 73–75
IDFT 209
IFFT 209
Initialisation 314–315
Inter-Symbol Interference 207
Introduction 21–22, 303–305, 331–332
Introduction to OFDM 21–40
Introduction to Peak-Power Reduction Techniques 45–46
Introduction to Space-Time Processing . . 255–258
Inverse Discrete Fourier Transform 209
Inverse Fast Fourier Transform 209
ISI 41, 207, 231
frequency error 105, 106
Gaussian approximation 105–107

J

Jamming 205
Joint Channel Estimation and MUD for SDMA OFDM 303–329
Joint Genetic Optimisation 315–317
Joint Optimisation Versus Separate Optimisation 327
Joint Optimisation versus Separate Optimisation 325
Joint Probability Density 140–141

K

Kalet 5
Kasami Sequences 222
decimation of m-sequences 222
efficient generator 222
generator 222
Welch lower bound 222
Kolb 5, 37

L

LFSR 219
Linear Interpolation for PSAM 71–73
LLR 293
Log-MAP
OHRSA 285

M

m-sequences 219–221
autocorrelation 220
Fibonacci construction 219, 220
Galois construction 219, 220
randomness properties 220
matrix
direct product 276
Maximal Ratio Combining 236
Maximum Likelihood Detection 243
MC-CDMA
frequency diversity 232
introduction 211–214

multi user detection 242–244
receiver schematic 213
signal 212
single user detection 235–242
synchronous 231
system model 233–235
Transmitter Model 234
transmitter schematic 212, 213
MC-DS-CDMA
introduction 214–215
spectrum 215
transmitter schematic 214
MCF 286
MIMO Channel Model 259–260
MIMO Robustness 327–329
Minimum Bit Error Ratio Detection of OFDM 332
ML Enhanced Sphere Decoding of MIMO-OFDM 253–301
MLD 243
MMSE-BDFE joint detector 246
Modem Implementation 32
Modified Hadamard Transform 223
Modulation by DFT 25–29
Modulation Scheme
16QAM 42
BPSK 42, 43
D8PSK 42
DBPSK 42
DQPSK 42
QPSK 42
modulation scheme
BPSK 277, 286
QAM 293
MRC 236
MT-CDMA
frequency separation 216
introduction 215–217
spectrum 215
transmitter schematic 216
MUI 206, 246
Multi-Carrier CDMA
overview 211–217
summary 217
Multi-Path Intensity Profile 245
Multi-Rate Orthogonal Gold Codes . . 226–228
example 228
Multi-User OFDM Employing GA-Aided MBER MUD 331–348
Multiple Access Frame Structure 117–119
Mutation Operator 316–317

N

Non-Stationary Channel 68–70
Nonlinear Amplification 43–50
amplitude statistics 45
backoff 45, 46, 50
clipping amplifier
BER results 44
interference 49
spectrum 47–49
Note 1: 265
Note 2: 265
Numerical Integration 141–144
Nyquist Filter 47

O

OFDM
adaptive loading 231
amplitude statistics 43, 44
bandwidth efficiency 38
BER performance
AWGN 42, 43
complex baseband representation . . . 208
cyclic extension 35
cyclic prefix 209, 210
DFT representation 209
disadvantage 210
milestones 7
modulation schemes 42
overview 208–211
peak power 45
reduction 45
spectrum 210
system schematic 34
transmitter schematic 209
virtual carriers 48
OFDM Bandwidth Efficiency 38–39
OFDM Channel
estimation 42
OFDM Modem 32, 55–57
OFDM Signal Amplitude Statistics 43–44
OFDM Symbol Synchronisation 120
OFDM Synchronisation 103–138
errors 103
OFDM System Performance over AWGN Channels 42–43
OFDM Transmission over Gaussian Channels 41–60
OFDM Transmission over Wideband Channels 61–102

OHRSA
Log-MAP 289
ML 277, 286
OHRSA-Aided Log-MAP SDM Detection 279–289
OHRSA-Aided ML SDM Detection . 263–267
One Phasor in AWGN Environment . 139–140
Optimised Hierarchy Reduced Search Algorithm-Aided SDM Detection 262
Optimised Hierarchy Reduced Search Algorithm-aided SDM Detection 299
ORC 241
Orthogonal Codes 223–228
Orthogonal Gold Codes 224–226
Orthogonality Restoring Combining 241
Overview of GAs 338–339

P

Peled 5
Perfect Channel Estimation 78–81, 89–90
Performance Analysis 296–299
Performance of a Four-User and Four-Receiver Antenna Scenario 343
Performance of the Four-Antenna Scenario versus the Number of Users . . 344–346
Performance of the Pilot Based Frequency Acquisition in AWGN Channels 126–129
Performance with Frequency and Timing Errors 103–114
Periodic Autocorrelation 220
Phase Distribution 141
Phase Noise 53–60
coloured 57
BER performance 59
interference 57
mask 57
effects 53
effects on serial modem 55
mask 53, 54, 57
phase jitter 53, 54
simulations 54
white 54
BER performance 54, 55, 58
interference 55, 56
Phase Noise - Summary 60
Phase Noise Simulations 54–59
Pilot Symbol Assisted Modulation 83–88, 111
Pilot Symbol Assisted Schemes 71–78
Pilot Symbol-Assisted Modulation 90
Pilot-Aided Initial Channel Estimation . . . 309
Pilot-aided Initial Channel Estimation 311
PN Sequences 219–222
Polar Coordinates 139–140
Pre-distortion 148
Pre-Equalisation 176
full channel inversion 178
limited dynamic range 179
with adaptive modulation 181
with sub-band blocking 179
Preuss 5
Principles of QAM-OFDM 23–25
Product of Two Noisy Phasors 140–144
Proof of Lemma 1: 265–267
PSAM 71, 108–109
BER performance 83, 90
linear interpolation 71
lowpass interpolation 73
number of pilots 73
Pulse Shaping 47

Q

QAM-FDM Principles 23

R

Rückriem 5
Ranging 205
Redundant Residue Number System 245
Reference Symbol 117–118, 124
Ruiz 5
Rule 1 271
Rule 2 271–272
Rule 3 272
Rule 4 272–274
Rule 4a 290–291
Rule 5 291
Rule 6 291–293

S

Schüssler 5
SDM-OFDM System Model 259–262
SDM-OFDM Transceiver Structure . . 260–262
SDMA MIMO Channel Model 305–306
search
branch 286
low likelihood 288
recursive 277
tree 288

Search Strategy 267–274
Serial Modem 55
Shortened WATM Channel 64
Signal Spectrum with Clipping Amplifier 47–50
Signalling Over Time-Dispersive OFDM Channels 70
Simulation Results 319–329, 343–346
SISO 293
Slowly-Varying Time-Dispersive Channel 88, 90
Soft-Output OHRSA-Aided Approximate Log-MAP Detection 289–299
Space Division Multiple Access 334–335
Space-Time Block Code 245
Spectrum of the OFDM Signal 104–108
Spreading Sequences 219–229
Static Time-Dispersive Channel 78–88
Summary 75–78
Summary of Time-Variant Channels 70
Synchronisation
  acquisition 115, 116
  algorithms 114–138
    auto-correlation 117
    comparison 133
    pilots 123
  BER performance 137
  errors 114
  frequency errors 103
    interference 103
    spectrum 104
  reference symbol 117, 124
  timing errors 110
  tracking 115, 116
Synchronisation Algorithms 114–133
Synchronisation by Auto-Correlation 117
Synchronisation Using Pilots 123–133
System Model 334–337
system model
  real-valued 276
System Overview 306
System Performance 78–90

T

TDMA 206
Time and Frequency Domain Synchronisation 103–144
Time Domain Channel Estimation 78
Time Domain Synchronisation Errors 110–114
Time Domain Synchronisation Errors - Summary 114
Transmission via Bandlimited Channels 29–32
Trellis Coded Modulation 244

U

UMTS 62
UMTS System 66
UMTS system 65
UMTS Type Channel 65–66

W

W-ATM Channel
  parameters 232
Walsh Codes 223–224
  efficient implementation 224
Walsh codes
  Hadamard Transform 223
WATM 61
WATM Channel
  impulse response 232
WATM channel 62–63
Weinstein 5, 37
White Phase Noise Model 54–57
Wireless Asynchronous Transfer Mode . . . 245
Wireless Asynchronous Transfer Mode System 62–64
Wireless Local Area Network System . . 64–65
WLAN 61
WLAN channel 65

Z

Zero Forcing 241
ZF 241

Author Index

A

Aaron, M.R. [423] 333
Aazhang, B. [428] 333
Abedi, S. [455] 339, 340
Adachi, F. [315] 223
Adami, O. [68] 8, 116, 117
Adeli, H. [447] 339
Ahmad Kamsani Samingan, [440] . . 332, 337, 338, 346
Ahmad, N.N. [460] 339
Ahmad, N.N. [464] 340
Ahmad, N.N. [439] 333
Al-Dhahir, N. [282] 216
Al-Susa, E. [91] 10, 11
Ala–Laurila, J. [172] 16
Alain Glavieux, [416] 320
Alamouti, S.M. [339] 244
Alamouti, S.M. [348] 245
Alard, M. [11] 5, 16, 21
Aldis, J. [173] 16
Alias, M.Y. [465] 340
Andreas Antoniou, [435] 333
Antoniou, A. [453] 339, 340
Anvari, K. [72] 8
Ariyavisitakul, S. [258] 207
Ariyavisitakul, S. [259] 207
Ariyavisitakul, S. [110] 11–13, 97
Ariyavisitakul, S. [382] 304, 309
Awater, G. [134] 14, 16
Awater, G. [172] 16
Awater, G. [133] 14, 16
Awater, G.A. [135] 14, 16
Awater, G.A. [142] 15, 16

B

Babak G. Nobary, [456] 339, 340
Bahai, A.S. [72] 8
Bahl, L.R. [224] 164, 170
Baier, P.W. [254] 206
Balaban, P. [363] 260
Balachandran, K. [5] 3
Bang, S.C. [316] 226
Barroso, V.A.N. [377] 304, 307
Barry, J.R. [427] 333
Barry, J.R. [429] 333
Barry, J.R. [430] 333
Barton, S.K. [49] 7, 45, 210
Barton, S.K. [48] 7, 45
Barton, S.K. [189] 64, 65
Barton, S.K. [262] 210
Batalama, S.N. [433] 333
Baum, C.W. [279] 216
Baum, K.L. [124] . . 14, 16, 191, 193, 198, 200
Belfiore, J.-C. [365] 262
Bell, M.R. [292] 216
Bello, P.A. [21] 6
Benjebbour, A. [143] 15, 16
Berens, F. [309] 216
Berens, F. [283] 216
Berens, P. [306] 216
Berrou, C. [223] 164, 170
Berrou, C. [415] 320
Berrou, C. [350] 245
Bhargava, V.K. [120] 12, 304
Bhargave, A. [145] 15, 16
Bingham, J.A.C. [234] 186, 187, 231
Bingham, J.A.C. [202] 116
Bingham, J.A.C. [214] 145, 186, 187
Bingham, J.A.C. [77] 9
Blanz, J. [247] 206, 246
Blogh, J. [217] . 145, 202, 242, 243, 253, 254, 257, 356

© 2006 John Wiley & Sons, Ltd

Blogh, J. [442] 335
Bogenfeld, E. [169] 16, 58
Bölcskei, H. [119] 12
Bonek, E. [354] 255
Börjesson, P.O. [79] 9, 11
Börjesson, P.O. [80] 9, 11
Börjesson, P.O. [69] 8, 116, 117
Borowski, J. [169] 16, 58
Borowski, J. [168] 16, 58
Borth, D.E. [313] 219–221, 223, 224, 226
Brajal, A. [71] 8, 211, 216, 217, 353
Brown, P.A. [165] 16
Brüninghaus, K. [67] 8
Brüninghaus, K. [317] 231
Burr, A.G. [165] 16
Burr, A.G. [209] 145
Busking, E. [173] 16

C

Caier, G. [366] 262
Calderbank, A.R. [349] 245
Calderbank, A.R. [347] 245
Calvo, M. [187] 53
Cao, Z. [140] 15, 16
Cao, Z. [92] 10, 11
Cao, Z. [103] 11
Cao, Z. [97] 10, 11
Carloni, M. [59] 7, 46
Cavers, J.K. [181] 38, 42, 71, 167
Cem Ergun, [454] 339, 340
Chang, K.H. [194] 91–98, 100
Chang, L.F. [258] 207
Chang, M-X. [101] 10, 11
Chang, R.W. [1] 1, 5, 7, 18, 21, 150, 208
Chang, R.W. [23] 6, 21
Chang, R.W. [261] 208
Chen, Q. [311] 216, 217
Chen, S. [437] 333
Chen, S. [460] 339
Chen, S. [464] 340
Chen, S. [422] 331, 333
Chen, S. [434] 333
Chen, S. [396] 305, 317
Chen, S. [465] 340
Chen, S. [436] 333
Chen, S. [420] 331–333, 335, 336
Chen, S. [432] 333
Chen, S. [431] 333
Chen, S. [438] 333
Chen, S. [426] 333
Chen, S. [439] 333
Chen-Chu Yeh, [419] 331, 333, 336
Cheng, R.S-K. [126] 14, 16
Cheng, R.S. [140] 15, 16
Cheng, R.S. [232] 186, 187
Cheng, R.S. [92] 10, 11
Cherriman, P. [7] 3, 145, 202, 356
Ching-Tai Chiang, [463] 340
Chkeif, A. [365] 262
Chng, E. [426] 333
Chng, E.S. [431] 333
Cho, Y-S. [287] 216
Cho, Y.S. [111] 11–13
Cho, Y.S. [194] 91–98, 100
Cho, Y.S. [115] 12
Cho, Y.S. [151] 13
Choi, B-J [75] 8, 247
Choi, B.J. [90] 8–10, 12–15, 38, 45, 60, 71, 78, 84, 145, 146, 148, 153, 202, 211, 217, 229, 243, 245, 246, 248, 255, 257–261, 264, 282, 296, 303–305, 309–311, 318, 331, 332, 334–336, 338, 353, 355
Choi, B.J. [334] 244
Choi, S. [151] 13
Chouly, A. [71] 8, 211, 216, 217, 353
Chow, J.S. [77] 9
Chow, P.S. [214] 145, 186, 187
Chow, P.S. [162] 16
Chow, P.S. [161] 16
Chow, P.S. [163] 16
Chua, S-G. [208] 145
Chua, S. [340] 244
Chuang, J.C-I. [152] 13
Chun-Yi Chang, [463] 342
Cimini, L.J. [10] 5–7, 21, 37, 208, 209
Cimini, L.J. [150] 13, 95, 97, 99, 191, 202
Cimini, L.J. [361] 259, 297
Cimini, L.J. [186] 48
Cimini, L.J. [86] 9, 11, 14
Cimini, L.J. Jr [59] 7, 46
Cimini, L.J. Jr [152] 13
Cioffi, J.M. [214] 145, 186, 187
Cioffi, J.M. [162] 16
Cioffi, J.M. [161] 16
Cioffi, J.M. [77] 9
Cioffi, J.M. [282] 216
Cioffi, J.M. [163] 16
Cioffi, J.M. [78] 9, 11
Ciotti, C. [168] 16, 58

Classen, F. [26] 6, 8, 115, 116
Classen, F. [27] 6, 116
Claude Berrou, [416] 320
Cocke, J. [224] 164, 170
Conner, K.F. [279] 216
Cooper, G.R. [240] 205, 206
Cruickshank, D.G.M. [266] 211
Czylwik, A. [213] 145, 186

D

Daffara, F. [68] 8, 116, 117
Damen, M.O. [365] 262
Damen, M.O. [366] 262
Daneshrad, B. [59] 7, 46
DaSilva, V.M. [263] 211, 214–217, 353
DaSilva, V.M. [298] 216
Dasilva, V.M. [280] 216
David E. Goldberg, [443] 339–342
David Gesbert, [421] 331
Dawid, H. [450] 339
de Couasnon, T. [203] 116
De Man, H.J. [136] 14–16
Deinzer, M. [166] 16
Deller, J.R. [104] 11
Deneire, L. [146] 15, 16
Derryberry, R.T. [352] 254
Di Benedetto, M.G. [170] 16, 58
Dinis, R. [57] 7
Dinis, R. [56] 7
Dinis, R. [58] 7
Dinis, R. [61] 8
Dohi, T. [315] 223
Drewes, C. [193] 91–93, 97, 100
Duel-Hallen, A. [106] 11
Duel-Hallen, A. [328] 243

E

Ebert, P.M. [9] 5–7, 21, 29, 32, 37, 209
Edfors, O. [79] 9, 11
Edfors, O. [80] 9, 11
Eltoft, T. [145] 15, 16
Engels, M. [29] 6, 331
Engels, M. [146] 15, 16
Engels, M. [130] 14
Engels, M. [156] 16
Engels, M.G.E. [136] 14–16
Ergün, C. [399] . 305, 313, 315, 317, 319, 327

F

Failli, M. [191] 65, 170
Falaschi, A. [204] 117, 123
Faulkner, M. [88] 9, 11
Fazel, K. [198] 115
Fazel, K. [25] 6
Fazel, K. [73] 8, 205, 211, 216, 217, 353
Feher, K. [250] 206
Fernandes, J. [58] 7
Fettweis, G. [25] 6
Fettweis, G. [72] 8
Fettweis, G. [296] 216, 217
Fettweis, G. [70] . . 8, 205, 211, 212, 214–217, 236, 239, 240, 353
Figueiredo, R.J.P. [145] 15, 16
Fincke, U. [364] 262
Fischer, R.F.H. [231] 186
Flannery, B.P. [320] 238
Flannery, B.P. [108] 11, 95
Foschini, G. Jr [357] 255, 303
Foschini, G.J. [137] 15, 16
Fragouli, C. [122] 12
Frenger, P. [81] 9, 11

G

Galko, P. [425] 333
Gamal, H.E. [366] 262
Gans, M. [357] 255, 303
Garcia, A. [187] 53
Gentle, J.E. [372] 265
Georghiades, C.N. [117] 12
Gesbert, D. [356] 255
Gesbert, D. [355] 255
Giannakis, G.B. [95] 10, 11
Gibby, R.A. [23] 6, 21
Gibby, R.A. [261] 208
Gibson, G. [431] 333
Gibson, G. [426] 333
Gilhousen, K.S. [244] 206
Glavieux, A. [223] 164, 170
Glavieux, A. [415] 320
Glavieux, A. [350] 245
Glisic, S. [325] 243
Godara, L.C. [332] 243
Godara, L.C. [235] 191, 192, 200
Goldberg, D.E. [359] 258, 304, 321
Goldfeld, L. [276] 216
Goldfield, L. [286] 216
Goldsmith, A. [340] 244
Goldsmith, A.J. [208] 145
Golomb, S.W. [314] 220
Gong, Y. [114] 12
Grant, P.M. [266] 211

Grant, P.M. [330] 243
Grant, P.M. [248] 206, 243
Grant, P.M. [132] 14, 16
Gray, S.D. [352] 254
Green, E.P. Jr [252] 206, 232
Grob, U. [253] 206
Grünheid, R. [317] 231
Gudmundson, M. [190] 65
Gui, X. [289] 216
Guo, Y.J. [189] 64, 65
Gusmao, A. [57] 7
Gusmao, A. [56] 7
Gusmao, A. [58] 7
Gusmao, A. [61] 8
Gyselinckx, B. [136] 14–16
Gyselinckx, B. [156] 16

H

Hacioglu, K. [399] . . 305, 313, 315, 317, 319, 327
Hallen, H. [106] 11
Hallmann, E. [174] 16
Hansen, J.H.L. [104] 11
Hanzo, L. [227] 171, 191, 194
Hanzo, L. [437] 333
Hanzo, L. [460] 339
Hanzo, L. [464] 340
Hanzo, L. [217] . 145, 202, 242, 243, 253, 254, 257, 356
Hanzo, L. [215] . 145, 146, 148, 202, 243, 356
Hanzo, L. [249] 206, 231, 239, 260
Hanzo, L. [323] . 242, 243, 304, 305, 313–317, 319–321, 327
Hanzo, L. [216] . 145, 146, 148, 202, 254, 257, 279, 297, 320
Hanzo, L. [90] 8–10, 12–15, 38, 45, 60, 71, 78, 84, 145, 146, 148, 153, 202, 211, 217, 229, 243, 245, 246, 248, 255, 257–261, 264, 279, 282, 296, 303–305, 309–311, 318, 331, 332, 334–336, 338, 353, 355
Hanzo, L. [177]21, 24, 30, 32, 38, 41, 42, 148, 153, 164, 170, 176
Hanzo, L. [7] 3, 145, 202, 356
Hanzo, L. [105] 11
Hanzo, L. [6] 3, 168, 170
Hanzo, L. [75] 8, 247
Hanzo, L. [300] 216, 217, 353
Hanzo, L. [442] 335
Hanzo, L. [211] 145, 149
Hanzo, L. [343] 245
Hanzo, L. [226] 168
Hanzo, L. [225] 168, 174, 177
Hanzo, L. [221] 150
Hanzo, L. [342] 245
Hanzo, L. [458] 339, 340
Hanzo, L. [457] 339, 340
Hanzo, L. [222] 153
Hanzo, L. [444] 339, 341
Hanzo, L. [344] 245
Hanzo, L. [358] 257
Hanzo, L. [153] 13
Hanzo, L. [197] 97, 99
Hanzo, L. [271] 216, 217
Hanzo, L. [272] 216, 217
Hanzo, L. [268] 216
Hanzo, L. [269] 216
Hanzo, L. [465] 340
Hanzo, L. [205] 117
Hanzo, L. [322] 242, 243
Hanzo, L. [4] 3
Hanzo, L. [2] . . 1, 3, 93, 95, 99, 206, 209, 231, 232, 245–249
Hanzo, L. [180] 26
Hanzo, L. [436] 333
Hanzo, L. [420] 331–333, 335, 336
Hanzo, L. [438] 333
Hanzo, L. [439] 333
Hanzo, L. [459] 339, 340
Hanzo, L. [192] 71
Hanzo, L. [212] 145, 149
Hanzo, L. [334] 244
Hanzo, L. [345] 245
Hanzo, L. [346] 245
Hara, S. [74] 8, 211, 214–217, 233
Hara, S. [265] 211, 214, 217
Hara, S. [284] 216
Harada, H. [167] 16
Harmuth, H.F. [182] 38
Harmuth, H.F. [183] 38, 39
Hasholzner, R. [193] 91–93, 97, 100
Hasholzner, R. [195] 91, 93–95, 98
Hassell Sweatman, C.Z.W. [132] 14, 16
Hatori, M. [333] 243
Hayashi, M. [220] 147
Hayashi, M. [219] 147
Haykin, S. [144] 15, 16
Heath, R.W. [119] 12
Higashi, A. [315] 223
Hirakawa, S. [337] 244

Hirosaki, B. [14] 5, 6, 21, 32, 34
Hirosaki, B. [20] 5–7
Hochwald, B.M. [176] 17, 262, 263, 301, 311, 355
Höher, P. [85] 9, 11
Höher, P. [84] 9, 11
Höher, P. [76] 9, 11
Hole, K.J. [341] 244
Holland, J. [408] 315
Holland, J. [445] 339–341
Holm, H. [341] 244
Holma, H. [375] 297
Holtzman, J. [328] 243
Holtzman, J. [245] 206
Holtzman, J.M. [257] 207
Homma, K. [220] 147
Homma, K. [219] 147
Hu, S. [106] 11
Huang, H.C. [137] 15, 16
Huber, J.B. [231] 186
Huber, J.B. [51] 7, 46
Hübner, J. [169] 16, 58
Hughes-Hartogs, D. [233] 186
Hung, S.L. [447] 339
Hutter, A. [193] 91–93, 97, 100
Hutter, A. [195] 91, 93–95, 98

I

Imai, H. [337] 244
Imai, H. [243] 206
Imai, H. [333] 243
Ionescu, D.M. [352] 254
Itami, M. [89] 9, 11
Itoh, K. [89] 9, 11

J

Jacobs, I.M. [244] 206
Jafarkhani, H. [285] 216
Jafarkhani, H. [349] 245
Jakes, W.C. Jr [362] 260
Jeanclaude, I. [65] 8, 16, 116, 211, 231
Jelinek, F. [224] 164, 170
Jeon, W.G. [111] 11–13
Jeon, W.G. [194] 91–98, 100
Jeon, W.G. [115] 12
Jeruchim, M.C. [363] 260
John J. Grefenstette, [446] 339
John R. Barry, [419] 331, 333, 336
Jones, A.E. [49] 7, 45, 210
Jorma O. Lilleberg, [452] 339, 340
Jourdan, S. [71] 8, 211, 216, 217, 353
Jung, P. [306] 216
Jung, P. [190] 65
Jung, P. [309] 216
Jung, P. [283] 216
Jung, P. [247] 206, 246
Juntti, M.J. [360] 258

K

Kaasila, V.-P. [199] 116
Kadri Hacioglu, [454] 339, 340
Kaiser, S. [198] 115
Kaiser, S. [85] 9, 11
Kaiser, S. [84] 9, 11
Kaiser, S. [319] 232–234, 243
Kalet, I. [19] 5, 6, 21, 145, 186
Kalet, I. [274] 216
Kallel, S. [339] 244
Kam Tai Chan, [461] 339, 340
Kamio, Y. [207] 145
Kammeyer, K.D. [55] 7
Kang, H-W. [287] 216
Karam, G. [65] 8, 16, 116, 211, 231
Kato, O. [220] 147
Kato, O. [219] 147
Kaufmann, H. [253] 206
Kay, S.M. [412] 318
Keller, T. [227] 171, 191, 194
Keller, T. [90] 8–10, 12–15, 38, 45, 60, 71, 78, 84, 145, 146, 148, 153, 202, 211, 217, 229, 243, 245, 246, 248, 255, 257–261, 264, 279, 282, 296, 303–305, 309–311, 318, 331, 332, 334–336, 338, 353, 355
Keller, T. [177] 21, 24, 30, 32, 38, 41, 42, 148, 153, 164, 170, 176
Keller, T. [343] 245
Keller, T. [226] 168
Keller, T. [225] 168, 174, 177
Keller, T. [221] 150
Keller, T. [342] 245
Keller, T. [153] 13
Keller, T. [205] 117
Keller, T. [2] . . 1, 3, 93, 95, 99, 206, 209, 231, 232, 245–249
Keller, T. [212] 145, 149
Khayata, R.E. [78] 9, 11
Kim, C.K. [151] 13
Kim, D.I. [120] 12, 304
Kim, J.-S. [307] 216

Kim, Y-H. [288] 216, 217
Kirsch, A.L. [8] 5, 6, 21
Kitade, T. [220] 147
Kitade, T. [219] 147
Kiviranta, M. [200] 116
Kleijne, T. [173] 16
Kohno, R. [243] 206
Kohno, R. [333] 243
Kohno, R. [251] 206, 207
Kolb, H.J. [178] 25
Kolb, H.J. [15] 5, 6, 21, 36, 37
Komaki, S. [60] 8
Komninakis, C. [122] 12
Kondo, S. [304] 216
Kondo, S. [297] 216
Koora, K. [169] 16, 58
Kopmeiners, R. [173] 16
Kramer, G. [190] 65
Kuan, E-L. [323]242, 243, 304, 305, 313–317, 319–321, 327
Kuan, E-L. [75] 8, 247
Kuan, E-L. [444] 339, 341
Kuan, E.L. [322] 242, 243
Kuchenbecker, H-P. [52] 7, 46
Kull, B. [169] 16, 58
Kumar, S. [5] 3
Kung, R. [253] 206
Kuronen, J. [199] 116
Kuwabara, M. [89] 9, 11

L

Lai, S.K. [232] 186, 187
Lajos Hanzo, [440] 332, 337, 338, 346
Lassalle, R. [11] 5, 16, 21
Laster, J.D. [329] 243
Lau, V.K.N. [210] 145
Lee, D-W. [301] 216
Lee, D-W. [307] 216
Lee, D-W. [295] 216
Lee, H. [307] 216
Lee, J.S. [238] 205, 207
Lehnert, J.S. [290] 216
Letaief, K.B. [114] 12
Letaief, K.B. [140] 15, 16
Letaief, K.B. [232] 186, 187
Letaief, K.B. [126] 14, 16
Letaief, K.B. [92] 10, 11
Letaief, K.B. [103] 11
Letaief, K.B. [97] 10, 11
Leung, C. [64] 8, 116
Levitt, B.K. [242] 205, 219–222
Li, J. [140] 15, 16
Li, R-Y. [275] 216
Li, X. [186] 48
Li, X. [137] 15, 16
Li, Y. [150] 13, 95, 97, 99, 191, 202
Li, Y. [361] 259, 297
Li, Y. [99] 10, 11
Li, Y. [148] 13
Li, Y. [112] 12, 13
Li, Y. [127] 14, 16
Li, Y. [93] 10, 11, 260
Li, Y. [118] 12, 304, 309
Li, Y. [149] 13, 191, 193, 201
Li, Y. [129] 14, 16
Li, Y. [110] 11–13, 97
Li, Y. [86] 9, 11, 14
Li, Y. [382] 304, 309
Li, Y. [236] 202
Li, Y. [147] 15, 16
Li, Z. [201] 116
Liew, T. [342] 245
Liew, T. [344] 245
Liew, T. [345] 245
Liew, T. [346] 245
Liew, T.H. [216] 145, 146, 148, 202, 254, 257, 279, 297, 320
Liew, T.H. [343] 245
Liew, T.H. [334] 244
Lilleberg, J.O. [360] 258
Lim, T.J. [308] 216
Lin, L. [152] 13
Lindner, J. [179] 25
Linnartz, J-P. [296] 216, 217
Linnartz, J-P. [70] . 8, 205, 211, 212, 214–217, 236, 239, 240, 353
Linnartz, J.P. [267] 212, 214, 242
Litva, J. [155] 16, 191–194, 200
Liu, K.J.R. [141] 15
Lo, T.K-Y. [155] 16, 191–194, 200
Lok, T-M. [290] 216
Lopes, L.B. [185] 47
Lopes, R.R. [430] 333
Lozano, A. [137] 15, 16
Lu, B. [98] 10, 11
Lu, W.-S. [453] 339, 340
Luo, J. [367] 263, 311
Luo, Z.-Q. [147] 15, 16
Lupas, R. [246] 206

M

Macleod, M.D. [210] 145
Mahrokh G. Shayesteh, [456] 339, 340
Mammela, A. [199] 116
Mammela, A. [200] 116
Mammela, A. [201] 116
Mammela, A. [171] 16, 58
Man, H.D. [130] 14
Man, H.D. [156] 16
Mandarini, P. [170] 16, 58
Mandarini, P. [204] 117, 123
Mandayam, N.B. [428] 333
Mandyam, G. [352] 254
Mann–Pelz, R. [173] 16
Mark, T. [173] 16
Markku J. Juntti, [452] 339, 340
Maseng, T. [88] 9, 11
Maseng, T. [83] 9, 11
Matsuoka, H. [207] 145
May, T. [53] 7, 46
McLaughlin, S. [266] 211
Meidan, R. [251] 206, 207
Mengali, U. [100] 10
Meyr, H. [26] 6, 8, 115, 116
Meyr, H. [27] 6, 116
Meyr, H. [131] 14, 16
Michale D. Vose, [449] 339
Mignone, V. [82] 9, 11
Miller, L.E. [238] 205, 207
Miller, S.L. [291] 216
Milstein, L.B. [301] 216
Milstein, L.B. [304] 216
Milstein, L.B. [251] 206, 207
Milstein, L.B. [293] 216
Milstein, L.B. [294] 216
Milstein, L.B. [295] 216
Milstein, L.B. [297] 216
Minn, H. [120] 12, 304
Mitchell, M. [462] 340, 341
Mitsuo Gen, [451] 339
Miya, K. [220] 147
Miya, K. [219] 147
Mody, A.N. [113] 12
Moeneclaey, M. [62] 8, 53, 211
Mohamad Yusoff Alias, [440] . . 332, 337, 338, 346
Mohammad B. Menhaj, [456] 339, 340
Molisch, A.F. [354] 255
Molisch, A.F. [353] 255
Monnier, R. [203] 116
Montezuma, P. [57] 7
Moon, T.K. [109] 11, 279, 317, 318
Moose, P.H. [66] 8, 116, 117
Morelli, M. [100] 10
Morello, A. [82] 9, 11
Morinaga, N. [207] 145
Moshavi, S. [327] 243
Moura, J.M.F. [377] 304, 307
Mueller-Roemer, F. [157] 16, 21
Muenster, M. [225] 168, 174, 177
Mulgrew, B. [422] 331, 333
Mulgrew, B. [434] 333
Mulgrew, B. [330] 243
Mulgrew, B. [248] 206, 243
Mulgrew, B. [436] 333
Mulgrew, B. [420] 331–333, 335, 336
Mulgrew, B. [432] 333
Mulgrew, B. [431] 333
Mulgrew, B. [438] 333
Mulgrew, B. [426] 333
Mulgrew, B. [132] 14, 16
Müller, S.H. [51] 7, 46
Münster, M. [90] 8–10, 12–15, 38, 45, 60, 71, 78, 84, 145, 146, 148, 153, 202, 211, 217, 229, 243, 245, 246, 248, 255, 257–261, 264, 279, 282, 296, 303–305, 309–311, 318, 331, 332, 334–336, 338, 353, 355
Münster, M. [153] 13
Münster, M. [197] 97, 99
Murata, H. [143] 15, 16
Murch, R.D. [232] 186, 187
Murch, R.D. [126] 14, 16
Murch, R.D. [139] 15, 16

N

Naguib, A. [355] 255
Naguib, A.F. [331] 243
Nakagawa, M. [310] 216
Nakagawa, M. [270] 216
Nanda, S. [5] 3
Necker, M.C. [102] 10, 11
Nettleton, R.W. [240] 205, 206
Ng, S.X. [358] 257
Ng, S.X. [459] 339, 340
Ng, T-S. [289] 216
Ng, T.S. [303] 216
Niemi, J. [171] 16, 58
Nikookar, H. [63] 8, 53
Nishijima, H. [60] 8

O

O'Neill, R. [185] 47
Ohno, K. [315] 223
Ohta, H. [89] 9, 11
Oien, G.E. [341] 244
Ojanperä, T. [190] 65
Ojanperä, T. [312] 217, 353
Okada, M. [60] 8
Okumura, Y. [315] 223
Omura, J.K. [242] 205, 219–222
Ormondroyd, R.F. [91] 10, 11

P

Pados, D.A. [433] 333
Padovani, R. [244] 206
Paik, K.H. [111] 11–13
Paik, K.H. [115] 12
Pal, S.K. [448] 341
Papke, L. [73] 8, 205, 211, 216, 217, 353
Park, S-R. [288] 216, 217
Pasupathy, S. [311] 216, 217
Pasupathy, S. [333] 243
Pasupathy, S. [425] 333
Patel, P. [245] 206
Pattipati, K.R. [367] 263, 311
Pauli, M. [52] 7, 46
Paulraj, A. [331] 243
Paulraj, A.J. [119] 12
Pearce, D.A. [209] 145
Peled, A. [13] 5, 6, 21
Peterson, R.L. [313] . . 219–221, 223, 224, 226
Pham, D. [367] 263, 311
Piazzo, L. [170] 16, 58
Piazzo, L. [229] 186–190
Pietikainen, M. [171] 16, 58
Pirhonen, R. [190] 65
Plechinger, J. [306] 216
Plechinger, J. [309] 216
Plechinger, J. [283] 216
Plenge, G. [158] 16, 21
Pohst, M. [364] 262
Pollet, T. [62] 8, 53, 211
Polydoros, A. [407] 314
Poor, H.V. [125] 14, 16
Popovic, B.M. [305] 216, 217
Povey, G.J.R. [266] 211
Powers, E.N. [22] 6, 21
Prasad, R. [28] 6
Prasad, R. [318] 232
Prasad, R. [74] 8, 211, 214–217, 233
Prasad, R. [265] 211, 214, 217
Prasad, R. [284] 216
Prasad, R. [63] 8, 53
Prasad, R. [312] 217, 353
Prasad, R. [167] 16
Prasad, R. [324] 243
Press, W.H. [320] 238
Press, W.H. [108] 11, 95
Preuss, K. [17] 5, 6, 21
Price, R. [252] 206, 232
Proakis, J.G. [260] . . . 208–210, 221, 222, 231, 232, 236, 238
Proakis, J.G. [104] 11
Psaromiligkos, I.N. [433] 333

R

Raghothaman, B. [352] 254
Raheli, R. [407] 314
Raimundo Sampaio-Neto, [418] 331–333
Rainbolt, B.J. [291] 216
Rashid-Farrokhi, F. [141] 15
Rasmussen, L.K. [308] 216
Rault, J.B. [203] 116
Rautio, J. [171] 16, 58
Rautio, T. [171] 16, 58
Rautiola, K. [171] 16, 58
Raviv, J. [224] 164, 170
Ray Liu, K.J. [96] 10, 11
Reed, J.H. [329] 243
Robertson, P. [198] 115
Robertson, P. [85] 9, 11
Robertson, P. [84] 9, 11
Robins, W.P. [188] 53
Rodrigo C. de Lamare, [418] 331–333
Rohling, H. [67] 8
Rohling, H. [174] 16
Rohling, H. [53] 7, 46
Rohling, H. [317] 231
Rowitch, D.N. [293] 216
Rowitch, D.N. [294] 216
Rückriem, R. [18] 5, 6, 21
Ruessel, M. [196] 94, 95
Ruf, M.J. [198] 115
Ruiz, A. [13] 5, 6, 21
Runwei Cheng, [451] 339

S

Saltzberg, B.R. [278] 216
Saltzberg, B.R. [24] 6, 7, 21, 208
Samingan, A.K. [437] 333

Samingan, A.K. [436] 333
Samingan, A.K. [420] 331–333, 335, 336
Sampei, S. [207] 145
Sanada, Y. [310] 216
Sandell, M. [79] 9, 11
Sandell, M. [80] 9, 11
Sandell, M. [69] 8, 116, 117
Sari, H. [65] 8, 16, 116, 211, 231
Sayed, A.H. [122] 12
Schafer, R.D. [374] 276, 278
Schlö, T. [360] 258
Schmidt, H. [55] 7
Schnell, M. [319] 232–234, 243
Scholtz, R.A. [239] 205
Scholtz, R.A. [242] 205, 219–222
Schüssler, H.W. [16] 5, 6, 21
Scott, D.I. [266] 211
Sellathurai, M. [144] 15, 16
Senst, A. [131] 14, 16
Seokho, [288] 216, 217
Seshadri, N. [110] 11–13, 97
Seshadri, N. [382] 304, 309
Seshadri, N. [406] 314
Seshadri, N. [347] 245
Shafi, M. [356] 255
Shafi, M. [355] 255
Shamash, E. [424] 333
Shanmugan, K.S. [363] 260
Sheng Chen, [440] 332, 337, 338, 346
Shepherd, S.J. [48] 7, 45
Shepherd, S.J. [262] 210
Shiu, D-S. [356] 255
Shiu, D-S. [355] 255
Simon, M.K. [242] 205, 219–222
Simpson, F. [257] 207
Sistanizadeh, K. [163] 16
Sköld, J. [190] 65
Slimane, S.B. [273] 216
Slimane, S.B. [121] 12
Smith, P.J. [356] 255
Smith, P.J. [355] 255
Sollenberger, N.R. [150] . . 13, 95, 97, 99, 191, 202
Sollenberger, N.R. [361] 259, 297
Sollenberger, N.R. [99] 10, 11
Sollenberger, N.R. [148] 13
Sollenberger, N.R. [127] 14, 16
Sollenberger, N.R. [149] . . . 13, 191, 193, 201
Sollenberger, N.R. [129] 14, 16
Sollenberger, N.R. [86] 9, 11, 14
Somerville, F.C.A. [105] 11
Somerville, F.C.A. [6] 3, 168, 170
Song, I. [288] 216, 217
Sourour, E.A. [270] 216
Sousa, E.S. [263] 211, 214–217, 353
Sousa, E.S. [311] 216, 217
Sousa, E.S. [280] 216
Sousa, E.S. [298] 216
Sousa, E.S. [277] 216
Speth, M. [131] 14, 16
Steele, R. [3] 3
Steele, R. [249] 206, 231, 239, 260
Steele, R. [335] 244
Steele, R. [206] 145
Steinbauer, M. [354] 255
Steiner, B. [302] 216
Stette, G. [275] 216
Stirling, W.C. [109] 11, 279, 317, 318
Stoger, M. [166] 16
Streit, J. [7] 3, 145, 202, 356
Stüber, G.L. [113] 12
Stüber, G.L. [102] 10, 11
Stüber, G.L. [196] 94, 95
Su, Y.T. [101] 10, 11
Svensson, A. [81] 9, 11

T

Tafazolli, R. [455] 339, 340
Tarokh, V. [285] 216
Tarokh, V. [349] 245
Tarokh, V. [347] 245
Tassiulas, L. [141] 15
Tellambura, C. [189] 64, 65
ten Brink, S. [176] 17, 262, 263, 301, 311, 355
Teukolshy, S.A. [108] 11, 95
Teukolsky, S.A. [320] 238
Thitimajshima, P. [223] 164, 170
Thitimajshima, P. [415] 320
Thoen, S. [146] 15, 16
Thoma, R.S. [354] 255
Thomas Schlosser, [452] 339, 340
Thomas, T.A. [116] 12, 304
Thompson, J.S. [330] 243
Thompson, J.S. [248] 206, 243
Thompson, J.S. [132] 14, 16
Toeltsch, M. [354] 255
Torrance, J.M. [211] 145, 149
Torrance, J.M. [222] 153
Torrance, J.M. [218] 146, 152, 156
Torrance, J.M. [192] 71

Torrance, J.M. [212] 145, 149
Toskala, A. [190] 65
Toskala, A. [375] 297
Tozer, T.C. [209] 145
Tranter, W.H. [356] 255
Tseng, S-M. [292] 216
Tu, J.C. [162] 16
Tu, J.C. [161] 16
Tufts, D.W. [423] 333
Tufvesson, F. [107] 11
Tufvesson, F. [88] 9, 11
Tufvesson, F. [83] 9, 11
Tzou, C-K. [407] 314

U

Ue, T. [219] 147
Ungerboeck, G. [338] 244

V

van Bladel, M. [62] 8, 53, 211
van de Beek, J-J. [69] 8, 116, 117
van de Beek, J.-J. [79] 9, 11
Van de Wiel, O. [281] 216
van den Beek, J. [80] 9, 11
Van Der Perre, L. [146] 15, 16
Van Der Perre, L. [136] 14–16
Van der Perre, L. [130] 14
Van der Perre, L. [156] 16
van der Perre, L. [29] 6, 331
Van Eetvelt, P. [262] 210
van Eetvelt, P.W.J. [48] 7, 45
van Nee, R. [173] 16
van Nee, R. [134] 14, 16
van Nee, R. [28] 6
van Nee, R. [133] 14, 16
van Nee, R. [135] 14, 16
van Nee, R. [142] 15, 16
van Zelst, A. [134] 14, 16
van Zelst, A. [133] 14, 16
van Zelst, A. [135] 14, 16
van Zelst, A. [142] 15, 16
Vandenameele, P. [29] 6, 331
Vandenameele, P. [130] 14
Vandenameele, P. [136] 14–16
Vandenameele, P. [156] 16
Vandendorpe, L. [281] 216
Vandendorpe, L. [299] 216
Vandendorpe, L. [264] 211, 216, 217, 353
Varanasi, M.K. [373] 269, 271
Verdú, S. [246] 206
Verdú, S. [321] 242, 243, 303, 304
Verdu, S. [154] 16
Vetterling, W.T. [320] 238
Vetterling, W.T. [108] 11, 95
Viterbi, A.J. [237] 205, 207
Viterbi, A.J. [256] 207
Viterbi, A.J. [244] 206
Viterbi, A.M. [256] 207
Vook, F.W. [116] 12, 304
Vook, F.W. [124] . . 14, 16, 191, 193, 198, 200
Vucetic, B. [325] 243
Vucetic, B. [336] 244
Vucetic, B.S. [326] 243

W

Wang, X. [98] 10, 11
Wang, X. [125] 14, 16
Wang, X. [96] 10, 11
Wang, X.F. [453] 339, 340
Warner, W.D. [64] 8, 116
Watanabe, M. [220] 147
Weaver, L.A. Jr [244] 206
Webb, W. [180] 26
Webb, W.T. [3] 3
Webb, W.T. [177] . . 21, 24, 30, 32, 38, 41, 42, 148, 153, 164, 170, 176
Webb, W.T. [335] 244
Webb, W.T. [206] 145
Webb, W.T. [2] 1, 3, 93, 95, 99, 206, 209, 231, 232, 245–249
Weinstein, S.B. [9] . . . 5–7, 21, 29, 32, 37, 209
Welti, A.L. [253] 206
Wesel, R.D. [122] 12
Wheatley, C.E. III [244] 206
Wilkinson, T.A. [49] 7, 45, 210
Willet, P.K. [367] 263, 311
Willink, T.J. [230] 186
Wilson, S.K. [79] 9, 11
Wilson, S.K. [80] 9, 11
Wilson, S.K. [78] 9, 11
Win, M.Z. [353] 255
Winters, J.H. [441] 334
Winters, J.H. [353] 255
Winters, J.H. [351] 253, 254
Wittke, P.H. [230] 186
Wolfgang, A. [460] 339
Wolfgang, A. [464] 340
Wong, C. [344] 245
Wong, C. [345] 245
Wong, C.H. [215]145, 146, 148, 202, 243, 356

Wong, K-K. [126] 14, 16
Wong, P.P. [448] 339
Wong, T-F. [290] 216
Woodard, J.P. [105] 11
Woodard, J.P. [6] 3, 168, 170
Woodard, J.P. [226] 168
Woodward, G. [326] 243
Wu, Y. [396] 305, 317
Wu-Sheng Lu, [435] 333
Wulich, D. [286] 216
Wulich, D. [276] 216
Wulich, D. [54] 7, 46
Wulich, D. [50] 7, 45
Wyatt–Millington, C.W. [48] 7, 45

X

Xavier, J.M.F. [377] 304, 307
Xiaofeng Wang, [435] 333
Xie, Y. [117] 12

Y

Yamashita, M. [89] 9, 11
Yang, B. [92] 10, 11
Yang, B. [103] 11
Yang, B. [97] 10, 11
Yang, L-L. [323] 242, 243, 304, 305, 313–317, 319–321, 327
Yang, L-L. [444] 339, 341
Yang, L-L. [271] 216, 217
Yang, L-L. [272] 216, 217
Yang, L-L. [268] 216
Yang, L-L. [269] 216
Yang, L.L. [300] 216, 217, 353
Yao, K. [424] 333
Yeap, B.L. [216] 145, 146, 148, 202, 254, 257, 279, 297, 320
Yeap, B.L. [358] 257
Yee, M. [346] 245
Yee, M.S. [215] . 145, 146, 148, 202, 243, 356
Yee, N. [296] 216, 217
Yee, N. [70] . . 8, 205, 211, 212, 214–217, 236, 239, 240, 353
Yee, N. [267] 212, 214, 242
Yeh, C.C. [427] 333
Yeh, C.C. [429] 333
Yeh, C.C. [430] 333
Yen, K. [323] . . . 242, 243, 304, 305, 313–317, 319–321, 327
Yen, K. [458] 339, 340
Yen, K. [457] 339, 340
Yen, K. [444] 339, 341
Yen, K. [459] 339, 340
Yinggang Du, [461] 339, 340
Yip, K.W. [303] 216
Yoon, Y.C. [243] 206
Yoshida, S. [143] 15, 16
Youn, D-H. [287] 216
Yue, O.C. [241] 205

Z

Zehavi, E. [256] 207
Zeisberg, S. [169] 16, 58
Zhou, S. [95] 10, 11
Zhu, X. [139] 15, 16
Ziemer, R.E. [313] . . . 219–221, 223, 224, 226
Zimmermann, M.S. [22] 6, 21
Zimmermann, M.S. [8] 5, 6, 21
Zollinger, E. [253] 206
Zvonar, Z. [328] 243